

Petrogenesis of the Mesoproterozoic anorthosite, syenite
and carbonatite suites of NW Namibia and their
contribution to the metasomatic formation of the
Swartbooisdrif sodalite deposits

*Dissertation zur Erlangung des
naturwissenschaftlichen Doktorgrades
der Bayerischen Julius-Maximilians-Universität Würzburg*

vorgelegt von

Kirsten Drüppel

aus Würzburg

Würzburg 2003

Eingereicht am:

1. Gutachter:
 2. Gutachter:
- der Dissertation

1. Prüfer:
 2. Prüfer:
- der mündlichen Prüfung

Tag der mündlichen Prüfung:
Doktorurkunde ausgehändigt am:

Drüppel, K. (2003): Petrogenesis of the Mesoproterozoic anorthosite, syenite and carbonatite suites of NW Namibia and their contribution to the metasomatic formation of the Swartbooisdrif sodalite deposits. Dr. rer. nat. thesis, University of Würzburg, 345 + 199 pp., 140 Figs., 24 Tables in the text, 4 Plates.

NATUR IST MAßLOS

(FRITZ MAUTHNER, 1901)

TABLE OF CONTENTS

ZUSAMMENFASSUNG	7
ABSTRACT	12
ACKNOWLEDGEMENTS.....	15
1 INTRODUCTION.....	17
1.1 LOCATION OF THE STUDY AREA.....	17
1.2 GEOLOGICAL FRAMEWORK	17
1.2.1 <i>The metamorphic Epupa Complex</i>	17
1.2.2 <i>The anorthositic Kunene Intrusive Complex</i>	18
1.2.3 <i>The syenite-carbonatite-lamprophyre suites of Swartbooisdrif and Epembe</i>	21
1.3 AVAILABLE GEOCHRONOLOGICAL DATA	22
1.4 PREVIOUS WORK ON THE MAGMATIC ROCKS OF NW NAMIBIA AND SW ANGOLA	24
1.5 METHODS OF INVESTIGATION.....	26
1.6 AIMS OF THE STUDY	26
PART I: THE GEOLOGY OF THE SODALITE MINING AREA AT SWARTBOOISDRIF.....	29
2 PHYSIOGRAPHY OF THE AREA MAPPED.....	29
2.1 LOCATION OF THE AREA MAPPED	29
2.2 GEOGRAPHIC AND GEOMORPHOLOGIC OVERVIEW	29
2.3 EXPLORATION HISTORY.....	31
3 GEOLOGY OF THE AREA MAPPED.....	32
3.1 GEOLOGICAL OVERVIEW	32
3.2 ROCK EXPOSURE	34
3.3 FIELD OBSERVATIONS.....	35
3.3.1 <i>The white anorthosite suite [A,w]</i>	35
3.3.2 <i>The dark anorthosite suite</i>	36
3.3.2.1 Anorthosites and leucogabbronorites [A,m]	36
3.3.2.2 Leucotroctolites [T,m].....	37
3.3.2.3 Brecciated anorthosites [A,b].....	38
3.3.3 <i>Ilmenite-magnetite ore [IM]</i>	38
3.3.4 <i>Syenites [S,a] and [S,f]</i>	40
3.3.5 <i>Nepheline Syenite [S,ne]</i>	42
3.3.6 <i>Carbonatites and associated rock types</i>	44
3.3.6.1 Carbonatitic breccia.....	44
3.3.6.1.1 Layered carbonatitic breccia [CB,l]	44
3.3.6.1.2 Sodalite-rich carbonatitic breccia [CB,so]	46
3.3.6.1.3 Massive carbonatitic breccia [CB,m]	52
3.3.6.2 K-feldspar-biotite-ilmenite-calcite rock.....	54
3.3.6.3 Ferrocarbonatite	55
3.3.7 <i>Dolerite [Dol]</i>	56
3.3.8 <i>Trachyte [Tr] and Andesite [An]</i>	56

3.3.9 <i>Sedimentary rocks</i>	57
3.3.9.1 Unconsolidated deposits of fluvial terraces [Qtz,p].....	57
3.3.9.2 Carbonate-cemented deposits of fluvial terraces [Cgl].....	58
3.3.9.3 River floor deposits [All]	58
3.3.9.4 Anorthositic talus deposits	59
3.3.9.5 Mining waste piles	59
3.4 ECONOMIC POTENTIAL	60
3.4.1 <i>Sodalite deposits</i>	60
3.4.2 <i>Leucotroctolites</i>	61
3.5 TECTONICS.....	62
3.5.1 <i>Tectonic overview</i>	62
3.5.1.1 The anorthosite problem	62
3.5.1.2 The structural setting of carbonatites	63
3.5.2 <i>Structural investigations of the mapped sheet and related areas</i>	64
3.5.2.1 The Zebra Mountain massif	64
3.5.2.2 The cogenetic syenite intrusions	69
3.5.2.3 The carbonatite dyke swarms.....	70
3.5.2.4 Dolerites	74
3.5.3 <i>Fault system</i>	75
PART II: PETROGENESIS AND EVOLUTION OF THE KUNENE INTRUSIVE COMPLEX AND THE SPATIALLY ASSOCIATED FELSIC SUITE	77
4 GENERAL REMARKS	77
5 PETROGRAPHY.....	79
5.1 PETROGRAPHY OF THE ANORTHOSITIC ROCK SUITE.....	79
5.1.1 <i>Igneous textures</i>	79
5.1.1.1 White anorthosite suite.....	79
5.1.1.2 Dark anorthosite suite	82
5.1.1.2.1 Pyroxene-bearing anorthosite and leucogabbronorite.....	83
5.1.1.2.2 Olivine-bearing anorthosite and leucotroctolite.....	85
5.1.2 <i>Structures of subsolidus origin</i>	88
5.1.2.1 Type I corona	88
5.1.2.2 Type II corona	89
5.1.2.3 Ilmenite-magnetite-orthopyroxene symplectites.....	91
5.2 PETROGRAPHY OF THE FELSIC ROCK SUITE.....	95
5.2.1 <i>Granite and quartz-syenite</i>	96
5.2.2 <i>Syenite</i>	98
6 MINERAL CHEMISTRY.....	102
6.1 FELDSPAR	102
6.1.1 <i>Anorthositic suite</i>	102
6.1.2 <i>Felsic suite</i>	104
6.2 OLIVINE	106
6.3 PYROXENE	107
6.3.1 <i>Orthopyroxene</i>	108
6.3.2 <i>Clinopyroxene</i>	111
6.4 AMPHIBOLE.....	111
6.5 BIOTITE.....	113

6.6 TITANITE	115
6.7 FE-TI OXIDES	115
6.7.1 <i>Ilmenite</i>	116
6.7.2 <i>Magnetite</i>	116
6.7.3 <i>Hematite</i>	117
6.8 GARNET	117
6.9 EPIDOTE	119
6.10 CHLORITE.....	119
6.11 COMPARATIVE APPROACH.....	120
7 GEOCHEMISTRY	122
7.1 MAJOR AND TRACE ELEMENT GEOCHEMISTRY	122
7.1.1 <i>Anorthositic suite</i>	122
7.1.2 <i>Felsic suite</i>	128
7.2 REE GEOCHEMISTRY.....	131
8 OXYGEN ISOTOPE CONSTRAINTS.....	135
8.1 ANORTHOSITIC SUITE	135
8.2 FELSIC SUITE	137
9 PRESSURE-TEMPERATURE CONDITIONS.....	140
9.1 THERMOBAROMETRY OF THE ANORTHOSITIC ROCKS.....	140
9.1.1 <i>Magmatic textures</i>	140
9.1.2 <i>Coronitic mineral assemblages</i>	142
9.1.3 <i>Symplectitic mineral assemblages</i>	148
9.2 THERMOBAROMETRY OF THE SYENITIC SUITE	148
9.3 P-T EVOLUTION OF THE KUNENE INTRUSIVE COMPLEX AND THE TEMPORALLY ASSOCIATED FELSIC SUITE.....	152
10 DISCUSSION	157
10.1 CONSTRAINTS ON THE SOURCE AND EVOLUTION OF THE ANORTHOSITIC AND SYENITIC MELTS	157
10.2 PETROGENETIC MODEL.....	160
11 COMPARISON WITH OTHER PARTS OF THE KIC.....	164
PART III: FENITIZING PROCESSES INDUCED BY FERROCARBONATITE MAGMATISM.....	165
12 INTRODUCTION.....	165
12.1 CARBONATITES AND FENITIZATION	165
12.2 SODALITE - A REVIEW	166
13 PETROGRAPHY.....	171
13.1 FENITIZED ANORTHOSITE	171
13.2 FENITIZED SYENITE	177
13.3 FENITIZED NEPHELINE SYENITE	179
13.4 FENITIZED ULTRAMAFIC XENOLITHS	182
13.5 CARBONATITIC BRECCIA	183
13.5.1 <i>Massive carbonatitic breccia</i>	184
13.5.2 <i>Layered carbonatitic breccia</i>	186
13.5.3 <i>Sodalite-rich carbonatitic breccia</i>	186

13.5.3.1 REE-poor samples.....	186
13.5.3.2 REE-rich samples.....	192
13.5.4 <i>Crystallization sequence of the carbonatitic breccia</i>	194
13.6 FERROCARBONATITE VEINS.....	195
13.7 K-FELDSPAR-BIOTITE-ILMENITE-CALCITE ROCK	197
14 MINERAL CHEMISTRY.....	198
14.1 CARBONATE MINERALS.....	198
14.1.1 <i>Ankerite-dolomite solid solution</i>	198
14.1.2 <i>Calcite</i>	204
14.1.3 <i>Siderite-magnesite solid solution</i>	206
14.1.3 <i>Carbocernaite</i>	207
14.1.4 <i>Strontianite</i>	208
14.2 FELDSPAR	208
14.2.1 <i>Potassium feldspar</i>	208
14.2.2 <i>Plagioclase</i>	209
14.3 NEPHELINE.....	211
14.4 SODALITE.....	212
14.5 CANCRINITE GROUP	215
14.6 ANALCITE	216
14.7 AEGIRINE	217
14.8 AMPHIBOLE.....	218
14.9 WHITE MICA.....	219
14.10 BIOTITE.....	221
14.11 APATITE.....	227
14.12 PYROCHLORE	229
14.13 FE-TI OXIDES.....	230
14.13.1 <i>Ilmenite</i>	230
14.13.2 <i>Magnetite</i>	231
14.13.3 <i>Hematite</i>	232
14.13.4 <i>Rutile</i>	232
14.14 SULPHIDES	233
14.14.1 <i>Pyrite</i>	233
14.14.2 <i>Chalcopyrite</i>	235
14.14.3 <i>Pyrrhotite</i>	235
14.14.4 <i>Pentlandite</i>	236
14.14.5 <i>Bornite</i>	236
14.14.6 <i>Chalcocite-digenite</i>	236
14.14.7 <i>Millerite</i>	237
14.14.8 <i>Siegenite</i>	239
14.14.9 <i>Violarite-polydymite</i>	239
14.14.10 <i>Fletcherite</i>	241
14.15 BARITE.....	242
14.16 UNSPECIFIED NA-AL PHASE	242
14.17 TRACE AND RARE EARTH ELEMENT CHEMISTRY OF SELECTED MINERALS – A COMBINED LA-ICPMS – SRXRF STUDY	245
14.17.1 <i>Carbonates</i>	245
14.17.2 <i>Sodalite</i>	248
14.17.3 <i>Biotite</i>	249
14.17.4 <i>Apatite</i>	249
14.17.5 <i>Pyrochlore</i>	252

15 GEOCHEMISTRY	255
15.1 MAJOR AND TRACE ELEMENT GEOCHEMISTRY	255
15.1.1 Fenitized anorthosite.....	256
15.1.2 Fenitized syenite.....	259
15.1.3 Fenitized nepheline syenite	261
15.1.4 Carbonatites	262
15.1.4.1 Carbonatitic breccia.....	262
15.1.4.2 Ferrocarbonatite veins	267
15.2 RARE EARTH ELEMENT GEOCHEMISTRY	268
15.3 DISCUSSION AND INTERPRETATION OF THE CARBONATITE EVOLUTION	271
15.4 COMPARISON WITH THE LUPONGOLA CARBONATITES	272
16 MASS BALANCE CALCULATIONS.....	273
16.1 THE GRESENS APPROACH	273
16.2 MASS CHANGE CALCULATIONS FOR THE FENITIZATION OF ANORTHOSITES AND SYENITES.....	274
16.3 ORIGIN AND NATURE OF THE FENITIZING SOLUTIONS	279
17 FLUID INCLUSION STUDIES.....	282
17.1 MICROTHERMOMETRIC STUDIES.....	282
17.1.1 H ₂ O-rich inclusions.....	283
17.1.1.1 Fluid inclusions in sodalite.....	283
17.1.1.2 Fluid inclusions in carbonate.....	285
17.1.1.3 Fluid inclusions in quartz	286
17.1.2 CO ₂ -rich inclusions	287
17.1.3 Discussion and interpretation	288
17.2 HIGH-RESOLUTION SYNCHROTRON MICRO-XRF ANALYSIS.....	290
17.3 IMPLICATIONS FOR THE EVOLUTION OF THE FENITIZING FLUIDS	293
18 STABLE ISOTOPE COMPOSITION.....	295
18.1 OXYGEN AND CARBON ISOTOPIC COMPOSITION	295
18.1.1 Oxygen isotopic composition of anorthositic rocks	295
18.1.2 Oxygen isotopic composition of fenitized syenites and nepheline syenites.....	296
18.1.3 Oxygen and carbon isotopic compositions of the carbonatitic breccia and the ferrocyanatite veins	297
18.2 SULPHUR ISOTOPIC COMPOSITION.....	300
19 P-T EVOLUTION OF THE CARBONATITIC MELTS AND FLUIDS.....	304
19.1 EMPLACEMENT AND CRYSTALLIZATION OF THE CARBONATITES	304
19.2.1 Biotite-apatite thermometry and HF barometry	305
19.2.2 Calcite-dolomite thermometry.....	309
19.1.3 Ankerite-magnetite oxygen isotope equilibria.....	309
19.1.4 Pyrite-chalcopyrite sulphur isotope equilibria	311
19.1.5 Stability relations of Co-Ni-Fe sulphides.....	311
19.2 EMPLACEMENT AND FENITIZATION OF THE NEPHELINE SYENITE	314
19.3 FENITIZATION OF ANORTHOSITIC XENOLITHS AND SYENITES– IMPLICATIONS FROM FLUID-INCLUSION ISOCHORE DATA.....	316
20 CONCLUSIONS.....	319
20.1 ORIGIN AND EVOLUTION OF THE SWARTBOOISDRIF CARBONATITES.....	319
20.2 THE BREAKDOWN OF IGNEOUS MINERALS DURING FENITIZATION.....	322
20.3 LINKS TO OTHER CARBONATITE COMPLEXES OF NW NAMIBIA AND SW ANGOLA.....	323
20.4 CONCLUDING REMARKS	324

21 REFERENCES..... 325

ZUSAMMENFASSUNG

Die mesoproterozoische Entwicklung Namibias ist durch wiederholte magmatische Aktivität gekennzeichnet, welche zur Intrusion verschiedener Gesteinsschmelzen führte. Zunächst erfolgte die Platznahme der anorthositischen Magmen des Kunene-Intrusiv-Komplexes (KIK), der mit einer Fläche von etwa 18000 km² das vermutlich größte Anorthosit-Massiv der Welt darstellt. Die Intrusion der anorthositischen Magmen erfolgte vor etwa 1385-1347 Ma innerhalb der amphibolit- bis granulitfaziell metamorphen Gesteine des paläo- bis meso-proterozoischen Epupa-Komplexes am Südwestrand des Kongo-Kratons. Der KIK, ein typischer *massif-type* Anorthosit-Komplex, ist in Form einer N-S ausgerichteten Intrusion über 300 km Länge und 30-80 km Breite im Südwesten Angolas und untergeordnet im Nordwesten Namibias aufgeschlossen. Er kann grob in zwei Haupteinheiten unterteilt werden, die durch einen Gürtel granitischer Intrusionen (1400-1300 Ma) getrennt sind: (1) Ein Grossteil des angolischen KIK zeigt eine ausgeprägte N-S Orientierung und setzt sich überwiegend aus schwach alterierten, dunkel gefärbten Anorthositen, Leukogabbros und Leukotroktolithen zusammen. (2) Dagegen zeigt der südliche Teil des KIK, inklusive des namibischen Teiles, eine deutliche E-W Orientierung. In dieser Region dominiert eine ältere, vollständig alterierte und weiß gefärbte Anorthosit-Varietät, der sogenannte weiße Anorthosit. Dieser wurde entlang von etwa E-W-streichenden, extensionsgebundenen Störungen von einer zweiten Anorthosit-Generation durchschlagen, die heute in Form von E-W-streichenden Höhenrücken aus den Ebenen von weißem Anorthosit herauspräpariert ist. Dieser kogenetisch entstandene Anorthosit-Typ entspricht in seinem Auftreten und seiner Mineralogie den Anorthositen der nördlichen Einheit und wird aufgrund seiner dunkelgrauen bis schwarzen Färbung als dunkler Anorthosit bezeichnet. Der Anorthosit-Komplex wurde nahe seiner südöstlichen Begrenzung, im Bereich der Siedlung Swartbooisdrif, von zahlreichen extensionsgebundenen Störungen und Scherzonen durchschlagen. In diese SE-NW und untergeordnet ENE-WSW streichenden Schwächezonen intrudierten Quarz-Syenite und Syenite, die ein Alter von etwa 1380-1340 Ma aufweisen, sowie jüngere ankeritische Karbonatite (ca. 1140-1120 Ma) und Nephelin-Syenite. Metasomatische Wechselwirkungen zwischen Fluiden der karbonatitischen Schmelzen und intensiv zerscherten Syeniten sowie Anorthositen führten innerhalb der Störungen zur Bildung ökonomisch bedeutsamer Sodalith-Vorkommen, die auf ein Areal von etwa 100 km², im Bereich der Siedlung Swartbooisdrif, begrenzt sind.

Ziel der mineralogisch-petrologisch-geochemischen Untersuchungen war eine vielfältige und vergleichende Analytik möglichst vieler Proben unterschiedlicher Lithologie. Diese wurden sowohl an den Anorthositen und Syeniten als auch an den jüngeren Karbonatiten und Nephelin-Syeniten durchgeführt und umfassten die petrographische Bearbeitung von Dünnschliff-Präparaten und deren detaillierte Mikrosonden-analytische Bearbeitung, geochemische Untersuchung der Gesamtgestein-Haupt- und Spurenelement-Analytik und der Gesamtgestein-Seltenerdelement-Analytik ausgesuchter Proben, mikrothermometrische Untersuchungen sowie Synchrotron-XRF-Untersuchungen von Fluid-Einschlüssen, Laser-ICPMS und Synchrotron-XRF Analysen der Spurenelement-Gehalte ausgesuchter Minerale sowie O-, C- und S-Isotopenanalytik. Hierdurch sollte eine umfassende Vorstellung über die genetische und zeitliche Stellung der verschiedenen Gesteinstypen und insbesondere über die mineralbildenden Vorgänge gewonnen werden, die zur Abscheidung der metasomatisch gebildeten Mineralparagenesen geführt haben.

Die Anorthosite des KIK und die assoziierten felsischen Gesteinseinheiten: Für den weißen und den dunklen Anorthosit konnten anhand der Feldbefunde, des Mineralbestandes und Mineralchemismus, des Gefüges sowie des Gesamtgesteinschemismus zwei zeitlich getrennte aber kogenetische magmatische Ereignisse charakterisiert werden. Die typische primär-magmatische Mineralogie in den Gesteinen des KIK umfasst: Plagioklas (weißer Anorthosit: An_{37-53} ; dunkler Anorthosit: An_{43-75}) \pm Olivin \pm Orthopyroxen \pm Klinopyroxen + Fe-Ti-Oxide + Apatit \pm Zirkon. Spätmagmatische Säume von Amphibol (meist Magnesio-Hastingsit/Pargasit) und Biotit umgeben die Pyroxene und Ilmenit. Weiße Anorthosite sind im Gegensatz zu den dunklen Anorthositen durch eine durchgreifende Sericitisierung, Saussuritisierung und Albitisierung der Plagioklase und Alteration der Fe-Mg Silikate charakterisiert. Geothermometrische Untersuchungen ergaben Temperaturen von 985-950°C für die spätmagmatische Kristallisation von Amphibol. Merkmale einer Reequilibrierung der Anorthosite unter granulit- bis amphibolitfaziellen Bedingungen sind in Leukotroktolithen zugegen. In diesen Gesteinen werden magmatische Olivine durch Orthopyroxen-Granat-Amphibol-Koronen und Ilmenite durch Biotit-Granat-Koronen umgeben. Anhand geothermobarometrischer Untersuchungen wurden Bedingungen von $760 \pm 100^\circ\text{C}$ und 7.3 ± 1 kbar für die Bildung der Koronen ermittelt, welche sich unter annähernd isobarer Abkühlung bis zu Temperaturen von 680-630°C und 6.2 ± 0.4 kbar fortsetzte. In Kombination mit den Kristallisationsbedingungen der spätmagmatischen Amphibole resultiert für die Anorthosite ein P-T-Pfad der annähernd isobaren Abkühlung unter amphibolit- bis granulit-faziellen Bedingungen.

In den zeitgleich intrudierten Quarz-Syeniten und Syeniten kristallisierten zunächst K-Feldspat, Plagioklas und Klinopyroxen und/oder Hastingsit, gefolgt von einer zweiten Generation von K-Feldspat, spät-magmatischem Hastingsit und Fe-Ti-Oxiden. Letztere werden vereinzelt durch schmale Titanit-Säume umgeben. In Folge einer Subsolidus-Reequilibrierung der Syenite wurde Hastingsit partiell durch Hastingsit-Ilmenit-Magnetit-Plagioklas-Symplektite ersetzt. Die magmatische Kristallisation von K-Feldspat fand unter Temperaturbedingungen von 890-790°C statt, welche vermutlich nahe des Liquidus der syenitischen Schmelzen liegen. Für die spät-magmatische Kristallisation von Hastingsit wurden Drucke von 6.5 ± 0.6 kbar ermittelt, welche gut mit den für die Anorthosite kalkulierten Drucken übereinstimmen. Die späte Bildung von Ilmenit-Magnetit-Plagioklas-Symplektiten erfolgte unter ähnlichen Druckbedingungen (6.6-6.9 kbar), welche auf eine annähernd isobare Abkühlung der Syenite hinweisen.

Mit dem Ziel, die Natur der Magmenquelle der Anorthosite und Syenite zu charakterisieren und die Frage zu klären, ob Syenite und Anorthosite eventuell aus einem gemeinsamen Stamm-Magma hervorgegangen sind, wurden geochemische Untersuchungen durchgeführt, sowie die Sauerstoff-Isotopie von Feldspat-Separaten bestimmt. Die Ergebnisse dieser Untersuchungen belegen, dass es die Stamm-Magmen der Anorthosite des KIK stark fraktionierte, basaltische Magmen darstellen. Die gewonnenen Sauerstoff-Isotopendaten für Plagioklas ($5.61-6.13 \text{ ‰ } \delta^{18}\text{O}$) legen zudem nahe, dass es sich hierbei um Schmelzen handelt, die durch partielle Aufschmelzung des Mantels entstanden sind. Ähnliche Werte wurden für Plagioklas-Separate aus Proben des durchgreifend alterierten weißen Anorthosits ermittelt ($5.35-6.14\text{‰}$). Die gute Übereinstimmung der $\delta^{18}\text{O}_{\text{SMOW}}$ -Werte von Plagioklasen weißer und dunkler Anorthosite lässt darauf schließen, dass es sich bei den Fluiden, die zur Überprägung des weißen Anorthosits führten, um magmatische Fluide anorthositischer Schmelzen handelte. Petrographische und geochemische Untersuchungen bestätigen, dass nahezu alle Anorthosite im Zuge ihres Aufstiegs eine variable Kontamination durch krustales Material erfuhren, die sich am stärksten auf die früh intrudierten Anorthosit-Magmen auswirkte. Die für die Syenite ermittelten Ergebnisse belegen eindeutig, dass es sich

bei Anorthositen und Syeniten um chemisch unabhängige Systeme handelt, da (1) chemische Kontinuität zwischen Anorthositen und Syeniten nicht beobachtet wurde, (2) die Spurenelementgehalte der felsischen Gesteine auf eine krustale oder zumindest eine gemischte Kruste-Mantel-Quelle hindeuten, (3) Chondritnormierte Seltenerd-Element-Muster der Syenite keine negative Eu-Anomalie aufweisen, wie sie von Fraktionierungsprodukten von Schmelzen, welche zuvor in großen Mengen Plagioklas kristallisierten, erwartet werden könnte und (4) die $\delta^{18}\text{O}_{\text{SMOW}}$ -Werte von magmatisch kristallisiertem Feldspat der Syenite mit 7.20-7.92 ‰ etwa 1.6 ‰ höher liegen als die der magmatisch gebildeten Plagioklase der Anorthosite. Dementsprechend sind die Anorthosite und Syenite zwar zeitgleich intrudiert, eine Entwicklung aus nur einem Stamm-Magma kann jedoch eindeutig ausgeschlossen werden. Vielmehr liegt ihre enge räumliche und zeitliche Assoziation darin begründet, dass der Aufstieg und die Platznahme der Stamm-Magmen der Anorthosite zum partiellen Aufschmelzen der Unterkruste und somit zur Bildung potentieller Stamm-Magmen der Syenite führten.

Die Karbonatite von Swartbooisdrif: Im Verlauf eines weiteren, jüngeren magmatischen Ereignisses erfolgte vor etwa 1140-1120 Ma zunächst die Platznahme einer ersten Karbonatit-Generation, welche in erheblichem Maße durch fragmentiertes, anorthositisches und syenitisches Gesteinsmaterial kontaminiert ist und daher entsprechend ihres makroskopischen Erscheinungsbildes als karbonatitische Brekzie bezeichnet wird. Diese wird von zahlreichen jüngeren und geringmächtigen Ferrokarbonatit-Adern durchschlagen, die sich durch eine nur geringe Kontamination mit Nebengesteinsmaterial auszeichnen. Die gewonnenen Ergebnisse der mineralogisch-petrologisch-geochemischen Untersuchungen der Karbonatite belegen eindeutig, dass die Karbonatiten beider Generationen magmatische Kristallisationsprodukte fraktionierter Mantelschmelzen und nicht hydrothermal gebildete Gesteinseinheiten darstellen. Die Karbonatite treten als Gänge und Adern auf, welche die ältere Gesteinseinheiten durchschlagen. Syenite und Anorthosite haben im Kontakt zu den Karbonatiten eine metasomatische Überprägung erfahren; Nebengesteinsklasten sind in der Fliessrichtung der Karbonatite orientiert, zum Teil rotiert und werden von Karbonat-reichen Lagen umflossen. Diese Annahme wird durch die Mineralogie beider Karbonatit-Generationen, i.e. (1) Ankerit + Kalzit + Magnetit + Biotit ± Ilmenit ± Apatit ± Pyrochlor ± Sulfide in der Karbonat-Matrix der karbonatitischen Brekzie und (2) Ankerit + Kalzit + Magnetit ± Pyrochlor ± Rutil der jüngeren, nahezu Xenolith-freien Ferrokarbonatit-Adern, ihren geochemischen Signaturen sowie durch die Sauerstoff- und Kohlenstoff-Isotopie separierter Ankerite (8.91-9.73 ‰ $\delta^{18}\text{O}$ und -6.73 bis -6.98 ‰ $\delta^{13}\text{C}$) bestätigt, wobei allerdings die O-Isotopendaten eine schwache hydrothermale Alteration beider Karbonatit-Typen nahe legen. Die Karbonatite beider Generationen können somit als Kristallisationsprodukte stark fraktionierter Mantelschmelzen mit ferrokarbonatitischer Zusammensetzung charakterisiert werden. Das Auftreten von Biotit, Apatit, Ilmenit und Sulfiden in der karbonatitischen Brekzie deutet darauf hin, dass diese Schmelzen durch vergleichsweise hohe Gehalte an Si, Al, K, Ti, S und P gekennzeichnet waren, was über geochemische Untersuchungen bestätigt werden konnte. Dagegen wurden diese Minerale in den jüngeren Ferrokarbonatit-Adern nicht beobachtet, welche zudem vergleichsweise geringe Gehalte an Fe, Mg, Si, Al, Ti, K, S und P aufweisen. Diese Ergebnisse legen nahe, dass die Bildung der späten Ferrokarbonatite im Anschluss an die Kristallisation von Biotit, Apatit, Ankerit, Ilmenit, Magnetit und den Sulfiden erfolgte. Die jüngeren Ferrokarbonatite stellen somit die Fraktionierungsprodukte der für die Bildung der karbonatitischen Brekzie verantwortlichen Karbonatit-Magmen dar. Allerdings belegen die geochemischen Signaturen der karbonatitischen Brekzie, dass diese Fraktionierungs-Prozesse bereits vor

der Intrusion der älteren Karbonatit-Einheit aktiv waren. Im Gegensatz hierzu können extreme Sr- und SEE-Anreicherungen zweier Proben der karbonatitischen Brekzie nicht über extreme Fraktionierung der Karbonatit-Schmelzen abgeleitet werden. In diesen Proben werden magmatische Ankerit-Kristalle randlich durch das SEE-Karbonat Carbocernait ersetzt. Zudem füllen Baryt und Strontianit Zwickel zwischen einzelnen Ankerit-Körnern. Diese Mineral-Umwandlungen und Neubildungen resultieren aus einer hydrothermalen Überprägung der Gesteine durch späte, Sr- und LSEE-reiche karbonatitische Fluide.

Prozesse der Fenitisierung: Feldbefunde in der Region Swartbooisdrif deuten darauf hin, dass die Devolatisierung früh intrudierender karbonatitischer Magmen zur metasomatischen Überprägung intensiv gescherter Anorthosite und Syenite im Kontakt zu den Karbonatit-Gängen führte. Zudem wirkte sich diese Fenitisierung auch auf die in den Karbonatiten eingeschlossenen Nebengesteinsbruchstücke aus. Im Zuge dieses Ereignisses wurden insbesondere Plagioklas und K-Feldspat der Anorthosite und Syenite sowie Nephelin eines Nephelin-Syenites in Albit und/oder Sodalith umgewandelt. Unter Verwendung konventioneller Geothermometrie in Kombination mit den für Fluid-Einschlüsse kalkulierten Isochoren konnten die Druck- und Temperaturbedingungen sowohl der Platznahme der Karbonatite als auch der im Zuge der Fenitisierung initiierten mineralum- und -neubildenden Prozesse bestimmt werden. Hierbei wurden die Entwicklung sowie die Zusammensetzung der fenitisierenden Fluide aus der zeitlichen Abfolge der Mineral-Reaktionen abgeschätzt. Quantitative Daten wurden über mikrothermometrische Untersuchungen und Synchrotron-XRF-Analysen von Fluid-Einschlüssen gewonnen, die in verschiedenen, metasomatisch neugebildeten und überprägten Mineralen eingeschlossen sind. Die hierbei gewonnenen Ergebnisse lassen folgende Rückschlüsse zu: (1) Im Zuge eines frühen metasomatischen Ereignisses erfolgte die Umbildung von Plagioklas der Anorthosite und K-Feldspat der Syenite in nahezu reinen Albit. Zeitgleich wurden wasserfreie Fe-Mg-Silikate der Anorthosite und Syenite in Biotit umgewandelt. Wie textuelle Beobachtungen belegen, fanden diese Prozesse bereits vor der Intrusion der Karbonatit-Magmen statt. Die metasomatischen Reaktionen implizieren, dass es sich bei den verantwortlichen Fluiden um Na-reiche, wässrige Lösungen handelte. (2) Im Anschluss an die Platznahme der karbonatitischen Brekzie in ca. 12-15 km Tiefe (4-5 kbar), erfolgte die Kristallisation von Apatit und Biotit über ein Temperaturintervall von 1200-630°C. Etwa zeitgleich kristallisierten die wasserfreien Minerale Ankerit und Magnetit, was eine erneute Wassersättigung des Karbonatit-Magmas zur Folge hatte. Unter Temperaturen von 800-530°C bewirkte die Zirkulation NaCl-reicher wässriger Fluide (19-30 Gew.% NaCl äquivalent) die Umwandlung von Albit der eingeschlossenen Nebengesteinsbruchstücke in Sodalith. Unter ähnlichen Temperaturen (ca. 775-700°C) wurde Nephelin eines angrenzenden Nephelin-Syenites zu Sodalith-Muskovit-Paragenesen abgebaut. Wie SRXRF-Analysen belegen, enthielten die fenitisierenden Fluide zudem geringe Konzentrationen an Sr, Ba, Fe, Nb und SEE. Ein großer Teil des in den Fluiden enthaltenen Natriums wurde während dieser Ereignisse aufgebraucht. Dementsprechend weisen sekundäre Fluid-Einschlüsse eines benachbarten Quarz-Syenit Ganges geringere Salinitäten (9-24 Gew.% NaCl äquivalent) und zugleich höhere Gehalte an K, Ca, Fe, Ti, Sr und Ba auf. Die hohen modalen Anteile an dem auf Kosten von Plagioklas neugebildeten Sodalith in der karbonatitischen Brekzie legen nahe, dass das Karbonatit-Magma vor der Fenitisierung erhebliche Gehalte an Natrium enthielt. Im Gegensatz zur karbonatitischen Brekzie konnten jedoch im Kontakt zu den jüngeren Ferrokarbonatit-Adern keine Fenit-Aureolen beobachtet werden; die Schmelzen scheinen dementsprechend ein nur geringes metasomatisches Potential besessen zu haben. (3) Während eines späten Stadiums der Fenitisierung bildeten sich Cancrinit und Muskovit auf Kosten von Albit der im Karbonatit eingeschlossenen Nebengesteinsbruchstücke. Es kann daher davon ausgegangen werden, dass es sich bei den fenitisierenden Fluiden noch immer um wässrige Lösungen handelte, die jedoch nicht

mehr ausreichend Natrium enthielten, um Sodalith zu bilden. Die Si-freie Zusammensetzung einer bislang unbekanntes Na-Al-Phase, welche sich später auf Kosten von Sodalith bildete, legt zudem nahe, dass auch späte fenitische Fluide stark Si-untersättigt waren.

Die vorliegende Arbeit zeigt, dass die Bildung der Ferrokarbonatite sowie die von ihnen verursachte Kontakt-Metasomatose das Resultat zahlreicher, miteinander eng verknüpfter magmatischer und metasomatischer Prozesse ist. Nahezu jeder dieser Prozesse kann mit spezifischen Mineralum- und -neubildenden Vorgängen in Zusammenhang gebracht werden, die letztendlich zur Überprägung der Anorthosite und Syenite zu Albit- und Sodalith-reichen Feniten führte.

ABSTRACT

During the Mesoproterozoic large volumes of magma were repeatedly emplaced within the Palaeoproterozoic basement of north-west Namibia. Magmatic activity started with the intrusion of the anorthositic rocks of the Kunene Intrusive Complex at 1,385-1,347 Ma which, with a total surface area of 18,000 km², is one of the largest anorthosite bodies of the world. At its south-eastern margin the Kunene Intrusive Complex was subsequently invaded by Mesoproterozoic quartz-syenite and syenite dykes (1,380-1,340 Ma) as well as by younger carbonatites (1,140-1,120 Ma) and nepheline syenites along ENE and SE trending faults. Older carbonatite intrusions, designated as carbonatitic breccia, frequently contain anorthositic and syenitic wallrock fragments set in a ferrocarnatite matrix, whereas subordinate veins of massive ferrocarnatite are almost xenolith-free and cut through the main carbonatite dykes. Metasomatic interaction between carbonatite-derived fluids and both neighbouring lithologies and incorporated anorthosite xenoliths led to the formation of economically important sodalite occurrences, confined to an area of about 100 km².

Investigated anorthosite samples display the typical magmatic mineral assemblage of plagioclase (An₃₇₋₇₅) ± olivine ± orthopyroxene ± clinopyroxene + ilmenite + magnetite + apatite ± zircon. Ilmenite and pyroxene are surrounded by narrow reaction rims of biotite as well as pargasite. During the subsolidus stage sporadic coronitic garnet-orthopyroxene-quartz assemblages around olivine and garnet-biotite assemblages around ilmenite were produced. Thermobarometry studies on amphiboles yielded temperatures of 985-950°C for the late-magmatic crystallization of the anorthositic rocks. The chemical compositions of garnet-orthopyroxene coronas and their textural relationships indicate, that the emplacement and crystallization of the anorthosites was followed by subsolidus re-equilibration of the plutonic body at conditions of 760 ± 100°C and 7.3 ± 1 kbar. Near-isobaric cooling proceeded to temperatures 680-630°C and pressures of 6.2 ± 0.4 kbar.

In the contemporaneously emplaced quartz-syenites and syenites potassium feldspar, plagioclase, hastingsite and/or clinopyroxene crystallized first, followed by a second generation of potassium feldspar as well as interstitial hastingsite and Fe-Ti oxides, which may in turn be surrounded by narrow rims of titanite. During the subsolidus re-equilibration of the syenites interstitial hastingsite was partially replaced by hastingsite-ilmenite-magnetite-plagioclase symplectites. Magmatic crystallization of potassium feldspar in the syenites occurred under temperatures of 890-790°C, which are presumably near the liquidus of the rocks. For the late-magmatic crystallization of hastingsite pressures of 6.5 ± 0.6 kbar have been obtained, which are similar to those derived for late-stage garnet-orthopyroxene coronas around olivine in the anorthosites. For the subsolidus formation of hastingsite-ilmenite-magnetite-plagioclase symplectites pressures of 6.6-6.9 kbar have been determined, implying that the syenite emplacement was followed by almost isobaric cooling.

In order to constrain the source rocks of the two suites, oxygen isotope analyses of feldspar from the anorthosites and syenites as well as geochemical bulk rock analyses were carried out. In case of the Kunene Intrusive Complex, the general geochemical characteristics of all anorthositic lithologies are in excellent agreement with a derivation from fractionated basaltic liquids, with the δ¹⁸O values obtained for magmatic plagioclase (5.88 ± 0.19 ‰ δ¹⁸O) proving their derivation from mantle-derived magmas. However, the mineralogical and isotopic data suggest that all studied anorthosite samples underwent a minor degree of crustal contamination, which was most prominent during the early intrusion stages. The

results obtained for the felsic suite, in turn, provide convincing evidence against consanguinity of the anorthosites and the syenites, i.e. (1) compositional gaps are developed between the major and trace element data of the two suites; chemical continuity is lacking, (2) trace element data of the felsic suite points to a crustal or at least a mixed crustal-mantle source of the felsic suite, (3) syenites do not exhibit ubiquitous negative Eu-anomalies in their REE patterns, which would be expected from fractionation products of melts that previously formed extensive plagioclase cumulates and (4) magmatic feldspar $\delta^{18}\text{O}$ values from both the quartz-syenite and the syenites fall in a restricted range of 7.20-7.92 ‰, which, however, are about 1.6 ‰ higher than the average magmatic plagioclase $\delta^{18}\text{O}$ of the anorthosites. Conformably, the crustal-derived felsic and the mantle-derived anorthositic suite are suggested to be coeval but not consanguineous. Their spatial and temporal association can be accounted for, if the heat necessary for crustal melting is provided by the upwelling and emplacement of mantle-derived melts, parental to the anorthosites.

In order to constrain the source of the 1,140-1,120 Ma carbonatites and to elucidate the fenitizing processes, which led to the formation of the sodalite occurrences of Swartbooisdrif, detailed mineralogical and geochemical investigations, stable isotope (C,O,S) analyses and fluid inclusion measurements (microthermometrical studies and synchrotron-micro-XRF analyses) of both the carbonatites and the fenitized lithologies have been combined.

There is striking evidence that carbonatites of both generations are magmatic rather than hydrothermal in origin. They occur as dykes and veins with cross-cutting relationships and margins disturbed by fenitic aureoles, and contain abundant flow-oriented xenoliths from the surrounding anorthosite and syenite. The mineral assemblage of both carbonatite generations of ankerite + calcite + ilmenite + magnetite + biotite \pm apatite \pm pyrochlore \pm sulphides in the main carbonatite body and ankerite + calcite + magnetite \pm pyrochlore \pm rutile in the younger and almost silicate-free ferrocarbonatite veins, their geochemical characteristics and the O and C isotope values (8.91 to 9.73 and -6.73 to -6.98, respectively) again indicate igneous derivation, with the $\delta^{18}\text{O}$ values suggesting only minor subsolidus alteration. Carbonatites of both generations can hence be described as mantle-derived, magmatic ferrocarbonatite magmas. The presence of apatite and biotite phenocrysts in the carbonatitic breccia is suggestive of a ferrocarbonatite melt that additionally contained minor amounts of P, K, Si and Al. The absence of these phases in the ferrocarbonatite veins implies that the ferrocarbonatite veins represent late-stage fractionation products of the ferrocarbonatite magma which formed the carbonatitic breccia, with their emplacement post-dating the extensive crystallization of biotite, ankerite, Fe-Ti oxides, apatite, and sulphides. However, the geochemical characteristics of the carbonatitic breccia itself provides evidence that these fractionation processes were already active previous to the emplacement of the older carbonatite unit. In contrast the extreme REE-enrichment, observed in two samples of the carbonatitic breccia, does not result from fractionation of the carbonatite melt, but is caused by a hydrothermal overprint by late-stage and highly evolved carbonatite fluids, which contained appreciable amounts of Sr and LREE.

NaCl-rich fluids, released from the early intruding carbonatite melt caused the fenitization of both, the incorporated wallrock xenoliths and the bordering anorthosite, syenite and nepheline syenite. This process is mainly characterized by the progressive transformation of Ca-rich plagioclase, K-feldspar and nepheline into albite and/or sodalite. Applying conventional geothermobarometry combined with fluid-inclusion isochore data, it was possible to reconstruct the P-T conditions for the carbonatite

emplacement and crystallization and for several mineral-forming processes during metasomatism. The composition and evolutionary trends of the fenitizing solution were estimated from both the sequence of metasomatic reactions within wallrock xenoliths in the carbonatitic breccia and fluid inclusion data (microthermometric measurements combined with synchrotron-micro-XRF analysis): (1) The formation of almost pure albite at the expense of former plagioclase and alkali-feldspar from anorthosite and syenite, respectively, and the transformation of anhydrous Fe-Mg-silicates and amphibole into biotite in the respective rock types predated the emplacement of the carbonatite melts. These metasomatic reactions require that Na and H₂O were the dominant components of this fluid. (2) After its final emplacement in the crust at c. 12-15 km (4-5 kbar), the carbonatite magma again reached water saturation following the contemporaneous formation of apatite and biotite at temperatures of c. 1200-630°C and fractionation of the anhydrous phases ankerite and magnetite. In a temperature range of 800-530°C the circulation of NaCl-rich aqueous brines (19-30 wt.% NaCl eq.) caused the transformation of albite of the incorporated anorthositic xenoliths into sodalite. The sodalitization of nepheline in a bordering nepheline syenite dyke occurred under similar temperatures (c. 775-700°C). Moreover, these fluids were capable of transporting minor amounts of Sr, Ba, Fe, Nb, and LREE. As most of the sodium contained in the fenitizing agents was consumed during this major sodalite-forming event, fluids trapped in quartz of a neighbouring quartz-syenite dyke display lower salinities of (9-24 wt.% NaCl eq.) but, at the same time, contain higher amounts of K, Ca, Fe, Ti, Sr, and Ba. The abundance of metasomatically formed sodalite in most samples of the carbonatitic breccia, formed at the expense of plagioclase from anorthosite xenoliths, suggests that these melts contained appreciable amounts of sodium before alkali-loss during fenitization. In contrast, late-stage ferrocarbonatite veins incorporate previously fenitized xenoliths but rarely show any wallrock alteration related to their emplacement. (3) During late stages of fenitization, cancrinite and muscovite replace albite from feldspar-rich xenoliths in the carbonatitic breccia, hence implying that the evolved fluids were still aqueous brines but no longer contained sufficient Na to form sodalite. The Si-free composition of a subsequently formed and yet unspecified Na-Al phase, grown at the expense of sodalite, provides evidence that even the late-stage carbonatite fluids were strongly deficient in Si.

This study demonstrates that the generation of ferrocarbonatite magmas and the associated contact metasomatism in the Swartbooisdrif area are the result of several magmatic and interrelated metasomatic processes, each inducing characteristic mineral reactions in the anorthositic and syenitic wall-rocks.

ACKNOWLEDGEMENTS

Special thanks are due to Professor Dr. M. Okrusch who initiated this project. His unrestricted support and encouragement as well as his never ending readiness for debates and discussions greatly contributed to the success of this project. To Professor Dr. V. Lorenz, I wish to express my gratitude for his guidance and interest during the field investigations and for his critical review of the manuscript.

Many thanks are due to Dr. habil. N. Cook (Geological Survey of Norway, Trondheim) and Dipl.-Min. S. Littmann (GeoForschungsZentrum Potsdam) who provided the sample material of 1997 and gave me a first insight into the geology of NW Namibia.

I am especially grateful to Dr. V. von Seckendorff for his always friendly willingness for discussions concerning the complex geology of the Swartbooisdrif area and his critical comments on the various manuscripts. Dipl.-Geol. S. Brandt is thanked for challenging discussions regarding the metamorphic Epupa Complex surrounding the investigated field area and for providing selected anorthosite and granite samples. I am grateful to Professor Dr. R. Klemd, Mrs. R. Baur and Dr. H. Brätz for their help and advise with the XRF- and LA-ICPMS-measurements and to Dr. habil. U. Schüssler for his ideas to improve the analytical approach of the EMP work. Thanks are also due to Dr. K. Hradil for her support with the XRD-measurements and to Mr. P. Späthe for his thorough preparation of the polished sections. Mrs. A. Kirchner is thanked for her always friendly administrative help.

I am greatly indebted to Professor Dr. J. Hoefs (Göttingen) for providing the oxygen- and carbon-isotope data and helping with their interpretation. Thanks are extended to Professor Dr. J. Erzinger, Dr. P. Dulski, Dr. E. Kramer, Dipl.-Min. S. Littmann and Mrs. S. Tonn (GeoForschungsZentrum Potsdam) for providing the opportunity to carry out REE analyses at the GeoForschungsZentrum Potsdam and their help and advice with the sample preparation and REE analysis. Many thanks go to Dr. K. Rickers (HASYLAB, Hamburg) for her introduction to and help with the Synchrotron-Micro-XRF analysis. I am indebted to Dr. T. Wagner (University of Tübingen) for performing the sulfur-isotope measurements, compiling the diagram of literature data for thiospinel compositions and for various valuable discussions. Dr. U. Hünken (KFA Jülich, Außenstelle Potsdam) is thanked for stimulating discussions, the assistance during the microthermometric measurements and the careful reading of the fluid inclusion chapter and

Dipl.-Min. A. Klimera (Fraunhofer ISC, Würzburg) for his help with the density determination at the Fraunhofer ISC, Würzburg.

The research project benefited from the support of the Geological Survey of Namibia. I am obliged to Dr. G. Schneider, Mr. V. Petzel, Mr. B. Rösener and Mr. R. Wackerle. The permission of Namibia Blue Sodalite Ltd. Company for access to, and sampling in the Swartbooisdrif sodalite mine and the kind assistance of Mr. F. Augustin and his son during the field studies is highly appreciated.

Many thanks are addressed to my friends and to the colleagues of the Institute of Mineralogy, Würzburg. Special thanks go to my family and to Sönke Brandt for their unrestricted encouragement and support during my work.

The financial support of Deutsche Forschungsgemeinschaft (grant Ok 2/64-1) is gratefully acknowledged.

1 Introduction

1.1 Location of the study area

The study area is located at the north-western border of Namibia, approximately 780 km north of the Namibian capital Windhoek (Fig.1.1). It is dominated by the anorthositic rocks of the Kunene Intrusive Complex (KIC) that, with a length of 350 km and a width of 30-80 km, extends from SW Angola into NW Namibia (Fig. 1.2). Towards the north and north-west the study area is restricted by the river Kunene, which marks the natural border between Namibia and Angola. The south-western and southern boundaries of the study area are formed by the metamorphic basement rocks of the Epupa Complex (EC). Rock samples were taken from a total area of approximately 2,800 km².

1.2 Geological framework

1.2.1 The metamorphic Epupa Complex

Metamorphic basement rocks in NW Namibia include the metamorphosed volcano-sedimentary sequence of the *Epupa Complex* (EC) which forms the southern extension of the Proterozoic Congo Craton (also referred to as the Angola-Kasai craton; see e.g. Clifford, 1970). The Namibian EC was subdivided into two units by Brandt et al. (2000, 2003; Fig. 1.3):

(1) Upper amphibolite-facies rocks of the *Orue Unit* are the dominant rock unit, mainly consisting of migmatitic granitic orthogneisses intruding subordinate migmatitic metasedimentary and metavolcanic rocks. A direct contact between the Orue Unit and the KIC has not been observed, since it has been intruded by dolerite and syenite dykes.

(2) To the south, about 10 km south of the KIC, a limited but well defined area of ultrahigh-temperature granulite-facies rocks has been recognized by Brandt et al. (2000, 2001, 2003), termed *Epembe Unit*. In its central part, this unit consists of a volcano-sedimentary sequence of interlayered felsic and mafic granulites, intercalated with subordinate migmatitic metasedimentary granulites. Rare sapphirine-bearing lenses of Mg-Al-rich granulites were observed in layers of migmatitic metagreywackes (Brandt et al., 2000, 2001, 2003). In contrast, the north-western and eastern parts of the Epembe Unit are dominated by massive mafic granulites. The Epembe Unit is separated from the Orue Unit by a sub-vertical E-W trending fault, termed Otjitambi-Ehomba Line, which was partly intruded by younger and unmetamorphosed gabbroic intrusions.

anorthosite bodies in the world (Ashwal & Twist, 1994). With a length of 350 km and a width of 30-80 km, the N-S elongated complex extends from SW Angola into NW Namibia (Fig. 1.2).

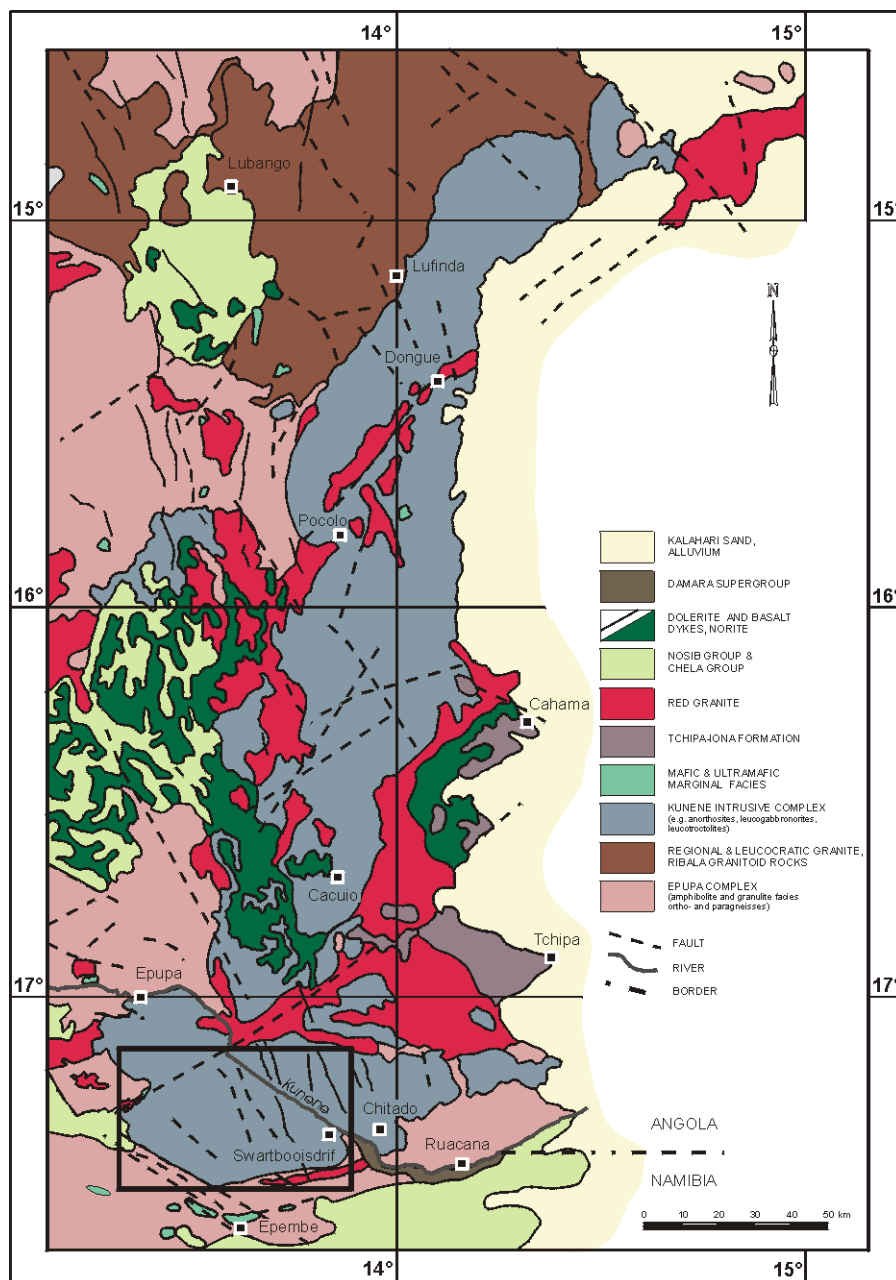


Fig. 1.2: Geologic overview map of the Kunene Intrusive Complex in SW Angola and NW Namibia. Map simplified and modified after Carvalho & Alves (1990). Outlined area marks the study area.

Only 2,500 km² of the KIC crop out on Namibian territory south of the Kunene River, building the mass of the Zebra Mountains. As already proposed by Morais et al. (1998) and Drüppel et al. (2001) the KIC may be subdivided into two major units, separated by a NE-SW trending belt of several granitoid intrusions:

(1) The majority of the Angolan part of the KIC displays a N-S elongation and is mainly composed of fresh to weakly altered, dark coloured anorthosites, leucogabbros and leucotroctolites with subordinate gabbros, norites and troctolites (e.g. Carvalho & Alves, 1990; Silva, 1992; Ashwal & Twist, 1994; Morais et al., 1998). Less than 10 % of these anorthositic rocks show igneous lamination with a pronounced NE-SW fabric, defined by a preferred orientation of plagioclase laths (Simpson, 1970; Morais et al., 1998).

(2) In contrast, the southernmost part of the KIC, including the Zebra Mountains (Fig. 1.3), has a pronounced E-W elongation. It mainly consists of whitish to greenish, heavily altered anorthosites and leucogabbros (cf. Simpson, 1970; Köstlin, 1974; Menge, 1996, 1998), the *white anorthosite* (about 60 %). In contrast, dark coloured, weakly altered anorthosites, leucotroctolites, leucogabbros and leuconorites, the *dark anorthosite*, are subordinate. Both the white and the dark anorthosite are characterized by a massive appearance, due to a homogeneous structure without preferred orientation of the plagioclase crystals. Cumulate textures are relatively widespread on a local scale; yet no evidence for extensive layering or igneous lamination was recognized, in contrast to the interpretation of aerial photographs by Menge (1996, 1998).

A conspicuous feature of the KIC are elliptic patches of Fe-Ti-ore concentrations (geological map), consisting predominantly of titanomagnetite and ilmenite with minor Fe-Mg-silicates (olivine and/or orthopyroxene) and sulphides. So far, neither geophysical data nor drill holes exist which might provide evidence for their exact three-dimensional shapes. These magnetite-ilmenite ores are restricted to the anorthositic rocks of the KIC and thus most probably resemble exsolution features of immiscible oxide and silicate.

A series of mafic and ultramafic intrusions of yet unknown age, the settings of which infer a genetic relationship to the anorthosite, crop out within the EC near the southern margin of the KIC (Fig. 1.3). Several individual mafic and ultramafic (dunite, pyroxenite, gabbro, leucogabbro, norite, hyperite, hornblende-hyperite, serpentinite) stocks and pipes that predominately intrude E-W and SE trending weakness zones have been mapped by Menge (1996). These rocks, the total volume of which is small compared to the KIC, have been generally assumed to be of an age comparable to that of the anorthosite, yet certain field relationships and geochemical patterns (Köstlin, 1967; Carvalho & Alves, 1990; Menge, 1996, 1998) suggest the intrusions to post-date the anorthosite emplacement.

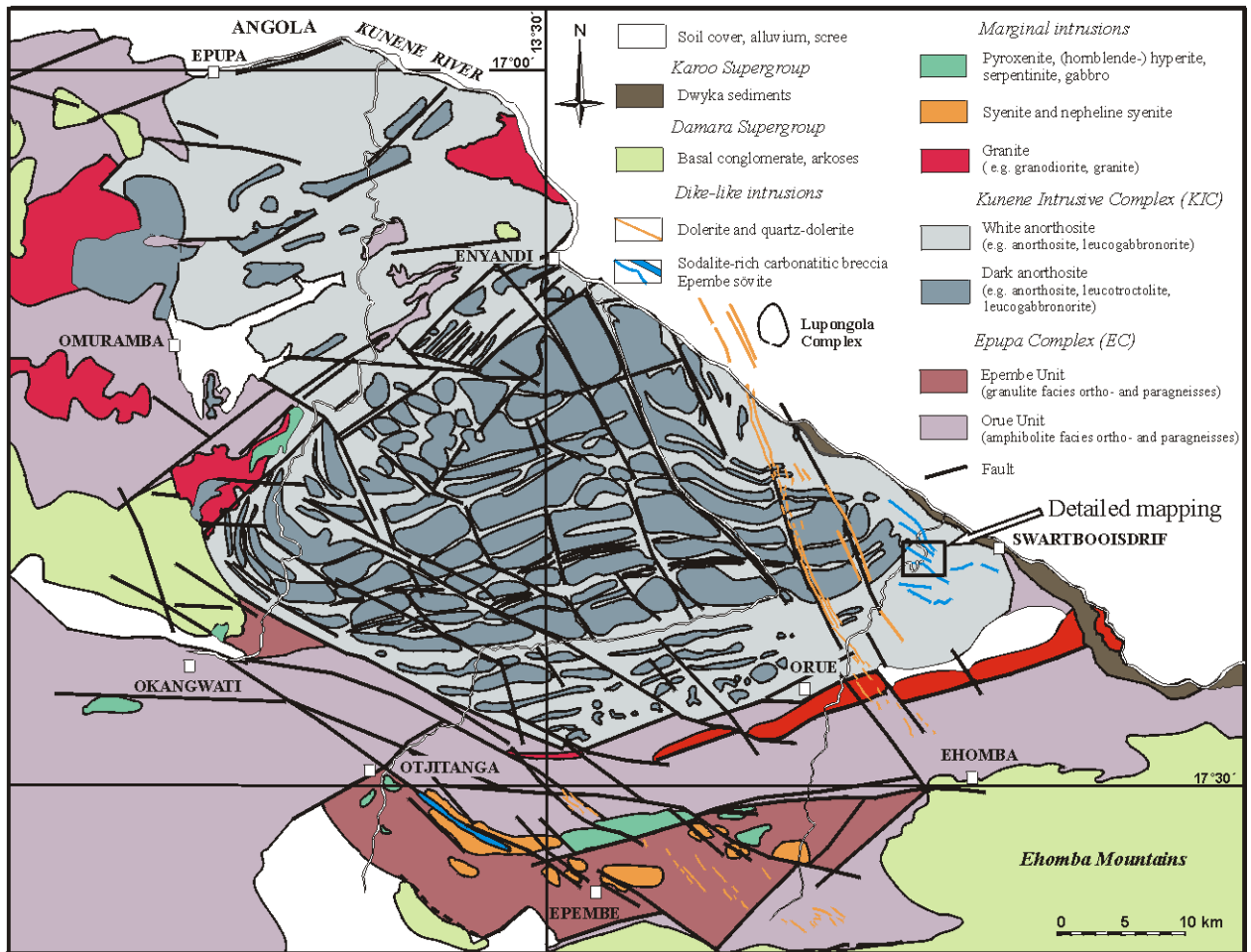


Fig. 1.3: Geologic overview map of the southern part of the Kunene Intrusive Complex. Map simplified and modified after Menge (1998).

1.2.3 The syenite-carbonatite-lamprophyre suites of Swartbooisdrif and Epembe

Close to the southern margin of the KIC, in the Epembe and Swartbooisdrif regions, both the KIC and the EC are transected by numerous SE and NE to ENE trending extensional faults and shear zones that were in parts intruded by various lamprophyre, carbonatite, nepheline syenite and syenite dykes (Fig. 1.3):

(1) In the Epembe area this alkaline suite mainly comprises small plugs and dykes of nepheline syenite and minor syenite intrusions emplaced within the metamorphic rocks of the Epupa Complex. These rocks clearly post-date the basic satellite intrusions, as evidenced by ultramafic xenoliths within the nepheline syenite (Littmann et al., 2003). Also assigned to the same alkaline suite are E-W-striking calciocarbonatite, ferrocyanatite and lamprophyre dykes (Ferguson et al., 1975).

(2) A second swarm of NE and SE striking dykes is exposed within the anorthositic rocks of the Kunene Intrusive Complex in the Swartbooisdrif area. This rock suite is distinct in appearance from that of the Epembe area. Felsic intrusives are mainly represented by syenite, which generally forms NE and SE striking dykes, crosscutting the anorthosite complex. A major swarm of ankeritic carbonatite dykes with a predominant SE, and a subordinate NE direction occurs in this area, dissecting both the syenite dykes and the anorthositic rocks of the KIC. These ankerite-rich carbonatites contain abundant xenoliths of anorthosite and syenite, surrounded by a laminated carbonatite matrix. Based on their macroscopic appearance these rocks are designated as *carbonatitic breccia*, even though they are clearly not a carbonatitic breccia sensu stricto. The carbonatitic breccia may contain variable amounts of sodalite, which are mined in an area of approximately 100 km², about 7.5 km NW of Swartbooisdrif (Fig. 1.3; Plate 1: geological map). A second generation of almost silicate-free ferrocarbonatite veins, transecting the carbonatitic breccia, is present in minor proportions.

1.3 Available geochronological data

The available geochronological data is summarised in Table 1. The age of the *EC* has been commonly regarded as Palaeo- to Mesoproterozoic (Martin 1965; Hedberg 1979). One date has been constrained by conventional U-Pb dating on zircons of a syntectonically intruded granite at Ruacana yielding an upper intercept age of 1,795 +33/-29 Ma (Tegtmeyer & Kröner, 1985). Recently however, Pb-Pb ages of about 1,460-1,430 Ma have been determined using garnets from granulite samples of the Epembe Unit (Seth et al., 2001), whereas the authors obtained conventional and SHRIMP U-Pb ages of 1,810-1,635 Ma and 1,520-1,510 Ma for zircon cores and rims, respectively. Unpublished U-Pb zircon age determinations from granitic gneiss and amphibolite samples of the EC (Burger, in Menge, 1996) yield slightly younger ages of 1,470 Ma and 1,394 Ma, respectively. These ages are in good accordance with Pb-Pb garnet ages obtained by Seth et al. (in prep.; 1,390-1,330 Ma) for samples of the amphibolite-facies Orue Unit.

In Angola, the Pre-Eburnian (late Archean to early Palaeoproterozoic) basement rocks were partly migmatized during the Eburnian orogeny (~ 2,200-1,800 Ma; Torquato & Oliviera, 1977) and intruded by large volumes of syntectonic granitoids (2,191 ± 60 Ma: Torquato et al., 1979; 1,847 ± 62 Ma: Carvalho et al., 1979). Subsequently, these rocks were by themselves transected by numerous syn- to post-tectonic granitoids with ages ranging between ~ 1,800-

1,600 Ma (e.g. Torquato & Oliviera, 1977; Carvalho et al., 1979, 2000; Torquato & Carvalho, 1992).

	<i>Lithostratigraphical unit</i>	<i>Lithology</i>	<i>Age (Ma)</i>
Basement rocks			
Angola	Regional granite	granite, granodiorite, tonalite	2,191 ± 60 (Rb-Sr 5 w.r.i., Torquato et al., 1979)
	Bale group	metasediments (conglomerate, siltstone, arkose, sandstone, greywacke, shale, quartzite)	2,162 ± 99 (Rb-Sr 5 w.r.i., Torquato & Oliviera, 1977)
	Quibala-type granite	granite, granodiorite	1,847 ± 62 (Rb-Sr 5 w.r.i., Carvalho et al., 1979)
	Eburnian gneiss	porphyroblastic gneiss	1,790 ± 32 (Rb-Sr 6 w.r.i., Carvalho et al., 2000)
	Leucocratic granite	granite	1,763 ± 21 (Rb-Sr 8 w.r.i., Carvalho et al., 1979)
	Caraculo granitoid	granite, granodiorite	1,686 ± 69 (Rb-Sr 1 w.r.i., Torquato & Carvalho, 1992)
	Bibala granitoid	granite, granodiorite	1,596 ± 86 (Rb-Sr 4 w.r.i., Torquato & Oliviera, 1977)
<hr/>			
Namibia (Epupa Complex)	Ruacana augengneiss	granitic gneiss	1,795 +33/-29 (U-Pb zircon, Tegtmeier & Kröner, 1985)
	EC (undifferentiated)	granitic gneiss	~1,470 (U-Pb zircon, Burger, in Menge, 1996)
	EC (undifferentiated)	amphibolite	~1,394 (U-Pb zircon, Burger, in Menge, 1996)
	Epembe Unit	granulite-facies ortho- and paragneisses	~1,460-1,430 (Pb-Pb garnet, Seth et al., 2001) ~1,520-1,510 (U-Pb zircon rims, Seth et al., subm.) ~1,810-1,635 (U-Pb zircon cores, Seth et al., subm.)
	Orue unit	amphibolite-facies ortho- and paragneisses	~1,390-1,330 (Pb-Pb garnet, Seth et al., in prep.)
<hr/>			
Kunene Intrusive Complex and associated felsic rocks			
Angola	Kunene Basic Complex	troctolite	1,347 ± 13 (U-Pb zircon, Mayer et al., 2000)
		troctolite	1,030 – 1,150 (internal Sm-Nd orthopyroxene-plagioclase isochron, Mayer et al., 2000)
	Mangerite dyke	mangerite	1,370 ± 4 (U-Pb zircon, Mayer et al., 2000)
	Red granite	granite	~1,400-1,300 (Rb-Sr w.r.i., Carvalho et al., 1979)
<hr/>			
Namibia	Kunene Intrusive Complex	leucogabbronorite	1,385 ± 25 (U-Pb zircon, Drüppel et al., 2000)
	Swartbooisdrif Syenite	Qtz-syenite syenite	1,376 (U-Pb zircon, Littmann et al., in prep.) 1,345 (U-Pb zircon, Littmann et al., in prep.)
<hr/>			
Alkaline suite			
Namibia	Epembe nepheline syenite	nepheline syenite	1,216 ± 2.4 & 1,213 ± 2.5 (U-Pb zircon, Littmann et al., 2000)
	Epembe carbonatite	sövite	1,204 (U-Pb titanite, Littmann et al., in prep.)
	Swartbooisdrif carbonatitic breccia	carbonatitic breccia	1,116 (U-Pb pyrochlore, Littmann et al., in prep.)
	Swartbooisdrif ferrocarnatite	ferrocarnatite veins	1,138 (U-Pb pyrochlore, Littmann et al., in prep.)

Table 1: Available geochronological data for Palaeo- to Mesoproterozoic rocks of north-western Namibia and south-western Angola.

A minimum age of the **KIC** has been provided by a Rb-Sr date of $1,190 \pm 90$ Ma using muscovite from a pegmatite dissecting the anorthosite massif (Simpson & Otto, 1960; recalculated by Cahen & Snelling, 1966). Recently, an internal biotite-plagioclase whole-rock Rb-Sr isochron date of $1,347 \pm 13$ Ma has been determined for one anorthosite sample of the Angolan part of the complex (Mayer et al., 2000). This age has been constrained by the same authors by an almost concordant U-Pb age of $1,370 \pm 4$ Ma using zircons from a cogenetic mangerite vein. These ages are in good accordance with an almost concordant U-Pb zircon age of $1,385 \pm 25$ Ma for a dark anorthosite sample of the Namibian part of the KIC (Drüppel et al., 2000). In contrast, two conspicuous internal plagioclase-orthopyroxene whole-rock Sm-Nd isochrons of 1.03 Ga and 1.15 Ga have been obtained for anorthosite samples of the northern Angolan part of the KIC by Mayer et al. (2000), which the authors interpret to reflect cooling episodes or re-crystallization after the emplacement of the anorthosite body. With Rb-Sr whole-rock ages of $1,350 \pm 50$ Ma (Carvalho et al., 1987) the **granite** belt (Red granite), that separates the northern and southern part of the KIC, is coeval with the anorthositic rocks of the KIC.

With U-Pb zircon ages of $\sim 1,380$ - $1,340$ Ma (Littmann et al., in prep.) the **syenite** dykes at Swartbooisdrif, although post-dating the emplacement of the main anorthosite body, seem to belong to the same magmatic event. In contrast, the **ankeritic carbonatites** of the Swartbooisdrif area are distinctly younger as is evidenced by U-Pb pyrochlore ages of $\sim 1,140$ - $1,120$ Ma (Littmann et al., in prep.).

The **nepheline syenite** intrusions, exposed within the basement rocks in the Epembe area, yielded U-Pb zircon ages of $1,216 \pm 2.4$ and $1,213 \pm 2.5$ Ma whereas an U-Pb zircon age of $1,204$ Ma has been constrained for the E-W trending **sövite** dykes of the same area (Littmann et al., 2000, in prep.). These age determinations rather suggest an independent formation of the Epembe and Swartbooisdrif suites.

1.4 Previous work on the magmatic rocks of NW Namibia and SW Angola

Based on petrologic and geochemical investigations, the **Kunene Intrusive Complex** has been interpreted as a massif-type anorthosite complex (Beetz, 1933; Simpson, 1970; Simpson & Otto, 1960; Vermaak, 1981), as a layered intrusion like the Great Dyke of Zimbabwe (Stone & Brown, 1958) and the Bushveld (Silva, 1990, 1992), as a transitional type between massif-type and layered intrusion like the Michikamau intrusion (Carvalho & Alves, 1990; Menge, 1998) or

as a composite massif-type anorthosite body (Ashwal & Twist, 1994; Morais et al., 1998; Slejko et al., 2002). In addition, the petrogenesis of the white anorthosite has been interpreted as a metasomatic transformation of the gneissic country rocks of the Epupa Complex (Köstlin, 1967, 1974). According to Köstlin (1974), the dark anorthosites intruded this white anorthosite massif along a series of concentric faults. In contrast to Menge (1998) and Köstlin (1974) recent detailed field and analytical studies of the Namibian part of the KIC (Drüppel, 1999) have shown that both the white and the dark anorthosite suite are typical Proterozoic massif-type anorthosites, the white anorthosite suite representing an older intrusion, crosscut by thick dykes of cogenetic dark anorthosite along E-W trending faults. This interpretation is mainly supported by (1) the excellent preservation of igneous mineralogy and textures in both anorthosite suites, (2) sharp intrusion contacts between the two anorthosite suites, (3) inclusions of angular clasts of white anorthosite up to 12 m across in the dark anorthosite and (4) high LREE abundances and xenocrysts of andradite-rich garnet in white anorthosite indicate a high degree of crustal contamination of this rock suite when compared to the dark anorthosite, consequently pointing to a different evolution of the parental melts of the two suites (Drüppel & Okrusch, 2000).

In contrast to the KIC, the *Epembe and Swartbooisdrif rock suites* are not widely known in the international literature. The sodalite occurrences were discovered by geologists of the Bethlehem Corporation in the early 60's. Simpson & Otto (1960) were the first to describe the sodalite-bearing lithologies of Swartbooisdrif. The authors describe fine-grained intergrowths of calcite, albite, sodalite and cancrinite with deep blue sodalite aggregates up to 20 cm in length. Unfortunately they misinterpreted the magmatic carbonatite-fenite mixtures as sedimentary deposits. A brief outline of the Swartbooisdrif carbonatite dykes is given in Martin (1965), who first recognized the intrusive nature of the carbonatites. He emphasised the fan-like distribution of the carbonatite dykes and the occurrence of conspicuous sodalite-cancrinite lenses within the carbonatites. A more detailed investigation, including a petrographic description, was given by Toerin (in Verwoerd, 1967). The author suggests, that both sodalite and cancrinite are of metasomatic origin, with the sodalite replacing nepheline of nepheline syenite fragments and the cancrinite replacing plagioclase of anorthositic xenoliths. The alkaline intrusive suite exposed in the Epembe area has been investigated in some detail by Ferguson et al. (1975). Their study concentrated on fenitic aureoles surrounding the nepheline syenite and carbonatite intrusions of Epembe, which, in clear contrast to the Swartbooisdrif carbonatite dykes, lack the extensive formation of sodalite. The latest review of the Swartbooisdrif sodalite occurrences is given by Menge (1986, 1996), who found the ankerite-rich carbonatite dykes to intrude older and heavily sheared syenites. He recognized the characteristic magmatic foliation of the carbonatite dykes

with alternating layers dominated by ankerite, sodalite, analcite, cancrinite, albite or magnetite, with the sodalite being formed by the interaction of carbonatitic fluids and the bordering lithologies.

1.5 Methods of investigation

Sampling of the anorthositic rock units concentrated on marginal zones of the KIC since the rugged topography of the Namibian KIC made a detailed investigation of its central parts without helicopter aid impossible. Mapping was conducted on topographic sheets (1:50,000) with the help of aerial photographs, landsat images and a Garmin Global Positioning System (GPS).

Detailed mapping (1 : 5,000) was carried out on the sodalite mining area of Namibia Blue Sodalite Ltd. (co.) in order to evaluate the complicate field relationships between the anorthosites of the KIC and the syenites and ferrocarnatites of the Swartbooisdrif area. Streets, dykes and geological borders were doubly measured with the help of the Garmin GPS. The general course of several larger carbonatite dykes was cross-checked with aerial photographs and landsat images.

1.6 Aims of the study

Objectives of this study are the anorthositic rocks of the Kunene Intrusive Complex and the spatially associated felsic suite as well as the younger carbonatites of the Swartbooisdrif area, including sodalite-rich lithologies. The present study tries to give a comprehensive insight into the Mesoproterozoic evolution of NW Namibia, with respect to the genesis and tectonothermal evolution of these rock suites. The study has been subdivided into three sub-units in order to solve certain special problems concerning the evolution of each individual rock unit:

The first part of this study outlines the complex field relationships between anorthosites, syenites and carbonatites.

- What are the structural controls for the emplacement of the anorthosites, syenites and carbonatites?
- Where does the sodalite exactly occur?

- Are there other rock units, which are possibly involved in the fenitizing processes?

The second part of this study is concerning with the petrogenesis of the anorthositic and the felsic suite.

- What are the source rocks of the anorthositic and the felsic rocks?
- What are the pressure and temperature conditions during their emplacement, crystallization and subsolidus re-equilibration?
- Are the two suites consanguineous or just coeval?
- Which processes led to their intrusion?

Part three of this study elucidates the magmatic and interrelated metasomatic processes of the Swartbooisdrif carbonatites and related rock units.

- What are the source rocks of the carbonatites?
- Of what kind are the relationships between the carbonatitic breccia and the late ferrocarbonatite veins?
- Under which pressure-temperature conditions did the carbonatites crystallize?
- Which processes led to the fenitization of anorthosites and syenites and the formation of sodalite?
- What is the nature and origin of the fenitizing solutions? Do they display an evolutionary history?
- What are the pressure-temperature conditions of the several mineral-forming, metasomatic processes?

The only work on the relation between the anorthosites of the KIC, the associated felsic rocks and the Swartbooisdrif sodalite deposits has been published by Menge in 1996, which however is mostly based on investigations performed 20 to 30 years ago. Since knowledge in structural geology, petrology and geochemistry tremendously increased during the last decades, a re-examination of the rock units using modern tools is most desirable.

PART I: The geology of the sodalite mining area at Swartbooisdrif

2 Physiography of the area mapped

2.1 Location of the area mapped

In order to evaluate the complicated relationships between anorthosite, syenite and ankerite carbonatites, a locally restricted sub-area of the study area has been mapped in detail (scale: 1 : 5,000; Plate 1: geological map). This area is located about 5 km south-west of the Namibian-Angolan border, marked by the river Kunene, and 6.8 km north-west of the settlement Swartbooisdrif (Fig. 1.3). It comprises an area of about 12 km², extending across longitudes of E 13°46.000' to E 13°48.000' and latitudes of S 17°20.000' to S 17°21.520' and is covered by a map section of the topographic map 1:50,000 Swartbooisdrif (sheet 1713BD). The mapped region is part of the mining area of Namibia Blue Sodalite Ltd. Company. It is transected by the ephemeral stream Ondoto and bordered by the NE-striking ridges of the Zebra Mountains in the north-west.

2.2 Geographic and geomorphologic overview

The topography of the study area is closely related to the relative age and mineralogical composition of the different lithologies and, to a certain extent, to regional tectonic structures.

The north-western part of the area mapped is dominated by ENE striking ridges with a strong positive relief, consisting of weakly altered and dark coloured anorthositic rocks. These rugged and steep mountains may rise to altitudes of about 940 m above sea-level and 150 m above the bordering plain. Physical weathering of the anorthositic rocks led to the in-situ formation of spheroidal boulders with diameters up to 10 m that cover the flanks of the ridges. Channelled eluviation of soil along a radial drainage system is responsible for plant life localised as belts, 20-50 m apart. The alternation of the uncovered and dark-coloured boulder belts and vegetation gives the ridges a striped appearance (Fig. 2.1a) which caused their regional name *Zebra Mountains*.

In clear contrast, the undulating plain south-east of the ridges has an average altitude of 790 m above sea-level with the topography changing about 30-50 m in height over short distances. It is underlain by white anorthosite as the dominant rock type of the major part of the study area. The pervasively altered and strongly weathered white anorthosite is transected by numerous SE- and subordinate NE-trending tension-fissures, that were in part filled by younger syenite and

carbonatite dykes. The topography of the low-lying sub-area is mainly characterized by an alternation of NW-striking and parallel running valleys and ridges that were most probably formed as a result of the faster denudation of the tectonised and weathered white anorthosite compared to the numerous younger syenite and carbonatite intrusions (Fig. 2.1b).

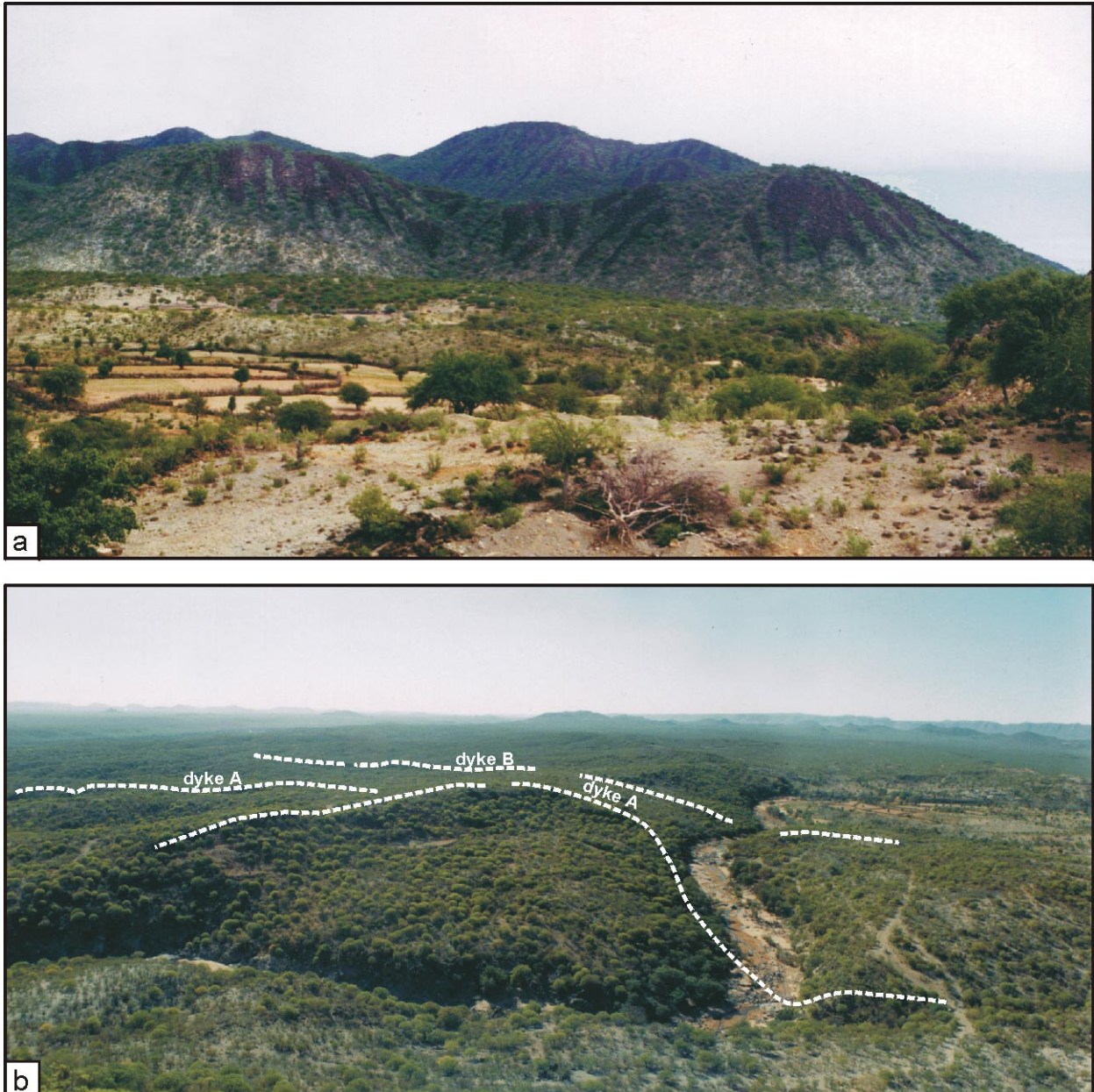


Fig. 2.1: *a)* Photography of the weathering resistant dark anorthosite ridges of the Zebra Mountains in the background of an undulating plain, underlain by white anorthosite (Locality: S 17°20.417', E 13°47.000'; NW-direction). *b)* Overview photography of the study area (Locality: S 17°20.075', E 13°46.016', S-direction), with the two major dykes of the sodalite-rich carbonatitic breccia (dyke A and B) marked.

The courses of the river valleys of the ephemeral stream Ondoto and the numerous smaller blind creeks are mainly controlled by the NE- and SE-trending fault system. Consequently, the deeply eroded river bed of the Ondoto shows the lowest topographic altitudes of the study area, i.e. 743 to 752 m above sea level. The drainage of the Ondoto is towards the Kunene River which is the only perennial river in NW Namibia. The Kunene spruits in Angola, follows the border of Angola and Namibia over a long distance and flows into the Atlantic. All blind creeks of the study area as well as the radial drainage system of the Zebra Mountains empty into the Ondoto.

The climate in NW Namibia is hot and subtropical. Rain falls mainly between December and April with an average annual rainfall of 300 mm (Swartbooisdrif). The daily temperature-maximum in the summer is 45°C, in the winter frost is common. As a consequence of these climatic conditions and the dominance of physical weathering soil formation is rare.

The vegetation exhibits seasonal and regional diversity. During the dry winter months, the barren vegetation is dominated by small bushes and trees (i.e. mopane: *Colophospermum Mopane* and *Copaifera Mopane*, paper bark tree: *Comuniphera*, wild fig tree: *Ficus Sycomorus*, and baobab: *Adansonia Digitata*), whereas the area is carpeted by several species of bushman grass (*Aristida Uniplumis*) in the summer months.

2.3 Exploration history

The sodalite occurrences were discovered by geologists of the Bethlehem Corporation in the early 60's. The exploration of the sodalite as a semiprecious stone was started in 1969 by Bantu Mining Corporation limited, Pretoria, South Africa. Between 1964 and 1979, about 700 t of sodalite-rich rocks were mined, the pits started on sodalite outcrops subsequently developed into small pits and opencastings. The use of ordinary TNT caused rupturing of the rocks and thus gave rise to a long-term damage to the sodalite-bearing lithologies. In 1979 all mining activities came to a standstill as a result of military operations in this area related to the Namibian-Angolan civil war. In 1985 the production and export of sodalite-bearing lithotypes as blocks of ornamental stone (1m x 1m x 2m), the Namibia Blue, was started. The mining area is now in possession of the Namibia Blue Sodalite Ltd. Company.

3 Geology of the area mapped

3.1 Geological overview

The study area is located near the south-eastern margin of the *KIC*. The dominant rock type in the central and southern part of the area mapped is a massive bright coloured anorthosite, the *white anorthosite* (heavily altered anorthosite and leucogabbonorite [A,w]), with a general white, green or violet appearance. In contrast, the north-western part is dominated by the steep ridges of the Zebra Mountains that are mainly composed of less altered *anorthosites and leucogabbonorites* [A,m] and *leucotroctolites* [T,m] of the *dark anorthosite* suite [A,d: comprising A,m and T,m]. Smaller, subsequently emplaced intrusions of dark anorthosite within the white anorthosite predominantly occur in central and eastern parts of the field area. In the vicinities of the river bed of the Ondoto, the dark anorthosite is strongly brecciated and weathered. Since it was impossible to assign the tectonised rocks to one particular anorthosite unit of the dark anorthosite suite, the *brecciated anorthosite* [A,b] was classified as an independent unit.

A conspicuous feature of the north-eastern part of the study area are elliptic accumulations of ilmenite-magnetite ore, which are mainly exposed within the white anorthosite. The general absence of exposed contacts between the weathered boulders of *ilmenite-magnetite ore* [IM] and the white anorthosite makes it difficult to unravel their chronological succession, yet the ores are suggested to be genetically and temporally linked to the anorthosite emplacement.

Fractures and near-extensional shear zones in the anorthositic rocks of the KIC were intruded by numerous SE and subordinate NE to ENE trending syenite and carbonatite dykes and veins. In a study area of about 12 km² a total of 288 dykes as well as numerous small veinlets of strongly varying lithology were mapped. Individual dykes may be interrupted over short distances and frequently change their strike and dip direction on a local scale.

The 82 *felsic dykes* are mainly represented by reddish to brownish, strongly altered K-feldspar-rich *syenite* [S,a] which forms NE and SE striking dykes, crosscutting the anorthosite complex. In shear zones intruded by both, syenites and carbonatites, the syenite is heavily strained and exhibits a pink to brownish colour. The colour-change of the syenites may be attributed to metasomatic exchange reactions between carbonatitic fluids and the syenite,

forming a *fenitized syenite* [S,f]. At one locality, a pegmatoidal *nepheline syenite* [S,ne] dyke, crosscutting the syenite intrusions, was observed in direct contact to a carbonatite dyke.

A major swarm of **carbonatite dykes** and veins occur in the area, dissecting the syenite dykes and the anorthosite body. The carbonatite dykes have variable trends with a predominant SE, and a subordinate NE direction. Two main periods of carbonatite emplacement have been recognized:

(1) The 187 dykes of the predominant carbonatite bodies, the *carbonatitic breccia*, are up to 80 m in width and frequently contain variable amounts of angular to sub-rounded fragments of fenitized wallrock anorthosite and syenite (70-95 vol.%), set in an ankeritic carbonatite matrix. Most of the xenoliths are pervasively fenitized and partially broken to small particles making up an interfragmental groundmass. A common feature of the carbonatitic breccia is a banded or streaky appearance due to an alternation of ankerite-, magnetite- and silicate-rich layers oriented sub-parallel to the dyke walls (*layered carbonatitic breccia* [Cb,l]). Flow-banding and impersistent magmatic folding on a millimetre to meter scale are common structures of this rock type. In places, where the grain size of the rocks decreases to very fine-grained, following syn- to post-emplacement shearing, the rocks exhibit a massive texture and a homogeneous grey colour (*massive carbonatitic breccia* [Cb,m]). Ankerite, albite and magnetite are the main minerals present in the carbonatitic breccia, although calcite, dolomite, cancrinite, biotite, muscovite, apatite, sulphides and sodalite are locally observed in significant concentrations. Variable amounts of sodalite occur as conspicuous deep blue lenses, layers and breccias in several of the larger dykes of the carbonatitic breccia (*sodalite-rich carbonatitic breccia* [Cb,so]), but are also abundant as metasomatic aureoles up to 1 m in width within the bordering dark anorthosite. Dark coloured *K-feldspar-biotite-ilmenite-calcite rocks*, strongly resembling lamprophyres but yet displaying conflict relationships to the carbonatitic breccia, are present in minor proportions.

(2) Both, the main carbonatite body and the K-feldspar-biotite-ilmenite-calcite rocks are transected by and intermingled with small veins and stringers of a second generation of almost silicate-free *ferrocarbonatite* [FV] veins and stringers, which may be present in strongly varying proportions. In contrast to the carbonatitic breccia, no effects of metasomatic alteration of the bordering rocks are visible on a macroscopic scale.

Sparse SE trending **dolerite** [Dol] dykes up to 70 m in width, which are most abundant throughout the eastern part of the investigated field area, cut both the syenites and the carbonatites. In addition, one **andesite** dyke [An] and one dyke of a **carbonate-rich trachyte** [Tr]

have been mapped. Due to their limited aerial extent, it was impossible to constrain clear temporal and structural relationships with the carbonatite, syenite and dolerite dykes.

The magmatic lithologies are overlain by different *sedimentary rock units*. Anorthositic *talus deposits* cover the steep ridges of the Zebra Mountains in the north-western part of the study area. The riverside of the ephemeral stream Ondoto is flanked by unconsolidated *quartzite pebble accumulations* [Qtz,p], which most probably represent variably eroded relics of former fluvial terraces. The youngest fluvial terrace generation, *carbonate-cemented immature conglomerates* [Cgl], border the Ondoto riverbed. The river floor of the Ondoto is filled by barren sand [All] intercalated with angular anorthosite and carbonatite fragments.

Mining waste piles in the vicinity of abandoned and active opencastings and the settlement Orotumba testify to the continuous pressure-production history.

3.2 Rock exposure

Due to the vegetation cover, many of the carbonatite outcrops are not accessed easy. In addition, the strong oxidation of ankerite under atmospheric conditions causes homogeneous brownish weathering surfaces of the carbonatitic breccia and thus makes it difficult to identify its mineralogy and texture. Good exposure of carbonatites and syenites and their contact relationships is confined to the numerous disused sodalite quarries formed by previous mining operations and the deeply eroded river valley of the Ondoto river. Excellent exposure is provided by the presently active sodalite quarry.

Since the KIC mountain ridges are generally covered by vegetation and anorthosite debris whereas the plains underlain by white anorthosite are covered by soil, mapping and sampling of the anorthositic rock types of area mapped concentrated on sodalite-quarries, the Ondoto river valley and scattered leucotroctolite outcrops occurring in the north-western part of the study area.

3.3 Field observations

3.3.1 The white anorthosite suite [A,w]

The study area is dominated by the *white anorthosite* that represents the oldest magmatic rock unit. In outcrops, the strongly tectonised white anorthosite displays a massive appearance, due to a homogeneous structure without preferred orientation of the coarse-grained plagioclase crystals (Fig. 3.1a). Accumulations of Fe-Ti-Oxides, associated with biotite and/or amphibole are rare.

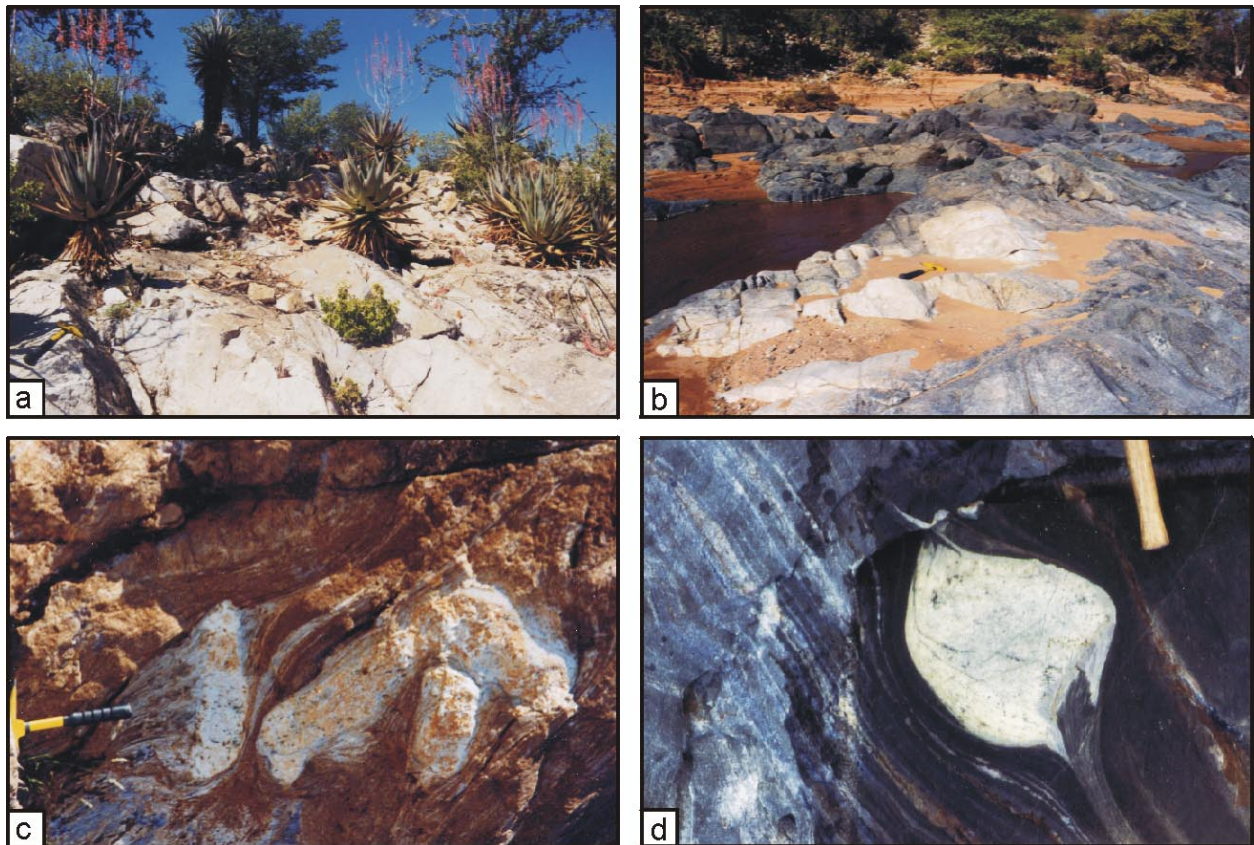


Fig. 3.1: *a)* Outcrop of massive white anorthosite, exposed in the river valley of the ephemeral stream Ondoto (Locality: S 17°20.437', E 13°46.860'). *b)* An angular clast of white anorthosite is enclosed by the grey coloured dark anorthosite (Locality: S 17°20.019', E 13°46.529'). *c)* In the carbonatitic breccia, clasts of the white anorthosite are wrapped by brownish ankerite-rich (Locality: S 17°21.045', E 13°47.078') or *d)* grey to blue silicate-rich layers (Sodalite opencasting 7, locality: S 17°20.850', E 13°46.824').

The hololeucocratic white anorthosite is characterized by a whitish to greenish or violet colour due to a pervasive sericitization and saussuritization of plagioclase and an alteration of Fe-Mg silicate phases. If exposed, intrusion contacts between the white anorthosite and the dark anorthosite are always sharp; inclusions of angular clasts of white anorthosite up to 12 m across in the younger dark anorthosite are a common feature in the investigated field area (Fig. 3.1b). In

addition, rotated and elongated fragments of the white anorthosite of up to 3 m across occur within the carbonatitic breccia (Fig. 3.1c, d).

Due to its strong alteration and brecciation the white anorthosite is generally weathered and deeply eroded, with the undulating erosion plains being covered by soil (Fig. 2.1a). Exposures of solid bedrock are rare, except in the Ondoto river valley and several disused sodalite quarries.

3.3.2 The dark anorthosite suite

3.3.2.1 Anorthosites and leucogabbronorites [A,m]

Irregular bounded anorthosite and leucogabbronorite (including leucogabbro and leuconorite) mounds with diameters of up to 300 m occur within the white anorthosite. These rocks dominate in the western part of the study area but may also occur in the centre and eastern regions. Due to their grey to greenish-grey colour and their resistance against alteration and weathering these rocks can be well distinguished from the white anorthosite on a macroscopic scale.

The anorthosites and leucogabbronorites are characterized by a massive texture with subhedral, coarse-grained plagioclase crystals of up to 26 cm in length (Fig. 3.2 a). Cumulations of Fe-Mg-silicates and Fe-Ti oxides of up to 0.5 m in diameter are relatively widespread on a local scale (Fig. 3.2 b). Leucogabbronorites can be distinguished from the anorthosites by their higher modal amounts of Fe-Mg silicates, i.e. clinopyroxene, orthopyroxene, biotite and amphibole. It has to be mentioned, however, that the boundaries between anorthosite and leucogabbronorite are generally transitional, thus the two rock units could not be distinguished as independent lithologies in the field.

Both rock types generally display sharp contacts against the older white anorthosite and the younger leucotroctolite. Commonly, dykes and small plugs of the leucotroctolites crosscut the older anorthosites and leucogabbronorites (Fig. 3.2 c). In the Ondoto river valley, the rocks may display a low angle banking structure which is most probably related to joint tectonics rather than representing magmatic layering as was proposed by Menge (1986).

Attaining up to 65-98 vol.%, plagioclase is the major constituent of these rock types. Minor phases are amphibole, clinopyroxene, orthopyroxene, biotite and Fe-Ti oxides with strongly varying amounts. When approaching the contact to dykes of the carbonatitic breccia, plagioclase is successively replaced by sodalite along fractures leading to a colour change of the

rocks from grey into purplish blue. In addition, accessory sulphides may fill small cracks in the anorthositic rocks. At the direct contact to the carbonatite dykes, the anorthositic rocks display a strong foliation oriented sub-parallel to the intrusion interfaces. In these zones, elongated plagioclase crystals are almost completely replaced by sodalite (Fig. 3.2 d), the anhydrous Fe-Mg silicates are altered to biotite and the amount of carbonate minerals increases drastically.

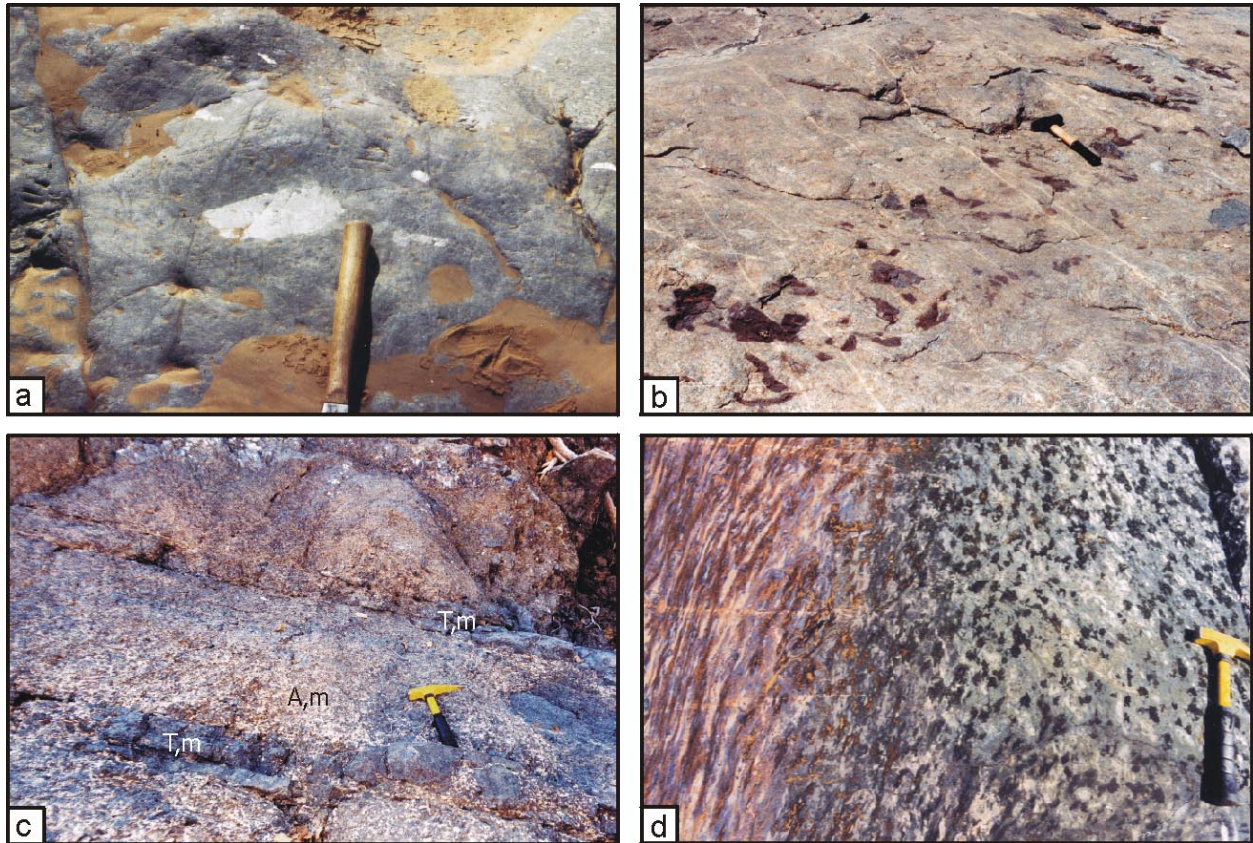


Fig. 3.2: *a)* Outcrop of the grey coloured dark anorthosite in the Ondoto riverbed. Note the homogeneous texture of the anorthosite, containing a plagioclase megacrysts of 18 cm length (Locality: S 17°20.019', E 13°46.529'). *b)* Accumulations of amphibole (brownish) in a transitional anorthosite/leucogabbro of the dark anorthosite suite, exposed at the south-western margin of the KIC (Locality: S 17°08.405', E 13°14.181'). *c)* Narrow leucotroctolite dykes (T,m) cut older leucogabbro (A,m) of the dark anorthosite suite (Locality: S 17°20.286', E 13°46.224'). *d)* The leucogabbro (left) in direct contact to the carbonatitic breccia (right) displays a weak foliation marked by ankerite- (brown), biotite- (black), sodalite- (blue) and plagioclase-rich (white) schlieren (Sodalite open-casting 8, locality: S 17°20.470', E 13°47.000').

3.3.2.2 Leucotroctolites [T,m]

Leucotroctolite [T,m], including leucotroctolite-anorthosite transitions, occurs near the western boundary of the study area as 19 independent rounded to oval shaped intrusions or narrow dykes

within both, the white anorthosite and the anorthosites/leucogabbronorites of the dark anorthosite suite. The biggest of these intrusions has a diameter of approximately 180 m. In addition, leucotroctolite occurs at the north-western boundary of the study area where it forms spectacular bolder belts covering the steep ridges of the Zebra Mountains (Fig. 3.3 a).

In fresh exposures leucotroctolites are characterized by dark grey to black colour. In clear contrast, the rocks display sacklike structures and brown coloured alteration rims in outcrops exposed to weathering. The leucotroctolites are commonly medium-grained with a homogeneous texture lacking a preferred orientation of the plagioclase crystals (Fig. 3.3 b). A conspicuous feature of the leucotroctolites is the strong iridescence of their plagioclase crystals, which makes these rocks most suitable for an exploitation as dimension stones.

The mineralogy of the leucotroctolites is much more restricted than that of the anorthosites and leucogabbronorites. Plagioclase (89-98 vol.%) is the dominant mineral accompanied by minor olivine (up to 8 vol.%). Accessory pyroxene, amphibole, biotite and Fe-Ti oxides may occur even though cumulate textures, as common in the leucogabbronorite, are lacking.

3.3.2.3 Brecciated anorthosites [A,b]

In the vicinity of the Ondoto river as well as along the numerous fault-related streamlets the anorthositic rocks are strongly tectonised. The diameter of the angular fragments rarely reaches 1.5 cm. The shatter zones are mainly composed of a porous plagioclase framework with the altered Fe-Mg silicates and Fe-Ti oxides being weathered and washed out (Fig. 3.3 c).

Contacts between the brecciated anorthosite and its undeformed counterparts are always sharp. Therefore, the brecciated anorthosites can not be assigned to one particular anorthosite unit and were thus mapped as an independent unit. The fact that narrow syenite dykes within the brecciated anorthosite are not affected by this deformation, strongly suggests that the brecciation of the anorthosites and the formation of the branched fault system predates the syenite emplacement.

3.3.3 Ilmenite-magnetite ore [IM]

Lensoidally bounded accumulations of weathered ilmenite-magnetite ore [IM] of up to 125 m in diameter particularly occur within the white anorthosite in the north-eastern part of the study

area but may also be present within leucogabbronorites and anorthosites of the dark anorthosite suite. If exposed, contacts between the black coloured Fe-Ti ore and the host anorthosite are generally transitional. However, outcrops of solid bedrock are generally rare in the study area, since the ilmenite-magnetite ore is mostly weathered to rounded pebbles which are up to 8 cm in diameter (Fig. 3.3d).

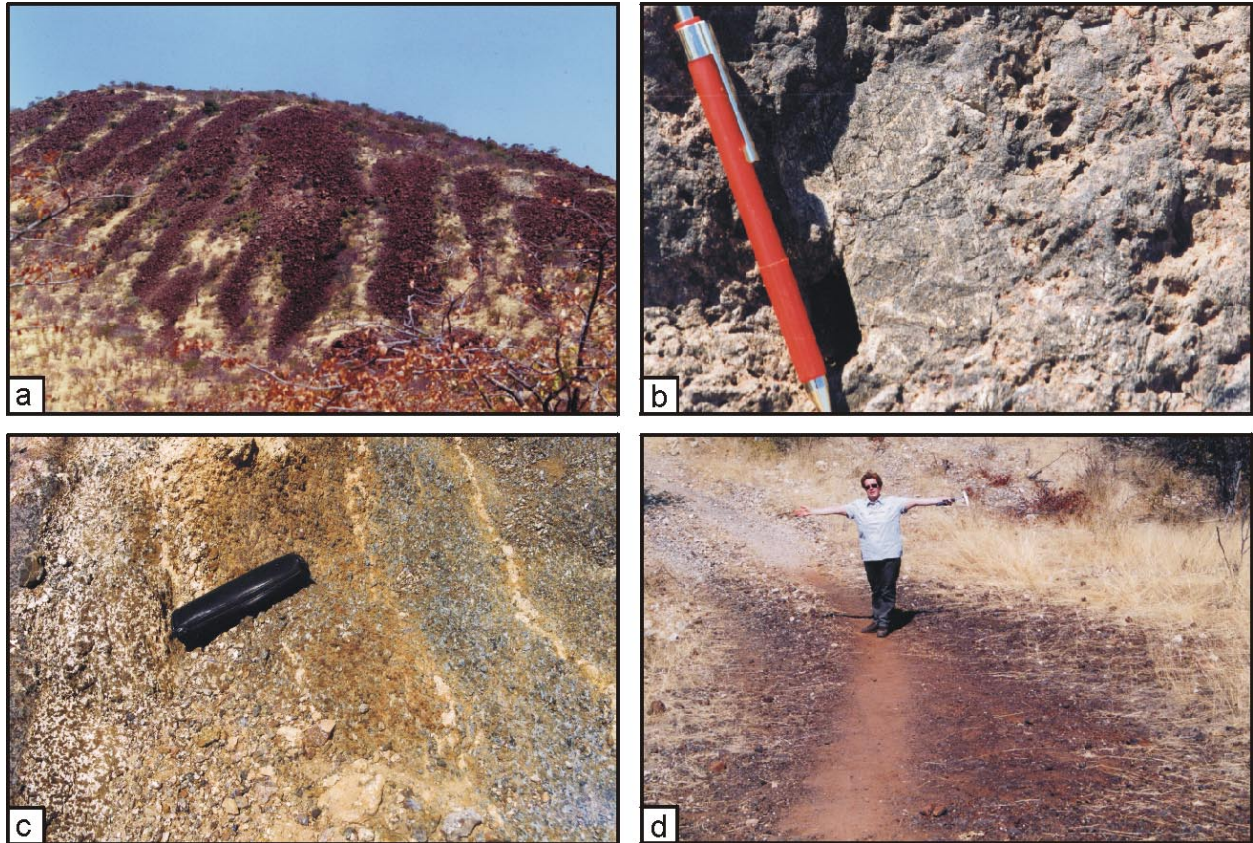


Fig. 3.3: *a)* Leucotroctolites exposed in the Zebra Mountain massif form boulder belts, that cover the ridges in zones of up to 20 m apart (Locality: S 17°20.126', E 13°46.524', W-direction). *b)* The commonly medium-grained, dark grey to black leucotroctolites may contain plagioclase crystals of up to 8 cm in length (Locality: S 17°26.830', E 13°37.995'). *c)* In the vicinity of a dyke of the carbonatitic breccia, the anorthositic rocks are brecciated. Plagioclase forms a porous framework, whereas the intercumulus Fe-Mg silicates and Fe-Ti oxides have been washed out (Locality: S 17°19.904', E 13°46.601'). *d)* Deposits of the ilmenite-magnetite ore are commonly exposed as accumulations of dark brown, rounded pebbles (Locality: S 17°20.126', E 13°46.524').

Ore minerals mainly consist of magnetite and ilmenite (> 90 vol.%) with the magnetite displaying macroscopically visible ilmenite exsolution lamellae. Interstices between the Fe-Ti oxide grains are filled by sulphides and relics of heavily altered Fe-Mg silicates. Cavities in the weathering surfaces of the ore boulders suggest that superficial Fe-Mg silicates were leached out.

The fact, that the exact 3-dimensional shape of the ore bodies is yet unknown and exposed wallrock contacts are rare, makes it difficult to unravel their temporal succession and their genetic setting. Most likely, however, the generation of the ilmenite-magnetite ores is genetically linked to the intrusion of the white anorthosite and the leucogabbro. The Fe-Ti ores may have separated by either (1) mechanical segregation of crystallising Fe-Ti oxide minerals following gravity settling or filter pressing or (2) oxide magma immiscibility followed by crystallization of Fe-Ti oxides from the separated liquid phase. Based on field investigations Morais et al. (1998) rather preferred the second model for similar ore bodies in the Angolan part of the KIC. Similar Fe-Ti ores have been found to be associated with anorthosites world-wide (e.g. Duchesne, 1999).

3.3.4 Syenites [S,a] and [S,f]

In the study area 82 major syenite dykes with a length of 10-650 m and a width of 15 cm to 15 m were mapped, not including numerous narrow veins and apophyses extending into the anorthositic rock units, which were too small to show them on the geological map. The syenites may be subdivided into two units:

(1) The vast majority of the felsic intrusives occurs in the south-eastern area as reddish to brownish, strongly altered and weathered K-feldspar-rich syenite to leucosyenite [S,a] which forms NE and subordinately SE trending dykes, exposed up to 600 m in length and 10 cm to 15 m in width and crosscutting the anorthosite complex. In most cases these syenites are heavily brecciated and/or sheared into small particles. Outcrops of solid bedrock are rare, commonly the syenites form accumulations of angular fragments (Fig. 3.4 a, b). When exposed in reactivated shear zones, the syenites are altered to epidote which may also be present as massive epidote rocks replacing the syenite dykes as a whole.

The medium-grained syenites are characterized by a homogeneous texture (Fig. 3.4b) without preferred orientation of the K-feldspar crystals (75-90 vol.%). Minor constituents are amphibole, biotite and Fe-Ti oxides. Contact-metamorphic phenomena have never been observed in the anorthositic rocks bordering the syenite dykes nor are chilled margins developed in the syenite itself. However, narrow syenite dykes may display a flow zoning, with the biotite crystal sizes increasing towards the dyke centre (Fig. 3.4c). It may thus be concluded that the anorthosites still had elevated temperatures during the syenite emplacement. However, in some of the dark anorthosite occurrences, syenitic fluids led to the contact-metasomatic formation of disseminated sulphides.

Angular fragments of syenite are incorporated in the carbonatitic breccia, locally reaching amounts of up to 40 vol.% (Fig. 3.4d). The brecciated and rotated xenoliths may approach diameters of up to 4 m. Since these syenite clasts are too big to be transported over long distances by the carbonatitic melt, the most successful model for the carbonatite emplacement is a passive intrusion mechanism following fault-related brecciation of the syenite.

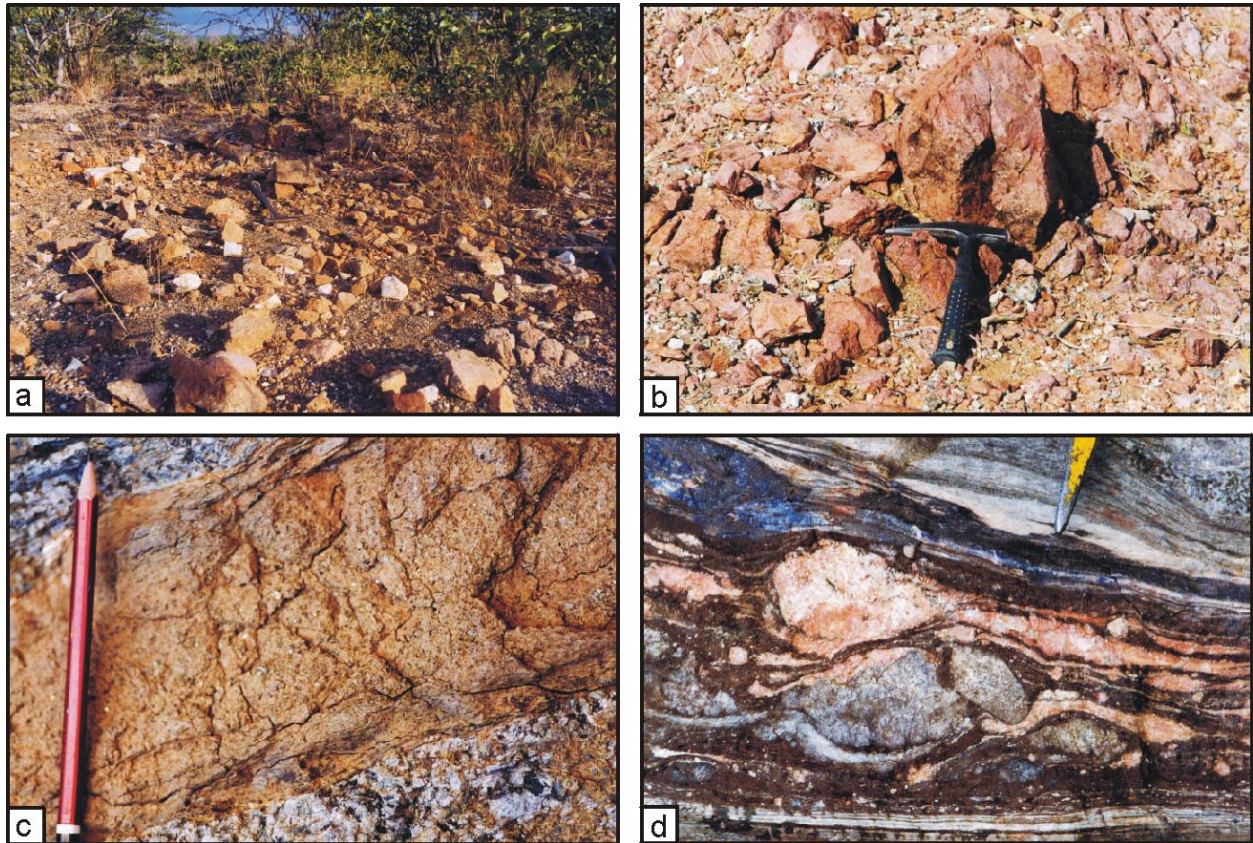


Fig. 3.4: *a)* Syenite commonly forms accumulations of weathered, angular syenite fragments (Locality: S 17°21.145', E 13°47.772'). *b)* In rare cases, the reddish syenite is exposed in small outcrops of solid bedrock (Locality: S 17°21.145', E 13°47.772'). *c)* A narrow biotite-bearing syenite dyke (brownish) transects an older leucogabbronorite (grey) of the dark anorthosite suite. The crystal sizes of biotite successively increase towards the centre of the syenite dyke (Locality: S 17°21.072', E 13°46.495'). *d)* Rotated fragments of the heavily tectonised syenite (pink) occur within the carbonatitic breccia, where they are wrapped by carbonate- (brown) and silicate-rich (grey, blue) layers (Locality: S 17°21.944', E 13°48.180').

(2) In the predominantly SE trending shear zones intruded by both, syenite and carbonatite, the syenites are heavily strained and mostly exhibit a pink colour (Fig. 3.5 a, b). The syenite occurs within and at the borders of the dykes of the carbonatitic breccia with a width ranging from < 3 m up to 15 m. The exposed contacts between syenite and carbonatite are

curvilinear (Fig. 3.5 a) but tectonic, since syenitic fragments in all stages of detachment can be observed in the bordering carbonatite (Fig. 3.5 b).

In clear contrast to the K-feldspar-rich syenite dykes, the coarse-grained fenitized syenites [S,f] are predominantly composed of subhedral albite crystals of up to 3 cm length, already visible on a macroscopic scale. When approaching the contacts to the carbonatite dykes, the fenitized syenite displays a weak foliation sub-parallel to the dyke walls. Joints in the fenitized syenites are commonly filled by clusters of euhedral magnetite crystals of up to 3 cm in length.

The colour-change of the syenites must be attributed to metasomatic exchange reactions between Na-rich carbonatitic fluids and the K-feldspar-rich syenite forming albite-rich fenitized syenites. It has to be mentioned, however, that the rarely exposed contacts between the syenite and the fenitized syenite are always sharp, the latter dissecting the former. Thus it may be concluded that the predominantly SE trending fenitized syenites are not only fenitized equivalents of the syenite but may additionally represent a second syenite generation emplaced in a younger, SE trending fault bundle.

Common features of both syenite dyke swarms are branching, dying out and curving of the dykes as well as dyke segmenting into an en-echelon set of intrusions, with the width of the dykes continuously decreasing from >10 m down to several tens of cm towards their terminations.

3.3.5 Nepheline Syenite [S,ne]

At one locality, in the eastern part of the mapped area (Locality: S 17°21.100', E 13°47.850'), a nepheline syenite dyke, crosscutting a syenite intrusion, was observed in direct contact to a dyke of the carbonatitic breccia. The dyke is exposed over just a short distance of about 6.5 m and a width of 3 m to 30 cm.

At distance to the carbonatite dykes, the pink nepheline syenite is characterized by a homogeneous texture with subhedral and medium-grained nepheline and K-feldspar being the major constituents, accompanied by minor biotite and Fe-Ti oxides. When approaching the carbonatite dykes, the texture of the nepheline syenite successively becomes inhomogeneous with fine-grained K-feldspar-rich zones alternating with irregular pegmatoidal zones, mainly composed of nepheline crystals of up to 5 cm in length (Fig. 3.5c). At the direct contact to the

carbonatite dykes the nepheline syenite exhibits a massive texture with euhedral nepheline crystals of up to 15 cm across. In these zones, nepheline exhibits a pale blue tint resulting from its partial replacement by sodalite (Fig. 3.5 d). The increase of the nepheline crystal size at the contact to the carbonatite dyke and the replacement of nepheline by sodalite may be attributed to the late influx of Na-rich carbonatitic fluids, but may also be due to the cogenetic formation of the two rock types.

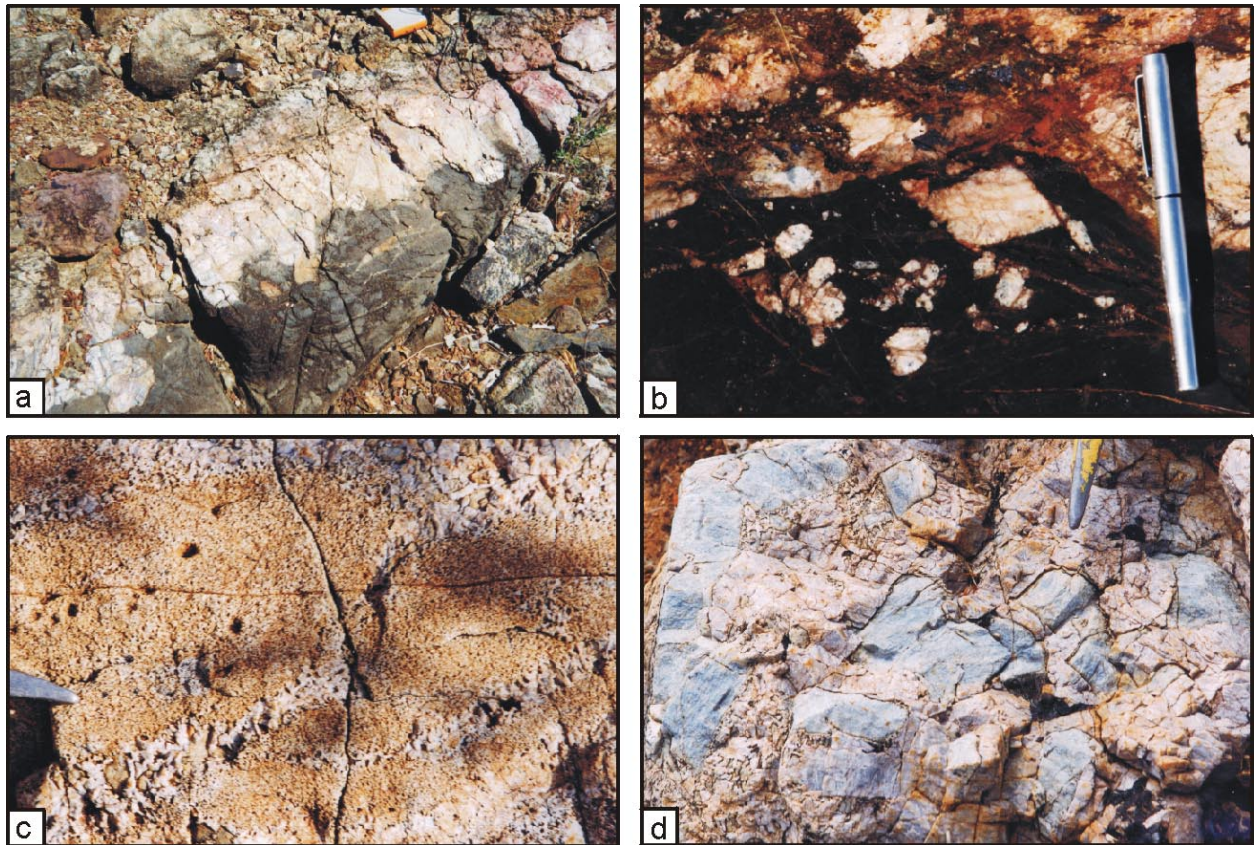


Fig. 3.5: *a)* From distance, the contacts between the pink coloured fenitized syenite and the carbonatitic breccia (dark grey) look curvilinear, thus suggesting a cogenetic origin of the two rock units (Locality: S 17°20.970', E 13°47.113'). *b)* However, in a more detailed view, syenite fragments (pink) in all stages of detachment can be observed in the bordering carbonatitic breccia (black), testifying to the intrusive nature of the younger carbonatites (Sodalite opencasting 7, locality: S 17°20.890', E 13°46.774'). *c)* The nepheline syenite in contact to the carbonatitic breccia displays an inhomogeneous texture, characterized by alternating K-feldspar- and nepheline-rich schlieren (Locality: S 17°21.101', E 13°47.854'). *d)* At the direct contact to the carbonatitic breccia, euhedral nepheline of the nepheline syenite exhibits a blue tint, resulting from its partial replacement by metasomatically formed sodalite (Locality: S 17°21.101', E 13°47.854').

3.3.6 Carbonatites and associated rock types

3.3.6.1 Carbonatitic breccia

A major swarm of 199 carbonatite dykes and veins occurs in the area, dissecting the syenite dykes and the anorthosite body. The carbonatite dykes have variable trends with a predominant SE, and a subordinate NE direction. Like the syenites, the dykes of all three carbonatite subgroups display features like dying out, branching, curving and en-echelon segmentation. The predominant carbonatite bodies, the *carbonatitic breccia*, are up to 80 m in width and frequently contain variable amounts of angular to sub-rounded fragments of wallrock anorthosite and syenite (~70-95 vol.%). The fragments range continuously from 8 m down to several millimetres in diameter, set in an ankeritic carbonatite matrix. Most of the xenoliths are pervasively fenitized and partially broken to small particles making up an interfragmental groundmass. Regarding both their macroscopic appearance and their general mineralogy, three subtypes of the carbonatitic breccia were established:

(1) The vast majority of the dykes of the carbonatitic breccia, i.e. 145 dykes, displays a banded or streaky appearance due to an alternation of ankerite-, magnetite- and silicate-rich layers oriented sub-parallel to the dyke walls. Flow-banding and impersistent magmatic folding on a millimetre to meter scale are common structures of the layered carbonatitic breccia [CB,l]. Sodalite is a minor constituent or even absent.

(2) In 45 more medium to coarse-grained dykes of the carbonatitic breccia, sodalite is concentrated in economic proportions of > 25 vol.%. Variable amounts of sodalite occur as conspicuous deep blue lenses, layers and breccias within the larger carbonatite dykes, but are also abundant as metasomatic aureoles up to 1 m in width within the bordering dark anorthosite. These rocks are referred to as sodalite-rich carbonatitic breccia [CB,so].

(3) In clear contrast, 12 dykes of the carbonatitic breccia are characterized by a massive appearance and a homogeneous grey colour with rare reddish feldspar-rich xenoliths. The grain sizes of the massive carbonatitic breccia [CB,m] range from fine-grained to very fine-grained, most probably following syn- to post-emplacement shearing. Sodalite has never been observed in these rocks on a macroscopic scale.

3.3.6.1.1 Layered carbonatitic breccia [CB,l]

Dykes of the banded carbonatitic breccia are spread over the whole study area. They are exposed over a length of 5-800 m with a varying thickness ranging between 20 cm and 18 m. The rocks are characterized by an impersistent layering sub-parallel to the wallrock interface, marked by an

alternation of bands rich in, or wholly composed of albite (pink to light grey) and biotite (dark brown to black), carbonates (brownish to yellowish) and oxides (black) whereas sodalite (blue), cancrinite (light yellow) and sulphides are minor constituents (Fig. 3.6 a, e, f).

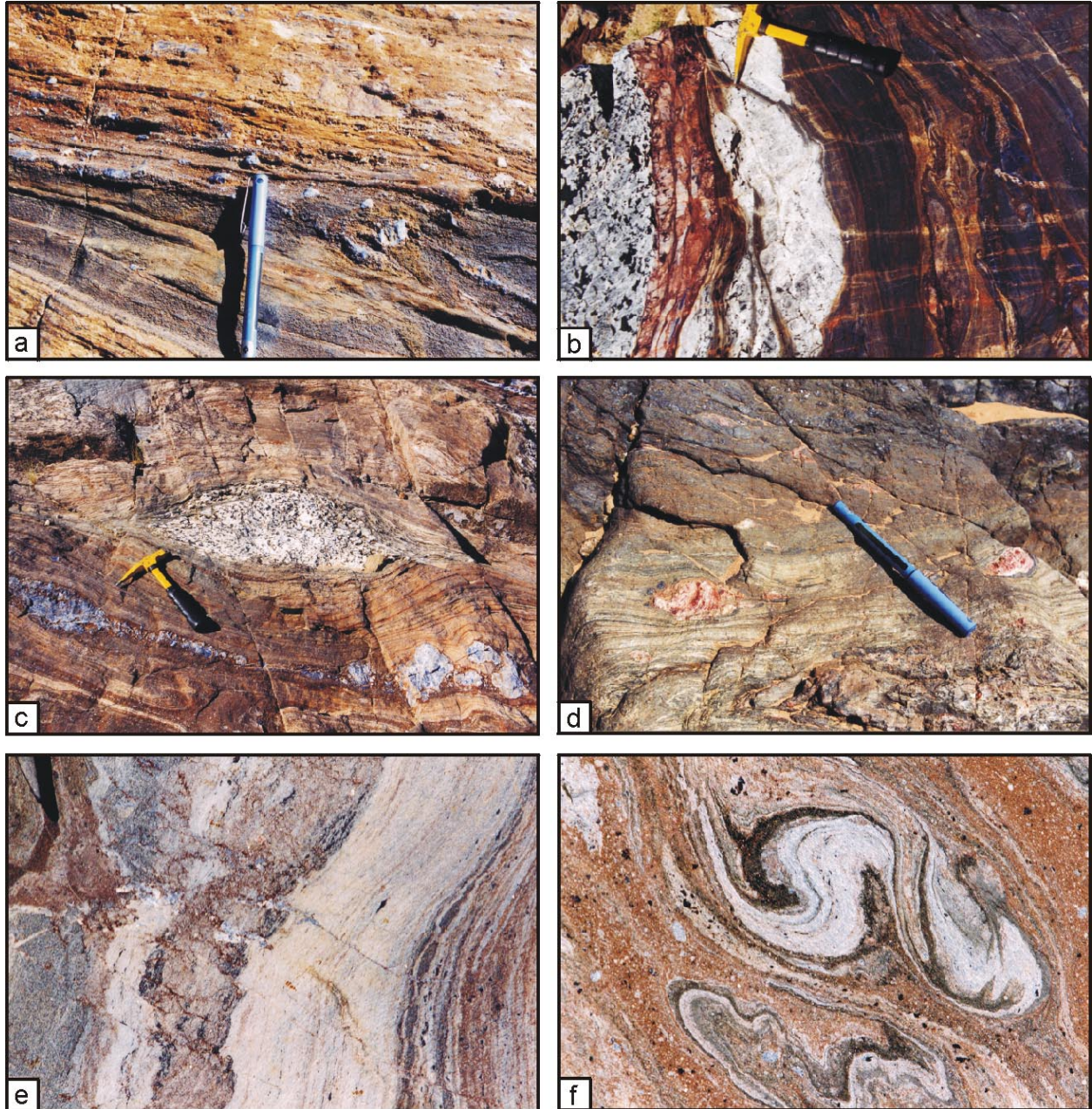


Fig. 3.6: *a)* Sub-parallel alternation of grey albite- and biotite-rich and brownish ankerite-rich layers of the layered carbonatitic breccia, containing dispersed, sodalite-rich xenoliths (Locality: S 17°20.066', E 13°46.524'). *b)* A dyke of the layered carbonatitic breccia (dark brown), displaying impersistent lamination, transects a leucogabbro (grey), which, by itself, is intruded by a syenite dyke (pink) (Sodalite opencasting 7, locality: S 17°20.890', E 13°46.774'). *c)* and *d)* The sub-parallel layering of the carbonatitic breccia, with the laminae wrapping rotated anorthosite (light grey), sodalite (blue) and syenite fragments (pink), gives the rock a mylonite-like appearance (Locality: S 17°20.147', E 13°46.662'). *e)* Common features of the carbonatitic breccia are the displacement of already completely crystallized laminae along impersistent brittle faults and *f)* discontinuous magmatic folding (Sodalite opencasting 4, Locality: S 17°20.967', E 13°47.722').

Contacts between individual layers may be both sharp or transitional (Fig. 3.6 b). Rotated angular fragments of altered anorthosite with sericitized plagioclase crystals (white to light grey; Fig. 3.6 c) and syenite (reddish to light pink; Fig. 3.6 d), with diameters ranging between several millimetres and 2.5 m, are commonly enveloped by ankerite-magnetite layers. Single laminae of the banded carbonatite breccia may run sub-parallel over a certain distance, giving the rock a mylonite-like appearance. In places, the laminae are displaced along small scaled brittle faults which die out after short distances of 5-90 cm (Fig. 3.6 e). In addition, the dykes may display discontinuous magmatic folding, with small scaled ductile shear zones being developed locally (Fig. 3.6 f). The occurrence of carbonatite rafts, oriented discordant to the magmatic foliation of the surrounding carbonatite matrix, supports evidence for repeated injections of carbonatite melt. The fact that ankeritic laminae fill even the narrowest joints in the bordering anorthosite and syenite prove that the carbonatite melt itself had a low viscosity, even though the textures displayed by carbonatite-xenolith mixtures, as described above, closely resemble those of high viscosity melts like rhyolites.

The numerous abandoned and active opencastings are exceptionally suitable for the investigation of the textural features described above (Fig. 3.6 b, e, f). In addition, these textures can be observed in outcrops exposed to weathering since the minerals contained in the carbonate- and the silicate-rich layers display a strongly differing weathering behaviour (Fig. 3.6 a, c, d).

3.3.6.1.2 Sodalite-rich carbonatitic breccia [CB,so]

Economic concentrations of sodalite occur in several of the larger carbonatite dykes exposed over a length of up to 2.8 km and a varying width of 10-90 m. Textural features of layered sodalite-rich lithologies resemble those of the sodalite-poor subgroup (see above). In contrast to the latter, sodalite-rich carbonatites may additionally contain massive ankerite-magnetite patches with subordinate contamination by wallrock-material and/or massive fenite zones, that are almost completely composed of albite and biotite. Within the carbonatite dykes, sodalite occurs in three different textural positions: (1) As pale blue monomineralic layers of up to 1.2 m in width in which sodalite replaces fine-grained, fragmented plagioclase (Fig. 3.7 a), (2) as deep blue and partially translucent sodalite pseudomorphs after fragmented plagioclase-rich xenoliths of up to 1.5 m in diameter enveloped by carbonate-rich laminae or massive albite-biotite fenite zones (Fig. 3.7 b) and (3) as deep blue to green sodalite aggregates partially replacing

subrounded, feldspar-rich fragments dispersed in the massive ankerite-rich patches (Fig. 3.7 c, d; Fig. 3.8 a, b).

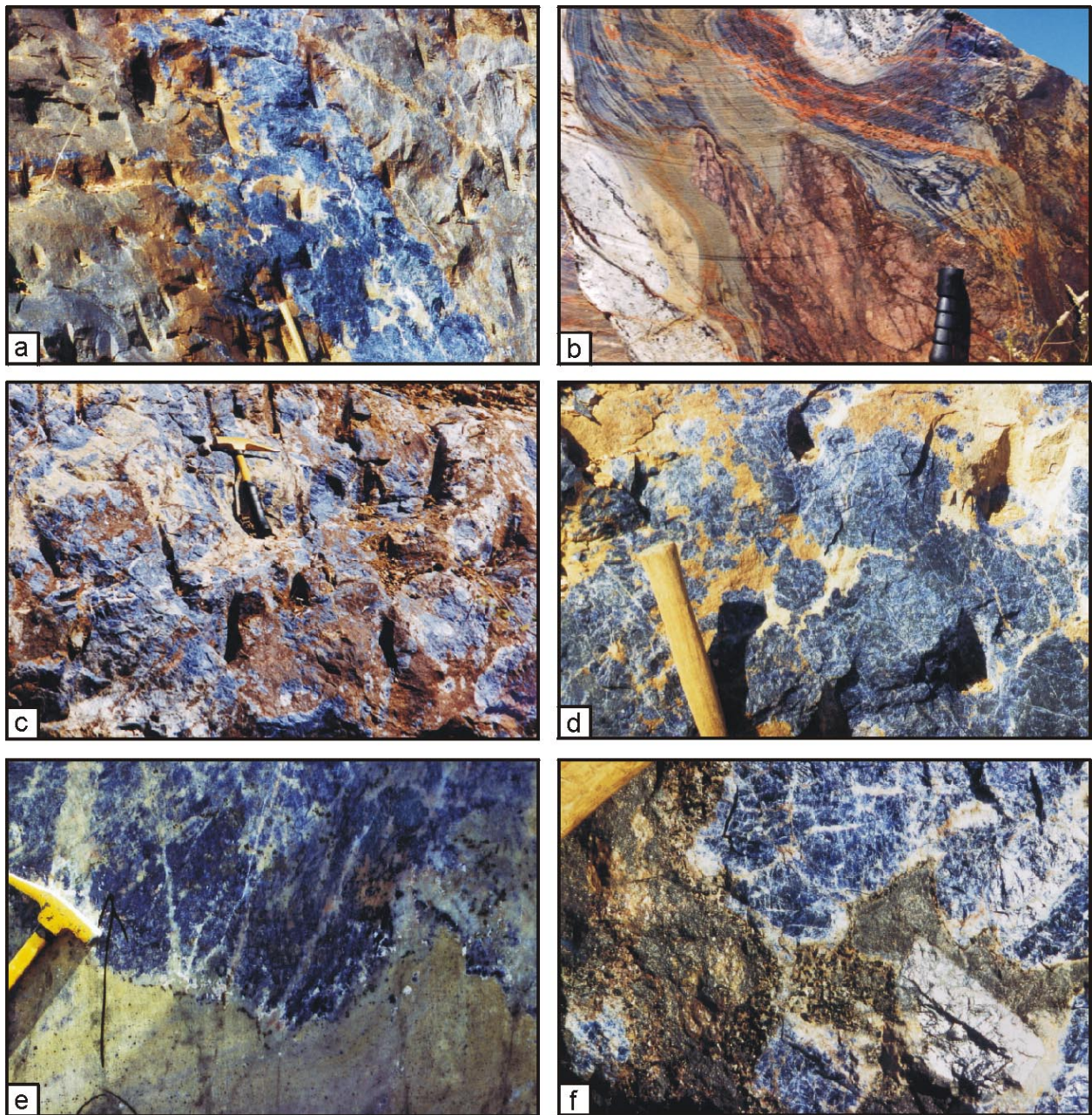


Fig. 3.7: *a)* A monomineralic layer of deep blue sodalite is exposed within a dyke of the sodalite-rich carbonatitic breccia (grey; Locality: S 17°19.904', E 13°46.601'). *b)* Low-viscosity carbonatite melts (light to dark brown) intruded a heavily brecciated anorthosite(grey)-syenite(pink) assemblage. Dark anorthosite fragments are partially replaced by sodalite and wrapped by carbonate-rich laminae (Sodalite opencasting 7, locality: S 17°20.890', E 13°46.774'). *c)* Sodalite-rich xenoliths (blue) are homogeneously dispersed in massive ankerite-rich patches (brown; Locality: S 17°20.567', E 13°47.605'). *d)* Same as (c) (Locality: S 17°20.902', E 13°45.823'). *e)* Trails of magnetite (black) mark the sodalite (blue) / carbonatite (yellowish) contacts (Sodalite opencasting 8, locality: S 17°20.417', E 13°47.000'). *f)* A rim of medium-grained biotite flakes (black) is developed around sodalite fragments (blue), enclosed by fine-grained albite-biotite zones (dark grey; Locality: S 17°20.902', E 13°45.823').

Trails of euhedral magnetite crystals mark the contacts between sodalite- and ankerite-rich zones (Fig. 3.7 e), whereas medium to coarse-grained biotite flakes crystallize in the vicinity of sodalite fragments, surrounded by fine-grained albite-biotite-rich zones (Fig. 3.7 f). The sodalite distribution within the dykes of the carbonatitic breccia is quite heterogeneous. Even within single dykes the amounts of sodalite commonly vary between 15 and 90 vol.%. In rare cases, sodalite may also be absent over a certain distance, a fact that complicates the mine layouts. It has to be mentioned, however, that sodalite is mostly difficult to identify in carbonatite outcrops exposed to weathering, since the oxidation of ankerite causes the formation of brownish alteration rims that may cover the whole rock. Sodalite concentrations of >90 vol.% containing sodalite fragments of up to 0.5 m in diameter predominantly occur in regions, where several large carbonatite dykes intersect at acute angles and the modal abundance of wallrock xenoliths increases, thus evidencing that sodalite is not a magmatic crystallization product of the carbonatites themselves but originates from the interaction of carbonatitic NaCl-rich fluids with the incorporated feldspar-rich xenoliths. This interpretation is constrained by the occurrence of sodalite in narrow metasomatic aureoles of up to 1 m in width within the anorthosites, that surround large dykes of the carbonatitic breccia (Fig. 3.2 d). Heavily tectonised cross-points of several large fractures intruded by large carbonatite dykes (geological map) seem to form exceptionally suitable pathways for large-scale fluid-flow.

In the following, a short description of the general characteristics of the 9 major active and abandoned opencastings, situated along the two major sodalite-rich dykes of the study area (*dyke A* in the north-eastern part and *dyke B* in the central part of the study area; Fig. 2.1a) will be given:

Sodalite opencasting 1 (dyke A, S 17°20.437', E 13°47.423')

In the abandoned opencasting (Ø: 40 m x 100 m) white anorthosite is transsected by a more or less E-W striking dyke of the sodalite-rich carbonatitic breccia dipping 30-35° to the S. The weathered dyke is exposed over a width of ~10 m and mainly composed of massive and coarse-grained ankeritic layers, alternating with narrow and fine-grained grey laminae, oriented sub-parallel to the dyke walls. Numerous sub-rounded and feldspar-rich xenoliths, partially replaced by sodalite, are scattered in the ankeritic zones giving the rock a speckled appearance. Anorthositic wallrock of the foot wall are tectonised whereas anorthosites of the hanging wall display a dyke-parallel foliation and a partial sodalitization of the elongated plagioclase crystals, most probably related to upward moving carbonatitic fluids. Metasomatic changes of the anorthositic mineralogy were observed in up to 1.5 m distance to the dyke contacts.

Sodalite opencasting 2a (dyke A, S 17°20.563', E 13°47.605' to S 17°20.599', E 13°47.614')

The disused sodalite digging (Ø: 140 m x 50 m) is in its main parts filled by mining debris. Due to the use of TNT during the early exploration activities, the outcropping carbonatite dyke is heavily shattered. The SE striking carbonatite dyke dips with angles between 35 to 70° to the SW and is dominated by brownish weathered, coarse-grained ankerite intermingled with large amounts of sub-rounded sodalite-rich wallrock fragments (~ 75 vol.%) with diameters of up to 1 m. Towards the hanging wall contacts, the carbonatite displays a discontinuous narrow foliation and asymmetric magmatic small scale folding. Anorthositic rocks in contact to the carbonatite display a dyke-parallel foliation.

Sodalite opencasting 2b (dyke A, S 17°20.553', E 13°47.685')

The abandoned opencasting (Ø: 20 m x 10 m) is an oval mine cavity in the centre of a 35-45° W to NW dipping dyke generated by blasting operations. The opened dyke forms the eastern extension of the carbonatite exposed in the sodalite opencastings (1) and (2). The outcropping carbonatite displays a banded texture, with sodalite being a major constituent (average amount: 45 vol.%).

Sodalite opencasting 3 and 4 (dyke A, S 17°20.790', E 13°47.689' - S 17°20.967', E 13°47.772')

In the disused opencastings (Ø: 10 m²) massive anorthosites and leucogabbroanorthosites are transected by a SSE striking dyke of the carbonatitic breccia dipping with angles between 30° and 50° to the SW. The 7-9.5 m thick dyke is characterized by an alternation of deep blue sodalite-rich laminae (ca. 55 vol.%) and brownish carbonate-rich layers, oriented sub-parallel to the intrusion contacts (Fig. 3.6 e; Fig. 3.20 c). The carbonatitic breccia exposed in sodalite opencasting 3 additionally exhibits a weak lineation (Fig. 3.20 d). Impersistent magmatic folding of the laminae dominates the centre parts of the dyke (Fig. 3.6 f; Fig. 3.20 a). In the bordering anorthositic rock units, no effects of a metasomatic alteration have been observed. The dyke is transected by a younger generation of almost silicate-free ferrocarbonatite veins, that dissect the magmatic foliation of the main carbonatite body.

Sodalite opencasting 5 (dyke B, S 17°21.492', E 13°47.509')

The small pit (5 m x 3 m) cuts a 8 m thick dyke of the sodalite-rich carbonatitic breccia that dips with 30-52° to the NE and transects the white anorthosite. In its central parts, the dyke is composed of a massive ankerite-rich zone that bears conspicuous light green and partly

translucent sodalite fragments (Fig. 3.8 a, b). The colour of these sodalite fragments may change from green to deep blue on a cm-scale (Fig. 3.8 a). Towards the dyke margins the massive ankerite zone is bordered by folded silicate- and carbonate-rich laminae.

Sodalite opencasting 6 a (dyke B, S 17°21.045', E 13°47.078')

The abandoned opencasting, situated ca. 120 m south-east of a former military fort, extends over an area of 15 m x 10 m. The mining operations concentrated on a 23 m thick sodalite-rich carbonatite dyke dipping 35-45° to SW with sodalite-accumulations, enriched as layers. In the strongly weathered carbonatite dyke anorthosite and fenite clasts have been observed, which are surrounded by the foliated carbonatite matrix. A contact aureole up to 5 m thick is developed in the neighbouring anorthosite, in which a contact parallel foliation is developed within the anorthosite.

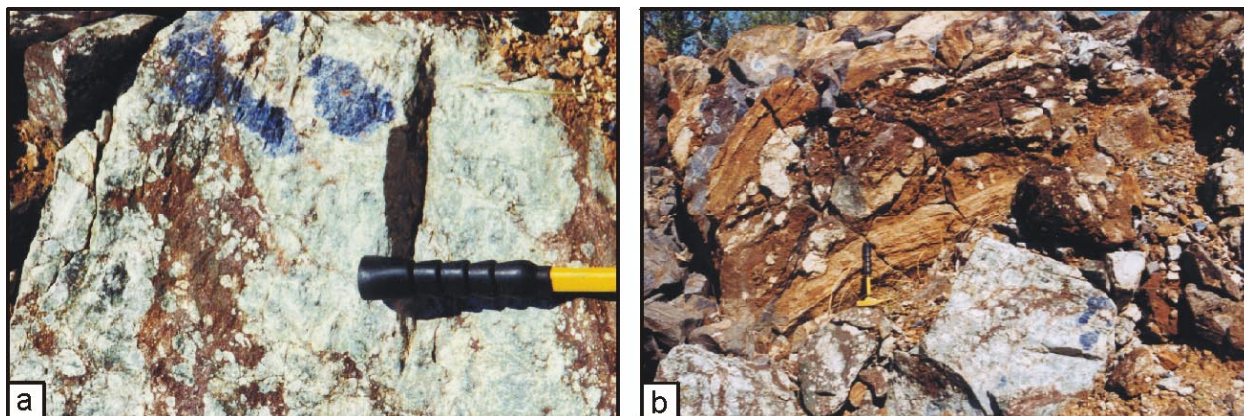


Fig. 3.8: Conspicuous light green coloured sodalite was observed at one locality (Sodalite opencasting 5, locality: S 17°21.492', E 13°47.509'). **a)** The colour of sodalite may change from green to deep blue on a cm-scale **b)** Both the green and the blue sodalite are concentrated in the central, ankerite-rich zones (brown) of a carbonatite dyke.

Sodalite opencasting 6 b (dyke B, S 17°21.006', E 13°47.010')

In this opencasting, the carbonatite dyke of the sodalite opencasting 6, as described above, is truncated at its surface. The crushed rock material has been used for the building-up of the nearby military fort.

Sodalite opencasting 7 (dyke B, S 17°20.890', E 13°46.774')

In the abandoned opencasting (120 m x 80 m) an up to 50 m thick carbonatite dyke is exposed dipping with angles between 45° to 80° to the SW. The dyke is characterized by the dominance

of strongly tectonised anorthositic and syenitic xenoliths, surrounded by layered carbonatite matrix (Fig. 3.1 d; 3.5 b; 3.6 b; 3.7 b; 3.10 d). Narrow fissures in the wallrock fragments are invaded by carbonatitic material; sodalite is a minor constituent (up to 10 vol.%) or even absent. The large diameter of the incorporated xenoliths (up to 2.3 m) and their high abundance in the carbonatite dyke argue against a long distance of transport by the carbonatitic melt, but rather suggest a passive emplacement of the carbonatite within previously tectonised shear-zones. A conspicuous feature of opencasting 7 is the exposure of albite-biotite-magnetite-carbonate rock remnants and schlieren within the carbonatitic breccia (Fig. 3.11 a, b), suggesting that its intrusion was synchronous with or even predated the carbonatite emplacement.

Sodalite opencasting 8 (dyke A, S 17°20.470', E 13°47.000')

The open mine (50 m x 30 m) is the only opencasting that is presently mined. It is situated in the central parts of a 26-30 m thick dyke of the sodalite-rich carbonatitic breccia (Fig. 3.9 a), dipping approximately 45° to SW. Sodalite accumulations are mined bench-like as dimension stones of 45m³ in a first step, with the mining floor situated approximately 18 m below the surface level (Fig. 3.9 b, c). For the export, these blocks are subsequently crushed to smaller blocks of 1 x 1 x 2 m.

In the central part of the carbonatite dyke sodalite is enriched in economic dimensions (up to 85 vol.%), replacing feldspar-rich xenoliths of up to 1.5 m in diameter surrounded by or intermingled with an ankerite-rich matrix (3.7 e; Fig. 3.9 d). Towards the dyke margins the banded carbonatite variety dominates. The carbonatitic breccia is transected by a younger generation of almost silicate-free ferrocarnatite veins and dykes (Fig. 3.12 a-d) and encloses rare and irregularly distributed ultramafic xenoliths (UMX). Anorthosites in contact to the main carbonatite dyke, exposed in the northern part of the opencasting, display a dyke-parallel foliation with the elongated plagioclase crystals being partly replaced by sodalite (Fig. 3.2 d). The changing modes of the anorthosite may be attributed to the interaction of hot carbonatitic fluids with the bordering anorthosite.

In the eastern part of the opencasting a conspicuous WNW striking dark coloured and sub-vertical dipping dyke of 1 m width is exposed that transects the carbonatitic breccia (Fig. 3.11 c, d). The medium to fine-grained rock is characterized by a massive texture with albite, biotite, ankerite and magnetite being the main constituents. It is invaded by coarse-grained schlieren of the younger ferrocarnatite generation. In the central part of the dyke well-developed magmatic flow textures can be observed. The dyke as well as the bordering lithologies have been sampled in order to investigate their oxide and sulphide mineralogy. The results of the

investigation have been described by von Seckendorff & Drüppel (1999) and von Seckendorff et al. (2000).

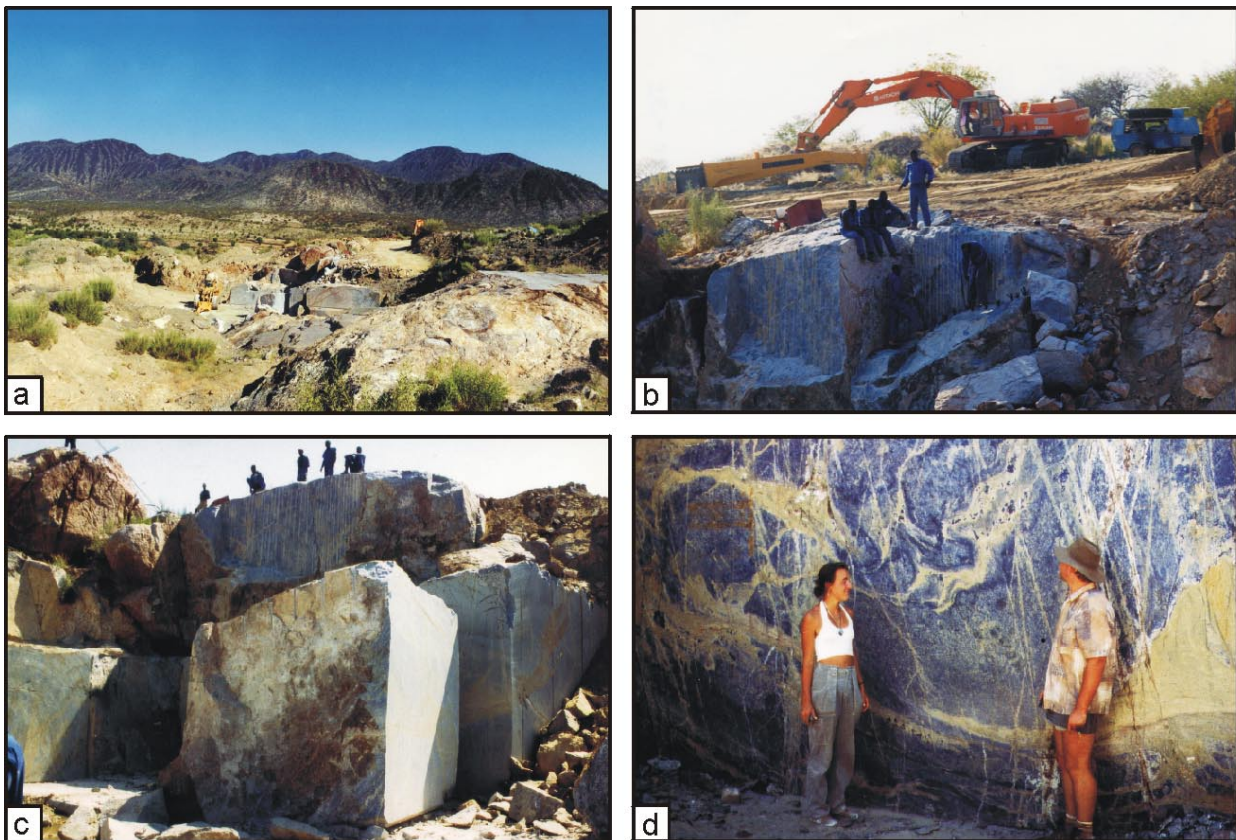


Fig. 3.9: Photographs of sodalite opencasting 8, which is the only opencasting that is presently mined (Locality: S 17°20.470', E 13°47.000'). **a)** The mine is situated in the central parts of a large carbonatite dyke, crosscutting leucogabbroites of the dark anorthosite suite. **b)** and **c)** Sodalite-rich lithologies are mined bench-like, with the sizes of the dimension stone blocks reaching up to 45 m³ in a first step. **d)** Sodalite is enriched in the central parts of the carbonatite dyke. In these zones, sodalite (blue) replaces feldspar-rich xenoliths of up to 1.5 m in diameter, that are in turn surrounded by and intermingled with ankerite-rich zones (yellowish).

3.3.6.1.3 Massive carbonatitic breccia [CB,m]

Twelve predominantly SE trending dykes of the massive variety of the carbonatitic breccia occur in the area, with the single dykes being exposed over a narrow width of 0.5-15 m and a length of 70-450 m. In outcrop, the fine-grained to very fine-grained massive carbonatitic breccia is characterized by a dark grey to black or brownish colour and a massive texture (Fig. 3.10 a, b). Due to the small grain sizes individual minerals cannot be identified on a macroscopic scale, however, the use of 5% HCl provides evidence for the presence of a certain amount of carbonate minerals. In places, the massive carbonatitic breccia contains fragmented and pink-coloured

syenite xenoliths with diameters of 2 mm to 8 cm whereas anorthosite- and sodalite fragments have never been observed on a macroscopic scale.

Narrow bands of the massive carbonatitic breccia may also occur interlayered with the banded carbonatitic breccia (Fig 3.10 c). The massive layers display sharp boundaries parallel to the dyke/wallrock interfaces, thus suggesting that the small grain sizes of the massive carbonatitic breccia are generated by localised post-emplacement shearing and mylonitisation rather than being a primary magmatic feature of this rock type. This interpretation is constrained by the localised occurrence of massive and very fine-grained carbonatite lithologies in small-scaled shear zones (Fig. 3.10 d) of the carbonatitic breccia.

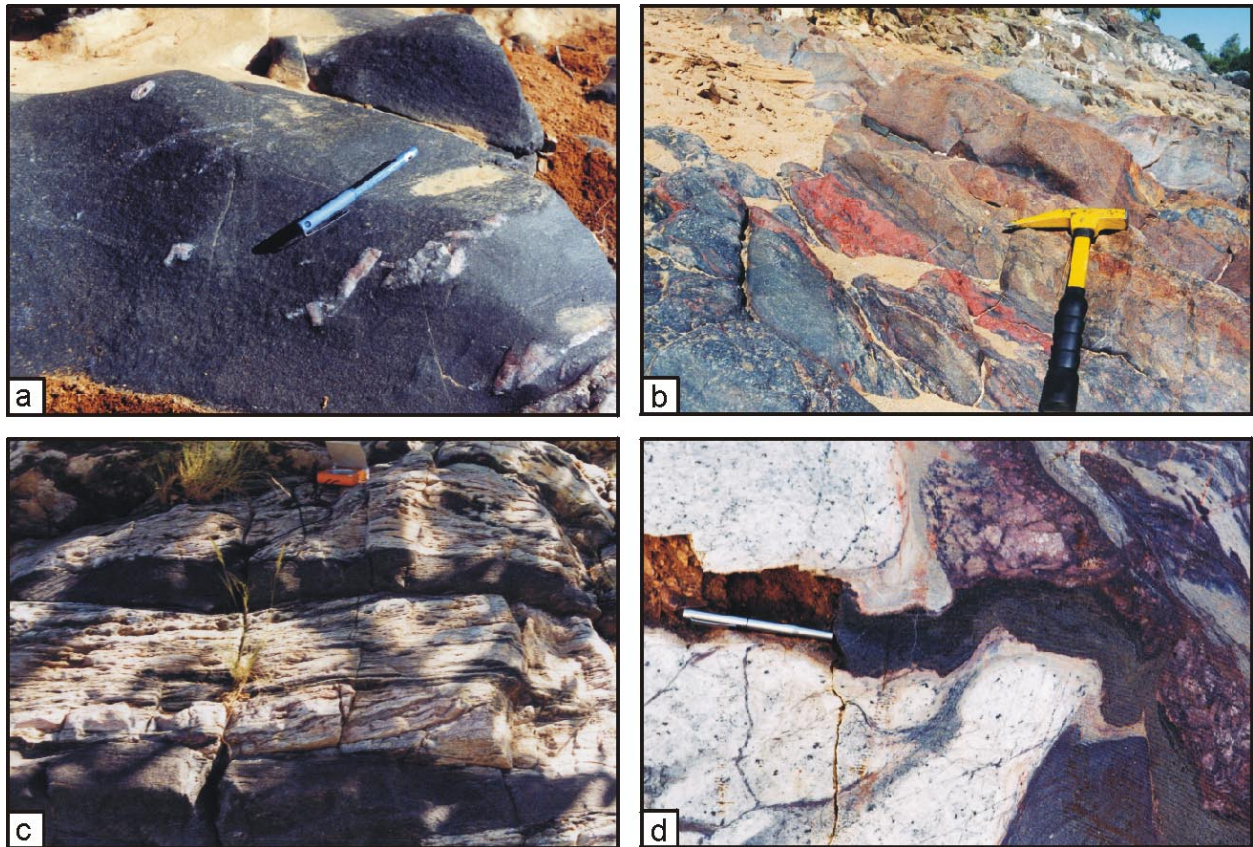


Fig. 3.10: *a)* On a macroscopic scale, the fine-grained massive carbonatitic breccia is generally characterized by a dark grey to black colour and a homogeneous texture, with rare reddish syenite-fragments being observed locally (Locality: S 17°20.066', E 13°46.524'). *b)* Dykes of the massive carbonatitic breccia, displaying alternations of massive brown, reddish and black coloured bands, most probably represent very fine-grained counterparts of the layered carbonatitic breccia (Locality: S 17°20.147', E 13°46.662'). *c)* Layers of the massive carbonatitic breccia (dark grey) may also be intercalated with the layered carbonatitic breccia (light grey; Locality: S 17°20.147', E 13°46.662') or *d)* occur within small scaled shear zones within brecciated anorthosite (light grey) and syenite (pink; Sodalite opencasting 7, locality: S 17°20.890', E 13°46.774').

3.3.6.2 K-feldspar-biotite-ilmenite-calcite rock

Rare irregular bodies of massive K-feldspar-biotite-ilmenite-calcite rocks (L) of up to 4 m in diameter have been observed in several of the larger dykes of both the banded and the sodalite-rich carbonatitic breccia (Fig. 3.11 a, b). Regarding their texture and macroscopic appearance, these massive, dark coloured and medium-grained rocks strongly resemble both, the albite-biotite-rich fenite zones of the carbonatitic breccia and the so-called "black dyke" (Fig. 3.11 c, d), which, however, never contain K-feldspar. Thus, the petrogenesis of the lamprophyre-like rocks remained uncertain.

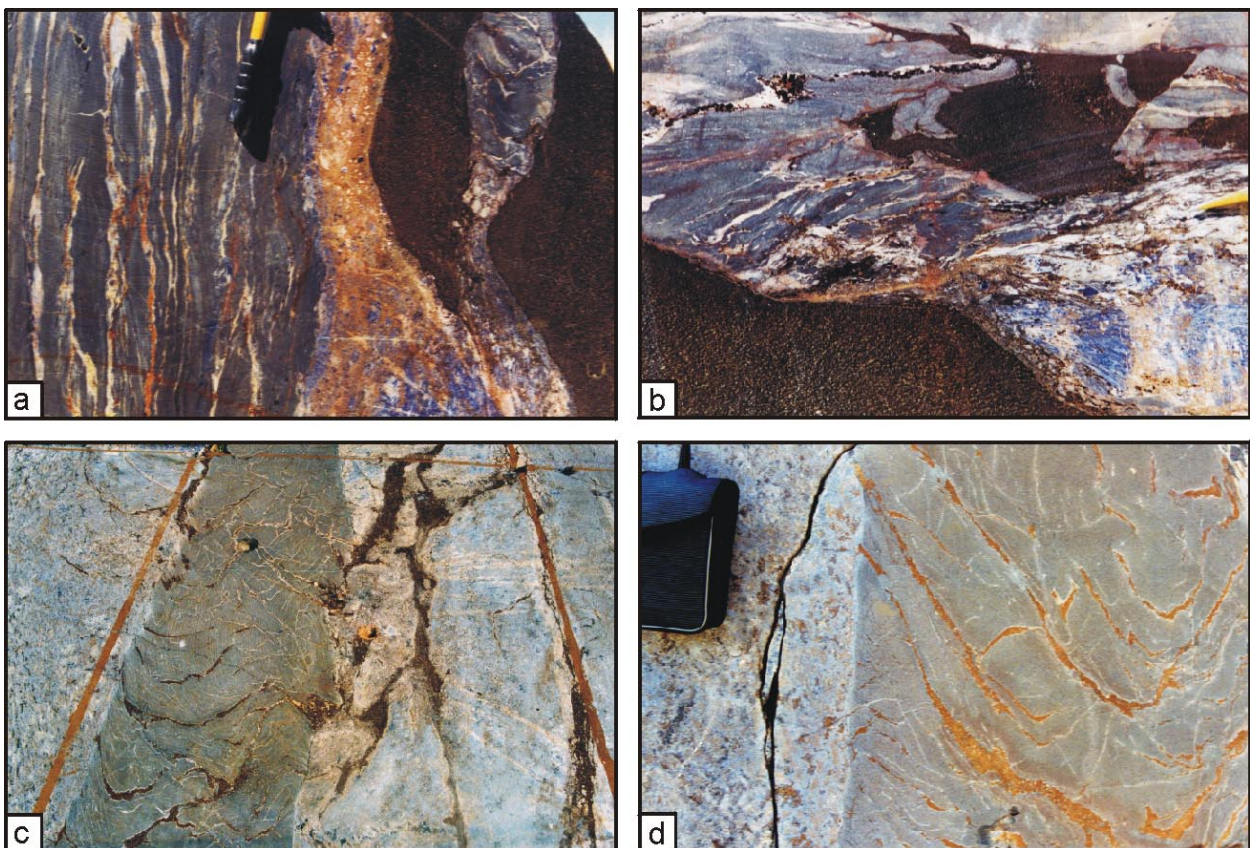


Fig. 3.11: *a*) and *b*) Remnants of the massive, black K-feldspar-biotite-ilmenite-calcite rock (black) are present within a dyke of the sodalite-rich carbonatitic breccia (layered, with alternating grey albite-biotite-rich, blue sodalite-rich and brown ankerite rich schlieren), thus suggesting that their emplacement predates the intrusion of the carbonatites. (Sodalite opencasting 7, locality: S 17°20.880', E 13°46.774'). *c*) and *d*) A grey dyke ("black dyke"), mainly composed of albite, biotite, magnetite, and ankerite, transsects the sodalite-rich carbonatitic breccia (light grey to bluish). This dyke is in turn invaded by younger ferrocyanite veins (brown; Sodalite opencasting 8, locality: S 17°20.417', E 13°47.000').

3.3.6.3 Ferrocarbonatite

Both, the main carbonatite dykes and the lamprophyres are transected by small veins and stringers of a second generation of almost silicate-free ferrocarbonatite intrusions, up to 1.5 m in width, which may be present in strongly varying proportions (Fig. 3.11 c, d; Fig. 3.12 a, b). The medium to coarse-grained magnetite-ankerite rocks are characterized by a brownish surface colour and a massive texture. Sub-rounded fragments of albite- and sodalite-rich xenoliths may occur locally, concentrated in the central parts of the veins (Fig. 3.12 c), whereas trails of euhedral magnetite grains mark the interfaces between the ferrocarbonatite veins and their

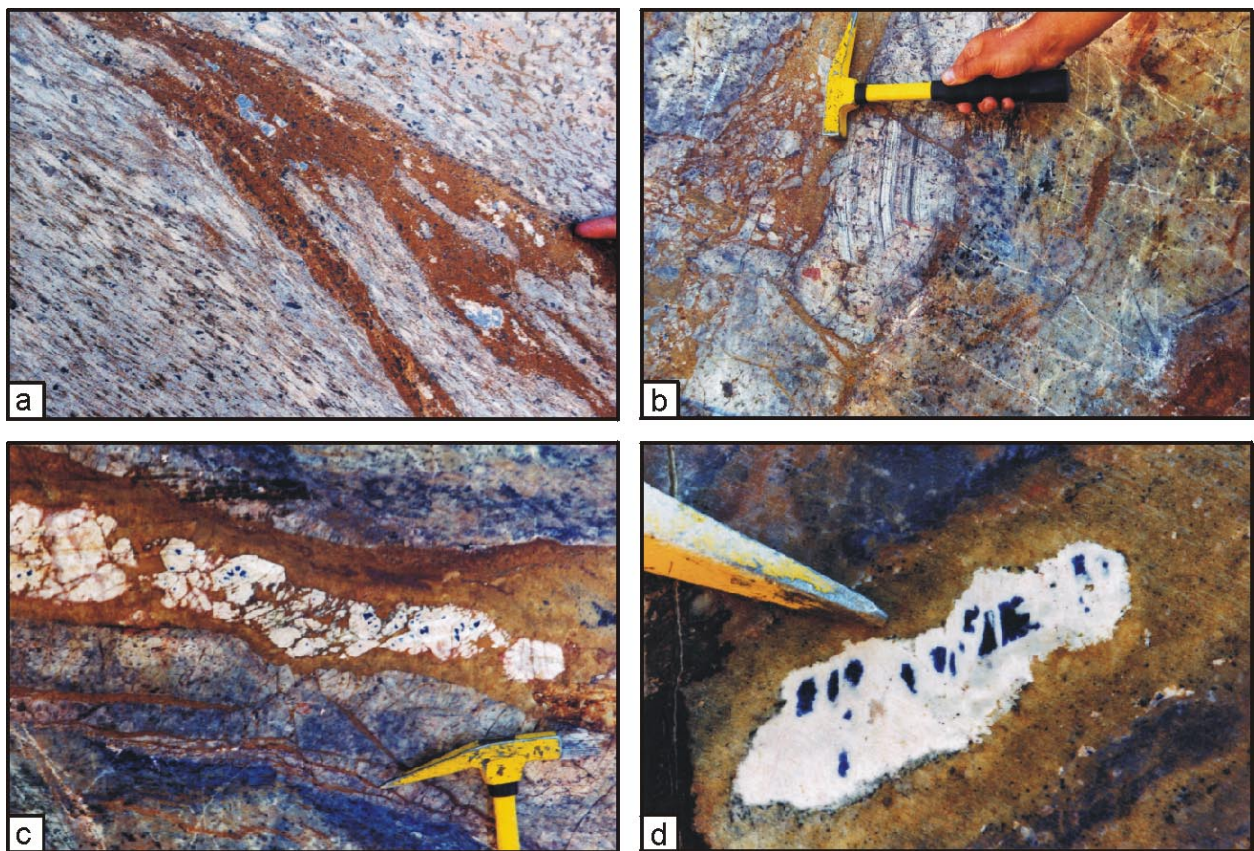


Fig. 3.12: Photographs of the late-stage ferrocarbonatite veins, exposed in the active opencasting 8 (Locality: S 17°20.470', E 13°47.000') *a)* Narrow, brown ferrocarbonatite veins and schlieren transsect and/or *b)* cement angular fragments of the older carbonatitic breccia (light grey to bluish). *c)* The ferrocarbonatite veins (brown) suffered minor wallrock contamination, when compared to the carbonatitic breccia (grey, pink, bluish). Xenoliths (white and blue) are generally concentrated in the central parts of the veins. *d)* The ferrocarbonatite (brown) encloses previously fenitized feldspar fragments (white to blue) but caused no metasomatic alteration of the wallrock by itself. Trails of subhedral magnetite crystals (black) mark the contacts between the ferrocarbonatite veins and the carbonatitic breccia.

wallrocks (Fig. 3.12 d). In contrast to the carbonatitic breccia, no effects of a metasomatic alteration of the bordering rocks are visible on a macroscopic scale.

3.3.7 Dolerite [Dol]

Five predominantly SE striking dolerite dykes transect the syenites, carbonatites and the anorthositic rocks. The sub-volcanic rocks, exposed over a width ranging from 3 m to 70 m and a length of up to 3.4 km, dominate in the eastern part of the study area. In natural outcrops the rocks are characterized by thin brownish weathering crusts and spheroidal weathering. Outcrops of solid bedrock are rare, mostly the fragments of bedrock are scattered as sub-rounded to angular boulders with diameters continuously ranging from 20 cm to 2.5 m (Fig. 3.13 a).

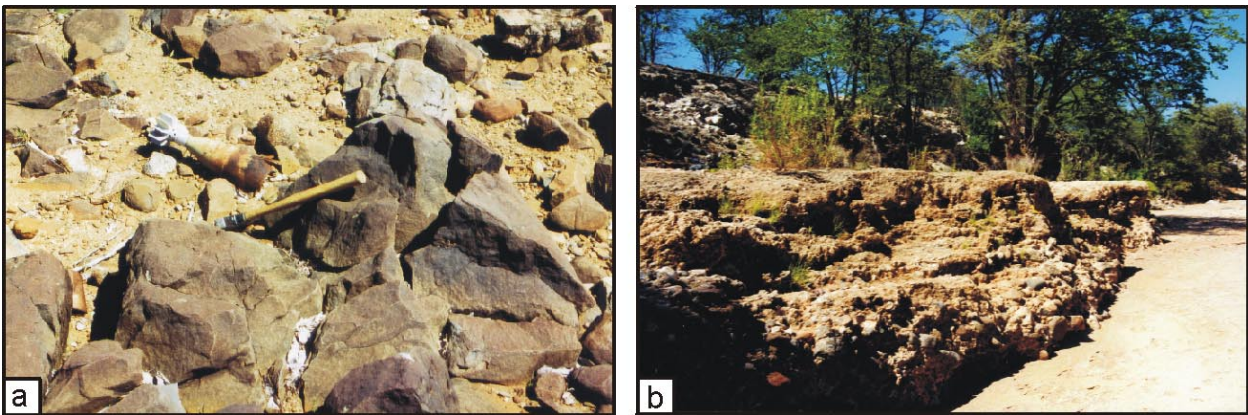


Fig. 3.13: *a*) Dolerite dykes are commonly exposed as accumulations of scattered angular to sub-rounded, brownish boulders (Locality: S 17°20.520', E 13°47.380'). *b*) Fluvial terrace deposits border the Ondoto riverbed. The carbonate-cemented immature conglomerate is mainly composed of well-rounded quartzite pebbles and gravel, with sub-rounded to sub-angular quartz, anorthosite and carbonatite fragments being minor constituents of the reversely graded terrace (Locality: S 17°21.060', E 13°46.529').

3.3.8 Trachyte [Tr] and Andesite [An]

In the northern part of the study area, a north-east trending carbonate-rich trachyte dyke is exposed over 90 m in length and 3-15 m in width within the white anorthosite. The trachyte differs from all other rock units investigated. It is characterized by spheroidal accumulation of reddish K-feldspar crystals (~10 vol.%) with diameters of up to 4 cm and euhedral biotite phenocrysts (~5 vol.%) set in a fine-grained dark-grey matrix mainly composed of carbonate, K-

feldspar, biotite, muscovite and euhedral magnetite. Due to the lack of exposed contacts between the trachyte and the carbonatites, no temporal succession could be established.

Also exposed in the same area is an E-W striking and 3-8 m thick andesite dyke with a length of 50 m. The grey andesite is characterized by narrow, reddish weathering surfaces. Porphyritic plagioclase (An₁₀₋₁₅), up to 2 mm in length, without a preferred orientation, is the main mineral present (~60-70 vol.%) accompanied by minor biotite and amphibole as well as accessory K-feldspar, magnetite and clinopyroxene. Since the andesite is solely exposed within the white anorthosite its genetic relation to the other rock units of the study area remains uncertain.

3.3.9 Sedimentary rocks

3.3.9.1 Unconsolidated deposits of fluvial terraces [Qtz,p]

Unconsolidated relics of fluvial terraces flank the ephemeral stream Ondoto. The variably eroded quartzite pebble accumulations are exposed on different altitudes above the actual river floor and thus allow the determination of their relative temporal succession.

The youngest generation of unconsolidated fluvial terrace deposits is exposed at an altitude of 775-785 m above sea-level and is mainly composed of sub-rounded quartzite pebbles (average: 80 %) with average diameters of 8 cm which mostly exhibit a reddish to brownish weathering surface. In addition, variable amounts of subangular quartz fragments, up to 5 cm in diameter, as well as fragments of epidote rocks (Ø: 1-4 cm), anorthosite (Ø: 0.2-0.5 m) and carbonatite (Ø: 0.1-0.4 m) may occur (Fig. 3.13 b).

Older fluvial terrace deposits occur at altitudes of 790-800 m and 805-818 m a.s.l., respectively. They differ from the younger terrace deposits by their higher amounts and larger average diameters of sub-rounded to subangular quartzite pebbles (up to 95 %). In contrast, small angular fragments of quartz, epidote rocks, anorthosite and carbonatite are rare. Single quartzite pebbles, scattered on the steep ridges of the Zebra Mountains, have been observed in altitudes of up to 915 m above sea-level.

In contrast to the epidote rocks, anorthosites and carbonatites, which are common rock units of the study area, and the quartz-rich pegmatites which occur in close neighbourhood to the sodalite mine, the quartzites are allochthonous rock material. The nearest occurrence of

quartzites of the Nosib Group, Damara supergroup, is actually situated approximately 40 km south-west of the study area in the headwater area of the stream Ondoto. The changes in composition and sizes of the three main fluvial terrace generations strongly suggest that the sediments of the Nosib Group were continuously eroded during terrace formation with the quartzite catchment area being displaced in further distance from the studied area. In addition, sedimentary deposits of the Nosib Group occur in the north-eastern part of the Zebra Mountains and thus strongly suggest that the whole anorthosite massif was once covered by the Neoproterozoic sediments.

3.3.9.2 Carbonate-cemented deposits of fluvial terraces [Cgl]

The youngest fluvial terrace generation, exposed at the margins of the Ondoto riverbed at an altitude of 743 to 752 m above sea level, is a carbonate-cemented immature conglomerate mainly composed of well-rounded quartzite pebbles and gravel (\varnothing : 1-15 cm). Sub-rounded to sub-angular quartz- (\varnothing : 0.2-4 cm) and anorthosite (\varnothing : 20-40 cm) fragments as well as carbonatite anguclasts of up to 0.5 m in length are minor constituents (20-30%). The reversely graded terrace has an average thickness of 2 m.

3.3.9.3 River floor deposits [All]

Both, the deposits of the ephemeral stream Ondoto and those of the numerous smaller blind creeks are referred to as river floor deposits. The strath alluvial valleys are characterized by a mostly plane river floor with strongly varying width depending on the stream-worn lithologies and the orientation of the stream. Thus, the NE trending Ondoto river floor, mostly incising the white anorthosite, is exposed over an average width of 300 m, whereas the width of the SE trending creek beds, crossing the weathering-resistant dark anorthosites, ranges between 10-230 m.

The river floor of the river Ondoto is covered by quartz-rich and poorly sorted fine to coarse sand together with minor sub-angular anorthosite, epidote and carbonatite fragments derived from the surrounding rock units. In clear contrast, the river floor deposits of the blind creeks are dominated by angular fragments of the closely neighbouring rocks.

3.3.9.4 Anorthositic talus deposits

Anorthositic talus deposits cover the steep mountains ridges in the north-western part of the study area. The spheroidal anorthosite boulders with diameters of up to 10 m cover the underlying dark anorthosite. The lack of hillwashes argues against a down-slope transport of the anorthositic rock material but rather suggests an in situ formation of the talus deposits. The radial drainage pattern of the Zebra Mountains causes the channelled eluviation of soil and thus causes a belt-like distribution of the vegetation in regions of undisturbed soil formation.

3.3.9.5 Mining waste piles

Waste piles occur in the vicinity of the numerous abandoned and the active opencastings, testifying to the continuous pressure-production history. In addition waste pile deposits have been used as upbuilding for the settlement Orotumba.

3.4 Economic potential

3.4.1 Sodalite deposits

The sodalite deposits of Swartbooisdrif are mined since 1969 even though, recently, the turnover of sodalite as a decorative stone is not without its problems. Because of the following reasons only one of several opencastings (sodalite opencasting 8) is actually mined:

1) Due to the quarry blasting during the early exploration activities, the sodalite-bearing lithologies are heavily ruptured. Narrow fissures and cracks, mostly invisible on a macroscopic scale, pass through all rock units exposed within the various opencastings. When the sodalite-bearing lithologies are extracted, the rock pressure of the enclosing rock is lacking and the cracks thus propagate fast until the whole block is penetrated and, as a result, disaggregates. The speed of fissuration is even accelerated by day and night changes of temperature, precipitous drops in temperature and chemical weathering.

2) The external use of sodalite as well as its use as wall coverings of kitchens or bathrooms is not practical since sodalite as a feldspathoid may be attacked by acid rain and weak acids as commonly contained in cleaning agents. As a result, the sodalite exhibits a pale blue tint. However, the carbonatitic breccia is not solely composed of sodalite but additionally contains variable amounts of ankerite. Even though ankerite is characterized by a bright whitish colour on fresh polished surfaces it is oxidised under atmospheric conditions after a certain time interval and thus changes its surface colour from white into brown.

3) The vast majority of superficial sodalite deposits have already been exploited during the long-lasting pressure-production history. Thus the exploration activity has to be expanded to deeper, not exposed levels of the carbonatite dyke. However, the sodalite distribution within the dykes of the carbonatitic breccia is quite heterogeneous, as has been mentioned before. In addition, the trends of the carbonatite dykes themselves are quite variable including structural features as dying out, branching and curving. Following this the transfer of the mining activity into greater depths bears risks.

As a conclusion the continuation of the exploration of the sodalite-rich lithologies as dimension stones is not longer profitable regarding the high costs of mining, transport, export and processing.

3.4.2 Leucotroctolites

In the Angolan part of the KIC medium-grained varieties of the black coloured leucotroctolites of the dark anorthosite suite, commonly displaying iridescence of their plagioclase crystals, are mined as ornamental stone, termed *Angola Nero*. In the Namibian part of the KIC, the dominance of the white anorthosite suite as well as the rugged topography of the Zebra Mountains argue against exploration activities concentrating on the dark anorthosite. However, the leucotroctolites could be exploited by the sodalite mining company as a by-product without causing considerable additional costs.

3.5 Tectonics

3.5.1 Tectonic overview

Following Trompette (1994), the study area is situated near the south-western margin of the Proterozoic Congo Craton, which, particularly in its central parts, is covered by Cenozoic to Quaternary sediments. Towards the north, south and west, the Congo Craton is bordered by four major mobile belts, i.e. the Oubanguide fold belt in the north, the Damara fold belt in the south, the Kaoko belt in the south-west and the West-Congo fold belt in the west, all of them being formed during the Panafrican orogeny (Trompette, 1994). Towards the east, the Congo Craton is limited by the Mesoproterozoic Kibara fold belt. Archaic to Palaeoproterozoic basement rocks are mainly exposed in the marginal zones of the Congo Craton and are subdivided into four major sub-zones (Trompette, 1994):

- (1) the Cameroon-Gabon-Congo block in the north-west,
- (2) the NE-Zaire block in the north-east,
- (3) the Kasai block in the eastern centre and
- (4) the Angolan block in the south-west.

Following this classification, the study area together with the Mesoproterozoic KIC and the metamorphic basement rocks of the EC form part of the Proterozoic Angolan block. It can thus be concluded that the EC, including the studied area, was stable part of the Angolan block during Pan-African times and hence records the pre-Pan-African crustal evolution.

3.5.1.1 The anorthosite problem

As yet, no successful model has been established for the precise tectonic setting of the large-scaled Proterozoic massif-type anorthosites, even though it is generally accepted that most of the yet known anorthosite bodies are emplaced in extensional environments (Ashwal, 1993). By now, a continental rift analogy is the preferred tectonic scenario which, however, has to differ significantly from modern-day examples by both its topology and timing, since it has to account for

- (1) the ponding of large amounts of basaltic melts in the lower crust,
- (2) an intrusion interval of several hundred million years,
- (3) the linearity of most anorthosite massifs,

- (4) the chemical bimodality and
- (5) the apparent restriction of massif type anorthosite magmatism to the Proterozoic.

A plausible model has been presented by Hoffman (1989) who suggested that a stationary supercontinent (Laurentia) was assembled during the early Proterozoic which acted as a thermal blanket, leading to a thermal insulation of the mantle and thus producing a mantle "superswell". It has to be tested, however, if a similar model may also account for the anorthosite magmatism of the southern hemisphere.

3.5.1.2 The structural setting of carbonatites

Carbonatites, in general, are widely believed to be emplaced in the stable central parts of continental areas. It has been demonstrated, however, that carbonatite magmatism may also be linked to orogenic activity along plate margins. The following tectonic models were established for carbonatite suites (see Woolley, 1989, for a review):

(1) *Rift valleys and lithosphere doming*: Nearly half of the yet known occurrences are emplaced within or nearby graben structures, as for example the Kaiserstuhl, Germany, and the carbonatites of the East African rift. It has to be mentioned, however, that particularly the carbonatite complexes of Southern Africa, including the Cretaceous carbonatites of Namibia and Angola, are apparently linked to structural domes, with much of the faulting and rifting being a response to the doming.

(2) *Major lineaments*: Intrusions of carbonatites may be emplaced along major lineaments ranging from ~10 km to several 1,000 km in length, as for example the Kapuskasing group, Canada, the mid-Zambezi-Luangwa lineament, East Africa, and the intrusion lines of Southern Africa, including Angola, Namibia and South Africa. Such lineaments, lying along and above deep seated fracture zones, may persist over long periods of time and even predate the carbonatite magmatism.

(3) *Orogenic activity*: Carbonatite magmatism may also be correlated with orogenic activity, with the carbonatites being emplaced in up to several 100 km wide zones adjacent to orogenic belts, as for example the carbonatites of the North Atlantic area (Vertainen & Woolley, 1974).

Until now, the most successful tectonic model for the carbonatites of the Swartbooisdrif area is their emplacement along major lineaments (model 2) which were already active before their emplacement, as is supported by the coincidence of the orientation of faults intruded by carbonatites with those used for the ascent of the older dark anorthosite melts. However, the

exact time span of anorthosite magmatism is yet unknown and may thus extend down to younger ages. Following this, the faulting and subsequent carbonatite emplacement may also be a response to structural doming induced by the intrusion of large masses of anorthositic melts, as is inferred by model (1).

3.5.2 Structural investigations of the mapped sheet and related areas

If possible, the structural trends of all rock units exposed in the study area have been investigated in some detail in order to constrain the temporal and spatial relationships between magmatism and faulting. Structural investigations on anorthosite and granitoids of other parts of the Namibian KIC as well as Landsat interpretations have been included in this study.

3.5.2.1 The Zebra Mountain massif

The KIC intruded as a generally N-S elongated intrusion in SW Angola, whereas it is exposed as a more or less E-W trending body in Namibia. This sub-zone, which, in clear contrast to the Angolan part of the KIC, is mainly composed of massive white anorthosite, most probably represents an individual anorthosite intrusion. In the central part of this sub-zone, the white anorthosite is transected by predominantly ENE trending dark anorthosite sheets of up to 10 km in width, which are responsible for the strong positive relief of the so-called Zebra Mountains (Fig. 3.14 a, b). A similar orientation is displayed by a broadly N75E trending granite dyke exposed near the southern margin of the KIC.

The Zebra Mountain massif extends over an area of approximately 1080 km². Towards the north-west, it is terminated by a N40E to N55E strike-slip fault bundle, up to 8 km in width, along which the dark anorthosite is heavily tectonised (Fig. 3.15). This fault bundle, termed *Serpa-Pinto-Lineament*, extends into Angola, where it is marked by intrusion-lines of granite, separating the northern and southern part of the KIC, but is also apparent in the basement rocks of the EC that border the KIC in the west. Thus, the Serpa-Pinto lineament can be interpreted as an old structure, that already existed before the dark anorthosite and granite emplacement. In the north-east, the Zebra Mountain massif is bordered by the S60E trending, fault-related river valley

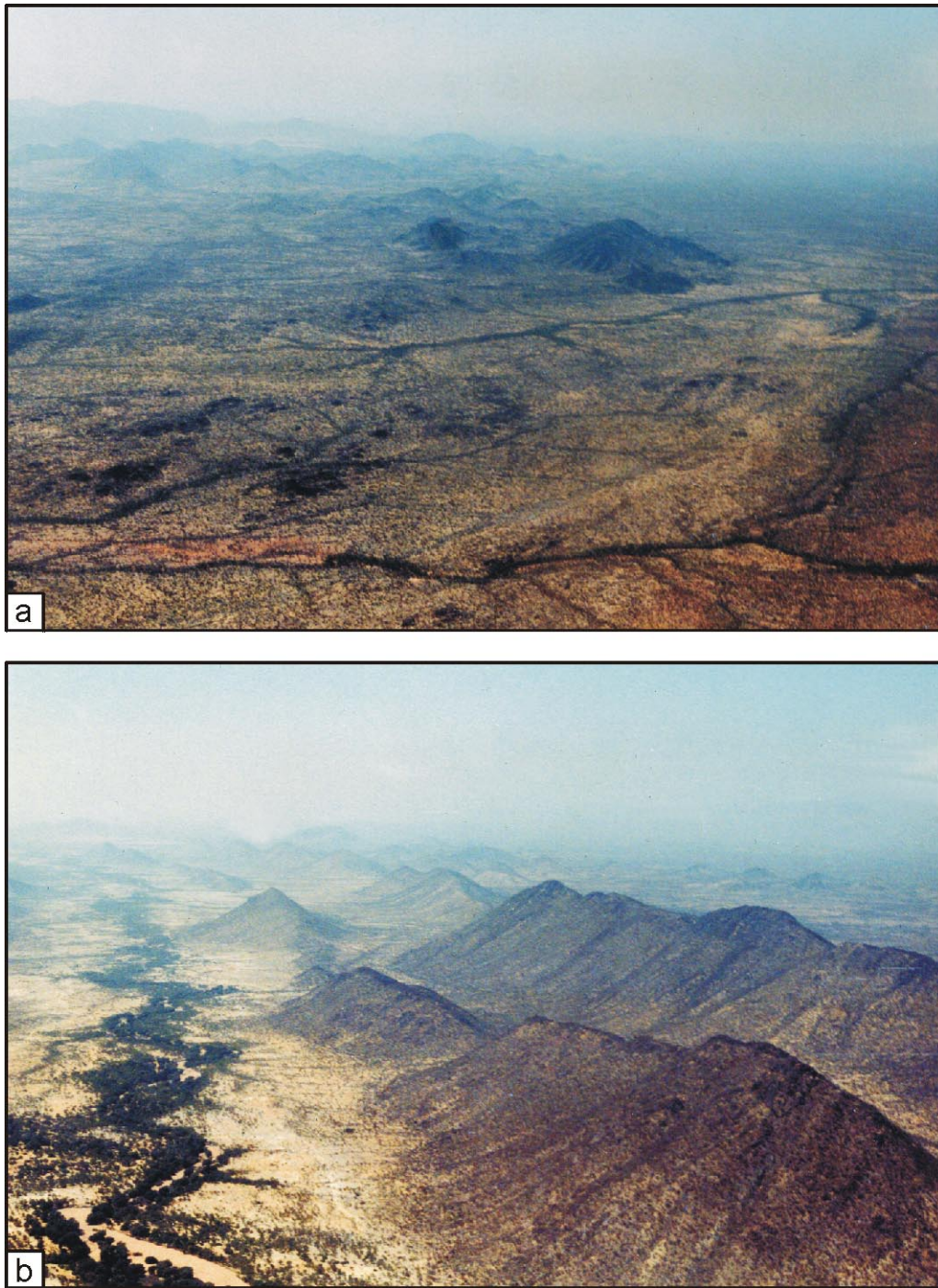


Fig. 3.14: Photography of the Namibian KIC, as observed from a Cessna plane *a)* North of the Serpa-Pinto lineament, the Namibian part of the KIC is dominated by the white anorthosite suite. Due to its low weathering resistance, the deeply eroded white anorthosite generally forms low-lying, undulating planes. Rare plugs of dark anorthosite are exposed as monadrocks (Locality: S 17°04.400', E 13°13.380', SE-direction). *b)* In clear contrast, the steep ridges of the dark anorthosite suite dominate the Zebra Mountain massif south of the Serpa-Pinto lineament. These rocks intruded the white anorthosite as generally E-W trending sheets (Locality: S 17°21.010', E 13°21.129', W-direction).

of the Kunene, whereas the tectonic contacts between the white anorthosite and the basement mark the southern termination of the Zebra Mountains. The dark anorthosite sheets reach their maximum width in the northern part of the Zebra Mountains as N65E to N75E trending ridges and smaller, oval shaped plutons. The thickness of the sheets successively narrows from north towards the southern margin of the KIC, where the dark anorthosite forms N70E to N85E trending intrusion lines, up to 1 km in width and dipping 25-40° towards the SSE. A conspicuous feature of the Zebra Mountains is the curving of the dark anorthosite sheets in the south-eastern

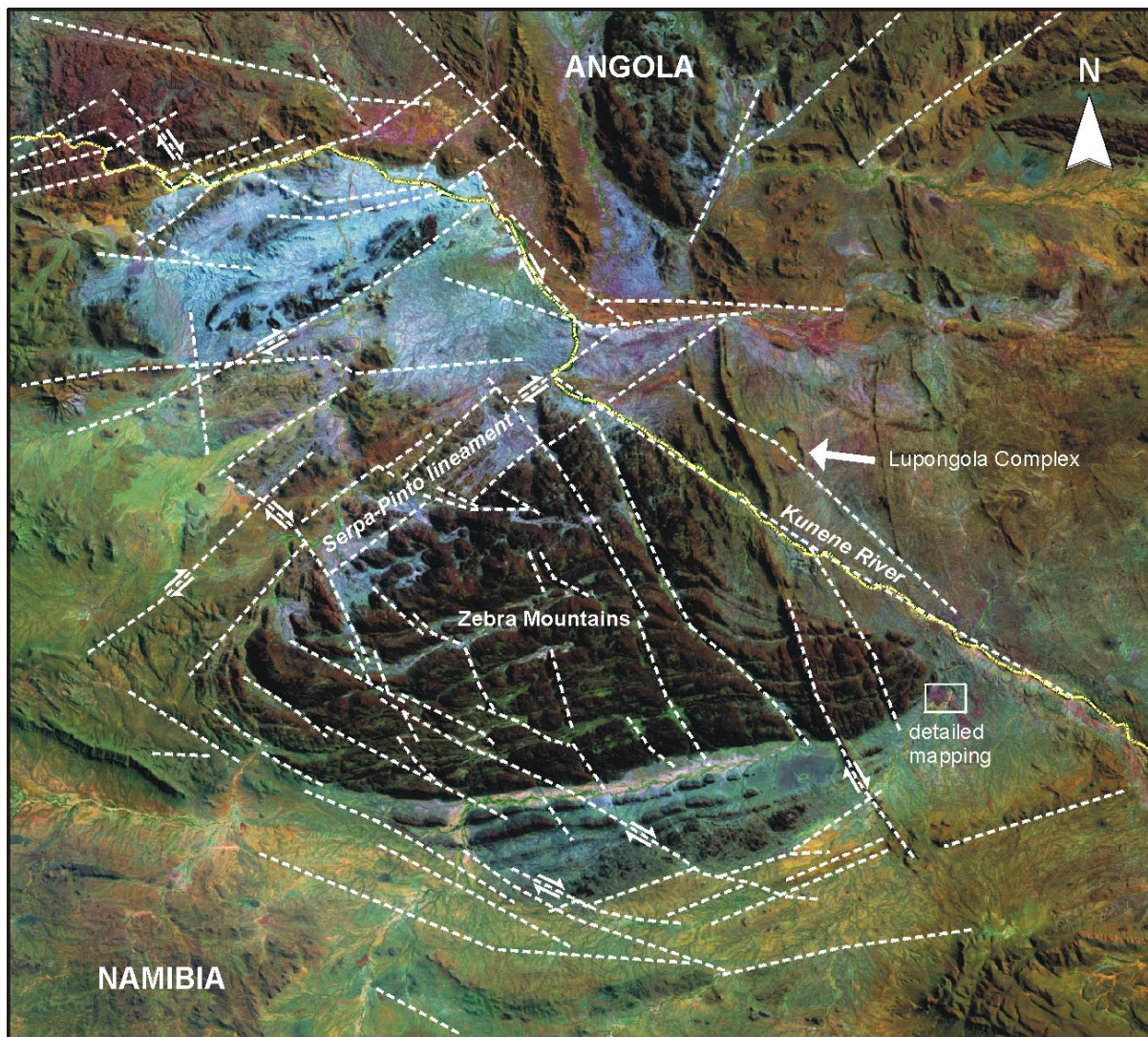


Fig. 3.15: Landsat image of the Namibian part of the KIC. Major lineaments and fault bundles are marked. Subset of Landsat TM Scene 181-72 (RGB: 7-4-1).

and south-western parts of the massif, where the intrusion-lines strongly narrow towards their tips and change their strike to run sub-parallel to the basement contacts.

The overall sheet-like shape of the Zebra Mountain massif makes a dyke-like ascent mechanism appealing, however, several features argue against this process: (1) the sheet margins are more curvilinear than is typical of dykes, (2) particularly in the central and marginal parts, the sheets display geometries intermediate between those of dykes and diapirs, (3) no faults extend in front of the narrow sheet tips. It is thus suggested, that the Namibian part of the KIC is constructed of at least two diapiric pulses, with the dark anorthosite crystal mushes being emplaced along pre-heated pathways. Following this, the sheet-like shape of the massif is mainly controlled by the internal structure and general geometry of the Namibian part of the KIC. In contrast, the overall shape of the E-W trending Namibian part of the KIC, including the white anorthosite, may be influenced by pre-existing zones of structural weakness, inherited during a Palaeoproterozoic collisional event, that affected the south-western margin of the Angolan block. As yet, the most plausible three-dimensional expression of the Zebra Mountain massif is an ENE elongated dome-like structure, as has already been proposed by Menge (1996). However, some sort of NNW extension must have occurred in response to the doming as is evident from (1) the general ENE trending orientation of both the dark anorthosite ridges and the elongated granite intrusion at the southern margin of the KIC (Fig. 3.16 a and b) and (2) the dextral shear sense of the NE trending Serpa-Pinto lineament, which was oriented oblique to the proposed 1,380 Ma net opening (Fig. 3.16 c).

After its emplacement, the Zebra Mountain massif was subjected to extensive dextral strike-slip faulting, that extends into the basement rocks of the EC in the south (Fig. 3.12). The shear zones trend S70E in the western part of the Zebra mountains but continuously change their strike towards S25E in the east. The strike-slip faults particularly displace the Serpa-Pinto lineament, the white anorthosite and the granite intrusion. The horizontal displacement locally reaches 3 km, giving the southern margin of the KIC a step-like appearance. In clear contrast, the dark anorthosite sheets are not displaced abruptly along the shear zones but curve in the direction of motion of the opposite block, giving the lineaments a drag fault appearance. The distortion of the sheets strongly suggests that the dark anorthosite, in clear contrast to the white anorthosite, still behaved in a ductile fashion during the displacement event, thus implying that the formation of the dextral shear zones preceded the complete crystallization of the dark anorthosite. It can thus be concluded that during late stages of cooling, the crystallising dark anorthosite sheets within the KIC became capable of transmitting stress. It may be possible, that the faulting reflects a regional stress field, characterized by an approximately E-W oriented maximum

horizontal extension, which became prominent as the repeated injection of anorthositic melt came to a standstill. A regional stress-field like this would be in good accordance with the general NNE trend of the Angolan part of the KIC, implying that opening was broadly E to SE, oblique to the expected sheet-perpendicular extension. However, the bad exposure of the faults complicated measurements of their dips and investigation of dislocation markers. Thus it was impossible to reconstruct the precise stress-field, responsible for the faulting.

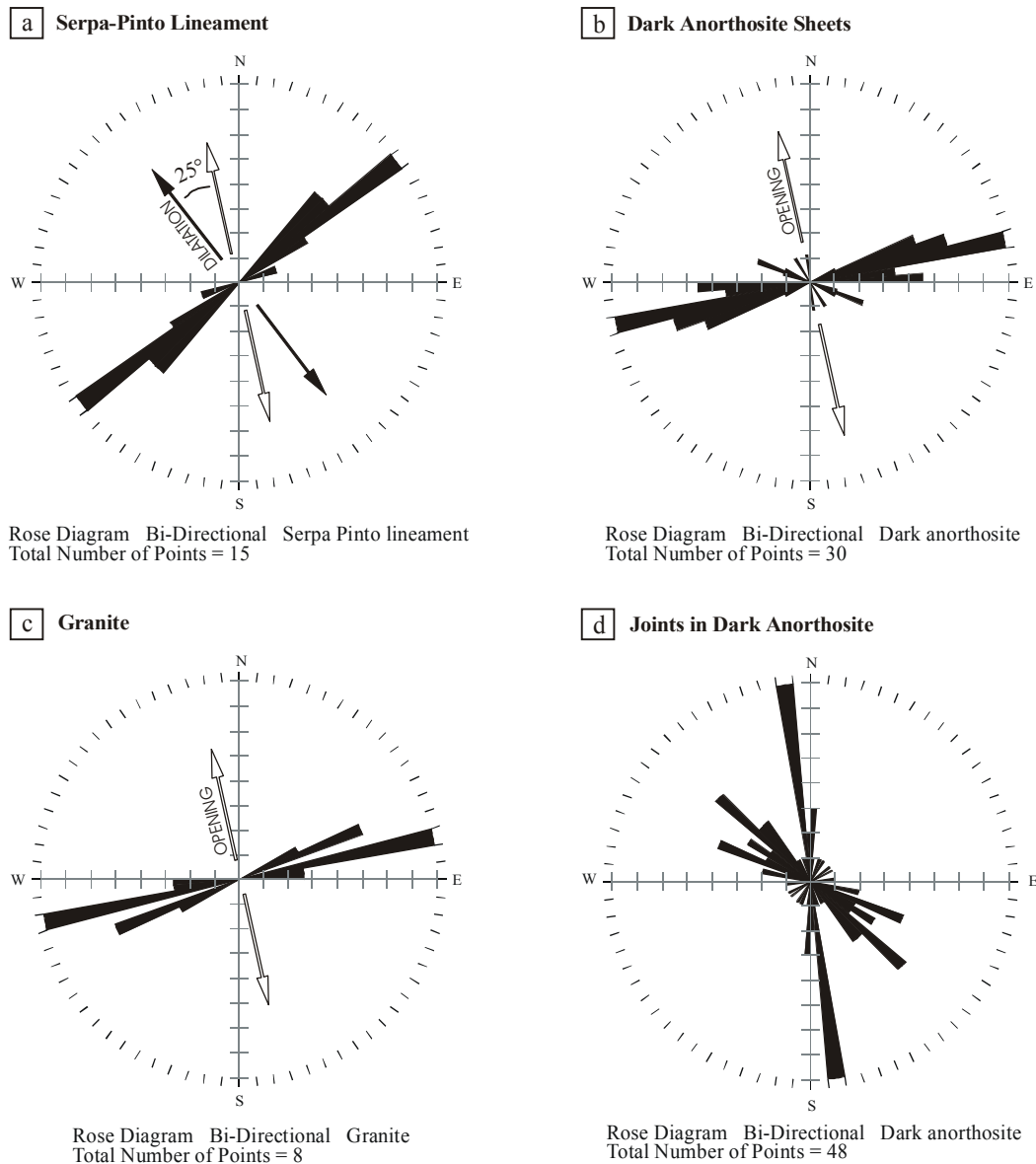


Fig. 3.16: Rose diagrams, illustrating the trends of the ~1,380 Ma rock units and structures in the study area. Net opening and dilatation are marked. **a)** Variation of strike of the dextral strike-slip fault bundle of the Serpa-Pinto lineament. **b)** Variation of strike of the dark anorthosite sheets. **c)** Variation of strike of the fabric of the granite intrusion. **d)** Variation of strike of joints in the dark anorthosite.

In contrast to the central part of the Zebra Mountains, the dark anorthosite plugs in the Swartbooisdrif area, that represents a marginal zone of the Zebra Mountain massif, are mostly irregularly bounded and rather display a irregularly scattered distribution within the white anorthosite. The overall lack of extensive outcrops of solid bedrock prevents detailed structural investigations of their fabric. However, the anorthositic rocks exposed in the Ondoto river valley are transected by numerous, SE trending fissures (Fig. 3.16 d). Joints in the rocks exhibit two major orientations, i.e. (1) S10E, dipping 15-38° to the NE and (2) S50E, dipping 25-64° to the SW. This structure does not copy a primary magmatic feature like extensive layering or igneous lamination but rather represents secondary faulting, post-dating the emplacement of the anorthositic magmas. Remarkably, the orientation of the joints correlates well with those of the SE trending carbonatite dykes, suggesting that at least part of the carbonatites were emplaced along pre-existing weakness zones within the anorthosite.

The structures in the anorthositic rocks of the Swartbooisdrif area are generally of brittle origin, testifying to their late stage origin. Only anorthosites in direct contact to the dykes of the carbonatitic breccia display a narrow zone of weak foliation marked by elongated plagioclase and biotite crystals oriented sub-parallel to the dyke walls. This ductile deformation most probably results from the local influx of heat and fluids released by the carbonatite melt.

3.5.2.2 The cogenetic syenite intrusions

Since the two syenite generations are genetically linked to, and were emplaced contemporaneously with the dark anorthosite suite, a investigation of their structural orientation should gain some general implications for the overall structural setting.

Measurements of the structural orientation of the first syenite generation are complicated, since outcrops of solid bedrock are rare. Thus only 15 measurements are reliable, showing the syenite to be emplaced as mainly E-W to S40E and minor S05E trending dykes, dipping 60-80° to the NE, 65-89° to the SW and sub-vertically to E (Fig. 3.17 a, b). The varying trends of the syenite dykes may reflect changes of the local stress-field, as discussed for the emplacement and subsequent faulting of the dark anorthosite.

In contrast, the fenitized syenite, comprising the younger syenite generation, predominantly trends S35E and S65E, mainly dipping between 45-60° to the SW and 60-75° to the NE (Fig. 3.18 a, 3.19 a). These orientations correlate well with those of the late-stage strike-

slip fault bundle, exposed in the Zebra Mountain massif. Most likely, these weakness zones provided excellent pathways for the emplacement of the younger syenite generation.

Both syenite dyke swarms are characterized by branching, dying out and curving of the dykes as well as dyke segmenting into an en-échelon sets of intrusions towards their terminations, suggesting minor changes in the maximum horizontal extension axis σ_3 during their emplacement. The brecciation of both syenite units is most probably related to repeated movements along the dextral strike-slip faults.

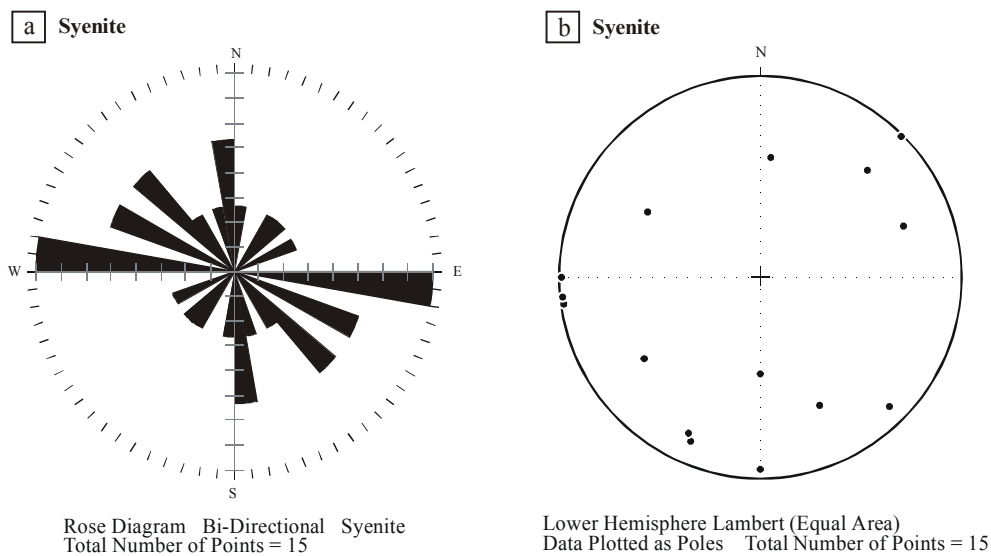


Fig. 3.17: *a*) Rose diagrams, illustrating the variation of strike of shearzones intruded by the ~1,380 Ma syenite. *b*) Variation of dip direction and dip of the syenite dykes, marked as poles to planes.

3.5.2.3 The carbonatite dyke swarms

Dyke swarms typically form perpendicular to the least compressive stress σ_3 and can thus be used to constrain the patterns of, and the changes in the regional stress field. However, dykes may also be injected along pre-existing fracture sets, opening in a direction oblique to their dyke walls. The orientation of the carbonatite dykes in the area mapped reflects a major fracture set, striking SE with a mean of 140° , thus implying a N50E trending, dyke-perpendicular maximum horizontal extension axis (Fig. 3.18 a-d). However, a maximum dyke width is displayed by rare S65E to S80E trending sodalite-rich carbonatites, which, at the same time, suffered negligible post-emplacement shearing (Fig. 3.18 c). In clear contrast, the numerous carbonatite dykes oriented oblique to this direction, i.e. S25E to S60E, contain weak ductile to brittle fabrics (3.18

a, b). Especially the massive carbonatitic breccia, trending S10E to S30E, was heavily sheared parallel to the wallrock contacts after its solidification giving the very fine-grained rock a mylonite-like appearance (3.18 d). Carbonatite dykes, oriented sub-perpendicular to the dominant set and trending N to N20E, do also occur but are mostly undeformed.

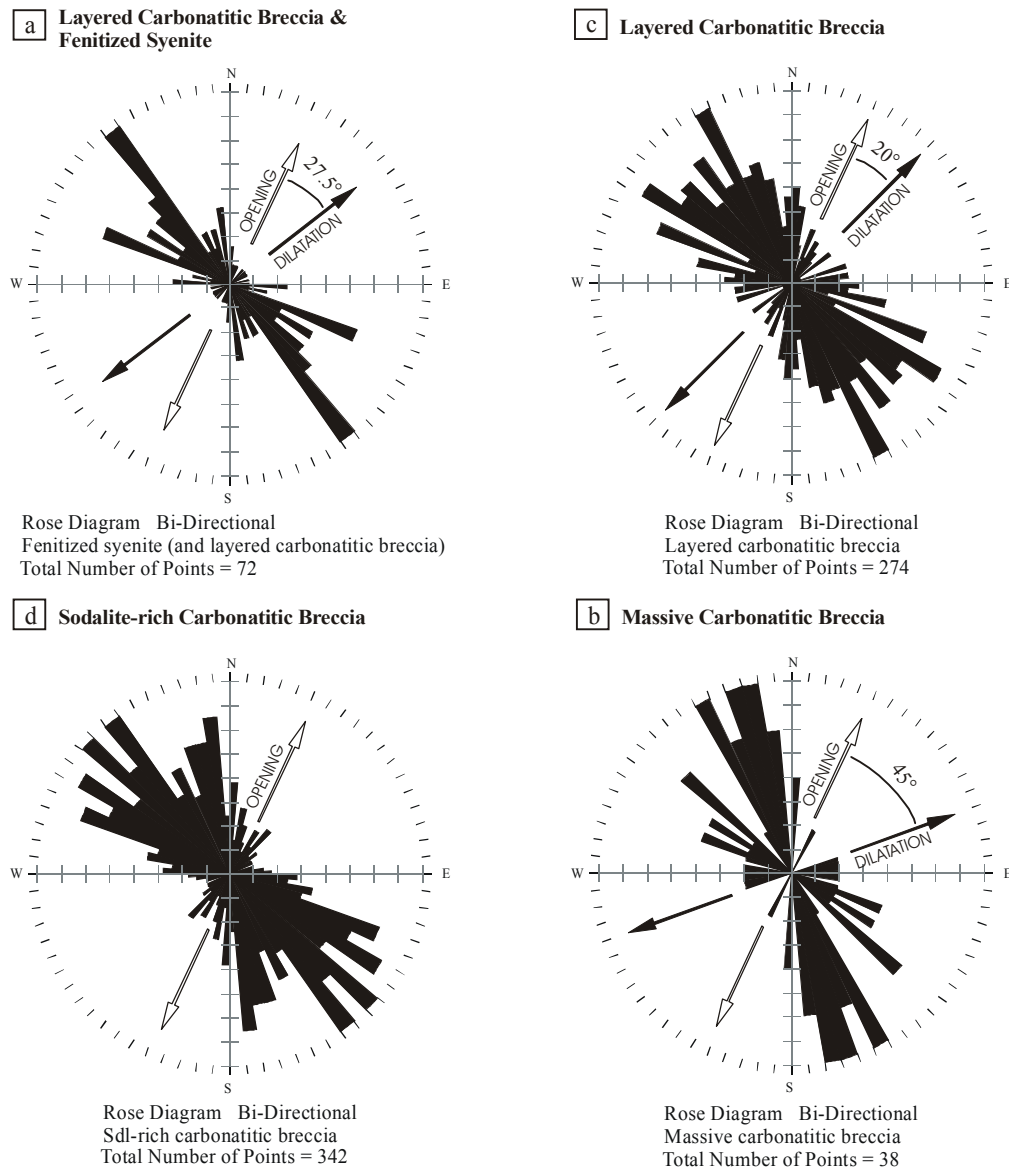


Fig. 3.18: Rose diagrams, illustrating the trends of faults intruded by the ~1,380-1,340 Ma dykes of the fenitized syenite (a) and the ~1,140-1,120 Ma carbonatite dykes (a-d). Net opening and dilatation are marked. **a)** Variation of strike of faults intruded by both, the fenitized syenite and the carbonatitic breccia. **b)** Variation of strike of dykes of the layered carbonatitic breccia. **c)** Variation of strike of dykes of the sodalite-rich carbonatitic breccia. **d)** Variation of strike of dykes of the massive carbonatitic breccia.

These observations suggest that the dykes opened in a N20E direction, that was mostly oblique to their walls. This is most likely to occur, if the carbonatite magma was injected in pre-

existing fracture sets, that were not perpendicular to the minimum horizontal extension axis at the time of carbonatite emplacement. This interpretation is confirmed by several features of the dykes, as for example (1) curving and branching of most of the dykes and (2) their dying out into a set of en-echelon segments. Remarkably, the trends of the sheared carbonatite dykes are in excellent agreement with those of the strike-slip faults, formed during or shortly after the emplacement of the dark anorthosite suite, thus suggesting that most of the carbonatites were injected along these older zones of weakness. It was impossible, however, to determine the amount and direction of displacement of the sheared dykes, since the carbonatitic breccia is generally characterized by a very inhomogeneous structure.

The dips of the carbonatite dykes are strongly variable, even within single dykes. In general, however, the SE trending dykes of the carbonatitic breccia dip with average values of 45-60° to the SW and, subordinately, with average values of 60-75° to the NE, whereas the rare NE trending dykes mainly dip between 55-65° to the NW and SE (Fig. 3.19 a-d). The general coincidence of the dyke orientations of the ~1,380-1,340 Ma syenite and the ~1,140-1,120 Ma carbonatite intrusions suggests that the two rock-units were emplaced along similar fracture sets, which already formed during the final stages of anorthosite magmatism. The lineaments survived a considerable time-span of >200 Ma, which makes an intervening orogenic event rather unlikely and thus characterizes the time gap as an era of continental stability.

All dykes of the carbonatitic breccia display a variety of internal structures. The extensive folding and layering of the carbonatitic breccia (Fig. 3.20a) have no preferred orientation and are thus interpreted as magmatic features, as typically developed in high-viscosity melts. However, the apparent high viscosity of the layered carbonatitic breccia is not a feature of the carbonatite melt itself but is rather caused by the incorporation of wallrock fragments. These brecciated and/or mylonitized xenoliths are present in strongly varying sizes and proportions. The large amount and average size of the anorthositic and syenitic clasts make a transport by the carbonatite unlikely but rather suggests that the carbonatite melts intruded previously sheared faults.

Rafts of the layered carbonatitic breccia, oriented discordantly to the magmatic layering of the surrounding carbonatite matrix (Fig. 3.20b), provide evidence for repeated injections of carbonatite melt. During the subsequent injections of melt, the older, already crystallized parts of the carbonatitic breccia suffered brittle deformation and displacement along small-scaled fractures (Fig. 3.20 b, c).

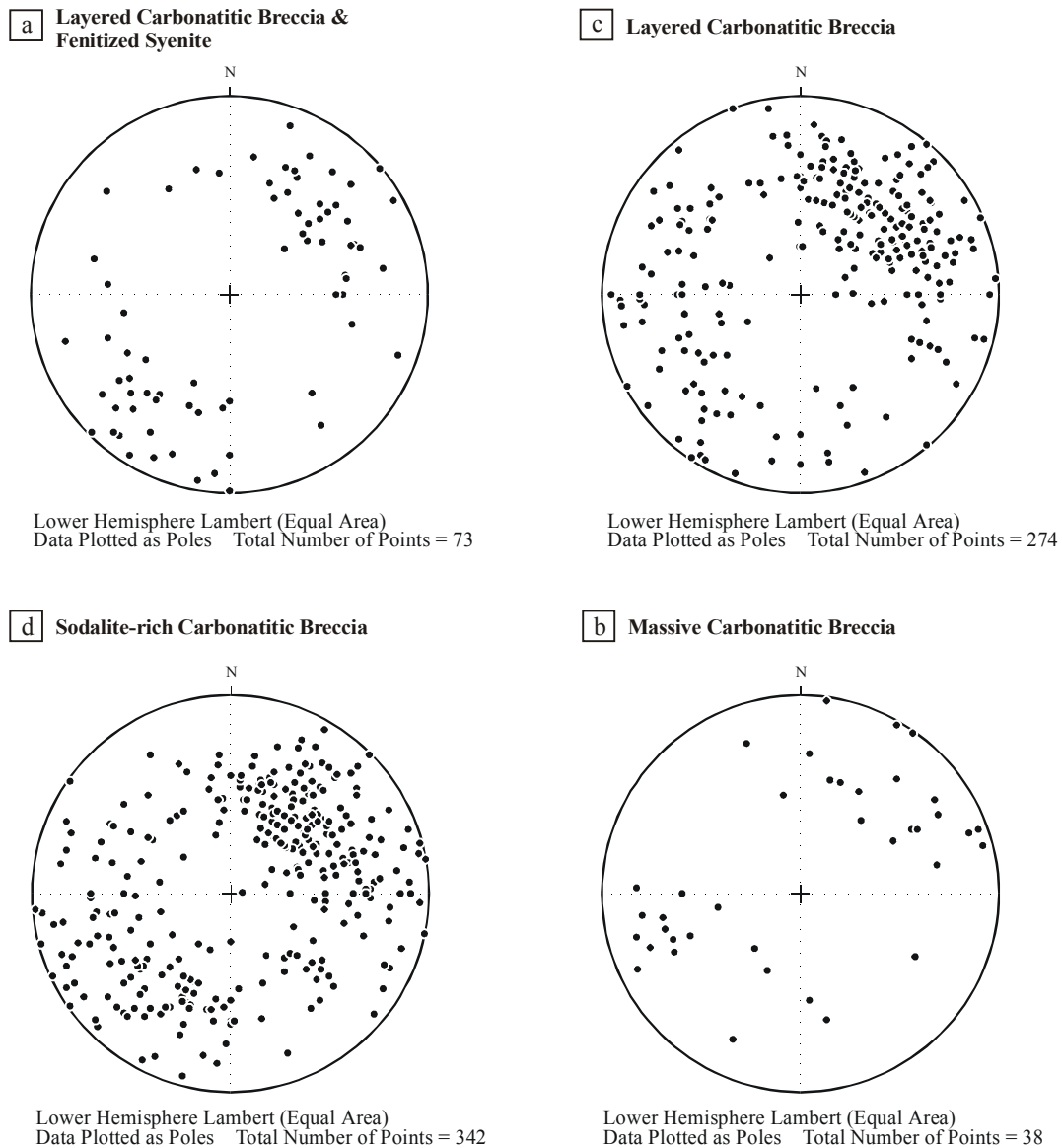


Fig. 3.19: Variation of dip direction and dip of the dyke contacts of the ~1,380-1,340 Ma fenitized syenite (a) and the ~1,140-1,120 Ma carbonatites (a-d), marked as poles to planes. **a)** Dip direction and dip of faults intruded by both, the fenitized syenite and the carbonatitic breccia. **b)** Dip direction and dip of dykes of the layered carbonatitic breccia. **c)** Dip direction and dip of dykes of the sodalite-rich carbonatitic breccia. **d)** Dip direction and dip of dykes of the massive carbonatitic breccia.

Locally the carbonatites may also display features of ductile deformation, as for example crystal-plastic deformation and re-crystallization of the matrix-carbonates. This holds true especially for the massive carbonatitic breccia. In rare cases a weak magmatic lineation is preserved in the carbonatitic breccia, marked by elongated mica, carbonate and magnetite crystals (Fig. 3.20 d). This lineation has been investigated in some detail in the opencastings of the two major dykes of the sodalite-rich carbonatitic breccia (dyke A and B; Fig. 2.1; Plate 2: tectonic map), in order to constrain the flow pattern of the carbonatite melts. These

investigations demonstrate that the carbonatite melt generally followed a straight path of upward-movement, rather than being injected obliquely to the fault planes.

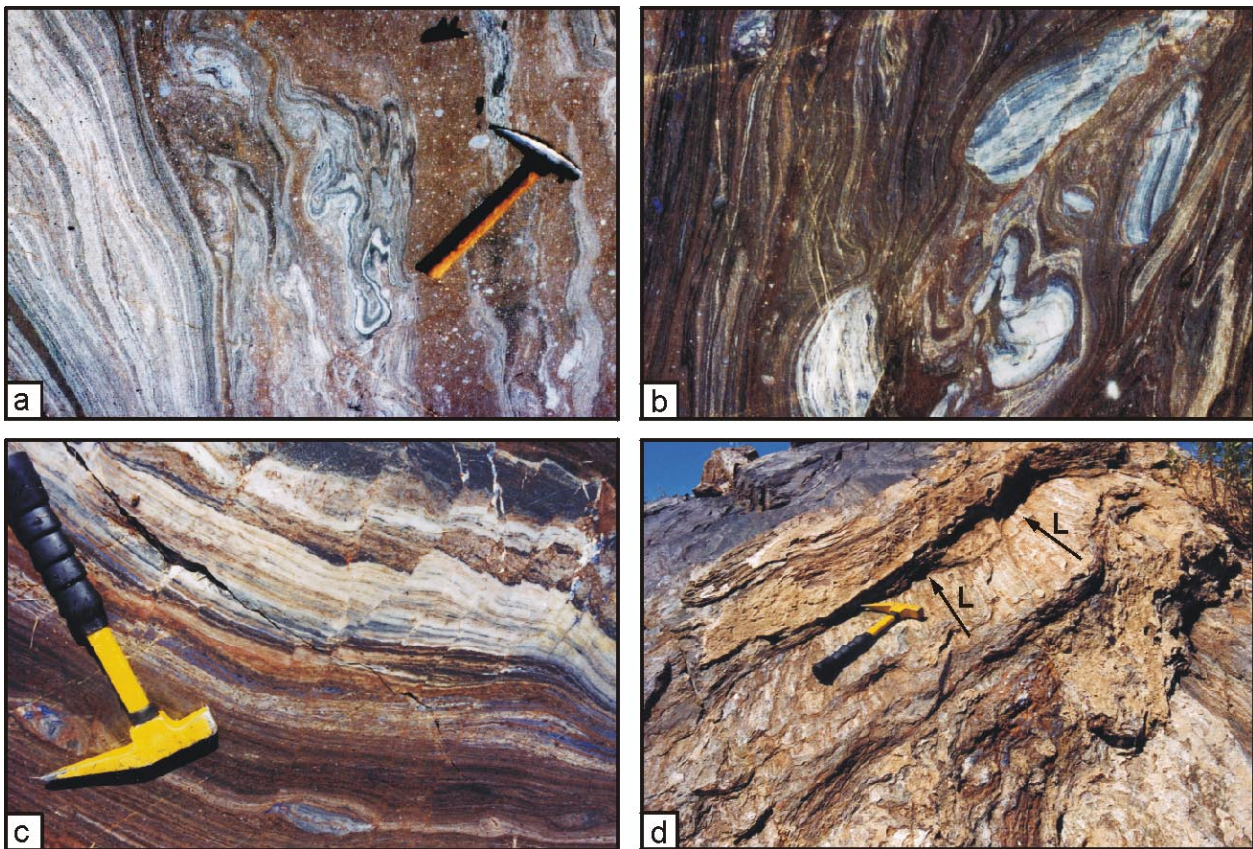


Fig. 3.20: Photographs of common internal structures of the carbonatitic breccia. **a)** Imperersistent magmatic folding (Sodalite opencasting 4, locality: S 17°20.947', E 13°47.752'). **b)** Rafts of the carbonatitic breccia (light grey to bluish), wrapped by a younger generation of layered carbonatite (brownish; Sodalite opencasting 4, locality: S 17°20.947', E 13°47.752'). **c)** Small-scale brittle deformation of already crystallized parts of the carbonatitic breccia, surrounded by undeformed carbonate (brown) and silicate layers (grey, white, blue; Sodalite opencasting 4, locality: S 17°20.967', E 13°47.722'). **d)** Lamination (L) of the layered carbonatitic breccia, marked by elongate ankerite crystals (Sodalite opencasting 3; locality: S 17°20.790', E 13°47.685').

3.5.2.4 Dolerites

The overall lack of well exposed possible dyke contacts allowed no detailed structural investigation of this rock type. Measurements show that the dolerites were emplaced along the same fracture set as the older intrusions of the carbonatitic breccia thus making major changes in the regional stress field accompanying and/or predating their emplacement rather unlikely. The

dykes mainly strike SSE and dip with 45-75° to the WSW, but, in clear contrast to the massive carbonatitic breccia, show no effects of syn- to post-emplacement shearing.

3.5.3 Fault system

Faults dominate in the southern part of the area mapped. They are exposed as mainly NE and subordinately SE trending fault bundles, mostly intruded by syenite. The fractures are mostly filled by massive epidote rocks, replacing the former syenite and/or cementing angular syenite clasts. Fault planes are never exposed but the conspicuous green colour of the epidote mineralization allowed to follow the path of the faults over a certain distance. However, the direction and value of fault-related movement could only be estimated by the relative displacement of the syenite, carbonatite and dolerite dykes. A method like this, however, bears risks, since it remains uncertain if the dyke displacement reflects a post-intrusive tectonic event. This holds true especially for most of the carbonatite and dolerite intrusions, which have been shown to be emplaced along a complex pre-existing fracture system.

Indeed, the various dykes appear to be displaced sinistrally and dextrally across both the NE and the SE trending faults, suggesting that this separation is the result of a jump-over to other faults. This interpretation is constrained by a dolerite dyke, that apparently suffered a sinistral displacement of 200 m, which, however, has not affected the neighbouring older syenite and carbonatite dykes.

PART II: Petrogenesis and evolution of the Kunene Intrusive Complex and the spatially associated felsic suite

4 General remarks

Massif-type anorthosite complexes, commonly associated with minor felsic rocks, are characteristic features of the Proterozoic crust. Their apparent temporal restriction to the Proterozoic testifies to specific tectono-thermal regimes and crust-forming processes that were operative during this period. However, the petrogenesis of Proterozoic anorthosite complexes is still a matter of debate. Thus, no general agreement has been reached on issues such as formation of parental magmas, monobaric *vs.* polybaric crystallization, mode and depth of emplacement and cooling history (*e.g.* Ashwal, 1993, for a review). Anorthosites, leucotroctolites and related gabbroic rocks commonly display late-magmatic and subsolidus reaction textures, among which garnet-bearing coronas are most conspicuous (*e.g.* Griffin & Heier, 1973; Whitney & McLelland, 1973; McLelland & Whitney, 1977, 1980a, b; Johnson & Essene, 1982; Bingen et al., 1984; Griffin et al., 1985; Grant, 1988; Johnson & Carlson, 1990; Ashwal et al., 1998). These textures may place constraints on at least two of the manifold problems pertaining to the petrogenesis of massif-type anorthosite complexes, namely (i) their intrusion depth, *i.e.* lower *vs.* upper crustal level, and (ii) their subsolidus evolution, *i.e.* slow isobaric cooling *vs.* a separate prograde metamorphic overprint.

As summarized by Ashwal (1993), the intrusion of massif-type anorthosites into the lowermost crust (*e.g.* Martignole & Schrijver, 1971; Taylor et al., 1984) is no longer generally accepted. Based on various evidence, a shallow intrusion depth has been invoked, for example for the Nain anorthosites of Labrador (Berg, 1977a, b), the Laramie anorthosite of Wyoming (Fuhrmann et al., 1988; Kolker & Lindsley, 1989; Grant & Frost, 1990) or for the Adirondack anorthosites of New York (Valley & O'Neil, 1982). A process of slow isobaric cooling for the subsolidus formation of corona structures was already proposed by Martignole & Schrijver (1971), Griffin (1971) and Bingen et al. (1984). In other cases, however, an alternative model, considering a separate event of prograde granulite facies metamorphism seems to be justified (McLelland & Whitney, 1977, 1980a, b; Johnson & Essene, 1982).

Most anorthosite massifs contain a small volume of temporally and spatially associated felsic plutonic rocks, characterized by a composition ranging from diorite to granite and a mostly anhydrous mineralogy. Commonly, intrusive contact relationships suggest these granitoids to be

younger than the associated anorthosite (e.g. de Waard, 1970; Seifert, 1978). The fact, that the mineral chemistry of the Fe-Mg silicates and plagioclase in the silicic suites appears to extend the compositional ranges of the anorthositic minerals to higher X_{Fe} and lower An-contents, has been interpreted in terms of consanguinity between the two rock suites (e.g. Fuhrman et al., 1988). An alternative model considers the granitoids to represent a chemically independent, crustal derived intrusive suite (e.g. Anderson, 1980; Anderson & Bender, 1989; Emslie, 1991; Emslie et al., 1994).

Focusing on these pairs of alternative models, the geochemical signatures as well as the magmatic and subsolidus reaction textures recorded by the anorthositic rocks of the Kunene Intrusive Complex and the spatially associated granitoid suite, have been investigated in some detail. Parts of this study have already been presented in Drüppel (1999) and Drüppel et al. (2001).

5 Petrography

5.1 Petrography of the anorthositic rock suite

5.1.1 Igneous textures

All anorthositic rock types are characterized by a massive appearance with coarse-grained plagioclase crystals without preferred orientation. The grain sizes of plagioclase commonly vary between 0.2-5 cm. Both, the white and the dark anorthosite suites display the typical magmatic assemblage of

plagioclase \pm orthopyroxene \pm clinopyroxene + ilmenite + magnetite + biotite + amphibole \pm apatite \pm zircon.

In contrast to the white anorthosite suite, the dark anorthosites may additionally contain variable amounts of olivine.

5.1.1.1 White anorthosite suite

Eight samples of the white anorthosite from the sodalite mining area have been investigated in detail.

White anorthosite (A,w): Ku-97-08b, Ku-97-33, Ku-97-33a, Ku-97-33b, Ku-97-44, Ku-97-99a, Ku-98-45, Ku-98-60

A characteristic feature of the white anorthosite is the dominance of anhedral cumulus plagioclase (87-99 vol.%), which, however, suffered an almost complete hydrothermal alteration (i.e. saussuritization, albitization and/or sericitization), responsible for the white to greenish colour of these rocks. Interstitial ortho- and clinopyroxene are minor phases. Late-magmatic biotite and pargasite form discontinuous rims around clinopyroxene and anhedral ilmenite. Olivine or its alteration products have never been observed in the investigated white anorthosite samples.

Due to a strong brittle deformation, plagioclase, pyroxene, amphibole and biotite are in most cases heavily brecciated. Locally, plagioclase is recrystallised to granular mosaics. Cracks in the rocks are filled by carbonate and/or epidote.

Anhedral, tabular **plagioclase** is virtually completely sericitized (Fig. 5.1a) or altered to fine-grained intergrowths of albite, epidote, actinolite and calcite (saussuritization, Fig. 5.1b). Plagioclase grain size is mostly coarse-grained with an average of 2.3 mm. Non-altered, twinned (albite-, pericline-, Carlsbad-law) plagioclase relics are preserved in the central parts of large plagioclase grains (Fig. 5.1a). The normally to slightly oscillatory zoned magmatic plagioclases fall in the compositional range of An₄₃₋₅₃ (andesine to labradorite). However, with an average of 2 mol.%, the differences in rim and core compositions are negligible. Locally, the primary-magmatic plagioclase crystals are recrystallised to granular mosaics (Fig. 5.1c). A characteristic feature of these secondary plagioclase crystals is the general lack of alteration and twinning (except rare albite-twins) and an inverse zonation, with An₃₋₄ cores and An₅₋₁₀ rims.

Intercumulus **orthopyroxene** (X_{Mg}: 0.71) is partially to completely replaced by chlorite. The fine-grained (grain size: < 0.5 mm), subhedral grains commonly display ilmenite exsolution lamellae ||(100) and are surrounded by narrow and impersistent chlorite and/or pargasite rims. Anhedral to subhedral intercumulus **clinopyroxene** is generally fine-grained (grain size: < 1mm) and heavily tectonised. Due to a hydrothermal overprint, the granular clinopyroxene grains are completely replaced by oriented and fine-grained actinolite intergrowths (Fig. 5.1 d). Clinopyroxene is enveloped by a narrow rim of late-magmatic, green pargasite.

Ore minerals, i.e. **magnetite** and **ilmenite**, are minor constituents of the white anorthosite. They occur as discrete anhedral grains in the interstices of cumulus plagioclase, suggesting their late-magmatic origin. However, subhedral magnetite may additionally be included in plagioclase. Commonly, ilmenite displays polysynthetic twinning. Both ore-minerals underwent subsolidus deformation along small-scaled shear zones (Fig. 5.1 e).

Light green to colourless **actinolite** replaces clinopyroxene, whereas late-magmatic green **pargasite** (X_{Mg}: 0.65-0.70), together with **biotite** (X_{Mg}: 0.48), forms narrow rims around intercumulus orthopyroxene, clinopyroxene and ilmenite (Fig. 5.1 e). Marginally, the biotite grains are replaced by fine-grained intergrowths of chlorite, calcite and epidote. Subhedral, prismatic **apatite** inclusions (average grain size: 0.1 mm) in clinopyroxene and ilmenite are a common accessory phase.

Chlorite and **epidote** replace biotite and plagioclase and additionally fill narrow fissures in the rocks. Intergranular **calcite** may be present in significant concentrations, reaching up to 4 vol.%.

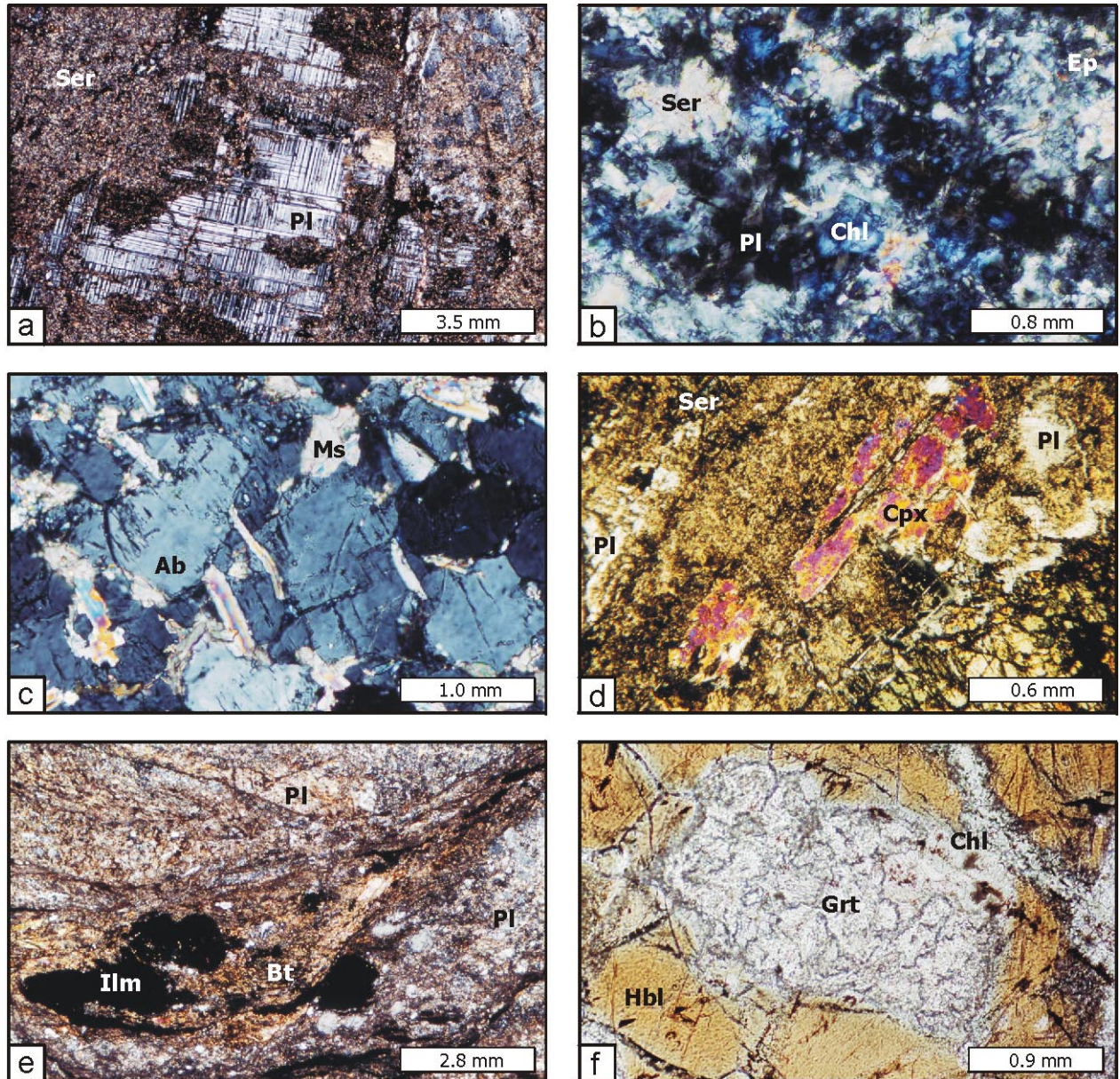


Fig. 5.1: Polished-section photomicrographs of the white anorthosite suite. Cross-polarized light (a-d). Plane-polarized light (e-f). *a*) In rare cases the cores of lath-shaped cumulus plagioclase are preserved whereas the rims are pervasively sericitized. *b*) Saussuritization of cumulus plagioclase. *c*) Granoblastic recrystallisation of cumulus plagioclase to almost pure albite. *d*) Pseudomorphous replacement of clinopyroxene by actinolite. *e*) Deformation along micro-shear zones causes the recrystallisation of late-magmatic biotite, surrounding interstitial ilmenite. *f*) A xenocryst of relict andradite-rich garnet, that is marginally replaced by retrograde chlorite, is surrounded by rims of late-magmatic amphibole.

Relic xenocrysts of andradite-rich **garnet** (average composition: $\text{And}_{72}\text{Grs}_{27}$), present in two of the nine investigated samples of white anorthosite, point to a contamination of the parental melt with calc-silicate country rock. The tectonised garnet grains are partially replaced by chlorite and surrounded by late-magmatic pargasite (Fig. 5.1f).

5.1.1.2 Dark anorthosite suite

In the investigated 59 dark anorthosite samples coarse-grained plagioclase is the dominant mineral (65-99 vol. %) with mostly anhedral to subhedral, tabular shape. Dust-like inclusions of Fe-Ti oxides in plagioclase are common in all samples of dark anorthosites but are most abundant in the leucotroctolites and thus most probably account for their dark-coloured appearance. A common feature is mortar texture, consisting of primary plagioclase, surrounded by re-crystallized grains of similar composition, possibly caused by the movement of the anorthositic crystal mushes (*e.g.* Longhi & Ashwal, 1985; Morse, 1968).

Minor post-cumulus orthopyroxene (En₅₉₋₆₃) and clinopyroxene (diopside with X_{Mg}: 0.66-0.76) are the dominant minerals (3-12 vol.%) among mafic silicates in the *leucogabbro and -norite samples*. They occur as relatively large, subhedral to anhedral intercumulus grains in subophitic relationship with cumulus plagioclase. In the *leucotroctolite* subordinate olivine (5-8 vol.%; Fo₅₄₋₆₅) occurs as small subhedral inclusions in plagioclase or as anhedral grains in the interstices between plagioclase crystals, partially rimmed by ortho- or clinopyroxene (up to 3 vol.%). The heavily strained intercumulus olivine is partially to completely replaced by fine-grained intergrowths of talc, carbonate and quartz, together with magnetite, forming irregular vein fillings in cracks of olivine. In contrast to the leucogabbro- and -norite and the leucotroctolite, *anorthosite sensu stricto* contains only minor amounts of pyroxene and/or olivine (0.5-3 vol.%).

Common accessories of all lithologies of the dark anorthosite suite are anhedral ilmenite and magnetite, with curved grain boundaries. The Fe-Ti ores form discrete grains in the interstices between plagioclase crystals, indicating a post-plagioclase formation. However, magnetite may additionally occur as fine-grained inclusions in plagioclase and olivine, pointing to its early crystallization. Intercumulus ilmenite, ortho- and clinopyroxene are partially surrounded by narrow rims of intergrowths of biotite (X_{Mg}: 0.39-0.67) and brown to yellowish amphibole (X_{Mg}: 0.55-0.67). In the leucogabbros and -norites amphibole and biotite of similar compositions also occur localised in patches, bearing abundant inclusions of fine-grained, euhedral apatite.

The well preserved magmatic textures as well as the analysed compositions of the magmatic mineral assemblages in the investigated leucotroctolite and anorthosite samples of the dark anorthosite suite resemble those reported for the Angolan part of the KIC (Ashwal & Twist,

1994; Carvalho & Alves, 1990; Morais et al., 1998; Silva, 1990, 1992; Simpson, 1970; Vermaak, 1981).

5.1.1.2.1 *Pyroxene-bearing anorthosite and leucogabbronorite*

Nine samples of pyroxene-bearing anorthosites and 25 samples of leucogabbronorites (comprising 1 sample of leucogabbro and 24 samples of leucogabbronorite s.s.) were taken from the Swartbooisdrif mine and the area around the settlement Swartbooisdrif.

Pyroxene-bearing anorthosite (A_{px}): Ku-97-02, Ku-97-12, Ku-97-13, Ku-97-31, Ku-97-92a, Ku-97-93, Ku-98-78, Ku-98-95, Ku-98-123

Leucogabbronorite s.s. (GN): Ku-97-03, Ku-97-03b, Ku-97-03c, Ku-97-04, Ku-97-05, Ku-97-06, Ku-97-08a, Ku-97-30, Ku-97-31b, Ku-98-71, Ku-98-72, Ku-98-79, Ku-98-84, Ku-98-92, Ku-98-126, Ku-98-128, Ku-98-129, Ku-98-222, Ku-01-19, Ku-01-20, Ku-01-21, Ku-01-22, Ku-01-23, B-98-101a

Leucogabbro (GN): Ku-98-68

Tabular **plagioclase**, with an average grain size of 1.8 mm, is the major constituent (65-98 vol.%) of the rock samples investigated (Fig. 5.2 a-c). Subordinate primocrysts of lath-shaped plagioclase have been observed in four samples (Fig. 5.2 f). The majority of the analysed plagioclase crystals (An₄₃₋₅₄) shows minor chemical oscillatory or patchy zoning. Marginally, the plagioclase crystals are recrystallised to medium-grained crystals (average grain size: 5 mm) of a similar compositional range. In one sample (Ku-98-84) plagioclase crystals adjacent to orthopyroxene display thin strongly reversed rims where the An content increases abruptly from 54 mol.% to 69 mol.%. According to Morse & Nolan (1984), these more calcic rims cannot be explained by subsolidus processes, but require an origin from intercumulus liquid. In contrast to the white anorthosite, plagioclase of the leucogabbronorites and the pyroxene-bearing anorthosites of the dark anorthosite suite suffered only minor sericitization, which occurs localised along small cracks or poecilitic magnetite inclusions. Alteration products formed by saussuritization are rare.

Minor post-cumulus **orthopyroxene** and **clinopyroxene** (X_{Mg} : 0.53-0.65), both lacking significant zoning, are the dominant minerals among mafic silicates. They occur as relatively

large (up to 1.5 cm), anhedral intercumulus grains (Fig. 5.2 a-c) or in subophitic relationship with cumulus plagioclase (Fig. 5.2 f). Clinopyroxene is commonly partially to completely replaced by colourless to light green, fibrous actinolite and surrounded by rims of late-magmatic

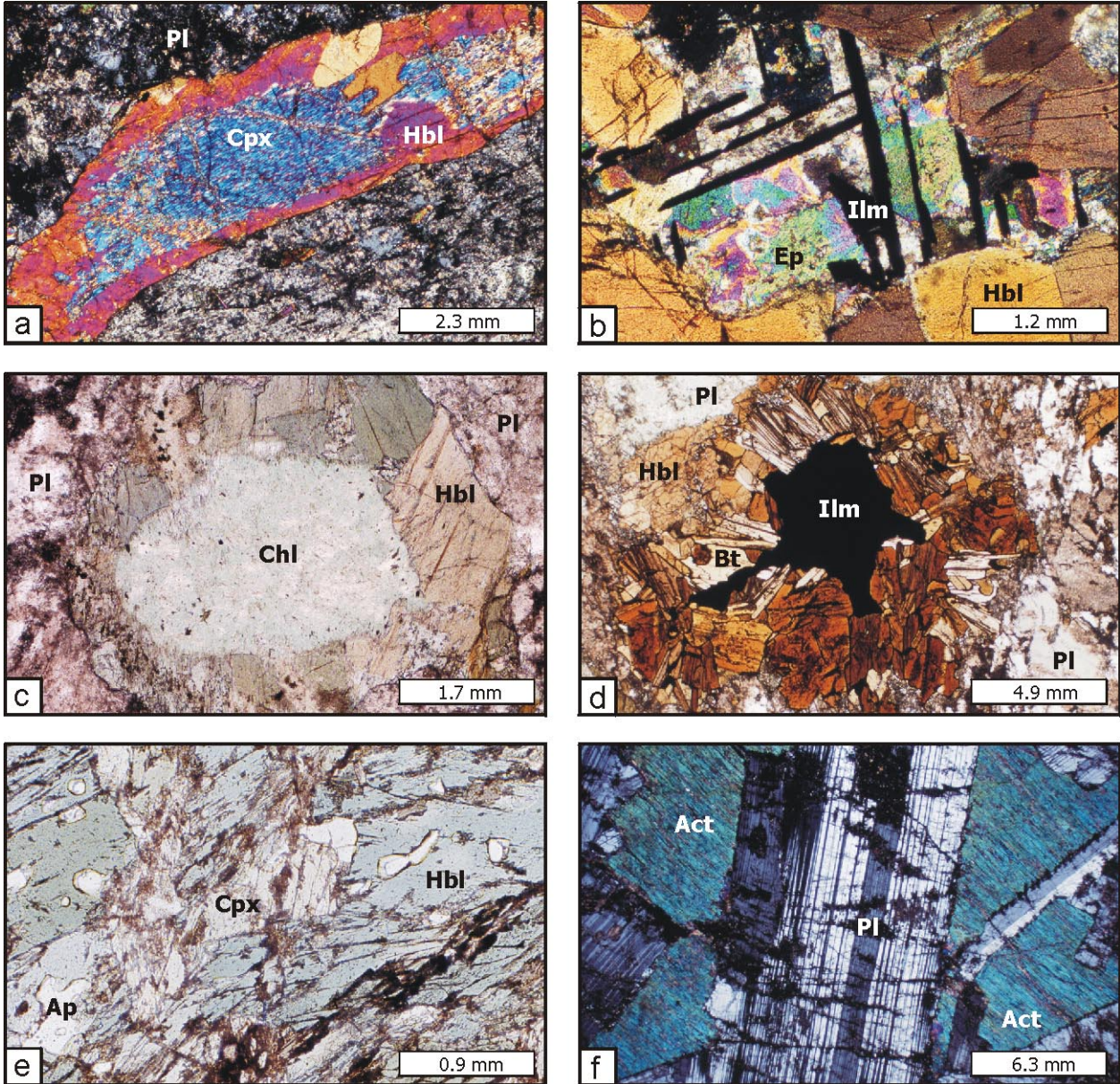


Fig. 5.2: a) Polished-section photomicrographs of the pyroxene-bearing anorthosites and the leucogabbronorite. Cross-polarized light (a-c, f). Plane-polarized light (d-e). **a)** Uralitised interstitial clinopyroxene fills the interstices between heavily sericitized cumulus plagioclase, and is surrounded by a rim of late-magmatic amphibole. **b)** Former pyroxene is replaced by epidote, whereby ilmenite-exsolution lamellae are preserved. **c)** Intercumulus orthopyroxene is commonly completely altered to chlorite and rimmed by late-magmatic amphibole. **d)** Brownish, strongly pleochroic biotite and amphibole aggregates surround anhedral, interstitial ilmenite grains. **e)** Poikiloblastic amphibole bears abundant apatite inclusions, both of them crystallized from trapped interstitial liquids. **f)** Subophitic texture displayed by interstitial, uralitized clinopyroxene and lath-shaped, subhedral plagioclase.

amphibole (Fig. 5.2 a). In clear contrast, orthopyroxene grains are always completely replaced by chlorite and/or epidote, whereby previously exsolved platelets of ilmenite, oriented \parallel (010) and \parallel (001), are preserved (Fig. 5.2 b-c).

Ubiquitous intercumulus ortho- and clinopyroxene as well as ilmenite, are partially surrounded by narrow rims of intergrowths of *biotite* (X_{Mg} : 0.39-0.48; Fig. 5.2 d) and greenish to brownish *amphibole* of mostly (ferro-)pargasitic to (magnesian-)hastingsitic composition (X_{Mg} : 0.46-0.73; Fig. 5.2 a). Amphibole and biotite of similar composition also occur localised in patches, bearing inclusions of fine-grained, euhedral apatite (Fig. 5.2 e). Exsolution of Ti-phases like ilmenite or rutile has not been observed in the amphiboles, indicating that they did not re-equilibrate with respect to Ti. The observed textural positions and compositions of biotite and amphibole are consistent with growth from pockets of interstitial magma trapped between the cumulus minerals and indicate that pargasite and biotite crystallized late in the magmatic history. In contrast, subordinate green to colourless, fibrous actinolite and magnesio-hornblende (Al : 0.27-0.98; Ti : < 0.04 ; X_{Mg} : 0.60-0.65) was formed by the alteration of intercumulus ortho- and clinopyroxene.

Anhedral intercumulus *ilmenite* with embayed grain boundaries (Fig. 5.2 d) is the dominant mineral among Fe-Ti oxides, whereas anhedral *magnetite* with ilmenite exsolution lamellae, oriented \parallel {111} and {100}, is rare. Common accessories are *zircon*, late-magmatic *apatite* as well as the alteration products *epidote* (Ps : 0.14-0.28), *chlorite* (X_{Mg} : 0.43-0.62), *clinozoisite*, *calcite* and *sericite*.

In the leucogabbro sample Ku-97-03, a xenocryst of a light pink andraditic *garnet* has been observed, which resembles the garnet contained in the white anorthosite sample Ku-97-08b, regarding both its composition and textural position. It can thus be concluded that the leucogabbro/anorthosite units of the dark anorthosite suite, like the older white anorthosite suite, underwent contamination by crustal calc-silicate lithologies during their uprise.

5.1.1.2 Olivine-bearing anorthosite and leucotroctolite

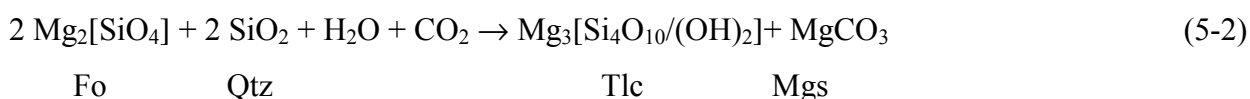
Eight samples of olivine-bearing anorthosite as well as 17 samples of leucotroctolite have been taken from the sodalite mining area and from the southern, northern and western margins of the Zebra mountains.

Olivine-bearing anorthosite (A,ol): Ku-97-28, Ku-97-28a, Ku-97-95, Ku-98-23, Ku-98-124, B-98-274a, B-98-274b, B-98-281b

Leucotroctolite (T): Ku-97-92, Ku-97-96, Ku-97-104, Ku-97-105, Ku-98-41, Ku-98-52, Ku-98-53, Ku-98-77, Ku-98-94, Ku-98-121, Ku-98-125, Ku-98-220, Ku-98-221a, Ku-98-221b, Ku-98-228, Ku-98-230, Ku-98-231

Subhedral to anhedral, tabular **plagioclase** with embayed grain boundaries is the main mineral present (75-96 vol.%). The crystals have an average grain size of 5 mm, which, however, strongly decreases in the vicinity of intercumulus pyroxene and olivine (Fig. 5.3 a). The majority of the weakly zoned plagioclase falls in the compositional range An₄₇ to An₆₇, whereas reversed rims of bytownitic composition may occur locally. Common features of plagioclase of the dark coloured leucotroctolite suite are (1) the overall presence of dust-like particles of Fe-Ti oxides (Fig. 5.3 b), (2) a weak sericitization and (3) the general lack of saussuritization products (Fig. 5.3 a-f).

Subordinate **olivine** (Fo₅₄₋₆₅) occurs as small subhedral inclusions of up to 0.2 mm in diameter in plagioclase or as anhedral grains (average grain size: 4 mm; Fig. 5.3 c) in the interstices between plagioclase crystals, partially rimmed by orthopyroxene, clinopyroxene and/or biotite (Fig. 5.3 d). Both olivine types may contain rounded magnetite inclusions (Fig. 5.3 c). In most cases, the heavily strained intercumulus olivine is partially to completely replaced by fine-grained intergrowths of talc, carbonate and quartz, together with magnetite, forming irregular vein fillings in cracks of olivine. As no relic serpentine mineral was observed, the replacement most probably is a direct reaction of the fayalite component to magnetite, producing the SiO₂ needed to transform the forsterite component to talc:



This replacement is the result of a weak hydrothermal alteration of the dark anorthosite suite.

Anhedral **clinopyroxene** (X_{Mg}: 0.60-0.74), **orthopyroxene** (X_{Mg}: 0.65-0.70), **ilmenite** and **magnetite**, with curved grain boundaries, form discrete grains in the interstices between

plagioclase crystals, indicating a post-plagioclase formation (Fig. 5.3 e). Clinopyroxene and orthopyroxene, together with biotite, may also form thin irregular rims around interstitial olivine (Fig. 5.3 a, d). Magnetite may additionally occur as fine-grained, rounded inclusions in plagioclase and olivine (Fig. 5.3 b-c), pointing to an early crystallization of magnetite.

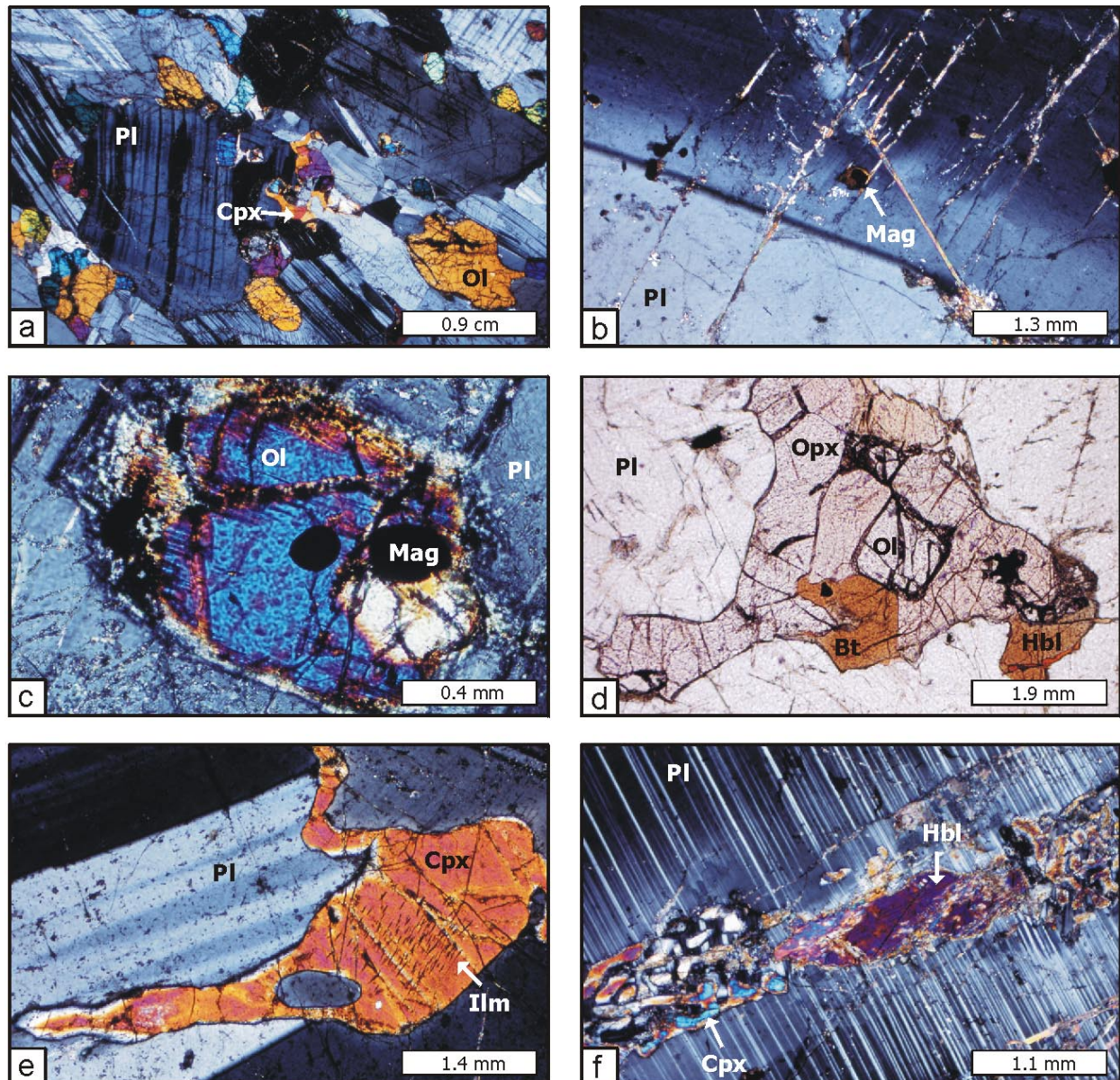


Fig. 5.3: Polished-section photomicrographs showing common magmatic textures of the olivine-bearing anorthosites and leucotroctolites. Cross-polarized light (a-c, e-f). Plane-polarized light (d). *a*) Interstices between coarse-grained cumulus plagioclase are filled by interstitial olivine, which in turn is surrounded by clinopyroxene rims. *b*) Fine-grained inclusions of cumulus magnetite in plagioclase account for the dark macroscopic colour of the leucotroctolites. *c*) Olivine may occur as sub-rounded inclusions in cumulus plagioclase, testifying to its early formation. *d*) Subhedral, interstitial olivine is surrounded by irregular rims of orthopyroxene and biotite, filling the open spaces between plagioclase crystals. *e*) Anhedral clinopyroxene with ilmenite-exsolution lamellae may form discrete intercumulus grains. *f*) Plagioclase encloses annealed cracks, filled by amphibole-clinopyroxene symplectites.

Ilmenite, spinel, clinopyroxene and olivine are partially surrounded by narrow rims of late-magmatic *biotite* (X_{Mg} : 0.45-0.48) and rare magnesio-hastingsitic to pargasitic *amphibole* (X_{Mg} : 0.77-0.86). Common accessories are epidote and chlorite (X_{Mg} : 0.71)

Small cracks in the rocks are filled by amphibole-clinopyroxene symplectites, that are locally overgrown by re-crystallized plagioclase (Fig. 5.3 f).

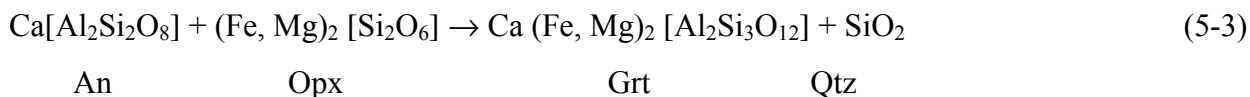
5.1.2 Structures of subsolidus origin

In five of the 17 leucotroctolite samples of the dark anorthosite suite (*Ku-97-104*, *Ku-97-105*, *Ku-98-220*, *Ku-98-221a*, *Ku-98-221b*), the igneous mineral assemblages and textures are locally obliterated by subsolidus reactions, leading to the development of two different types of garnet-bearing corona textures, surrounding olivine and ilmenite, respectively.

In addition, conspicuous ilmenite-magnetite-orthopyroxene symplectites developed in the vicinity of olivine in five anorthosite and leucotroctolite samples (*Ku-97-52*, *Ku-97-104*, *Ku-98-57*, *Ku-98-79*, *Ku-98-221b*). Both types of corona textures have been investigated in some detail by Drüppel et al. (2001).

5.1.2.1 Type I corona

In five leucotroctolite samples, olivine in contact with plagioclase (An_{59-75}) is rimmed by block-like, euhedral orthopyroxene (En_{62-71}) which, in turn, is surrounded by isolated euhedral garnet grains (average composition: $Prp_{28.6}Sps_{3.4}Alm_{54.9}GrS_{8.6}And_{4.5}$; X_{Mg} : 0.31-0.42) (Fig. 5.4 a-c). Subordinate quartz may appear in small grains next to garnet. In a simplified way, the observed garnet-forming reaction can be written as



Using the actual mineral compositions, the reaction cannot be balanced isochemically, but would lead to excess Na, Ca and Si in the reaction products. At the contacts with plagioclase, garnet and orthopyroxene are replaced by fibrous green to colourless pargasite to magnesio-hastingsite (Al : 2.73-3.15; Ti : < 0.01; X_{Mg} : 0.77-0.87) (Fig. 5.4 a-c) or biotite (X_{Mg} : 0.61-0.75).

In reality, this reaction is much more complex and presumably allochemical. Compared to the type-I corona textures, such a reaction mechanism is supported by the slightly lower X_{Mg} of garnets in type-II coronas, which may be the consequence of Fe-Ti oxide participation in the garnet forming reaction (5-5).

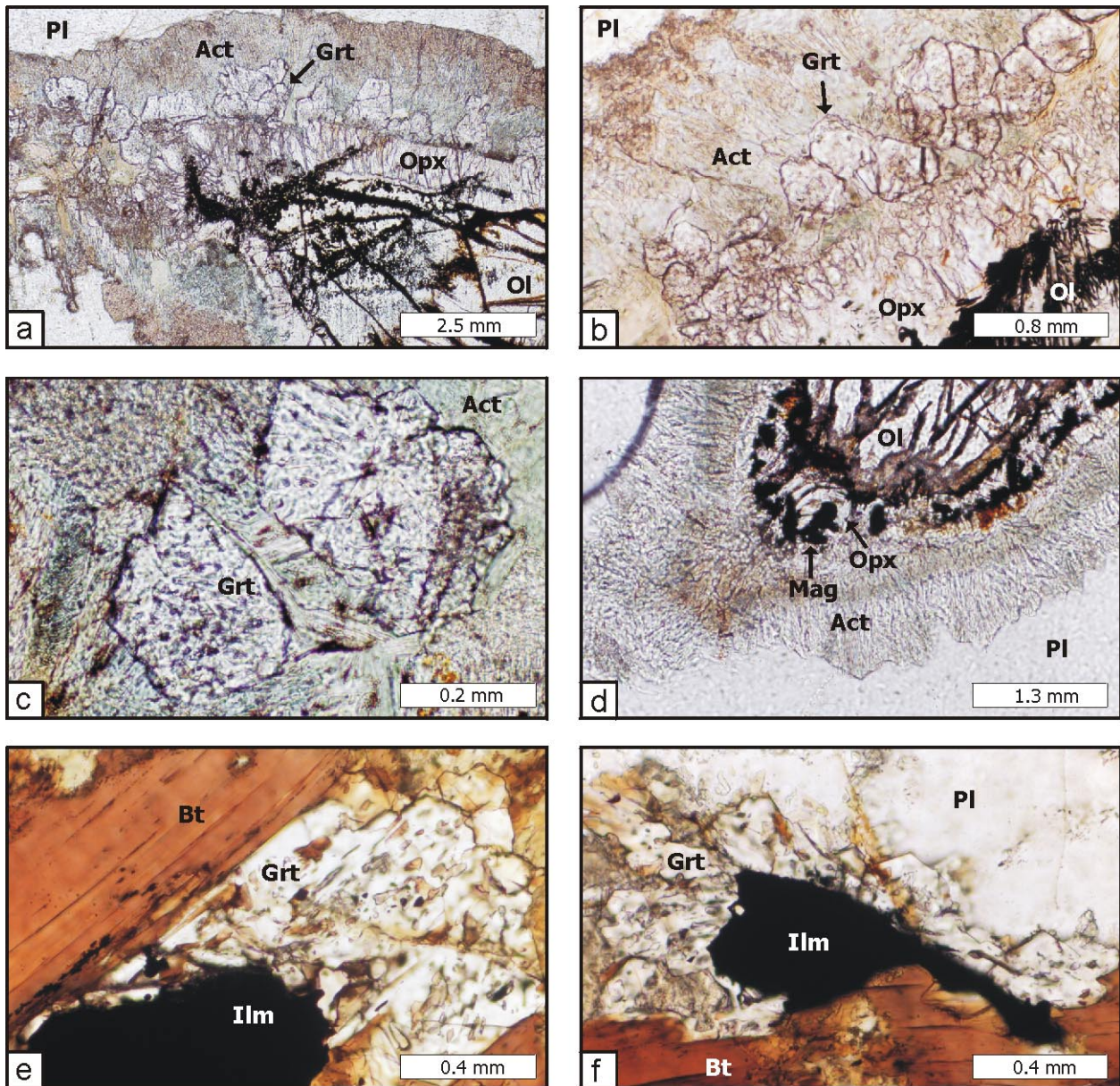
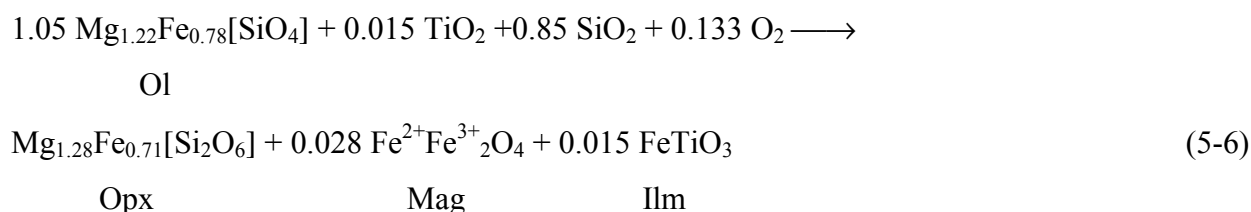


Fig. 5.4: Polished-section photomicrographs of garnet-bearing corona textures, developed in the leucotroctolites of the Kunene Intrusive Complex. Plane-polarized light. *a)* Olivine, partially replaced by subsolidus orthopyroxene, which in turn is surrounded by garnet. In contact to plagioclase, both garnet and orthopyroxene are altered to fibrous actinolite. *b)* Rim of block-like orthopyroxene, surrounded by euhedral garnet grains and fibrous actinolite. *c)* Partially corroded garnet grains, surrounded by actinolite as an alteration product. *d)* Block-like orthopyroxene, intergrown with fine-grained magnetite surrounds altered olivine. *e)* Euhedral garnet, bearing abundant biotite inclusions and being intimately associated with tabular biotite surrounds igneous ilmenite. *f)* Garnet-biotite corona around orthomagmatic ilmenite. Both, garnet and biotite are in direct contact to ilmenite.

5.1.2.3 Ilmenite-magnetite-orthopyroxene symplectites

In five more leucotroctolite samples, one of them containing type-I corona structures, conspicuous ilmenite-magnetite-orthopyroxene symplectites (IMOS) developed between intercumulus olivine (Fo₅₄₋₆₅) and magmatic Fe-Ti oxides.

Both the symplectites and the bordering olivine are enclosed by a continuous rim of block-like orthopyroxene (Fig. 5.5 a) that also separates the symplectites from the magmatic Fe-Ti oxide grains. The IMOS probably formed at the expense of olivine and magmatic Fe-Ti oxides, following the balanced reaction



Since the reaction was not isochemical, the formation of ilmenite in the symplectites is only possible if Ti is introduced into the system. This may explain the presence of symplectites in close proximity to magmatic ilmenite. Where olivine is in contact with the symplectite bodies, it is usually altered to talc, carbonate and magnetite, as described above. EMP analyses revealed that block-like orthopyroxene around olivine is richer in MgO than orthopyroxene in contact to symplectites and igneous Fe-Ti oxides (En₆₇₋₇₁ vs. En₅₈₋₆₁).

The symplectite bodies bordering olivine are irregular in shape, with diameters varying from 0.2 to 5 mm (Fig. 5.5 a-c). They mainly consist of magnetite with ilmenite oxy-exsolution lamellae set in a polycrystalline orthopyroxene matrix displaying the same composition (En₅₈₋₆₁) as the associated block-like orthopyroxene rim. Within distinct orthopyroxene grains of the IMOS, two different types of magnetite are intergrown with orthopyroxene, *i.e.* (i) lamellar-planar, with magnetite grains of 30-60 μm length and 1-7 μm width, and (ii) vermicular, with magnetite grains of 2-8 μm size (Fig. 5.5 a-f). As shown in perpendicular sections of the same region, the lamellar-planar and the vermicular types of IMOS are not due to an effect of the third dimension. In most cases, only one type of intergrowth is present within one individual orthopyroxene grain, called a symplectitic domain (Fig. 5.5 c). In the lamellar-planar

intergrowths, the magnetite lamellae are commonly curved (Fig. 5.5 a-d). Rarely, lamellar growth-forms grade into vermicular intergrowths within a single symplectitic domain (Fig. 5.5b).

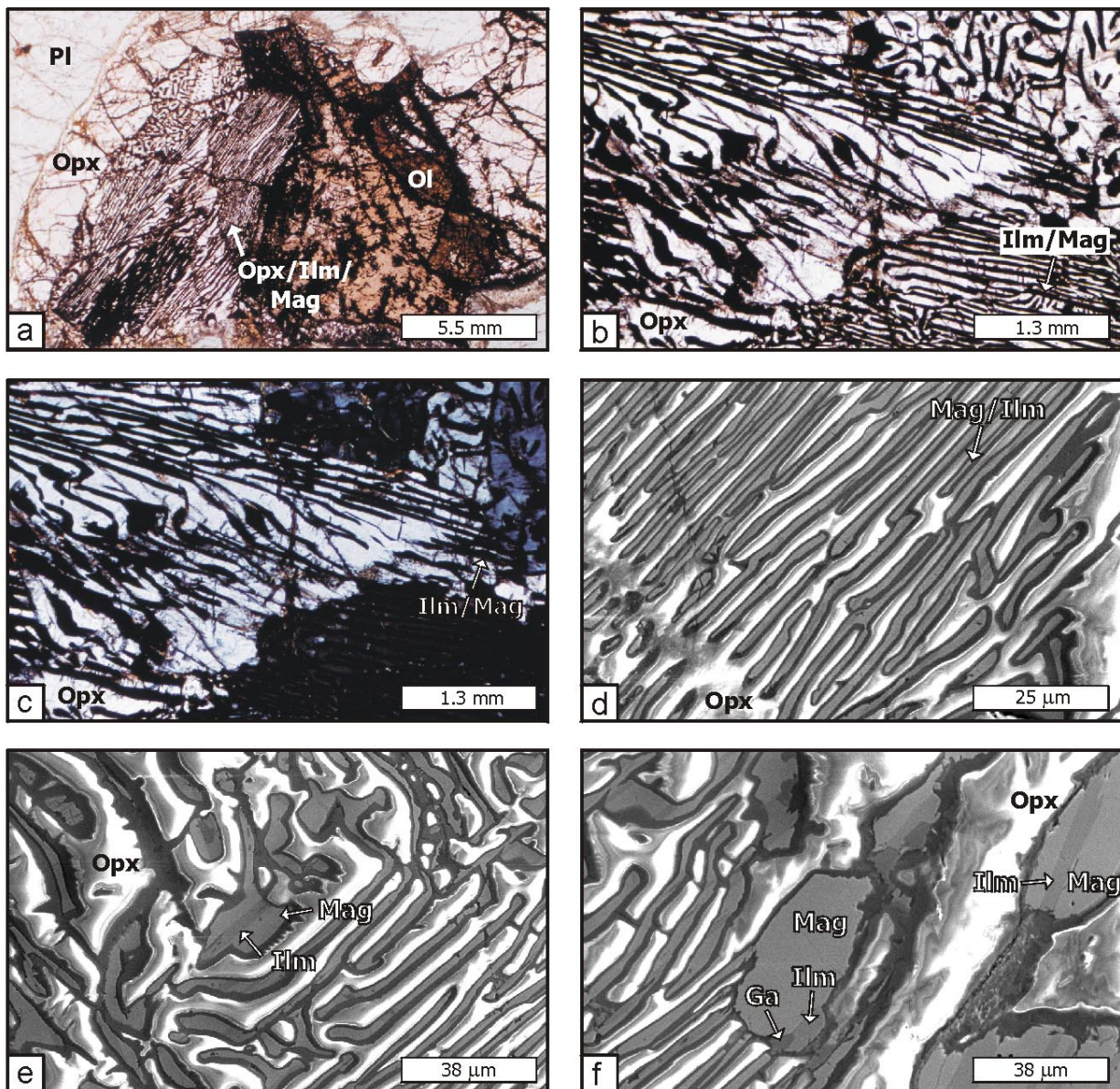


Fig. 5.5: Polished-section photomicrographs (a-c) and scanning electron microprobe images (e-f) of ilmenite-magnetite-orthopyroxene symplectites, developed in the leucotroctolites of the Kunene Intrusive Complex. Plane-polarized light (a-b). Cross-polarized light (c). **a)** Ilmenite-magnetite-orthopyroxene symplectite in contact to igneous olivine. Both, the symplectite and olivine are rimmed by a continuous corona of orthopyroxene. **b)** Within the whole symplectite body the two types of intergrowths between magnetite and orthopyroxene, i.e. vermicular and lamellar, are juxtaposed. **c)** In most cases, only one type of intergrowth occurs within each single orthopyroxene grain displaying different grey values under half-crossed polarizers. **d)** One-directional set of ilmenite exsolution lamellae in lamellar magnetite-orthopyroxene intergrowths. **e)** Lamellar growthform of magnetite and orthopyroxene, transitionally grading outward into vermicular intergrowths. **f)** Anhedral gahnite and ilmenite occur in patches, with gahnite displaying irregular grain boundaries against magnetite.

The size of the orthopyroxene grains decreases from 4 mm to 0.5 mm when approaching olivine. An analogous change in grain size is reflected by the Fe-Ti oxides. In direct contact with olivine, the grain size of the orthopyroxene diminishes to 0.03-1.5 mm, with a simultaneous decrease in the grain size of the Fe-Ti-oxide lamellae to 3-5 μm length and 0.5-1 μm width (Fig. 5.5 a). As a result, these intergrowths appear opaque in transmitted light.

The proportions of orthopyroxene and Fe-Ti oxides in the IMOS have been determined by volumetric integration of the SEM images, utilising a computer-controlled LEICA microscope with VIDS (video image digitalizing system) software, hosted in the Institute of Geology, University of Würzburg. It is interesting to note that at the contact to olivine, the fine-grained IMOS contains 29-31 (± 1) vol.% of Fe-Ti oxide, whereas in the coarsest domains, close to intercumulus ilmenite, the Fe-Ti oxide content decreases to 13-16 (± 1) vol.%. The average oxide content, integrated across the whole symplectite body is 18 (± 1) vol.%. Notwithstanding the textural differences, compositions of orthopyroxene and magnetite (average composition: $\text{Mt}_{99.1}\text{Ulv}_{0.2}\text{Chr}_{0.6}\text{Gl}_{0.1}$) remain constant in all symplectite domains. The magnetite itself displays complex oxy-exsolution of ilmenite (average composition: $\text{Ilm}_{93.6}\text{Pph}_{4.4}\text{Gkl}_{0.9}\text{Hem}_{1.1}$) lamellae oriented $\parallel (111)$ and $\parallel (100)$. In addition, ilmenite of the same composition occurs in irregular patches within magnetite (Fig. 5.5 f). Subordinate anhedral gahnite (average composition: $\text{Mt}_{7.5}\text{Hc}_{32.3}\text{Sp}_{23.1}\text{Ga}_{37.1}$), with grain sizes varying from 1 to 7.5 μm , is associated with ilmenite in patches, both displaying irregular boundaries against magnetite (Fig. 5.5 f).

SEM studies were undertaken to establish the textural relationships between orthopyroxene, Fe-Ti oxides and gahnite with the aid of back-scattered electron images (Fig. 5.5 d-f). Depending on the size of the magnetite lamellae, within one single orthopyroxene grain, two different orientation relationships between magnetite and ilmenite were observed:

(1) Within one symplectite domain, lamellar or vermicular magnetite contains a one-directional set of parallel ilmenite lamellae oriented parallel to the elongation of the lamellar magnetite. The orientation of the ilmenite exsolution lamellae is not changed even if the magnetite host is bent, or by the transition from lamellar to vermicular magnetite (Fig. 5.5 d, e). Within single magnetite lamellae, the width of the ilmenite oxy-exsolution lamellae is constant in most cases (Fig. 5.5 d). This feature suggests that individual magnetite lamellae are monocrystalline, whereas different lamellae represent different crystals. Larger equant magnetite grains (45-60 μm in size), which occur besides the lamellar magnetite, are presumably

polycrystalline, since the ilmenite lamellae in these grains may be interrupted or changed in width.

(2) In contrast to (1), one large polycrystalline magnetite aggregate contains ilmenite lamellae with variable orientation. This may be due to the development of different ilmenite exsolution-lamellae systems, but may also reflect different orientations of individual magnetite grains.

In conclusion, the textures suggest an oriented intergrowth of orthopyroxene with magnetite in a similar way as described by Barton et al. (1991), such that (111) of the magnetite lamellae is oriented parallel to (100) of orthopyroxene. According to Barton et al. (1991) the similarity of the symplectites with products of eutectoidal reaction and the absence of hydrous phases like amphibole or biotite in the symplectites is indicative of nucleation and growth during subsolidus cooling under static, dry conditions. Small-sized equivalents of the IMOS may occur within altered olivine crystals, where they nucleated in contact to veins, filled with exsolved magnetite.

5.2 Petrography of the felsic rock suite

Two samples of quartz-syenite, 4 samples of granite and 29 samples of syenite have been taken from the sodalite mining area, from a granite intrusion near the southern margin of the Zebra mountains and along the Kunene River road. It has to be mentioned, however, that more than half of the 29 syenite samples from the Swartbooisdrif area (N=17) underwent a metasomatic alteration, and will thus be described later (see Chapter 13.2).

Granite (G): B-98-170a, B-98-180a, B-99-410, Ku-01-16

Quartz-syenite (S,qtz): Ku-98-07, Ku-98-40

Syenite (S,fs): Ku-98-24, Ku-98-93, Ku-98-111, Ku-99-03, Ku-99-11, Ku-99-12, Ku-99-13, Ku-99-14, Ku-99-16, Ku-99-20, Ku-99-21, Ku-01-13

Both, the alkali-feldspar granite and the quartz-syenite lithologies are characterized by a equigranular to weakly porphyritic appearance, dominated by medium to fine-grained **potassium feldspar** (microcline or orthoclase; 55-75 vol.%) and **plagioclase** (5-35 vol.%), mostly lacking a preferred orientation. Dust-like inclusions of hematite-rich Fe-Ti oxides are present in most of the K-feldspar crystals, accounting for the generally reddish to brownish macroscopic colour of the rocks. Both the K-feldspar and plagioclase suffered a certain amount of sericitization, which, however, predominantly affected the K-feldspar and plagioclase cores.

Minor subhedral to euhedral **clinopyroxene** (3-8 vol.%), locally displaying narrow rims of euhedral epidote and carbonate, as well as late subhedral to anhedral **quartz** (5-10 vol.%) are restricted to the alkali-feldspar granites and the quartz-syenite lithologies. A common feature of the syenites is the enrichment of Fe-Mg silicates and Fe-Ti oxides, when compared to their quartz-bearing counterparts. In these rocks subhedral to anhedral **hastingsite** is the dominant mineral among Fe-Mg-silicates (5-23 vol.%). The grains of hastingsitic amphibole may in turn be marginally replaced by symplectitic intergrowths of hastingsite, plagioclase and Fe-Ti oxide.

Common accessories of the felsic rocks are **apatite**, **titanite**, **epidote**, **ilmenite**, **magnetite** and **zircon**. Due to a brittle deformation event, the feldspar crystals are locally brecciated and

marginally re-crystallized to fine-grained, granular albite mosaics. Cracks in the rocks are commonly filled by epidote and/or carbonate.

5.2.1 Granite and quartz-syenite

Both the granite (G) and quartz-syenite (S,qtz) samples are mainly composed of micro- to mesoperthitic *potassium feldspar* (microcline and occasional orthoclase; Or₉₄₋₉₈), containing albite exsolution lamellae (An₁₋₄). It occurs as medium to coarse-grained, subhedral to anhedral, tabular grains or laths of up to 1.5 cm in length with embayed to straight grain boundaries. The K-feldspar most probably crystallized as sanidine which partially to completely retrogressed to orthoclase and microcline during cooling. Commonly the crystals display Carlsbad twinning and a strong perthitic exsolution (Fig. 5.6 a, b). String perthite, transgressing into patch and block perthite is most common (Fig. 5.6 a), whereas other exsolution textures like braid, vein, plate or flame perthite are rare (Fig. 5.6 b). In places, chess-board albite develops at the expense of microcline, suggesting an alteration of K-feldspar by auto-metasomatism or fenitization. A second generation of later microcline may occur, forming separate, anhedral grains, lacking exsolution textures (Fig. 5.6 c). Both K-feldspar generations are marginally recrystallised to granular and twinned albite, forming mosaics. Most of the feldspar crystals show a variable degree of sericitization, commonly concentrated in the crystal core. Exsolved hematite occurs as very fine-grained inclusions in some of the larger K-feldspar grains or is concentrated along the grain margins of recrystallised albite.

Weakly reverse zoned, platy *plagioclase* (An₁₃₋₁₈) phenocrysts, with mostly subhedral to euhedral shape (Fig. 5.6 d) may be present in varying amounts but are always less abundant than potassium feldspar. The fact that the oligoclase displays straight grain boundaries against the first generation of potassium feldspar is taken as evidence for a contemporaneous crystallization of plagioclase and potassium feldspar, as is typical for subsolvus granites. In one granite sample, an anti-rapakivi texture is developed, bearing orthoclase with marginal trails of quartz-inclusion that surrounds heavily sericitized plagioclase cores. Almost pure albite (An₁₋₃) occurs as fine-grained, granular recrystallisation product of the potassium feldspars and as chess-board albite, replacing microcline.

Subhedral to anhedral, greenish *clinopyroxene* (X_{Mg}: 0.45-0.51) occurs in the interstices between feldspar crystals, but may also be present as inclusions in these minerals (Fig 5.6 e). In

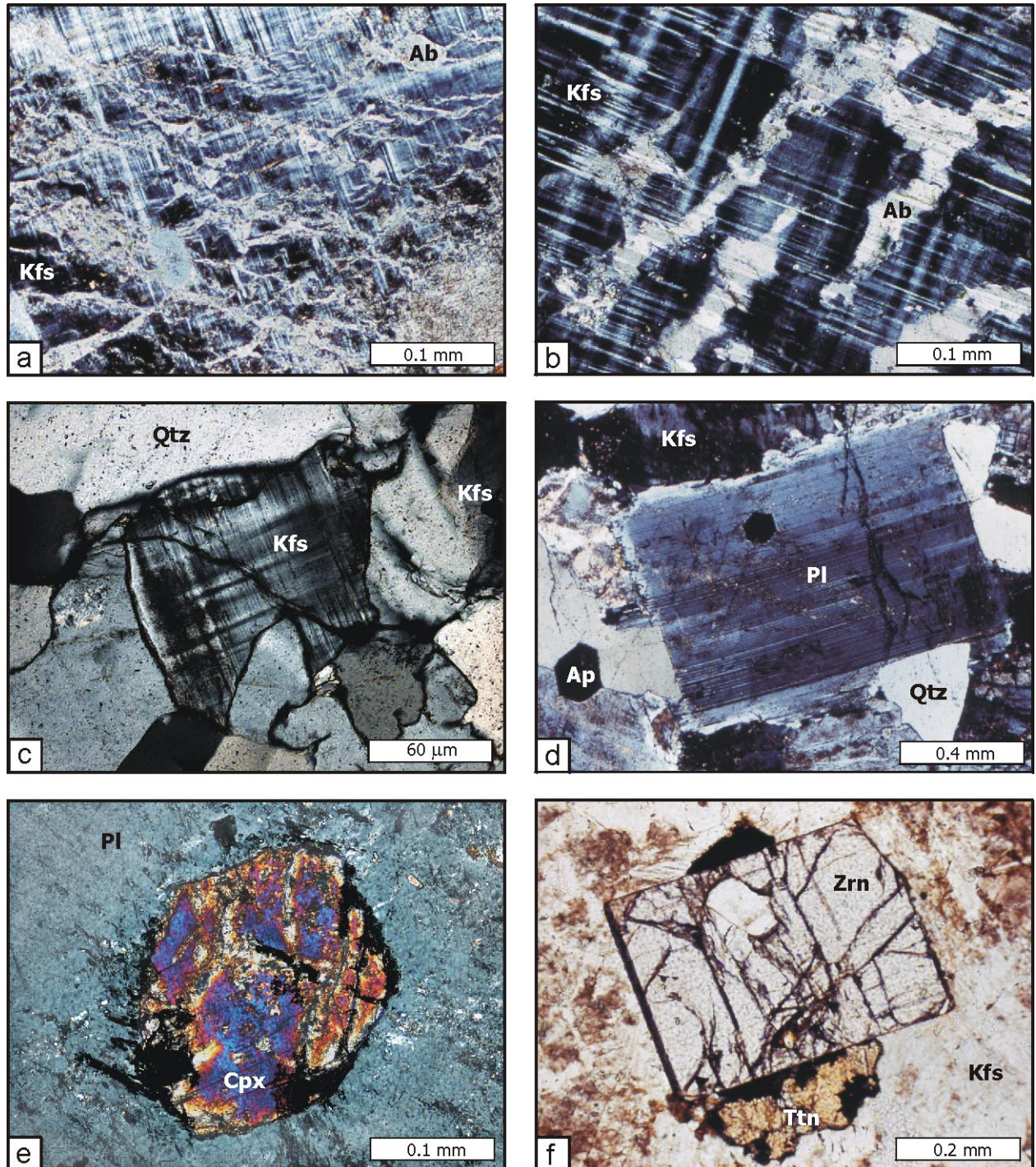


Fig. 5.6: Polished-section photomicrographs of the granite and the quartz-syenite. Cross-polarized light (a-e). Plane-polarized light (f). *a*) String perthite grading into blocky patch perthite. *b*) Vein perthite. *c*) Late, anhedral microcline fills the interstices between large K-feldspar crystals. *d*) Euhedral, tabular plagioclase, bearing an apatite inclusion, displays straight grain boundaries against K-feldspar of the first generation (upper left). *e*) Euhedral clinopyroxene inclusion in plagioclase. *f*) Anhedral titanite surrounding an euhedral zircon crystal.

cases, the clinopyroxene is replaced by fine-grained intergrowths of epidote, carbonate and chlorite. These altered clinopyroxenes are locally rimmed by euhedral epidote, which in turn is surrounded by impersistent rims of granular carbonate.

Anhedral *magnetite* displaying oxidative exsolution of ilmenite-lamellae $\{111\}$ and $\{100\}$ as well as late anhedral *quartz* (bearing abundant fluid inclusions) occur as separate grains, filling the interstices between individual feldspar crystals.

Titanite (aSph: 0.87-0.90), as large anhedral grains, is the most common accessory phase, associated with zircon, epidote or Fe-Ti oxides (Fig. 5.6 f). *Apatite* occurs as stubby prisms, commonly included in plagioclase, whereas *zircon* is found as isolated, euhedral crystals. Secondary enrichment of *epidote* ($P_{S_{21-32}}$) in clusters is common in samples, where hydrothermal alteration is more pronounced. *Sericite* is an alteration product of the feldspars, whereas very fine-grained epidote, *chlorite* and *carbonate* replace former Fe-Mg silicates.

5.2.2 Syenite

Strongly exsolved, micro- to mesoperthitic *potassium feldspar* (Or_{91-97}) is the main constituent of the medium-grained syenite. It occurs as subhedral to euhedral, elongated laths of 1-4 mm in length, commonly displaying Carlsbad twinning (Fig. 5.7 a). Former orthoclase was partially to completely replaced by microcline during cooling. Common perthite textures are string, patch, block, plate, braid and hair perthite, whereas flame perthite has only been observed sporadically (Fig. 5.7 b-d). Like their quartz-bearing counterparts, the syenites contain a second generation of microcline, forming homogeneous, fine-grained and anhedral crystals. Along their margins and cracks the potassium feldspars are recrystallised to fine-grained albite mosaics or are replaced by irregularly bounded aggregates of chess-board albite (Fig. 5.7 f).

Tabular to lathshaped, medium-grained *plagioclase* is reversely zoned albite to oligoclase, with the An-contents increasing slightly from core (An_{9-11}) towards the rim (An_{11-14}). Straight grain boundaries against potassium feldspar are common (Fig. 5.7 e). Plagioclase of similar composition occurs in fine-grained, symplectitic intergrowths with amphibole and Fe-Ti oxides. In clear contrast, plagioclase, grown at the expense of former potassium feldspar (Fig. 5.7 f), exhibits a weak normal zonation ($An_{4.5} \rightarrow An_{0.2}$) or is the unzoned, almost pure albite endmember. Alkali-feldspar inclusions may be preserved in the reversely zoned plagioclase

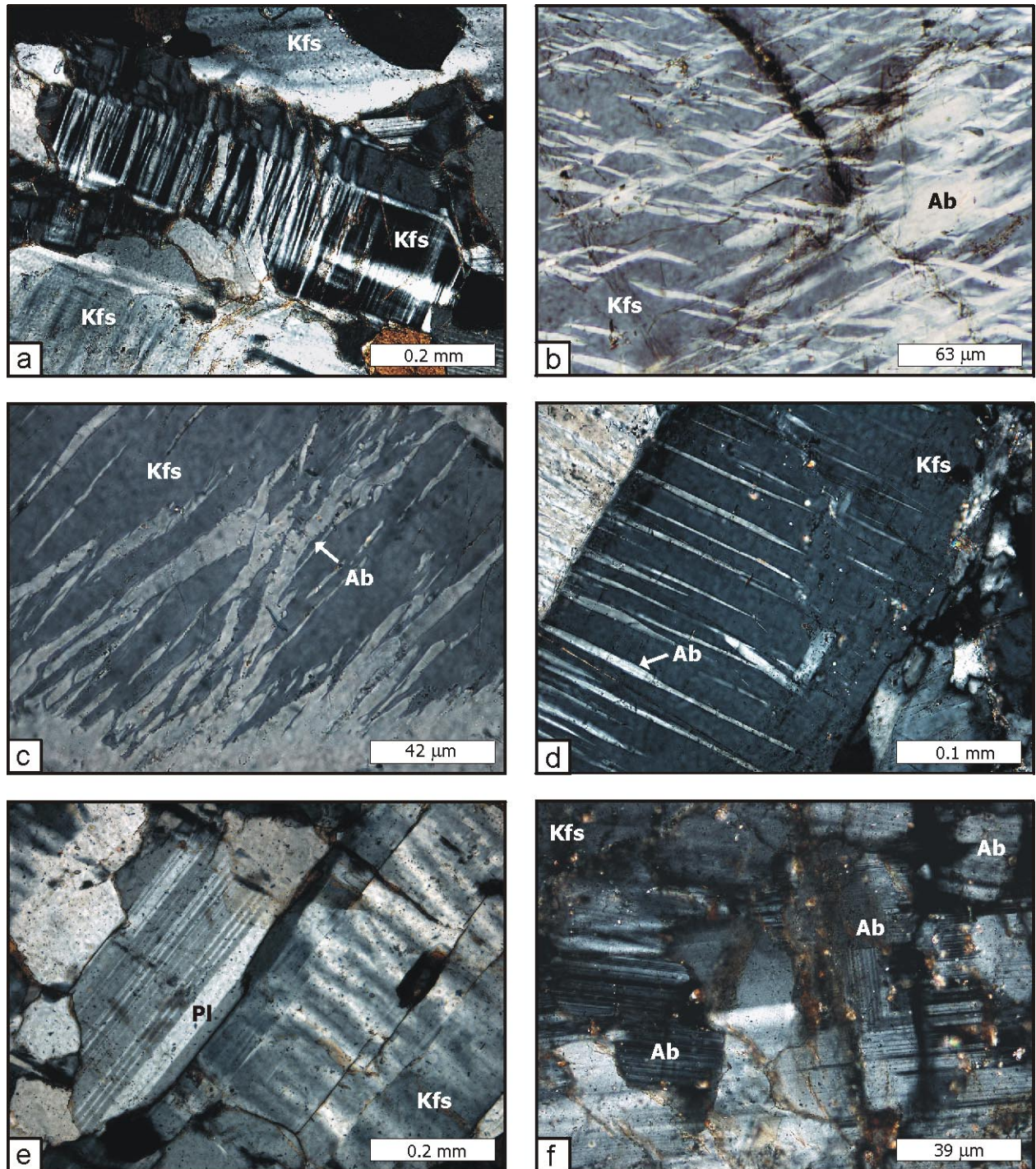


Fig. 5.7: Polished-section photomicrographs of the syenite. Cross-polarized light (a-f). *a*) Lathshaped, perthitic microcline, displaying Carlsbad-twinning. *b*) K-feldspar braid perthite. *c*) K-feldspar flame perthite. *d*) K-feldspar plate perthite. *e*) Magmatic plagioclase, displaying straight grain boundaries against K-feldspar. *f*) Chess-board albite, replacing K-feldspar.

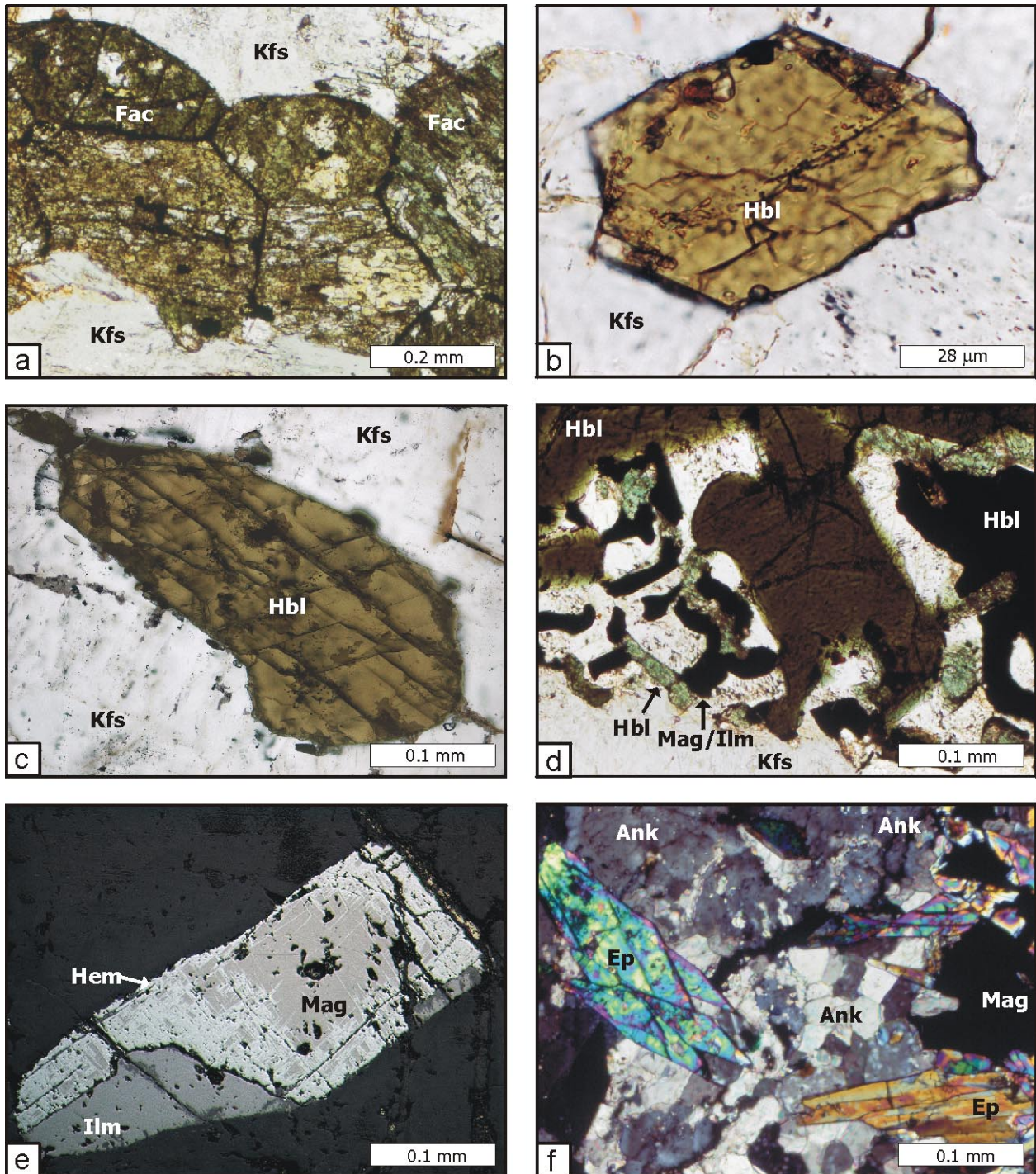


Fig. 5.8: Polished-section (a-d, f) and ore section (e) photomicrographs of the syenite. Cross-polarized light (f). Plane-polarized light (a-d). *a)* Early, euhedral to subhedral clinopyroxene, being completely replaced by fibrous ferro-hornblende to ferro-actinolite. *b)* Euhedral hastingsite inclusion in plagioclase. *c)* Subhedral, interstitial hastingsite. *d)* Hastingsite-plagioclase-magnetite-ilmenite symplectite surrounding interstitial hastingsite. *e)* Magnetite, displaying curved grain boundaries against ilmenite, is partially replaced by hematite. *f)* Epidote-ankerite-magnetite assemblage, surrounding an altered clinopyroxene.

crystals. In two syenite samples rapakivi-type textures with plagioclase rims on perthitic orthoclase have been observed. In all other samples, the respective feldspars form discrete grains.

Texturally early, euhedral to subhedral clinopyroxene is commonly completely replaced by fibrous *ferro-hornblende* to *ferro-actinolite* (X_{Mg} : 0.23-0.31; Fig. 5.8 a). Subhedral to euhedral *hastingsite* (X_{Mg} : 0.01-0.06) is included in plagioclase (Fig. 5.8 b). Hastingsite of a similar composition may also fill the interstices between individual feldspar crystals (5.8 c). or form symplectitic intergrowths with plagioclase and Fe-Ti oxides, surrounding interstitial amphibole (Fig. 5.8 d).

Large, anhedral *magnetite* is commonly spatially associated with *ilmenite*, forming clusters (Fig. 5.8 e). Martitisation of magnetite was observed in various stages of progression, and may even be advanced to the point where the texture consists of larger *hematite* areas, intergrown with relict magnetite. The Fe-Ti oxides are partially surrounded by narrow rims of titanite. In addition, both ilmenite and magnetite have been observed in very fine-grained symplectites replacing interstitial hastingsite, where the oxides are accompanied by amphibole and plagioclase, and as small, isolated grains.

Euhedral, prismatic *apatite*, anhedral grains and irregular rims of *titanite* (aSph: 0.79-0.85) as well as subhedral to euhedral *epidote* ($P_{S_{27-34}}$), intimately associated with magnetite and *ankerite* (Fig. 5.8 f), are common accessories (Fig. 5.8 f). Euhedral *zircon* is less abundant than in the quartz-syenites and granites. *Chlorite* (X_{Mg} : 0.09-0.11) and *sericite*, formed at the expense of hastingsite and feldspar, respectively, are the most common alteration products.

6 Mineral chemistry

The mineral chemistry of 26 selected samples of the rock types described in Chapter 4.2 (Petrography) has been investigated with the aid of electron-microprobe (EMP) analysis.

White anorthosite (A,w):

Ku-97-08b, Ku-97-33, Ku-97-33a, Ku-97-44

Leucogabbronorite (GN) and pyroxene-bearing anorthosite (A,px):

Ku-97-03, Ku-97-04, Ku-97-13, Ku-97-93, Ku-98-68, Ku-98-71, Ku-98-78, Ku-98-79,
Ku-98-84

Leucotroctolite (T) and olivine-bearing anorthosite (A,ol):

Ku-97-92, Ku-97-95, Ku-97-104, Ku-97-105, Ku-98-52, Ku-98-221a, Ku-98-221b

Quartz-syenite (S,qtz):

Ku-98-07, Ku-98-40

Syenite (S,fs):

Ku-99-11, Ku-99-12, Ku-99-13, Ku-99-14

Representative analyses are compiled in Tables A.5.1.1 to A.5.1.12 of the Appendix A.5.1. Analytical conditions are provided in Appendix A.2.3.

6.1 Feldspar

Calculation of the feldspar formula is based on 8 oxygens. Representative analyses of feldspar are depicted in Table A.5.1.1a and b in the Appendix A.5.1.

6.1.1 Anorthositic suite

The vast majority of the analysed cumulus plagioclase of the anorthositic rock suites shows minor chemical zoning, with the anorthite contents falling in the compositional range of andesine

Plagioclase from *leucogabbronorites* and *pyroxene-bearing anorthosites* (Fig. 6.1 b) of the dark anorthosite suite shows oscillatory zoning with the An-contents (An₄₃₋₅₄) being similar to those obtained for the white anorthosites. A tendency of decreasing An-contents towards the rims is common. A narrow rim of strongly reversed plagioclase was observed in one sample (Ku-98-84), where the An-content increases abruptly from 55 mol.% to 69 mol.%.

In clear contrast, plagioclase of the *olivine-bearing anorthosites* and *leucotroctolites* (Fig. 6.1 c) shows reverse to oscillatory zoning (An₄₇₋₇₅), with the highest An-contents being displayed by the *garnet-bearing leucotroctolite* (Fig. 6.1 d) samples. The most extreme difference between rim and core compositions is 14 mol.%; however, in most of the plagioclases the An-increase reaches a maximum of 3 mol.%. Plagioclase inclusions in olivine generally display similar An-contents as the matrix plagioclase. Strongly reversely zoned rims have been analysed in one sample (Ku-97-95).

In summary, the results indicate an increase of the An-content of plagioclase in the sequence (1) white anorthosite, leucogabbronorite and pyroxene-bearing anorthosite → (2) leucotroctolite and olivine-bearing anorthosite → (3) garnet-bearing leucotroctolite, which is in good accordance with the relative timing of their emplacement. Anderson & Morin (1968) proposed a subdivision of anorthosite massifs based on the An-contents of plagioclase. Following their classification, the white anorthosite as well as the leucogabbronorite and pyroxene-bearing anorthosite of the dark anorthosite suite could be considered as *andesine-type massifs*, whereas the younger leucotroctolites and olivine-bearing anorthosites would represent *labradorite-type massifs*, even though the compositions of plagioclase overlap. Regarding the Kunene Intrusive Complex, the increase in the An-content of plagioclase coincides with a decrease in crustal contamination, as is evidenced by the lack of crustal xenoliths in the leucotroctolites and olivine-bearing anorthosites. A similar model has also been proposed by Ashwal (1993) for other anorthosite massifs.

6.1.2 Felsic suite

Potassium feldspar in both, the *quartz-syenite* and the *syenite*, exhibits strong perthitic exsolution, with a potassium feldspar host (Or₉₁₋₉₈), containing albite (Ab₉₅₋₉₉) exsolution lamellae (Fig. 6.2). Recalculation of the magmatic compositions of K-feldspar before exsolution

concentrated on rare crystals, which lack extensive recrystallization and the secondary formation of chess-board albite.

Reintegrated compositions of K-feldspar cores of the syenite, analysed with a defocused beam of 20 μm size (Fig. 6.3), fall in the range of $\text{Ab}_{43.3}\text{An}_{1.9}\text{Or}_{54.8}$ – $\text{Ab}_{85.8}\text{An}_{4.1}\text{Or}_{10.1}$ whereas the feldspar rims have a more albite-rich composition ($\text{Ab}_{86.8}\text{An}_{2.6}\text{Or}_{10.6}$ – $\text{Ab}_{88.3}\text{An}_{3.1}\text{Or}_{8.6}$) or are the almost pure albite endmember ($\text{Ab}_{95.99}$).

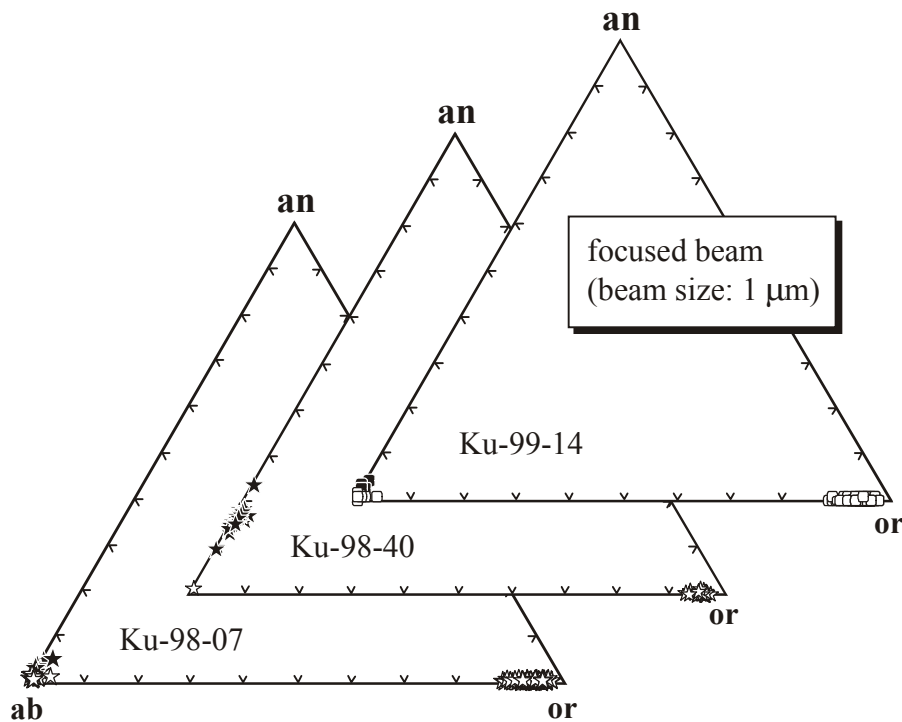


Fig. 6.2: Compositional variability of K-feldspar (mesoperthitic orthoclase/microcline; white symbols) and plagioclase (black symbols) in the quartz-syenites Ku-98-07 and Ku-98-40 and the syenite Ku-99-14, analysed with a focused beam of 1 μm size and expressed in the ternary diagram anorthite-albite-orthoclase.

A K-feldspar inclusion, preserved in a reversely zoned plagioclase crystal of the syenite Ku-99-11, displays an average Or-content of $\text{Ab}_{48.5}\text{An}_{3.1}\text{Or}_{48.4}$. The quite variable reintegrated core compositions of the analysed feldspars most probably reflect compositional modifications during late-stage coarsening of the mesoperthitic texture or continued cation exchange.

Plagioclase of the felsic suite generally displays lower An contents when compared to the anorthositic rocks. Based on their compositions and zoning patterns, plagioclase may be subdivided into two groups: Plagioclase of the *quartz-syenite* (sample Ku-98-40), containing abundant clinopyroxene inclusions, is almost unzoned oligoclase (An_{13-18}) with a slight rimward

increase of its An contents (Fig. 6.2). In contrast, plagioclase coexisting with amphibole and/or surrounding K-feldspar in the *syenite* (sample Ku-99-11) is mostly albite to oligoclase (Fig. 6.3), that displays a reverse zonation with the An-contents increasing slightly from core (An_{9-11}) to rim (An_{11-14}). Recrystallized plagioclase and chess-board albite of both the quartz-syenite (Ku-98-07) and the syenite (Ku-99-11, Ku-99-13, Ku-99-14) exhibits a weak normal zonation ($An_{4-5} \rightarrow An_{0-2}$) or is the almost pure albite endmember (An_{0-2} ; Fig. 6.2, 6.3).

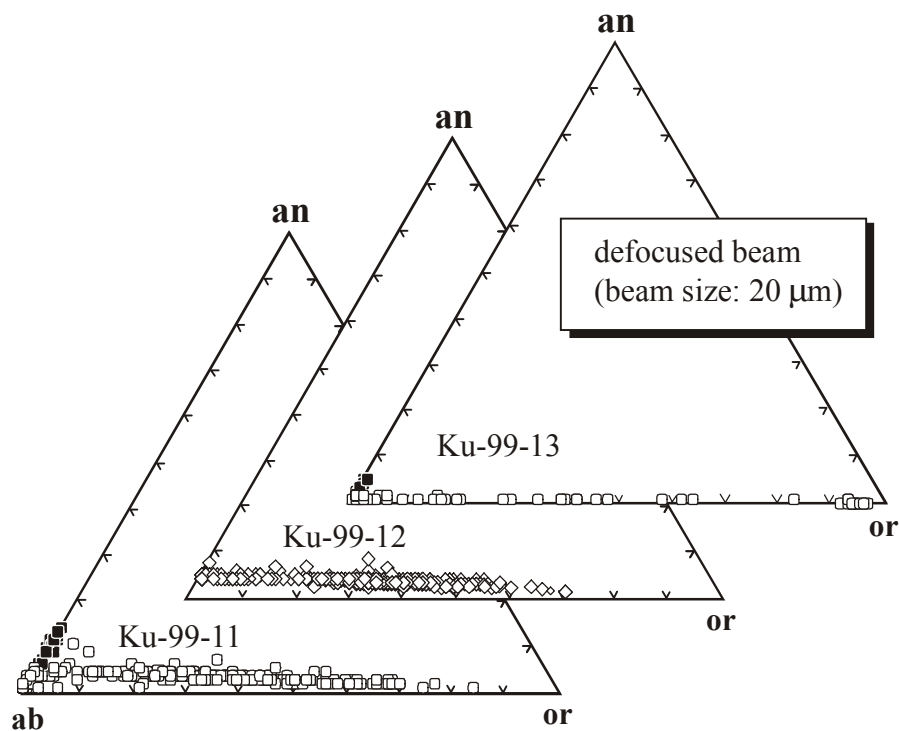


Fig. 6.3: Compositional variability of K-feldspar (micro-perthitic orthoclase/microcline, grey symbols) and plagioclase (black symbols) in the syenite, analysed with a defocused beam of 20 μm size and expressed in the ternary diagram anorthite-albite-orthoclase.

6.2 Olivine

Microprobe analysis was carried out for olivine from leucotroctolites of the dark anorthosite suite. Olivine formulae were calculated on the basis of 4 oxygens. Representative analyses are listed in Table A.5.1.2 in the Appendix A.5.1.

In general the olivines display a restricted, Mg-rich composition, ranging from 54-64 mol.% forsterite (Fo). All olivines are chemically unzoned with respect to the elements analysed. The Fo-content of olivine versus An-content of plagioclase diagram of Emslie (1985) allows a

comparison between mafic layered and massif-type intrusions in general. The analysed olivines of the KIC display only minor compositional variations when compared to the coexisting plagioclase, the samples thus plot in the field of massif-type anorthosite complexes and show no affinity to layered intrusions (Fig. 6.4).

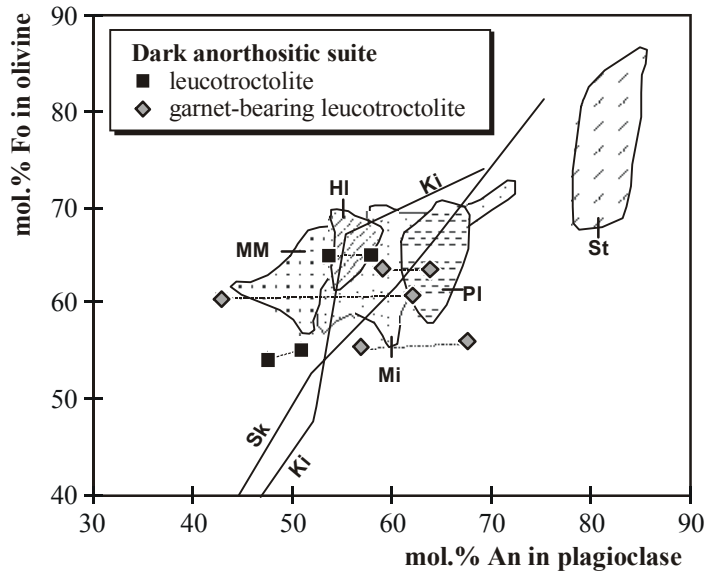


Fig. 6.4: Compositions of coexisting plagioclase and olivine from olivine-bearing anorthosites and leucotroctolites of the Kunene Intrusive Complex compared to those of other massif-type anorthosites and mafic layered intrusions (HI: Harp Lake; MI: Michikamau; MM: Mealy Mountains; PI: Paul Island. Layered intrusions: KI: Kiglapait; SK: Skaergaard; ST: Stillwater).

The distinctly higher Mg# of olivine when compared to the bulk-rock composition of the corresponding sample is most probably caused by the additional formation of intercumulus ilmenite and magnetite. However, the Mg-content of the analysed olivines is strongly controlled by the composition of the intercumulus melt as is suggested by the positive correlation of $Mg\#_{\text{olivine}}$ and $Mg\#_{\text{bulk rock}}$.

6.3 Pyroxene

Orthopyroxene has only been analysed in leucotroctolite and white anorthosite samples, since the analysis of the heavily altered orthopyroxene in the leucogabbroanorthosites and pyroxene-bearing anorthosites gave no reliable results. Clinopyroxene compositions were determined in leucogabbroanorthosites and leucotroctolites of the dark anorthosite suite and the felsic suite. The

calculation of the pyroxene formula followed the method of Papike & Cameron (1980) on the basis of 8 oxygens (Table A.5.1.3 in the Appendix A.5.1).

6.3.1 Orthopyroxene

Following the classification of Morimoto (1988) all orthopyroxenes of the anorthositic rocks of the KIC are enstatites, whereas they can be designated as hypersthene and bronzite after Poldervaart & Hess (1951). The composition of orthopyroxene strongly depends on the

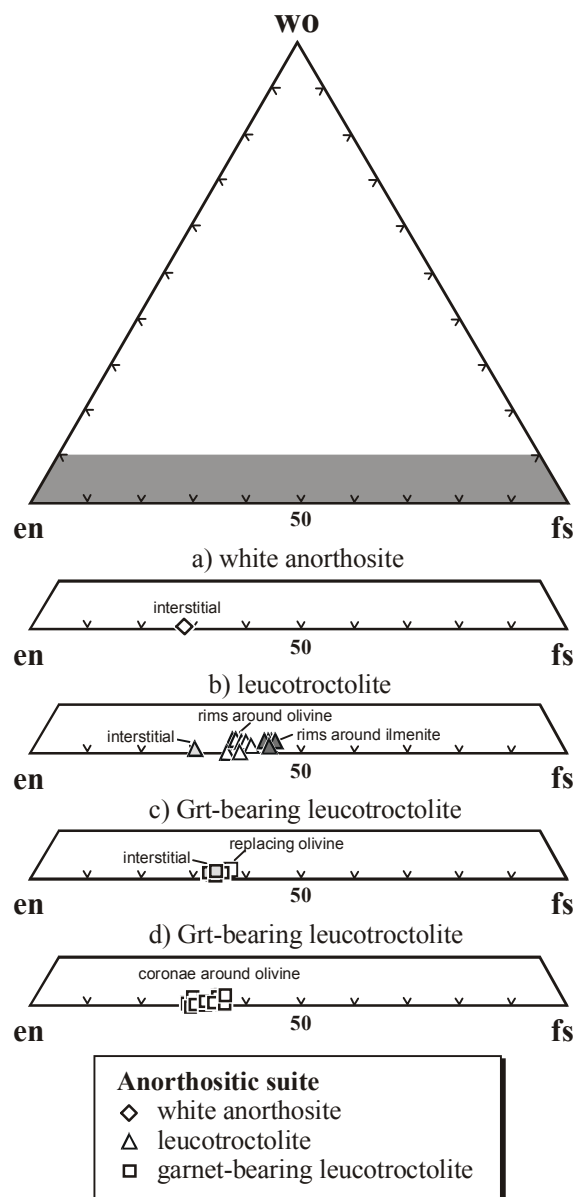


Fig. 6.5: Compositional variability of the composition of orthopyroxene from the white anorthosite and the leucotroctolite expressed in the diagram wollastonite-enstatite-ferrosilite.

bordering minerals. Intercumulus grains generally have the highest En-content, which however, decreases in the sequence white anorthosite → leucotroctolite → Grt-bearing leucotroctolite. In contrast, the highest Fs-content is displayed by late-magmatic orthopyroxene surrounding ilmenite and orthopyroxene occurring in symplectitic textures replacing former olivine. Late-magmatic orthopyroxene rims and recrystallised orthopyroxene coronas around olivine display similar, intermediate compositions, thus suggesting that the recrystallisation was an isochemical process.

The En-content of orthopyroxene versus An-content of plagioclase diagram of Emslie (1985) allows a comparison of the analysed orthopyroxene with that of other anorthosite intrusions. Orthopyroxenes of the KIC display only minor compositional variations when compared to the coexisting plagioclase, the samples thus clearly do not display a layered intrusion trend. It has to be mentioned, however, that the En-content of orthopyroxene is also distinctly higher than that of all other yet known massif-type anorthosite complexes.

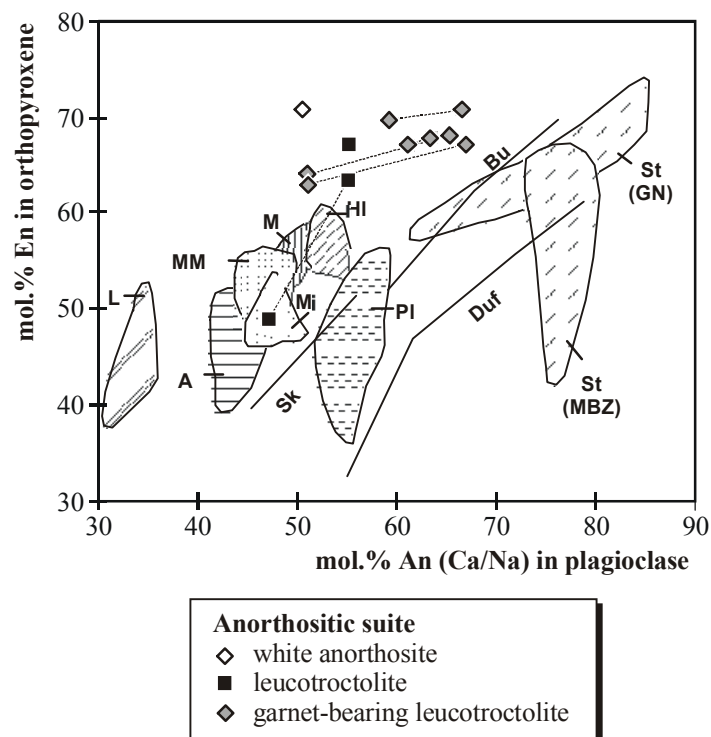


Fig. 6.6: Compositions of coexisting plagioclase and orthopyroxene from the white anorthosite and the leucotroctolites of the Kunene Intrusive Complex compared to those of other massif-type anorthosites and mafic layered intrusions (*A*: Adirondack; *HI*: Harp Lake; *L*: Labrieville; *M*: Morin; *Mi*: Michikamau; *MM*: Mealy Mountains; *PI*: Paul Island. *Layered intrusions*: *Bu*: Bushveld; *Duf*: Dufek; *Sk*: Skaergaard; *St*: Stillwater; *MBZ*: middle banded zone).

A weak positive correlation of the $Mg^{\#}_{\text{orthopyroxene}}$ and the $Mg^{\#}_{\text{bulk rock}}$ of the corresponding sample is displayed by most samples of the dark anorthosite suite. However, orthopyroxene from the white anorthosite does not follow this trend. The most plausible explanation for this deviation is the low resistance of Mg-Fe silicates against alteration when compared to Fe-Ti oxides. The hydrothermal overprint of the white anorthosite could thus have caused a relative decrease in the bulk rock $Mg^{\#}$.

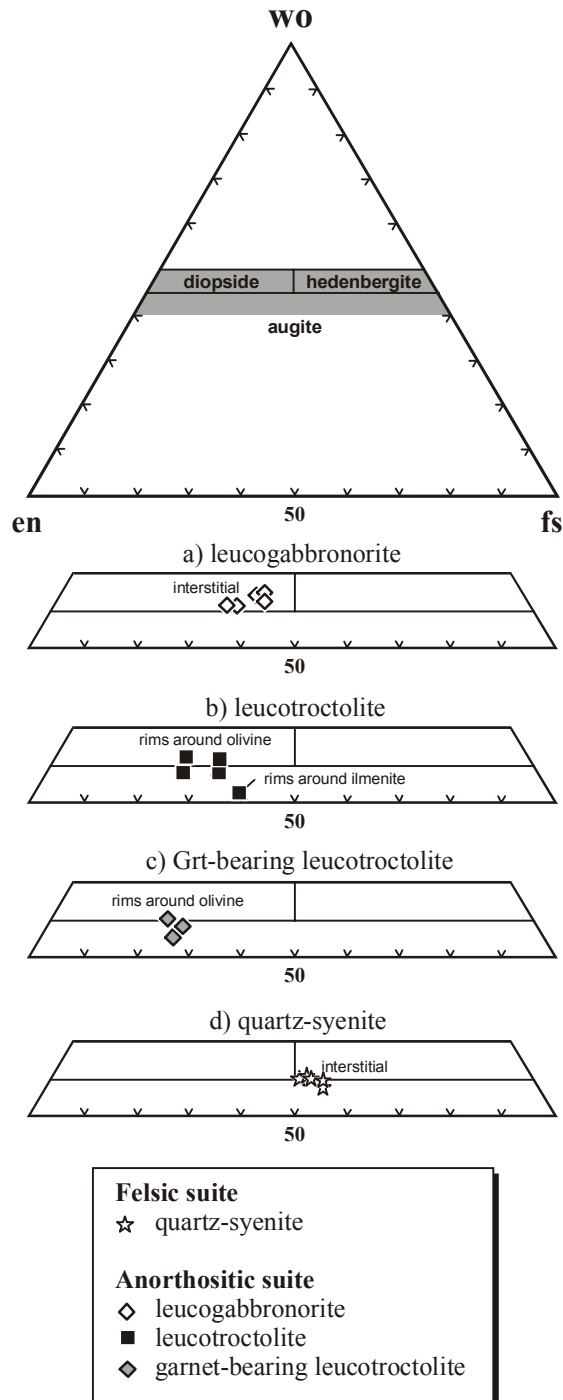


Fig. 6.7: Compositional variability of clinopyroxene from the white anorthosite and the leucotroctolite of the KIC and the quartz-syenite of the felsic suite, expressed in the diagram wollastonite-enstatite-ferrosilite.

6.3.2 Clinopyroxene

Following Poldervaart & Hess (1951) clinopyroxene of the *leucogabbronorites* is salite ($\text{Wo}_{44.4}\text{En}_{32.6}\text{Fs}_{18.3}$ – $\text{Wo}_{45.7}\text{En}_{27.8}\text{Fs}_{20.7}$), whereas clinopyroxene from the *leucotroctolites* ($\text{Wo}_{40.03}\text{En}_{34.4}\text{Fs}_{21.5}$ – $\text{Wo}_{43.5}\text{En}_{35.9}\text{Fs}_{12.4}$) and *garnet-bearing leucotroctolites* ($\text{Wo}_{42.3}\text{En}_{38.3}\text{Fs}_{14.2}$ – $\text{Wo}_{45.7}\text{En}_{39.1}\text{Fs}_{12.3}$) is salite to augite. After the IMA-classification of Morimoto (1988) all clinopyroxenes of the anorthositic rocks plot in the fields of diopside and augite (Fig. 6.7). The Al_2O_3 content of clinopyroxene from the anorthositic rocks is relatively high, increasing from leuconorite (Al_2O_3 : 1.49-1.92 wt.%) towards (garnet-bearing) leucotroctolite (Al_2O_3 : 1.65-3.25 wt.%).

The $\text{Mg}^\#$ of clinopyroxene of the anorthositic suite is quite homogeneous but generally higher than the $\text{Mg}^\#$ of orthopyroxene from similar samples. The $\text{Mg}^\#_{\text{clinopyroxene}}$ and the $\text{Mg}^\#_{\text{bulk rock}}$ exhibit a positive correlation.

In clear contrast, clinopyroxene from the *quartz-syenite* is more hedenbergitic in composition ($\text{Wo}_{43.8}\text{En}_{23.1}\text{Fs}_{28.0}$ – $\text{Wo}_{45.1}\text{En}_{25.4}\text{Fs}_{24.3}$; $X_{\text{Mg}} = 0.45$ -0.51) when compared to the anorthositic rocks. The Al contents are generally near the detection limit (Al_2O_3 : 0.41-0.79 wt.%), reflecting the Al-poor whole-rock composition of these rocks.

6.4 Amphibole

Minor amphibole occurs in almost all anorthositic rocks and is the dominant phase among Fe-Mg silicates in the syenites. Amphibole compositions are listed in Table A.5.1.4 in the Appendix A.5.1. The structural formula of amphibole was calculated on an anhydrous 23-oxygen basis. In both rock suites the amphiboles can be classified as calcic amphiboles in the sense of Leake et al. (1997). For the estimation of minimum and maximum Fe^{3+} contents a calculation modulus on the basis of 15 cations (excluding Na and K) and 13 cations (excluding Na, K and Ca), respectively, was chosen, following Spear & Kimball (1984). For the calculation of the average Fe^{3+} contents the mean value between the two extreme compositions was calculated, following the method of Papike et al. (1974), modified by Franz & Häussinger (1990).

Following the classification scheme of Leake et al. (1997) the vast majority of the late-magmatic amphiboles from the *anorthosite suites*, i.e. white anorthosite (Al p.f.u.: 2.42-2.97;

X_{Mg} : 0.65-0.70), leucogabbronorite (Al p.f.u.: 1.96-2.51; X_{Mg} : 0.51-0.73) and pyroxene-bearing anorthosite (Al p.f.u.: 1.82-2.29; X_{Mg} : 0.46-0.55) are magnesio-hastingsites/pargasites to ferro-pargasites/hastingsites (Fig. 6.8). The Ti contents of the amphiboles are variable (Ti p.f.u.: 0.02-0.40), depending on their textural position, e.g. amphiboles surrounding Fe-Ti oxides are generally characterized by the highest Ti contents. Magnesio-hastingsites and pargasites from garnet-bearing corona structures around olivine in the leucotroctolite are characterized by distinctly higher Mg and Al contents (Al p.f.u.: 2.73-2.81; X_{Mg} : 0.77-0.86), which may reflect the whole rock geochemistry of these rocks.

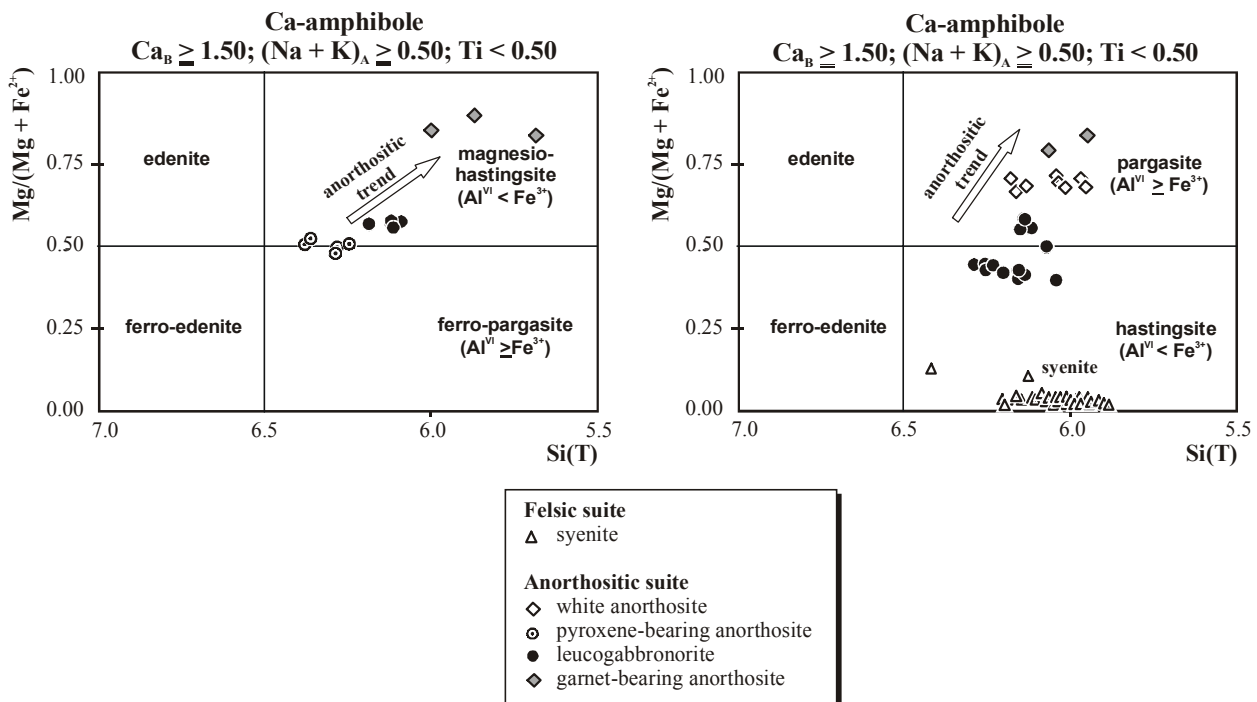


Fig. 6.8: Compositional ranges of primary magmatic Ca-amphiboles from the anorthositic rocks of the KIC and the syenites of the felsic suite expressed in the classification diagram of Leake et al. (1997).

In clear contrast, secondary amphibole formed at the expense of clinopyroxene in the leucogabbronorite and olivine in the leucotroctolites is mostly actinolite and rarely magnesio-hornblende (Al p.f.u.: 0.20-0.98; X_{Mg} : 0.60-0.65; Fig. 6.9).

Primary magmatic amphibole from the *syenites* is always hastingsite (Fig. 6.8), which, however, displays a distinctly lower X_{Mg} and Al contents (Al p.f.u.: 1.91-2.10; Ti p.f.u.: 0.07-0.26; X_{Mg} : 0.01-0.06) when compared to late-magmatic amphiboles of the anorthosite suite, whereas the Ti contents fall in a similar range.

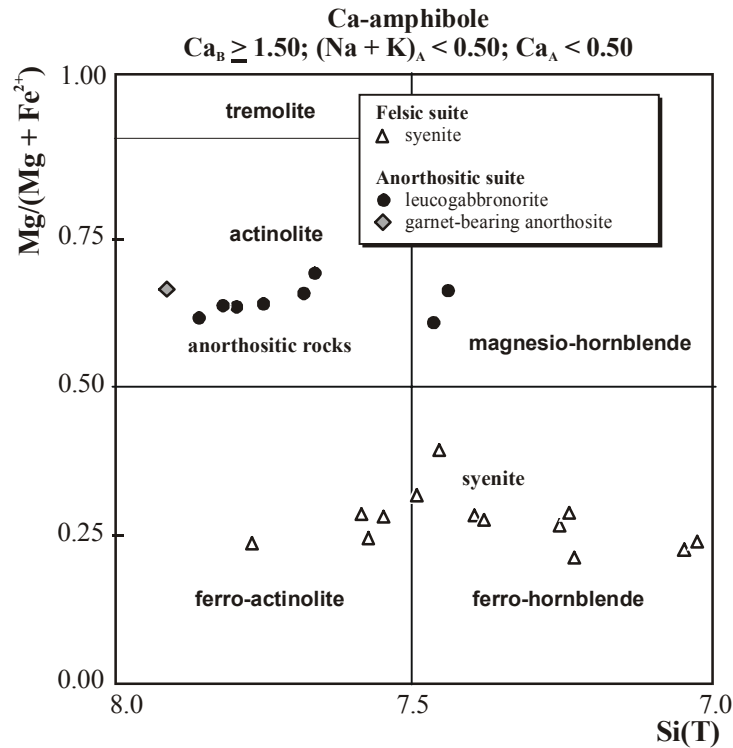


Fig. 6.9: Compositional ranges of secondary Ca-amphiboles from the anorthositic rocks of the KIC and the syenites of the felsic suite expressed in the classification diagram of Leake et al. (1997).

Secondary amphibole, formed by the hydrothermal alteration of clinopyroxene, is ferro-hornblende to ferro-actinolite (Al p.f.u.: 0.22-1.00; X_{Mg} : 0.23-0.31; Fig. 6.9). Its higher X_{Mg} , when compared to the magmatic amphiboles of the same samples, is most probably inherited from the former clinopyroxene.

6.5 Biotite

Microprobe analyses were carried out for biotite from the different anorthositic lithologies. Biotite formulae were calculated on the basis of 22 oxygens. Representative analyses are depicted in Table A.5.1.5 in the Appendix A.5.1.

The composition of the analysed biotites is strongly dependent on their respective textural position and rock type. The classification of Foster (1960; in Tröger, 1982) characterizes the majority of the unzoned late-magmatic biotite, surrounding ilmenite in the white anorthosite (X_{Mg} : 0.48; Al^{VI} : 0.87; Ti p.f.u.: 0.12), pyroxene-bearing anorthosite (X_{Mg} : 0.39-0.46; Al^{VI} : 0.35-0.45;

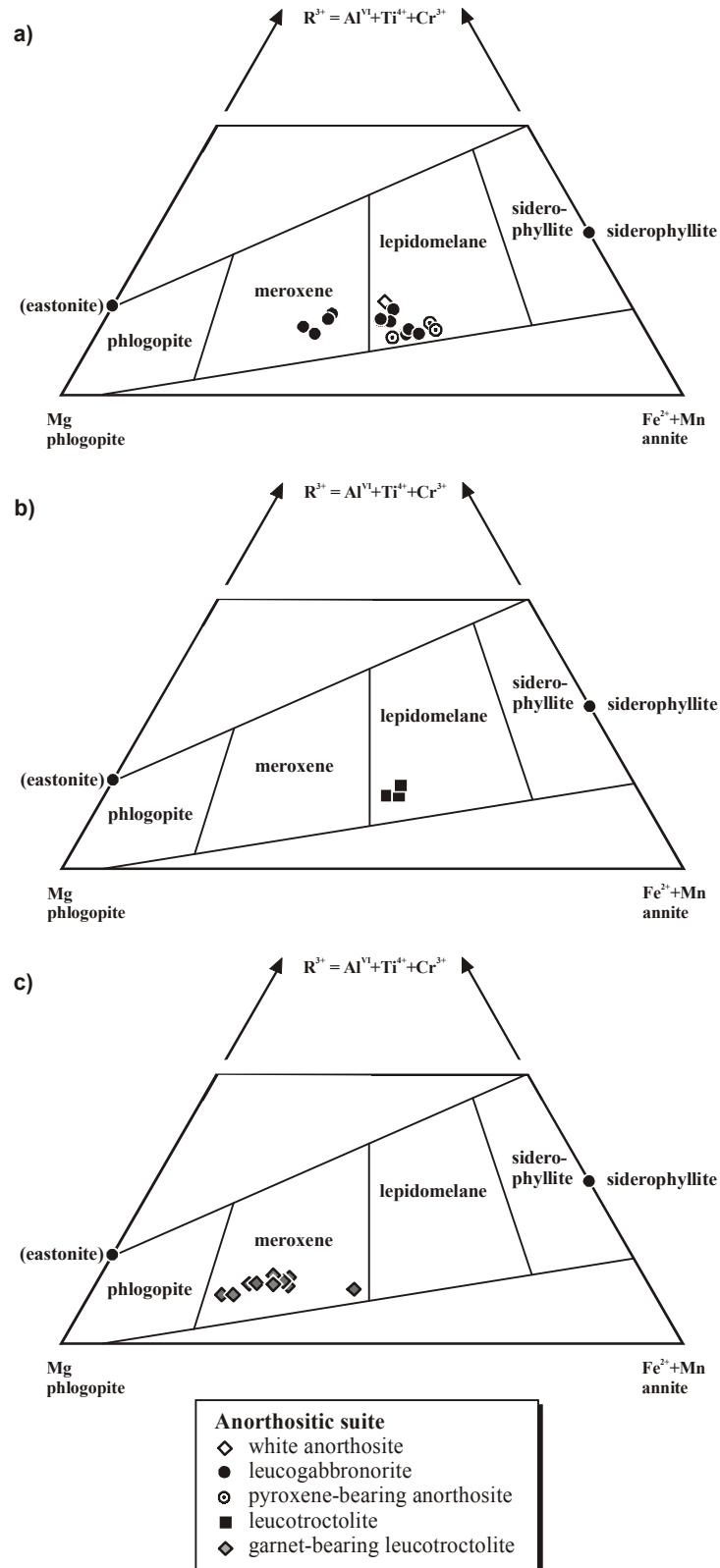


Fig. 6.10: Classification of biotite from the anorthositic rocks of the KIC in the modified ($Fe^{2+}=Fe^{tot}$) triangle R^{3+} ($Al^{VI}+Ti+Cr$)-Mg-($Fe^{2+}+Mn$) after Foster (1960, in Tröger, 1982). **a)** Magmatic biotite from the white anorthosite, pyroxene-bearing anorthosite and leucogabbro. **b)** Magmatic biotite from the leucotroctolite. **c)** Secondary biotite from the garnet-bearing leucotroctolite.

Ti p.f.u.: 0.25-0.28), leucogabbronorite (X_{Mg} : 0.42-0.48; Al^{VI} : 0.43-0.65; Ti p.f.u.: 0.17-0.26) and garnet-free leucotroctolite (X_{Mg} : 0.45-0.48; Al^{VI} : 0.54-0.71; Ti p.f.u.: 0.21-0.26) as lepidomelanes, whereas meroxenes are rare (Fig. 6.10 a-b). In clear contrast, all biotites formed by subsolidus processes in the garnet-bearing leucotroctolite samples are meroxenes (Fig. 6.10 c), even though they occur in different textural positions, i.e. as coronas surrounding ilmenite (X_{Mg} : 0.66-0.77; Al^{VI} : 0.20-0.27; Ti p.f.u.: 0.36-0.48) and olivine (X_{Mg} : 0.75; Al^{VI} : 0.24; Ti p.f.u.: 0.34), as fine-grained inclusions in garnet (X_{Mg} : 0.68; Al^{VI} : 0.22; Ti p.f.u.: 0.45) and intergrown with garnet (X_{Mg} : 0.0.72-0.73; Al^{VI} : 0.34-0.44; Ti p.f.u.: 0.26-0.33). The fact that late-magmatic biotite together with amphibole are abundant phases in almost all investigated samples, suggests that the crystallization from the latest stage liquid differentiates occurred under a high water fugacity.

6.6 Titanite

Titanite was analysed in samples of the quartz-syenite and the syenite. Titanite formulae were calculated anhydrous on a 20-oxygens basis (Table A.5.1.6 in the Appendix A.5.1).

Titanite from both the quartz-syenite and the syenite contains appreciable amounts of Al (Al p.f.u.: 0.28-0.36 and 0.69-0.90, respectively) and Fe^{3+} (Fe p.f.u.: 0.27-0.44 and 0.21-0.43, respectively), thus deviating significantly from the ideal formula $CaTi[O/SiO_4]$. For the formation of these so-called grothites, a charge balance by the coupled substitution of $(Al, Fe^{3+}) + (F, OH^-) = Ti^{4+} + O^{2-}$ (Oberti et al., 1991) is required, which also accounts for the low total sums of the analyses.

6.7 Fe-Ti oxides

Ilmenite and magnetite are ubiquitous accessory constituents of both the anorthositic and the felsic rock suite, whereas martitisation of magnetite is restricted to the syenite samples. The calculation of the ilmenite and hematite formula was based on 6 oxygens whereas magnetite was calculated on a 4-oxygens basis. For the estimation of the Fe^{3+} contents of ilmenite/hematite and magnetite a calculation modulus on the basis of 4 and 3 cations, respectively, was chosen.

Representative analyses of ilmenite, magnetite and hematite are listed in Tables A.5.1.7, A.5.1.8 and A.5.1.9, respectively, in the Appendix A.5.1.

6.7.1 Ilmenite

In the *anorthositic rock suite*, ilmenite occurs in three different textural positions, i.e. (1) as discrete grains in the interstices between plagioclase crystals, (2) as ilmenite exsolution lamellae in magnetite and (3) in symplectitic intergrowth with orthopyroxene and magnetite. EMP analyses revealed ilmenite compositions with minor amounts of the Mn end-member pyrophanite and quite variable contents of hematite. The Mn and Fe³⁺ contents of intercumulus ilmenite (MnO: 0.74-3.09 wt.%, Hem: 0.00-4.09 mol.%) slightly increase in the sequence white anorthosite (MnO: 0.74-2.62), leucogabbronorite and pyroxene-bearing anorthosite (MnO: 1.82-2.91) towards leucotroctolite and olivine-bearing anorthosite (MnO: 1.28-3.09).

In clear contrast, the MnO contents of ilmenite oxy-exsolution lamellae in magnetite are distinctly lower, ranging from 0.92-0.99 wt.% (leucotroctolite) to 0.55-1.10 wt.% (leucogabbronorite). Ilmenite of the ilmenite-magnetite-orthopyroxene symplectites (IMOS) is characterized by relatively high MnO contents of 1.50-2.09 wt.% in the leucogabbronorites, 1.14-1.24 wt.% in the leucotroctolites and 2.17-3.54 wt.% in the garnet-bearing leucotroctolite samples. The hematite contents of both ilmenite types fall in a range of 0.00-1.83 mol.%.

Discrete grains of ilmenite in the *syenite* are characterized by high MnO amounts of 5.37-6.04 wt.% and a low hematite content of 0.00-2.25 mol.%. In contrast, ilmenite oxy-exsolution lamellae in magnetite of the *quartz-syenite* display higher FeO^{tot}/MnO ratios, containing lower amounts of MnO (4.88-4.94 wt.%) but displaying higher hematite contents (2.39-2.44 mol.%).

6.7.2 Magnetite

Magnetite from the *anorthositic rock suite* occurs as (1) inclusions in plagioclase, (2) homogeneous intercumulus grains, (3) intercumulus grains with ilmenite-exsolution lamellae and (4) in intergrowths with symplectitic ilmenite and orthopyroxene in the IMOS. Depending on their respective textural position, magnetites display minor differences in their TiO₂ contents, with ranges of 0.59-0.65 wt.% in discrete magnetite grains from the leucotroctolites, 0.03-0.11 wt.% in magnetite displaying ilmenite oxy-exsolution lamellae and 0.02-0.17 wt.% in magnetite

from symplectitic intergrowths, replacing olivine and pyroxene. Magnetite inclusions in plagioclase are too small, to obtain reliable analyses.

Magnetite from the *felsic suite*, displaying ilmenite oxy-exsolution lamellae, is generally characterized by low Ti contents (TiO_2 : 0.00-0.13 wt.%). The Ti content of magnetite in symplectitic intergrowth with amphibole and plagioclase in the syenites is similar (TiO_2 : 0.02 wt.%).

6.7.3 Hematite

Hematite, formed by martitisation of magnetite from the *syenite* was found to be almost pure Fe_2O_3 . The TiO_2 contents are generally low, ranging from 0.03-0.18 wt.% whereas Cr_2O_3 , MgO and MnO are generally below the detection limit.

6.8 Garnet

Andradite-garnet has been observed in one white anorthosite (Ku-97-08b) and one leucogabbronorite sample (Ku-97-03), where it occurs as xenocrysts that are marginally replaced by chlorite. In addition, almandine-pyrope garnet surrounding intercumulus olivine and ilmenite is present in some of the leucotroctolite samples (Ku-97-104, Ku-97-105, Ku-98-57, Ku-98-220, Ku-98-221a, Ku-98-221b). In contrast to the former, these garnets were formed during a subsolidus re-equilibration of the leucotroctolites under upper amphibolite to granulite-facies conditions. Garnet formulae were calculated on a 24-oxygen basis. For the estimation of the Fe^{3+} contents of garnet a calculation modulus on the basis of 16 cations was chosen. End-member calculation followed the sequence uvarovite, andradite, grossular, almandine, spessartine and pyrope. Representative analyses are depicted in Table A.5.1.10 in the Appendix A.5.1.

Garnet xenocrysts in the white anorthosite and leucogabbronorite belong to the andradite-grossular solid-solution series, ranging between $\text{And}_{72.3}\text{Grs}_{26.9}$ in sample Ku-97-08b and $\text{And}_{94.9}\text{Grs}_{4.4}$ in the leucogabbronorite sample Ku-97-03 and containing negligible amounts of Ti, Mg and Mn. The compositional range of the analysed garnets agrees well with that known from typical calc-silicate rocks and skarn assemblages. Indeed, scattered outcrops of calc-silicate rocks have been observed in both the Namibian (Brandt, in prep.) and the Angolan part of the Epupa Complex (Carvalho & Alves, 1990), thus suggesting that the early generations of

anorthositic crystal mushes incorporated crustal calc-silicate material during their ascent. However, such calc-silicate rocks are rare in the exposed parts of the Epupa Complex, which mainly consist of metabasites, metapelites, metasepites and granitic gneisses (Brandt et al., 2003). The fact that xenoliths of the latter lithologies have never been observed in the anorthositic rocks is taken as evidence that the lower, not exposed zones of the EC differ in composition from its superficial parts by containing significant amounts of calc-silicate material.

Garnet of the leucotroctolites is always almandine-pyrope with a high grossular component (X_{Grs} : 0.04-0.18), reflecting the Ca-rich whole-rock geochemistry of the leucotroctolites. Spessartine is generally low (X_{Sps} : 0.02-0.04) and unzoned, indicating intracrystalline diffusional exchange and/or rapid growth. Depending on their mineral assemblage the analysed garnets display significant compositional differences (Fig. 6.11):

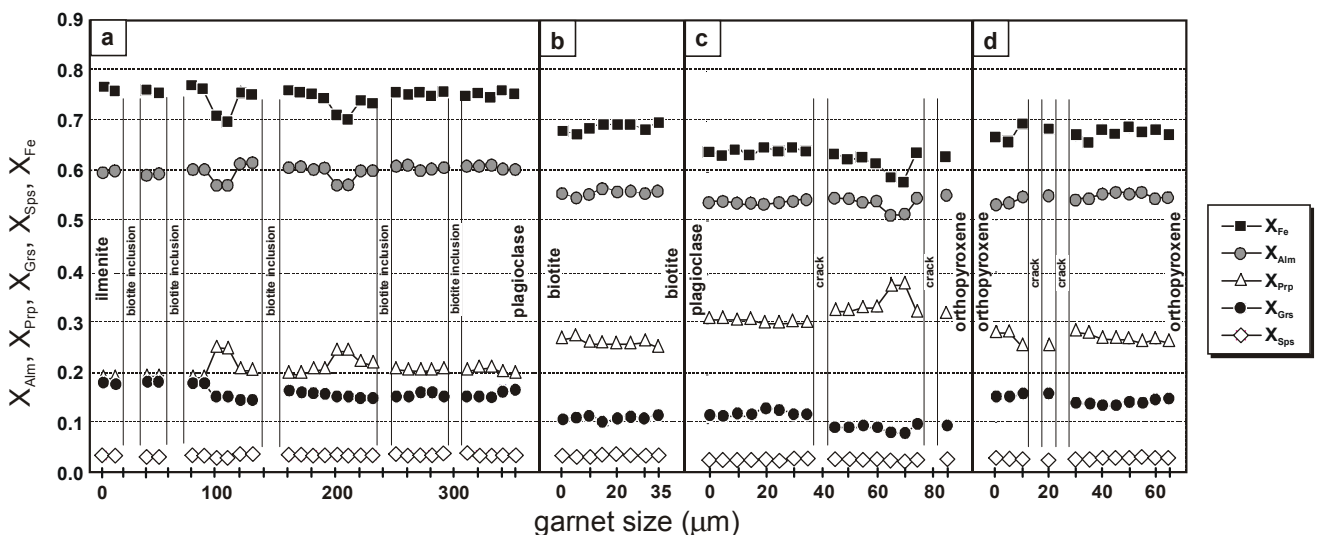


Fig. 6.11: Zoning profiles of garnet from the garnet-bearing leucotroctolites of the KIC. **a)** Poikiloblastic garnet from a garnet-biotite corona surrounding ilmenite in sample Ku-98-221b. **b)** Inclusion-free garnet from a garnet-biotite corona surrounding ilmenite in sample Ku-98-221b. **c)** Garnet from a garnet-orthopyroxene-quartz corona surrounding olivine in sample Ku-98-221b. **d)** Garnet from a garnet-orthopyroxene-quartz corona surrounding olivine in sample Ku-98-221a.

- Garnet in corona textures surrounding olivine has an average composition of $\text{Prp}_{28.6}\text{Sp}_{3.4}\text{Alm}_{54.9}\text{Grs}_{8.6}\text{And}_{4.5}$ (X_{Mg} : 0.31-0.42; Fig. 6.11 c-d). When bordered by plagioclase and orthopyroxene garnets from type I coronas exhibit a weakly developed asymmetric zonation, involving slight decreases in X_{Prp} and X_{Grs} and increases in X_{Alm} and X_{Fe} with increasing proximity to orthopyroxene (Fig. 6.11 c). The highest pyrope contents are preserved in narrow zones, which presumably remained unaffected during the retrograde re-equilibration.

- When compared to garnet surrounding olivine, garnet from type II corona textures around ilmenite is characterized by distinctly lower pyrope contents (average composition: Prp_{22.7}Sps_{3.3}Alm_{59.2}Grs_{10.6}And_{4.2}; X_{Mg}: 0.23-0.30; Fig. 6.11 a-b) and lacks significant zoning patterns. Lowest pyrope contents were obtained for a poikiloblastic garnet, bearing abundant biotite inclusions (Fig. 6.11 a), whereas inclusion-free garnet generally exhibits significantly higher pyrope contents (Fig. 6.11 b). It can thus be concluded, that poikiloblastic garnet was affected by retrograde Fe-Mg exchange with the included biotite, resulting in an almost complete homogenization of the garnet host, whereas the X_{Alm} and X_{Prp} of inclusion-free garnet remained almost unchanged.

6.9 Epidote

Accessory epidote minerals occur in almost all rock samples of both the anorthositic and felsic suite as a retrograde phenomenon. Epidote formulae were calculated on an anhydrous basis of 25 oxygens. Representative analyses are compiled in Table A.5.1.11 in the Appendix A.5.1. Compositional variations can be expressed in terms of the pistacite (Ps) component of epidote (mole fraction of Ca₂Fe₃Si₃O₁₂(OH)). Significant core-rim relationships of the epidotes do not occur.

In the anorthositic rock suite, the pistacite component of epidote varies between 0.14-0.28 mol.%, corresponding to Al-epidotes in the sense of Holdaway (1972), whereas epidotes of the quartz-syenites (Ps: 0.21-0.32 mol.%) and syenites (Ps: 0.27-0.34 mol.%) are generally more Fe-rich and can thus be described as Fe-epidotes.

6.10 Chlorite

Chlorite in both the anorthositic and felsic suite is formed by the hydrothermal alteration of Fe-Mg silicates (biotite and pyroxene in the anorthositic suite and amphibole in the syenites). Calculation of the formula is based on 28 oxygens, excluding H₂O. The estimation of Fe³⁺ followed the method of Laird & Albee (1981). Due to the small grain size of chlorite and its intimate association with biotite, amphibole, carbonate, epidote or actinolite only a few reliable analyses were obtained (Table A.5.1.12 in the Appendix A.5.1).

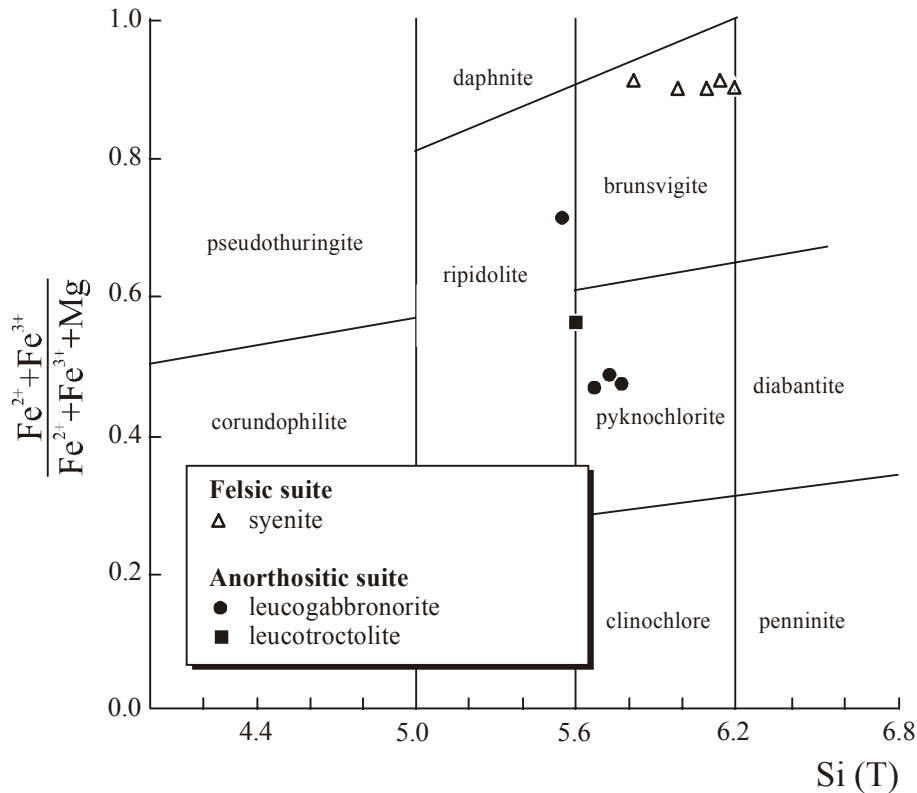


Fig. 6.12: Classification of chlorite from the anorthositic rocks of the KIC and the syenites of the felsic suite in the classification diagram of Hey (1954).

Following the classification of Hey (1954), chlorites formed by the alteration of biotite from the anorthositic rock suite is pyknochlorite, whereas those growing at the expense of pyroxene are ripidolite (Fig. 6.12). In clear contrast, the chlorites in the syenites can be classified as Fe-rich brunsvigite (Fig. 6.12).

6.11 Comparative approach

In summary, the respective mineral compositions of the granitoid suite appear to extend the compositional range of the anorthositic rocks towards higher Fe/Mg ratios and lower Al of the Fe-Mg silicates (clinopyroxene, orthopyroxene, amphibole, epidote and chlorite) and lower An contents of plagioclase. The relative changes in the mineral compositions could provide evidence for a consanguinity between the two rock suites.

However, intermediate mineral compositions in between those of the anorthositic and the felsic suite are missing. Moreover, the relative changes of the mineral chemistry, displayed by the subsequently emplaced anorthosite lithologies themselves rather imply an opposite

evolutionary trend, including an increase of the X_{Mg} of amphibole and the An-content of plagioclase with subsequent intrusion. Based on the mineral chemistry, the two rock suites are thus interpreted to represent chemically independent suites.

7 Geochemistry

7.1 Major and trace element geochemistry

Geochemical data was obtained for 56 rock samples of the two anorthosite suites and 12 rock samples of the felsic suite. The investigation of the bulk rock geochemistry shall serve as a tool for characterising the nature and magmatic evolution of the basic and the felsic melts. Thus, samples affected by secondary metasomatic alteration were excluded from this part of the study but will be discussed later. The obtained major and trace element chemical data are given in Table A.5.4.1 in the Appendix A.5.4. Analytical conditions are given in the Appendix A.2.4.

Felsic suite

Granite (G): B-98-170a, B-98-180a, B-99-410

Quartz-syenite (S,qtz): Ku-98-40

Syenite (S,fs): Ku-98-93, Ku-99-03, Ku-99-11, Ku-99-12, Ku-99-13, Ku-99-14, Ku-99-16, Ku-99-20

White anorthosite suite (A,w)

Ku-97-08b, Ku-97-33, Ku-97-33aw and Ku-97-33ag (i.e. the white and the green portions of sample Ku-97-33a), Ku-97-33b, Ku-97-44, Ku-97-99a, Ku-98-45, Ku-98-60

Dark anorthosite suite

Pyroxene-bearing anorthosite (A,px): Ku-97-02, Ku-97-12, Ku-97-13, Ku-97-31, Ku-97-92a, Ku-97-93, Ku-98-123

Leucogabbronorite (GN): Ku-97-03, Ku-97-03b, Ku-97-03c, Ku-97-04, Ku-97-05, Ku-97-06, Ku-97-08a, Ku-97-30, Ku-97-31b, Ku-98-68, Ku-98-92, Ku-98-126, Ku-98-128, Ku-98-129, Ku-98-222, B-98-101a

Olivine-bearing anorthosite (A,ol): Ku-97-28, Ku-97-28a, Ku-97-95, Ku-98-23, Ku-98-124, B-98-274a, B-98-274b, B-98-281b

Leucotroctolite (T): Ku-97-92, Ku-97-96, Ku-98-41, Ku-98-52, Ku-98-53, Ku-98-94, Ku-98-121, Ku-98-125, Ku-98-228, Ku-98-230, Ku-98-231

including the garnet-bearing samples (T,grt): Ku-97-104, Ku-97-105, Ku-98-220, Ku-98-221a, Ku-98-221b

7.1.1 Anorthositic suite

Following the classification of Tischendorf (in Seim & Tischendorf, 1990) most unaltered samples of the dark anorthosite suite indeed fall into the compositional range of anorthosites

(Fig. 7.1). However, the pervasively altered white anorthosite samples strongly deviate from the average anorthosite composition due to the use of Na_2O and K_2O as discrimination factors, which were strongly enriched by secondary processes affecting these rocks.

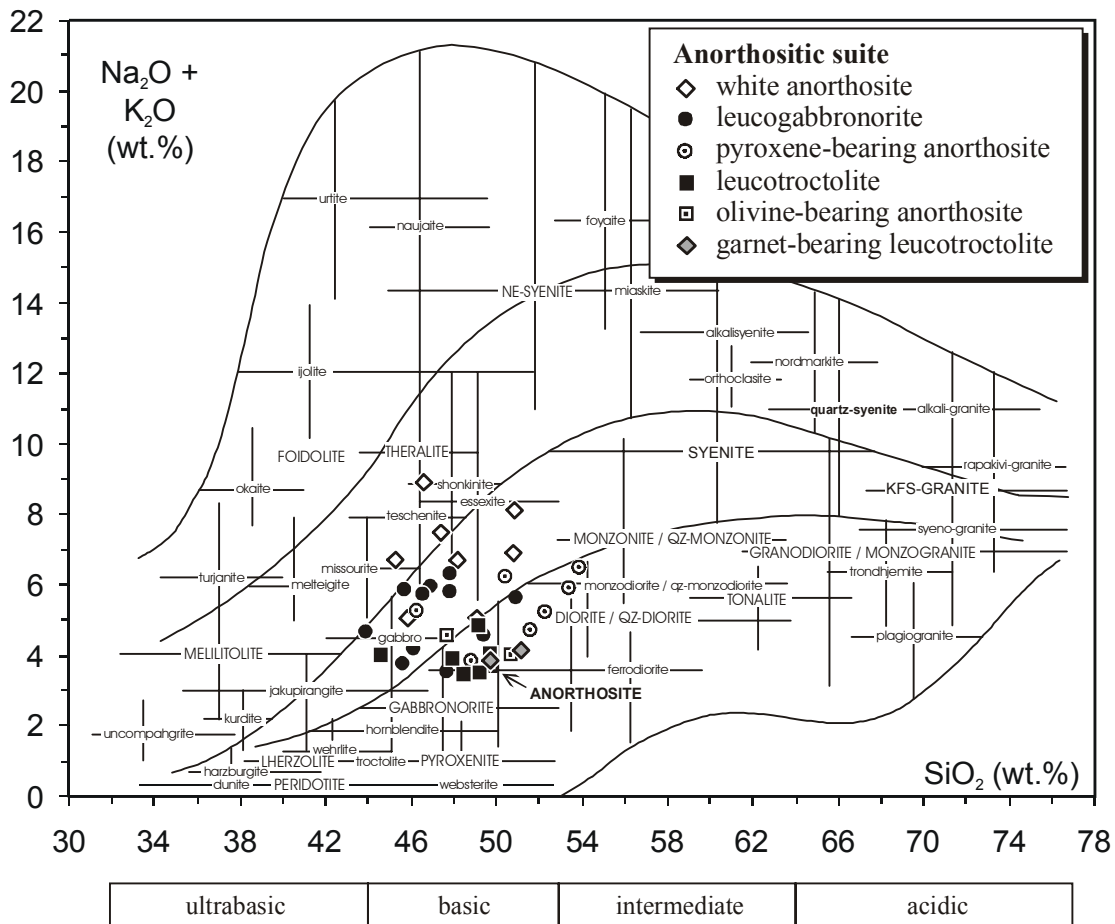


Fig. 7.1: Compositional variability of the anorthositic rocks of the KIC expressed in the classification diagram of Tischendorf (in Seim & Tischendorf, 1990).

In order to constrain the particular style of hydrothermal alteration, which affected the white anorthosite, the graphical representation of alteration indexes ("alteration box plot") by Large et al. (2001) is used (Fig. 7.2). In clear contrast to the least altered samples of the dark anorthosite suite, white anorthosite samples mainly follow a trend of albitization/chloritization, which is also displayed by altered leucogabbronorite samples of the dark anorthosite suite.

Both the white and the dark anorthosite suite are enriched in Al_2O_3 (21-29 and 16-30 wt.%), CaO (4-13 and 7-13 wt.%), Na_2O (4-9 and 3-6 wt.%) and SiO_2 (45-51 and 38-54 wt.%), reflecting high amounts of cumulus plagioclase, whereas they are deficient in all other oxides. $\text{CaO}/\text{Na}_2\text{O}$ is quite variable, but weakly increases in the sequence white anorthosite and

leucogabbro towards leucotroctolite, reflecting differences in their respective plagioclase compositions.

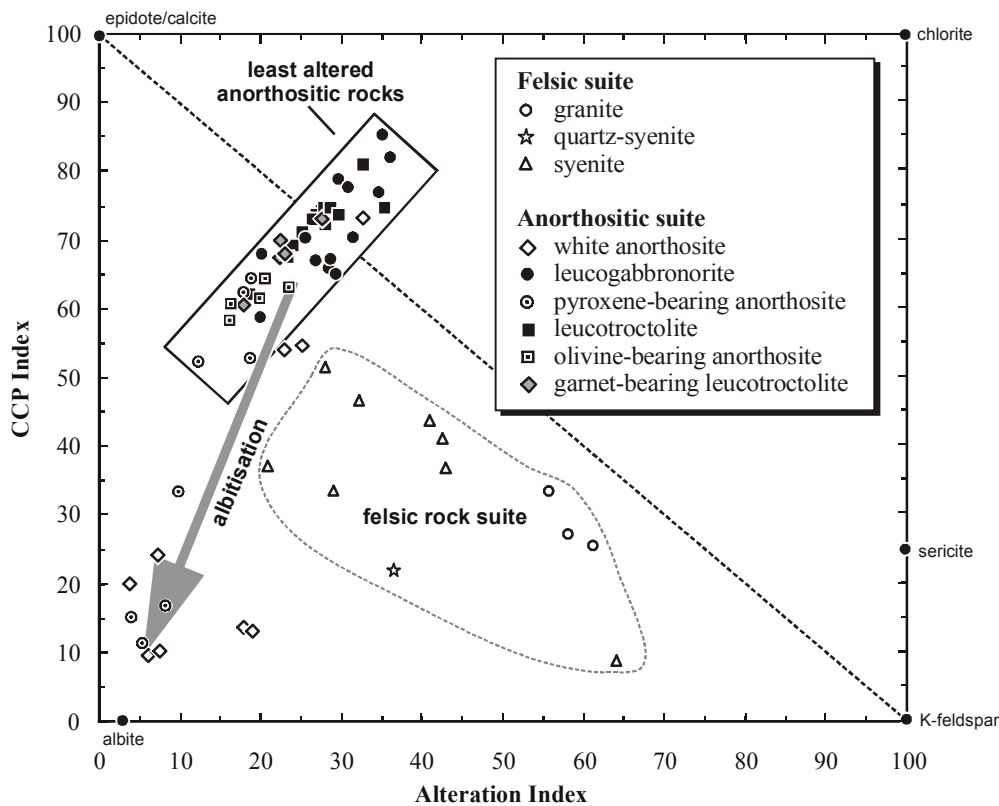


Fig. 7.2: Alteration styles of the white anorthosite suite and altered samples of the dark anorthosite suite of the Kunene Intrusive Complex, expressed in the modified alteration box plot of Large et al. (2001). Compositional ranges of the granite, quartz-syenite and syenite of the felsic suite are given for comparison. (CCP Index:

$$CCPI = \frac{100 \times (MgO + FeO)}{(MgO + FeO + Na_2O + K_2O)}, \text{ Alteration Index: } AI = \frac{100 \times (K_2O + MgO)}{(K_2O + MgO + Na_2O + CaO)}.$$

The $Fe^{tot}/(Fe^{tot}+Mg)$ ratio is generally intermediate (> 0.28), pointing to anorthosite crystallization from fractionated melts. However, the highest values are displayed by the white anorthosite (0.51-0.74) and the leucogabbro (0.31-0.66), which both were affected by crustal contamination. The geochemical trends of the major elements of least altered samples of the dark anorthosite suite, as demonstrated in various Harker diagrams (Fig. 7.3), correlate well with varying proportions of cumulus plagioclase and intercumulus phases (i.e. Fe-Mg silicates and Fe-Ti oxides). Decreases of Si, Al, Ca and Na are accompanied by increases of Fe, Mn and Mg from anorthosite and troctolite towards leucogabbro of the dark anorthosite suite.

Leucogabbros generally display the highest values of K and P, reflecting variable but generally high amounts of late-magmatic biotite and apatite, which crystallized from pockets of intercumulus melt. Trends of the white anorthosite are mostly indistinguishable from those of the

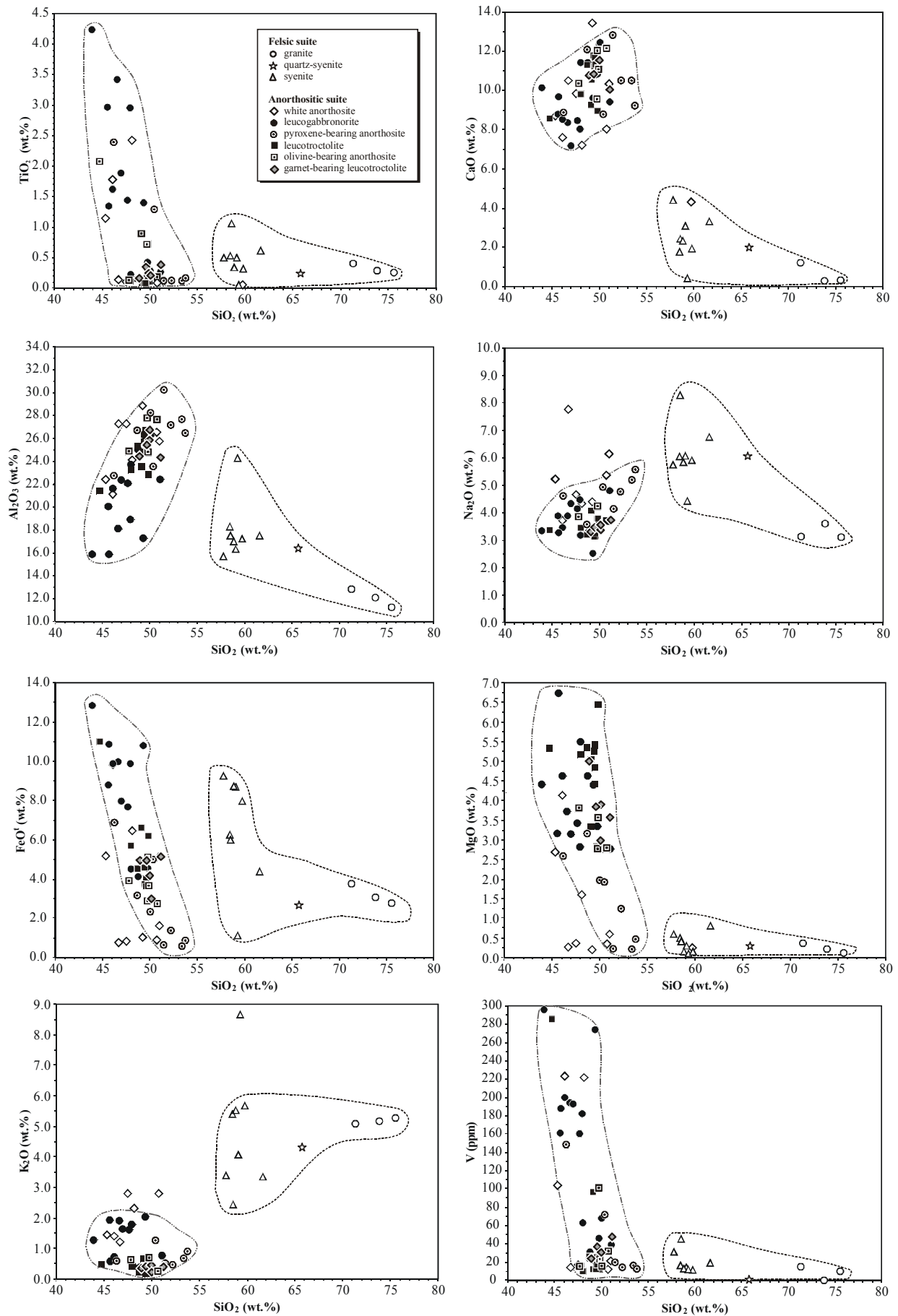


Fig. 7.3: Variation of major element contents of the anorthositic rocks of the Kunene Intrusive Complex and the granites, quartz-syenites and syenites of the felsic suite.

dark anorthosite suite, with the exception of Na and K, that were strongly enriched during the hydrothermal alteration.

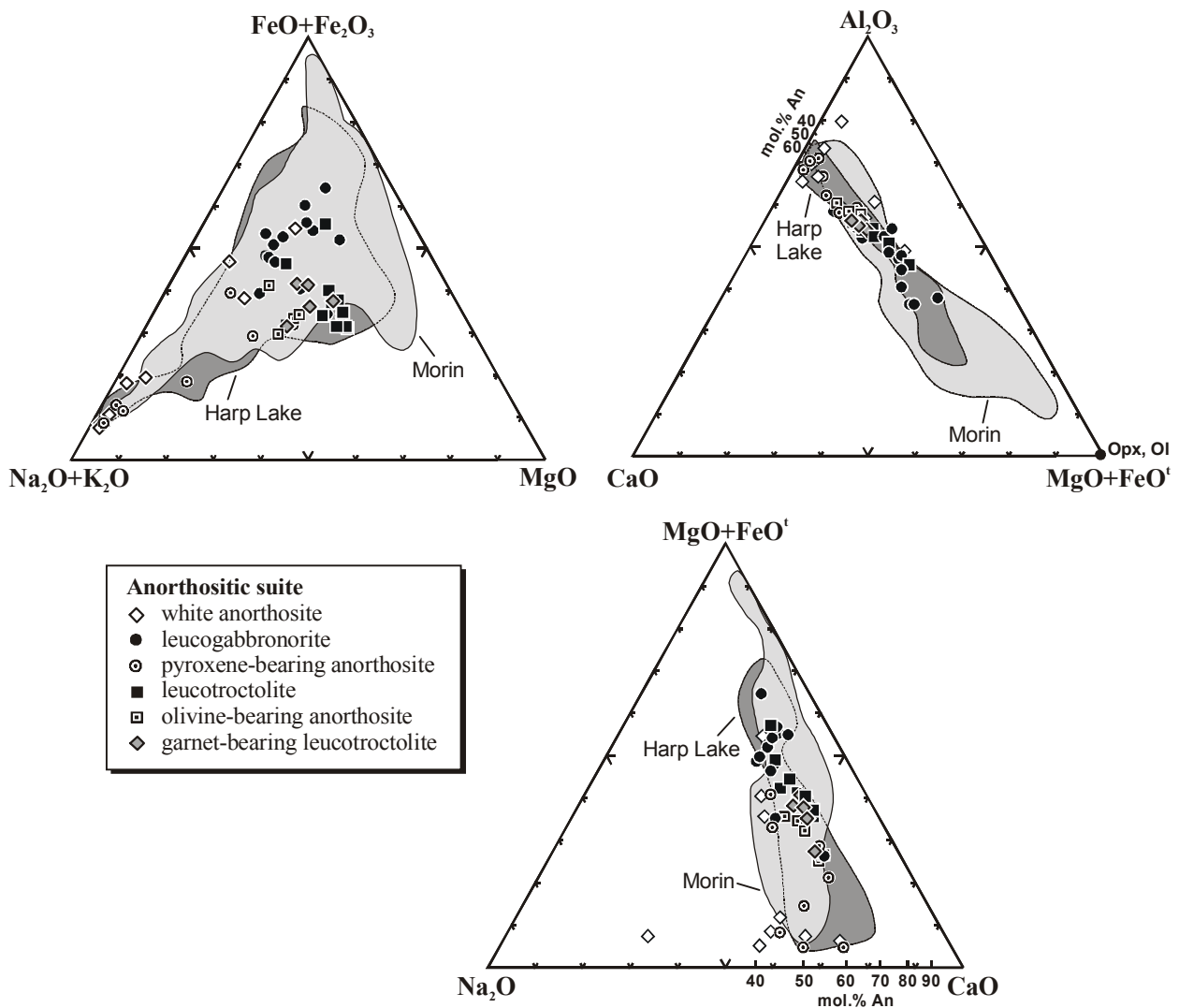


Fig. 7.4: Composition of the anorthositic rocks of the KIC, expressed in triangular diagrams (AFM-, ACF- and FNC-diagrams). Geochemical data for the Harp Lake massif, Labrador (Emslie, 1980) and the Morin massif, Quebec (Martignole, 1974; Emslie, 1975b) was plotted for comparison.

In order to compare the major element geochemistry of the KIC with metamorphosed and not metamorphosed anorthosite massifs, a set of triangular diagrams (AFM, FNC and ACF diagrams; Fig. 7.4) was used. The anorthositic rock samples of the KIC are characterized by a wide range of rock compositions, which, however, display a certain continuity throughout all diagrams. The scattering of data points in the ACF and FNC diagrams illustrate the variability of plagioclase compositions of the white and the dark anorthosite suite, whereas the trends towards higher $\text{FeO}+\text{MgO}$ are reflected by increasing amounts of intercumulus silicates and oxides, which reach highest contents in the leucogabbronorites and leucotroctolites. Trends of the white

anorthosite and the dark anorthosite suite are nearly indistinguishable, thus suggesting that the older white anorthosite suite was composed of a variety of anorthositic lithologies before its pervasive alteration. The obtained compositional ranges of the dark anorthosite suite correlate best with those obtained for the Harp Lake massif, Labrador, whereas they deviate from those of the metamorphosed Morin massif, Quebec (Fig. 7.4).

The highest values for Ni are obtained for the olivine-bearing anorthosites and leucotroctolites, corresponding to increasing modal amounts olivine in these rocks. In contrast, the high V and Zn contents of the leucogabbroites are reflected by higher modal amounts of intercumulus ilmenite and pyroxene.

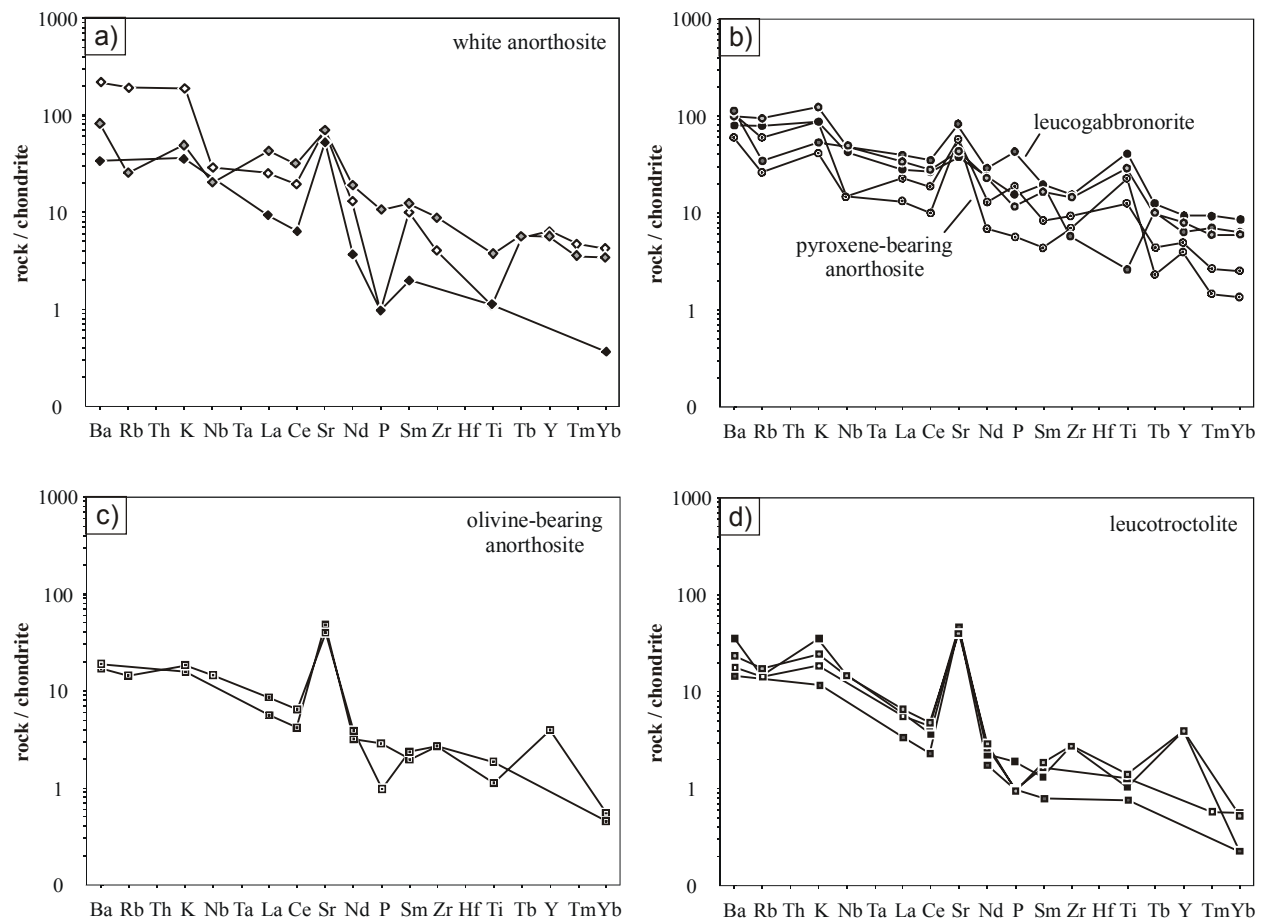


Fig. 7.5: Chondrite-normalized (except K, Rb and P) trace element abundance diagrams (spider-grams) for the white anorthosite suite and the dark anorthosite suite of the Kunene Intrusive Complex, using the normalization factors of Thompson et al. (1983; see Thompson, 1982, for details on the selection of normalization factors for K, Rb and P).

Chondrite normalized trace element plots of all rock samples investigated show a strong negative slope, with enrichment in Ba, Rb, K and Sr relative to Tb, Y, Tm and Yb (Fig. 7.5). A variably

accentuated positive Sr anomaly is displayed by all lithologies, pointing to a Sr-enriched parental melt and thus ruling out extensive plagioclase crystallization prior to the emplacement of the anorthosite massifs. The highest Sr-concentrations have been obtained for the white anorthosite samples (540-1250 ppm; Fig. 7.5 a) and the pyroxene-bearing anorthosites and leucogabbronorites (380-980 ppm; Fig. 7.5 b) of the dark anorthosite suite, which, at the same time, exhibit the highest overall trace element abundances and the lowest An contents of plagioclase. In contrast, the lowest average Sr concentrations (470-640 ppm) have been obtained for the youngest intrusives, the olivine-bearing anorthosites (Fig. 7.5 c) and leucotroctolites (Fig. 7.5 d), corresponding with the highest average An-contents of plagioclase and low total sums of incompatible trace elements. An inverse correlation between Sr and the An-content is a common feature of layered intrusions and is commonly attributed to plagioclase fractionation, causing a decrease of the Sr content in the melt (see Ashwal, 1993, for a review). However, in the case of the Kunene Intrusive Complex, this trend is rather caused by decreasing degrees of crustal contamination during the subsequent intrusion of the anorthosite massifs. This interpretation is constrained by comparably high values of K, Rb and Ba of both the white anorthosites and the leucogabbronorite samples. However, in case of the white anorthosite, these trends may also be influenced by a hydrothermal alteration.

7.1.2 Felsic suite

According to the classification of Tischendorf (in Seim & Tischendorf, 1990) the felsic suite can be subdivided in K-feldspar granites, quartz-syenites and syenites (Fig. 7.6). The SiO₂ contents of the granites range between 71-76 wt.%, whereas those of the quartz-syenite (SiO₂: 66 wt.%) and the syenites (SiO₂: 58-62 wt.%) are distinctly lower (Fig. 7.3). In clear contrast to the anorthositic rock suite, all felsic samples are enriched in K₂O (2.4-8.7 wt.%) and Na₂O (3.1-8.3 wt.%) relative to CaO (0.3-4.4 wt.%). The data for samples of the felsic rock suite form coherent arrays on major element variation diagrams, involving a negative correlation of Si with Ti, Al, Fe, Mn, Mg, Ca, Na and P whereas K increases in the same direction (Fig. 7.3). In case of Al, Ca and Na these trends are unequal to those obtained for the anorthositic rocks and thus strongly argue against a chemical relation between the two suites. The high scatter of data points for Al, Na and K are reflected by local variations in the abundances of K-feldspar and plagioclase. The ratio $\text{FeO}^{\text{tot}}/(\text{MgO}+\text{FeO}^{\text{tot}})$ is constantly high, ranging between 0.91-0.96 in the granite and quartz-syenite and 0.85-0.98 in the syenite and thus plotting in the ferroan field of Frost et al. (2002; Fig. 7.7 a). Syenites and the quartz-syenite are alkalic, whereas the granites are alkali-

calcic (Fig. 7.7 b). Most of the felsic samples analysed are metaluminous to slightly peraluminous with increasing SiO_2 , except for one peraluminous syenite sample (Ku-99-16; Fig. 7.7c). However, none of the samples is peralkaline, as would be typical for mantle-derived melts.

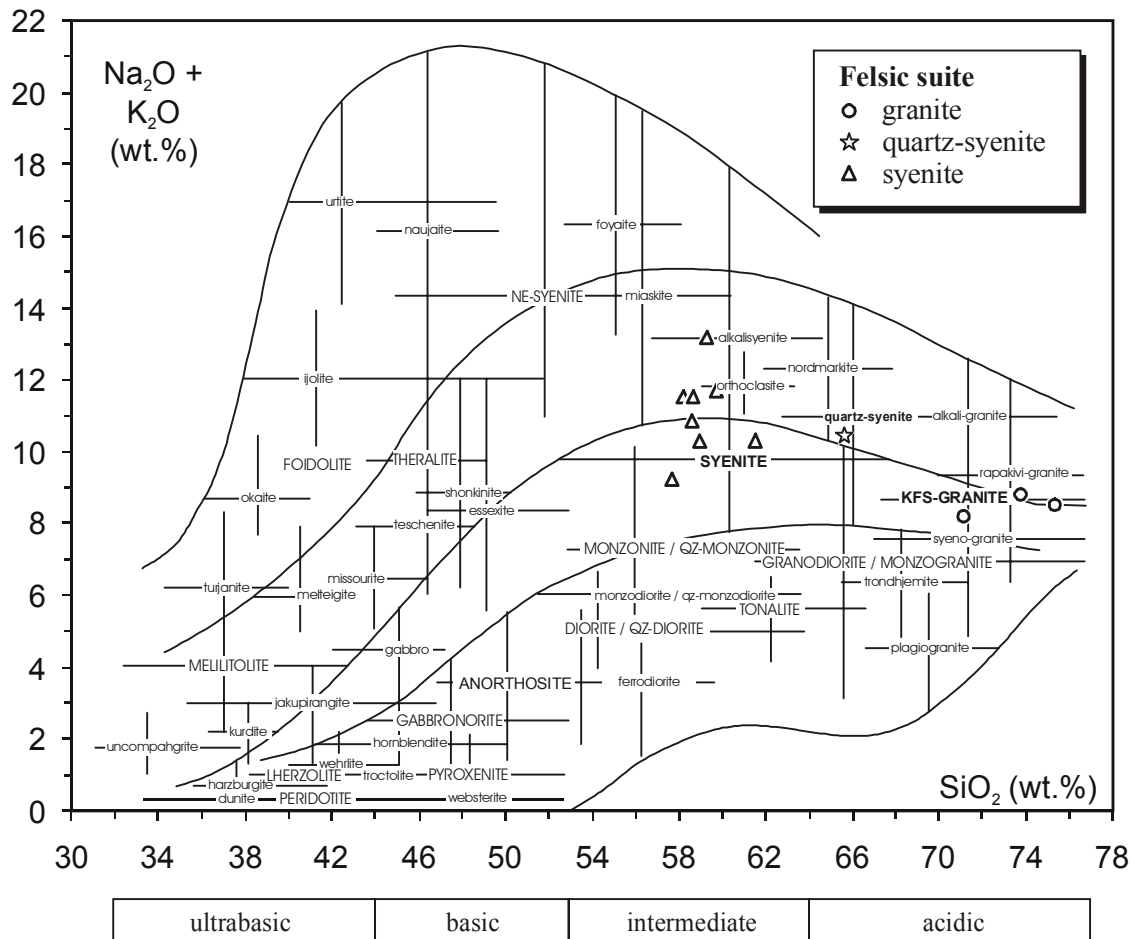


Fig. 7.6: Compositional variability of the felsic rock suite (granite, quartz-syenite and syenite), expressed in the classification diagram of Tischendorf (in Seim & Tischendorf, 1990).

All samples contain abundant LIL (Rb, Ba, REE) and HFS elements (Zr, Y, Nb), typical of anorogenic (A-type) granites (Fig. 7.7 d). In the discrimination diagrams Y against Nb and (Y+Nb) against Rb of Pearce et al. (1984) all samples plot in the field of within-plate granites (WPG; Fig. 7.7 e-f), broadly following a continental rift trend as defined by Pearce et al. (1984).

Chondrite normalized trace element plots show depletion in Nb, Sr, P and Ti and a strong negative slope, except the accentuated positive Zr anomaly (Fig. 7.8). Remarkably, the trace-element patterns of the quartz-syenite and the syenite are quite similar to those of common upper continental crust rocks as granites or metapelites (see Thompson et al., 1983, for a review), thus suggesting that the felsic rocks have evolved from mixtures of crustal and mantle sources.

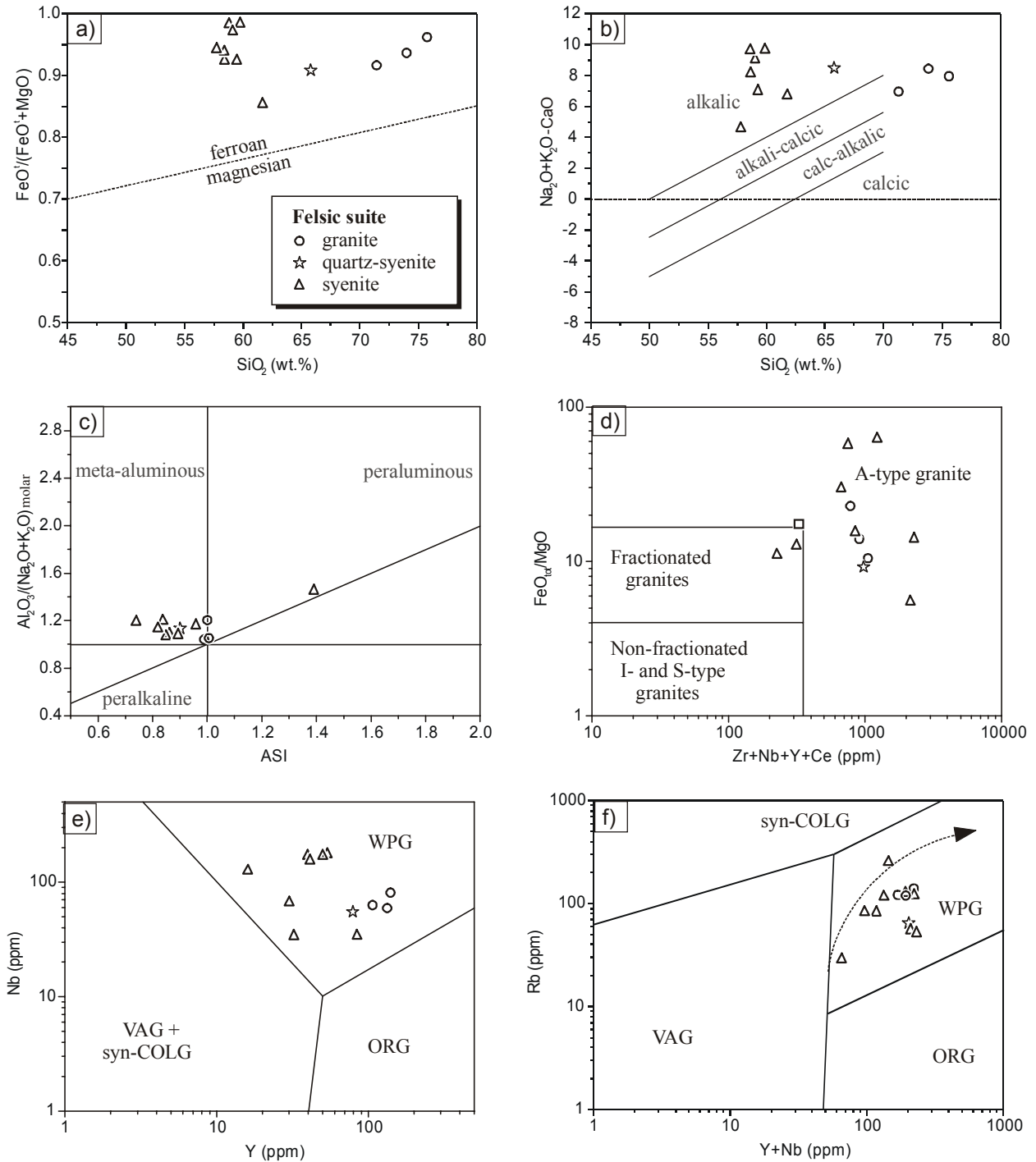


Fig. 7.7: Compositional characteristics of the felsic suite expressed in various binary discrimination diagrams. **a)** Plot of $\text{FeO}^{\text{tot}}/(\text{FeO}^{\text{tot}}+\text{MgO})$ against SiO_2 with the boundary between ferroan and magnesian fields given by Frost et al. (2002). **b)** Plot of the modified alkali-lime index $\text{Na}_2\text{O}+\text{K}_2\text{O}-\text{CaO}$ against SiO_2 (Frost et al., 2002). **c)** Shand's alkalinity index (plot of $\text{Al}_2\text{O}_3/(\text{Na}_2\text{O}+\text{K}_2\text{O})_{\text{molar}}$ against $\text{Al}_2\text{O}_3/(\text{Na}_2\text{O}+\text{K}_2\text{O}+\text{CaO})_{\text{molar}}$). **d)** A-type granitoid discrimination diagram after Whalen et al. (1987). **e)** and **f)** Tectonic environment discrimination diagrams after Pearce et al. (1984).

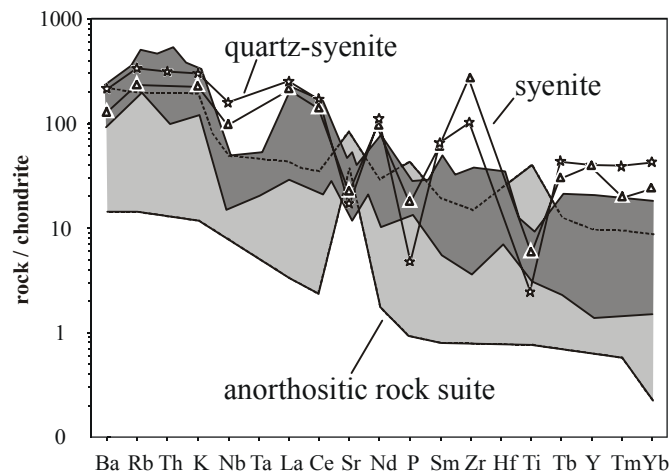


Fig. 7.8: Chondrite-normalized (except Rb, K, P) trace element abundance diagrams (spider-grams) for the syenites of the felsic suite. Compositional ranges of the anorthositic rocks of the Kunene Intrusive Complex (light grey) and representative fusible rock types of the continental crust (Thompson et al., 1983; dark grey) are marked for comparison.

7.2 REE geochemistry

REE-analyses were carried out on fourteen samples of the anorthositic suite and on two samples of the felsic suite. Analytical results are given in Table A.5.4.2 in the Appendix A.5.4.

Regarding their rare earth element (REE) patterns, all **anorthositic rocks** are characterized by a variable enrichment of the light REE (La_N/Yb_N : 3.3-26.9), a strong positive Eu (Eu/Eu^* : 1.3-11.2) anomaly and flattening in the heavy REE (Fig. 7.9). In the dark anorthosite, the overall abundance of REE increases in the sequence leucotroctolite (Eu/Eu^* : 5.1-11.2; La_N/Yb_N : 10.1-26.9) – olivine-bearing anorthosite (Eu/Eu^* : 4.4-5.2; La_N/Yb_N : 12.8-16.3) - pyroxene-bearing anorthosite (Eu/Eu^* : 3.0-4.0, La_N/Yb_N : 8.9-9.9) – leucogabbronorite (Eu/Eu^* : 1.3-1.8, La_N/Yb_N : 3.3-6.3), resulting in a relative decrease of the Eu anomaly. The white anorthosite shows strongly varying REE patterns, one (Ku-97-45; Eu/Eu^* : 7.1, La_N/Yb_N : 26.9) resembling that of the leucotroctolites of the dark anorthosite suite whereas two other patterns (Ku-98-44, Ku-97-33b; Eu/Eu^* : 1.6-2.3; La_N/Yb_N : 5.9-12.6) agree well with those of the leucogabbronorites and pyroxene-bearing anorthosites. It may thus be concluded that the white anorthosite, like the dark anorthosite, represents a suite of different anorthositic lithologies rather than an anorthosite *sensu stricto* as was proposed by Menge (1998). When compared to the corresponding lithologies of the dark anorthosite suite, all three white anorthosite samples display a slight enrichment in light the REE and a relative decrease of the heavy REE as

evidenced by their La_N/Yb_N ratios. This steeping of their REE patterns supports evidence for an elevated amount of crustal contamination and/or the pervasive alteration during their intrusion.

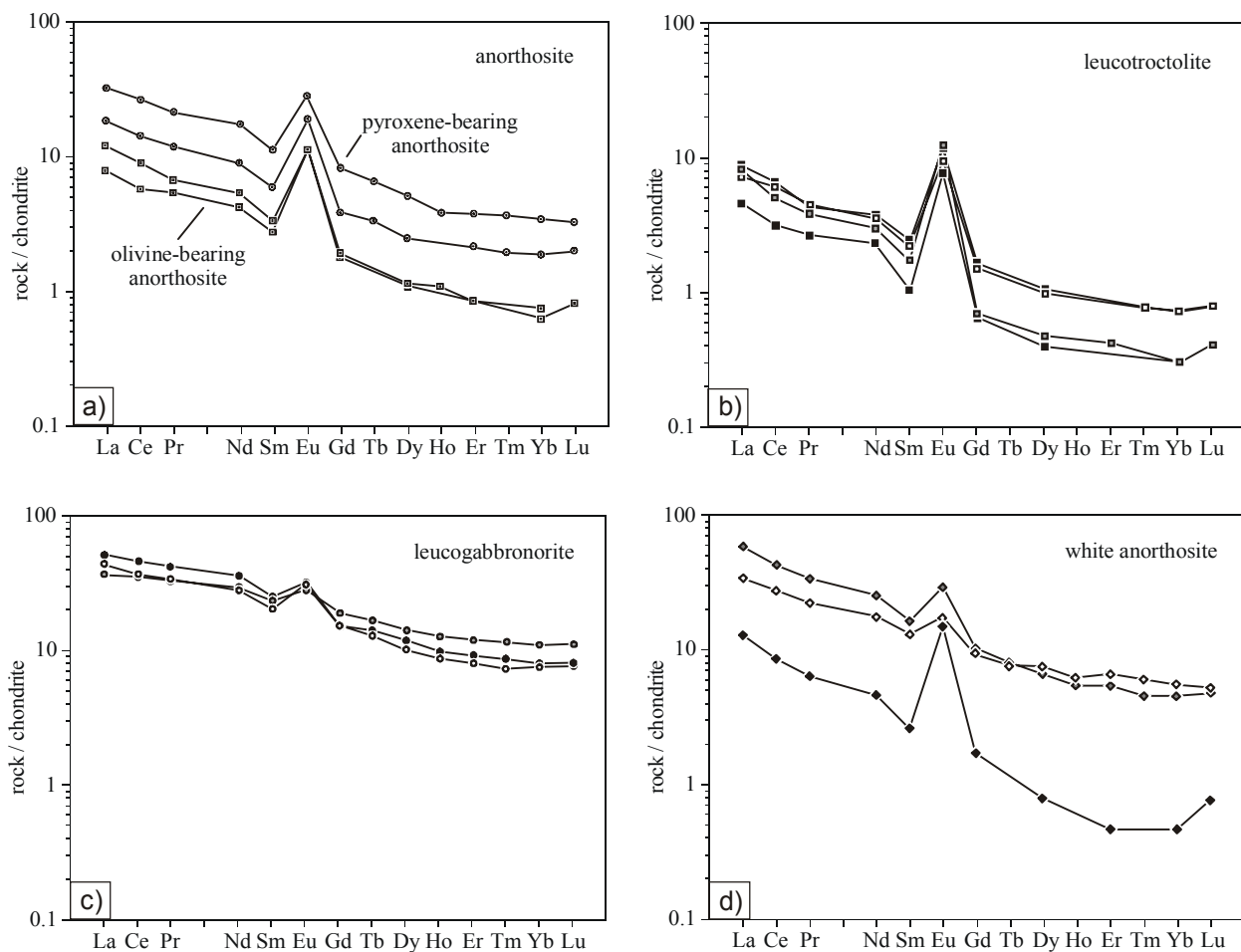


Fig. 7.9: Diagrams showing the variations in chondrite-normalized rare earth element (REE) abundances for the anorthositic rocks of the KIC. **a)** Olivine-bearing anorthosite (Ku-97-28, Ku-98-23) and pyroxene-bearing anorthosite (Ku-97-13, Ku-97-31). **b)** leucotroctolite (Ku-97-92, Ku-97-104, Ku-98-41, Ku-98-230). **c)** leucogabbronorite (Ku-97-04, Ku-97-05, Ku-97-31b, Ku-98-68). **d)** white anorthosite (Ku-97-33b, Ku-97-44, Ku-98-45).

Chondrite-normalized REE plots of the *quartz-syenite* and the *syenite* are almost identical. Low La_N/Yb_N ratios of 5.9-9.5 indicate a moderate LREE enrichment (Fig. 7.10). With Eu/Eu^* ratios varying from 1.01 to 1.06, the rocks lack an accentuated europium anomaly. An extensive plagioclase accumulation prior to their emplacement, as evidenced by an accentuated Sr trough in the chondrite normalized trace element plots, can thus be ruled out.

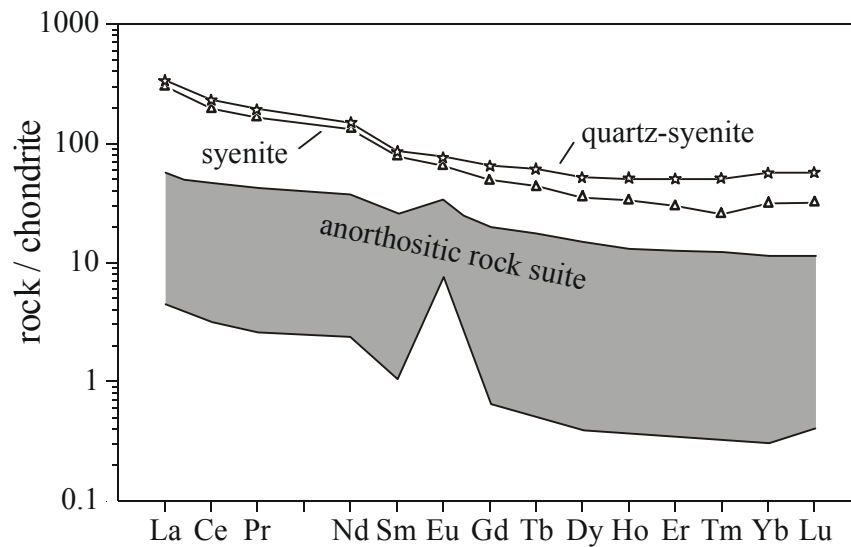


Fig. 7.10: Diagrams showing the variations in chondrite-normalized REE abundances for the syenites of the felsic suite compared to those of the anorthositic rocks of the KIC (*quartz-syenite* Ku-98-40, *syenite* Ku-99-20).

The results obtained strongly suggest that the anorthositic and the felsic lithologies represent two chemically independent suites, with the melts parental to the anorthositic rocks being mantle-derived liquids, that were modified by only minor crustal contamination during their uprise, whereas the felsic melts parental to the granitoids are suggested to have been generated in the crust.

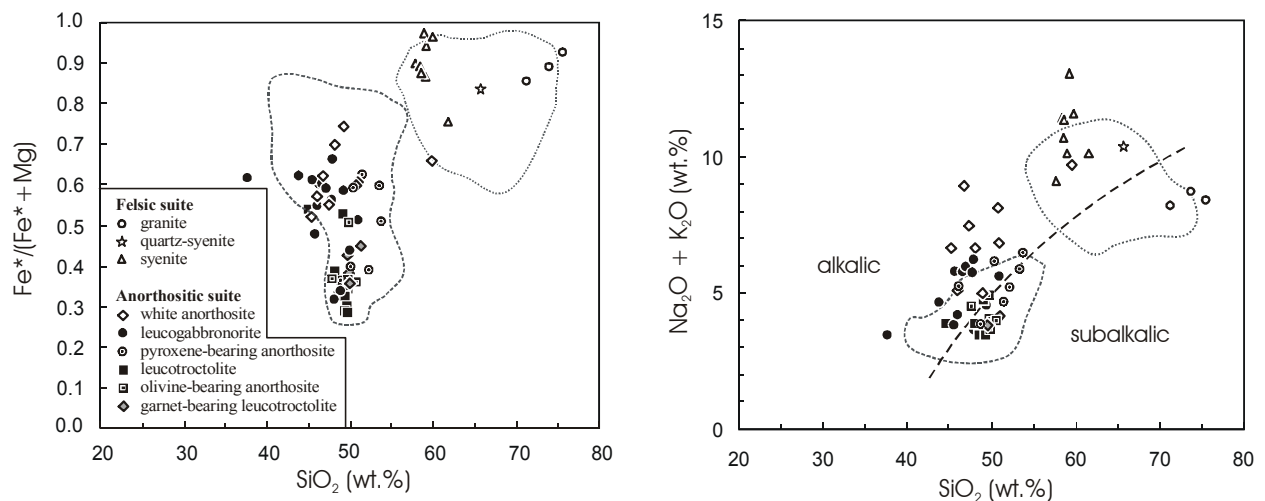


Fig. 7.11: Compositional variability of both the anorthositic and the felsic rock suite compared to similar lithologies of the Harp Lake massif, Labrador (stippled boundaries; Emslie, 1980) **a)** Plot of molar $\text{Fe}^{\text{tot}}/(\text{Fe}^{\text{tot}}+\text{Mg})$ against SiO_2 and **b)** $\text{Na}_2\text{O}+\text{K}_2\text{O}$ against SiO_2 .

Like the Harp Lake massif, Labrador, the two Namibian rock suites are characterized by chemical discontinuities, reflecting the lack of rock types of intermittent chemical composition (Fig. 7.11). Following Ashwal (1993), this separation of data points is a common feature of unmetamorphosed anorthosite massifs. In clear contrast, metamorphosed anorthosite complexes display an apparent chemical continuity between the anorthosite and granitoid suites, which the Ashwal (1993) interprets to have been caused by secondary processes.

8 Oxygen isotope constraints

The utility of stable isotopes as monitors for the source rocks and processes like crustal assimilation and hydrothermal alteration of anorthosites and related rocks has been demonstrated in various studies (Taylor, 1968; Valley & O'Neill, 1982; Morrison & Valley, 1988; O'Connor & Morrison, 1999; Peck & Valley, 2000).

The stable isotope analyses were carried out at the Geowissenschaftliches Zentrum, Abteilung Isotopengeologie, Universität Göttingen. For analyses of the oxygen isotopic composition of the anorthositic suite, plagioclase was separated from 8 samples of the dark anorthosite and 6 samples of the white anorthosite suite. In addition, one olivine separate of a leucotroctolite sample has been analysed. Oxygen isotopic compositions of the felsic suite were determined for K-feldspar and plagioclase separates for one quartz-syenite and 4 syenite samples. The obtained plagioclase and K-feldspar ^{18}O values are a good proxy for the bulk rock $\delta^{18}\text{O}$ since both, the anorthosites and syenites are almost entirely composed of feldspar. A description of the analytical techniques is given in the Appendix A.2.6.1. Analytical results are listed in Table A.5.5.1 in the Appendix A.5.5.

8.1 Anorthositic suite

Almost all plagioclase separates from pyroxene-bearing anorthosite (Ku-97-31, Ku-97-92a), olivine-bearing anorthosite and leucotroctolite (Ku-97-95, Ku-97-125, Ku-98-220) and leucogabbro (Ku-98-128, Ku-98-222) of the dark anorthosite suite exhibit a narrow range in $\delta^{18}\text{O}$ (5.61-6.13 ‰; Fig. 8.1), well in accordance with typical values of 5.8-7.6 ‰ for magmatic anorthosite from occurrences world-wide (e.g. Ashwal, 1993). The obtained $^{18}\text{O}/^{16}\text{O}$ ratios are similar to those from typical basalts and gabbros and are thus consistent with uncontaminated mantle-derived parental melts (Fig. 8.2). Pyroxene from leucotroctolite Ku-97-95 of the dark anorthosite suite is distinctly lower in $\delta^{18}\text{O}$ (3.07 ‰) when compared to plagioclase (5.90 ‰) from the same sample, suggesting subsolidus diffusional exchange.

Just one leucotroctolite sample (Ku-97-105), taken from a fault zone near the border between the KIC and the amphibolite-facies rocks of the Epupa Complex, has a considerably lower plagioclase $\delta^{18}\text{O}$ of 3.19 ‰. The low oxygen isotopic value is most probably related to an exchange with heated meteoric or hydrothermal fluids, restricted to the weak contact zones between the anorthosite massif and its country rocks. This interpretation is in excellent

agreement with the occurrence of hydrothermally formed fibrous actinolite in the sample, which is a late-stage replacement-product of garnet in the coronas textures surrounding olivine. Extremely low $\delta^{18}\text{O}$ values of down to -6‰ have also been analysed for the Boehls Butte, Idaho and Bitterroot, Montana anorthosite complexes (Mora & Valley, 1988) which the authors interpret to have resulted from subsolidus alteration of these rocks.

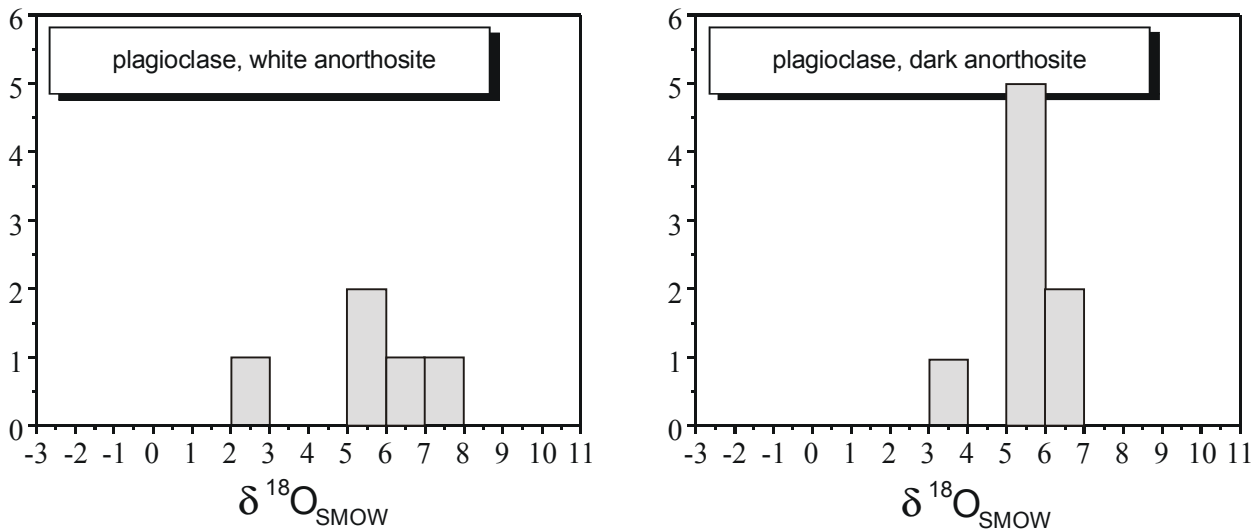


Fig. 8.1: Oxygen isotope composition histograms of magmatic plagioclase from the white and the dark anorthosite suite of the Kunene Intrusive Complex.

Three of five samples of the white anorthosite (Ku-97-33, Ku-97-33a, Ku-98-60) display plagioclase $\delta^{18}\text{O}$ contents of 5.35-6.14 in the range of unaltered plagioclase from the dark anorthosite (Fig. 8.1). Thus, a pervasive alteration by circulating crustal fluids or by meteoric water seems rather unlikely. A more convincing model is, that the alteration of the white anorthosite results from autometasomatism or metasomatism by fluids released by the younger anorthositic melts of the dark anorthosite suite, since only fluids like these would have no effects on the isotopic composition of the plagioclases. This interpretation is in excellent agreement with the preservation of magmatic REE patterns of the white anorthosite.

One conspicuously high $\delta^{18}\text{O}$ value of 7.30 has been determined for plagioclase from one white anorthosite sample (Ku-97-33b), which is ~ 1.4 ‰ higher than the values found in the "normal", magmatic plagioclase of the white and dark anorthosite. This date most probably reflects contamination with crustal calc-silicate material, since the homogeneous and lower $\delta^{18}\text{O}$ values of almost all other samples strongly argue against a regional interaction with crustal-derived, high $\delta^{18}\text{O}$ fluids. In contrast, one brecciated and completely re-crystallized white anorthosite sample (Ku-98-45), taken from a major fault zone, exhibits a lower $\delta^{18}\text{O}$ value of

2.36, which agrees well with the one obtained for the altered leucotroctolite sample from a similar tectonic setting.

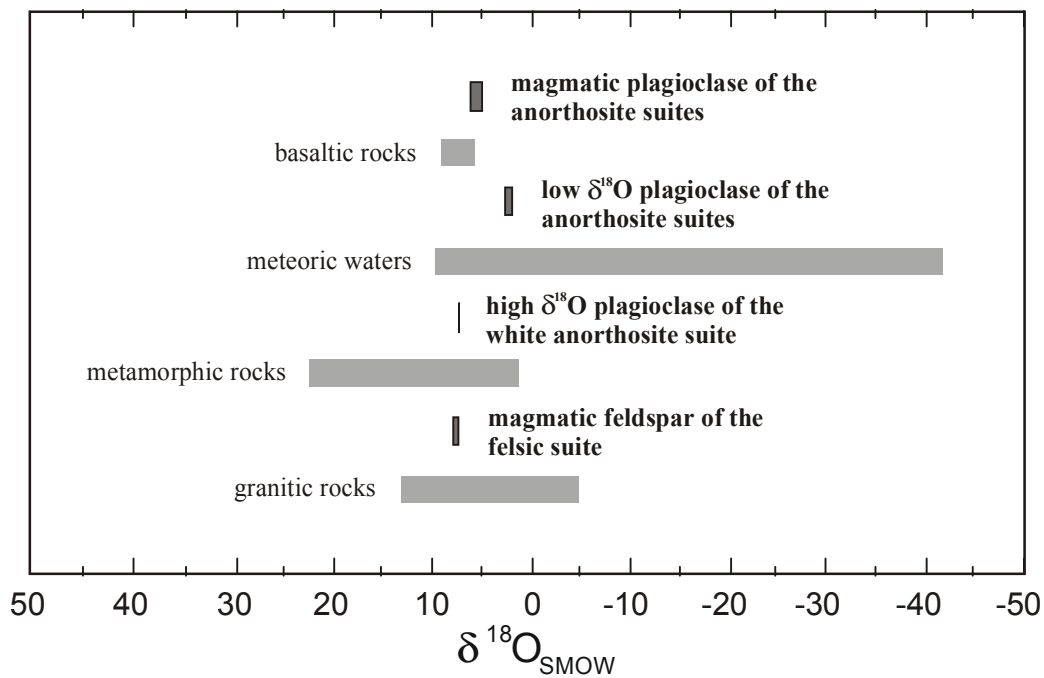


Fig. 8.2: Comparison of the $\delta^{18}\text{O}$ values of feldspar from the anorthositic suites of the KIC and the felsic suite with oxygen isotope data from important oxygen-containing compounds of the lithosphere after Hoefs (1997).

In conclusion, the intermediate plagioclase $\delta^{18}\text{O}$ values (average: 5.88 ± 0.19 ‰ $\delta^{18}\text{O}$) of both the dark and the white anorthosite suite are interpreted to be magmatic in origin, lower plagioclase $\delta^{18}\text{O}$ values (2.36-3.19 ‰ $\delta^{18}\text{O}$) to have resulted from the influx of meteoric waters restricted to faults and the higher $\delta^{18}\text{O}$ value (7.30 ‰ $\delta^{18}\text{O}$) to have been caused by crustal contamination.

8.2 Felsic suite

The $\delta^{18}\text{O}$ values of 4 K-feldspar separates from both the quartz-syenite (Ku-98-40) and the syenites (Ku-99-13, Ku-99-20, Ku-99-21) falls in a restricted range of 7.22-7.92 ‰ (mean: 7.50 ± 0.26 ‰; Fig. 8.3). Almost identical values have been obtained for plagioclase separates of the respective samples (7.20-7.52 ‰; mean: 7.36 ± 0.16 ‰; Fig. 8.3), suggesting equilibrium crystallization of the two feldspars. The obtained values are interpreted to be magmatic, since the small shift of $\delta^{18}\text{O}$ values and the coincidence of the $^{18}\text{O}/^{16}\text{O}$ ratios of K-feldspar and plagioclase in the syenites are inconsistent with low-temperature alteration. It has to be mentioned, however, that the average $\delta^{18}\text{O}$ value of feldspar from the syenites is about 1.6 ‰ higher than the average

plagioclase $\delta^{18}\text{O}$ of the anorthosites. Following Taylor & Sheppard (1986) there is indeed a general increase in $\delta^{18}\text{O}$ with increasing SiO_2 during closed-system crystal fractionation, since silica tends to concentrate the heavy oxygen isotope.

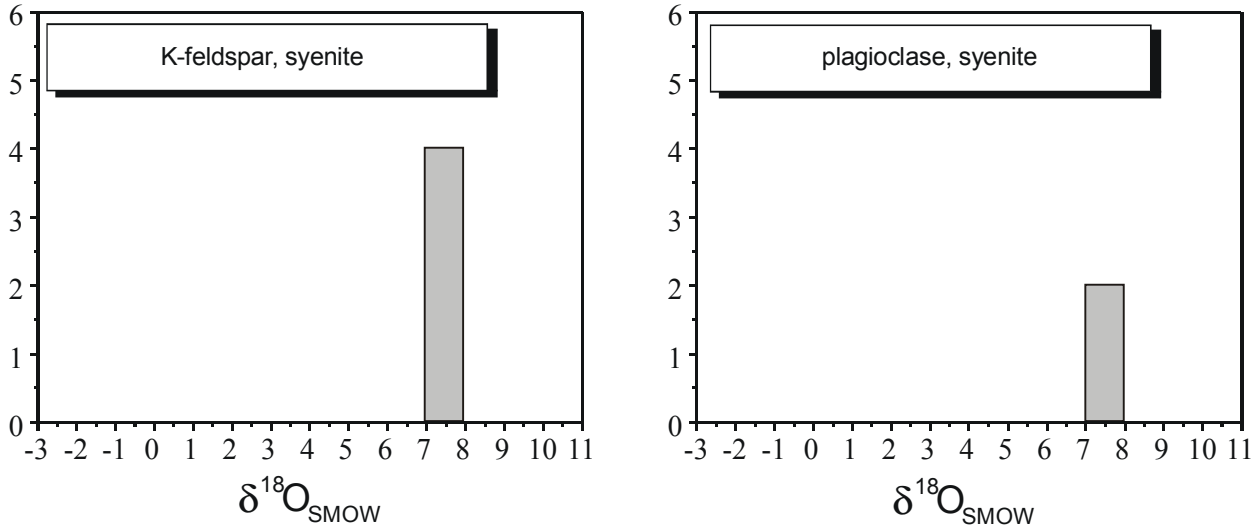


Fig. 8.3: Oxygen isotope composition histograms of magmatic K-feldspar and plagioclase from the syenite of the felsic suite.

However, following these authors, even for an increase of 75% for silica the concomitant ^{18}O increase is generally $< 1\%$, for a given fractionation temperature of $> 900^\circ\text{C}$. This ^{18}O increase

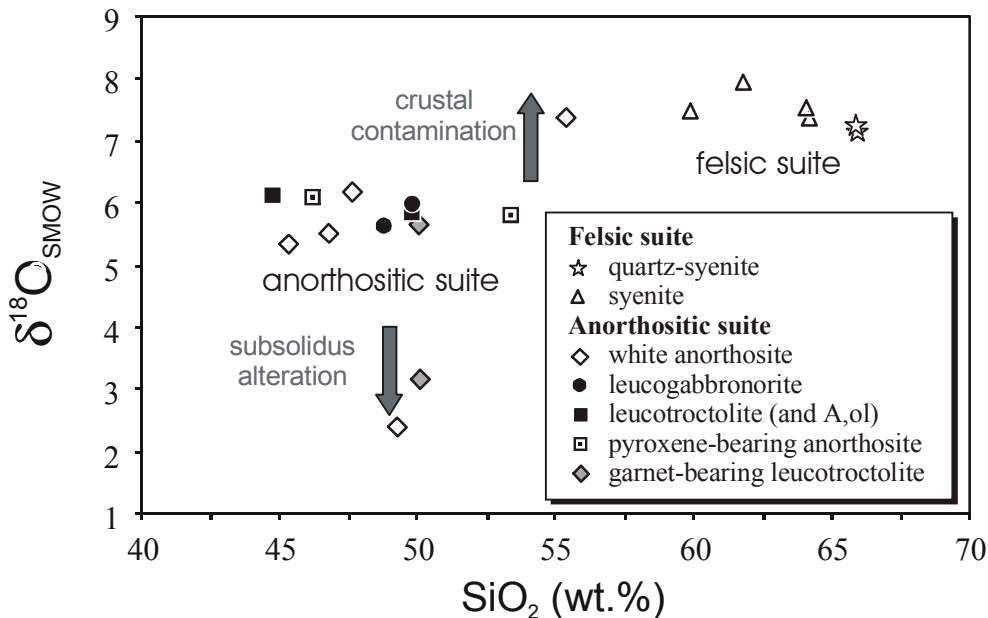


Fig. 8.4: Plot of $\delta^{18}\text{O}$ against SiO_2 for the anorthositic rocks of the KIC and the felsic suite (see text for discussion).

is significantly lower than that obtained for the granitic and anorthositic suites which, at the same time, only display a relative silica increase of $\sim 30\%$ (Fig. 8.4). The great difference in the

magmatic $^{18}\text{O}/^{16}\text{O}$ ratios of feldspars from syenites and anorthositic rocks rather suggests a non-comagmatic relationship of the two suites. A possible explanation for the gap between the isotopic compositions is the incorporation of crustal components into the granitic melts. The rather homogeneous $\delta^{18}\text{O}$ values of the syenitic feldspars point to a crustal origin or mixed mantle and crust sources for the felsic suite.

9 Pressure-temperature conditions

The P-T conditions for magmatic crystallization and subsolidus re-equilibration of the anorthositic suite (Drüppel et al., 2001) and the felsic suite can be estimated from the chemical compositions and textural relationships of their respective mineral assemblages. The results of the various calculations are summarized in the P-T plot of Fig. 9.3.

9.1 Thermobarometry of the anorthositic rocks

9.1.1 Magmatic textures

The following magmatic crystallization sequence was established for samples of the dark anorthosite suite:

cumulus plagioclase + Fe-Ti oxides + olivine →
intercumulus Fe-Ti oxides + olivine + orthopyroxene + clinopyroxene →
late-magmatic amphibole + biotite

Plagioclase and part of the Fe-Ti-oxides and olivine are of cumulus origin, followed by intercumulus Fe-Ti oxides, olivine, orthopyroxene and clinopyroxene. If both, olivine and pyroxenes are present, the latter commonly form rims around olivine. Late-magmatic rims of amphibole and biotite, crystallized from pockets of trapped melt, surround intercumulus pyroxenes and the Fe-Ti oxides.

Orthopyroxene-clinopyroxene thermometry

In order to constrain the crystallization temperatures of the anorthositic rocks, the temperatures of 3 pairs of coexisting interstitial ortho- and clinopyroxene in the dark anorthosite were calculated using the thermometer formulation of Brey & Köhler (1990; their equation 9), based on the transfer reaction of enstatite in Opx and Cpx. For an assumed pressure range of 6-8 kbar (for a detailed discussion on the reasons for the pressure assumption see Chapter 9.3), temperatures of 730-780°C (Ku-98-52) and 740-745°C (Ku-98-221b) were calculated (Table 9.1). The accuracy of the calculation in natural systems is $\pm 16^\circ\text{C}$. The estimated temperatures resemble those derived with the pyroxene-solvus diagram of Lindsley (1983), with the solvus

isotherms of coexisting orthopyroxene and clinopyroxene displayed in the quadrilateral pyroxene system Di-Hd-En-Fs.

The obtained temperature range is lower than expected for magmatic phases and lies even below the temperatures calculated from amphibole compositions (see below). This points to a subsolidus re-equilibration, that strongly affected the Ca-Mg-Fe-exchange in the mafic silicates.

rock type	sample	assemblage	B&K	
			7.0 kbar	7.5 kbar
leucotroctolite	Ku-98-52	opx2-2-cpx1-7	776°C	778°C
		opx1-5-cpx1-1	727°C	729°C
leucotroctolite	Ku-98-221b	opx2-1-cpx1-2	742°C	744°C

Table 9.1: Representative T estimates for magmatic orthopyroxene-clinopyroxene pairs of leucotroctolite samples of the dark anorthosite suite (B&K Brey & Köhler, 1990).

Hornblende thermometry

For the determination of the T conditions during the late-magmatic crystallization of the anorthositic rocks the amphibole thermometer of Helz (1973, 1976) was used. Experimental studies of Helz (1973), at conditions of 700-1000°C and 5 kbar, have shown that the Ti content of hornblende increases with temperature and is independent of the whole-rock composition if ilmenite is present and the oxygen fugacity is near the QFM buffer. According to Otten (1984) the thermometer is applicable to amphiboles of both magmatic and subsolidus origin. In the presence of ilmenite the amphiboles crystallized from the interstitial magma will contain the maximum amount of Ti, and the thermometer will yield the crystallization temperature. In contrast, the Ti-content of amphiboles formed during subsolidus reactions will strongly depend on the local availability of Ti so that the respective amphiboles may not contain the maximum possible amount of Ti. Conformably, the thermometer will yield minimum temperatures for subsolidus amphiboles.

In the dark anorthosite suite of the KIC eighteen amphiboles of presumably late-magmatic origin surrounding ilmenite, were investigated. The number of Ti cations per formula unit (23 O) varies between 0.27 and 0.40, pointing to crystallization temperatures of 951-986°C.

The absence of exsolved Ti-phases like ilmenite or rutile demonstrates that the original Ti content is preserved in the amphiboles. Consequently, the calculated high temperatures are interpreted to give the late-magmatic crystallization temperature of the dark anorthosite suite. These temperature estimates are in good agreement with temperatures determined for similar amphiboles of the Artfjället dolerites, Sweden (Otten, 1984) and the Frankenstein gabbro, Odenwald, Germany (Kreher, 1992), which are supposed to be near-solidus.

Ilmenite-magnetite thermometry and oxygen barometry

The estimation of temperatures and oxygen fugacities for unexsolved, cogenetic ilmenite and magnetite was performed using the $\text{Ilm}_{\text{ss}}\text{-Mt}_{\text{ss}}$ thermometer-oxy-barometer of Spencer & Lindsley (1981), based on hydrothermal exchange-equilibrium experiments in a temperature range of 500-1000°C by Spencer & Lindsley (1978). The thermometer is applicable for a wide variety of igneous and metamorphic rocks. The choice of pressure conditions does not influence the obtained results.

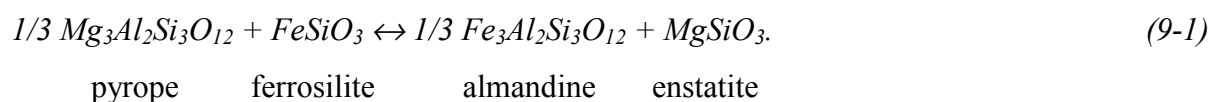
The calculation yields temperatures in the range of 680-730°C with corresponding oxygen fugacities of 10^{-17} - 10^{-19} , lying near the QFM buffer (Table 9.5; Fig. 9.2). Since ilmenite and magnetite commonly predate amphibole, the temperatures indicate re-equilibration of the Fe-Ti oxides as in the case of coexisting pyroxenes.

9.1.2 Coronitic mineral assemblages

In some of the leucotroctolite samples, the primary magmatic textures are partially obliterated by garnet-bearing corona structures around interstitial olivine and Fe-Ti oxides, pointing to a subsolidus re-equilibration of the rocks. Thus, the obtained quantitative P-T estimates should shed some light on the post-emplacement evolution of the Kunene Intrusive Complex.

Garnet-orthopyroxene thermometry

Temperatures during corona formation around olivine were estimated with the thermometers of Lee & Ganguly (1988) and Bhattacharya et al. (1991), based on temperature-dependent Fe-Mg exchange between coexisting garnet and orthopyroxene, expressed by the reaction:



The reaction has been calibrated as a thermometer by two independent experimental studies (Harley, 1984; Lee & Ganguly, 1988). The calibration of Bhattacharya et al. (1991) is based on the experimental data of Lee & Ganguly (1988), combined with the better constrained values of mixing parameters for the pyrope-almandine binary of Geiger et al. (1987). The Harley (1984) calibration has been excluded, since it is very sensitive to retrograde re-equilibration and thus mostly yields unrealistically low temperatures.

sample	assemblage	L&G		B	
		7.0 kbar	7.5 kbar	7.0 kbar	7.5 kbar
Ku-97-104	gt1-opx1	680°C	683°C	663°C	667°C
	gt2-opx2	676°C	679°C	658°C	663°C
Ku-97-105	gt1-opx1	632°C	635°C	620°C	624°C
Ku-98-221a	1-gt1-opx1	774°C	777°C	732°C	737°C
	2-gt1-opx2	747°C	750°C	710°C	714°C
	3-gt1-opx1	759°C	762°C	716°C	719°C
	3-gt2-opx2	765°C	768°C	725°C	730°C
Ku-98-221b	3-gt1-opx3	800°C	803°C	757°C	763°C
	3-gt2-opx2	766°C	768°C	729°C	734°C
	5-gt1-opx2	854°C	857°C	803°C	808°C

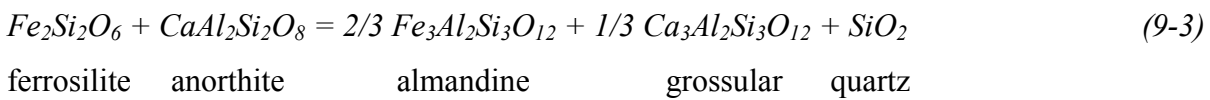
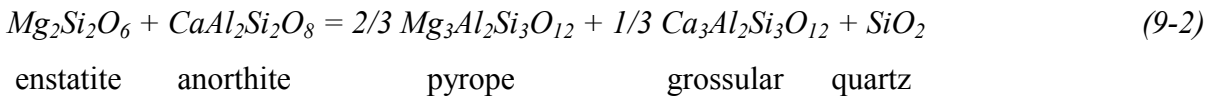
Table 9.2: Representative T estimates for garnet-orthopyroxene pairs of Type I coronas in leucotroctolite samples of the dark anorthosite suite (Thermometer calibrations: *B* Bhattacharya, 1991; *L&G* Lee & Ganguly, 1988).

For the applied thermometers a pressure range of 7.0 – 7.5 kbar was assumed (for a detailed discussion on the reasons for the pressure assumption see Chapter 9.3), yielding a range of temperatures for the four analysed samples, i.e. 630-860°C (Lee & Ganguly, 1988) and 620-810°C (Bhattacharya et al., 1991; Table 9.2). However, temperatures obtained for garnet-orthopyroxene pairs from individual samples are quite homogeneous, ranging from 632-635°C in sample Ku-97-105, 676-683°C in sample Ku-97-104, 747-777°C in sample Ku-98-221a and 766-857°C in sample Ku-98-221b. Remarkably, in the same direction the modal amount as well as the grain sizes of garnet increase, indicating that the garnets from samples Ku-97-104 and –

105 may have re-equilibrated, following diffusional exchange with the bordering Fe-Mg silicates (e.g. orthopyroxene, actinolite), even though continuous garnet formation under decreasing temperatures during cooling cannot be ruled out, as will be discussed in some detail below.

Garnet-orthopyroxene-plagioclase-quartz barometry

Pressures of the corona formation in the leucotroctolite samples were calculated using the garnet-orthopyroxene-plagioclase-quartz barometer, based on the net-transfer reaction $Pl + Opx = Grt + Qtz$. Two barometers are applicable for the P calculation of granulite-facies metabasites and charnockites, based on the following two end-member reactions:



For the pressure estimation based on the Mg-exchange reaction (9-2) the barometer calibrations of Newton & Perkins (1982), Powell & Holland (1988) and Eckert et al. (1991) were used, whereas pressure estimates following the Fe-exchange reaction (9-3) were calculated with the barometer calibrations of Bohlen et al. (1983) and Moecher et al. (1988).

For an assumed intermediate temperature of 750°C pressures of 6.3-8.1 kbar, 5.8-7.4 kbar and 5.8-7.6 kbar were calculated using the calibrations of Newton & Perkins (1982), Powell & Holland (1988) and Eckert et al. (1991), respectively. In contrast, the pressures obtained for the Fe-exchange barometer calibrations of Bohlen et al. (1983) and Moecher et al. (1988) for the same temperature range yield distinctly higher values of 9.2-11.2 kbar and 9.8-11.2 kbar, respectively (Table 9.3). In addition, the pressure estimates calculated from reaction (9-3) are very sensitive to changes in the assumed T, reflecting a considerably steeper slope of the Fe end member reaction when compared to reaction (9-2). Moreover, it has to be mentioned, that the calculated P values are maximum pressures because quartz is present in only minor proportions and the applied net-transfer reactions are shifted to lower pressures with a decreasing activity of SiO₂. Thus, the lower P ranges derived by reaction (9-2) are considered as more reasonable and trustworthy results.

sample	assemblage	N&P (Mg)			H&P (Mg)			E (Mg)		
		700°C	750°C	800°C	700°C	750°C	800°C	700°C	750°C	800°C
Ku-97-104	gt1-opx1-pl1	6.2 kbar	6.3 kbar	6.4 kbar	5.7 kbar	5.8 kbar	5.8 kbar	5.8 kbar	5.8 kbar	5.9 kbar
	gt2-opx2-pl2	6.4 kbar	6.5 kbar	6.6 kbar	5.8 kbar	5.9 kbar	5.9 kbar	5.9 kbar	6.0 kbar	6.1 kbar
Ku-97-105	gt1-opx1-pl1	6.4 kbar	6.5 kbar	6.6 kbar	5.8 kbar	5.9 kbar	5.9 kbar	5.9 kbar	6.0 kbar	6.1 kbar
Ku-98-221a	1-gt1-opx1-pl1	7.4 kbar	7.5 kbar	7.7 kbar	6.9 kbar	7.1 kbar	7.2 kbar	7.0 kbar	7.2 kbar	7.4 kbar
	2-gt1-opx2-pl1	6.9 kbar	7.0 kbar	7.1 kbar	6.4 kbar	6.4 kbar	6.5 kbar	6.4 kbar	6.5 kbar	6.6 kbar
	3-gt1-opx1-pl1	6.9 kbar	7.1 kbar	7.2 kbar	6.4 kbar	6.5 kbar	6.6 kbar	6.5 kbar	6.6 kbar	6.7 kbar
	3-gt2-opx2-pl2	7.1 kbar	7.0 kbar	7.4 kbar	6.6 kbar	6.8 kbar	6.9 kbar	6.7 kbar	6.8 kbar	7.0 kbar
Ku-98-221b	3-gt1-opx3-pl1	7.4 kbar	7.6 kbar	7.8 kbar	6.9 kbar	7.1 kbar	7.3 kbar	7.0 kbar	7.2 kbar	7.4 kbar
	3-gt2-opx2-pl2	7.0 kbar	7.3 kbar	7.5 kbar	6.6 kbar	6.7 kbar	6.9 kbar	6.6 kbar	6.8 kbar	7.0 kbar
	5-gt1-opx2-pl1	7.9 kbar	8.1 kbar	8.3 kbar	7.2 kbar	7.4 kbar	7.5 kbar	7.4 kbar	7.6 kbar	7.8 kbar

sample	assemblage	B (Fe)			M (Fe)		
		700°C	750°C	800°C	700°C	750°C	800°C
Ku-97-104	gt1-opx1-pl1	9.5 kbar	10.2 kbar	10.8 kbar	9.4 kbar	9.9 kbar	10.5 kbar
	gt2-opx2-pl2	9.8 kbar	10.5 kbar	11.6 kbar	10.3 kbar	11.0 kbar	12.0 kbar
Ku-97-105	gt1-opx1-pl1	10.2 kbar	10.9 kbar	11.6 kbar	10.5 kbar	11.2 kbar	11.9 kbar
Ku-98-221a	1-gt1-opx1-pl1	9.6 kbar	10.2 kbar	10.8 kbar	9.5 kbar	10.2 kbar	10.9 kbar
	2-gt1-opx2-pl1	8.7 kbar	9.2 kbar	9.8 kbar	9.2 kbar	9.8 kbar	10.5 kbar
	3-gt1-opx1-pl1	8.7 kbar	9.3 kbar	9.8 kbar	9.2 kbar	9.9 kbar	10.6 kbar
	3-gt2-opx2-pl2	8.9 kbar	9.4 kbar	9.9 kbar	9.4 kbar	10.0 kbar	10.7 kbar
Ku-98-221b	3-gt1-opx3-pl1	10.1 kbar	10.7 kbar	11.3 kbar	9.2 kbar	9.9 kbar	10.6 kbar
	3-gt2-opx2-pl2	10.2 kbar	10.8 kbar	11.4 kbar	9.3 kbar	10.0 kbar	10.7 kbar
	5-gt1-opx2-pl1	10.6 kbar	11.2 kbar	11.8 kbar	9.6 kbar	10.3 kbar	10.9 kbar

Table 9.3: Representative P estimates, calculated using the garnet-orthopyroxene-plagioclase-quartz barometer for garnet-orthopyroxene-plagioclase-quartz assemblages of Type I coronas in leucotroctolite samples of the dark anorthosite suite. (Barometer calibrations: *B* Bohlen et al., 1983; *E* Eckert et al., 1991; *M* Moecher et al., 1988; *N&P* Newton & Perkins, 1982, *P&H* Powell & Holland, 1988).

Like the T estimates for coexisting garnet and orthopyroxene of the leucotroctolite samples the calculated P for the T_{ref} of 750°C range can be subdivided into two groups, with the highest pressures of 6.4-8.1 kbar (7.3 ± 0.9 kbar) obtained for samples Ku-98-221a and Ku-98-221b, which at the same time yield highest Grt-Opx temperatures (750-860°C), whereas lower pressures were calculated for samples Ku-97-104 and Ku-97-105 (6.2 ± 0.4 kbar), corresponding to lower Grt-Opx temperatures (630-680°C; Table 9.3).

The most plausible explanation for these results is a garnet formation in at least two stages, the first generation predating and the second one post-dating a weak exhumation of the anorthosite body from ~7.3 (stage I) to ~6.2 kbar (stage II). Such an uplift of about 3 km (~1 kbar) would be in excellent accordance with the currently preferred tectonic setting of Proterozoic massif-type anorthosites, i.e. their emplacement in extensional environments (Ashwal, 1993). It has to be mentioned, however, that the low P and T estimates of Ku-97-104 and Ku-97-105 may also result from a later re-equilibration of their coronitic mineral assemblages with respect to Fe, Mg and Ca.

Garnet-biotite thermometry

The thermometer is based on the temperature-dependent Mg-Fe exchange between coexisting garnet and biotite, expressed by the reaction:



almandine phlogopite pyrope annite

sample	assemblage	I&M		K&R		P	
		7.0 kbar	7.5 kbar	7.0 kbar	7.5 kbar	7.0 kbar	7.5 kbar
Ku-98-221b	4-bt incl-gt1	541°C	542°C	596°C	598°C	573°C	574°C
	4-bt1-gt2	703°C	705°C	747°C	749°C	725°C	726°C
	2-bt1-gt3	704°C	706°C	748°C	751°C	726°C	727°C
	3-bt2-gt3	698°C	700°C	735°C	738°C	720°C	721°C

sample	assemblage	B		F&S		H&S	
		7.0 kbar	7.5 kbar	7.0 kbar	7.5 kbar	7.0 kbar	7.5 kbar
Ku-98-221b	4-bt2-gt1	620°C	620°C	566°C	567°C	625°C	627°C
	4-bt1-gt2	712°C	713°C	727°C	729°C	788°C	790°C
	2-bt1-gt3	713°C	713°C	726°C	729°C	788°C	791°C
	3-bt2-gt3	710°C	710°C	724°C	726°C	785°C	787°C

Table 9.4: Representative T estimates for garnet-biotite pairs of Type II coronas in leucotroctolite samples of the dark anorthosite suite (Thermometer calibrations: *B* Bhattacharya et al., 1992; *F&S* Ferry & Spear, 1978; *H&S* Hodges & Spear, 1982; *I&M* Indares & Martignole, 1985, *K&R* Kleemann & Reinhardt, 1994; *P* Perchuk & Lavrent'eva, 1983).

The reaction was calibrated as a thermometer by many authors. For the calculation of the pressure conditions of the garnet-biotite corona formation in the leucotroctolite sample Ku-98-221b, the thermometer formulations of Ferry & Spear (1978), Hodges & Spear (1982), Perchuk & Lavrent'eva (1983), Indares & Martignole (1985), Bhattacharya et al. (1992) and Kleemann & Reinhardt (1994) were used.

For an assumed pressure range of 7.0-7.5 kbar (for a detailed discussion on the reasons for the pressure assumption see Chapter 9.3), the calculated temperatures for core compositions of inclusion-free garnet and matrix biotite range between 660-790°C, the highest values being obtained with the Hodges & Spear (1982), and the lowest with the Indares & Martignole (1985) formulations (Table 9.4). In contrast, the T estimate using the composition of poikilitic garnet and a biotite inclusion deviates significantly from these results by yielding unrealistically low temperatures of 540-630°C. This low T range most probably results from diffusional Fe-Mg exchange between the poikilitic garnet and the included biotite, which, however, has not affected inclusion free garnet and matrix biotite (see Chapter 6.8).

9.1.3 Symplectitic mineral assemblages

Ilmenite-magnetite thermometry and oxygen barometry: Temperatures and oxygen fugacities for symplectitic ilmenite-magnetite pairs were estimated using the two-oxide thermometer of Spencer & Lindsley (1981).

The calculated temperatures are in the range of 490-570°C, with corresponding oxygen fugacities of 10^{-20} - 10^{-26} , indicating symplectite formation or re-equilibration at temperatures distinctly lower than those calculated for the interstitial oxide pairs, which however still plot near the QFM buffer (Table 9.5; Fig. 9.2).

rock type	sample	textural position	T (°C)	log ₁₀ fO ₂
leucotroctolite	Ku-97-105	interstitial	728	-17.60
			723	-17.50
			723	-17.50
			727	-17.60
leucotroctolite	Ku-98-221b	interstitial	680	-19.50
leucotroctolite	Ku-98-52	symplectitic	487	-24.90
			489	-26.60
			507	-24.50
leucogabbronorite	Ku-98-79	symplectitic	518	-23.90
leucogabbronorite	Ku-98-84	symplectitic	574	-19.80
			558	-20.80

Table 9.5: Representative T and Log₁₀fO₂ estimates for ilmenite-magnetite pairs from anorthositic rock samples of the dark anorthosite suite.

9.2 Thermobarometry of the syenitic suite

Feldspar thermometry

The determination of temperatures during K-feldspar crystallization of the syenites, followed the feldspar thermometer of Fuhrman & Lindsley (1988), which is based on a ternary solution model that accounts for the effects of K in plagioclase and of Ca in K-feldspar. This thermometer is thus highly applicable for feldspars formed under high temperatures, where the effects of ternary

solution become increasingly important. Reintegrated compositions of perthitic K-feldspar from the syenite have been plotted in the ternary feldspar diagram. Solvi for temperatures of 600–1100°C at an assumed pressure of 6.5 kbar were calculated with the program SOLVCALC (Wen & Nekvasil, 1994), applying the feldspar activity model of Fuhrman & Lindsley (1988).

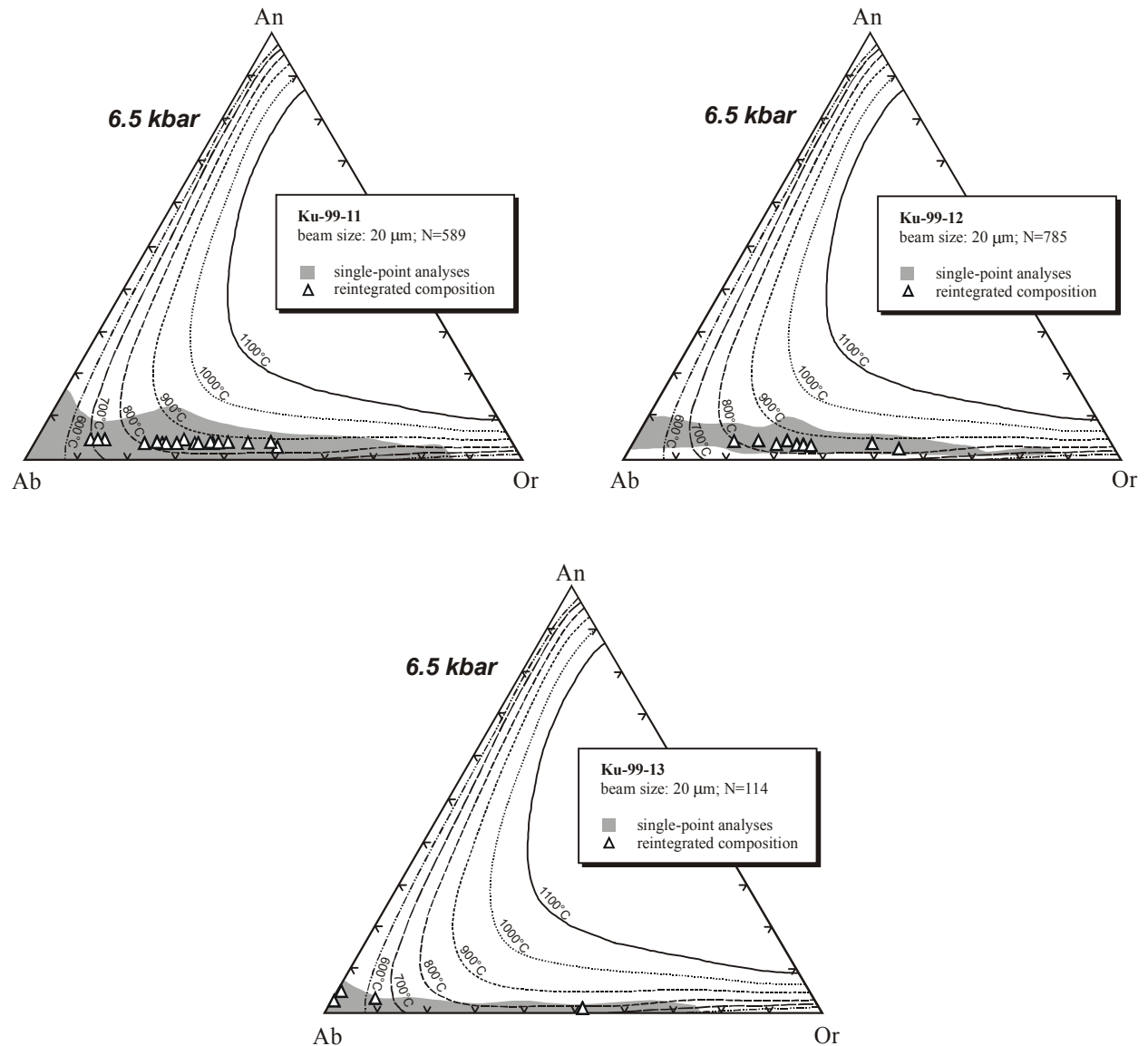


Fig. 9.1: T estimates for re-integrated compositions of perthitic K-feldspar from the syenites, plotted in the ternary feldspar diagram. Solvi at 6.5 kbar were calculated with the program SOLVCALC (Wen & Nekvasil, 1994) applying the feldspar activity model of Fuhrman & Lindsley (1988).

Feldspar core compositions of the three syenite samples investigated mostly plot between the 800°C and the 900°C isotherm or slightly below the 800°C isotherm, pointing to crystallization temperatures of 790–890°C, which are presumably near the liquidus of the

syenites (Fig. 9.1). In clear contrast, the rim compositions of the feldspars analysed generally yield temperatures below 750°C.

Amphibole barometry

The experimental studies of Hammarstrom & Zen (1983, 1985, 1986) have shown that the Al content in amphibole generally increases with increasing pressure. Based on this observation, the authors compiled a barometer formulation, based on the amount of Al^{tot} (total amount of Al calculated anhydrous on a 23-oxygen basis) in amphibole from calc-alkaline plutons and calibrated for a T range of 500-1100°C and P ranges of 1.5-3 kbar and 7-10 kbar, respectively. The barometer has been extended by Hollister et al. (1987) by including pressures between 3 and 7 kbar. Since the hornblende composition varies significantly with the rock composition, samples containing plagioclase, quartz, hornblende, biotite, potassium feldspar, magnetite and titanite are most suitable for pressure calculations (Hammarstrom & Zen, 1986).

The amount of Al^{tot} of hastingsite from the syenite samples varies between 1.91-2.10, corresponding to crystallization pressures of 6.0-7.1 kbar (Table 9.6). A similar pressure range has been determined for symplectitic amphibole from sample Ku-99-11 (P = 6.6-6.9 kbar), thus suggesting that the syenite emplacement was followed by almost isobaric cooling under P conditions of 6.5 ± 0.6 kbar.

rock type	sample	textural position	P _{min}	P _{max}	P _{average}	σ	N
syenite	Ku-99-11	interstitial	6.3 kbar	7.1 kbar	6.5 kbar	0.21	21
		symplectitic	6.6 kbar	6.9 kbar	6.8 kbar	0.10	5
	Ku-99-13	interstitial	6.0 kbar	6.8 kbar	6.4 kbar	0.19	32
	Ku-99-14	interstitial	6.0 kbar	7.1 kbar	6.6 kbar	0.26	43

Table 9.6: P estimates for magmatic amphibole of the syenite, calculated by using the Al in hornblende barometer calibration of Hollister et al. (1987).

Taken into account the overall uncertainties in conventional geothermobarometry, these pressure estimates are in good accordance with those obtained for the second stage of corona formation in the leucotroctolites (6.2 ± 0.4 kbar).

Ilmenite-magnetite thermometry and oxygen barometry

Temperatures calculated with the two-oxide thermometer of Spencer & Lindsley (1981) for interstitial ilmenite and magnetite from the quartz-syenite range between 600-620°C with corresponding oxygen fugacities of 10^{-18} (Table 9.7).

rock type	sample	textural position	T (°C)	$\log_{10}fO_2$
quartz-syenite	Ku-98-40	interstitial	622	-18.10
			624	-18.00
			599	-17.90
syenite	Ku-99-11	symplectitic	540	-18.10

Table 9.7: Representative T and $\log_{10}fO_2$ estimates for ilmenite-magnetite pairs from quartz-syenite and syenite of the felsic suite.

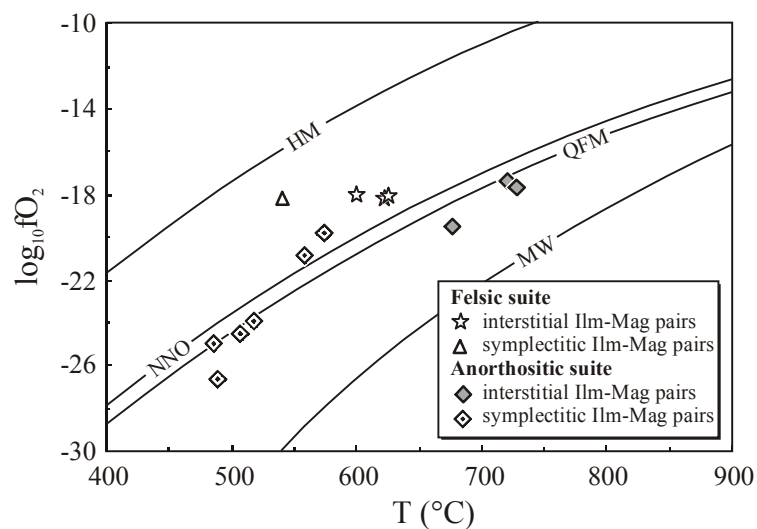


Fig. 9.2: Plot of $\log_{10}fO_2$ against temperature (°C) calculated for coexisting ilmenite-magnetite pairs occurring in different textural positions in both the anorthositic and the felsic suite (*HM* hematite-magnetite buffer, *MW* magnetite-wuestite buffer, *NNO* Ni-NiO buffer, *QFM* quartz-fayalite-magnetite buffer).

The temperature obtained for ilmenite and magnetite in symplectitic intergrowth with amphibole and plagioclase in the syenite is lower (540°C), but yields a similar value for the oxygen fugacity ($\log_{10}fO_2$: 10^{-18}). In contrast to those of anorthositic ilmenite-magnetite pairs, these oxygen fugacities are higher than the QFM buffer (Fig. 9.2), indicating a relatively oxidised environment, which is consistent with the presence of hematite and the absence of olivine from the felsic rocks.

9.3 P-T evolution of the Kunene Intrusive Complex and the temporally associated felsic suite

In the *dark anorthosite suite*, plagioclase was the first mineral to crystallize, accompanied and followed by cumulus to intercumulus magnetite and olivine. The next minerals appearing in the crystallization sequence are interstitial orthopyroxene, clinopyroxene and ilmenite. Ilmenite as well as the pyroxenes are partially surrounded by rims of pargasitic to hastingsitic amphibole and biotite. A late-magmatic crystallization rather than a subsolidus formation of amphibole is suggested by the following observations: (1) amphiboles of similar composition occur in different textural positions, *i.e.* isolated or as rims locally surrounding pyroxene or ilmenite. (2) In contrast to pyroxene, amphibole frequently contains inclusions of euhedral apatite grains, pointing to the late-magmatic crystallization of apatite and pargasitic to hastingsitic amphibole from P₂O₅-rich residual liquids. (3) A subsolidus replacement of pyroxene seems to be unlikely, since no crystallographic relationship between ortho- and clinopyroxene and amphibole has been observed. (4) In contrast to the pargasitic to hastingsitic amphiboles, actinolite formed by topotactic subsolidus replacement of orthopyroxene includes platelets of ilmenite exsolved from the precursor orthopyroxene. (5) The high Ti-contents of the pargasitic to hastingsitic amphiboles are suggestive of igneous crystallization, as subsolidus re-equilibration would typically result in exsolution of rutile or ilmenite (Otten, 1984). (6) If the analysed amphiboles have been crystallized under subsolidus conditions, the obtained temperatures of ~970°C would reflect minimum temperatures of the amphibole formation, due to the restricted availability of Ti (Otten, 1984). Subsolidus temperatures of > 970°C, however, would necessitate a high-T ductile deformation event that was not observed. (7) The absence of hydrous silicates in the ilmenite-magnetite-orthopyroxene symplectites contradicts the presence of a H₂O-rich fluid phase in the subsolidus stage.

Following these arguments, the average T of 970°C obtained from the amphibole thermometer of Helz (1973) is interpreted to be the late-magmatic crystallization temperature of the dark anorthosite (Fig. 9.3). This late-magmatic crystallization of amphibole must have occurred after the emplacement of the anorthositic crystal mushes.

After solidification, the formation of a first generation of garnet-orthopyroxene coronas around olivine and of garnet-biotite coronas around ilmenite occurred under P-T conditions of around $760 \pm 100^\circ\text{C}$ and 7.3 ± 0.9 kbar. Similar temperature ranges of $720\text{--}780^\circ\text{C}$ and $680\text{--}730^\circ\text{C}$, respectively, are obtained for magmatic orthopyroxene-clinopyroxene and ilmenite-magnetite pairs. These P-T conditions are indicative of an overall re-equilibration of the plutonic

mass at conditions near the amphibolite- to granulite-facies transition (Fig. 9.3), as already described for various massif-type anorthosite complexes (*e.g.* Martignole & Schrijver, 1971; Griffin, 1971; Bingen *et al.*; 1984, Ashwal *et al.*, 1998). Since there is no evidence for a high-grade metamorphic event post-dating the anorthosite emplacement both on the Namibian part (Drüppel *et al.*, 2001) and the Angolan part of the KIC (*e.g.* Ashwal & Twist, 1994; Morais *et al.*, 1998; Mayer *et al.*, 2000) the garnet-bearing corona structures are suggested to reflect cooling of the anorthosite body rather than a separate event of prograde metamorphism. This interpretation is mainly based on the following observations: (1) Deformation textures like shear zones and foliation are absent in the two anorthosite suites, both on the macroscopic and microscopic scale. (2) Metamorphic textures as well as corona structures have not been observed in samples of the white anorthosite suite, which obviously predates the dark anorthosite emplacement and consequently should have been affected by a prograde metamorphic event as well. (3) The preservation of hydrothermal alteration in the white anorthosite is unlikely in case of a pervasive high-grade metamorphic overprint. If, however, the alteration of the white anorthosite took place during retrograde greenschist-facies metamorphism along major E-W trending faults, these should extend from the KIC to the surrounding basement. This has never been observed. (4) Garnet-bearing corona structures have not yet been observed in most of the KIC and occur only in a few leucotroctolite samples of the dark anorthosite suite. Even within single samples they are found just sporadically. (5) On the microscopic scale, igneous textures are preserved in all investigated samples, whereas metamorphic effects like granoblastic textures, expulsion of Fe-Ti oxide inclusions from plagioclase or reduction of the grain size have not been observed.

Following these arguments, the pressures of around 7.3 ± 0.9 kbar, calculated with the garnet-orthopyroxene-plagioclase-quartz barometer for the subsolidus formation of garnet and orthopyroxene, are interpreted to reflect the emplacement depth (*c.* 22 km) of the anorthositic crystal mushes. Consequently, pressures of *c.* 7.3 kbar can also be assumed for the late-magmatic crystallization of pargasite. In two leucotroctolite samples, bearing minor and very fine-grained garnet, garnet orthopyroxene thermometry and garnet-orthopyroxene-plagioclase-quartz barometry yielded slightly lower temperature and pressure ranges, suggesting their formation under PT conditions of 630-680°C and 6.2 ± 0.4 kbar. The PT estimates indicate an exhumation of the anorthosite massif of about 3 km (~ 1 kbar) during the end-stages of the anorthosite emplacement (Fig. 9.3), which is in excellent agreement with the widely held belief that massif-type anorthosites are emplaced in extensional settings. It cannot be ruled out, however, that the small grain size of garnet in these two leucotroctolite samples favoured retrograde cation exchange with the bordering orthopyroxene and plagioclase, thus yielding re-equilibration

temperatures and pressures. As no symplectitic breakdown of coronitic garnet was observed, it can be concluded that pressure conditions of about 6-7 kbar outlasted the garnet formation for a certain period of time. These results invoke an emplacement in the middle crust followed by near-isobaric cooling of the anorthosite complex.

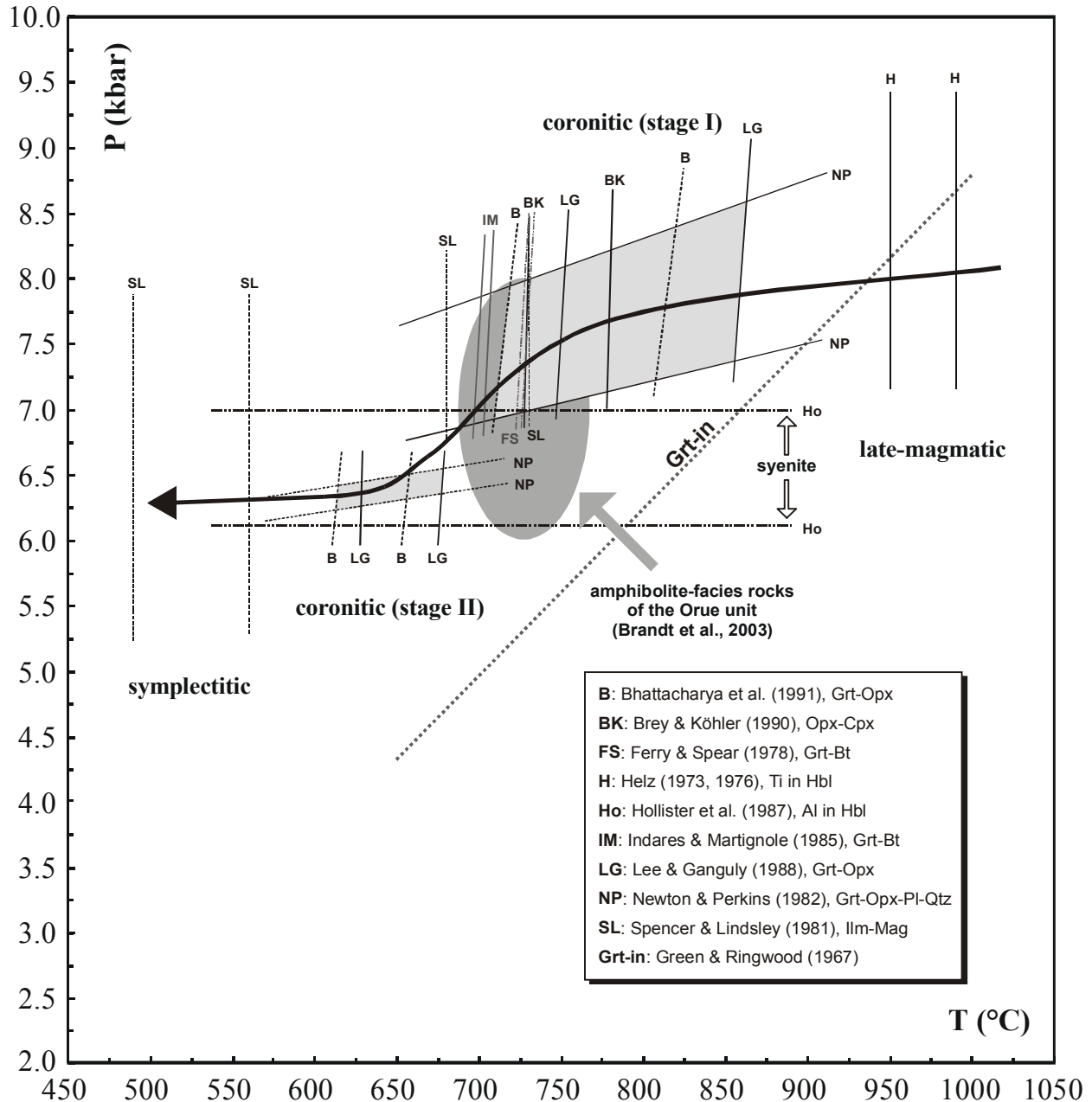


Fig. 9.3: P-T evolution of the dark anorthosite suite of the Kunene Intrusive Complex (see text for detail). The results of conventional geothermometry and geobarometry are indicated as the respective maximum and minimum estimates. For comparison, the P-T conditions of the bordering amphibolite-facies Orue Unit (Brandt et al., 2003) and the P conditions of the emplacement and cooling of the syenite suite are marked. (arrow suggested subsolidus P-T path for the dark anorthosite suite, grey stippled line experimentally determined reaction curve for plagioclase-olivine reaction and garnet-formation in olivine-tholeiites by Green & Ringwood, 1967).

The corona formation is followed by the development of ilmenite-magnetite-orthopyroxene symplectites at the expense of olivine and igneous Fe-Ti oxide following reaction (6): The formation of these symplectites necessitates that the QFM buffer curve was reached or crossed with decreasing temperature. In the case of the dark anorthosite suite, the calculated $f(\text{O}_2)$ -T path starts from 10^{-17} - 10^{-19} , 680-730°C of the orthomagmatic ilmenite-magnetite pairs down to 10^{-20} - 10^{-26} , 490-570°C calculated for the symplectites. On isobaric cooling, the QFM buffer curve is crossed, if a CO-CO₂-bearing fluid phase is involved, since the $f(\text{O}_2)$ -T curves of the solid buffer assemblages are transected by solid-gas buffer curves like graphite-CO-CO₂ (*cf.* Fig. L-20 in Lindsley, 1976). Support for this model is given by the presence of graphite precipitates on small fractures observed in one dark anorthosite sample. Both the orientation relationship between symplectitic orthopyroxene, magnetite and ilmenite, and the respective chemical compositions are compatible with those described by Barton & van Gaans (1988) and Barton et al. (1991), suggesting a subsolidus formation during cooling under dry conditions. The final stage of the late-magmatic evolution is marked by the formation of actinolite in the garnet-bearing coronas around olivine and the alteration of olivine to talc, magnetite and carbonate.

In the (*quartz-*)*syenites of the felsic suite* potassium feldspar, plagioclase and part of the hastingsite/clinopyroxene crystallized first, followed by interstitial hastingsite, Fe-Ti oxides, which may in turn be surrounded by narrow rims of titanite, which may additionally occur as discrete, anhedral grains together with a second generation of potassium feldspar (microcline). During the subsolidus re-equilibration of the syenites interstitial hastingsite was partially replaced by hastingsite-ilmenite-magnetite-plagioclase symplectites. A weak hydrothermal alteration of the syenites caused the replacement of clinopyroxene by fibrous ferro-hornblende to ferro-actinolite and/or epidote-calcite, the marginal alteration of hastingsite to chlorite, the sericitization of the feldspars and the martitisation of magnetite, whereas the recrystallisation of feldspars to granular plagioclase mosaics testifies to a post-emplacement deformation of the rocks.

For the magmatic to late-magmatic crystallization of hastingsite pressures of 6.5 ± 0.6 kbar have been obtained, which is similar to those derived for stage II garnet-orthopyroxene coronas around olivine (6.2 ± 0.4 kbar). These pressure estimates are interpreted to reflect the emplacement depth of the syenites (~ 19 km; Fig. 9.3), thus suggesting that the intrusion of the syenites in the middle crust post-dated the ~ 3 km exhumation of the dark anorthosite suite. Conformably, field observations and age determinations generally confirm an intrusive relationship between the two suites, with the felsic rocks being younger than the spatially associated anorthositic rocks (see Part I).

Magmatic crystallization of potassium feldspar in the syenites occurred under temperatures of 790-890°C, which are presumably near the liquidus of the rocks, whereas the (partially re-crystallized) feldspar rims formed at distinctly lower T of <750°C. Magmatic ilmenite-magnetite pairs of the quartz-syenite and syenite yield oxygen fugacities of 10^{-18} and comparably low temperatures of 600-620°C and 540°C, respectively, which are suggested to reflect re-equilibration conditions.

For the subsolidus formation of hastingsite-ilmenite-magnetite-plagioclase symplectites pressures of 6.6-6.9 kbar have been determined, implying that the syenite emplacement was followed by almost isobaric cooling, that has also been proposed for the dark anorthosite suite.

In summary, the results indicate that the emplacement of the dark anorthosite suite of the Kunene Intrusive Complex in the middle crust ($P = 7.3 \pm 0.9$ kbar, $T = 950-990^\circ\text{C}$) was followed by near-isobaric cooling to temperatures <600°C and pressures of 6.2 ± 0.4 kbar. The intrusion of the dark anorthosite suite was followed by the emplacement of numerous syenite dykes under PT conditions of 6.5 ± 0.6 kbar and 790-890°C. Like the anorthosites, the syenites cooled under almost isobaric conditions to temperatures <600°C. A prograde metamorphic event is precluded for the analysed samples, for reasons discussed in some detail above. This model of mid-crustal emplacement and cooling is constrained by PT conditions obtained for the bordering amphibolite-facies Orue Unit by Brandt et al. (2003). For these rocks, which locally even underwent contact-metamorphism by the anorthositic melts, the authors calculated temperatures of ~650-750°C at pressures of ~6-8 kbar, which agree well with the PT estimates for the emplacement and re-equilibration of both the anorthositic and the felsic suite (Fig. 9.3).

10 Discussion

The Kunene Intrusive Complex displays many of the typical features of massif-type anorthosite complexes as summarized by Ashwal (1993):

- The KIC has an extraordinary large areal extent of at least 18,000 km², being composed of several plutonic bodies.
- The massif mainly consists of anorthosite, leucogabbro and leucotroctolite, whereas mafic and ultramafic rocks are rare.
- Minor concentrations of ilmenite-magnetite ore occur in the marginal parts of the complex.
- The KIC is associated with minor volumes of K-rich felsic rocks, ranging in composition from syenite to granite.
- Plagioclase has an average composition of An_{50±20} and is generally coarse-grained.

Features like the mortar texture and the block-structure as well as the occurrence of anorthositic dykes crosscutting the main massif and the lack of layering additionally confirm the massif-type character of the KIC; a layered intrusion affinity of the KIC can be ruled out.

10.1 Constraints on the source and evolution of the anorthositic and syenitic melts

Much has been speculated about the magmas parental to anorthositic and associated granitic melts, however, no general consensus has been reached yet (*e.g.* Ashwal, 1993, for a review). A first decision to be made is whether the felsic rocks represent late-stage fractionation products from the magma parental to the anorthosites, or if the two suites are chemically unrelated.

In the case of the Kunene Intrusive Complex, evidence against consanguinity of the two suites is striking: (1) Field observations show the syenite dykes to be intrusive into the anorthositic rocks. In addition, granitoid plutons may form isolated bodies, crosscutting the bordering amphibolite-facies Epembe Unit of the Epupa Complex. (2) The mineral compositions of the granitoid suite appear to extend the compositional range of the respective minerals from the anorthositic rocks towards higher Fe/Mg ratios and lower Al of the Fe-Mg silicates and lower An contents of plagioclase. However, intermediate mineral compositions are missing. Moreover, the relative changes of the mineral chemistry, displayed by the subsequently emplaced

anorthosite bodies themselves, rather imply an opposite evolutionary trend (towards higher An of plagioclase and lower Fe/Mg ratios of the Fe-Mg silicates). (3) A compositional gap is developed between the major and trace element data of the two suites; chemical continuity, as commonly observed for most metamorphosed anorthosite massifs, is lacking. (4) The felsic rocks are typical of Proterozoic crustally derived A-type granites (K-rich, ferroan, subalkaline to alkaline, metaluminous to marginally peraluminous A-type granitoids). (5) Trace element data of the felsic suite, plotted in spider diagrams, provides evidence for a crustal or at least a mixed crustal-mantle source. (6) The syenites do not exhibit ubiquitous negative Eu-anomalies in their REE patterns, which would, however, be expected from fractionation products of melts that previously formed extensive plagioclase cumulates. (7) The magmatic feldspar $\delta^{18}\text{O}$ values from both the quartz-syenite and the syenites fall in a restricted range of 7.20-7.92 ‰, which, however, are about 1.6 ‰ higher than the average magmatic plagioclase $\delta^{18}\text{O}$ of the anorthosites.

Following these arguments, the felsic suite was at least not formed by closed-system fractionation from the melts parental to the anorthositic rocks of the Kunene Intrusive Complex. The question then becomes, were the felsic rocks formed (1) by fractional crystallization from residual liquids of the anorthosites, contaminated by crustal material during their uprise or (2) by crustal fusion with the heat necessary being provided by the upwelling and emplacement of mantle-derived melts at the base of the crust. This can not be answered easily, since in either case the originally dry magmas will be affected by fractional crystallization and crustal contamination as they ascend and thus both models could account for most of the features observed for the granitoids. However, judging from the data set so far available, a crustal origin of the felsic suite is the preferred working hypothesis, since data constraining a mixed mantle-crust source is equivocal, whereas evidence for a crustal source of the investigated syenites and granites is impressive. However, isotopic work on both rock suites is in progress (Littmann et al., in prep.) and will hopefully allow a final decision for one particular case.

There is no consensus on the magmas parental to massif-type anorthosites, but many investigators suggest that they are broadly basaltic in nature (e.g. Morse, 1968, 1982; Duchesne, 1984; Emslie, 1985; Wiebe, 1986; 1994, Olson & Morse, 1990; Ashwal, 1993; Longhi et al., 1999). In case of the KIC, the general geochemical characteristics of all anorthositic lithologies (i.e. high Al_2O_3 , CaO, Sr and Eu, intermediate to high Mg numbers of 0.37-0.74, Ne- and/or Ol-normative compositions) are in excellent agreement with a derivation from fractionated basaltic liquids. Mineral compositions of both anorthosite suites constrain this model, by being generally in the range of those commonly found in evolved gabbros and basalts. Following this, the

parental melts of the investigated anorthosites are suggested to be fractionated, Sr-enriched, high-Al gabbroic magmas.

Regarding the petrogenesis of the melts parental to massif type anorthosites, two different models have attained some popularity: (1) Most investigators suggest a petrogenetic scheme involving (i) the ponding of mantle-derived, broadly basaltic melts at the mantle-crust boundary, followed by (ii) extensive crystallization of olivine and highly aluminous pyroxene, with the residual liquids becoming more aluminous and Fe-rich, until (iii) plagioclase reaches the liquidus, leading to the formation of plagioclase suspensions in Fe-rich, high-Al gabbroic liquids, which (iiii) subsequently intrude middle to upper crustal levels (see Ashwal, 1993, for a review). This model is mainly constrained by the presence of high-Al orthopyroxene megacrysts within most anorthosite massifs, which testify to a high pressure stage of crystallization (e.g. Emslie, 1975a; Ashwal, 1993). (2) In contrast, the alternative petrogenetic model of Longhi et al. (1999) suggests the melts parental to massif-type anorthosites to be generated by partial melting of mafic source regions of the lower crust. With the help of equilibria experiments, Longhi et al. (1999) demonstrated that mantle-derived basaltic liquids, fractionating high-Al orthopyroxene in a first step, would reach plagioclase saturation at low normative Si contents and would thus become Ne-normative with further fractionation and assimilation of lower crustal material. The authors argue, that without extensive low-P assimilation of at least 20 % of a granitic component, such parental magmas could not produce the lithological variety observed in many anorthosite massifs (e.g. Ne-normative troctolitic and gabbroic lithologies to Qtz-normative noritic lithologies). Since the primitive isotopic compositions of these anorthosite massifs do not permit such an extensive assimilation of granitic material, Longhi et al. (1999) suggest mafic regions of the lower continental crust (mafic granulites or foundered mafic plutons) to be more suitable sources for the liquids parental to massif-type anorthosite complexes. However, no general agreement has yet been reached on either of these models.

The $\delta^{18}\text{O}$ values obtained for magmatic plagioclase from both anorthosite suites of the KIC prove their derivation from mantle-derived magmas, in good accordance with model (1). Moreover, the restricted chemical composition of the anorthositic lithologies of the Kunene Intrusive Complex and the general lack of Qtz-normative noritic assemblages does not require model (2), the melts parental to the anorthosites of the KIC are thus suggested to have formed by fractionation of a mantle-derived magma ponded near the base of the crust. However, magma generation by re-melting of mantle-derived gabbroic plutons, which were previously emplaced in the lower continental crust, can not yet be ruled out. The fact that UHT metamorphism recorded by granulites of the Epupa Complex is interpreted in favour of magmatic underplating at ~1,500 Ma (Brandt et al., 2003), might provide evidence for model (2) or a combination of both models.

The mineralogical and isotopic data suggests that all studied anorthosite samples underwent a certain degree of crustal contamination, which, however, was most prominent during the early intrusion stages of the white anorthosite and leucogabbro-norite: (1) Xenoliths of andradite-rich garnet, incorporated from calc-silicate crustal lithologies, were observed in one white anorthosite and one leucogabbro-norite sample but never in the younger leucotroctolites. (2) In contrast, late-magmatic biotite and amphibole are abundant phases in almost all investigated samples, suggesting a crustal contribution to the anorthositic melts of both suites, that was most possibly achieved during their ascent into middle crustal levels. (3) Highest values of $\text{Fe}^{\text{tot}}/(\text{Fe}^{\text{tot}}+\text{Mg})$, Na, K, P and Ba are recorded by the white anorthosite and the leucogabbro-norite and may indicate a granitic component. (4) Regarding their REE patterns white anorthosite samples display a slight enrichment in the light REE and a relative decrease in the heavy REE when compared with the corresponding lithologies of the dark anorthosite suite, supporting evidence for an elevated amount of crustal contamination of these rocks. (5) Last but not least, oxygen isotope data for one white anorthosite sample provides clear evidence for incorporation of crustal material.

To summarize, the crustal-derived felsic and the mantle-derived anorthositic suite are suggested to be coeval but not consanguineous. Their spatial and temporal association can be accounted for, if the heat necessary for crustal melting is provided by the anorthositic melts. The studied samples of the two anorthosite suites are representative of distinct intrusions, which underwent different degrees of crustal contamination, that, however, was most extensive during the early intrusion stages of the white anorthosite and the leucogabbro-norite.

10.2 Petrogenetic model

Mid-Proterozoic continental within-plate magmatism of anorthositic and associated felsic melts is recognized as an essential part of the early continental evolution of the Earth (e.g. Anderson, 1983; Ashwal, 1993). These rocks are widespread in what were probably large continental landmasses. The tectonic environment is generally considered to be extensional, even though their precise tectonic setting is yet under discussion (see Chapter 3.5.1.1). The most favoured model is a continental rift analogy, which may account for both, the bimodality of anorthosite-granitoid suites and the apparent linearity of anorthosite massifs.

The KIC is a broadly N-S elongated body, straddling the Namibian-Angolan border. In the Namibian part of the KIC, at least two distinct intrusive bodies were distinguished: (1) the older one mainly consists of light-coloured, strongly altered and tectonically overprinted massive anorthosites, leucotroctolites and leucogabbronorites, the white anorthosite, and is intruded by (2) less altered, dark-coloured anorthosites, leucotroctolites and leucogabbronorites, the dark anorthosite, along E-W-trending extensional faults. Based on the petrographic and geochemical investigations provided in this study combined with models published previously (e.g. Morse, 1968; Emslie, 1978, 1980; Ashwal, 1993), the following petrogenetic model is suggested for the evolution of both the KIC and the felsic suite:

1st stage

A significant thermal anomaly leads to the heating and partial melting of the upper mantle and/or lower crust. The magma ponds at the mantle-crust transition (magmatic underplating), building a large-scaled magma chamber (Fig. 10.1 a).

2nd stage

Continuing influx of magma and/or assimilation of lower crustal residues causes an expansion of the magma chamber. The melt increases in Al and Fe/Mg until plagioclase reaches the liquidus, precipitates and floats, forming plagioclase flotation cumulates. Density contrasts between the plagioclase-rich mushes and the surrounding country rocks of the lower crust (with density differences of 0.2-0.6 g/cm³ being estimated by Longhi & Ashwal (1985)) lead to the diapiric ascent of the crystal mushes and their emplacement in middle crustal levels (Fig. 10.1 a). During this ascent calc-silicates of the EC are assimilated, as is suggested by andraditic garnet xenocrysts within white anorthosites.

Late-stage oxide-melt segregations are foundered in the crystal mushes and crystallize the Fe-Ti ores. Fluid activity, induced by devolatilization of younger anorthositic crystal mushes, leads to a pervasive hydrothermal alteration of the white anorthosite suite, but, however, only weakly affects its REE.

3rd stage

Deep-crustal, ENE trending lineaments are intruded by a second generation of anorthositic crystal mush, the dark anorthosite (Fig. 10.1 b). These faults were most probably installed long before the anorthosite intrusion, since their attitude resembles that of both the foliation of and the ductile shear-zones within the basement rocks of the Epupa Complex, which were formed during the Eburnian orogeny at ~ 1.8-1.6 Ga (Brandt et al., 2003). Remarkably, however, the second

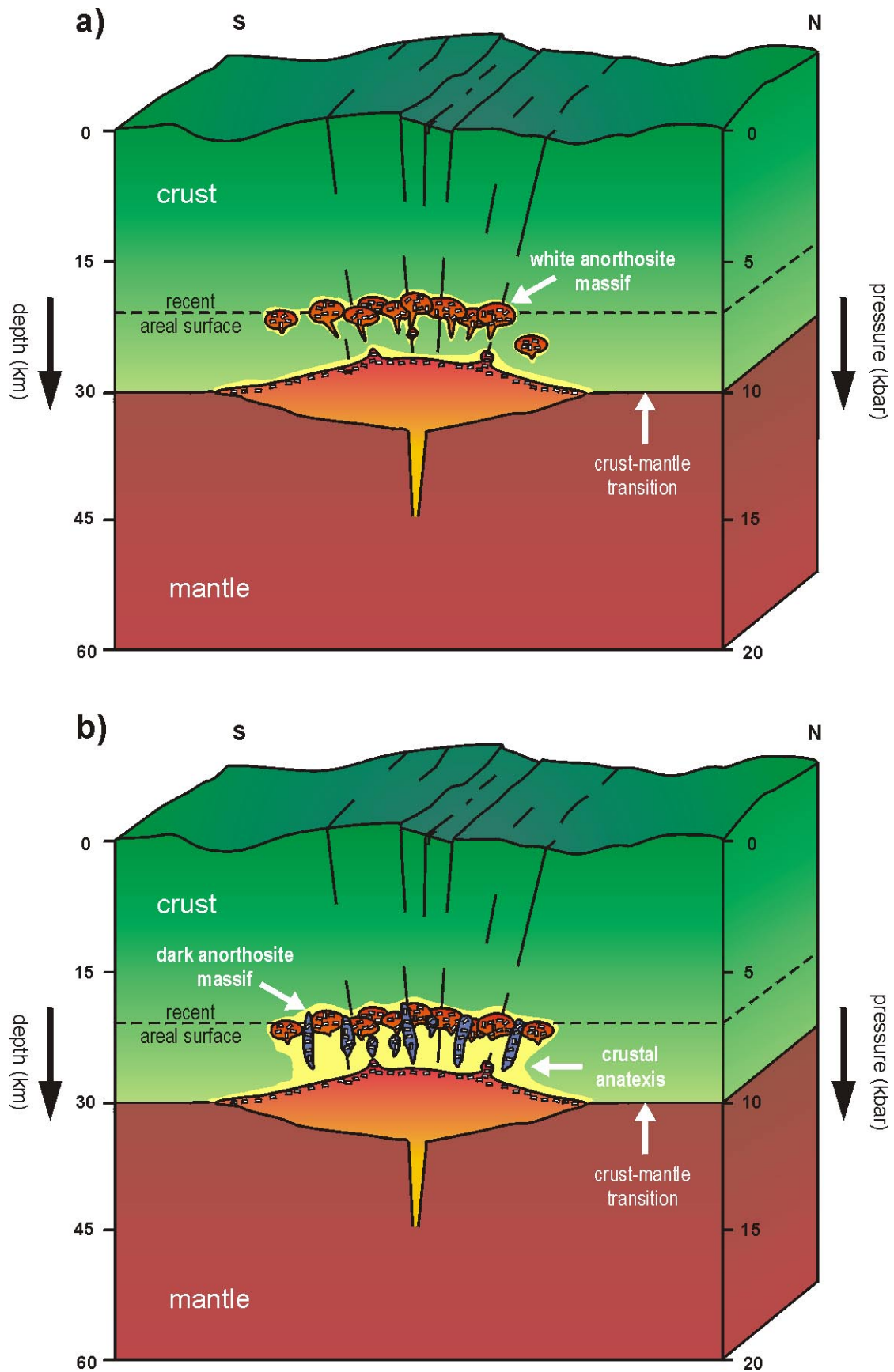


Fig. 10.1: Schematic petrogenetic model for the Kunene Intrusive Complex and the associated felsic suite (see text for details).

generation of anorthositic crystal mushes never intruded into the bordering basement rocks but solely occurs within the white anorthosite massif, concentrated in its central parts. It can thus be concluded that the white anorthosite massif itself behaved as a major zone of weakness and was not fully crystallized during the intrusion of the dark anorthosite.

This model also accounts for the decrease in crustal contamination with continuous intrusion, since younger melts most probably used similar pathways like the previously ascending crystal mushes and hence incorporated older anorthositic rather than crustal material. The emplacement of the dark anorthosite in the middle crust (~ 22 km) was followed by a period of near-isobaric cooling, leading to a re-equilibration of the magmatic mineral assemblages under conditions near the amphibolite- to granulite-facies transition.

4th stage

Continued heating of the lower crust finally causes crustal anatexis, hereby forming silicic melts parental to the granite and syenite of the felsic suite (Fig. 10.1 b). Like the dark anorthosites, the felsic melts predominantly use E-W trending weakness zones for their ascent. The fact, that the granitoids are concentrated near the boundaries between the Epupa Complex and the anorthosite massif, suggests that at least part of the felsic melts are formed by contact-metamorphic anatexis of the neighbouring basement rocks during the ascent of the anorthositic crystal mushes. The dyke-like emplacement of the syenites and granites in the middle crust (~ 19 km) is followed by isobaric cooling.

An extensional setting like the one described could also account for the uplift of the deep-crustal granulites of the Epembe Unit into mid-crustal levels along E-W trending sub-vertical faults (Brandt et al., 2003). In addition, the emplacement and crystallization of the large volumes of anorthositic and felsic melts during the period of ~ 1.38-1.35 Ga must have caused a significant heating of the lower and middle crust (regional "contact-metamorphism"), and may thus account for the comparably young ages of 1.37-1.33 Ga constrained for the neighbouring amphibolite-facies rocks of the Epupa-Complex by Seth et al. (in prep.).

11 Comparison with other parts of the KIC

As it is evident from Fig. 1.2 the KIC may be subdivided in at least two major structural parts. This interpretation is in accordance with the satellite imagery interpretation of Ashwal & Twist (1994) who recognized at least twelve distinct anorthosite bodies with probably individual petrogenetic evolution and consequently interpreted the KIC as a composite massif-type anorthosite. It has to be mentioned however that, due to difficult access during the civil war, most studies of the northern part of the KIC are based on old field data and sampling (Carvalho & Alves, 1990, 1993; Silva, 1990, 1992). Recent detailed field work in combination with petrographical investigations is lacking for most of the Angolan part of the KIC, except restricted areas around Lufinda, Dongue and Chiange in Angola (Ashwal & Twist, 1994; Morais et al., 1998, Slejko et al., 2002).

In the Angolan part granitoids are present in minor proportions, mainly represented by irregular bodies of rapakivi-type granite, graphic granite, leucocratic microgranite and sparse mangerite dykes (Morais et al., 1998). Like the felsic rocks investigated in this study, these granitoids are interpreted to be coeval but not consanguineous with the Kunene Intrusive Complex (Morais et al., 1998). In case of the mangerite dykes this model has been constrained by age determinations of both the felsic rocks and the KIC (Mayer et al., 2000).

The magmatic features of the leucotroctolite and anorthosite samples of the dark anorthosite suite investigated in this study resemble those reported for the northern part of the KIC (Simpson, 1970; Vermaak, 1981; Silva, 1990, 1992; Ashwal & Twist, 1994; Morais et al., 1998). However, subsolidus reaction textures like garnet-bearing corona structures of the dark anorthosite have not been described until now. In the Lufinda-Dongue area, the presence of cogenetic dolerites and mangerites is interpreted in favour of a shallow emplacement level of the anorthosite (Morais et al., 1998; Slejko et al., 2002), with pressures of 3-5 kbar being estimated by Slejko et al. (2002) for the subsolidus re-equilibration of pyroxenes. In clear contrast, the present study of the dark anorthosite of the Zebra Mountains is indicative of emplacement in the middle crust followed by isobaric cooling. It has to be mentioned, however, that the two respective study areas are at least 150 km apart from each other (Fig. 1.2). Therefore, detailed field work, petrographic and geochronological investigation of both anorthosite and country rocks for the intermittent southern Angolan part of the KIC is needed to decide whether the apparent differences in erosion level are due to a continuous gradient in exposed crustal depth or due to offsets by deep fracture zones as for example the Serpa-Pinto lineament or the Kunene River fault.

PART III: Fenitizing processes induced by ferrocarnatite magmatism

12 Introduction

12.1 Carbonatites and fenitization

The majority of the carbonatite complexes known from world-wide localities are predominantly composed of calcium- and magnesium-rich carbonatites. In these carbonatite centres late-stage ferrocarnatite dykes may occur, which are characterized by strong enrichments of Fe, Mg, Ba, Sr, REE, Th and U. These ferrocarnatites are commonly interpreted as the end-products of fractional crystallization and related differentiation processes of the main Ca-Mg carbonatite body (Le Bas, 1977, 1981, 1989, 1999; Gittins, 1989; Woolley & Kempe, 1989). In clear contrast, magmatic natrocarbonatite is known only as the extrusive product of the Oldoinyo Lengai volcano, Tanzania, which, at the same time, is the only active volcano (see Bell & Keller, 1995, for a review). However, the close spatial association of Na- and/or K-rich fenites and carbonatites (Morogan, 1994) suggests that carbonatites, which are now Ca-Mg-Fe carbonatites, were alkali-rich when they intruded and expelled alkali-metals and volatiles during their differentiation and crystallization. This model has been confirmed by experimental studies (Watkinson & Wyllie, 1971; Freestone & Hamilton, 1980).

Where carbonatitic centres are surrounded by metasomatic aureoles, the composition of the solidified carbonatite will differ significantly from that of the pristine carbonatite magma due to material losses and gains during differentiation, crystallization or post-magmatic re-equilibration. In this case, the carbonatites only preserve an incomplete memory of their magmatic history. The investigation of metasomatic mineral reactions at the magma to wall-rock interface and of fluid inclusions of the fenitizing agents can thus give important information about the geochemical nature and evolution of the liquids responsible.

The carbonatite dykes of Swartbooisdrif, NW Namibia are an ideal study object since they are well-exposed, mostly unweathered and suffered only minor subsolidus alteration. These ferrocarnatite dykes are not widely known in the international carbonatite literature, even though their emplacement led to the formation of deep blue sodalite-rich fenites, which are used as a deposit for ornamental stone, the "Namibia Blue", since 1960. They differ from all other known carbonatite occurrences in (1) their exotic fenite mineral assemblage, (2) the uncommon

anorthositic mineralogy of their wall-rocks involved in the metasomatic processes and (3) the general lack of associated Ca-Mg carbonatites and felsic intrusives. The aim of the present study is to characterize the magmatic evolution of the carbonatite intrusions and to elucidate the interrelated metasomatic processes, which led to the formation of the sodalite occurrences.

12.2 Sodalite - a review

Sodalite is one member of the sodalite group, a group of rock-forming framework silicates, including the end-members sodalite ($\text{Na}_8[\text{Al}_6\text{Si}_6\text{O}_{24}]\text{Cl}_2$), nosean ($\text{Na}_8[\text{Al}_6\text{Si}_6\text{O}_{24}]\text{SO}_4$) and h a yne ($(\text{Na,Ca})_{4-8}[\text{Al}_6\text{Si}_6\text{O}_{24}](\text{SO}_4,\text{S})_{1-2}$). Sodalite differs from the other minerals of the group in being the most Na-rich member and in containing chlorine as an essential constituent. The name sodalite (Thomson, 1811) refers to its sodium-rich composition. Variations in the Na content of sodalite are commonly minor, since the substitution of Na by both K and Ca reaches only a limited extent. The same holds true for the replacement of Al by Fe^{3+} . In the sodalite variety hackmanite, sulphur may be present in minor amounts.

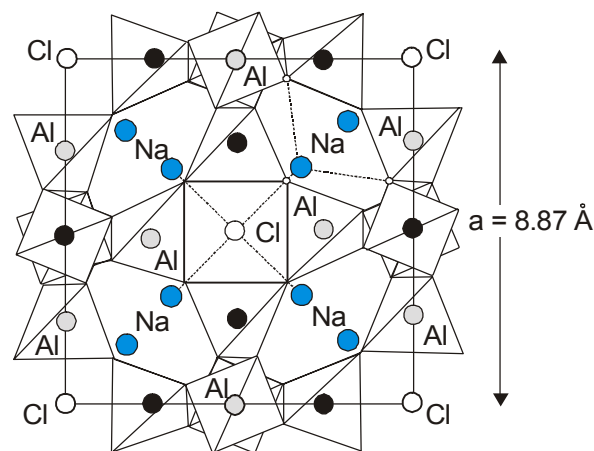


Fig. 12.1: The framework of tetrahedral groups in the structure of sodalite after Bragg & Claringbull (1965).

The structure of sodalite has been described by Bragg & Claringbull (1965) as an aluminosilicate framework, formed by almost equal amounts of linked SiO_4 - and AlO_4 -tetrahedra, with Al and Si being completely ordered (Fig. 12.1). Six rings of four tetrahedra $\parallel\{100\}$ and eight rings of tetrahedra $\parallel\{111\}$ form cage-like cubo-octahedral units. Six-membered rings define sets of channels, which are occupied by chlorine at their intersections. The Cl^- ions themselves are centred in Na^+ tetrahedra. The overall structure is cubic with $a = 8.1\text{Å}$ and a bimolecular unit cell.

The natural occurrence of sodalite is largely restricted to magmatic environments. The feldspathoid most commonly occurs in SiO₂-undersaturated alkaline igneous rocks (nepheline syenites, phonolites and related rocks), where sodalite is either a magmatic crystallization product or formed by the hydrothermal alteration of nepheline (Deer et al., 1992). In addition, sodalite has been described from meteorites (e.g. Berg et al., 1997) and from ejected volcanic blocks, where it was observed in cavities (e.g. Deer et al., 1992). Sodalite is commonly associated with nepheline, K-feldspar, albite, cancrinite, natrolite, melanite, calcite and fluorite. Prominent natural localities of sodalite include phonolites of the Cantal Massif, France (e.g. Brousse et al., 1969), sodalite foyaite, lujavrite and nauyaite of the Ilimaussaq intrusion, southern Greenland (e.g. Hamilton, 1964; Sørensen, 1970; Markl et al., 2001), nepheline syenite pegmatite of the Langesundsfjord, Norway (e.g. Taylor et al., 1967), contact-metamorphic carbonate and shale sequences of the Oslo Rift, Norway (e.g. Jamtveit et al., 1997), nepheline syenites, urtites and foyaites of the Lovozero Alkali Massif, Russia (e.g. Sørensen, 1970), lamprophyres of Kola Peninsula, Russia (e.g. Beard et al., 1996), and sodalite syenite and nepheline syenite of Mont Saint-Hilaire, Quebec (e.g. Currie et al., 1986).

(1) Experimental investigations of the stability of sodalite have been performed by several authors (e.g. Wellman, 1970; Barker, 1976; Binsted, 1981; Sharp et al., 1989; Kostel'nikov & Zhorniyak, 1995). Results of the most recent studies of Sharp et al. (1989) and Kostel'nikov & Zhorniyak (1995) are summarized below:

Sharp et al. (1989) studied the stability relations of phases in the system NaAlSiO₄-SiO₂-NaCl at 1 bar and elevated pressures of 7.4-10 kbar over temperature intervals of 1644-1652 K and 923-1173 K, using natural samples of sodalite-syenites from Mont St-Hilaire, Quebec. Phases in the system NaAlSiO₄-NaCl include halite (NaCl(s)), liquid NaCl (NaCl(l)) and vapour NaCl (NaCl(v)), nepheline (α -nepheline (289-467K), β -nepheline (467-1180K) and γ -nepheline (1180-1525K)), carnegieite (δ -carnegieite (298-980K) and β -carnegieite (980-1700K)) and sodalite. In order to calculate the stability field of sodalite, the authors combined available thermodynamic data for the above mentioned phases (see Sharp et al., 1989, for details) with experimental equilibrium reversals for the reaction



The authors found sodalite to be a high-temperature, low-pressure phase, which is stable even above the solidus in sodic, silica-undersaturated and NaCl-rich magmas, with the presence of sodalite constraining the NaCl-activities in the magmas. The experimental results of Sharp et al. (1989) are illustrated in two selected phase diagrams (Fig. 12.2a, b).

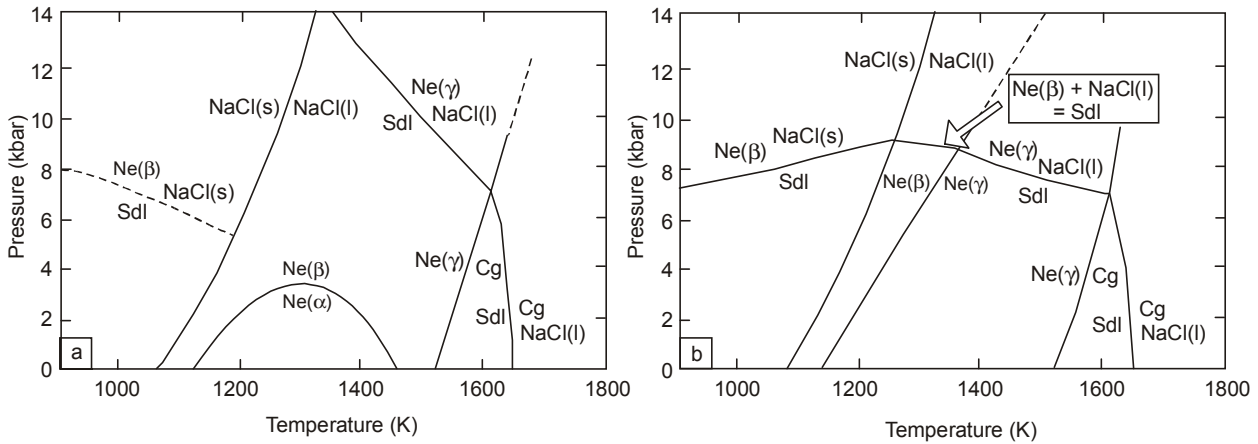
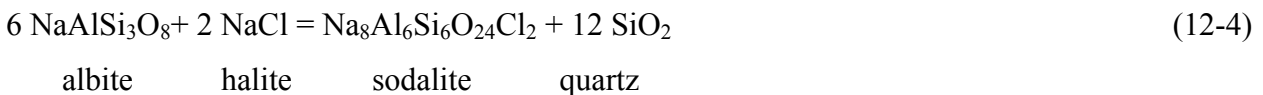
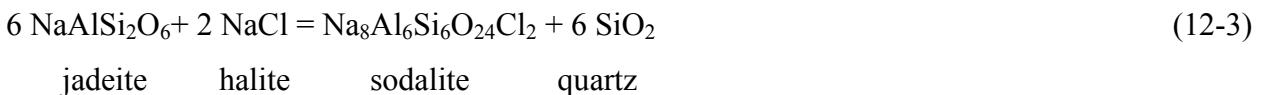
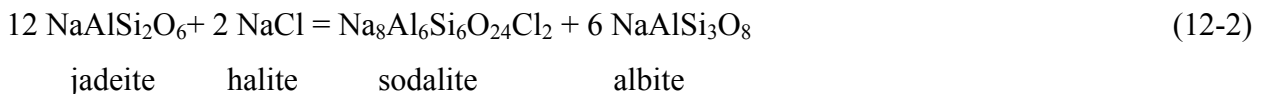


Fig. 12.2: Stability relation of phases in the system NaAlSiO₄-SiO₂-NaCl after Sharp et al. (1989). (Cg carnegieite, Ne nepheline, Sdl sodalite, see Sharp et al., 1989, for details). **a)** Uses the measured entropy of sodalite at 298 K. Sodalite-bearing reactions constrained by the 1 bar, 1649-1652 K reversals, except reaction Ne(β) + NaCl(s) = Sdl, which is determined for high-pressure, 923K and 973 K reversals. **b)** Includes an excess entropy term for sodalite of 61.7 J/mol·K. Generated curves coincide with experiments above 973 K.

When expanding the system NaAlSiO₄-NaCl to include SiO₂, the phases jadeite, albite and quartz are added along the NaAlSiO₄-SiO₂ join. In this system three more sodalite-forming reactions can be generated (Sharp et al., 1989), i.e.



Reaction (12-4) may be responsible for formation of sodalite in the Swartbooisdrif fenites. However, Sharp et al. (1989) found the stability field of quartz + sodalite, limited by reactions (12-3) and (12-4), to lie at temperatures below 298 K, and thus at geologically unreasonable low temperatures. Conformably, natural equilibrium assemblages of sodalite + jadeite and sodalite +

quartz have never been reported, as holds also true for the Swartbooisdrif fenite samples of this study.

(2) The stability of sodalite under hydrothermal conditions has been studied by Kostel'nikov & Zhornyak (1995), assuming the stability of sodalite to be defined by reaction (12-2). However, in contrast to Sharp et al. (1989), the authors determined a stability field of sodalite depending on temperature and salt concentrations in hydrothermal solutions. Starting minerals were natural nepheline (with the potassium being removed by treatment with molten NaCl), natural sodalite (hackmanite variety) and synthetic sodalite. The experiments were performed at a constant pressure of 3 kbar and 600-800°C, with the starting minerals being treated with fluids of variable salt concentrations of 10.0-42.5 wt.%. Only two phases were found in the system, i.e. sodalite and nepheline, with the stability of sodalite with respect to nepheline increasing with increasing NaCl-concentrations of the fluid. As temperatures rise, more NaCl is needed to stabilise sodalite. Results of the experimental investigations of Kostel'nikov & Zhornyak (1995) are shown in the T-X diagram of Fig. 12.3.

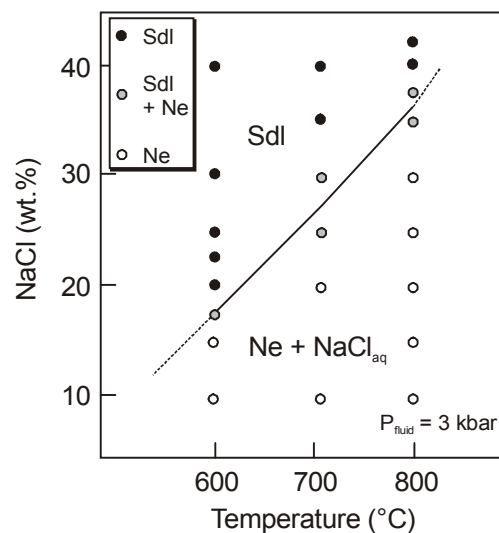


Fig. 12.3: Stability of sodalite in relation to temperature and NaCl concentration, determined by Kostel'nikov & Zhornyak (1995).

However, both experimental investigations are of only restricted use for the determination of the P-T conditions of the sodalite-formation in the studied samples, since sodalite of the Swartbooisdrif area is clearly not an orthomagmatic crystallization phase, nor is it exclusively formed by the hydrothermal alteration of nepheline (except in one nepheline syenite sample), but represents a replacement product of plagioclase from fenitized anorthositic rocks

incorporated by and bordering carbonatite centres (see Chapter 13). Moreover, quartz has never been observed in these samples, hence suggesting sodalite formation under contemporaneous desilication of the fenites. Unfortunately, stability relations for a conspicuous system like this are still wanting.

13 Petrography

13.1 Fenitized anorthosite

The magmatic petrography and mineral chemistry of the anorthositic rocks of the KIC was discussed in detail in chapters 5.1 and 6. In summary, both, the white and the dark anorthosite suite, display the primary magmatic assemblage of plagioclase (An_{37-53} and An_{43-75} , respectively) \pm olivine ($X_{Mg}: 0.54-0.65$) \pm orthopyroxene ($X_{Mg}: 0.53-0.71$) \pm clinopyroxene ($X_{Mg}: 0.66-0.76$) \pm biotite ($X_{Mg}: 0.39-0.67$) + ilmenite + magnetite. In contrast to the dark anorthosite, the white anorthosite is characterized by a pervasive alteration of all silicate phases, sericitization and saussuritization of the feldspars and chloritization of the Mg-Fe silicates.

White anorthosite in contact to the carbonatitic breccia is of no great use for this study, as the pervasive hydrothermal alteration of its primary magmatic mineral assemblage prevents a clear distinction between late-magmatic hydrothermal processes and the subsequent metasomatism by fenitizing fluids. Thus, this part of the study concentrates on the following dark anorthosite samples:

Weakly fenitized pyroxene-bearing anorthosite: Ku-98-78

Weakly fenitized leucogabbronorite: Ku-98-71, Ku-98-72, Ku-98-79, Ku-98-84

Weakly fenitized leucotroctolite: Ku-98-77

Fenitized anorthosite: Ku-98-19, Ku-98-36, Ku-98-54, Ku-98-114, Ku-98-120, Ku-99-01, Ku-99-02

Fenitized anorthosite xenoliths in the CB: Ku-98-55, Ku-98-89

Sample Ku-98-77, -78, -79 and -84 were collected at a distance of *c.* 2.0, 2.5, 2.5, and <0.1 m from the contact with a dyke of the carbonatitic breccia, respectively, in an outcrop located about 2 km N of the operating quarry. Samples Ku-98-71 and -72 are sampled in 20 cm and 2 m distance from the contact with another dyke. Samples Ku-98-19, -36, -54, -114, -120 and Ku-99-01 and -02 were taken from direct contact zones between anorthosite and dykes of the carbonatitic breccia, where the fenitizing processes reached a maximum magnitude.

When approaching the contact to dykes of the carbonatitic breccia, plagioclase (An_{49-54}) of the dark anorthosite suite still shows oscillatory zoning but is progressively altered to sericite/muscovite and albite to oligoclase (An_{1-17} ; Fig. 13.1a). Clinopyroxene, orthopyroxene and/or olivine are increasingly replaced by assemblages of deep green biotite (Fig. 13.1b),

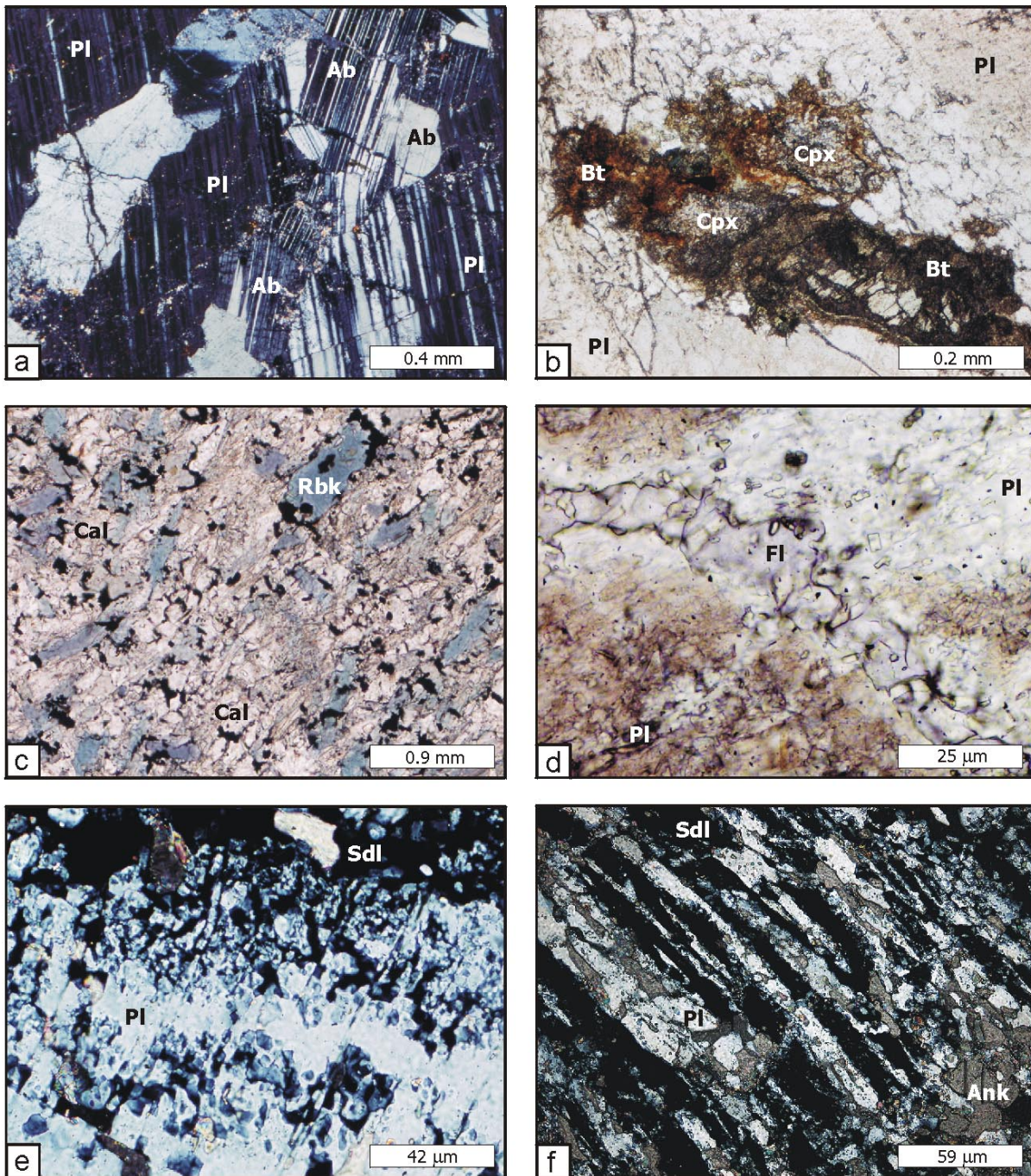


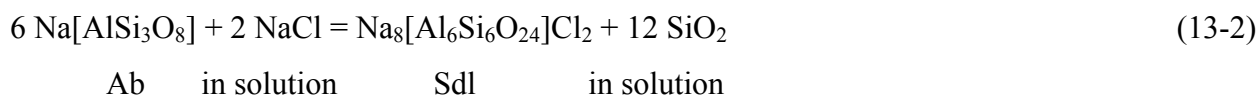
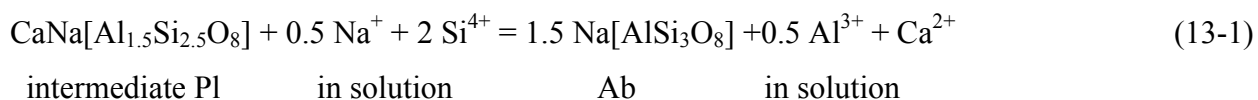
Fig. 13.1: Polished-section photomicrographs illustrating the mineralogical changes of anorthositic rocks during progressive fenitization. Cross-polarized light (a, e-f). Plane-polarized light (b-d). *a)* Replacement of orthomagmatic plagioclase by albite. *b)* Alteration of pyroxene to biotite. *c)* Replacement of clinopyroxene by fine-grained calcite-magnesio-riebeckite assemblages. *d)* Anhedral fluorite grains filling cracks in plagioclase. *e)* Sodalite replacing plagioclase along both its grain margins and albite-twin lamellae. *f)* Sodalite and ankerite replacing plagioclase along its twin lamellae.

subhedral epidote and granular calcite, chlorite-calcite intergrowths, and/or fine-grained intergrowths of bluish magnesio-riebeckite and calcite (Fig. 13.1c). The amount of apatite, associated with biotite and calcite/ankerite, strongly increases in the same direction. As is suggested by the brecciation of plagioclase, the deformation of Fe-Ti oxides and the increasing abundance of cracks in the rocks, the investigated dark anorthosite samples underwent an intense deformation prior to, or contemporaneous with the carbonatite emplacement. Joints in the rocks are commonly filled by epidote-calcite and magnesio-riebeckite-calcite intergrowths (Ku-98-71). In one sample (Ku-98-89), fissures in the altered plagioclase are filled by conspicuous anhedral fluorite grains, displaying a patchy colour zonation from light blue to lilac (Fig. 13.1d).

At the direct contact to large dykes of the carbonatitic breccia, the dark anorthosites are almost completely transformed into purplish-blue coloured anorthositic fenites, with the magmatic precursor mineralogy and textures being obliterated by the fenitizing processes. The rocks generally exhibit a banded appearance due to an alternation of albite ($An_{0.3}$)/sodalite -, ankerite- and biotite-rich layers.

Plagioclase of the fenites is commonly heavily strained. Most of the coarse-grained crystals are broken down to fine-grained angular particles, displaying undulose extinction. If preserved, the primary-magmatic cumulus plagioclase is completely replaced by almost pure albite ($An_{0.3}$), that exhibits bent and diffuse albite twin lamellae and may be associated with minor ankerite. Locally, plagioclase is recrystallised to mosaics of granular, twinned to untwinned albite (An_0). Poikilitic secondary albites have been observed, enclosing abundant biotite, muscovite and carbonate inclusions, hence suggesting that biotite and muscovite formation as well as carbonate injection was synchronous with the plagioclase recrystallisation. Sodalite, causing the purplish macroscopic colour of the anorthositic fenite, is restricted to the albite-rich zones, where it was formed at the expense of plagioclase. Various styles of replacement have been observed, i.e. (1) sodalite replacing the marginal zones of relict cumulus plagioclase (Fig 13.1e), (2) sodalite exclusively grown at the expense of the albite twin lamellae of relict cumulus plagioclase (Fig. 13.1f), (3) sodalite pseudomorphing the shape of secondary, granular albite and (4) sodalite replacing accumulations of broken plagioclase particles, forming almost monomineralic, diffuse schlieren (Fig. 13.2a). In addition, sodalite forms narrow rims around biotite-ankerite accumulations and magnetite. These almost monomineralic rims are interpreted in terms of an elevated fluid activity, that mainly affected the weak contacts and interstices between individual plagioclase crystals. Sodalite of all textural positions bears inclusions of biotite, albite and/or ankerite, giving the grains a poikilitic appearance (Fig. 13.2b). The fact that plagioclase relics, preserved in sodalite are always pure albite is taken as evidence

that the transformation of Ca-rich, primary-magmatic plagioclase into albite predates the sodalite formation. Thus, sodalitization of plagioclase is at least a two-stage process, according to the following simplified reactions:



Albitization of plagioclase following reaction (13-1) could thus have produced part of the Ca, needed for the formation of the associated ankerite. Remarkably, this reaction is in need for a certain amount of Si, which is a rather unlikely species for carbonatite-derived fluids, thus suggesting that either (1) the Si necessary for the reaction was produced by additional, Si-releasing reactions or (2) that both Si and Al behaved mobile during metasomatism, leading to misfits when balancing for Al. In clear contrast, reaction (13-2) is in excellent agreement with fenitization, caused by Si-undersaturated, NaCl-rich fluids as could be released by carbonatite melts.

Greenish to brownish biotite is mostly recrystallised to polygonal grains, forming irregularly bounded clusters (Fig. 13.2c). However, even the recrystallised grains display undulose extinction, pointing to multiple deformation events. The mica is commonly associated with minor ankerite and fine-grained magnetite, with the latter being expelled from biotite during the recrystallisation event. The fact, that biotite is not evenly distributed within single thin sections but forms mafic enclaves, similar in shape and distribution to those of unaffected anorthosites, is taken as evidence that biotite was mainly formed at the expense of magmatic accumulations of intercumulus clinopyroxene, orthopyroxene, olivine and/or late-magmatic amphibole. However none of these minerals nor their alteration products have been observed in the investigated samples, hence suggesting that the fenitization of these rocks reached a pervasive extent.

Granular ankerite, an abundant phase in the anorthositic fenite, is commonly associated with biotite, displaying straight grain boundaries against the latter (Fig. 3.2.d). Recrystallisation of ankerite to granular mosaics is a common feature. In addition, ankerite is enriched in almost monomineralic, irregularly bounded schlieren and fills small cracks in the rock.

Predominant ore minerals of all samples investigated are magnetite and ilmenite. Many of the magnetites display oxidative exsolution of ilmenite lamellae // {111} and {100}, similar in composition to larger ilmenite grains. Along the two lamellar systems and along cracks,

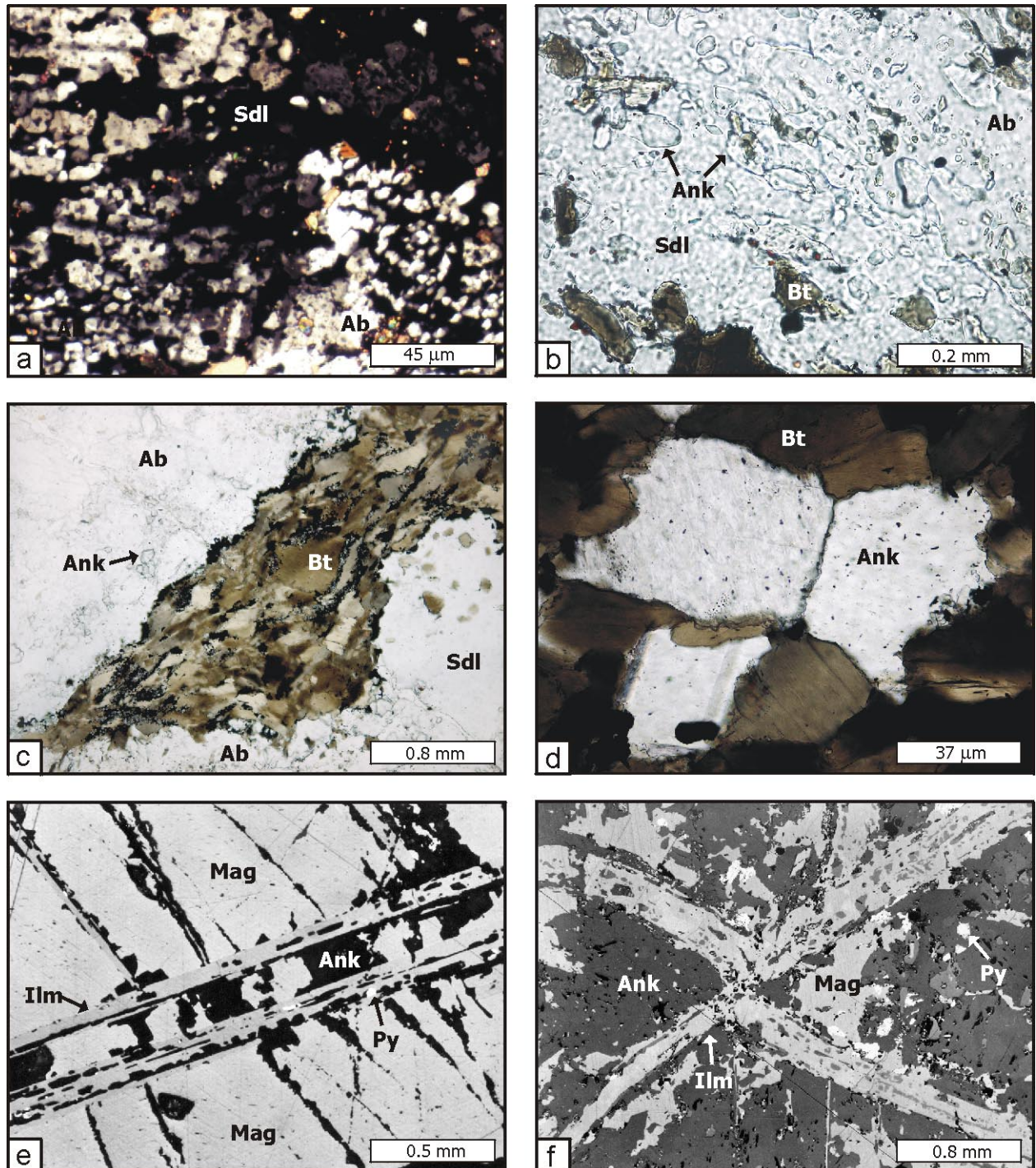


Fig. 13.2: Polished-section (a-d) and ore section (e-f) photomicrographs illustrating the mineralogical changes of anorthositic rocks during progressive fenitization. Cross-polarized light (a). Plane-polarized light (b-d). *a*) Sodalite forming diffuse schlieren, replacing fragmented plagioclase particles. *b*) Poikilitic sodalite, bearing abundant inclusions of ankerite and biotite. *c*) Heavily strained biotite, recrystallised to polygonal grains. *d*) Anhedra, granular ankerite, displaying straight grain boundaries against biotite. *e*) Replacement of magnetite by ankerite, whereby ilmenite exsolution lamellae are preserved. *f*) Isolated pyrite grains, occurring in the vicinity of ilmenite-exsolution lamellae.

magnetite is partially altered to hematite, which is in turn replaced by ankerite, whereby ilmenite exsolution lamellae are mostly preserved (Fig. 3.2e, f). Along ilmenite lamellae, small, isolated, anhedral grains of pyrite have formed (Fig. 3.2e, f), whereas cracks in larger ilmenite grains are often filled with massive pyrite aggregates. In addition, ilmenite may be surrounded by narrow rutile rims. In sample Ku-98-79, a large pyrite grain is overgrown by pyrite of a second generation. The former {100} grain boundary of the pyrite crystal is marked by trails of fluid inclusions. The amount of sulphides as well as the intensity of carbonate replacement of the oxides increase towards the contact with the carbonatite dykes. In sample Ku-98-71, shear bands in oxides and δ clasts of ilmenite testify to strong deformation at the dyke contacts. The observed reaction relationship of the Fe-Ti oxides with ankerite and pyrite suggests that carbonitization and sulphidation took place due to the interaction of ilmenite and magnetite with O_2 , S_2 and CO_2 in the fenitizing fluid phase. Carbonatization of the Fe-Ti oxides produced rutile, hematite and the siderite-component in ankerite following the simplified reactions (Yang, 1987)



Sulphidation of Fe-Ti oxides appears to be a multiple event, which is obviously related to the metasomatic overprint. Sulphidation of ilmenite and magnetite, according to the reactions (Barton and Skinner, 1979)



takes place in most anorthosite samples in contact with dykes of the carbonatitic breccia. A two-stage replacement is clearly indicated by the pyrite overgrowths on a larger pyrite crystal in the anorthosite sample Ku-98-79. Since no early-magmatic sulphide phases were recorded in the KIC rock types investigated, the sulphidation must be related to the repeated influx of S-rich fenitizing fluids, presumably released by the intruding carbonatite melts.

The absence of anhydrous Fe-Mg silicates and the progressive transformation of calcic plagioclase into pure albite and sodalite provides evidence for the hydrous and alkali-rich nature of the fenitizing fluid. The extensive formation of biotite, suggests that these fluids additionally contained a certain amount of K. Judging from the total of newly grown minerals, formed during

metasomatism, further species of the fluid must include certain amounts of CO₂, P, Cl, F, S and Fe³⁺.

13.2 Fenitized syenite

Syenite unaffected by metasomatism (see Chapter 5.2 and Chapter 6) is characterized by a homogeneous texture with coarse to medium-grained K-feldspar crystals without preferred orientation. The main minerals present are perthitic K-feldspar (orthoclase/microcline) and plagioclase (An₀₋₁₈). Late magmatic quartz, clinopyroxene (X_{Mg} : 0.45-0.51) and hastingsite (X_{Mg} : 0.01-0.06) may be present in varying amounts, forming discrete grains in the interstices between feldspar crystals. Common accessories include titanite, chlorite, epidote, Fe-Ti oxides and zircon. For the investigation of the fenitizing processes, affecting syenites emplaced in shear zones subsequently intruded by carbonatites, the following 16 samples have been studied in detail:

Fenitized syenite: Ku-97-05a, Ku-98-59, Ku-98-66, Ku-98-69, Ku-98-70s, Ku-98-73s, Ku-98-74, Ku-98-93, Ku-98-103s, Ku-98-105, Ku-98-106, Ku-98-107, Ku-99-06, Ku-99-09, Ku-99-10, Ku-99-18, Ku-99-19s

When approaching the carbonatitic breccia, the grain size of syenite decreases from medium- to fine-grained, following shearing and recrystallisation previous to and outlasting the emplacement of the carbonatites. The main constituent of the granular matrix is mostly untwinned and subordinately twinned and subrounded albite (An_{0.5}) with undulose extinction (Fig. 13.3 a, b), together with minor aggregates of recrystallized biotite (Fig. 13.3 a) and/or fine-grained, isometric muscovite (Fig. 13.3b), presumably formed at the expense of former K-feldspar. Fragmented relics of fine-grained microcline, which are apparently completely replaced by chess-board albite (Fig. 13.3c), support this interpretation, suggesting K-feldspar replacement according to the simplified reaction:



providing the K needed for the simultaneous muscovite formation. The alteration of K-feldspar under simultaneous formation of equal amounts of albite and muscovite can be written as Al-conservative reaction:

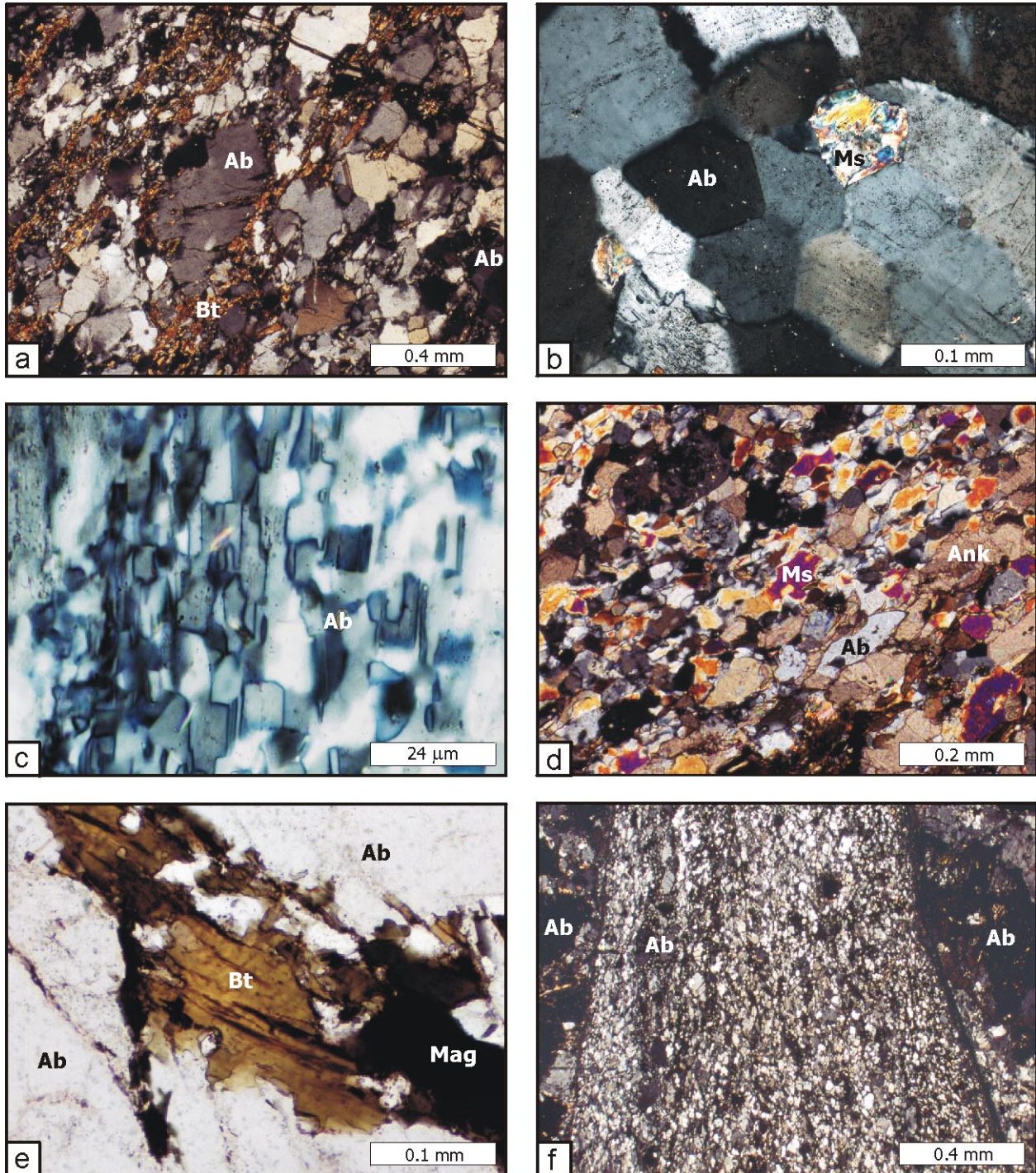
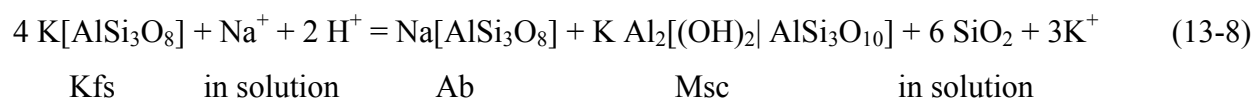


Fig. 13.3: Polished-section photomicrographs illustrating the mineralogical changes of syenites during progressive fenitization. Cross-polarized light (a-d, f). Plane-polarized light (e). *a*) Fine-grained, granular albite, displaying undulose extinction, is the main constituent of the fenitized syenites, associated by minor and strongly recrystallized biotite. *b*) Albite associated by fine-grained, isometric muscovite. *c*) Relics of microcline, replaced by chess-board albite are preserved locally. *d*) Granular ankerite, muscovite and albite, forming part of the even grained matrix. *e*) Magnetite and biotite, accumulated in irregular streaks. *f*) Micro-shearzones in the fenitized syenites testify to a strong deformation of the rocks.



which, in contrast to reaction (13-7), additionally accounts for the generally Si-deficient nature of carbonatite-derived fluids. The lack of dust-like Fe oxide inclusions (magnetite/hematite) in the secondary albite of the fenitized syenite is responsible for the white to pale pink colour of these rocks.

Fine-grained and granular ankerite is evenly distributed in the matrix, intimately associated by albite and muscovite (Fig. 13.3d). Minor heavily strained and partially recrystallised biotite, as well as anhedral to subhedral magnetite and ilmenite grains occur as patches or as intensely deformed irregular streaks (Fig. 13.3e). Pyrite, chlorite, epidote and apatite are common accessories. The amount of zircon generally increases with progressive fenitization; locally, zircon of a second generation forms rims around presumably magmatic zircon cores. Micro-shearzones (Fig. 13.3f) and repeated recrystallisation testify to several deformation events during the subsequent injections of carbonatite melts and/or repeated movements along the hosting faults. Fissures in the rock are invaded by magnetite and ankerite.

Hastingsite or clinopyroxene relics or their alteration products have never been observed in the investigated samples, suggesting that the syenites were pervasively altered by the circulating hydrous fluids. Remarkably, however, sodalite replacing secondary albite of the fenitized syenites is virtually completely absent (except one sample, Ku-98-59b). A possible explanation for this lack of a second stage of transformation is that the highly mobile, NaCl saturated fluids migrated in the anorthositic lithologies bordering the shear zones, thus leaving back fluids which contained insufficient NaCl to form sodalite. Accessory, very fine-grained analcite, replacing albite, has been observed in one sample (Ku-98-59b)

Contacts between the syenites and the carbonatitic breccia are always sharp. Syenite fragments in all stages of detachment can be observed in the carbonatitic breccia, hence constraining an intrusive relationship between the two units, with the younger carbonatites crosscutting the previously emplaced syenites.

13.3 Fenitized nepheline syenite

Nepheline syenite (Ku-99-15a, -15b, -15c and -15d) was observed at only one locality of the mapped area, where the small and impersistent dyke borders the carbonatitic breccia. The rock is

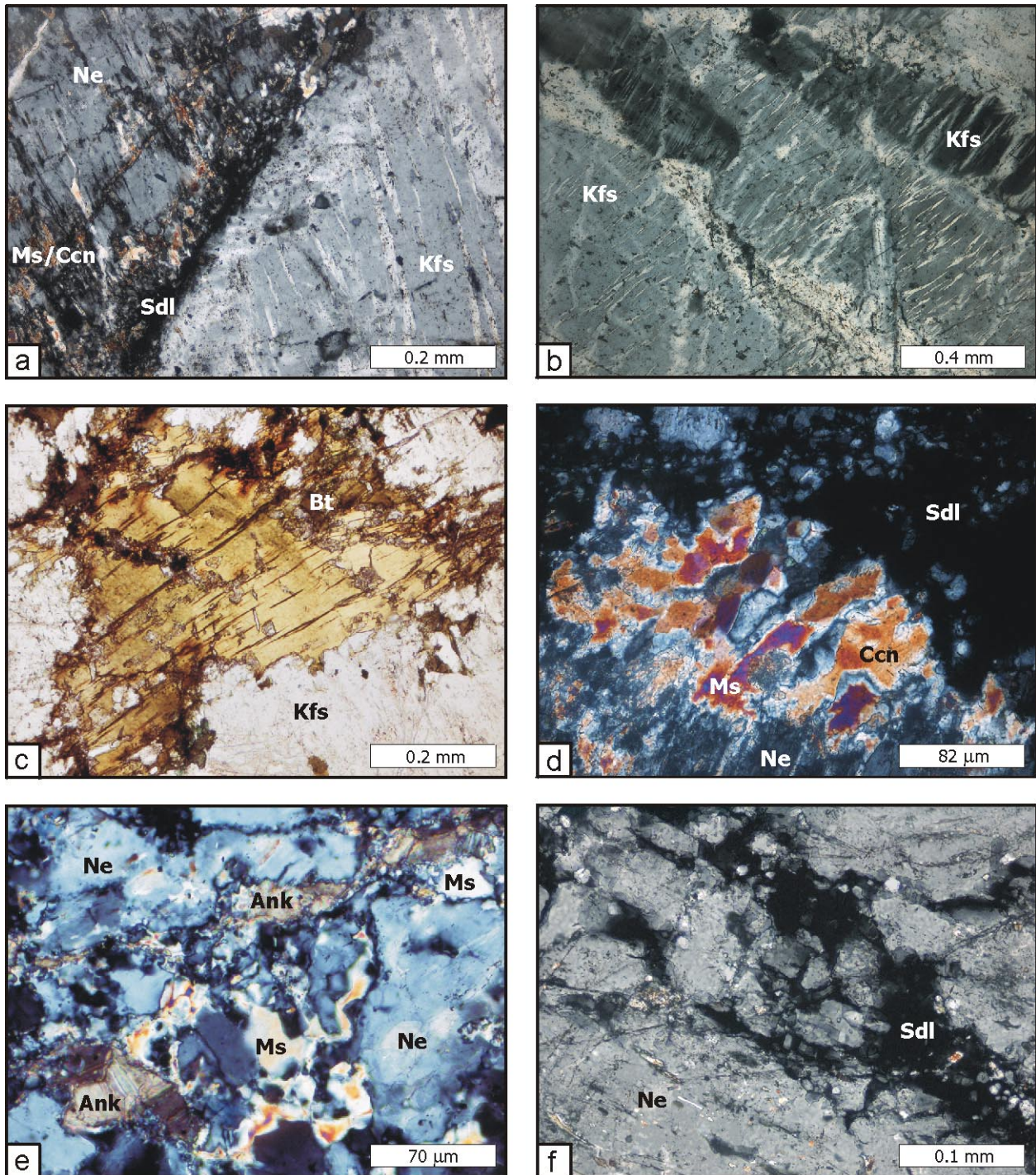


Fig. 13.4: Polished-section photomicrographs illustrating the mineralogical changes of the nepheline syenite during progressive fenitization. Cross-polarized light (a-b, d-f). Plane-polarized light (c). *a)* Contact between marginally altered nepheline and K-feldspar, the latter being unaffected by the fenitization. *b)* Medium-grained, perthitic K-feldspar laths. *c)* Anhedronal and heavily strained biotite, filling the interstices between individual K-feldspar crystals. *d)* Cancrinite-muscovite-sodalite assemblage, replacing nepheline. *e)* Anhedronal ankerite and muscovite, filling cracks in nepheline. *f)* Sodalite, replacing nepheline along cracks.

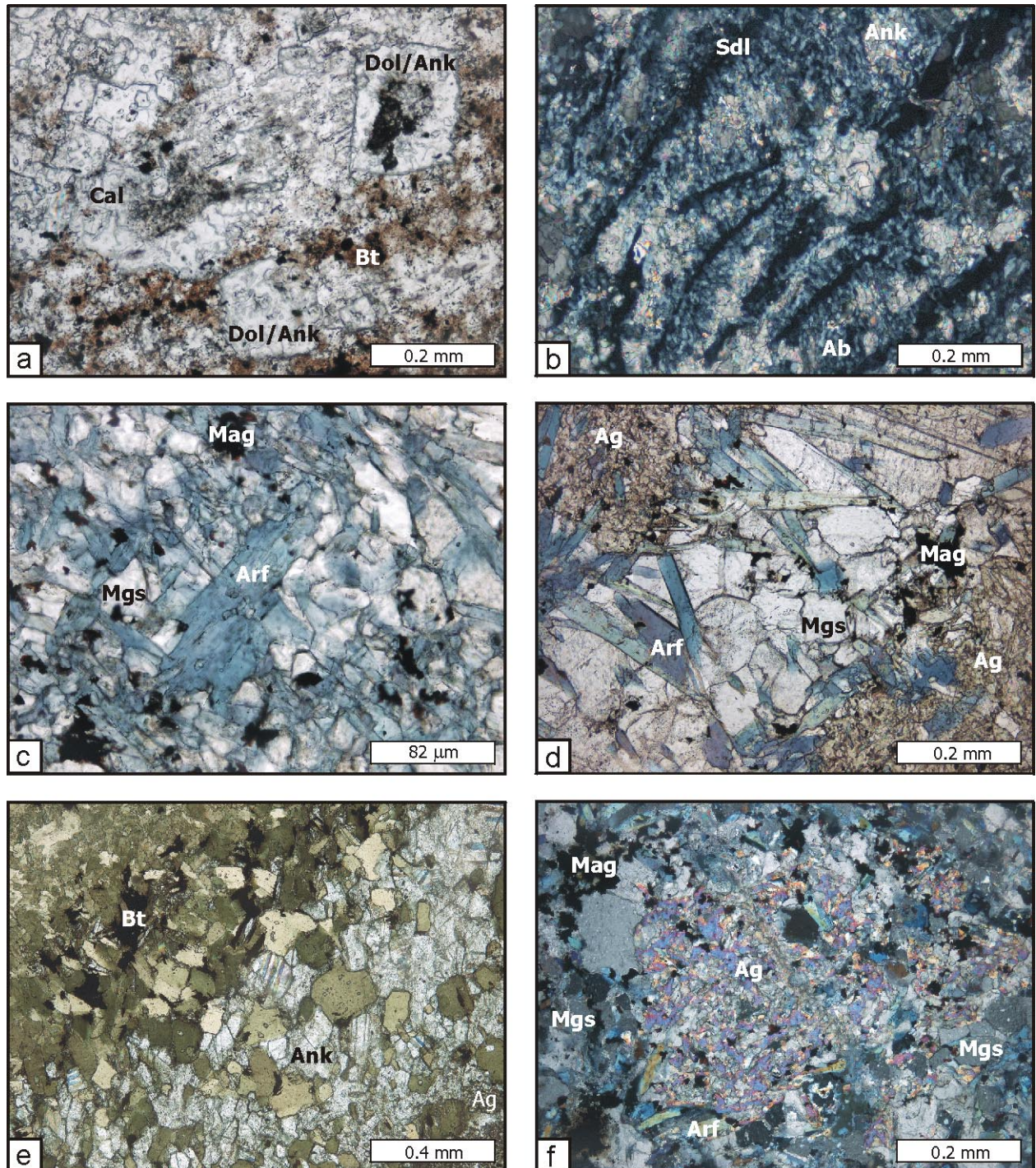
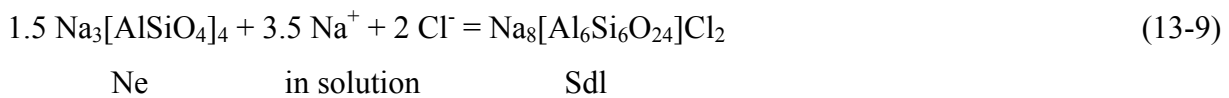


Fig. 13.5: Polished-section photomicrographs of the carbonatitic breccia and an enclosed ultramafic xenolith, that underwent extensive fenitization. Cross-polarized light (a, c-e). Plane-polarized light (b, f). *a*) Subhedral dolomite, as well as anhedral calcite, biotite and magnetite are the main constituents of the enclosing carbonatitic breccia. *b*) Anorthositic wallrock-xenoliths in the carbonatitic breccia are mainly composed of albite, with the latter being partially replaced by sodalite and ankerite. *c*) Fine-grained magnesite, magnesio-arfvedsonite and magnetite are the major constituents of the fine-grained matrix of the ultramafic xenoliths. *d*) Magnesite, magnetite and magnesio-arfvedsonite, forming veins. *e*) The contacts between the ultramafic xenoliths and the enclosing carbonatitic breccia are marked by two-fold corona structures, being composed of biotite and ankerite. *f*) Anhedral, poikilitic aegirine grain.

characterized by a streaky appearance due to changes in the grain sizes of its major phases nepheline and K-feldspar from medium- to coarse-grained.

Rare unaffected parts of nepheline syenite show the medium- to coarse-grained euhedral nepheline (Fig. 13.4 a) and subhedral tabular to lath-shaped, mesoperthitic K-feldspar (Fig. 13.4 a, b) to be the cumulus phases of the rock. Minor post-cumulus biotite, filling the interstices between individual nepheline and K-feldspar crystals (Fig. 13.4c), is the dominant mineral among mafic silicates. It occurs as small anhedral and heavily strained grains. Accessory, late stage epidote is localised in patches.

When reaching the ferrocarbonatite contacts, the grain size of nepheline attains maximum diameters of 15 cm, suggesting that the carbonatite emplacement triggered the nepheline growth. Muscovite and cancrinite are mainly localised at triple junctions between individual nepheline grains (Fig. 13.4 d), but may also occur in small fissures transecting nepheline (Fig. 13.4 e). The textural relationships strongly suggest that both muscovite and cancrinite were formed at the expense of nepheline, following the injection of fenitizing fluids. Granular ankerite fills cracks in the rock (Fig. 13.4e). Along its margins and irregular cracks, nepheline is replaced by sodalite (Fig. 13.4f), according to reaction



Reaction (13-9) implies an introduction of Na and Cl to the system and thus agrees well with the interpretation, that NaCl-rich, carbonatite-derived fluids migrated through country rocks neighbouring the carbonatite centres. Moreover, the replacement of nepheline by sodalite accounts for the macroscopically observed colour change of nepheline from pale yellow to pale blue when reaching the contacts to the carbonatite.

13.4 Fenitized ultramafic xenoliths

Ultramafic rocks (Ku-97-43a, Ku-97-43b) occur as angular xenoliths within one large dyke of the sodalite-rich carbonatitic breccia.

The matrix of the *enclosing carbonatitic breccia* is mainly composed of euhedral to subhedral ankerite/dolomite, interstitial calcite and anhedral magnetite grains (Fig. 13.5 a). Abundant anorthositic wallrock fragments are surrounded by the carbonatite matrix, and mainly consist of albite, being largely replaced by sodalite and ankerite (Fig. 13.5 b), and minor, heavily strained biotite.

Subhedral magnesite (53-68 vol.%), bluish to pale bluish magnesio-arfvedsonite (30-45 vol.%) and granular magnetite (~ 5 vol.%) are the major constituents of the fine-grained, equigranular matrix of the *finitized ultramafic xenoliths* whereas ankerite is present in minor proportions (Fig. 13.5c). Granular magnesite and subhedral to euhedral, lath-shaped magnesio-arfvedsonite may also form fine to medium-grained veins and schlieren (Fig. 13.5d). Medium-grained biotite and ankerite occur localised in patches and, more common, as two-fold corona structures at the contacts between the xenoliths and the enveloping carbonatite (Fig. 13.5e). In the latter textural position biotite together with minor magnetite marks the outer contact zones, whereas the inner parts of the corona are almost completely composed of ankerite. Fine-grained, anhedral aegirine grains of up to 1.2 mm in diameter have been observed in the magnesite-magnesio-arfvedsonite-magnetite matrix. The aegirines are always strongly poikilitic, bearing abundant magnesite, magnesio-arfvedsonite and ankerite inclusions (Fig. 13.5f).

Magnesite was most probably formed by replacement of former Fe-Mg silicates (presumably olivine), caused by the injection of CO₂-rich fluids. Such a finitization process would be in excellent accordance with an interaction between the ultramafic xenoliths and the volatile-rich carbonatite melt which brought them to the surface.

13.5 Carbonatitic breccia

Since the composition and internal structure of the carbonatitic breccia are intricate and change on a millimetre scale, only a simplified description of this rock type can be given. Predominant minerals are albite, ankerite, calcite, biotite, sodalite, muscovite and Fe-Ti oxides. Apatite, cancrinite, pyrochlore and sulphides are rare. A detailed description of the sulphide- and oxide-mineralogy and textures of this rock-type has been presented by von Seckendorff & Drüppel (1999) and von Seckendorff et al. (2000). Based on field observations the carbonatitic breccia has been subdivided into three units, i.e. (1) massive carbonatitic breccia, (2) layered carbonatitic breccia and (3) sodalite-rich carbonatitic breccia (see Chapter 3.3.6.1). Investigated samples of these units include:

Massive carbonatitic breccia: Ku-98-08, Ku-98-12, Ku-98-63, Ku-98-73c, Ku-98-103c, Ku-98-104, Ku-98-105, Ku-98-106

Layered carbonatitic breccia : Ku-98-05, Ku-98-14, Ku-98-28, Ku-98-48, Ku-98-51, Ku-98-55, Ku-98-56, Ku-98-62, Ku-98-64, Ku-98-69, Ku-98-70c, Ku-98-87, Ku-98-89, Ku-98-118, Ku-99-04, Ku-99-17, Ku-99-18, Ku-99-19c

Sodalite-rich carbonatitic breccia: Ku-97-15, -15a, -15b, -15c, -15d, -15e, -15g, -15i, -15k, 15l, -15n, -15o, -15q, -15r, -15s, -15t, -15u, -15v, Ku-97-19, Ku-97-24, Ku-97-26, Ku-98-17, Ku-98-18, Ku-98-27, Ku-98-31, Ku-98-47, Ku-98-57a, Ku-98-57b, Ku-98-58a, Ku-98-58b, Ku-98-80, Ku-98-83, Ku-98-131, Ku-99-05, Ku-99-06, Ku-99-07, Ku-99-08, Ku-99-SA8, Ku-99-SA11, Ku-01-OD1, Ku-01-OD2, Ku-01-OD3

REE-rich samples: Ku-98-130a and Ku-98-130b

13.5.1 Massive carbonatitic breccia

This sub-unit of the carbonatitic breccia is characterized by a macroscopically massive appearance. However, on a microscopic scale, almost all samples investigated display a narrow lamination and small-scaled magmatic folding (Fig. 13.6a). The erroneously macroscopic impression of textural homogeneity of the massive carbonatitic breccia is caused by the small grain sizes of the heavily brecciated and partially recrystallised minerals in this rock type, which commonly range between 1-30 μm and rarely exceed 0.5 mm.

The main minerals present are anhedral ankerite (50-75 vol.%) and subrounded fragments of albite (10-25 vol.%). Locally, larger relics of plagioclase with diameters of up to 500 μm have been observed. The bent and fissured, anhedral grains are surrounded by the laminated ankerite-albite matrix, giving the rock a mylonite-like appearance on a microscopic scale (Fig. 13.6 b). Subordinate fragmented magnetite is dispersed in the groundmass. Rare sodalite replaces schlieren of fragmented plagioclase. Other phases are present in only minor amounts (< 3 vol.%) and too small to be identified either microscopically or with the help of EMP or XRD analysis.

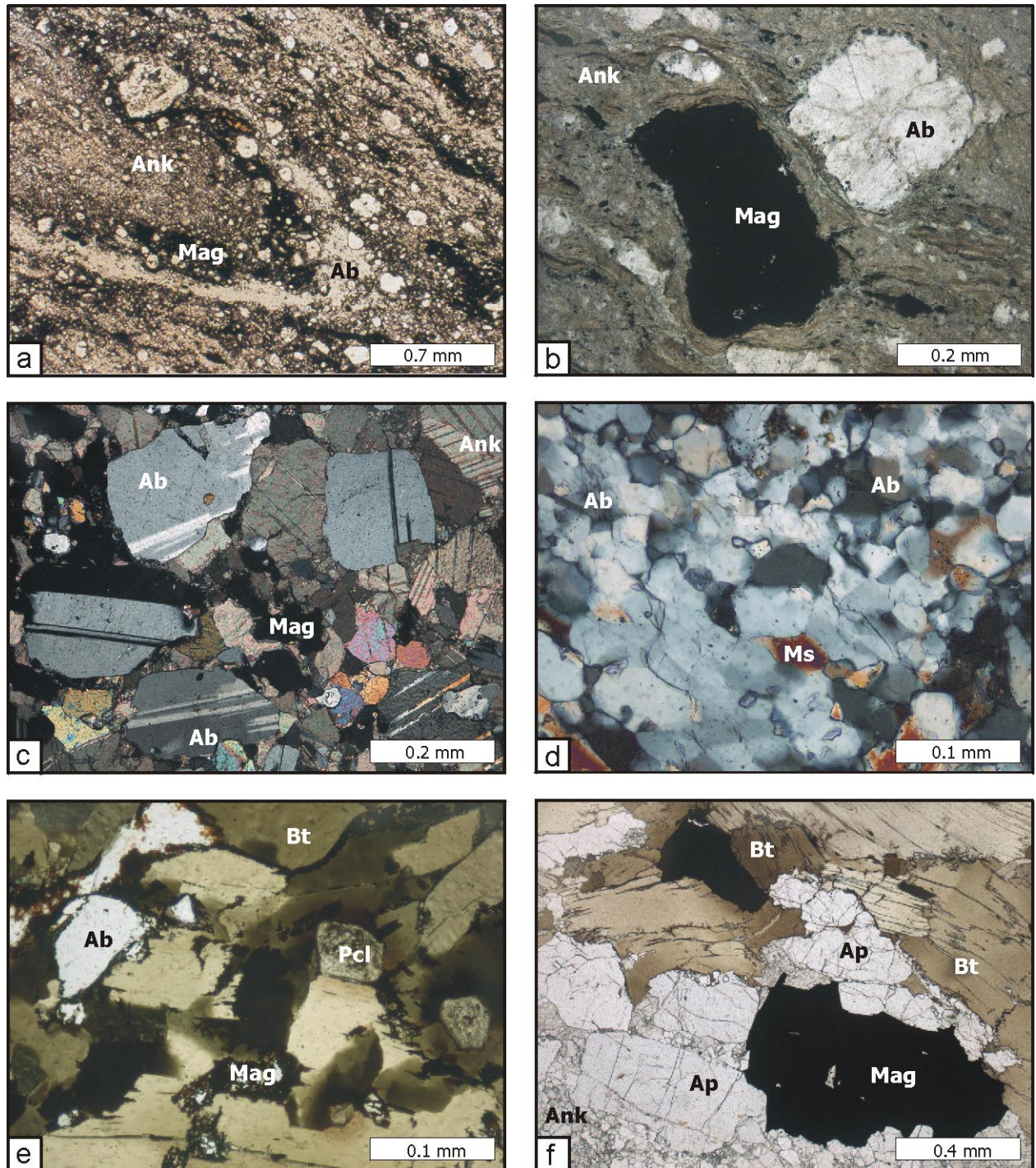


Fig. 13.6: Polished-section photomicrographs of the massive carbonatitic breccia (a-b) and the layered carbonatitic breccia (c-f). Cross-polarized light (c-d). Plane-polarized light (a-b, e-f). *a)* Small-scaled lamination and magmatic folding of the massive carbonatitic breccia. *b)* Very fine-grained, laminated carbonatite, surrounding a rotated wallrock xenolith. *c)* Layer composed of granular ankerite, magnetite and twinned albite. *d)* Layer composed of heavily strained albite fragments, displaying undulose extinction and being partially replaced by muscovite. *e)* Layer composed of biotite, magnetite, albite, and euhedral pyrochlore. *f)* Layer composed of orthomagmatic apatite, biotite, magnetite, and minor ankerite.

13.5.2 Layered carbonatitic breccia

Samples of the layered carbonatitic breccia display an indistinct layering and magmatic folding on a mm to cm scale, with extremely variable grain sizes ranging from fine- to coarse-grained in different layers. Single layers are commonly composed of (1) irregularly bounded ankerite grains, partially displaying undulose extinction (65-80 vol.%), associated by oval-shaped and twinned albite (18-35 vol.%), bearing carbonate and magnetite inclusions, rare schlieren of sodalite and dispersed, granular magnetite (Fig. 13.6c), (2) fragmented anhedral to subrounded albite, displaying patchy, undulose extinction (Fig. 13.6d), (3) partially recrystallised greenish biotite (37-50 vol.%), together with minor anhedral magnetite, anhedral, embayed albite grains (45-57 vol.%) and accessory pyrochlore (Fig. 13.6e) and (4) greenish biotite, subhedral to euhedral apatite prisms, granular ankerite and minor magnetite (Fig. 13.6f). Sodalite is a minor constituent of these rocks, even though it locally forms diffuse schlieren, pseudomorphing fragmented albite. Monomineralic cancrinite laminae are mainly restricted to the contact zones between carbonate- and feldspar-rich layers and are thus suggested to be formed by metasomatic exchange between the incorporated feldspar-rich xenoliths and the carbonatite melt. However, the intermingling of carbonatitic and xenolithic material in a first step and the subsequent separation of minerals into individual layers make it difficult to unravel the exact temporally succession of processes.

13.5.3 Sodalite-rich carbonatitic breccia

13.5.3.1 REE-poor samples

The mostly medium to coarse grain size of the sodalite-rich carbonatitic breccia, makes the separation between the crystallized carbonatite on the one hand and xenolithic material on the other hand a lot easier. In the samples investigated, subhedral to anhedral and partially recrystallised granular ankerite (5-40 vol.%) is the main constituent of the cementing ferrocyanatite matrix, whereas subordinate anhedral calcite fills the interstices between individual ankerite grains (Fig. 13.7a). Two generations of ankerite can be distinguished: (1) a first generation of subhedral and Mg-rich ankerite is preserved in rare cases (Fig. 13.5 a), and (2) a second generation of anhedral, granular and locally recrystallised ankerite (Fig. 13.7 a, b), differing from the former in its distinctly higher Fe-contents. In addition, small grains of Mn-rich ankerite were observed in the vicinity of fragmented Fe-Ti oxide grains.

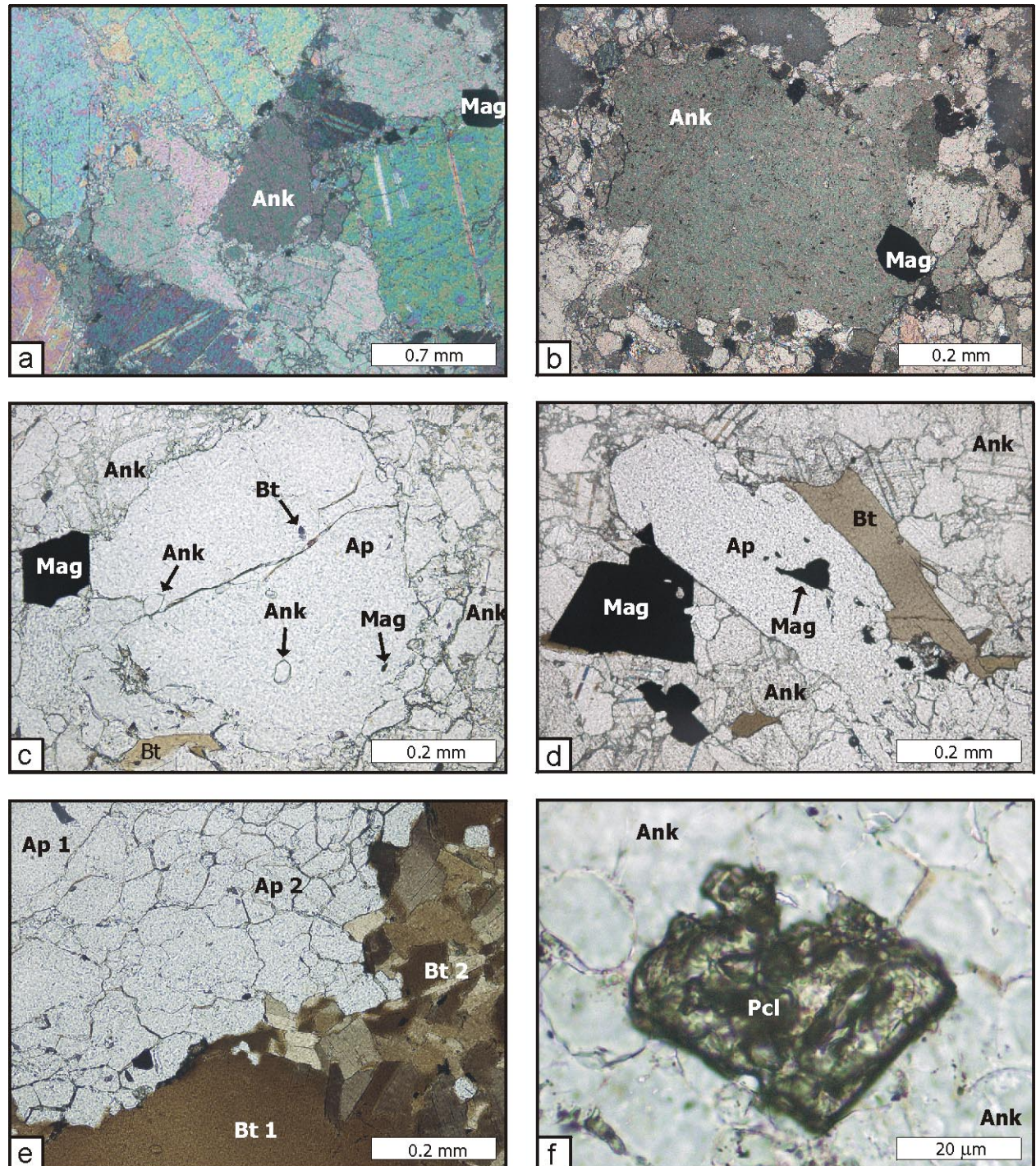


Fig. 13.7: Polished-section photomicrographs of carbonatite minerals from the sodalite-rich carbonatitic breccia. Cross-polarized light (a-b). Plane-polarized light (c-f). *a*) Anhedronal, granular ankerite, associated by minor magnetite, forming an even grained matrix. *b*) Ankerite, marginally recrystallised to polygonal grains. *c*) Apatite, bearing abundant inclusions of albite, magnetite and ankerite. *d*) Straight grain boundaries are developed between early crystallized apatite, biotite and magnetite. *e*) Marginally, both biotite and apatite are recrystallised to polygonal grains. *f*) Fine-grained pyrochlore, altered to very fine-grained intergrowths of secondary minerals.

Accumulations of optically zoned apatite grains have been observed in two samples of the sodalite-rich carbonatitic breccia. The euhedral to subhedral apatite prisms frequently contain inclusions of ankerite, magnetite and minor albite (Fig. 13.7 c, d). Rarely, biotite is included in large apatite grains (Fig. 13.7 c). Apatite is intimately associated with, and displays straight grain boundaries against subhedral biotite and a first generation of euhedral to anhedral and almost inclusion-free magnetite of up to 0.5 mm in diameter (Fig. 13.7d). Apatite, biotite and magnetite appear to have co-crystallized early in the magmatic history of the carbonatite, even though biotite and magnetite have overgrown apatite locally and thus outlasted the apatite formation. At their margins, both biotite and apatite are partially recrystallised to granular mosaics, supporting evidence that shearing outlasted the carbonatite emplacement and crystallization (Fig. 13.7 e). Small, unzoned pyrochlore crystals of up to 100 μm in diameter are common accessories of the cementing carbonatite matrix (Fig. 13.7 f). However these crystals are virtually completely replaced by fine-grained intergrowths of alteration products, which, however, were too small to be unambiguously identified.

Layers enriched in relict fenitized wallrock material are mainly composed of irregularly bounded fragments of fine-grained to very fine-grained albite displaying diffuse undulose extinction and containing abundant biotite inclusions (Fig. 13.8 a). In layers composed of both ankerite and albite, the latter has the tendency to develop a subrounded shape, suggesting solution of the albite grain margins by the carbonatite magma. In clear contrast to the angular albite fragments, these albites contain abundant ankerite, biotite and magnetite inclusions, mostly lack undulose extinction and may or may not display albite twinning (Fig. 13.8 b). In cases where twinning is missing, these feldspars strongly resemble quartz. In addition accumulations of twinned to untwinned albite (An_{0-1} ; 25-90 vol.%), in places associated with brownish to greenish, heavily strained biotite and fine-grained magnetite, form irregularly bounded zones pseudomorphing former xenolith boundaries. The latter are rotated and surrounded by narrow, carbonate-rich laminae.

The replacement of albite by sodalite started during the end-stages of biotite formation as is evidenced by biotite-sodalite inclusion-relationships. Sodalite occurs in different textural positions, i.e. (1) as virtually monomineralic layers, where sodalite replaces very fine-grained fragmented albite or relics of chess-board albite (Fig. 13.8 c), (2) as a replacement product of brecciated and albite-rich wallrock xenoliths, where the feldspathoid may be accompanied by ankerite (Fig. 13.8 d) and surrounded by narrow reaction rims of subhedral biotite and/or small euhedral magnetite grains and (3) as almost monomineralic rims around biotite-apatite patches and magnetite. Sodalite is mostly poikilitic, bearing abundant inclusions

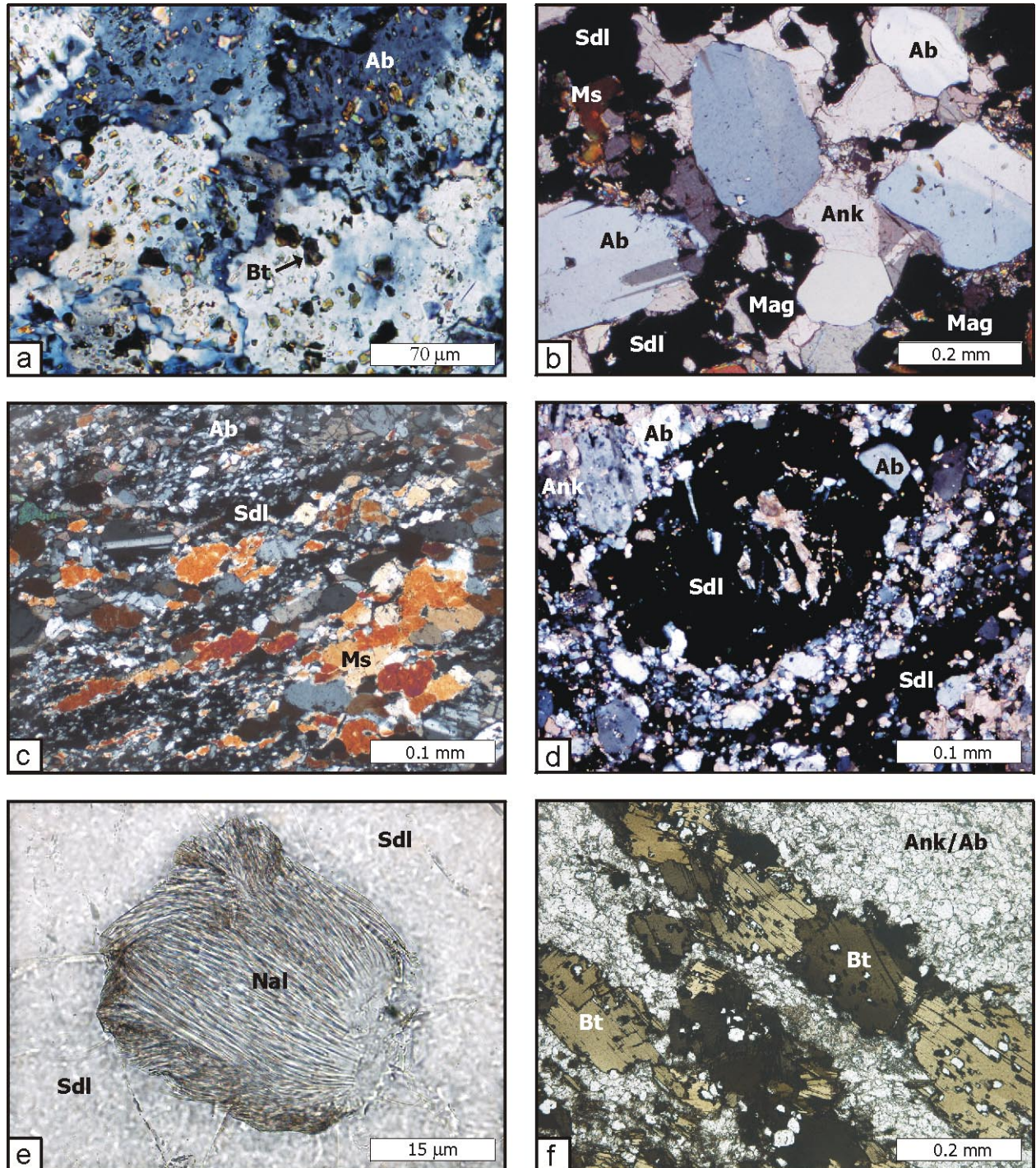


Fig. 13.8: Polished-section photomicrographs of the sodalite-rich carbonatitic breccia. Cross-polarized light (a-d). Plane-polarized light (e-f). *a*) Fragmented albite, displaying undulose extinction and containing abundant biotite inclusions, is the main constituent of the incorporated wall-rock xenoliths. *b*) In layers predominantly composed of ankerite, twinned to untwinned albite displays a rather oval shape. *c*) Sodalite occurring in schlieren, replacing fragmented albite. *d*) Sodalite replacing rotated, albite-rich anorthositic xenoliths. *e*) A yet unspecified Na-Al phase, displaying a fibrous morphology, replaces sodalite. *f*) Metasomatically formed biotite occurs in almost monomineralic schlieren, oriented parallel to the overall texture of the rock.

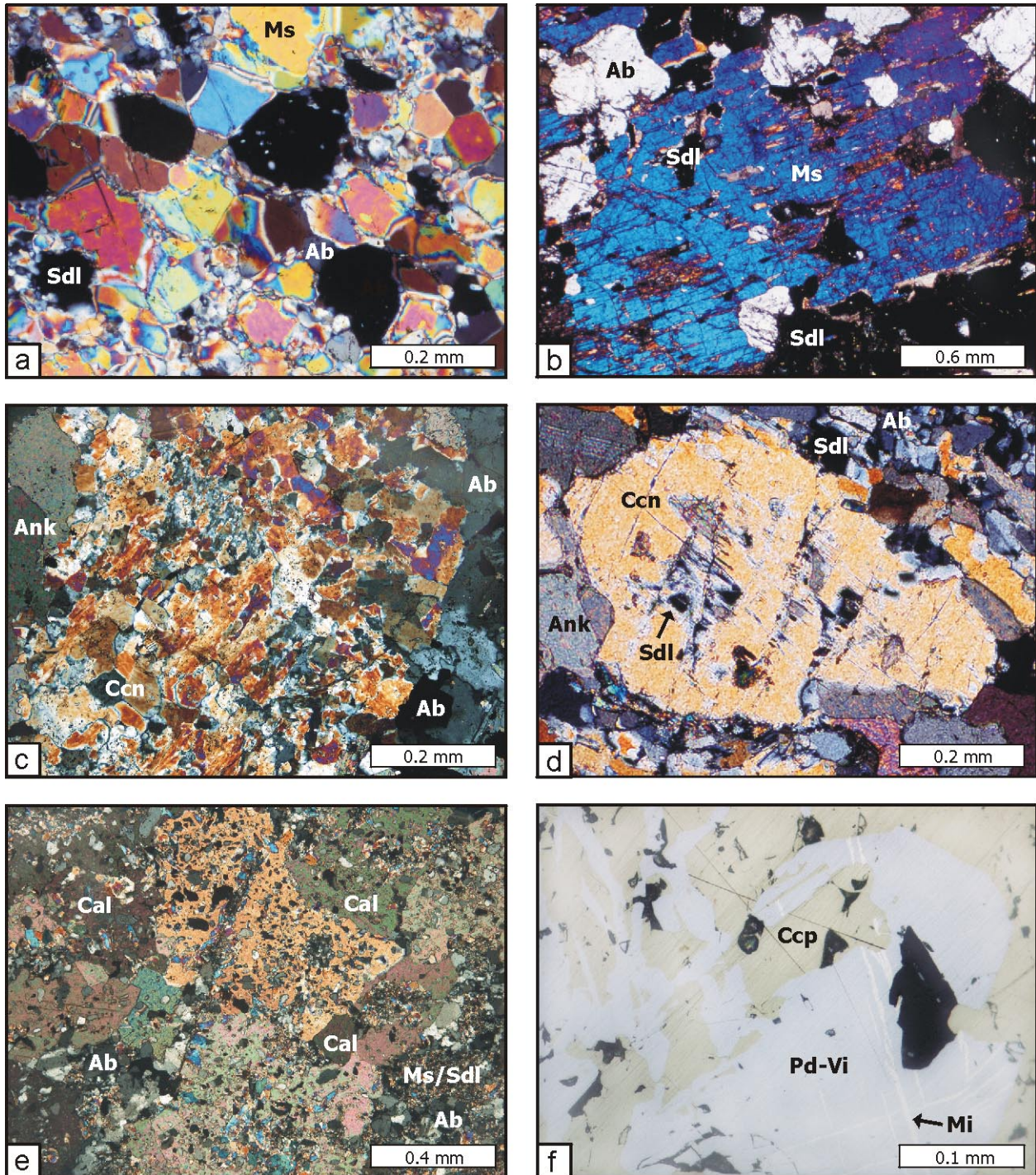


Fig. 13.9: Polished-section (a-e) and ore section (f) photomicrographs of the carbonatitic breccia. Cross-polarized light (a-e). **a)** Granular albite, either replaced by muscovite or sodalite. **b)** Muscovite replacing albite, whereby early formed sodalite is preserved. **c)** At the contacts between sodalite and carbonate-rich layers, narrow monomineralic cancrinite rims are developed. **d)** Late-stage cancrinite, replacing sodalitized albite. **e)** Late-stage, poikilitic calcite, bearing abundant inclusions of the matrix minerals. **f)** Millerite lamellae in thiospinel of the polydymite-violarite group, replaced by chalcopyrite.

of fine-grained ankerite and magnetite. Along both its margins and cracks sodalite is altered to a yet unknown silicate-free sodium-aluminium phase (Drüppel et al., in prep.). This phase commonly forms bunches of concentrically radiating fibres, with individual crystallites being up to 30 μm in length and $< 1 \mu\text{m}$ in width (Fig. 13.8 e).

Dark green biotite occurs in sodalite-rich and more commonly in albite-magnetite layers and patches, where the anhedral, embayed mica grains are heavily stained. In addition, biotite has been observed in carbonate-rich zones, where it forms schlieren of recrystallised grains, elongated parallel to the layering of the rocks (Fig. 13.8 f). Biotite of both textural positions is interpreted to be a relict phase of the incorporated anorthositic xenoliths.

Subordinate isometric muscovite and cancrinite locally replace fine-grained, fragmented albite, whereby early formed sodalite is preserved (Fig. 13.9 a, b, d). Cancrinite may also be present as reaction rims around albite- and sodalite-rich patches, separating carbonate-rich from silicate-rich zones (Fig. 13.9 c). Both minerals are rarely included in sodalite but are commonly enclosed by magnetite of a second generation. Late-stage calcite occurs in most of the samples, where it overgrows all previously mentioned minerals (Fig. 13.9 e). Chlorite and epidote are common accessories.

Magnetite is the dominant mineral among Fe-Ti oxides in the sodalite-rich carbonatitic breccia. A first generation of almost inclusion-free magnetite has been observed in carbonate-rich zones, where the oxide occurs as a widespread fine-grained matrix mineral, but may also form larger grains of up to 4 mm in size. Individual grains are subhedral to anhedral and display straight, curved or embayed grain boundaries with ankerite, biotite and apatite. The second generation of magnetite may reach grain sizes of up to 2 cm in diameter, frequently displaying inclusions of albite, sodalite, apatite, biotite and ankerite as well as rare muscovite and cancrinite (Fig. 13.9e). In either case, most of the magnetite grains are anhedral with undulating grain boundaries, embayments and cavities, whereas subhedral to euhedral grains are rare. Many of the magnetite grains are rotated and fragmented, the fractures being filled with carbonate or pyrite. Additionally, magnetite has been observed as vein fillings, where it is intergrown with titanohematite. The coexistence of hematite and magnetite points to T - $f(\text{O}_2)$ conditions at the hematite-magnetite buffer. Martitisation was observed in various stages of progression, in some cases advanced to the point where the texture consists of larger hematite areas containing relict magnetite. In addition, hematite forms fine-grained, anhedral or amoeboidal overgrowths on magnetite, preferentially at grain contacts with ankerite. Subhedral ilmenite forms either single grains or has developed several deformed subgrains. Lamellar twins after $\{10\text{-}11\}$ are common but often bent due to post-crystalline deformation. In irregularly bounded zones, ilmenite is

altered to very fine-grained symplectitic aggregates of magnetite and rutile. Titanohematite was found as an alteration product of ilmenite, invading the latter along cracks. Rutile is present in various textures, i.e. (1) as large, anhedral grains, either isolated or in contact with magnetite, (2) as groups of small, nearly euhedral to subhedral grains, as fine-grained overgrowths on magnetite where it is associated with ankerite and (3) as lamellae in magnetite, where it may be intergrown with hematite.

Pyrite is the dominant sulphide mineral. A first generation of pyrite occurs as subhedral to euhedral grains, either (1) dispersed in the matrix, (2) in the vicinity of magnetite or (3) as inclusions in chalcopyrite. Narrow fractures in the rocks are filled with a later generation of late pyrite. Minor amounts of chalcopyrite, millerite, siegenite and violarite-polydymite were identified, testifying to different cooling stages. The sulphides are frequently concentrated in irregular sulphide veins or patches and elongate lenses where they may be associated with minor magnetite and pyrite, but they may also form isolated grains in the matrix. Individual millerite grains underwent partial or total replacement by thiospinels of the violarite-polydymite group (Fig. 13.9 f). Sulphides, represented by members of the chalcocite-digenite group, associated with rare chalcopyrite and bornite, were observed only in one sample (Ku-97-15d), where they form small grains or grain aggregates, which are either dispersed in the matrix or, more frequently, form inclusions in magnetite. Pyrrhotite may be present in small amounts (Ku-97-19) forming single grains and irregular aggregates, concentrated in layer-parallel patches. In larger pyrrhotite grains two systems of pentlandite lamellae may be developed. Conspicuous oxide-sulphide aggregates have been observed locally, which have been investigated in some detail by von Seckendorff et al. (2000). The inner parts of the aggregates mainly consist of granular intergrowths of sub- to euhedral pyrite with anhedral magnetite, chalcopyrite and rare millerite. The broad outer zones of the domains are characterized by lamellar intergrowths of pyrite, hematite and magnetite with rare chalcopyrite, millerite and polydymite. In the outermost regions of these domains, pyrite lamellae are replaced by millerite, together with polydymite and chalcopyrite. These conspicuous aggregates have been interpreted to be formed by contemporaneous sulphidation and oxidation of a suspected precursor pyrrhotite (see von Seckendorff et al., 2000, for a detailed discussion).

13.5.3.2 REE-rich samples

The two REE-rich samples of the sodalite-rich carbonatitic breccia (Ku-98-130a, Ku-98-130b) are characterized by a pale pink macroscopic colour (except abundant deep blue sodalite fragments). Ankerite occurs as large anhedral grains with embayed grain boundaries, intimately

associated with magnetite. The magnetite grains are generally anhedral with undulating grain boundaries, embayments and cavities. Albite is the main constituent of fragmented xenoliths. In these zones, however, albite is only rarely preserved, since most of the grains are pervasively altered to fine-grained intergrowths of ankerite and sodalite, with the latter in turn being replaced by fibrous bunches of the Na-Al phase (Fig. 13.10 a).

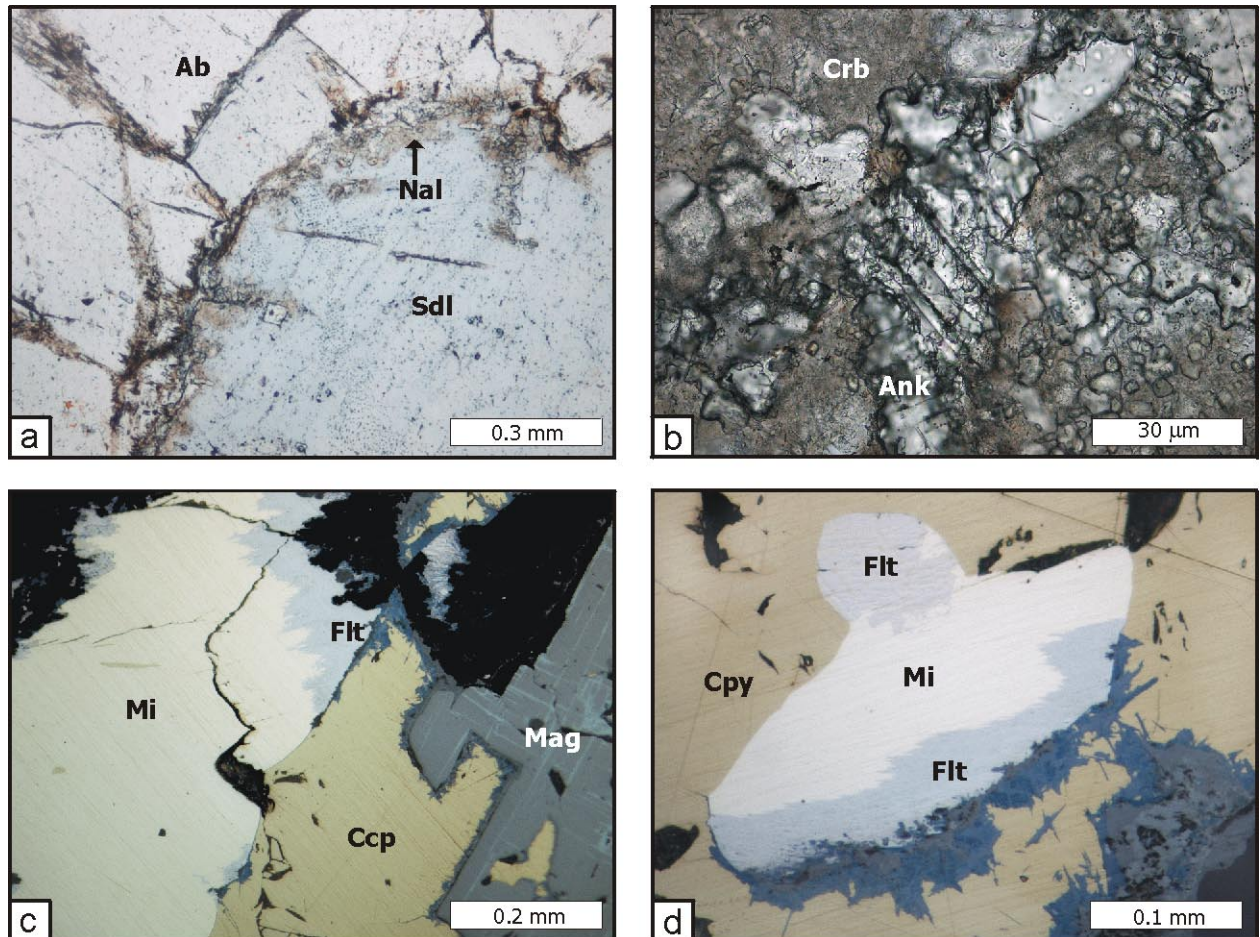


Fig. 13.10: Polished-section photomicrographs of the REE-rich samples of the carbonatitic breccia. *a)* Albite altered to sodalite, which in turn is replaced by the unspecified Na-Al phase. *b)* Brownish carbonate aggregates, with the inner parts being mainly composed of ankerite whereas the outer zones are dominated by carbocernaite. *c)* Late-stage sulphide vein, composed of chalcopyrite, magnetite and millerite, with the latter being partially replaced by fletcherite. *d)* Millerite in contact to chalcopyrite is replaced by a yet unknown member of the fletcherite group.

The REE are concentrated in conspicuous large, brownish carbonate aggregates, most probably pseudomorphing the shape of a suspected subhedral precursor carbonate (presumably calcite or ankerite), situated between large ankerite and magnetite grains. The carbonate aggregates can be subdivided into at least two different zones. The inner, pale-coloured parts are either composed of ankerite or consist of lamellar to patchy intergrowths of calcite and minor

siderite. In clear contrast, the brownish outer zones of the domains are dominated by dark brown carbocernaite (general formula: $(\text{Ca,Na})(\text{Sr,Ce,Ba})(\text{CO}_3)_2$; up to 15 vol.%) and ankerite (Fig. 3.10 b). It seems rather likely that these aggregates formed by metasomatic exchange between ankerite and late-stage, REE-rich fluids. Late subhedral barite and anhedral strontianite grains of up to 40 μm in diameter are localised in the interstices between large ankerite and magnetite grains and the carbocernaite aggregates, testifying to autometasomatism of the rocks, caused by the injection of late-stage Ba- and Sr-rich fluids.

Chalcopyrite and pyrite occur isolated in the matrix or, more commonly, as irregular sulphide veins or patches, where the sulphides are associated with magnetite (Fig. 13.10 c). Millerite is present in only minor proportions and is partially replaced by chalcopyrite. Additionally, millerite is altered along its margins and along cracks to a yet unknown member of the fletcherite group (Fig. 13.10 d). These fletcherites differ from those yet described by containing variable but high amounts of Cu, whereas the Co and Fe contents are negligible.

13.5.4 Crystallization sequence of the carbonatitic breccia

In summary, the following magmatic and metasomatic crystallization sequence can be established for the sodalite-rich carbonatitic breccia:

(1) In the cementing carbonatitic matrix magnetite, apatite, pyrochlore and biotite were the first minerals to crystallize, followed by ankerite, the suspected precursor pyrrhotite and late interstitial calcite. Chalcopyrite and pyrite are most probably synchronous with the second magnetite generation. During the end-stages of, and outlasting the carbonatite crystallization and fenitizing processes millerite, polydymite/violarite, chalcocite/digenite, bornite as well as late hematite, chlorite, barite, strontianite and calcite of the second generation were formed.

(2) In layers composed of fragmented fenitized wallrock anorthosite, albite is the first mineral to be formed during fenitization. Since albite is commonly included in apatite and biotite of the cementing carbonate matrix, whereas both An-rich plagioclase and K-feldspar have never been observed, it can be concluded that the transformation of feldspars of the wallrock anorthosite and syenite into almost pure albite predated the emplacement of the carbonatitic melt. The absence of Fe-Mg silicates common in anorthosite and syenite (e.g. pyroxene, olivine and/or amphibole) provides evidence that biotite, like albite, was formed during an early fenitizing event. After the emplacement of the carbonatitic melts, the repeated release of fenitizing fluids caused the formation of sodalite at the expense of albite. This process started

during, and outlasted the crystallization of biotite in the ankerite-rich zones. The replacement of albite by muscovite and cancrinite started during the final stages and outlasted the formation of sodalite in the fenitic zones and of the second magnetite generation in the carbonatite matrix. The end-stages of the fenitization are marked by the formation of chlorite, hematite, rutile and epidote.

13.6 Ferrocarbonatite veins

The younger ferrocarbonatite dykes and veins transsect both the massive and the banded variety of the main carbonatite body and are almost free of wallrock-material, even though the veins may locally be intermingled with the carbonatitic breccia. The following samples have been investigated in detail:

Ferrocarbonatite: Ku-97-15f, -15h, -15j, -15m, -15p, Ku-98-32, Ku-98-34, Ku-98-91, Ku-01-03, Ku-01-04, Ku-01-05

Major phases of the massive ferrocarbonatites are subhedral to anhedral ankerite grains with curved grain boundaries together with subordinate, subhedral to anhedral, angular to irregularly shaped magnetite grains that frequently display albite inclusions (Fig. 13.11 a). Martitisation of magnetite is mainly initiated from grain margins. Minor calcite fills the interstices between ankerite grains whereas rutile occurs as rims surrounding magnetite (Fig. 13.11 b). In one sample optically zoned pyrochlore euhedra, containing inclusions of pure albite (An_0), have been observed in the vicinity of magnetite grains (Fig. 13.11 c). The contacts between the ferrocarbonatite veins and the carbonatitic breccia are locally marked by trails of euhedral magnetite grains within the ferrocarbonatite. In two samples, cancrinite rims, up to 2 mm across, are developed between the Si-poor ferrocarbonatite and the main, xenolith-rich carbonatite intrusion, pointing to a minor degree of metasomatic exchange between the two rock units. Rounded fragments of sodalite and mostly untwinned albite (An_{0-1}) with undulose extinction, derived from the fenitized wallrock anorthosite and/or fenite xenoliths within the carbonatitic breccia, may form a subordinate constituents of this rock type (Fig. 13.11 d). Thompson et al. (2002) additionally described the presence of quartz within the ferrocarbonatite veins, incorporated from the fenitized wallrock anorthosite. In clear contrast to these authors, quartz was never observed in the samples investigated in this study, comprising both the

carbonatitic breccia and the younger ferrocarnatite veins. The lack of quartz agrees well with the general absence of quartz in the anorthosites of the KIC (Drüppel et al., 2001) and their

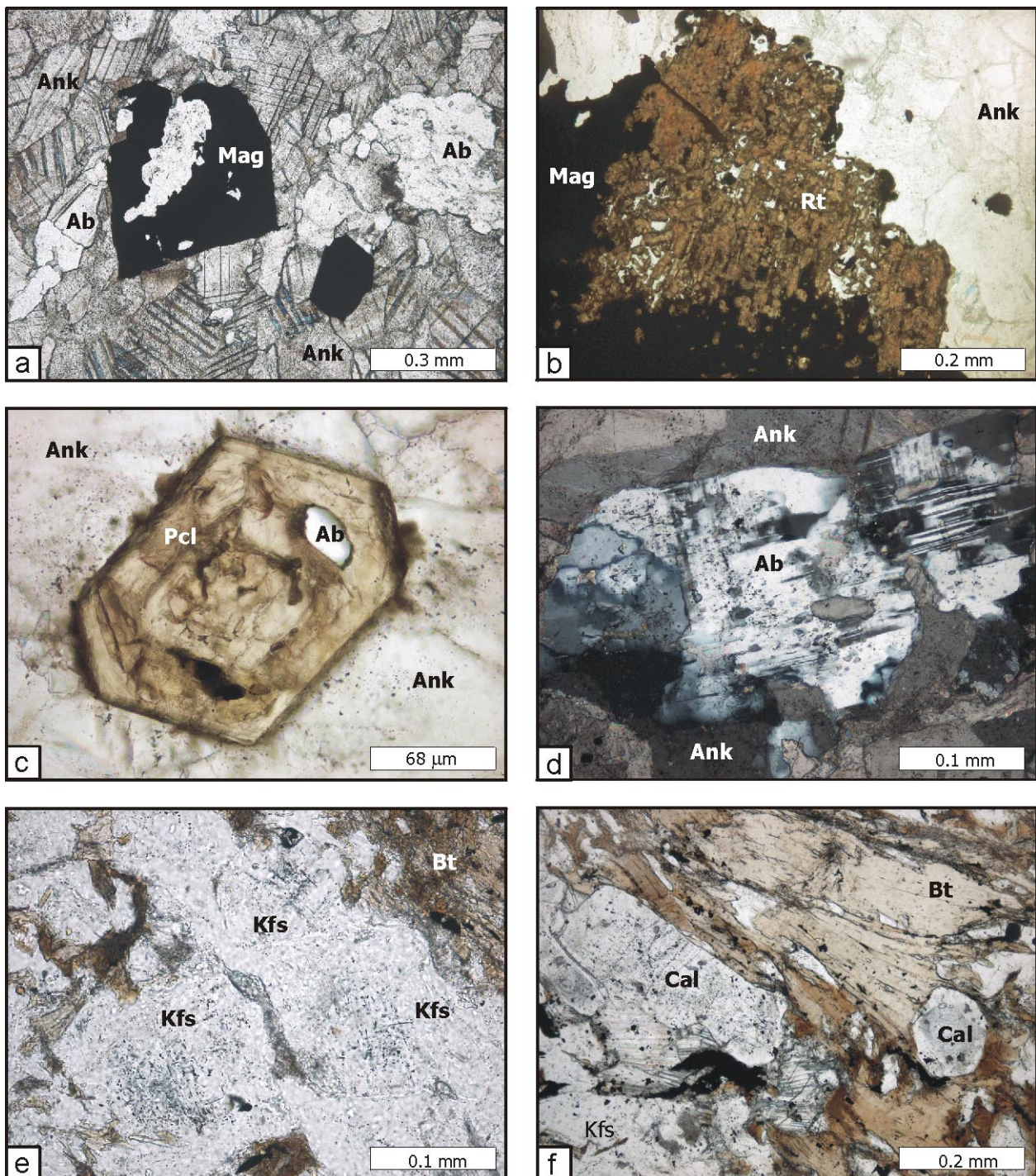


Fig. 13.11: Polished-section photomicrographs of the ferrocarnatite veins (a-d) and the feldspar-biotite-ilmenite-calcite rock (e-f). Cross-polarized light (d). Plane-polarized light (a-c, e-f). *a*) Granular ankerite and subhedral to euhedral magnetite, the latter bearing albite inclusions. *b*) Broad rutile rims are developed around magnetite. *c*) Optically zoned, euhedral pyrochlore, bearing an albite inclusions. *d*) Fragmented relict of albite, displaying undulose extinction. *e*) Homogeneous K-feldspar grains and anhedral to subhedral biotite flakes are the main constituents of the feldspar-biotite-ilmenite-calcite rock. *f*) Biotite, bearing abundant inclusions of euhedral calcite.

fenitization products and its rare occurrence in the syenites.

13.7 K-feldspar-biotite-ilmenite-calcite rock

The K-feldspar-biotite-ilmenite-calcite rock (Ku-98-25) forms part of a large dyke of the sodalite-rich carbonatitic breccia. The black, medium-grained rock displays curved contacts with the carbonatitic breccia and, in clear contrast to the latter, is characterized by a massive appearance.

The main minerals present are medium-grained, subhedral to anhedral, tabular K-feldspar (55 vol.%), mostly lacking exsolution phenomena, and subhedral to anhedral biotite flakes (35 vol.%; Fig. 13.11 e). Porphyric biotite was observed locally. Calcite (8 vol.%) forms either (1) discrete, subhedral to anhedral grains in the matrix, filling K-feldspar interstices and displaying straight grain boundaries against biotite or (2) euhedral inclusions in the latter (Fig. 13.11 f). Anhedral ilmenite showing abundant lamellar twins after {10-11} is present in minor amounts, filling the interstices between individual K-feldspar crystals. Accessory, fine-grained pyrite is dispersed in the matrix.

The rock differs significantly from the investigated fenites in containing K-feldspar as a major constituent and deviates from the syenites by the lack of exsolution features of potassium feldspar and its comparably high modal amount of magmatic calcite. It can thus be concluded, that the K-feldspar-biotite-ilmenite-calcite rock represents an independent magmatic unit, displaying similarities with lamprophyres.

14 Mineral chemistry

The mineral chemistry of 27 selected samples of the rock types described in Chapter 13 has been investigated with the aid of electron-microprobe (EMP) analysis. Analytical conditions are provided in the Appendix A.2.3.

<i>Fenitized anorthosite (A,f):</i>	Ku-98-71, Ku-98-78, Ku-98-79, Ku-98-84, Ku-99-02
<i>Fenitized syenite (S,f):</i>	Ku-98-59b
<i>Fenitized nepheline syenite (S,ne):</i>	Ku-99-15a
<i>Fenitized ultramafic xenolith (UMX):</i>	Ku-97-43a
<i>Sodalite-rich carbonatitic breccia (CB,so):</i>	Ku-97-15, Ku-97-15a, Ku-97-15d, Ku-97-15e, Ku-97-19, Ku-97-24, Ku-98-57a, Ku-98-58a, Ku-98-80, Ku-98-131, Ku-99-05, Ku-99-SA8
<i>REE-rich samples (CB,REE):</i>	Ku-98-130a, Ku-98-130b
<i>Layered carbonatitic breccia (CB,l):</i>	Ku-98-14, Ku-98-48, Ku-98-56b
<i>Ferrocarnatite veins (FV):</i>	Ku-01-04
<i>Kfs-Bt-Ilm-Cal rock (L):</i>	Ku-98-25

14.1 Carbonate minerals

Carbonates are the main constituents of the ferrocarnatite veins, the fenitized ultramafic xenoliths and the cementing carbonatite matrix of the carbonatitic breccia. In addition, they are ubiquitous accessory phases of the Kfs-Bt-Ilm-Cal rock and of both the anorthositic and fenitized syenitic lithologies. The calculation of the ankerite, dolomite and carbocearnite formulae was based on 2 cations whereas calcite, siderite, magnesite and strontianite were calculated on a 1-cation basis. Representative analyses are listed in Tables A.5.1.13 to A.5.1.17 in the Appendix A.5.1.

14.1.1 Ankerite-dolomite solid solution

The vast majority of the carbonates analysed has an Mg/(Mg+Fe) ratio of < 0.8 and can thus be classified as ankerites. The MnO contents of the carbonates are generally high, whereas their Ce,

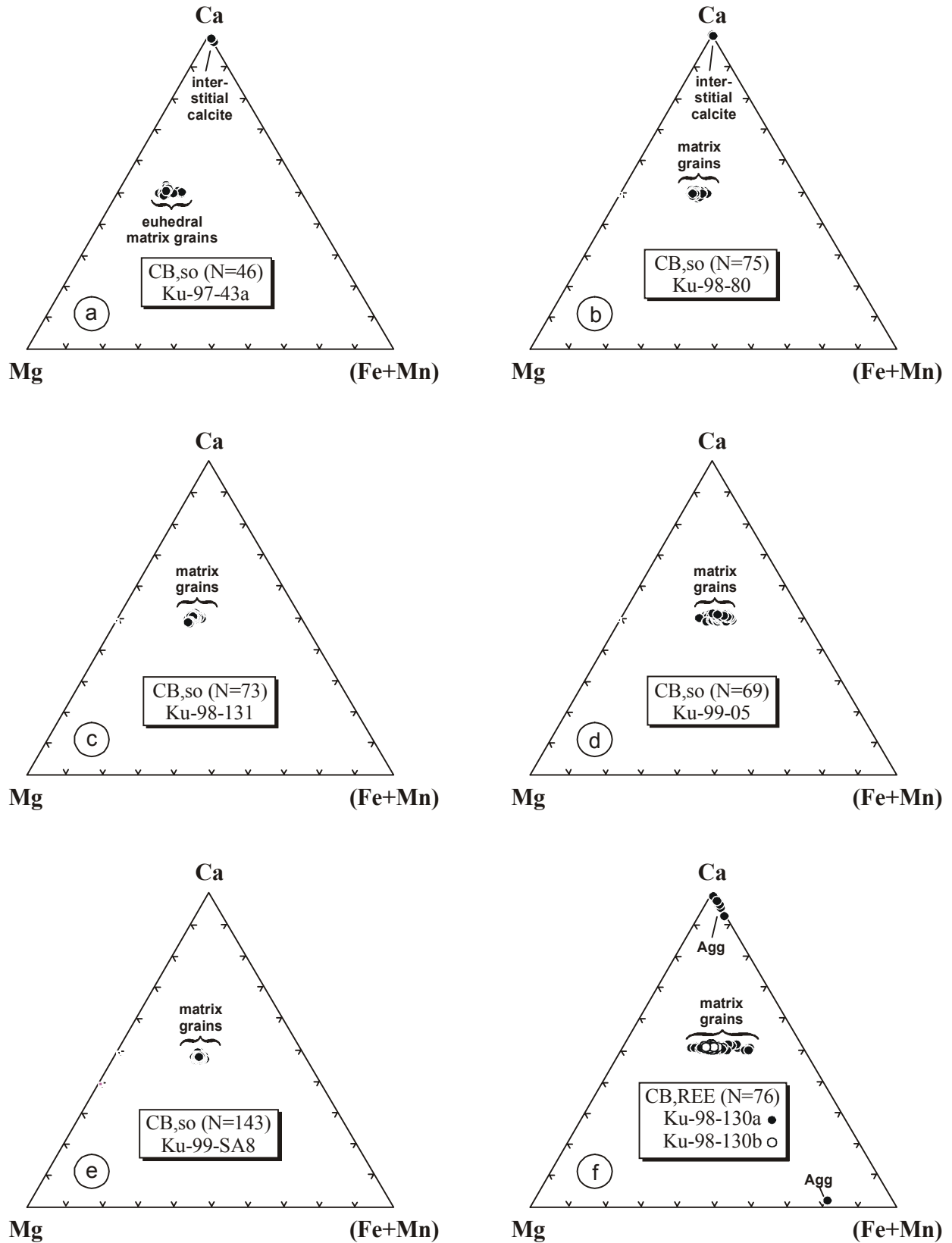


Fig. 14.1: Compositional variability of carbonate from the sodalite-rich carbonatitic breccia, expressed in the ternary diagram Ca-Mg-(Fe+Mn). (*Agg* carbonates from brownish carbonate aggregates).

La and Na contents are near or below the detection limit. Representative analyses are listed in Table A.5.1.13 in the Appendix A.5.1; average compositions of ankerite/dolomite of the investigated samples are compiled in Table 14.1.

Carbonates with X_{Mg} at or near the ankerite-dolomite transition were observed in two samples of the *carbonatitic breccia*, where they occur in different textural positions: (1) as euhedral, early crystallized carbonates (X_{Mg} : 0.61-0.77) in the sodalite-rich carbonatitic breccia, enclosing abundant ultramafic xenoliths (Ku-97-43a; Fig. 14.1a) and (2) as carbonate inclusions (X_{Mg} : 0.79-0.84) in magnetite of the first generation in sample Ku-98-14 of the sodalite-free carbonatitic breccia (Fig. 14.2a). In clear contrast, anhedral matrix carbonates of the main carbonatite body display distinctly lower Mg-contents, that slightly decrease in the sequence of layered carbonatitic breccia (X_{Mg} : 0.56-0.74; Fig. 14.2) – REE-poor samples of the sodalite-rich carbonatitic breccia (X_{Mg} : 0.43-0.64; Fig. 14.1a-e) - REE-rich samples of the sodalite-rich carbonatitic breccia (X_{Mg} : 0.25-0.61; Fig. 14.1f). All analysed ankerite crystals show minor oscillatory to patchy zoning with the Mg-contents commonly decreasing from core towards the rim (Fig. 14.4a-d). Only the biotite-free sample Ku-99-05 (Fig. 14.4e) displays an opposite zoning, with the Fe-content decreasing towards the rim. The observed trends of decreasing X_{Mg} of the carbonates with subsequent crystallization most probably reflects the extensive, synchronous biotite formation in these samples. In the same direction both MnO and SrO increase from values 0.6 to 2.5 wt.% and 0.1 to 0.8 wt.%, respectively.

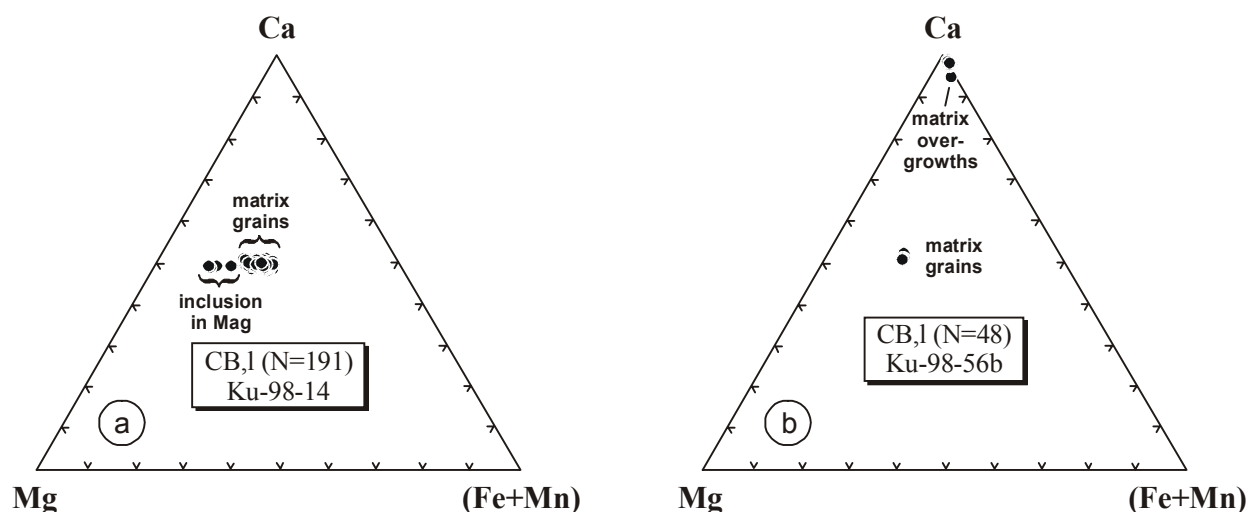


Fig. 14.2: Compositional variability of carbonate from the layered carbonatitic breccia, expressed in the ternary diagram Ca-Mg-(Fe+Mn).

In clear contrast, the rimward Fe-increase of the biotite-free sample Ku-99-04 is suggested to reflect the onset of magnetite crystallization.

Ankerite from samples of the younger *ferrocarbonatite veins* (X_{Mg} : 0.43-0.64; Fig. 14.3a) has Mg amounts comparable to those of ankerites from the sodalite-rich carbonatitic breccia, but, at the same time, distinctly higher MnO contents of 2.3-3.4 wt.%, suggesting its crystallization from a more fractionated melt. In clear contrast to carbonates of the main carbonatite body, most of these ankerites preserve nearly unzoned Fe-rich cores (X_{Mg} : 0.43-0.49) and display strongly reversed rims (X_{Mg} : 0.55-0.64) where the Mg content increases abruptly (Fig. 14.4f). This increase is suggested to be related to the onset of magnetite crystallization in the ferrocarbonatite, which in contrast to the carbonatitic breccia, lacks an Mg-fractionating phase like biotite.

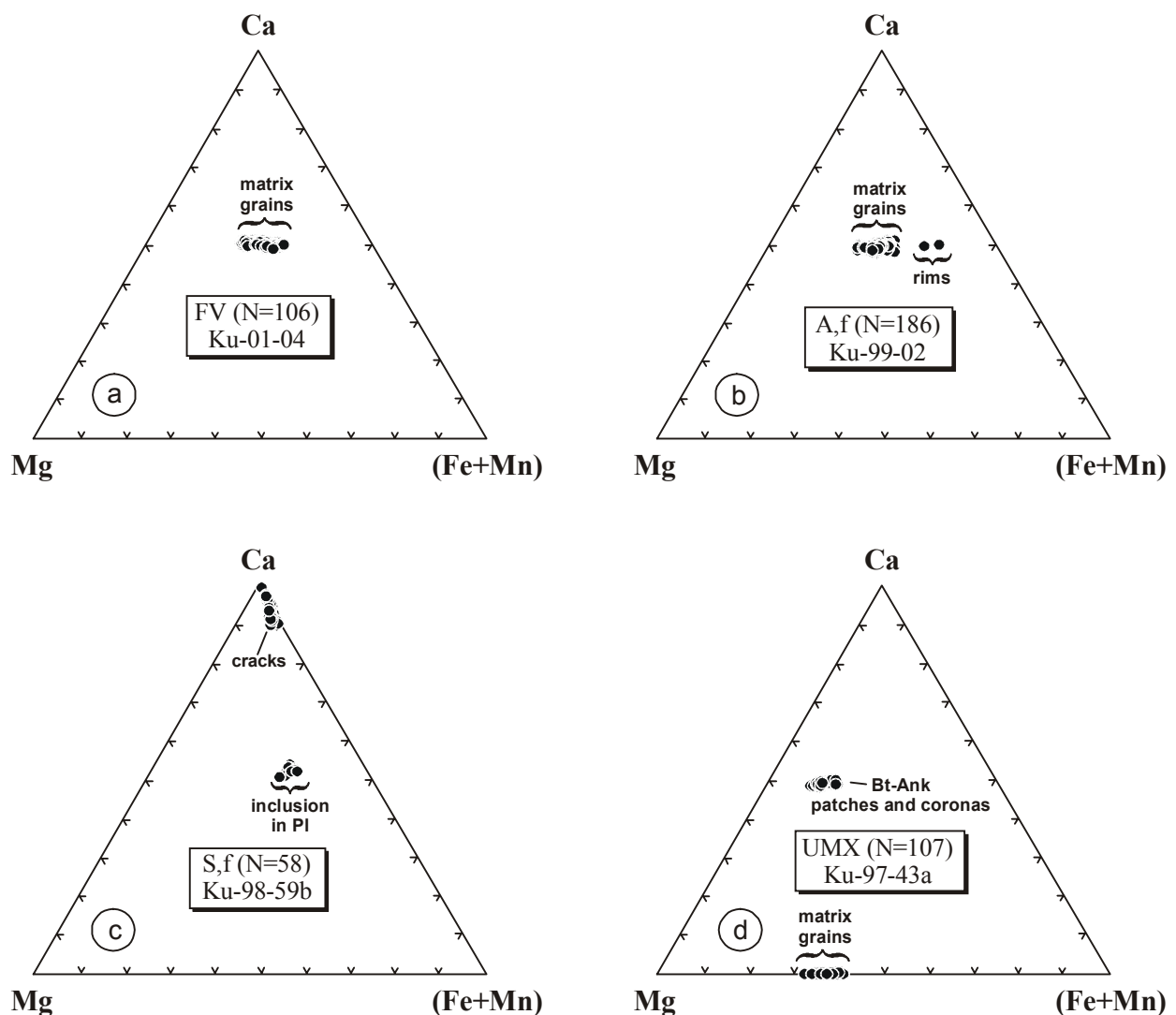


Fig. 14.3: Compositional variability of carbonate, expressed in the ternary diagram Ca-Mg-(Fe+Mn). *a)* Ferrocarbonatite vein. *b)* Fenitized anorthosite. *c)* Fenitized syenite. *d)* Fenitized ultramafic xenolith.

Carbonates in the bordering *fenitized anorthosites* (Ku-99-02) are ankerites with a patchy zoning and Mg/Fe ratios (X_{Mg} : 0.48-0.64) in the range of the main carbonatite body (Fig. 14.3b),

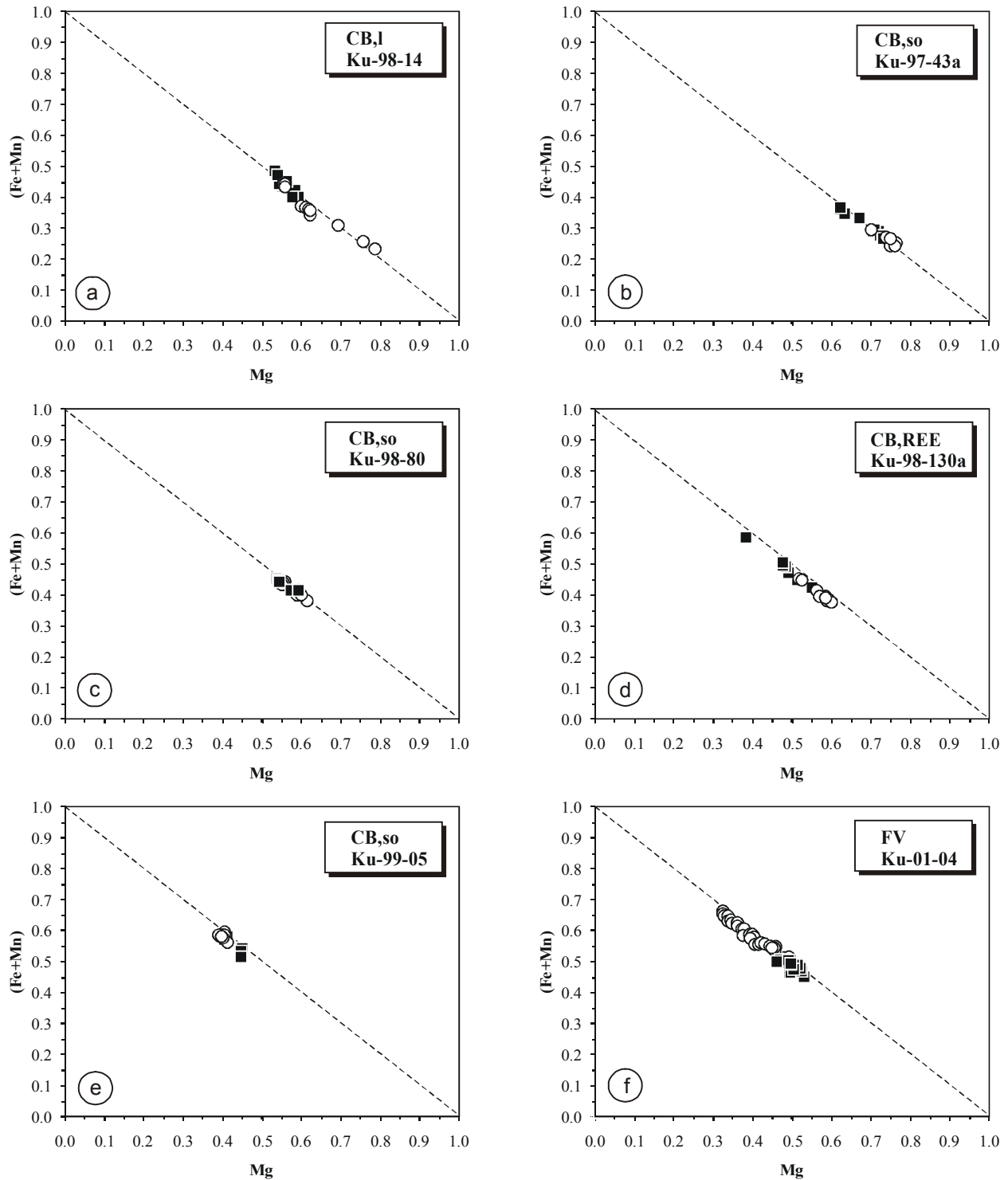


Fig. 14.4: Core (white symbols) and rim (black symbols) compositions of ankerite from selected samples of the carbonatitic breccia (*a-e*) and the younger ferrocarnatite veins (*f*). Note that biotite-rich samples (*a-d*) display a rimward increase of the Fe-content, whereas biotite-free samples (*e-f*) are characterized by an opposite trend of increasing Mg.

indicating that the wallrock-fenitization is related to the injection of carbonatite melt. With a Mg/(Mg+Fe) of 0.27-0.34, narrow ankerite rims on the matrix ankerite grains display the highest

sample; wt.%	textural position	MgO	CaO	MnO	FeO	SrO	BaO	CO ₂	Sum
CB,I									
<i>Ku-98-14</i>	inclusion in Mag	15.80	27.99	1.96	6.68	0.11	0.02	44.59	97.16
σ (N=4)		0.38	0.17	0.64	0.80	0.04	0.02	0.42	0.83
<i>Ku-98-14</i>	anhedral matrix grains	11.30	27.00	2.40	12.60	0.80	0.03	43.07	97.19
σ (N=187)		0.57	0.34	0.16	0.89	0.10	0.04	0.36	0.72
<i>Ku-98-56b</i>	anhedral matrix grains	13.62	29.21	1.90	10.12	0.70	0.00	45.47	101.03
σ (N=4)		0.20	0.41	0.13	0.21	0.11	0.00	0.21	0.41
CB,so									
<i>Ku-97-43a</i>	euhedral matrix grains	14.97	28.82	0.57	9.11	0.22	0.03	44.99	98.70
σ (N=31)		0.77	0.43	0.09	1.24	0.07	0.03	0.39	0.76
<i>Ku-98-80</i>	anhedral matrix grains	11.62	28.04	1.60	13.74	0.77	0.03	44.44	100.25
σ (N=72)		0.53	0.26	0.08	0.74	0.08	0.04	0.30	0.62
<i>Ku-98-131</i>	anhedral matrix grains	11.63	28.60	1.25	13.76	0.59	0.03	44.60	100.46
σ (N=73)		0.46	0.35	0.19	0.58	0.12	0.04	0.34	0.78
<i>Ku-99-SA8</i>	anhedral matrix grains	11.52	26.79	2.49	13.72	0.71	0.03	43.87	99.13
σ (N=143)		0.23	0.35	0.16	0.34	0.08	0.04	0.27	0.63
<i>Ku-99-05</i>	anhedral matrix grains	8.51	27.00	2.30	16.52	0.64	0.03	42.31	97.30
σ (N=69)		0.96	0.50	0.28	1.51	0.12	0.04	0.61	1.10
CB,REE									
<i>Ku-98-130a</i>	anhedral matrix grains	9.41	28.27	1.75	16.41	0.53	0.02	43.84	100.24
σ (N=53)		1.81	0.47	0.17	2.89	0.17	0.03	0.66	0.91
<i>Ku-98-130b</i>	anhedral matrix grains	10.31	28.58	1.70	15.03	0.60	0.04	41.64	98.24
σ (N=28)		0.65	0.55	0.16	0.65	0.35	0.05	0.49	0.60
FV									
<i>Ku-01-04</i>	anhedral matrix grains	9.78	28.37	2.73	15.05	0.62	0.03	41.45	98.14
σ (N=106)		1.29	0.58	0.27	2.26	0.09	0.04	0.64	1.11
A,f									
<i>Ku-99-02</i>	anhedral matrix grains	10.43	26.90	1.98	15.12	0.56	0.02	43.24	98.26
σ (N=184)		0.85	0.34	0.35	1.14	0.14	0.03	0.38	0.65
<i>Ku-99-02</i>	rims on matrix grains	5.64	26.39	1.30	23.17	0.45	0.04	42.07	99.06
σ (N=2)		0.72	0.26	0.00	0.69	0.06	0.04	0.53	0.72
S,f									
<i>Ku-98-59b</i>	anhedral matrix grains	6.14	29.85	2.14	16.66	0.46	0.02	41.86	97.11
σ (N=11)		1.02	3.59	0.38	2.64	0.12	0.02	0.65	1.23
UMX									
<i>Ku-97-43a</i>	patches and coronas	15.80	28.27	0.43	8.77	0.37	0.03	45.24	98.91
σ (N=68)		0.78	0.69	0.09	1.02	0.08	0.04	0.35	0.65

Table 14.1: Average compositions of ankerite/dolomite from different samples and textural positions (σ standard deviation).

Fe-contents of all ankerites analysed, and, moreover, seem to extend the yet known compositional range of natural ankerite to the most extreme Fe-rich composition (Fig. 14.3b).

Ankerite of the *fenitized syenite* (Ku-98-59b) has a comparably low X_{Mg} (0.36-0.44; Fig. 14.3c), according to high MnO amounts of 1.9-2.9 wt.%. The Fe-rich nature of the carbonates reflects the Fe-rich whole-rock composition of the syenites, and thus suggests some sort of chemical interaction between the intruding carbonatite melt and the bordering lithologies during fenitization.

Ankerite/dolomite from the *fenitized ultramafic xenolith* (Ku-97-43a), occurring in biotite-ankerite patches, schlieren and corona textures, has quite homogeneous MgO contents (X_{Mg} : 0.71-0.81; Fig. 14.3d), which, however, are higher than those of ankerite/dolomite in the enclosing carbonatitic breccia (Fig. 14.1a). Like in the case of the fenitized syenite, these changes in the mineral compositions of ankerite/dolomite are suggested to reflect chemical interaction between the carbonatite melt and the high-Mg ultramafic xenoliths.

14.1.2 Calcite

Calcite of the *carbonatitic breccia* occurs in 3 different textural positions, i.e. (1) in the interstices between individual ankerite grains (Ku-97-43a, Ku-98-14, Ku-98-80, Ku-98-130a),

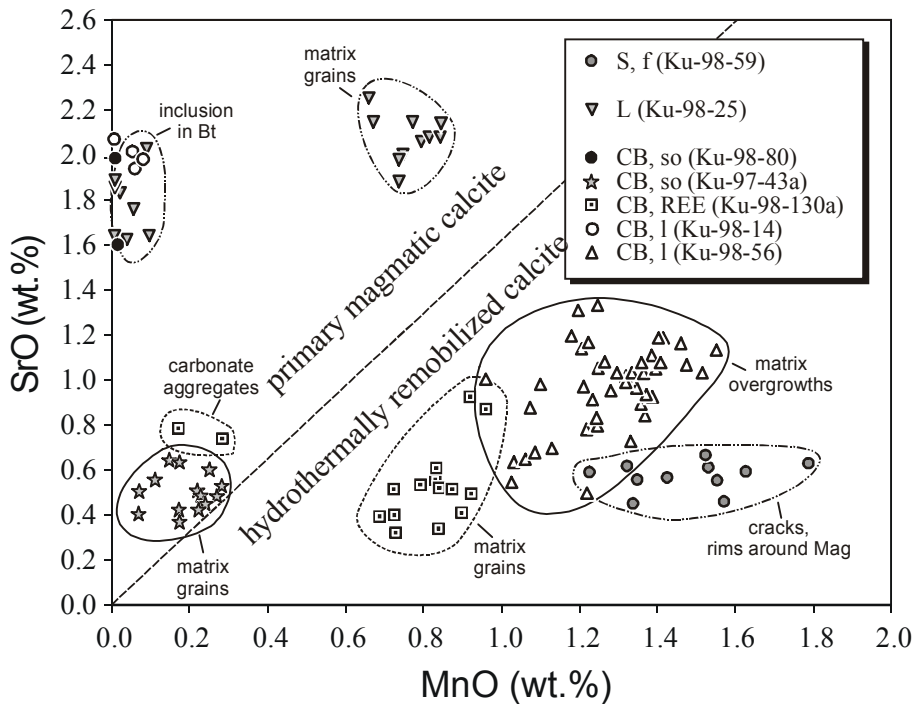


Fig. 14.5: Compositional variability of calcite, plotted as SrO against MnO (*CB,l* layered carbonatitic breccia, *CB,REE* REE-rich samples of the sodalite-rich carbonatitic breccia, *CB,so* sodalite-rich carbonatitic breccia, *L* K-feldspar-biotite-ilmenite-calcite rock, *S,f* fenitized syenite).

(2) as late matrix overgrowths (Ku-98-56b) and (3) in brownish carbonate aggregates, where it is intimately associated by siderite and carbocearnite (Ku-98-130a). Orthomagmatic, interstitial calcites of samples Ku-98-14 (MnO: <0.08, SrO: 1.9-2.1), Ku-98-80 (MnO: <0.02, SrO: 1.6-2.2) and Ku-98-43a (MnO: 0.1-0.3, SrO: 0.4-0.7) are characterized by high Sr/Mn ratios (Fig. 14.5). Presumably also orthomagmatic is calcite from the brownish carbonate aggregates (MnO: 0.2-0.3, SrO: 0.7-0.8) of the REE-rich carbonatitic breccia Ku-98-130a (Fig. 14.5).

sample; wt.%	textural position	MgO	CaO	MnO	FeO	SrO	BaO	CO ₂	Sum
S, f									
Ku-98-59b	cracks, rims around	0.56	51.27	1.48	2.42	0.57	0.06	43.52	99.89
σ (N=48)	Mag, matrix	0.31	1.09	0.16	0.93	0.06	0.06	0.34	0.81
Kfs-Bt-Ilm-Cal rock									
Ku-98-25	inclusions in Bt	0.01	54.52	0.04	0.16	1.80	0.03	43.70	100.26
σ (N=8)		0.02	0.32	0.04	0.10	0.13	0.04	0.24	0.58
Ku-98-25	anhedral matrix grains	0.99	50.76	0.76	1.95	2.09	0.05	43.49	100.09
σ (N=10)		0.30	0.22	0.06	0.12	0.10	0.06	0.34	0.67
CB,so									
Ku-97-43a	anhedral matrix grains	0.03	54.31	0.19	0.99	0.51	0.04	43.61	99.68
σ (N=15)		0.04	0.48	0.07	0.11	0.08	0.04	0.43	0.99
Ku-98-80	anhedral matrix grains	0.00	53.43	0.01	0.08	1.66	0.00	42.69	97.86
σ (N=3)		0.00	0.11	0.01	0.06	0.25	0.00	0.09	0.31
CB,REE									
Ku-98-130a	brownish carbonate	0.12	54.31	0.23	0.37	0.76	0.14	43.49	99.42
σ (N=2)	aggregates	0.03	0.05	0.06	0.02	0.03	0.03	0.05	0.14
Ku-98-130a	anhedral matrix grains	0.20	51.69	0.91	2.95	0.67	0.07	43.46	99.95
σ (N=21)		0.55	4.71	0.31	4.13	0.60	0.06	0.57	0.98
CB,l									
Ku-98-14	anhedral matrix grains	0.00	52.86	0.05	0.10	2.00	0.06	41.03	98.82
σ (N=4)		0.00	0.54	0.03	0.07	0.04	0.07	0.37	0.97
Ku-98-56b	matrix overgrowths	0.08	53.23	1.28	0.79	0.96	0.03	43.56	99.93
σ (N=44)		0.08	0.61	0.13	0.27	0.19	0.04	0.34	0.80

Table 14.2: Average compositions of calcite from different samples and textural positions (σ standard deviation).

In clear contrast, anhedral matrix calcite of the *REE-rich carbonatitic breccia* Ku-98-130a, has comparably high MnO contents of 0.7-1.0 wt.% and intermediate SrO contents of 0.3-0.9 wt.%, well in accordance with a secondary origin of calcite during hydrothermal alteration (Fig. 14.5). Similar Sr/Mn ratios have been obtained for texturally late calcite of sample Ku-98-56b (MnO: 1.0-1.6 wt.%, SrO: 0.5-1.3 wt.%).

Calcite is the dominant mineral among carbonates in the *fenitized syenite*, where the carbonate occurs in cracks within feldspar and as rims around magnetite. With MnO contents of

1.2-1.8 wt.% and SrO contents of 0.5-0.6 wt.%, it has the lowest Sr/Mn of all calcites analysed, and is thus presumably of secondary origin (Fig. 14.5).

Calcite of the *K-feldspar-biotite-ilmenite-calcite rock* has been observed in two textural positions, (1) as inclusions in biotite and (2) as anhedral matrix grains. Calcite of both textures has constantly high SrO contents (1.6-2.2 wt.%) but quite variable MnO values, ranging between 0.0–0.1 wt.% in calcite inclusions and 0.7–0.9 wt.% in matrix grains. However, calcite of both generations is presumably of magmatic origin (Fig. 14.5).

14.1.3 Siderite-magnesite solid solution

Siderite was observed in the central parts of the brownish carbonate aggregates of the *REE-rich carbonatitic breccia*. Since siderite has grown close to calcite, only one reliable analysis was obtained, whereas all others revealed mixtures between calcite and siderite. Siderite is characterized by a high X_{Fe} of 0.81 and high MnO and CaO contents of 3.3 wt.% and 1.35 wt.%, respectively (Fig. 14.6), whereas Sr and Ba are below the detection limit. Siderite is suggested to be exsolved from a Fe-rich precursor carbonate (presumably calcite or ankerite) during cooling.

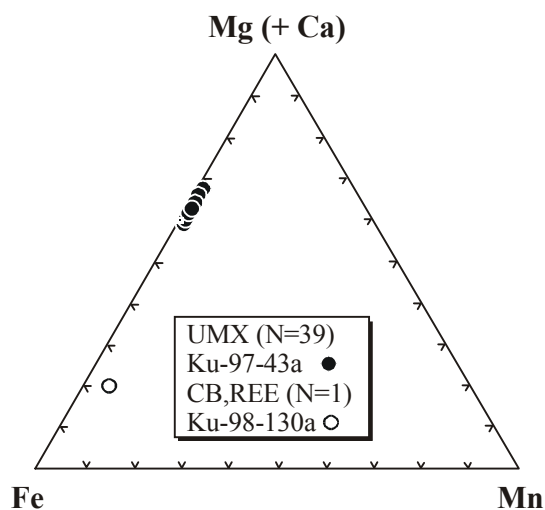


Fig. 14.6: Compositional variability of magnesite and siderite, expressed in the ternary diagram Mg(+Ca)-Fe-Mn. Note that both magnesite and siderite contain only minor Ca with respect to Mg.

Magnesite is a major constituent of the *fenitized ultramafic xenoliths*, where it is intimately associated with aegirine and magnesio-arfvedsonite. All magnesites analysed contain between 20-38 mol.% FeCO_3 and can thus be classified as breunnerite, the ferroan magnesite

variety (Fig. 14.6). The breunnerites contain only minor amounts of Sr and Ba, whereas MnO and CaO range between 0.7-1.1 % and 0.2-0.3 wt.% , respectively. All analysed breunnerites

sample; wt.%	textural position	MgO	CaO	MnO	FeO	SrO	BaO	CO ₂	Sum
CB,REE									
<i>Ku-98-130a</i>	carbonate aggregates	6.29	1.35	3.34	47.84	0.00	0.02	39.31	98.15
UMX									
<i>Ku-97-43a</i>	anhedral matrix grains	26.08	0.25	0.88	27.17	0.02	0.03	45.88	100.31
σ (N=39)		1.12	0.04	0.09	1.49	0.03	0.03	0.44	0.77

Table 14.3: Average compositions of members of the siderite-magnesite solid solution series (σ standard deviation).

exhibit a weak concentric zonation, with the MgO contents slightly decreasing from core towards the rim (X_{Mg} : 0.60-0.63 \rightarrow X_{Mg} : 0.64-0.68). The Mg-rich composition of the analysed magnesites strongly suggests their formation by alteration of former Fe-Mg silicates (presumably olivine or its alteration products), following the injection of CO₂-rich fluids of the carbonatite melt. Judging from the zonation patterns of breunnerites, these fluids must have contained certain amounts of Fe. The obtained results strongly suggest, that the fenitization of the ultramafic xenoliths was caused by the Fe-rich carbonatitic melts, which transported them into upper crustal levels.

14.1.3 Carbocernaite

Carbocernaite (Ca,Na)(Sr,Ce,La)(CO₃)₂ has been analysed in two REE-rich samples of the carbonatitic breccia (Ku-98-130a, Ku-98-130b). It has been distinguished from the chemically similar mineral burbankite (Na,Ca,Sr,Ba,Ce)₆(CO₃)₅ by X-ray diffraction and its stoichiometry, which is rather 6:6 than 6:5 regarding the cation:carbonate ratio.

The analysed carbocernaite grains (Table A.5.1.16 in the Appendix A.5.1) have a rather variable composition with the CaO and SrO contents ranging between 14.3-18.1 wt.% and 13.6-18.6 wt.%, respectively. In most cases the REE carbonates display oscillatory zoning patterns. Decreases of Ca and Sr in the analyses are generally accompanied by increases of the Na₂O (1.2-2.2 wt.%), Ce₂O₃ (15.1-20.1 wt.%) and La₂O₃ (10.7-14.4 wt.%) contents. The compositions of the analysed carbocernaite range from (Ca_{1.01}Na_{0.09}Sr_{0.58}Ba_{0.06}Ce_{0.15}La_{0.11})(CO₃)₂ and (Ca_{0.97}Na_{0.10}Sr_{0.50}Ba_{0.03}Ce_{0.23}La_{0.17})(CO₃)₂.

The chemistry of the analysed carbocernaite is in good agreement with that obtained by Wall et al. (1993) for carbocernaite exsolution lamellae in calcite in a REE-rich carbonatite dyke from Rajasthan, India. The close association of carbocernaite with calcite-siderite intergrowths might suggest that carbocernaite, like siderite, was exsolved from a high-REE precursor calcite, which additionally contained a certain amount of Fe. However, a cotectic crystallization of calcite and carbocernaite, followed by an exsolution of siderite-component of calcite can not yet be ruled out.

14.1.4 Strontianite

Strontianite is a rare mineral in the Swartbooisdrif carbonatitic breccia. It was observed as rims around carbocernaite in the marginal parts of the brownish carbonate aggregates of the REE-rich sample Ku-98-130a. The only reliable analysis of the very fine-grained strontianite (Table A.5.1.17 in the Appendix A.5.1) revealed exceptionally high CaO contents of 18.3 wt. %, which is equivalent to 42 mol.% CaCO₃. The relation of strontianite to the carbocernaite remains somewhat unclear, however, detailed EMP analysis and backscattered imagery on the conspicuous fine-grained carbonate aggregates is in progress.

14.2 Feldspar

Representative analyses of potassium feldspar and plagioclase are depicted in Table A.5.1.1 in the Appendix A.5.1.

14.2.1 Potassium feldspar

K-feldspar is a major orthomagmatic phase of the *nepheline syenite* (Ku-99-15a), where it forms large, subhedral grains. The feldspar grains exhibit strong perthitic exsolution, with a potassium feldspar host (Or₉₆₋₉₇), bearing plagioclase (Ab₉₈₋₁₀₀) exsolution lamellae (Fig. 14.7a). The An- and Ce-contents of both the K-feldspar host and the albite exsolution lamellae are generally below 0.5 mol.%. Due to the coarse grain sizes of the exsolution lamellae, reintegrating measurements with a broad, defocused beam yielded no reliable results.

Unexsolved potassium feldspar is the main constituent of the *K-feldspar-biotite-ilmenite-calcite rock*. The K-feldspar is characterized by a weak normal zonation, with both the Ab and the Ce contents increasing from core ($\text{Or}_{96.3}\text{Ab}_{3.7}\text{Ce}_{0.0}$ - $\text{Or}_{92.6}\text{Ab}_{4.9}\text{Ce}_{2.5}$) towards the rim ($\text{Or}_{91.1}\text{Ab}_{5.9}\text{Ce}_{3.0}$ - $\text{Or}_{86.0}\text{Ab}_{8.2}\text{Ce}_{5.8}$), whereas the An contents are generally below the detection limit (Fig. 14.7b).

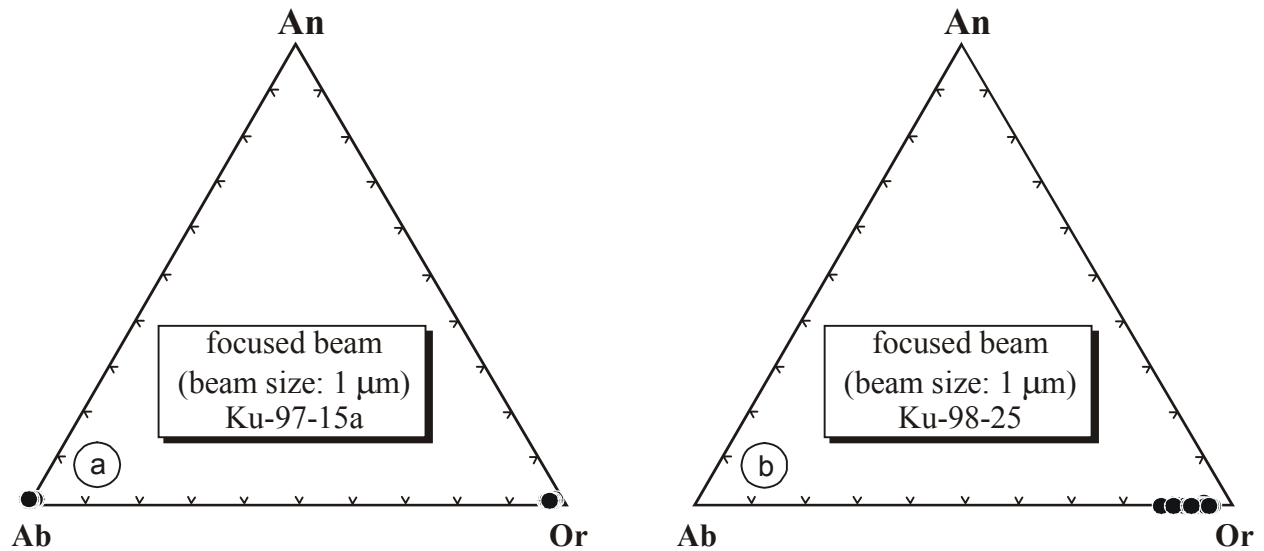


Fig. 14.7: Compositional variability of potassium feldspar of (a) the nepheline syenite and (b) the K-feldspar-biotite-ilmenite-calcite rock, expressed in the ternary diagram An-Ab-Or.

Feldspar relics of former microcline, observed in the *fenitized syenite* sample Ku-98-59b, are virtually pure albite. Despite the fact, that most feldspar fragments were extensively analysed, not one single K-feldspar analysis was obtained, suggesting that the fenitization of the syenite resulted in a complete replacement of K-feldspar by chess-board albite.

14.2.2 Plagioclase

Metasomatically formed feldspar from the *fenitized syenite*, the *carbonatitic breccia* and the late *ferrocarbonatite veins* is almost pure, homogeneous albite (Ab_{99-100} ; Table 14.4). The same compositional range was obtained for albite inclusions in pyrochlore of the ferrocarbonatite veins (Table 14.4). The homogeneity of the values is striking, hence suggesting that all above mentioned lithologies must have re-equilibrated with large amounts of Na-rich fluids, expelled by the carbonatite magma.

sample	SiO ₂	Al ₂ O ₃	CaO	FeO	BaO	Na ₂ O	K ₂ O	Sum	An	Ab	Or	Ce
CB,so												
<i>Ku-97-15</i>	68.77	20.08	0.02	0.07	0.02	11.66	0.07	100.68	0.12	99.48	0.37	0.03
σ (N=33)	0.61	0.32	0.03	0.06	0.02	0.15	0.03	0.77	0.14	0.19	0.16	0.04
<i>Ku-98-57a</i>	67.76	19.55	0.05	0.21	0.02	11.65	0.04	99.31	0.23	99.50	0.24	0.03
σ (N=38)	0.83	0.24	0.05	0.83	0.03	0.15	0.02	0.50	0.21	0.21	0.10	0.05
<i>Ku-98-80</i>	69.02	20.25	0.03	0.29	0.03	11.50	0.07	101.20	0.16	99.38	0.41	0.05
σ (N=28)	0.45	0.31	0.03	0.33	0.03	0.11	0.02	0.57	0.16	0.22	0.13	0.05
<i>Ku-98-131</i>	69.18	20.21	0.03	0.08	0.03	11.45	0.07	101.13	0.13	99.41	0.41	0.05
σ (N=14)	0.79	0.30	0.02	0.17	0.02	0.24	0.02	0.73	0.09	0.12	0.09	0.03
<i>Ku-99-05</i>	67.79	19.41	0.04	0.11	0.03	11.57	0.06	99.02	0.17	99.45	0.32	0.05
σ (N=21)	0.25	0.11	0.03	0.04	0.03	0.12	0.02	0.33	0.15	0.22	0.14	0.05
CB,REE												
<i>Ku-98-130a</i>	68.26	20.15	0.02	0.04	0.01	11.56	0.05	100.10	0.10	99.60	0.30	0.01
σ (N=2)	0.64	0.07	0.02	0.01	0.01	0.17	0.01	0.70	0.08	0.15	0.05	0.01
CB,l												
<i>Ku-98-14</i>	67.28	19.35	0.03	0.11	0.02	11.60	0.06	98.47	0.16	99.46	0.34	0.04
σ (N=24)	0.35	0.14	0.06	0.09	0.03	0.17	0.02	0.47	0.29	0.29	0.13	0.05
<i>Ku-98-48</i>	68.95	20.27	0.03	0.18	0.02	11.52	0.09	101.07	0.14	99.30	0.52	0.04
σ (N=18)	0.60	0.35	0.03	0.18	0.02	0.26	0.02	0.88	0.13	0.21	0.14	0.04
<i>Ku-98-56</i>	68.78	20.22	0.01	0.02	0.00	11.73	0.05	100.82	0.03	99.68	0.29	0.00
FV												
<i>Ku-01-04</i>	67.64	19.45	0.04	0.18	0.02	11.56	0.05	98.95	0.18	99.49	0.30	0.00
σ (N=15)	0.61	0.25	0.02	0.18	0.02	0.19	0.02	0.54	0.11	0.09	0.10	0.00
S, f												
<i>Ku-98-59b</i>	68.05	20.23	0.06	0.05	0.03	11.50	0.06	99.99	0.30	99.32	0.33	0.05
σ (N=139)	0.78	0.39	0.07	0.08	0.03	0.31	0.04	0.87	0.36	0.41	0.21	0.06
A, f												
<i>Ku-99-02</i>	68.63	20.25	0.06	0.03	0.06	11.39	0.05	100.49	0.28	99.34	0.27	0.10
σ (N=13)	0.59	0.29	0.05	0.02	0.04	0.17	0.03	0.74	0.24	0.27	0.15	0.07
<i>Ku-98-71</i>	68.29	20.33	0.32	0.09	0.14	11.46	0.03	100.68	1.52	98.06	0.18	0.25
<i>Ku-98-71</i>	66.68	19.95	1.92	0.14	0.00	11.87	0.01	100.56	8.19	91.77	0.05	0.00
<i>Ku-98-79</i>	63.17	22.17	3.04	1.09	0.08	8.69	0.02	98.30	16.13	83.59	0.13	0.15
<i>Ku-98-79</i>	63.73	22.32	3.37	0.10	0.00	8.84	0.10	98.49	17.29	82.08	0.63	0.00
<i>Ku-98-79</i>	66.79	20.88	1.33	0.03	0.04	9.92	0.03	99.01	6.88	92.87	0.18	0.07
<i>Ku-98-79</i>	68.22	20.40	0.74	0.05	0.04	10.23	0.05	99.72	3.82	95.82	0.29	0.07

Table 14.4: Average compositions of plagioclase (σ standard deviation).

Magmatic plagioclase (An₃₇₋₇₅) of the *fenitized anorthosites* (Ku-98-71, Ku-98-79) bordering the carbonatitic breccia is replaced, to an increasing extent, by sodium-rich plagioclase (An₁₋₁₇). At the direct contact to the carbonatite dykes, fenitization reached pervasive extent. In the anorthositic fenite sample Ku-99-02, taken from a foliated contact zone, the magmatic plagioclase is completely transformed into homogeneous and virtually pure albite (Ab₉₉₋₁₀₀; Table 14.4).

During the transformation of both, potassium feldspar of the syenite and of plagioclase of the anorthosite into almost pure albite, appreciable amounts of K and Ca must have been released, which most probably account for the close association of albite and muscovite in the fenitized syenite and of albite and carbonate in the fenitized anorthosite.

14.3 Nepheline

Euhedral to subhedral nepheline is a major constituent of the *nepheline syenite*, whereas anhedral, metasomatically formed nepheline is an accessory phase. Formulae of nepheline were calculated on a basis of 32 oxygens (Table A.5.1.18 in the Appendix A.5.1).

The analysed compositions of magmatic nepheline are in the range of $\text{Ne}_{68.4}\text{Ks}_{19.1}\text{Qtz}_{12.5}$ to $\text{Ne}_{73.6}\text{Ks}_{18.6}\text{Qtz}_{7.8}$. In most cases the grains display a continuous growth zonation, with SiO_2 decreasing towards the rim (Fig. 14.8). When approaching the outermost margins or cracks nepheline is significantly richer in the Ne component ($\text{Ne}_{73.1}\text{Ks}_{21.4}\text{Qtz}_{5.5}$ – $\text{Ne}_{80.3}\text{Ks}_{11.2}\text{Qtz}_{8.5}$).

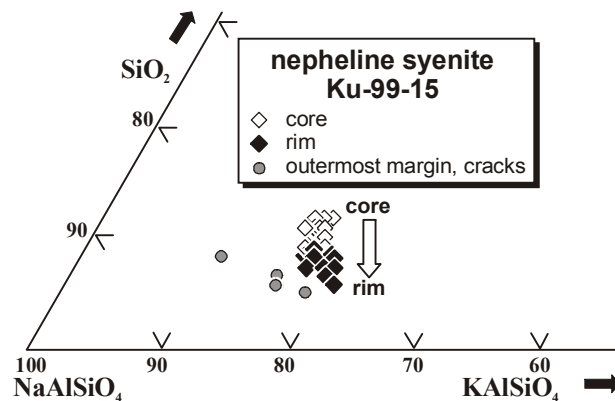


Fig. 14.8: Compositional variability of nepheline from the nepheline syenite, expressed in the ternary diagram SiO_2 - NaAlSiO_4 - KAlSiO_4 .

These chemical variations suggest an interaction between the nepheline-syenite and the Na-rich and Si-deficient carbonatite magma. Since both, the petrographical observations and the analyses of the nepheline mineral chemistry point to continuous nepheline growth, it might be possible that Na was introduced to the system before nepheline was fully crystallized, hence pointing to a contemporaneous carbonatite-nepheline syenite emplacement.

Remarkably, secondary, metasomatically formed nepheline differs significantly from those of magmatic origin in containing significant amounts of Ca (1.0-1.5 a.p.f.u.) in addition to Na (6.5-6.9 a.p.f.u.), but only minor amounts of K (0.1-0.2 a.p.f.u.). Presumably, secondary nepheline was formed instead of cancrinite by the interaction between magmatic nephelines and the Na- and Ca-rich carbonatitic magma.

14.4 Sodalite

In the Swartbooisdrif area, sodalite occurs in different rock types and textural positions, i.e. (1) in the *fenitized wallrock anorthosite*, replacing plagioclase, (2) as a replacement product of nepheline in the *nepheline syenites*, (3) as replacement product of feldspar-rich anorthositic wallrock fragments, incorporated by the *carbonatitic breccia*, (4) in the late *ferrocarbonatite veins*, replacing albite-xenocrysts and, quite less common, (5) in the *fenitized syenite*, replacing chess-board albite. The sodalites from the different rock types have been analysed with the help of EMP analysis. In order to prevent migration of sodium during electron bombardment, sodalite has been measured with a broad beam of 10 μm across. Sodalite formulae were calculated on the basis of 24 oxygens, assuming charge balance. Representative analyses are listed in Table A.5.1.19 in the Appendix A.5.1, average analyses are provided in Table 14.5.

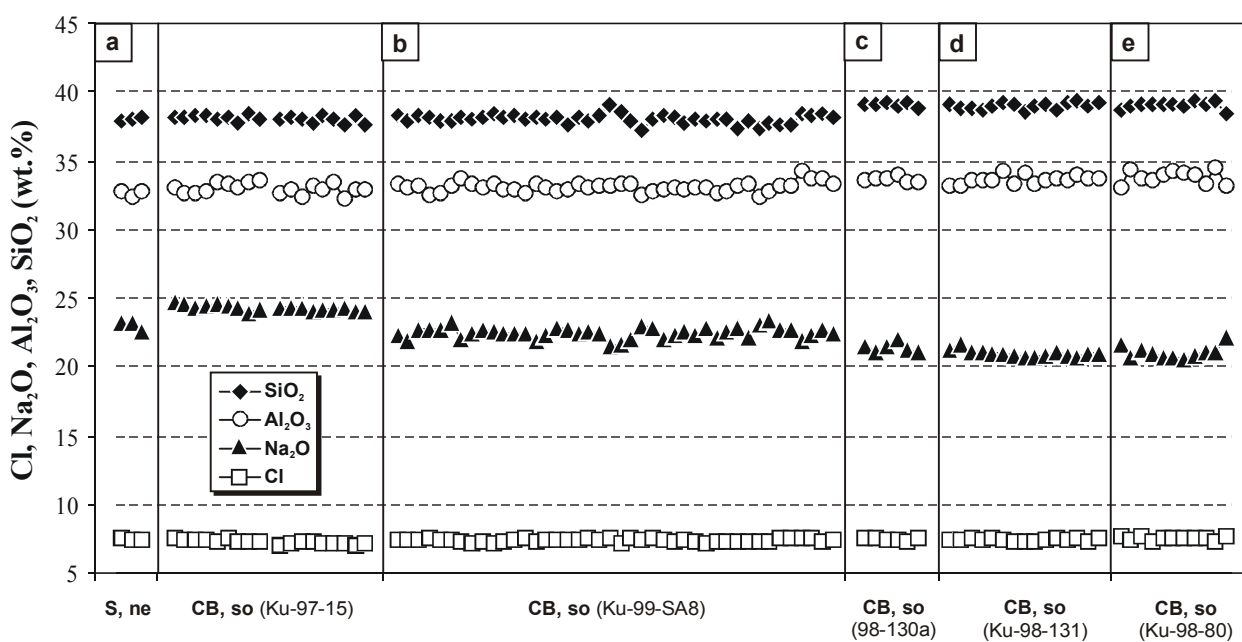


Fig. 14.9: Zoning patterns of sodalite from the nepheline syenite (*a*) and the sodalite-rich carbonatitic breccia (*b-e*).

Sodalite of all rock units is the almost pure sodalite endmember, generally displaying Fe_2O_3 , CaO , K_2O , S and F contents <0.1 wt.%. However, most of the analysed sodalites deviate from the ideal sodalite composition $\text{Na}_8[\text{Cl}_2(\text{AlSiO}_4)_6]$ in containing too low Na and too high Si and Al, with the sodalite formulae ranging between $\text{Na}_{7.0}[\text{Cl}_{2.0}(\text{Al}_{6.2}\text{Si}_{6.1}\text{O}_{24})]$ and $\text{Na}_{7.3}[\text{Cl}_{2.0}(\text{Al}_{6.2}\text{Si}_{6.0}\text{O}_{24})]$ in the nepheline syenite and between $\text{Na}_{6.3}[\text{Cl}_{2.0}(\text{Al}_{6.4}\text{Si}_{6.2}\text{O}_{24})]$ and $\text{Na}_{7.7}[\text{Cl}_{2.0}(\text{Al}_{6.1}\text{Si}_{6.0}\text{O}_{24})]$ in the carbonatitic breccia. Remarkably, both Si and Al apparently increase with decreasing Na, whereas Cl remains constant (Fig. 14.9).

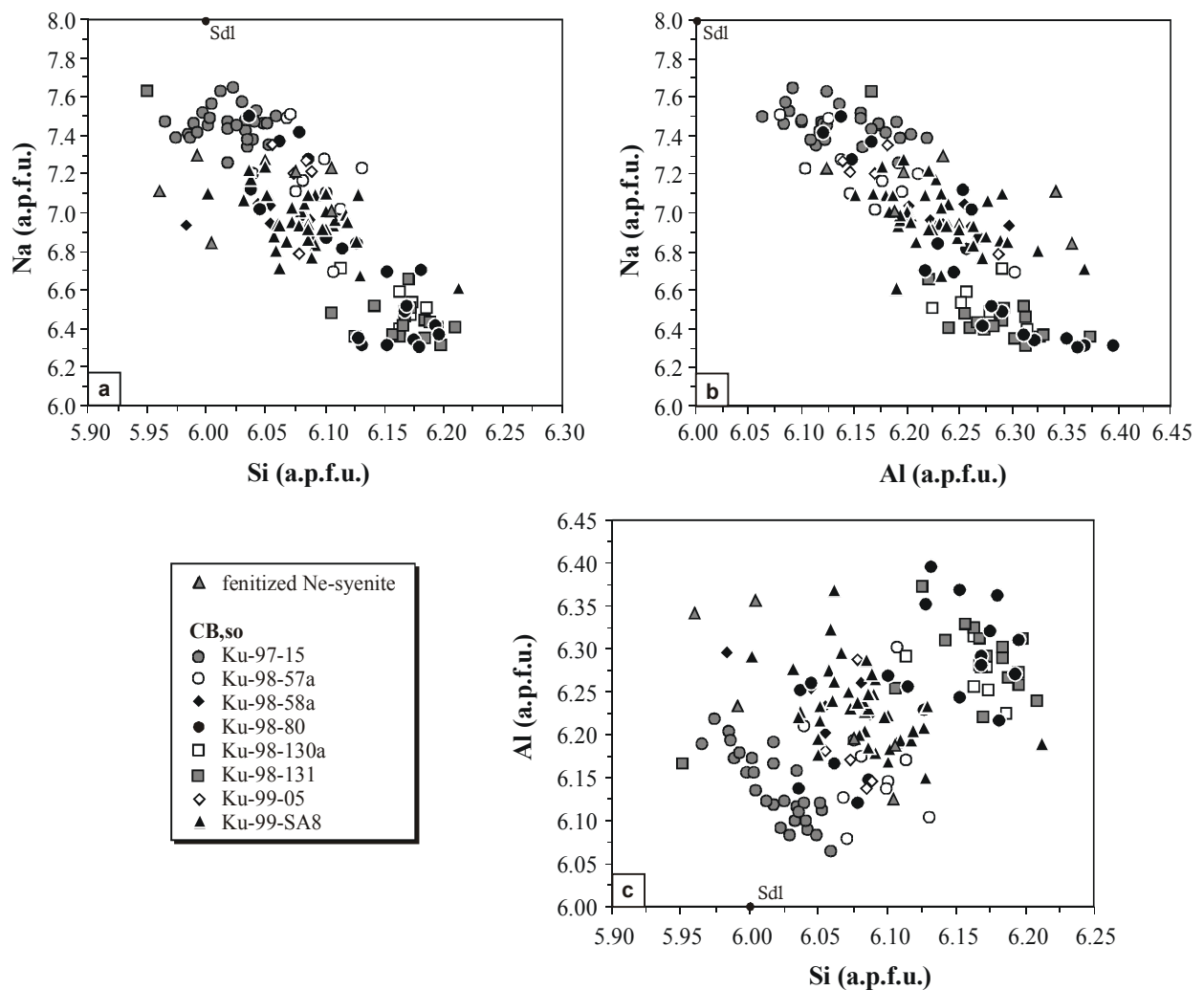
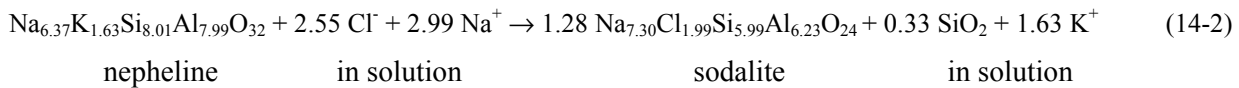
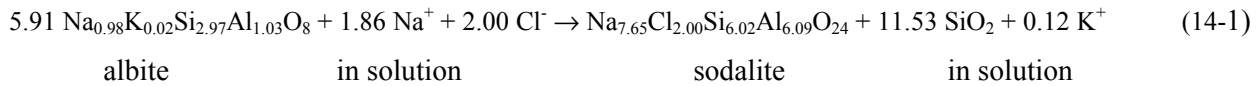


Fig. 14.10: Correlation patterns of Na, Si and Al p.f.u. (formula calculation based on 24 oxygens) in sodalite. **a)** Si against Na. **b)** Al against Na. **c)** Si against Al. *Sdl* marks ideal sodalite composition.

Such a crystal chemical behaviour has so far never been observed for natural sodalites. The apparent negative correlation of Na with both Al and Si (Fig. 14.10) may thus be related to the conspicuous crystallization history of sodalite, i.e. its subsolidus formation at the expense of albite under Si-deficient conditions. It may be possible, that albite was not completely transformed into sodalite during fenitization, depending on the fluid:rock ratio and the local

availability of Na, Si and Al. This possibility, however, has to be examined with the help of detailed TEM studies.

The transformation of albite of the fenitized anorthosites and syenites and of nepheline of the nepheline syenites into sodalite necessitates the introduction of large amounts of NaCl, whereas Si and K will be released, as is evidenced by the following two reactions (balanced for Al):



The release of K and SiO₂ during the sodalitization of nepheline may account for the close spatial association of sodalite and muscovite in the nepheline syenite, whereas it remains

sample	SiO ₂	Al ₂ O ₃	Fe ₂ O ₃	CaO	Na ₂ O	K ₂ O	Cl	F	S	Total	O-Cl,S,F	Sum
CB,so												
Ku-97-15	38.03	32.92	0.03	0.02	24.31	0.02	7.30	0.00	0.02	102.65	1.68	100.97
σ (N=28)	0.24	0.35	0.03	0.02	0.22	0.02	0.14	0.00	0.03	0.53	0.05	0.52
Ku-97-43a	39.05	32.68	0.02	0.04	22.36	0.03	7.15	0.05	0.01	101.39	1.65	99.74
σ (N=4)	0.98	0.13	0.03	0.02	0.29	0.01	0.13	0.08	0.01	0.65	0.05	0.69
Ku-98-130a	39.21	33.95	0.03	0.02	21.13	0.03	7.47	0.04	0.01	101.89	1.72	100.17
σ (N=8)	0.38	0.58	0.02	0.02	0.67	0.02	0.07	0.05	0.01	0.56	0.03	0.54
Ku-98-131	38.92	33.64	0.05	0.02	21.17	0.01	7.42	0.04	0.02	101.29	1.72	99.57
σ (N=19)	0.40	0.33	0.17	0.02	0.89	0.03	0.10	0.05	0.02	0.53	0.04	0.53
Ku-98-57a	38.17	32.68	0.04	0.02	23.09	0.01	7.42	0.06	0.01	101.50	1.72	99.78
σ (N=11)	0.49	0.54	0.03	0.02	0.58	0.01	0.14	0.07	0.01	0.50	0.05	0.48
Ku-98-58a	38.16	33.42	0.31	0.02	22.69	0.04	7.47	0.05	0.01	102.16	1.72	100.44
σ (N=6)	0.19	0.24	0.21	0.02	0.16	0.02	0.07	0.05	0.01	0.45	0.02	0.46
Ku-98-80	38.58	33.44	0.01	0.01	21.87	0.02	7.55	0.04	0.02	101.55	1.74	99.81
σ (N=21)	0.59	0.69	0.02	0.02	1.11	0.01	0.11	0.05	0.01	0.46	0.04	0.47
Ku-99-05	38.03	32.23	0.02	0.01	22.51	0.06	7.15	0.09	0.01	100.12	1.67	98.45
σ (N=7)	0.89	0.51	0.02	0.01	0.73	0.01	0.20	0.06	0.01	0.29	0.05	0.28
Ku-99-SA8	38.05	33.09	0.03	0.02	22.49	0.03	7.37	0.03	0.01	101.12	1.69	99.43
σ (N=42)	0.35	0.35	0.03	0.01	0.39	0.01	0.12	0.05	0.01	0.45	0.04	0.45
S, f												
Ku-98-59b	38.68	33.58	0.17	0.02	22.95	0.03	7.30	0.05	0.01	102.78	1.68	101.09
σ (N=2)	0.26	0.06	0.03	0.01	1.95	0.01	0.07	0.05	0.01	2.09	0.01	2.10
S, ne												
Ku-99-15a	37.87	33.20	0.01	0.04	23.02	0.01	7.40	0.03	0.01	101.62	1.71	99.91
σ (N=6)	0.18	0.59	0.02	0.03	0.52	0.01	0.07	0.06	0.01	0.59	0.03	0.59

Table 14.5: Average compositions of sodalite (σ standard deviation).

unclear what happened to SiO₂, released during the sodalitization of albite in all other rock types. In the investigated samples of the fenitized wallrock lithologies, the carbonatitic breccia and the late ferrocarbonatite veins, free quartz has never been observed. Two explanations may account for this observation: (1) SiO₂ is incorporated into other silicate phases (i.e. biotite, cancrinite, muscovite) formed during the fenitization, or (2) SiO₂ was removed into higher and not exposed crustal levels.

14.5 Cancrinite group

Na-Ca feldspathoids, which, based on their optical properties, have been assigned to the cancrinite group occur sporadically in both the *carbonatitic breccia* and the fenitized *nepheline syenite*, where they formed as an alteration product of albite and nepheline, respectively. Formulae were calculated on an anhydrous 24-oxygen basis (Table A.5.1.20 in the Appendix A.5.1). Remarkably, all analysed Na-Ca feldspathoids deviate significantly from the ideal cancrinite formula (Na,Ca)₇₋₈[Al₆Si₆O₂₄](CO₃,SO₄,Cl)_{1.5-2.0}·1-5H₂O in containing variable but generally too low amounts of Na, which apparently increase with decreasing Si (Fig. 14.11).

The calculated formulae of the Ca-Na feldspathoids range between Na_{4.0}Ca_{0.9}K_{0.2}[Al₆Si₆O₂₄] (nepheline syenite) and Na_{2.2}Ca_{1.0}[Al₆Si_{6.5}O₂₄] (carbonatitic breccia). Regarding their chemical characteristics (e.g. deficiencies of 9-11 wt.% in the total sums of analyses, not calculating CO₂ and H₂O; Si/Al ratios of ~ 1:1) the phases resemble selected members of the zeolite group, such as thomsonite; however, their uniaxial and optically negative character as well as their granular morphology strongly argue against this possibility. From the chemically similar mineral nepheline the Ca-Na feldspathoids have been distinguished by optical properties (stronger birefringence), low totals of analyses (89-91 wt.%) and higher SO₃- and Cl- contents of up to 0.5 wt.% and up to 0.6 wt.%, respectively.

It can thus be concluded that either (1) the Ca-Na feldspathoids represent a yet unknown, low-Na member of the cancrinite-group or, more likely, (2) the conspicuous compositions are caused by submicroscopic intergrowths between cancrinite and at least a second phase, which contains higher Si and lower Na (such as albite and/or analcite). By now, possibility (2) is the preferred model, since the apparent negative correlation of Si and Na is quite untypical of

feldspathoids, which, on the contrary, are generally characterized by substitution of the type $\text{NaSi} \leftrightarrow \text{CaAl}$ (Fig. 14.11).

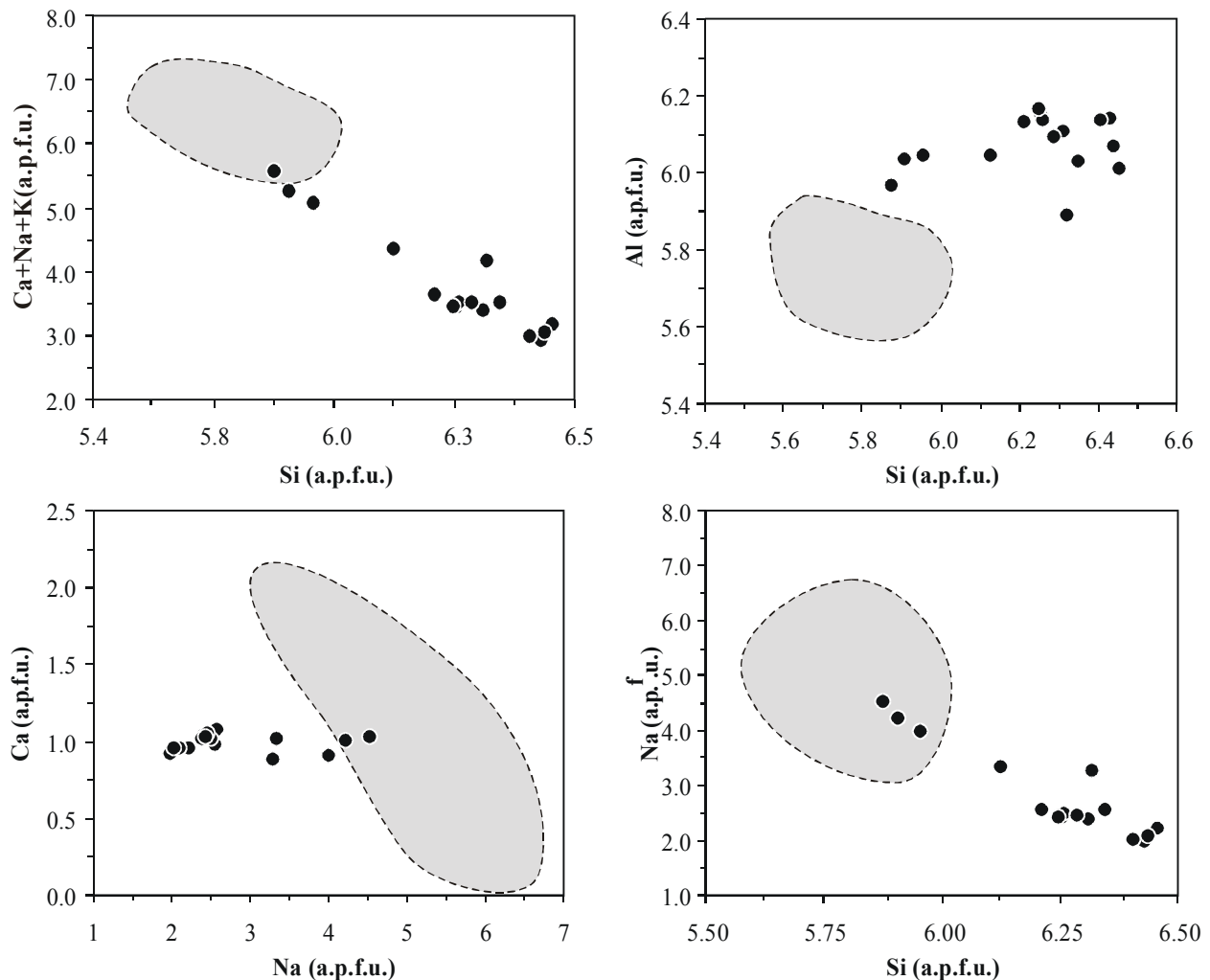
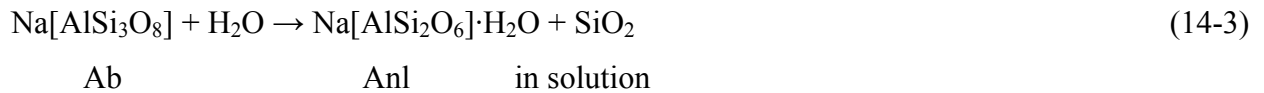


Fig. 14.11: Correlation patterns of Si, Na, Ca, K and Al p.f.u. (formula calculation based on 24 oxygens) in the Ca-Na feldspathoids (black dots). Compositional ranges of members of the cancrinite-vishnevite series (grey shaded fields), summarized by Deer et al. (1963) are illustrated for comparison

14.6 Analcite

Analcite (general formula $\text{Na}[\text{AlSi}_2\text{O}_6] \cdot \text{H}_2\text{O}$) has been observed in the *finitized syenite* Ku-98-59b, where it replaces metasomatically formed albite. Analcite formulae have been calculated on a basis of 7 oxygens. Due to the small grain sizes of analcite only a few reliable analyses were obtained, which are listed in Table A.5.1.21 in the Appendix A.5.1.

The analysed analcites have an almost ideal composition. The amounts of K_2O , CaO and Na_2O are generally near the detection limit. The metasomatic formation of analcite at the expense of albite can be written as:



The reaction constrains the interaction of syenite with Si-deficient, Na-rich hydrous fenitizing fluids, most probably released by the carbonatite melt.

14.7 Aegirine

Clinopyroxene has been analysed in the *fenitized ultramafic xenoliths*, where it is intimately associated with magnesio-arfvedsonite and breunnerite. The calculation of the pyroxene formula followed the method of Papike & Cameron (1980) on the basis of 8 oxygens. For the estimation of the Fe^{3+} contents a calculation modulus on the basis of 4 cations was chosen. Representative analyses are listed in Table A.5.1.22 in the Appendix A.5.1.

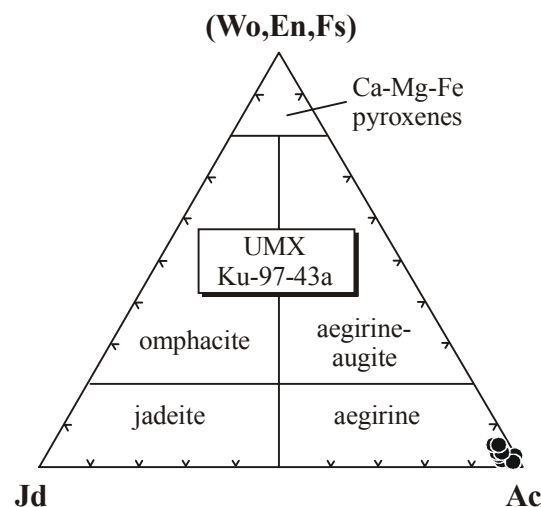


Fig. 14.12: Compositional variability of clinopyroxene from the fenitized ultramafic xenolith, expressed in the ternary diagram Jd ($NaAlSi_2O_6$) – Ac ($NaFe^{3+}Si_2O_6$) – (Wo,En,Fs)((Ca,Mg,Fe) $_2Si_2O_6$).

Following the classification of Morimoto (1988) all clinopyroxenes of the fenitized ultramafic xenoliths are aegirine, next to a pure aegirine composition (Fig. 14.12). The Jd content of the aegirines is generally below 3.3 mol.%, whereas the amounts of (En+Fs+Wo) may reach up to 5.6 mol.%.

The analysed aegirines are most probably not a primary magmatic constituent of the ultramafic xenoliths, but were formed during fenitization, which additionally led to the replacement of olivine by magnesite and to the formation of hydrous Fe-Mg silicates (biotite and amphibole).

14.8 Amphibole

Minor bluish amphibole occurs in both the fenitized anorthosites and in the fenitized ultramafic xenoliths. The structural formula of amphibole was calculated on an anhydrous 23-oxygen basis (Table A.5.1.4 in the Appendix A.5.1). For the estimation of minimum and maximum Fe^{3+} contents a calculation modus on the basis $\Sigma\text{Na}=15$ and $\Sigma\text{Mn}=13$, respectively, was chosen (Spear & Kimball, 1984). The average Fe^{3+} contents were calculated as mean value between the two extreme compositions, following the method of Papike et al. (1974), modified by Franz & Häussinger (1990). Amphiboles from both rock suites can be classified as sodic amphiboles in the sense of Leake et al. (1997).

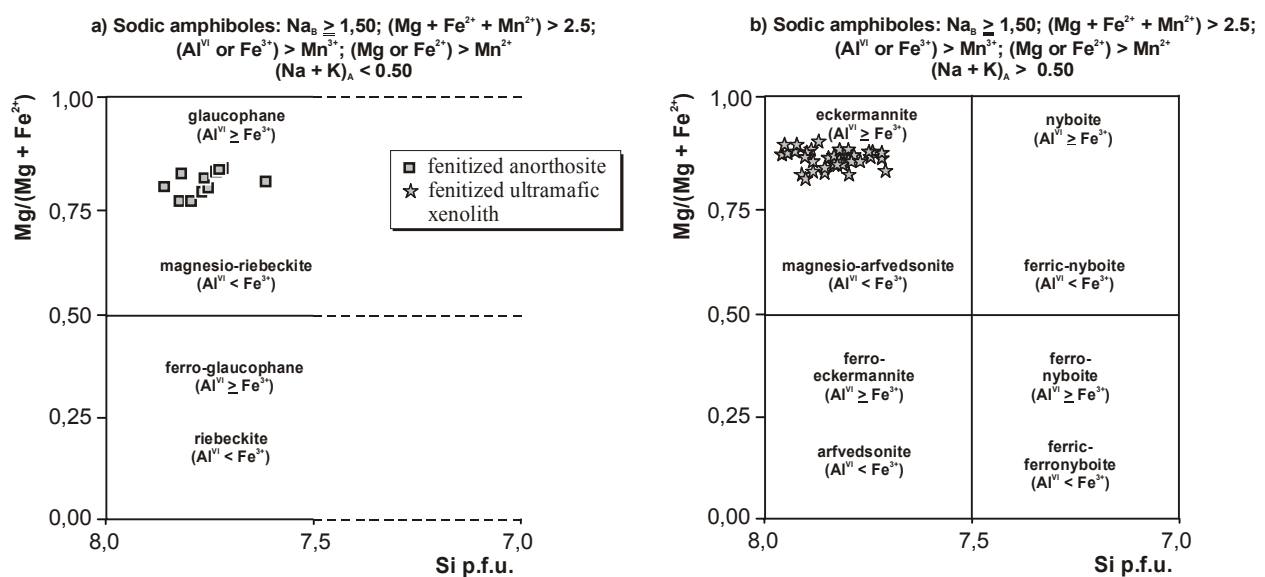


Fig. 14.13: Compositional variability of sodic amphibole from the fenitized anorthosite (a) and the fenitized ultramafic xenoliths (b), expressed in the classification diagram of Leake et al. (1997).

Following Leake et al. (1997) sodic amphiboles from the *fenitized anorthosite* (Ku-98-71), sampled in ~20 cm distance from the contact with a large dyke of the sodalite-rich carbonatitic breccia, are magnesio-riebeckites (Fig. 14.13a). The Si contents of the amphiboles are variable (Si p.f.u.: 7.4-7.9), whereas the X_{Mg} is relatively constant (X_{Mg} : 0.75-0.82). The

formation of the magnesio-riebeckites at the expense of unhydrous Fe-Mg silicates (presumably pyroxene) most probably results from the injection of Na-rich, hydrous and oxidising fluids, released by the intruding carbonatite magma. The fact, that sodic amphibole is lacking in anorthositic rocks in direct contact to the carbonatites, which, in contrast, contain abundant biotite, is taken as evidence for a chemical zonation of the fenitic aureoles with respect to Na and K.

Sodic amphiboles, which together with aegirine and magnesite, constitute the fine-grained matrix of the *fenitized ultramafic xenoliths*, are magnesio-arfvedsonites (Fig 14.13b). The amphiboles are characterized by high Si (Si p.f.u.: 7.7-8.0) and Na contents (Na p.f.u.: 2.1-2.6) and a high X_{Mg} of 0.81-0.89. The intimate association of magnesio-arfvedsonite with secondary magnesite suggests a secondary formation of the amphibole, caused by interactions between the xenoliths and Na- and H₂O-rich fluids.

14.9 White mica

Microprobe analyses were carried out for muscovite from the *fenitized syenite*, the *fenitized nepheline syenite* and the *carbonatitic breccia*. Muscovite formulae were calculated on an anhydrous basis of 22 oxygens. Representative analyses are depicted in Table A.5.1.23 in the Appendix A.5.1.

As shown in Fig. 14.14, the compositional variation of the analyzed white micas from the fenitized nepheline syenite and the carbonatitic breccia is in excellent agreement with a Tschermak's substitution mechanism ($Al^{IV} + Al^{IV} = R^{2+} + Si^{4+}$), even though micas from the carbonatitic breccia generally plot below this line, indicating an increased substitution of Fe³⁺ for Al^{VI}. In clear contrast, the trend displayed by data points of white mica of the fenitized syenite rather implies edenite exchange ($NaAl^{IV}O_{.1}Si_{.1}$; "o" = vacancy).

The analysed white micas display significant differences in their composition depending on the respective rock type. White micas of the carbonatitic breccia (Si p.f.u. 5.91-6.07, Fe p.f.u.: 0.02-0.31, Na p.f.u.: 0.02-0.34) are generally characterized by higher Na and Fe contents when compared to those of the fenitized nepheline syenite (Si p.f.u. 5.93-5.99, Fe p.f.u.: 0.01-0.09, Na p.f.u.: 0.03-0.09) and the fenitized syenite (Si p.f.u. 5.74-6.06, Fe p.f.u.: 0.02-0.19, Na p.f.u.:

0.02-0.09). The white micas are characterized by a high X_{Fe} , ranging between 0.67 and 0.95 (carbonatitic breccia), 0.55 and 1.00 (fentitized syenite) and 0.83-1.00 (fentitized nepheline syenite). Chlorine and fluorine contents of all white micas analysed are generally below the detection limit.

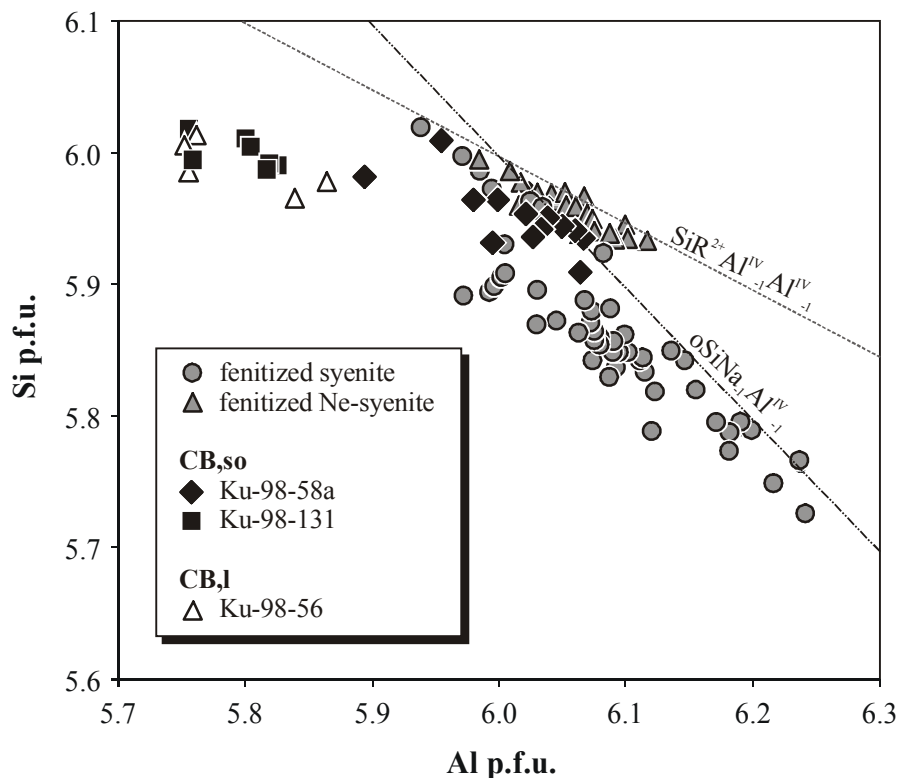


Fig. 14.14: Variation of Si versus Al in white micas of the fenitized syenite, the fenitized nepheline syenite and the carbonatitic breccia.

Following the classification of Schliestedt (1980) the composition of the analysed white micas is muscovite-dominated, with variable amounts of the paragonite and the celadonite components, which, however, are more prominent in white micas of the carbonatitic breccia (Fig. 14.15). The differences in the Na and Fe-contents between muscovites from the carbonatitic breccia and those of the fenitized syenite and the fenitized nepheline syenite may be explained by their different crystallization histories. Judging from its textural position, muscovite from the nepheline syenite and the syenite crystallized synchronously with the Na-fractionating phases sodalite and albite, respectively. In clear contrast, muscovite from the carbonatitic breccia clearly post-dates albite and sodalite and thus may have incorporated the maximum possible amount of Na available in the respective stage of metasomatism.

In one sample of the layered carbonatitic breccia (Ku-98-14), white mica has a somewhat unusual composition, deviating significantly from that of muscovite. The micas contain large amounts of Na_2O (1.16-1.19 a.p.f.u.) and minor Ba (0.1 a.p.f.u.), both substituting K (0.67-0.75 a.p.f.u.). Remarkably, these micas plot in the compositional gap of muscovite-paragonite solid solution in the ternary diagram paragonite-muscovite-celadonite after Schliestedt (1980; Fig. 14.15). The conspicuous apparent composition of the white mica could be caused by submicroscopic changes in its interlayer occupations, that are predominantly occupied by either Na or K. This interpretation, however, has to be examined with the help of detailed TEM studies.

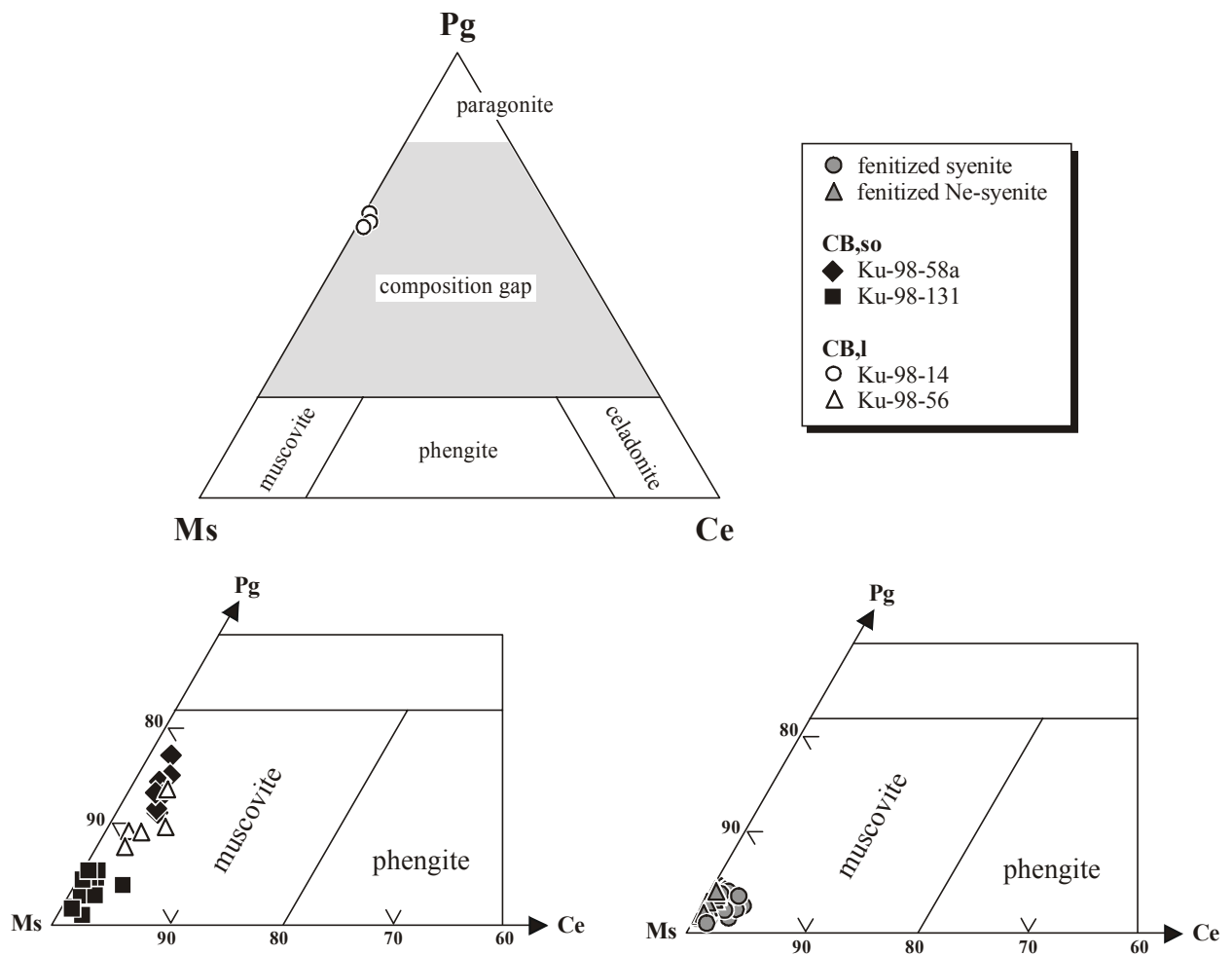


Fig. 14.15: Classification of metasomatically formed white micas in the study area, expressed in the paragonite-muscovite-celadonite diagram according to Schliestedt (1980).

14.10 Biotite

Biotite is a major constituent of the fenitized anorthosite, the carbonatitic breccia and the fenitized ultramafic xenoliths. Moreover biotite occurs as a minor orthomagmatic phase in

nepheline syenite. Biotite formulae were calculated on an anhydrous 22-oxygen basis. Representative analyses are depicted in Table A.5.1.5 in the Appendix A.5.1.

The analysed biotites display considerable compositional variations, between both rock types and individual samples and were thus subdivided into the following seven groups:

- metasomatically formed biotite from sodalite-biotite-assemblages of xenoliths of the fenitized anorthosite incorporated by the *sodalite-rich carbonatitic breccia* (Bt1),
- magmatic biotite in intimate association with apatite in samples of the *sodalite-rich carbonatitic breccia* (Bt2),
- magmatic biotite associated with apatite in sodalite-free samples of the *layered carbonatitic breccia* (Bt3)
- metasomatically formed biotite from the *fenitized syenite* (Bt4)
- orthomagmatic biotite from the *nepheline syenite* (Bt5) and
- metasomatically formed biotite from biotite-ankerite patches and schlieren of the *fenitized ultramafic xenoliths* (Bt6)
- orthomagmatic biotite from the *K-feldspar-biotite-ilmenite-calcite rock* (Bt7).

In assemblage (1), where biotite from the *carbonatitic breccia* coexists with sodalite, X_{Mg} clusters around 0.43 (X_{Mg} : 0.37-0.60) whereas the biotite in assemblage (2) and (3) exhibits average X_{Mg} values of 0.49 (0.44-0.57) and 0.44 (0.37-0.52), respectively. All biotites are characterized by high Ti contents (Bt1: Ti p.f.u.: 0.23-0.32; Bt2: Ti p.f.u.: 0.12-0.38 and Bt3: Ti p.f.u.: 0.16-0.41) and minor oscillatory to concentric zoning, involving a core preference for Al, whereas the rim trends to higher Si, pointing to a progressively lower availability of Al in the carbonatite magma. Decreases in Al are accompanied by increases of the X_{Mg} , suggesting that Fe was consumed during the synchronous crystallization of magnetite. Following the modified classification diagram of Foster (1960, in Tröger, 1982) the biotites are meroxenes to lepidomelanes (Fig. 14.16). The fact, that most of the magmatic biotites, coexisting with apatite in the carbonate-rich zones, plot slightly below the meroxene and lepidomelane fields is taken as evidence for elevated Fe^{3+} contents of the micas when compared to those coexisting with sodalite in the xenolith-rich zones. This interpretation is confirmed by Al-deficiencies of the tetrahedral position of the biotites which may be compensated by either Ti or Fe^{3+} .

Metasomatically formed biotite from the *fenitized syenite* (Bt4) is lepidomelane with patchy zonation (Ti p.f.u.: 0.15-0.34; Fig. 14.17a). The X_{Mg} attains comparably low values of

0.26-0.39, reflecting the Fe-rich composition of the primary magmatic Fe-Mg silicates (pyroxene and amphibole), which were replaced by biotite during the metasomatic alteration of the syenites. Magmatic biotites from the *nepheline syenite* (Bt5) are unzoned meroxenes to lepidomelanes (X_{Mg} : 0.50-0.57; Ti p.f.u.: 0.23-0.26; Fig. 14.17b) whereas magmatic biotites from the *K-feldspar-biotite-ilmenite-calcite rock* (Bt7) are unzoned meroxenes (X_{Mg} of 0.61-0.63; Ti p.f.u.: 0.31-0.36; Fig. 14.17c).

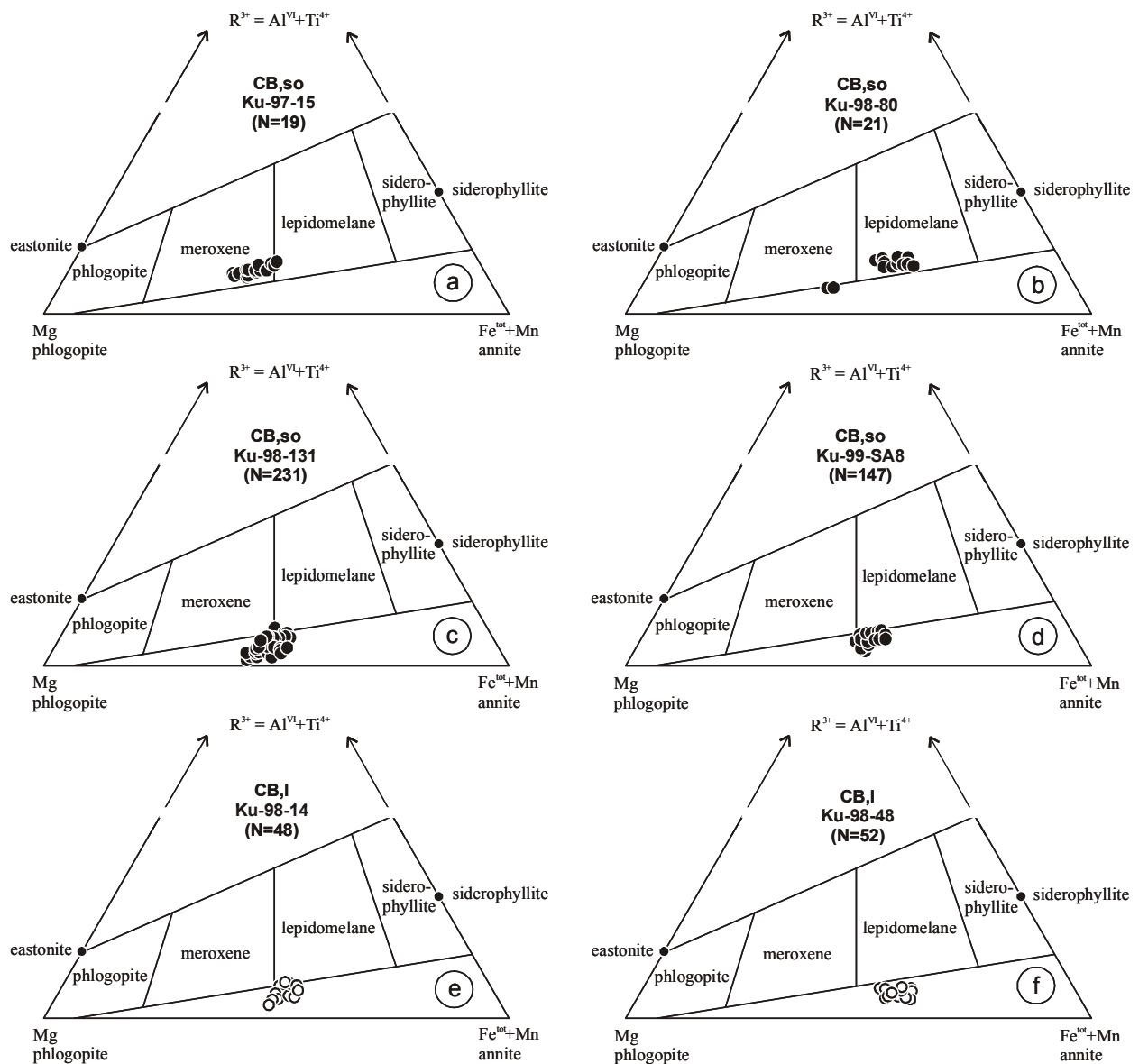


Fig. 14.16: Biotite classification in the modified ($Fe^{2+}=Fe^{tot}$) triangle $R^{3+}(Al^{VI}+Ti)$ -Mg-($Fe^{tot}+Mn$) after Foster (1960, in Tröger, 1982). *a)* and *b)* Metasomatically formed biotite (Bt1) from the sodalite-rich carbonatitic breccia. *c)* and *d)* Magmatic biotite (Bt2) from the sodalite-rich carbonatitic breccia. *e)* and *f)* Magmatic biotite (Bt3) from the layered carbonatitic breccia.

The highest overall Mg and lowest Ti contents are displayed by biotite from the *fenitized ultramafic xenoliths* (Bt6; X_{Mg} : 0.67-0.77; Ti p.f.u.: 0.03-0.06), in good accordance with the Mg-rich compositions of coexisting ankerites/dolomites. Due to the low Al and Ti amounts of the biotites, there was still some deficiency left in the tetrahedral site ($Si+Al^{IV}+Ti^{IV}$) of the calculated biotite formulae. Thus an appropriate amount of Fe was recast as Fe^{3+} in order to complete the tetrahedral site occupancy, following the equation $Fe^{3+}=8-Si-Al^{IV}-Ti^{IV}$. All analysed biotites from different textural positions such as biotite in ankerite-biotite patches in the xenoliths and biotite in reaction rims between the xenoliths and the enclosing carbonatitic breccia are meroxenes in the sense of Foster (1960, in Tröger, 1982) and show no significant differences in the chemical compositions (Fig. 14.17d). It can thus be concluded that the formation of all biotites of the ultramafic xenoliths was caused by the interaction between the ultramafic xenolith and the transporting carbonatite magma under high oxygen fugacities.

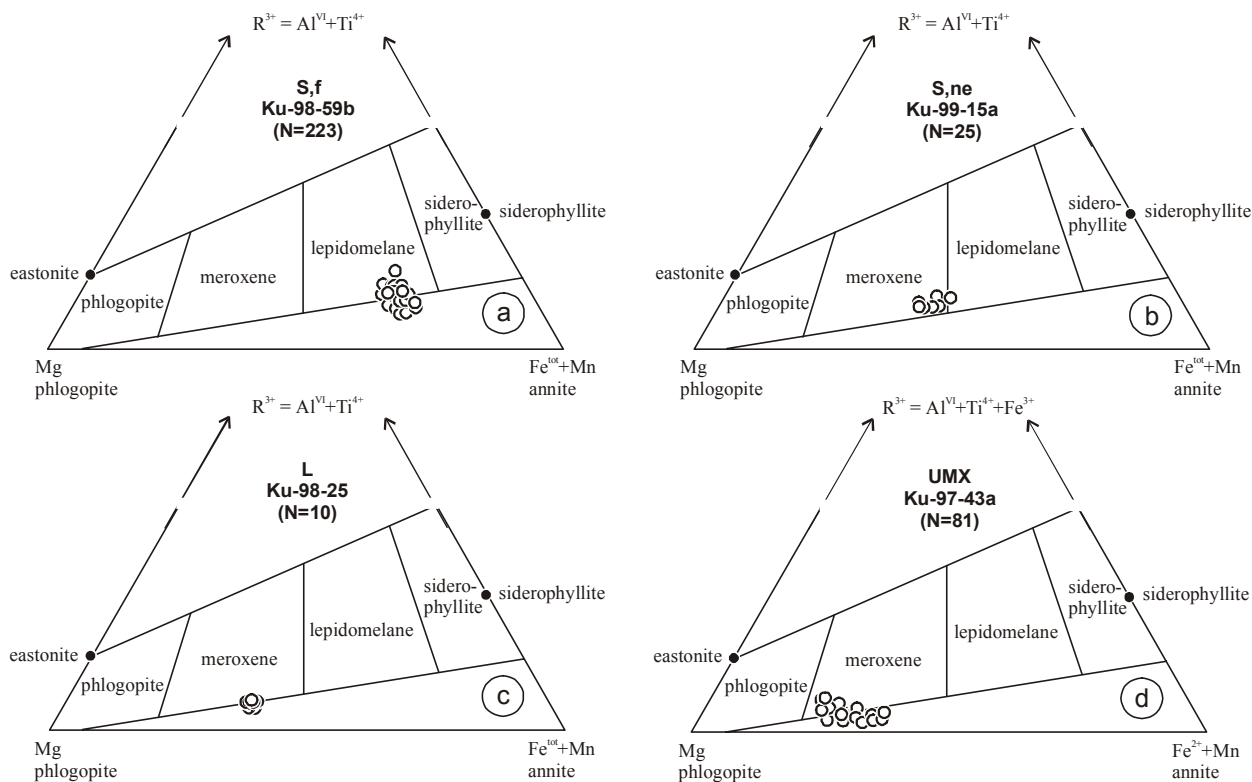


Fig. 14.17: Biotite classification in the modified triangle $R^{3+}(Al^{VI}+Ti)-Mg-(Fe^{tot}+Mn)$ (a-c) and the triangle $R^{3+}(Al^{VI}+Ti+Fe^{3+})-Mg-(Fe^{2+}+Mn)$ (d) after Foster (1960, in Tröger, 1982). **a)** Metasomatically formed biotite (Bt4) from the fenitized syenite. **b)** Magmatic biotite (Bt5) from the fenitized nepheline syenite. **c)** Magmatic biotite (Bt7) from the K-feldspar-biotite-ilmenite-calcite rock. (Bt7) **d)** Metasomatically formed biotite (Bt6) from the ultramafic xenoliths (Fe^{3+} contents recalculated).

In the discrimination diagram MgO versus TiO_2 (Fig. 14.18), both the orthomagmatic biotites of the carbonatitic breccia (Bt2 and Bt3) and the metasomatically formed biotites of the

ultramafic xenoliths (Bt6) mostly plot within the field of biotite from carbonatites as defined by Gaspar & Wyllie (1987). Metasomatic biotites from the carbonatitic breccia (Bt1) compositionally resemble those of magmatic origin. In clear contrast, metasomatically formed biotites from the fenitized syenites deviate from this composition in displaying lower Ti and Mg contents, reflecting the Fe-rich and Ti-poor whole-rock composition of the syenites (Fig. 14.18).

Distinct trends are also displayed by the Si/Al-ratios of the different biotite subgroups (Fig. 14.19). Magmatic biotite of the K-feldspar-biotite-ilmenite-calcite rock (Bt7) plots near the ideal biotite composition. In contrast, both, Bt1 and Bt4 have Al in excess of that necessary to fill the tetrahedral site in addition to Si. The biotites exhibit a scattered distribution in the Si versus Al diagram but mainly plot within the compositional field of late-magmatic biotite of the

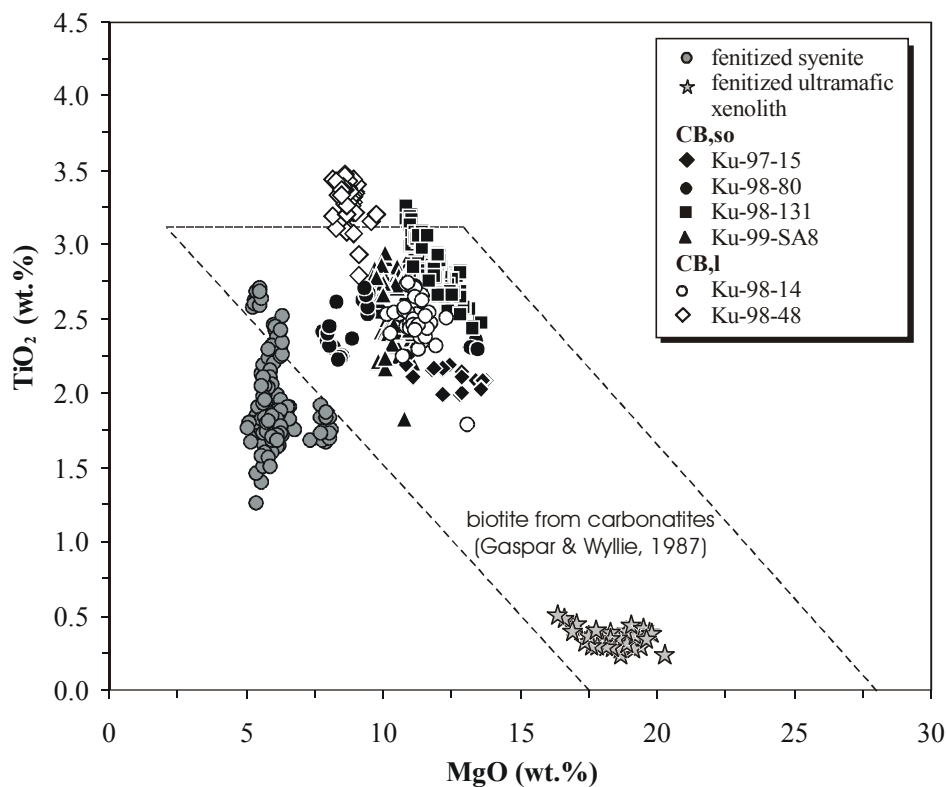


Fig. 14.18: Compositional range of magmatic and metasomatically formed biotite from the carbonatitic breccia, the fenitized syenite and the fenitized ultramafic xenoliths, expressed in the diagram MgO versus TiO₂ after Gaspar & Wyllie (1987).

unaltered anorthosite lithologies and in the range of magmatic biotite of the nepheline syenite (Bt4). This is taken as supporting evidence, that Bt1 and Bt4 were formed by interaction between the carbonatite magma and the bordering anorthosites and syenites, respectively, with the latter two providing the necessary Al. Bt2 and Bt3, which both crystallized from the carbonatite melt display a distinct trend, reaching from high Al values towards Al deficit compared to ideal biotite, evidencing that either (1) the carbonatite melt contained only minor Al amounts, that

were consumed during the biotite formation or that (2) the biotites crystallized under progressively increasing fO_2 , causing substitution of Fe^{3+} for Al. Low Al contents of Bt1, Bt2, Bt3 and Bt4 are accompanied by high Mg and/or low Na and high Si, suggesting the most important substitution mechanism could be $Al^{VI} + Al^{IV} = Mg^{VI} + 2Si^{IV}$ (tschermak), and, far less frequently, $Na + Al^{IV} = O + 2Si^{IV}$ (edenite scheme). In Bt2 and Bt3 Fe^{3+} increases with decreasing Al^{IV} , suggesting an additional substitution scheme of $Fe^{3+} \leftrightarrow Al^{IV}$. Bt6, coexisting with ankerite/dolomite in the fenitized ultramafic xenoliths, is Al- and Ti-poor, hence strongly suggesting substitution of Fe^{3+} for Al. The low Al contents of these micas most probably result from the generally Al-poor composition of both the ultramafic xenoliths and the transporting carbonatite magma.

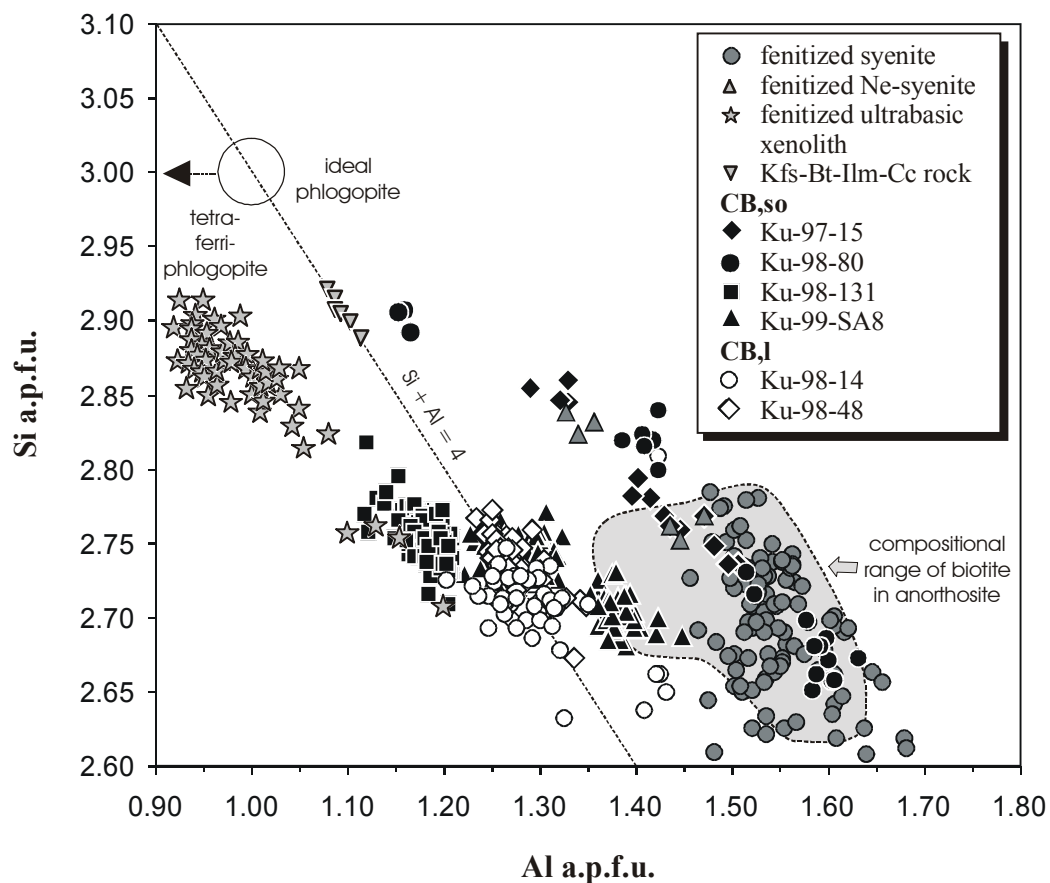


Fig. 14.19: Variation of Si versus Al in biotites of the study area.

The highest but most variable Cl contents of up to 0.24 wt.% are displayed by Bt4 of the fenitized syenite (X_{Mg} : 0.26-0.39; Fig. 14.20), which at the same time contains the lowest F contents (0.4-1.5 wt.%). In clear contrast, orthomagmatic Bt2 and Bt3 in assemblage with apatite contain Cl amounts at or below the detection limit (up to 0.11 wt.%; Fig. 14.20) corresponding to F contents (0.3-2.7 wt.%) and a higher X_{Mg} (0.37-0.57). Lowest Cl contents of 0–0.05 wt.% are

revealed by the Mg-rich biotites (X_{Mg} : 0.62-0.73) of the fenitized ultramafic xenoliths (Fig. 14.20), which, however, are characterized by the highest F contents (1.5-3.8 wt.%).

The results are in good agreement with experimental studies of Munoz & Swenson (1981) and Volfinger et al. (1985), who suggest a preferential incorporation of Cl into Fe-rich biotites, even though the predicted trend of “Mg-Cl-avoidance” is not very pronounced in the rock-samples investigated. Especially Bt4 in sample Ku-98-59b, has Cl contents, which are much more variable than the corresponding X_{Mg} . Therefore, it appears that Cl incorporation in biotite is not solely governed by the Mg-Cl-avoidance but may additionally result from the interaction of biotite with compositionally changing metasomatic fluids. Following this, fluid-flow outlasted the biotite formation.

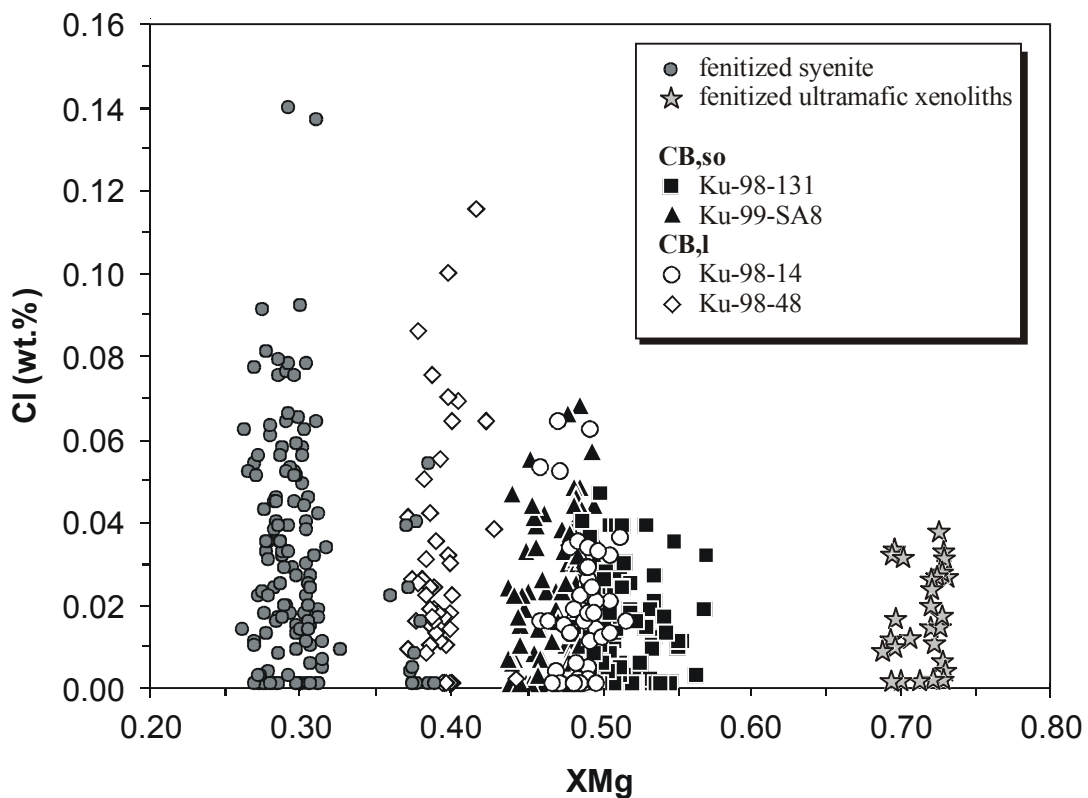


Fig. 14.20: Chlorine contents (wt.%) of magmatic and metasomatic biotites plotted against the respective mole fraction of Mg.

14.11 Apatite

Apatite is a minor constituent of both the layered and the sodalite-rich carbonatitic breccia. Apatite compositions were investigated in great detail, since the mineral may incorporate F, Cl

and OH and thus gives additional information on the composition of the carbonatite magma. Representative analyses are presented in Table A.5.1.24 in the Appendix A.5.1. Mineral formulae were calculated on a 25-oxygen basis. Apatites from both the *layered carbonatitic breccia* and the *sodalite-rich carbonatitic breccia* contain significant amounts of F (1.3-5.1 wt.%) and Sr (1.1-2.5 wt.%) and can thus be classified as strontian fluorapatites.

The F-contents of apatite increase from an average value of 2.80 wt.% (1.3-4.8 wt.%) in sodalite-rich samples to 3.64 wt.% (2.2-5.1 wt.%) in the layered carbonatitic breccia. In the same sequence of samples the concentrations of Na₂O (0.33-1.09 wt.%) and BaO (0-0.14 wt.%) and Sr increase. Most of the investigated apatites exhibit only minor amounts of Cl, which, however, may reach values of up to 0.31 wt.% in single apatites, corresponding to 0.1 Cl atoms per formula unit.

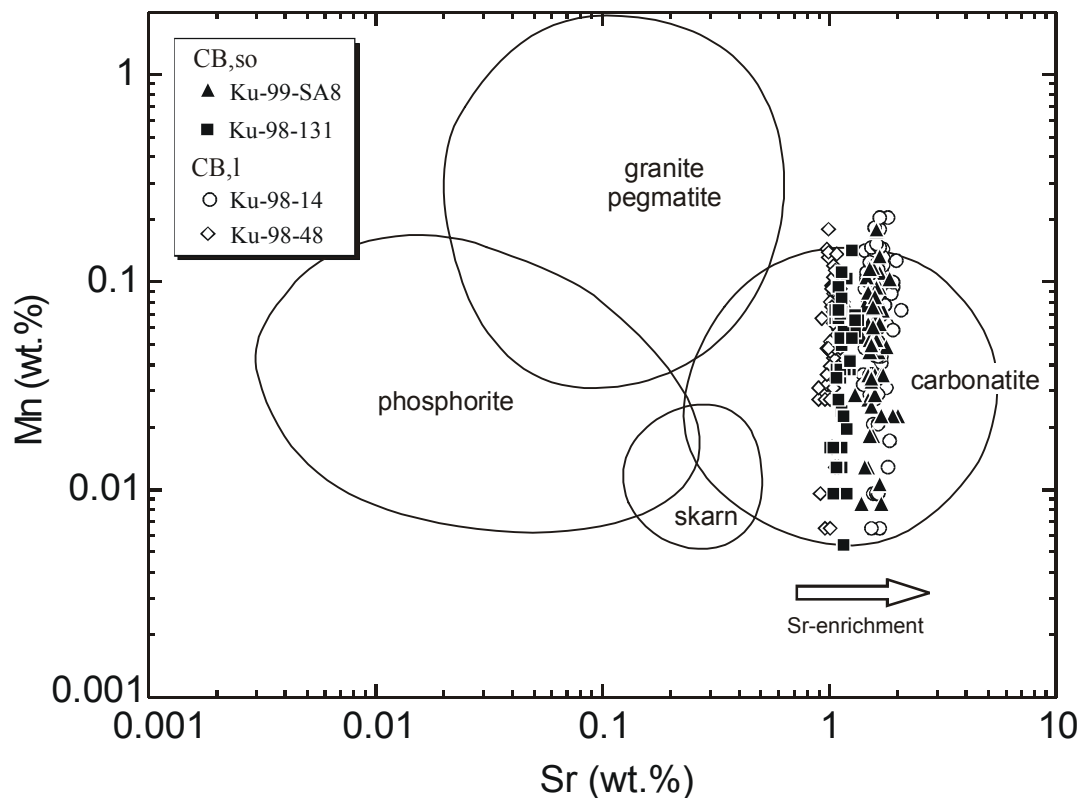


Fig. 14.21: Mn-Sr fields of apatite from skarn, phosphorite, granite pegmatite and carbonatite from world-wide localities (compiled by Hogarth, 1989). Note that all apatites from the Swartbooisdrif carbonatites plot in the carbonatite field.

Trace element contents of FeO (<0.54 wt.%), MnO (<0.16 wt.%) and MgO (0.0 wt.%) are generally extremely low. Consistently low total sums of analyses of apatite from one sample of the layered carbonatitic breccia (Ku-98-14) might be explained by the additional incorporation of carbon. However, the exact substitution scheme remains unclear, since chemical analyses of

OH^- and $[\text{CO}_3]^{2-}$ are still wanting. In the Sr versus Mn diagram (Fig. 14.21) all analysed apatites from the carbonatitic breccia fall in the compositional range of apatites from carbonatites.

14.12 Pyrochlore

Medium- to very fine-grained and optically zoned pyrochlore occurs as an accessory phase in both the late *ferrocarbonatite veins* and the *carbonatitic breccia*. However, the small pyrochlore grains from the carbonatitic breccia are completely altered to fine-grained intergrowths of secondary phases and hence attained unreasonable and highly variable EMP analyses. Formula properties of pyrochlore from the ferrocarbonatite veins have been calculated on the basis of total occupation on the B-site of pyrochlore ($\text{Nb} + \text{Si} + \text{Ti} = 2$), according to the general formula

<i>A-ion characterization</i>		<i>Pyrochlore subgroup</i> $\text{Nb} + \text{Ta} > 2\text{Ti}; \text{Nb} > \text{Ta}$	<i>Microlite subgroup</i> $\text{Nb} + \text{Ta} > 2\text{Ti}; \text{Ta} \geq \text{Nb}$	<i>Betafite subgroup</i> $2\text{Ti} \geq \text{Nb} + \text{Ta}$
<i>Na + Ca but no other A-atom</i> > 20% total A-atoms		PYROCHLORE	microlite	calciobetafite
<i>One ore more A-atoms, other than Na or Ca, > 20 % total A-atoms</i>	K Cs Sn Ba Sr	kalipyrochlore bariopyrochlore (un-named)	 cestibtantite stannomicrolite bariomicrolite	
<i>Species named by most abundant A-atom, other than Na or Ca</i>	REE ($\Sigma\text{Ce} > \Sigma\text{Y}$) REE ($\Sigma\text{Y} > \Sigma\text{Ce}$) Bi Sb Pb U Th	ceriopyrochlore yttropyrochlore plumbopyrochlore uranpyrochlore (un-named)	 bismutomicrolite plumbomicrolite uranmicrolite	yttrobetafite stibiobetafite plumbobetafite betafite

Table 14.6: Classification of the pyrochlore group after Bonshtedt-Kupletskaya (1966; in Hogarth, 1989) and Hogarth (1977) ($\text{REE} = \text{lanthanides} + \text{Y}$, $\Sigma\text{Ce} = (\text{La} \rightarrow \text{Eu})$, $\Sigma\text{Y} = (\text{Gd} \rightarrow \text{Lu}) + \text{Y}$, pyrochlore species found in the Swartbooisdrif carbonatite is in capitals).

$(\text{A})_{2-m}\text{B}_2\text{O}_6(\text{O}, \text{OH}, \text{F})_{1-n} p\text{H}_2\text{O}$ (Hogarth, 1977). However, with values of 1.64-1.88, the totals of the remaining cations in the A-site (Fe, Ce, Ca, Sr, Ba, Na) of the analysed pyrochlores are distinctly lower than those given by the ideal formula $(\text{Ca}, \text{Na})_2\text{Nb}_2\text{O}_6(\text{OH}, \text{F})_2$. These deficiencies in the A-site is a common feature of pyrochlores from carbonatites and are generally attributed to either (1) vacancies in the A-site or (2) strong hydration. Representative analyses of pyrochlore are given in Table A.5.1.25 in the Appendix A.5.1.

The characterization of pyrochlores followed the classification scheme of Bonshtedt-Kupletskaya (1966; in Hogarth, 1989) and Hogarth (1977), which is based on the B-site and A-site characterization of pyrochlore (Table 14.6). Following this classification scheme, pyrochlores are first subdivided into three subgroups, i.e. (1) pyrochlore $Nb+Ta > 2Ti$, $Nb > Ta$, (2) microlite $Nb+Ta > 2Ti$, $Ta \geq Nb$ and (3) betafite $2Ti \geq Nb+Ta$. Subsequently, subspecies of the subgroups are defined as (i) Na and Ca but no other A-atom exceeding 20 at.% of the totals of A-atoms and (ii) one or more A-atoms other than Ca and Na exceeding 20 at.%. With an average formula of $Ca_{0.83}Na_{0.85}Sr_{0.05}Ce_{0.03}Fe_{0.01}Nb_{1.90}Ti_{0.08}Si_{0.02}O_6(OH,F)_2$, all investigated pyrochlores plot in the field of the pyrochlore subspecies.

EMP analyses generally reveal high SrO and Na_2O contents of 0.96-2.24 wt.% and 6.54-7.98 wt.%, respectively, whereas the Ta contents are < 0.7 wt.%. The fine-scaled oscillatory zonation of pyrochlore, observed microscopically, is also displayed by its mineral chemistry. All analysed grains show a concentric zoning pattern with a core preference for Ca and Ti, whereas Si, Fe, Ba, Sr and Ce trend to rim.

14.13 Fe-Ti Oxides

Ilmenite, hematite, rutile and magnetite are ubiquitous accessory constituents of most samples investigated. The calculation of the ilmenite and hematite formula was based on 6 oxygens whereas magnetite was calculated on a 4-oxygen basis. For the estimation of the Fe^{3+} contents of ilmenite/hematite and magnetite a calculation modulus on the basis of 4 and 3 cations, respectively, was chosen. Rutile was calculated on a 2-oxygen basis. Representative analyses of ilmenite, magnetite and hematite are given in Tables A.5.1.7, A.5.1.A and A.5.1.9 in the Appendix A.5.1. Rutile analyses are listed in Table A.5.1.26 in the Appendix A.5.1.

14.13.1 Ilmenite

Ilmenite occurs in several different textural positions and rock samples, i.e. (1) as oxy-exsolution lamellae in magnetite from the fenitized anorthosites, (2) as anhedral, heavily tectonised grains in the fenitized syenite, (3) as late-magmatic, anhedral grains in the K-feldspar-biotite-ilmenite-calcite rock and (4) as small, irregularly bounded grains in the carbonatitic breccia.

The MnO contents of ilmenite oxy-exsolution lamellae in magnetite from the *fenitized anorthosite* are generally low, ranging from 0.6-0.7 wt.%. The hematite contents of these ilmenite types fall in a range of 0.4-0.6 mol.%.

In contrast, discrete grains of ilmenite in the *fenitized syenite* are characterized by comparably high MnO amounts of 5.37-6.04 wt.% and an extremely low hematite content of <0.01 mol.%, in good accordance with the ilmenite compositions from unaltered syenites.

In the *K-feldspar-biotite-ilmenite-calcite rock*, ilmenite occurs as discrete grains in the interstices between plagioclase and biotite crystals. EMP analyses reveal ilmenite compositions with minor amounts of the Mn end-member pyrophanite (3.2-4.1 mol.%; MnO: 1.5-1.9 wt.%) and low but quite variable contents of hematite (0.1-1.3 mol.%).

Anhedral ilmenite occurs in rare samples of the *carbonatitic breccia*, where the oxide generally forms single grains, bearing abundant inclusions of matrix minerals. In places, ilmenite is marginally replaced by rutile or altered to titanohematite along cracks. EMP analyses along various profiles reveal high hematite contents of 1.6-4.3 mol.% and low MnO values of 0.8-1.1 wt.%.

14.13.2 Magnetite

Magnetite is a common accessory phase in the fenitized anorthosites, the fenitized syenites, the carbonatitic breccia, the late ferrocarbonatite veins and the fenitized ultramafic xenoliths.

Magnetite from the *fenitized anorthosites* occurs as intercumulus grains with ilmenite-exsolution lamellae. However, along the lamellar systems and along cracks magnetite is mostly completely altered to hematite replaced by ankerite, whereby ilmenite exsolution lamellae are preserved. Thus only few reliable analyses of magnetite were obtained, revealing TiO₂ contents of 0.02-0.13, which are in the range of those obtained for similar magnetites from the unaltered anorthositic rocks.

Magnetite from the *fenitized syenite* occurs as large anhedral grains, displaying embayed grain boundaries and containing abundant albite inclusions. The homogeneous magnetites attain Ti contents of 0.0-0.3 wt.%, in good accordance with the Ti values obtained for magnetites of unaltered syenites.

In the *carbonatitic breccia*, magnetite occurs in two different textural positions, i.e. (1) as inclusion-free magnetite dispersed in the matrix and in places forming large grains of up to 4 mm in size and (2) as irregularly bounded grains of up to 2 cm in diameter, which frequently display inclusions of matrix minerals. However, magnetites from both textural position are almost identical in composition, containing extremely low Ti contents of < 0.9 wt.%, suggesting subsolidus re-equilibration of all oxides during the final stages of metasomatism. In the late *ferrocarbonatite veins*, angular or irregularly shaped magnetite grains are evenly distributed in the ankerite matrix. Analysis profiles across magnetite reveal extremely low values of TiO₂ (0.00-0.08 wt.%) and MnO (0.00-0.04 wt.%), both slightly decreasing from core towards the rim.

Magnetite is a minor constituent of the *fenitized ultramafic xenoliths*, where the oxide is intimately associated with ankerite/dolomite and biotite in irregular patches. Magnetite was found to be virtually pure FeFe₂O₄, containing minor amounts of Ti (0.06-0.11 wt.%) in the range of magnetite from the late ferrocarbonatite veins.

14.13.3 Hematite

Hematite is a common alteration product of both magnetite and ilmenite in samples of the *carbonatitic breccia*. Depending on their textural position, the hematites display significant differences in their chemical composition. When formed by the martitisation of magnetite, hematite was found to be virtually pure Fe₂O₃ (TiO₂ < 0.1 wt.%), whereas hematite replacing ilmenite attains distinctly higher TiO₂ amounts of 2.1-7.0 wt.%. Individual grains of titanohematite may be zoned with the Ti-contents increasing from core towards the rim. Cr₂O₃, MgO and MnO are generally below the detection limit.

14.13.4 Rutile

Rutile is present in various textures in the fenitized anorthosites, the carbonatitic breccia and the late ferrocarbonatite veins, i.e. (1) as large, anhedral grains of rutile, either isolated or in contact with magnetite from both the ferrocarbonatite veins and the carbonatitic breccia, (2) as fine-grained overgrowths of rutile and carbonate, on magnetite and (3) in intergrowths with hematite, replacing magnetite twin lamellae and/or ilmenite oxy-exsolution lamellae in magnetite.

Rutile from the *carbonatitic breccia* and the *fenitized anorthosites* commonly attains high Fe₂O₃ contents, ranging between 0.6-2.2 wt.%, but displaying no significant differences with respect to their textural positions.

Rutile in contact to magnetite and pyrochlore in the late *ferrocarbonatite veins* reveals overall high Fe₂O₃ amounts of 2.2-3.1 wt.%. Low total sums of oxides of the analysed rutiles (< 97.5 wt.%), suggest that the Ti-oxides may additionally contain significant amounts of Nb.

14.14 Sulphides

Sulphides occur as accessory phases in the fenitized anorthosites, the fenitized syenites, the carbonatitic breccia and the K-feldspar-biotite-ilmenite-calcite rock. It has to be mentioned however, that the sulphides are quite heterogeneously distributed within the respective rock types, and are thus lacking in most of the samples investigated.

14.14.1 Pyrite

Pyrite is a common accessory phase of the fenitized anorthosites, the fenitized syenites and the carbonatitic breccia. In the latter, the sulphides are concentrated in samples which presumably suffered autometasomatism by late-stage, highly evolved fenitizing fluids, such as the REE-rich carbonatitic breccia. In addition, dispersed pyrite grains were observed in the K-feldspar-biotite-ilmenite-calcite rock. Representative pyrite analyses are listed in Table A.5.1.27 in the Appendix A.5.1. Compositional ranges of the analysed pyrites are illustrated in the ternary diagram CoS₂-NiS₂-FeS₂ after Nickel (1970; Fig. 14.22).

Pyrite from the *fenitized anorthosite* occurs in two different textural positions, i.e. as (1) strongly corroded, euhedral grains in contact to magnetite, overgrown by (2) pyrite of a second generation. The latter may also occur as small, subhedral grains, dispersed in the rocks. Pyrite of the first generation reveal Co contents near the detection limit, whereas the Ni contents range between 0.0-1.6 wt.%, with the Ni increasing from core towards the rim (Fig. 14.22a). In clear contrast, texturally late pyrite is characterized by Ni contents below the detection limit and Co-contents varying between 0.0 wt.% (core) and 3.5 wt.% (rim; Fig. 14.22b). The formation of the

pyrites is most probably linked to the sulphidation of orthomagmatic magnetite, following the injection of the fenitizing carbonatite fluids.

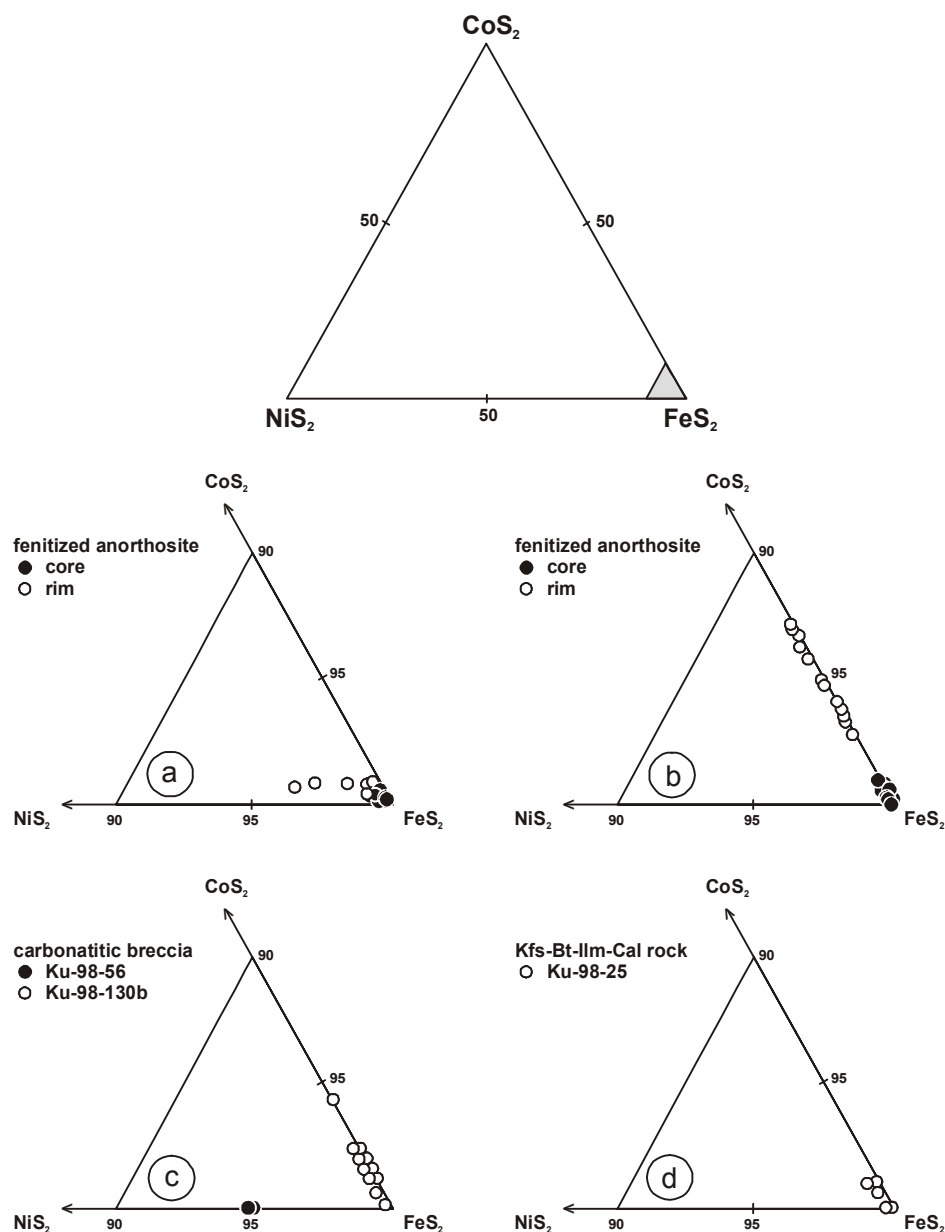


Fig. 14.22: Compositional variation of pyrite from the studied samples, expressed in the ternary diagram CoS_2 - NiS_2 - FeS_2 after Nickel (1970). **a)** First pyrite generation of the fenitized anorthosites. **b)** Second pyrite generation of the fenitized anorthosites. **c)** Pyrite from the carbonatitic breccia. **d)** Late-magmatic pyrite from the K-feldspar-biotite-ilmenite-calcite rock.

Two pyrite generations are distinguished in samples of the *carbonatitic breccia*. A first generation of pyrite forms small, subhedral grains, which are dispersed in the carbonatite matrix (Ku-98-56). These pyrites attain high Ni contents of 2.5-2.7 wt.% and Co contents below the detection limit (Fig. 14.22c). In contrast, pyrite of the second generation is localised in sulphide

patches and veins, where it is intimately associated by millerite and chalcopyrite (Ku-98-130b). The Ni values of these late-stage pyrites are generally < 0.1 wt.% whereas Co ranges between 0.1 wt.% and 2.3 wt.% (Fig. 14.22c). The evolutionary trend of the pyrites towards higher Co and lower Ni contents is in excellent accordance with the findings for the two pyrite generations from the fenitized anorthosites, hence suggesting that the composition of the fenitizing fluids changed during metasomatism. Following this, early fenitizing fluids must have transported certain amounts of Ni, whereas Co dominates over Ni in the late-stage fluids.

Subhedral pyrite grains of the *K-feldspar-biotite-ilmenite-calcite rock* are found to be virtually pure FeS₂. Both the Co and the Ni contents are generally low, ranging between 0.0 and 0.5 wt.% and 0.0 and 0.2 wt.%, respectively (Fig. 14.22d). Judging from their textural position and their chemical composition, these pyrites are suggested to represent a late-magmatic crystallization product of the K-feldspar-biotite-ilmenite-calcite rocks, unrelated to metasomatic processes.

14.14.2 Chalcopyrite

Chalcopyrite is closely associated with pyrite in the fenitized anorthosite. In the carbonatitic breccia, chalcopyrite either occurs as small dispersed grains or localised in sulphide veins and patches. Representative analyses of chalcopyrite are depicted in Table A.5.1.28 in the Appendix A.5.1.

Ni and Co contents of chalcopyrites from the *fenitized anorthosite* are generally below the detection limit, irrespective of their textural position. The same holds true for late-stage chalcopyrite of the *carbonatitic breccia*, which is intimately intergrown with millerite. In clear contrast, dispersed grains of early chalcopyrite from the carbonatitic breccia reveal slightly higher Ni contents of up to 0.12 wt.%, hence supporting the interpretation that early fenitizing fluids are richer in Ni than their late-stage counterparts.

14.14.3 Pyrrhotite

Pyrrhotite was observed in only one sample of the *carbonatitic breccia* (Ku-97-19; von Seckendorff & Drüppel, 1999; von Seckendorff et al., 2000). In this rock, pyrrhotite and pyrite

form either single grains or irregular, layer-parallel patches. Representative pyrrhotite analyses are compiled in Table A.5.1.29 in the Appendix A.5.1.

EMP analyses revealed Ni contents of 0.75 wt.% for a pyrrhotite inclusion in pyrite, whereas matrix pyrrhotite, bearing abundant pentlandite lamellae, is virtually Ni-free (Ni < 0.15 wt.%). The composition of the investigated pyrrhotites ranges between Fe_{0.97}S and FeS.

14.14.4 Pentlandite

Pentlandite occurs as lamellae in pyrrhotite of one sample of the carbonatitic breccia (Ku-97-19; von Seckendorff & Drüppel, 1999; von Seckendorff et al., 2000) and as small, isolated grains in the fenitized anorthosite. The formula of pentlandite has been calculated on an 8-sulphur basis. Representative analyses are listed in Table A.5.1.30 in the Appendix A.5.1.

Pentlandite of the *fenitized anorthosite* has a rather homogeneous composition of Fe_{3.5}Ni_{4.8}Co_{0.3}S₈, whereas the compositional range of pentlandite lamellae in pyrrhotite from the *carbonatitic breccia* can be described as Fe_{4.5-5.3}Ni_{3.3-4.4}S₈, with Co contents below the detection limit. Higher Fe and lower Ni contents of the latter pentlandites, when compared to those of the fenitized anorthosites, are most probably related to the Fe-rich and Ni-poor composition of the pyrrhotite host.

14.14.5 Bornite

Small bornite grains were observed in one sample of the *carbonatitic breccia* (Ku-97-15d), where the sulphide is associated by chalcocite-digenite (von Seckendorff & Drüppel, 1999; von Seckendorff et al., 2000). The analysed bornite was found to be virtually pure Cu₅FeS₄ (Table A.5.1.31 in the Appendix A.5.1).

14.14.6 Chalcocite-digenite

Members of the chalcocite-digenite group have been observed in only one sample of the *carbonatitic breccia* (Ku-97-15d), either as single grains or, in association with bornite, as irregular grain aggregates (von Seckendorff & Drüppel, 1999; von Seckendorff et al., 2000).

EMP analyses of chalcocite-digenite (Table A.5.1.32 in the Appendix A.5.1) yielded two chemically distinct compositional groups with different Fe-contents. The Fe-poor group is near-binary, generally with compositions of $\text{Cu}_{1.91}\text{S}$ - $\text{Cu}_{1.94}\text{S}$ and Fe contents of 0.05-0.07 wt. %, whereas the second group reveals Fe values of 1.2-3 wt. %. The data points do not plot exactly in the digenite field delineated by Yund & Kullerud (1966), but close to the most Fe-rich chalcocite composition. Traces of Hg, As, Sb, Bi, Se and Te are present, but are mostly below the detection limit.

14.14.7 Millerite

Millerite is a comparably common accessory phase of the *carbonatitic breccia*. Representative analyses are listed in Table A.5.1.33 in the Appendix A.5.1. Average compositions are given in Table 14.7. Compositional variations of the investigated millerites are illustrated in the ternary diagram Co-Ni-Fe (at.%; Fig. 14.23).

sample; wt.%		Cu	Fe	Mn	Co	Ni	As	Sb	S	Se	Total
Ku-97-24	lamellae in sg	0.00	2.60	0.00	1.32	62.30	0.00	0.00	35.40	0.00	101.62
N=2		0.00	0.45	0.00	0.09	0.30	0.00	0.00	0.20	0.00	0.46
Ku-97-24	matrix, isolated	0.00	0.37	0.00	0.23	63.50	0.00	0.00	35.20	0.06	99.36
Ku-97-24	late-stage veins	0.00	2.87	0.00	0.27	62.40	0.00	0.00	35.45	0.03	101.01
N=2		0.00	0.14	0.00	0.00	0.90	0.00	0.00	0.35	0.03	1.38
Ku-98-56	lamellae in pd	0.08	1.56	0.02	1.49	60.17	0.00	0.00	36.53	0.03	99.92
N=2		0.04	0.15	0.01	0.32	1.04	0.00	0.00	0.31	0.03	0.36
Ku-98-130°	matrix, next to cpy	0.08	0.27	0.01	0.15	64.18	0.01	0.01	35.60	0.11	100.42
N=36		0.08	0.15	0.02	0.03	0.36	0.02	0.02	0.17	0.05	0.38
Ku-98-130a	matrix next to py	0.21	0.35	0.01	0.56	63.28	0.01	0.01	35.36	0.10	99.89
N=27		0.22	0.23	0.01	0.03	0.55	0.02	0.02	0.26	0.05	0.59
Ku-98-130a	matrix, next to mag	0.36	0.97	0.01	0.53	62.80	0.02	0.01	35.66	0.16	100.52
N=14		0.14	0.23	0.01	0.03	0.43	0.03	0.02	0.15	0.05	0.32

Table 14.7: Average compositions millerite (σ standard deviation; values for sample Ku-97-24 are taken from von Seckendorff et al., 2000).

The investigated millerites display significant differences in both their Fe and Co contents depending on their respective textural positions, i.e.

- (i) as lamellae in ferroan siegenite (Co: 1.2- 1.5 wt.%; Fe: 2.1-3.1 wt.%; Fig. 14.23 b),
- (ii) as a constituent of late sulphide veins (Co: 0.2-0.3 wt.%; Fe: 2.7-3.0 wt.%; Fig. 14.23b),

- (iii) (v) as lamellae in polydymite-violarite (Co: 1.2-1.8 wt.%; Fe: 1.4-1.7 wt.%; Fig. 14.23c),

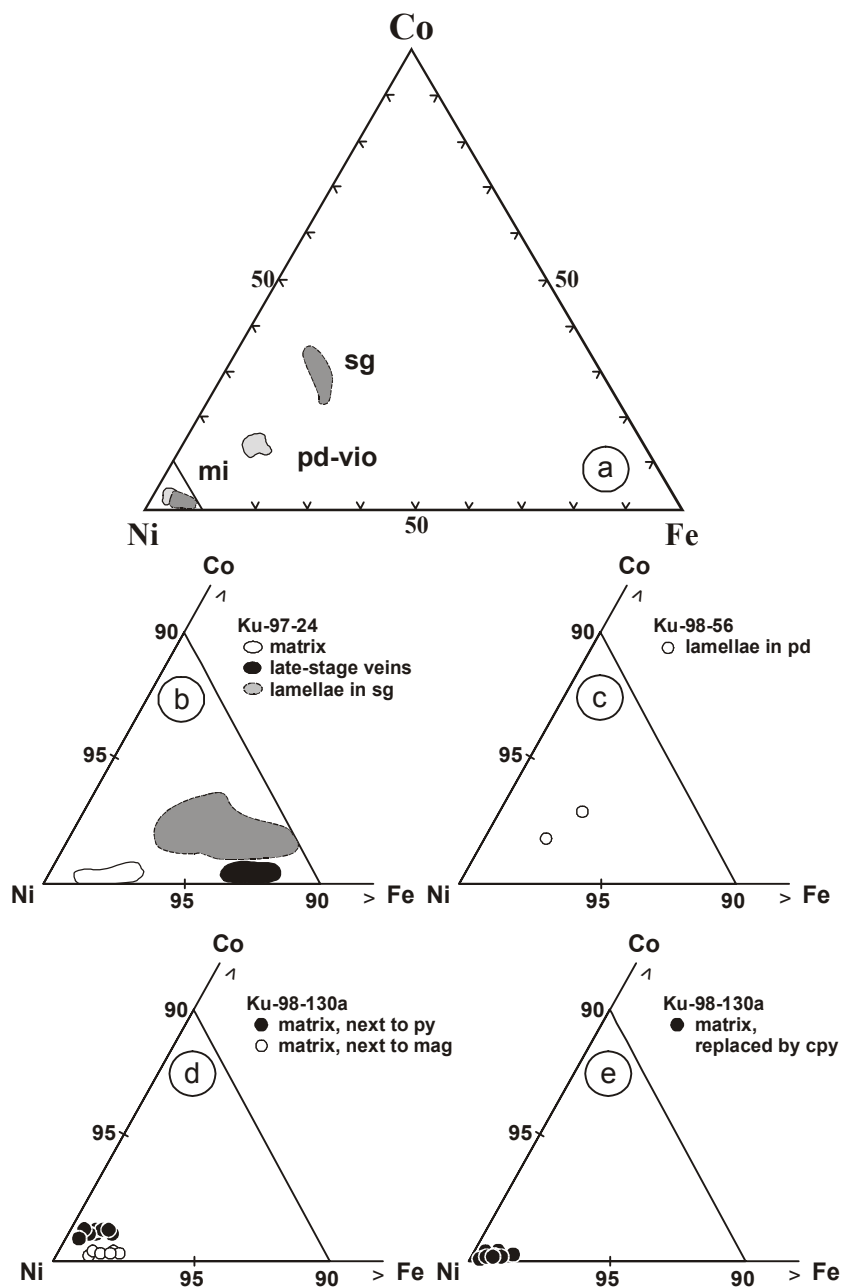


Fig. 14.23: Compositional variation of millerite from the studied samples, expressed in the ternary diagram Co-Ni-Fe (at.%). **a)** Dark grey fields designate the compositions of millerites, coexisting with ferroan siegenite in sample Ku-97-24 (von Seckendorff et al., 2000), light grey fields designate the compositional variation of violarite-polydymite bearing millerite-lamellae in sample Ku-98-56. **b)** Enlarged section displaying the compositional variation of millerite in sample Ku-97-24 (von Seckendorff et al., 2000), **c)** Enlarged section displaying the compositional variation of millerite in sample Ku-98-56, **d)** and **e)** Enlarged section displaying the compositional variation of millerites in sample Ku-98-130a.

- (iv) as matrix grains bordered by pyrite (Co: 0.5-0.6 wt.%; Fe: 0.1-1.0 wt.%; Fig. 14.23d),

- (v) as matrix grains bordered by magnetite (Co: 0.5-0.6 wt.%; Fe: 0.7-1.4 wt.%; Fig. 14.23d),
- (vi) as isolated matrix grains, subsequently replaced by chalcopyrite and/or fletcherite (Co: 0.1-0.2 wt.%; Fe: 0.1-0.8 wt.%; Fig. 14.23e).

Remarkably, millerites in assemblage (i) and (iii) reveal quite similar Fe:Co ratios like the coexisting ferroan siegenite and polydymite-violarite, respectively (Fig. 14.23a). The generally low contents of both Fe and Co of the matrix millerites (iv), (v) and (vi) are in good agreement with their precipitation from Ni-rich and Co-poor fluids, whereas the elevated Fe-contents of millerites in the subsequently formed sulphide veins point to changes in the physico-chemical conditions during fenitization, extending the availability of iron in late-stage fluids. This interpretation is constrained by concentric zoning patterns of matrix millerites in textures (iv) and (vi), involving a rimward increase of the Fe-contents of millerite towards the bordering pyrite and chalcopyrite, respectively.

14.14.8 Siegenite

Siegenite was observed in one sample of the *carbonatitic breccia* (Ku-97-24) by von Seckendorff & Drüppel (1999) and von Seckendorff et al. (2000). In addition to its occurrence in the matrix, siegenite may form a constituent of late-stage sulphide veins. In all textural positions, siegenite contains lamellae of millerite. The formula of siegenite has been calculated on a 4-sulphur basis (Table A.5.1.34 in the Appendix A.5.1). EMP analyses of siegenite generally reveal high Fe contents of 7-12 wt. %. Traces of Cu may reach values of up to 0.5 wt.%.

14.14.9 Violarite-polydymite

In the *carbonatitic breccia* sample Ku-97-24, polydymite was found as a replacement product of millerite (von Seckendorff et al., 2000), whereas millerite in sample Ku-98-56 forms lamellae in polydymite-violarite grains. Formulae of polydymite-violarite have been calculated on a 4 sulphur basis. Representative analyses are listed in Table A.5.1.35 in the Appendix A.5.1.

With Fe-contents of 2.1-3.2 wt.% and Co-contents of 0.2-0.4 wt.% polydymite of sample Ku-97-24 has a composition near to the polydymite end-member (von Seckendorff et al., 2000).

In clear contrast, thiospinels of sample Ku-98-56 display quite variable ratios of Fe/Ni and Fe/Co. Their formulae can be expressed as $\text{Fe}_{0.3}\text{Co}_{0.3}\text{Ni}_{2.4}\text{S}_4$ to $\text{Fe}_{0.7}\text{Co}_{0.3}\text{Ni}_{2.0}\text{S}_4$. Most grains are oscillatory zoned, pointing to episodically changing chemical compositions of the fenitizing fluids. The compositional range of the thiospinels can be expressed in the subsystem Fe-Co-Ni forming part of the complex Cu-Fe-Co-Ni system (Fig. 14.24), where the thiospinels of sample Ku-98-56 predominantly plot within the field of the polydymite-violarite solid solution series (Ni_3S_4 - Fe_3S_4).

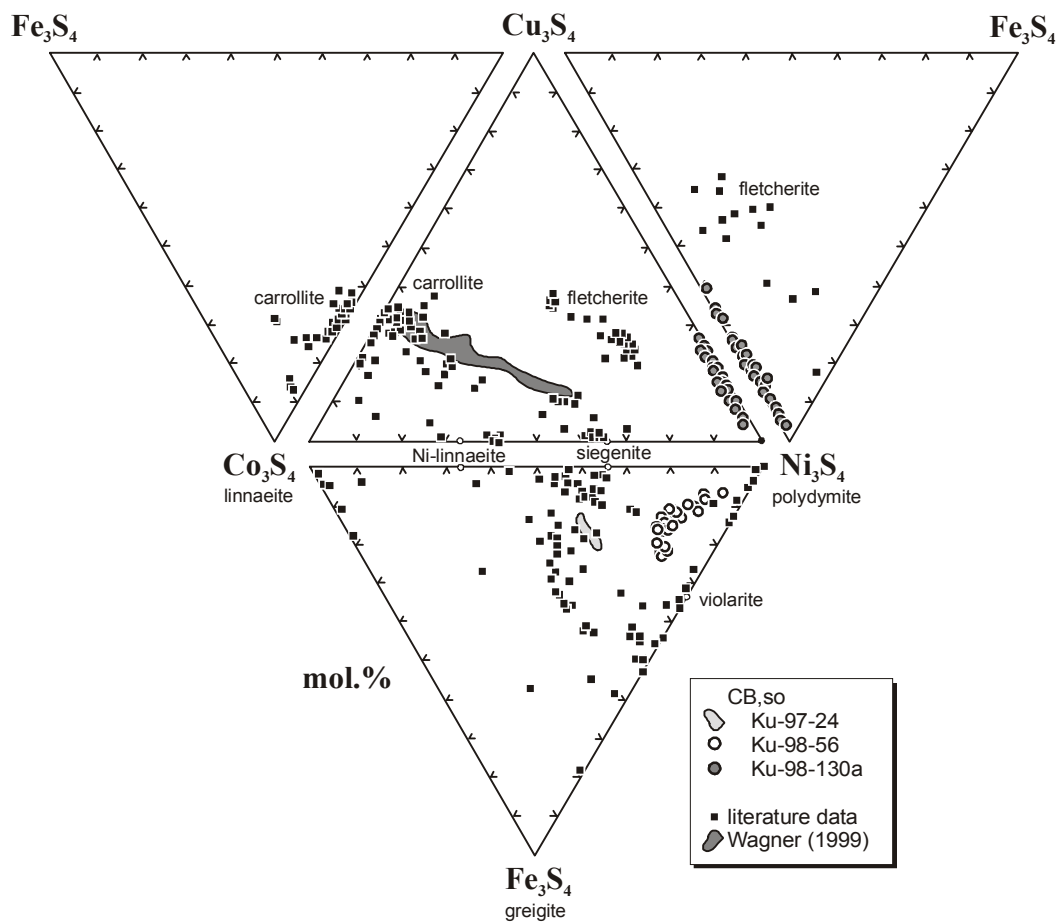


Fig. 14.24: Comparison of analysed polydymite-violarite and fletcherite with thiospinel from the literature in the pseudo-quaternary diagram Co_3S_4 - Ni_3S_4 - Cu_3S_4 - Fe_3S_4 (mol.%). Literature data (black squares) were compiled by Wagner (1999) using Craig (1971), Vaughan et al. (1971), Craig & Higgins (1975), Minceva-Stefanova & Kostov (1976), Minceva-Stefanova (1978), Ostwald (1978), Craig et al. (1979), Riley (1980), D'Orey (1983), Pignolet & Hagni (1983), Vaughan & Craig (1985), Ixer & Stanley (1996), and references therein. Analyses of thiospinels from sample Ku-97-24 (von Seckendorff et al., 2000; light grey shaded field) and of carrollites (Wagner, 1999; dark grey shaded field) are marked for comparison.

14.14.10 Fletcherite

Fletcherite occurs in one sample of the *carbonatitic breccia* (Ku-98-130a), where it replaces millerite along its grain margins and along cracks. The formula of fletcherite has been calculated on a 4 sulphur basis (Table A.5.1.36 in the Appendix A.5.1).

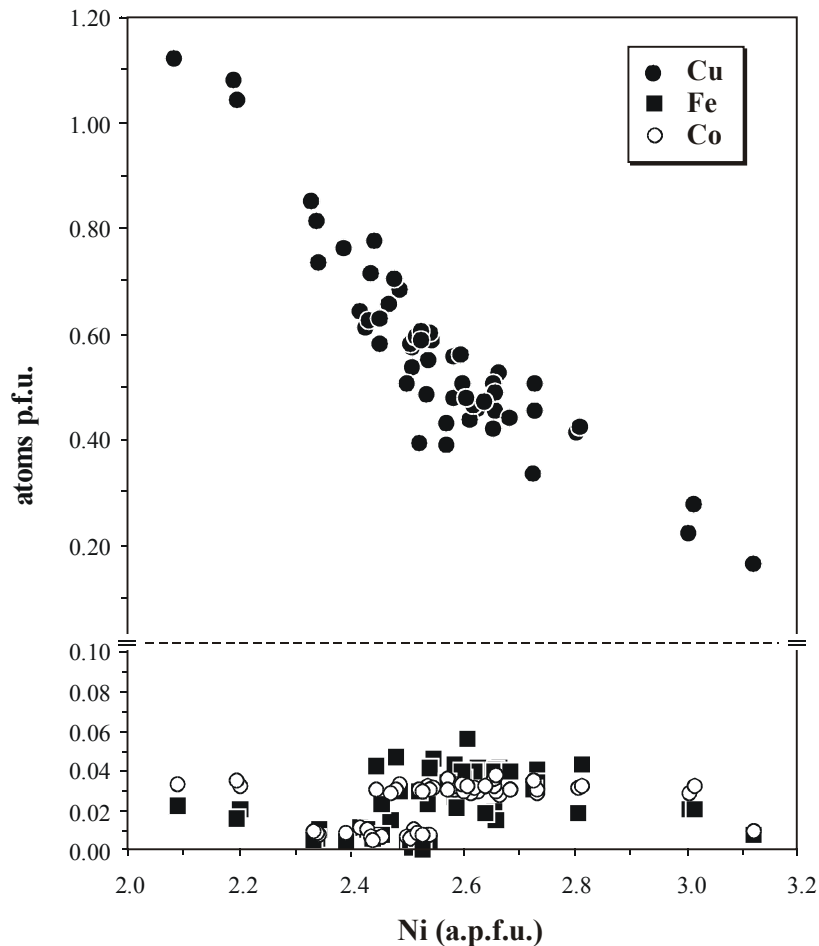


Fig. 14.25: Correlation patterns of Cu, Fe and Ni p.f.u. (formula calculation based on 4 sulphurs) in fletcherite from the REE-rich carbonatitic breccia (Ku-98-130a).

The investigated fletcherites have a quite conspicuous composition, implying the existence of a new solid-solution series in the Cu-Fe-Co-Ni-S system (Drüppel & Wagner, in prep.; Fig. 14.24). The fletcherites are near-binary, generally with compositions of $\text{Cu}_{0.2}\text{Ni}_{3.1}\text{S}_4$ – $\text{Cu}_{1.1}\text{Ni}_{2.1}\text{S}_4$ and low Fe- and Co-contents of 0.0-1.6 wt. % and 0.1-0.7 wt.%, respectively. Most grains exhibit an asymmetric zoning pattern, involving decreases of Ni and increases of Cu with increasing distance from millerite. Thus, the typifying feature of the investigated fletcherites is a pronounced Cu substitution into the structure, reaching a maximum of 21.4 wt.% at the grain margins, corresponding to 1.1 Cu atoms per formula unit (Fig. 14.25). The solid-solution series extends from the end-member polydymite towards what is considered as Co- and Fe-poor

fletcherite. The substitution scheme for the observed linear correlation trends, relating Ni and Cu but not Ni and Co or Ni and Fe, suggests a substitution of Cu^{2+} for Ni^{2+} on the tetrahedral sites of thiospinel.

Remarkably, fletcherite has only been observed in sample Ku-98-130a, where millerite is intimately associated by chalcopyrite, thus suggesting that the replacement of millerite by fletcherite is accompanied by the breakdown of chalcopyrite, the latter providing the Cu incorporated by the Cu-Ni fletcherite.

14.15 Barite

Barite has been observed in one sample of the *REE-rich carbonatitic breccia* (Ku-98-130b), where the very fine-grained sulphate is localised in the interstices between large ankerite grains and brownish carbocernaite aggregates. Representative analyses are given in Table A.5.1.37 in the Appendix A.5.1.

The composition of the analysed barites differs from the ideal formula in revealing significant amounts of both CaO (0.2-1.4 wt.%) and Ce_2O_3 (2.5-3.1 wt.%), whereas the Sr contents are near the detection limit, thus suggesting, that the available Sr was incorporated by the synchronously crystallising strontianite. The precipitation of barite may be related to late-stage oxidation of the reduced sulphur species to sulphate in the evolved carbonatitic solutions carrying significant amounts of both Ba and Ce. This interpretation is in good accordance with the high LREE contents of the co-crystallising strontianite. The fact that barite occurs as a texturally late phase in the REE-carbonatite, whereas all other S-bearing minerals predating the barite formation are sulphides, strongly suggests an increase of the oxidising conditions during carbonatite evolution.

14.16 Unspecified Na-Al phase

The unspecified Na-Al phase occurs as a late-stage alteration product of sodalite in the sodalite-rich carbonatitic breccia, where it replaces the sodalite along its margins and cracks. The transparent Na-Al phase is characterized by a fibrous morphology, with the hair-like needles of <

0.1 μm in width and 0.5-3 μm in length, commonly found in radiating clusters. Regarding the above mentioned properties the phase strongly resembles natrolite, which indeed is a common alteration product of sodalite.

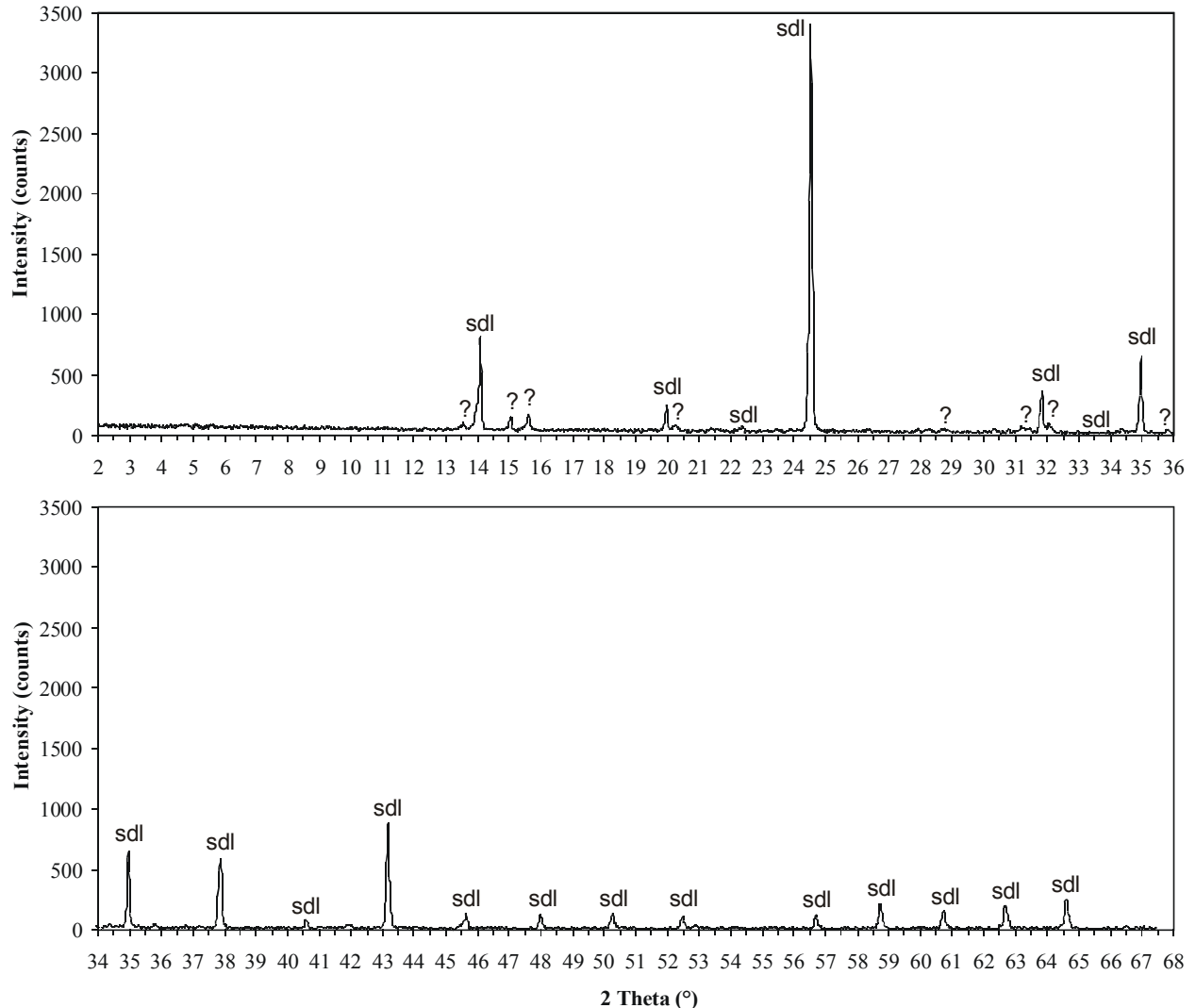


Fig. 14.26: Powder X-ray diffractometry spectra of the unspecified Na-Al phase (peaks marked as ?), which is intimately intergrown with sodalite (peaks marked as sdl).

Remarkably, however, the Na-Al phase contains large amounts of Al (40-43 wt.%) and Na (7.6-9.5 wt.%) with a molecular ratio of approximately 4:1 (Table A.5.1.38 in the Appendix A.5.1), whereas the amounts of all other elements detectable with the help of EMP (EDA spectra), including Si, are negligible (Table A.5.1.38 in the Appendix A.5.1) and, if analysed, are obviously caused by the interference with the intimately intergrown sodalite. Thus, the elements remaining as possible additional constituents of the Na-Al phase include H, C, N and O. Only two natural occurring phases are yet known, being composed of the above mentioned chemical species, i.e. dawsonite $\text{NaAlCO}_3(\text{OH})_2$ and diaoyudaoite $\text{NaAl}_{11}\text{O}_{17}$. However, the stoichiometry

of both minerals differs significantly from that of the Na-Al phase. The same holds true for yet known synthetic Na-Al phases. A best-fit formula was reached by calculating the Na-Al phase as an oxide, leaving a deficiency of 10 wt.% in the total sum of oxides, which was subsequently converted into a corresponding amount of H₂O. Following this calculation, the formula would be close to NaAl₄O_{6.5}·1.5H₂O.

In order to constrain its crystal structure, the Na-Al phase was separated from the rock samples Ku-98-18 and Ku-98-130b, powdered and investigated with the help of powder X-ray diffractionmetry (XRD). However, due to the intimate intergrowth of the Na-Al phase with sodalite, measurements yielded insufficient results, with the spectra being largely dominated by the sodalite patterns. Thus, only minor and very small peaks deviating from those of sodalite were identified, which may be representative of the Na-Al phase (Fig. 14.26). Remarkably, however, none of the yet known synthetic and natural phases fits the remaining 2 Theta values, thus suggesting that the Na-Al phase represents a new mineral species.

The Si-free composition of the phase and its high Al:Na ratio of 4:1 when compared to sodalite (Al/Na < 1) strongly suggests that even the late-stage carbonatite fluids were still strongly deficient in Si but contained only minor amounts of Na.

14.17 Trace and rare earth element chemistry of selected minerals – a combined LA-ICPMS – SRXRF study

14.17.1 Carbonates

In order to investigate the trace element composition of carbonates, formed during different stages of carbonatite evolution, magmatic calcite from one sample of the carbonatitic breccia (Ku-98-14) as well as magmatic ankerites from two samples of the carbonatitic breccia (CB,l: Ku-98-18 and CB,REE: Ku-98-130a) and one ferrocarbonatite sample (Ku-01-04) were analysed for rare-earth and other trace elements with the help of high-resolution synchrotron micro-XRF. Analytical results for ankerite and calcite are compiled in Tables A.5.2.1 and A.5.2.2, respectively, in the Appendix A.5.2.

Interstitial calcite of the *carbonatitic breccia* sample Ku-98-14 is rich in SrO (1.6-1.8 wt.%) and the LREE (La: 0.5-0.6 wt.%, Ce: 0.9-1.3 wt.%, Nd: 0.4-0.5 wt.%, Sm: 0.03-0.06 wt.%, Eu: 0.02-0.03 wt.%, Gd: 0.02-0.03), whereas Zn (8-31 ppm), Kr (6-11 ppm), Nb (16-54 ppm), Ba (0-196 ppm) and the HREE (Tb: 22-40 ppm, Dy: 151-240 ppm, Ho: 9-27 ppm, Er: 56-94, Tm: 0-9 ppm, Yb: 49-78 ppm, Lu-14-39 ppm) are present in only minor amounts. The analysed calcite displays a concentric zoning pattern, involving a core preference for the REE and Sr, whereas Ca, Fe and Mn trend to rim. The Σ REE in calcite ranges between 1.9 wt.% (rim) and 2.5 wt.% (core). The calcite is characterized by positively correlated $(\text{La/Nd})_{\text{cn}}$ and $(\text{La/Yb})_{\text{cn}}$ ratios increasing from 2.3 (core) to 2.6 (rim) and from 50 (core) to 78 (rim), respectively. The calcites display straight REE patterns and strong positive $(\text{Eu/Eu}^*)_{\text{cn}}$ anomalies (1.7-1.9). An accentuated negative trough for Sm is developed for all REE patterns.

Regarding their Fe, Mg and Ca contents all investigated ankerite crystals show a quite homogeneous composition with the X_{Mg} ranging between 0.57 and 0.64. Traces of Zn (6-290 ppm), Kr (8-116 ppm) and Nb (6-132 ppm) are present in all analysed ankerites. However, the carbonates show considerable variations of the REE between individual samples.

(1) Anhedral matrix ankerite from the *layered carbonatitic breccia* (Ku-98-14) has a Σ REE ranging between 0.1 wt.% and 0.8 wt.%, distinctly lower than those of the coexisting calcite. The REE patterns of the ankerites are straight, with high $(\text{La/Nd})_{\text{cn}}$ and $(\text{La/Yb})_{\text{cn}}$ ratios of 2.6-2.9 and 42, respectively (Fig. 14.27a). A strong positive $(\text{Eu/Eu}^*)_{\text{cn}}$ anomaly (1.8) and negative Sm and Tm anomalies have been observed for one ankerite with elevated REE contents.

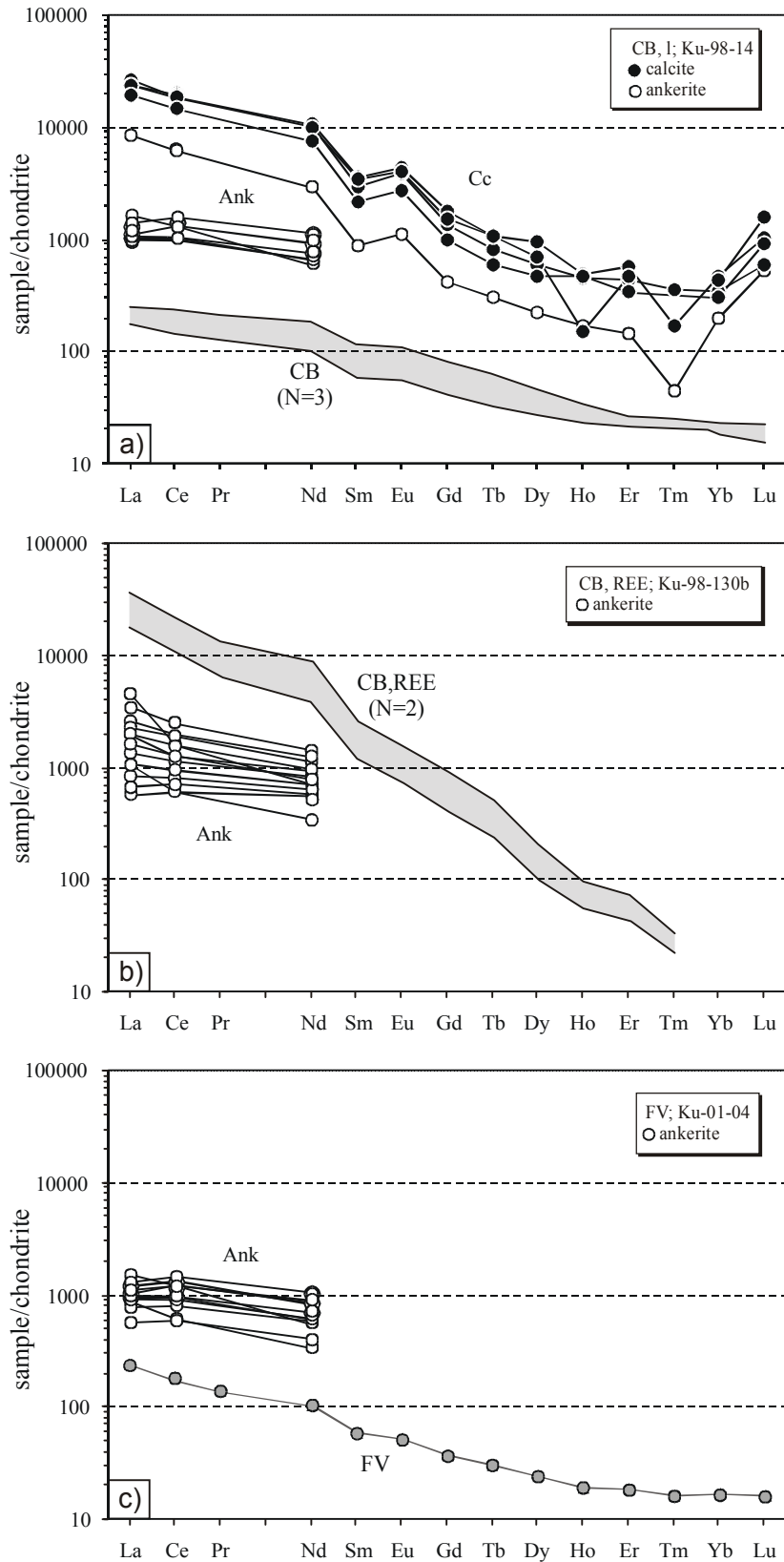


Fig. 14.27: Chondrite-normalized rare-earth element patterns of carbonates from the Swartbooisdrif carbonatitic breccia (analyzed by SRXRF). Chondrite-normalized rare-earth element patterns of the respective rock samples (grey; analyzed by ICP-AES and ICPMS) are illustrated for comparison. **a)** Layered carbonatitic breccia. **b)** REE-rich sample of the sodalite-rich carbonatitic breccia. **c)** Ferrocarbonatite vein.

The REE patterns of ankerite are in excellent accordance with those obtained for calcite and the corresponding rock samples, even though the totals of REE in ankerite are lower than those of calcite and higher than those of the carbonatitic breccia.

(2) Matrix ankerite from a *REE-rich sample of the sodalite-rich carbonatitic breccia* (Ku-98-130b) has comparably low Σ REE of 0.1-0.3 wt.%, which, however, may increase to values of up to 0.8 wt.% when reaching bordering carbocernaite. Their $(\text{La}/\text{Nd})_{\text{cn}}$ ratios are generally high but variable, ranging between 1.1-5.4. Values of REE heavier than Nd are below the detection limit. Regarding the high $(\text{La}/\text{Nd})_{\text{cn}}$ ratios, the REE patterns of the ankerites agree well with those of the corresponding rock samples of the REE-rich carbonatitic breccia (Fig. 14.27b). However, in clear contrast to the latter, ankerites contain distinctly lower totals of REE, thus suggesting that the high REE amounts of the rock samples are rather caused by high modal amounts of carbocernaite. SRXRF analyses of carbocernaite were performed, but attained mostly unreasonable and highly variable trace element values.

(3) With values of 0.1-0.2 wt.%, anhedral grains of matrix ankerite from the late *ferrocarbonatite vein* (Ku-01-04) reveal the lowest average Σ REE of all ankerites investigated. Values of REE heavier than Nd are too low to be detected with help of SRXRF (Fig. 14.27c). The $(\text{La}/\text{Nd})_{\text{cn}}$ ratios of the ankerites (1.1-1.4) are comparably low, in good accordance with those of the corresponding rock sample, which, however, contains significantly lower Σ REE.

In summary, the following evolutionary trend can be established for carbonates of the Swartbooisdrif carbonatites. Ankerites from the first carbonatite generation, the carbonatitic breccia, generally reveal higher Σ REE and $(\text{La}/\text{Nd})_{\text{cn}}$ ratios than those of the late ferrocarbonatite veins. The LREE contents of ankerite from both the carbonatitic breccia and the ferrocarbonatite veins are higher than those of the corresponding rock samples, thus suggesting that the carbonates contain almost the bulk of LREE of the respective samples. In clear contrast, ankerites from the REE-rich samples of the carbonatitic breccia display distinctly lower Σ REE and $(\text{La}/\text{Nd})_{\text{cn}}$ ratios than the corresponding rock samples, hence implying that the high overall amounts of LREE in these samples are caused by their high modal amounts of carbocernaite. The fact, that Σ REE of the early crystallized ankerites from the REE-rich carbonatitic breccia are in the range of those of ankerites from the ferrocarbonatite veins and even lower than those of ankerites from the REE-poor carbonatitic breccia, strongly suggests that the enrichment of REE in these rock samples is not a primary feature of the carbonatite melt but was caused by secondary processes, such as hydrothermal alteration.

14.17.2 Sodalite

In order to constrain the origin of sodalite from the *sodalite-rich carbonatitic breccia*, X-ray fluorescence (XRF) measurements of hand-picked sodalite separates and in situ LA-ICPMS analyses have been performed. XRF analyses of sodalite separates, however, attained mostly unreasonable and highly variable trace element values, resulting from a variable but generally high amount of mineral and fluid inclusions contained in the sodalite and are thus excluded. Analytical results for the LA-ICPMS analysis are compiled in Table A.5.3.1 in the Appendix A.5.3. A description of the analytical technique is given in the Appendix A.2.5

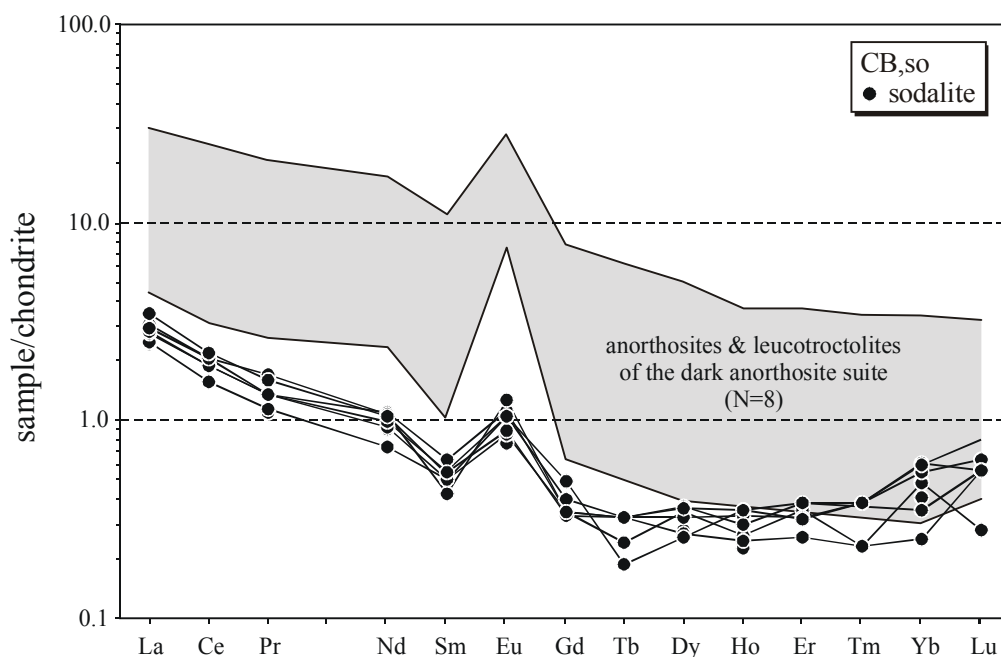


Fig. 14.28: Chondrite-normalized rare-earth element patterns of sodalite from the Swartbooisdrif carbonatitic breccia and anorthosites of the Kunene Intrusive Complex (analysed by LA-ICPMS and ICP-AES, respectively).

The REE contents of sodalite determined by LA-ICPMS are generally low (ΣREE : 2.5-3.3 ppm), whereas remarkably high values of As (422-657 ppm), Ti (38-57 ppm), Sn (14-51 ppm) and Ba (57-92 ppm) have been recorded. The Rb and Sr contents of sodalite are in the range of 9-13 ppm and 10-14 ppm, respectively. Regarding their REE-patterns, all analysed sodalites are characterized by an enrichment of the light REE ($(\text{La}/\text{Yb})_{\text{cn}}$: 4.6-12.1) and flattening in the heavy REE (Fig. 14.28). All REE-patterns display a strong positive Eu anomaly ($(\text{Eu}/\text{Eu}^*)_{\text{cn}}$: 1.5-3.3) although the Ca-contents of sodalite are below the detection limit. These REE-patterns are quite similar to those obtained for anorthosite and leucotroctolite samples of the dark anorthosite suite, thus suggesting that most of the sodalite, abundant in the sodalite-rich

carbonatitic breccia, was formed at the expense of plagioclase of both the bordering anorthosites and the incorporated anorthositic xenoliths. Following this argument, the relative decrease of the absolute amounts of the REE in the sodalite may be related to a volume increase during the transformation of plagioclase (specific gravity: 2.7 g/cm³) into the less dense sodalite (specific gravity: 2.3 g/cm³).

14.17.3 Biotite

In order to investigate the rare earth and trace element composition of biotite coexisting with apatite in samples of the *carbonatitic breccia* (Ku-98-14), SRXRF analyses were performed (Table A.5.2.3 in the Appendix A.5.2).

However, the REE contents of all analysed biotites remain below the detection limit, thus confirming that almost the bulk of the available REE was incorporated by synchronously crystallising apatite and/or ankerite. Minor amounts of Zn (881-1654 ppm), Rb (282-524 ppm), Sr (13-72 ppm), Sn (35-287 ppm), Ba (100-5200 ppm) were detected, displaying oscillatory zoning in the analysed biotite grains. A core preference for Zn was observed for one biotite, which is inversely correlated with Fe. Ba trends to rim, whereas a patchy to oscillatory zoning was observed for the Rb, Sr and Sn.

14.17.4 Apatite

Apatite is a geochemical and petrogenetic indicator mineral of carbonatites (e.g. Le Bas et al., 1992; Rae et al., 1996; Bühn et al., 2001), with its REE chemistry suggested to be linked to the degree of carbonatite differentiation (Bühn et al., 2001). Therefore, the REE contents of optically zoned apatites from a sodalite-free sample of the *layered carbonatitic breccia* (Ku-98-14) have been investigated in some detail with the help of high-resolution synchrotron micro-XRF (SRXRF) analysis (Drüppel et al., 2002b; Table A.5.2.4 in the Appendix A.5.2).

In sample Ku-98-14, apatite occurs in two different textural positions, i.e. (1) as large subhedral matrix grains and (2) as medium- to fine-grained inclusions in biotite, which, at the same time, are characterized by the highest Na contents. All analysed fluorapatites display a weak chemical zonation, with the preserved cores being concentrically zoned, involving a decrease of F, Fe and the REE as well as an increase of Ba towards the core-rim contacts. Small

apatite grains, lacking a distinct core zoning, as well as rims of large apatite grains are characterized by an oscillatory zoning with respect to Cl, Mn, Ba, F, and the REE, whereas Fe and Y increase towards the outer margins. The apatites involve at least two substitution mechanisms (Fig. 14.29), i.e. (1) the "belovite scheme" $\text{Ca}^{2+} + \text{Ca}^{2+} \rightarrow \text{Na}^{+} + \text{REE}^{3+}$ (Rønso, 1989), which is a quite common substitution mechanism of apatites from carbonatites, and, much less frequently, (2) the "britholite scheme" $\text{Ca}^{2+} + \text{P}^{5+} \rightarrow \text{Si}^{4+} + \text{REE}^{3+}$ (Hogarth, 1989).

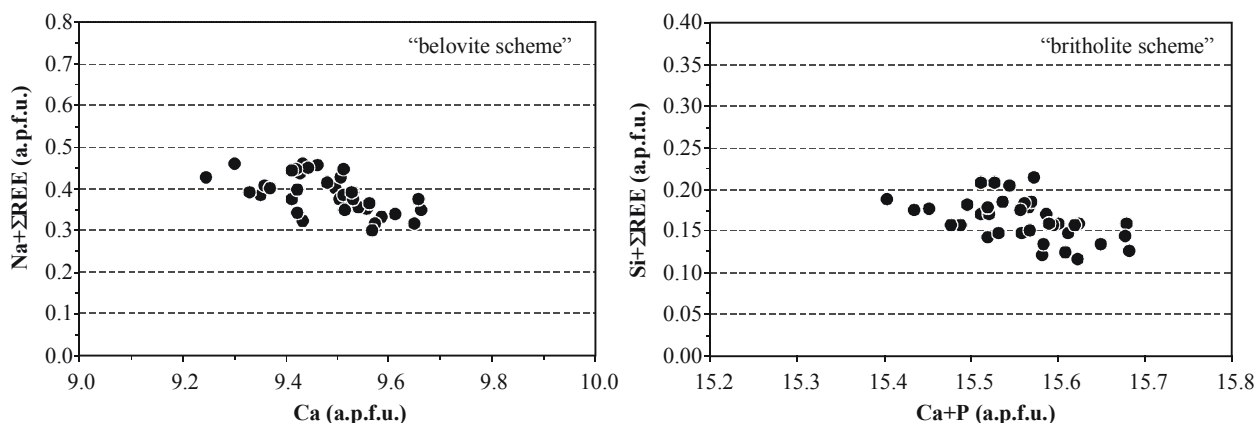


Fig. 14.29: Correlation patterns of Ca versus Na+REE and Ca+P versus Na+Si (a.p.f.u.; formula calculation based on 25 oxygens) in apatite from the carbonatitic breccia (Ku-98-14).

The ΣREE in apatite ranges between 0.9 and 3.1 wt.%, with the highest values obtained for matrix apatite. The fluorapatites have relatively high La contents of 0.2-0.7 wt.% and high, positively correlated $(\text{La}/\text{Nd})_{\text{cn}}$ and $(\text{La}/\text{Yb})_{\text{cn}}$ ratios increasing from 1.5 to 4.4 and from 33 to 240 (except one value of 488), respectively. All fluorapatites display straight REE patterns and weakly positive to distinctly negative $(\text{Eu}/\text{Eu}^*)_{\text{cn}}$ anomalies of 0.3-1.3 (Fig. 14.30). Accentuated negative Tb, Er and Yb troughs are mainly displayed by apatite included in biotite, but may also be prominent in matrix apatite when reaching the contacts to the bordering biotite. This depletion of the HREE may be related to the early crystallization of pyrochlore in the investigated sample, which, however, was too small to obtain reliable results with the help of EMP or SRXRF analysis. With values of 26-163 ppm the Y concentrations of all fluorapatites are extremely low, with the Y/Ho ratios (0.6-7.8) lying even below the chondritic value of 28. A weak positive correlation is seen between the Sr and the Y contents of the fluorapatites.

The high ΣREE , $(\text{La}/\text{Nd})_{\text{cn}}$ and $(\text{La}/\text{Yb})_{\text{cn}}$ ratios and extremely low Y/Ho ratios of the analysed apatites as well as their straight REE patterns agree well with the findings of Böhn et al. (2001) for fluorapatites from strongly fractionated carbonatites. The wide range of $(\text{Eu}/\text{Eu}^*)_{\text{cn}}$ anomalies (0.3-1.3) of the fluorapatites, which are not displayed by the whole-rocks, may

indicate the presence of coexisting hydrous fluids which might have extracted Eu^{2+} from the carbonatite melt, a process proposed by Böhn et al. (2001). In contrast, the accentuated negative anomalies for Tb, Er and Yb displayed by the Swartbooisdrif fluorapatites have not been described so far for other apatites from carbonatites world-wide. The fact, that none of the anomalies is observed in the corresponding whole rocks may either suggest partitioning of the elements into a coexisting fluid, or, more probable, fractionation of the compatible elements Tb, Er and Yb in a HREE-rich phase, such as early crystallising pyrochlore.

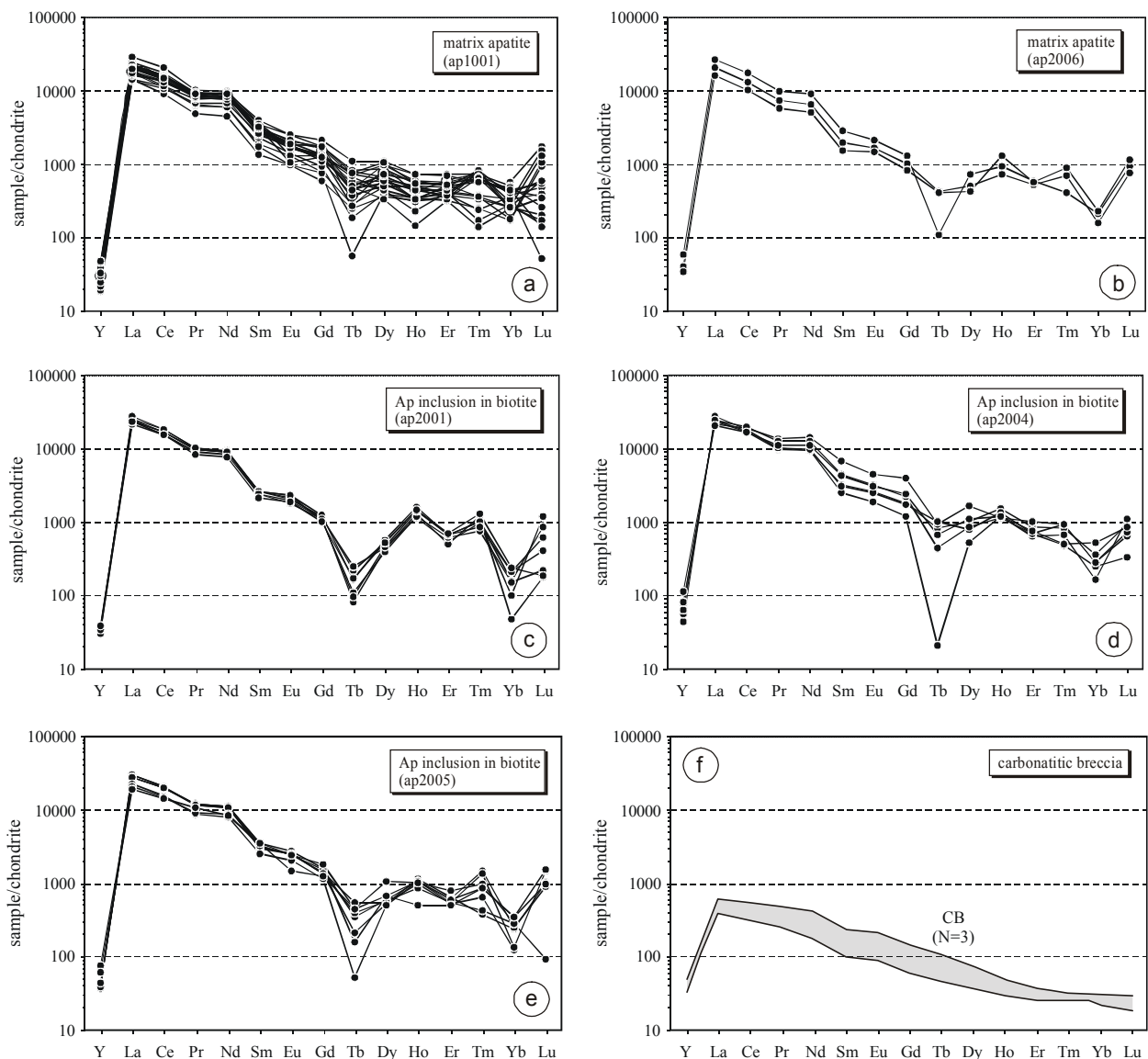


Fig. 14.30: a) to e) Chondrite-normalized rare-earth element patterns of apatite from the Swartbooisdrif carbonatitic breccia (analysed by SRXRF). f) REE-patterns of the carbonatitic breccia itself (ICP-AES analyses) are given for comparison.

Figure 14.31 compares the trace-element composition of the Swartbooisdrif carbonatites with that of fluorapatites from calciocarbonatites and from metasomatized country rocks of other

carbonatite complexes elsewhere investigated by Böhn et al. (2001). The $(\text{La}/\text{Nd})_{\text{cn}}$ and $(\text{La}/\text{Yb})_{\text{cn}}$ ratios as well as La_{cn} and the $(\text{La}/\text{Yb})_{\text{cn}}$ ratios display a positive correlation whereas CaO and $\Sigma\text{REE}_{\text{cn}}$ are negatively correlated, in good accordance with the findings of Böhn et al. (2001) for magmatic fluorapatites from calciocarbonatites. However, in clear contrast to the latter, the Swartbooisdrif fluorapatites are characterized by a weak positive correlation of the $(\text{La}/\text{Yb})_{\text{cn}}$ and $(\text{Eu}/\text{Eu}^*)_{\text{cn}}$ ratios, which was also observed for metasomatically formed fluorapatites from the Okoruso carbonatite, Namibia (Böhn et al., 2001). This distinct behaviour of the Swartbooisdrif apatites, when compared to orthomagmatic apatites from calciocarbonatites, may imply that the fractionation mechanisms in ferrocarbonatite magmas differ from those of calciocarbonatites with respect to Eu.

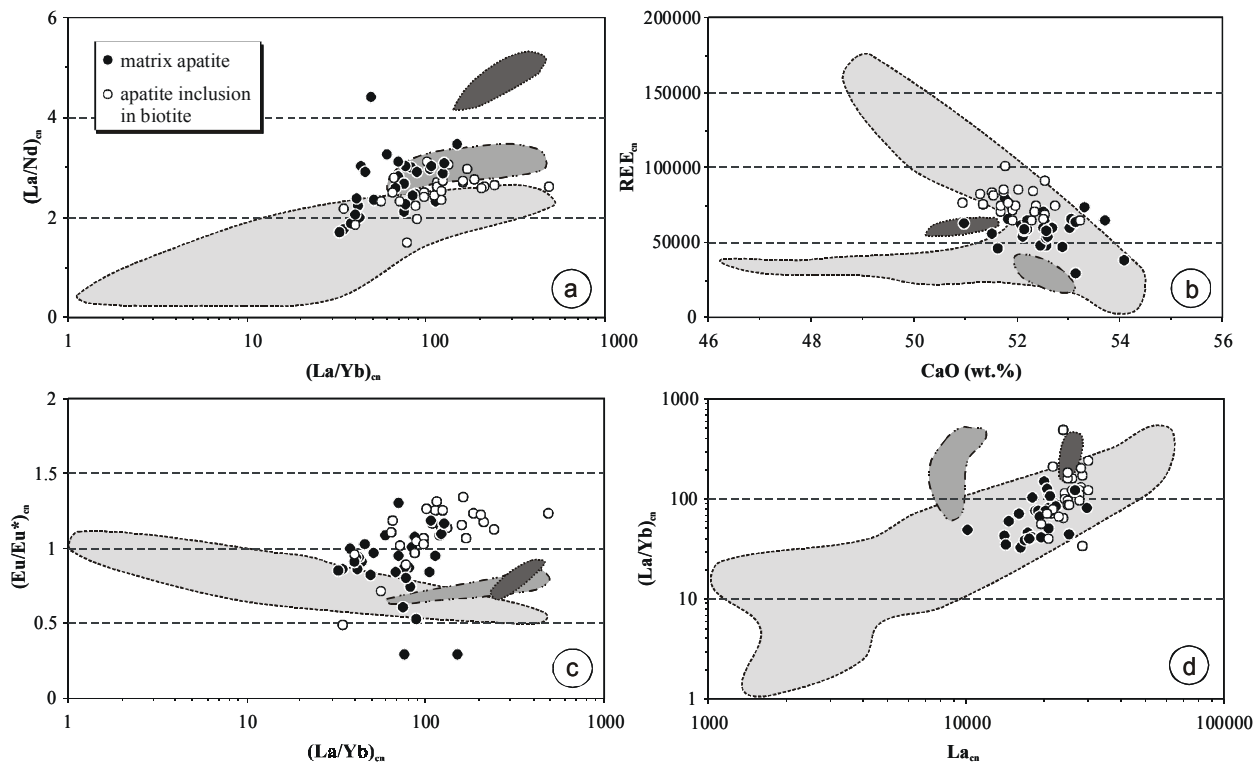


Fig. 14.31: Trace element characteristics of the Swartbooisdrif fluorapatite compared the data of Böhn et al. (2001) for fluorapatites from calciocarbonatites (light grey shaded fields), from a brecciated fluorapatite layer in calciocarbonatite (dark grey shaded fields) and from a metasomatized marble country rock in contact to a calciocarbonatite (middle grey shaded fields).

14.17.5 Pyrochlore

Optically zoned pyrochlore crystals of the sample Ku-01-04, taken from a late-stage *ferrocarbonatite vein*, have been investigated in some detail with the help of SRXRF analysis

(Table A.5.2.5 in the Appendix A.5.2), which generally reveals high amounts of Cr (0.2-3.2 wt.%), Ta (0.2-0.9 wt.%), W (0.2-0.8 wt.%) and part of the REE (La: 0.4-1.1 wt.%, Ce: 0.8-2.3

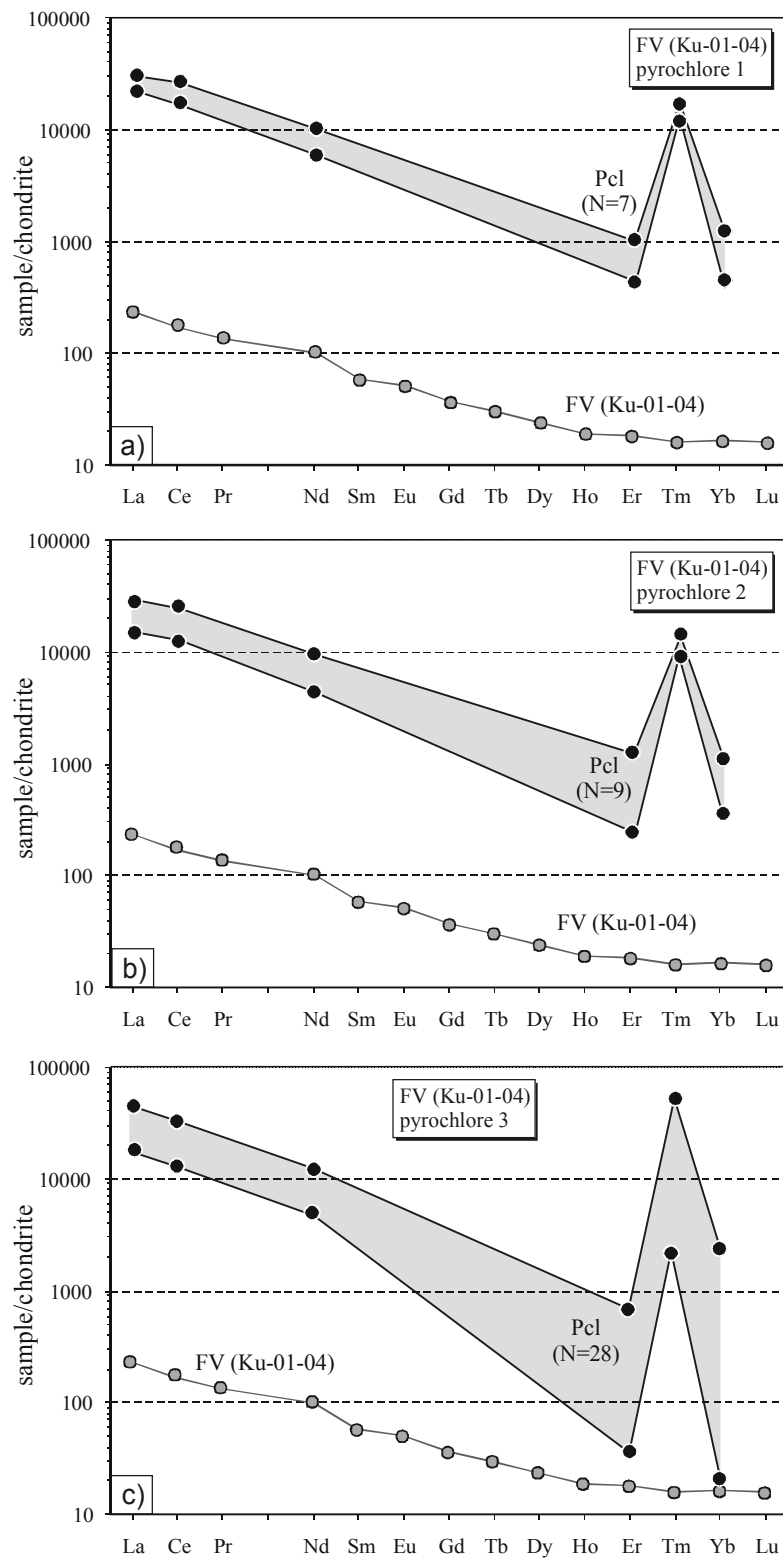


Fig. 14.32: Chondrite-normalized rare-earth element patterns of pyrochlore from a ferrocarnatite vein (Ku-01-04), analysed by SRXRF. REE-patterns of the corresponding whole-rock (ICP-AES analyses) are given for comparison. **a)** and **b)** Small matrix grains of pyrochlore (ca. 0.1 mm). **c)** large pyrochlore grain (0.9 mm).

wt.%, Nd: 0.2-0.8 wt.%, Er: 6-201 ppm, Tm: 243-1308 ppm, Yb: 24-375 ppm). The fine-scaled oscillatory zoning of pyrochlore, observed microscopically, is also displayed by its trace element chemistry. All analysed grains show a concentric zonation pattern with a rim preference for the LREE, Yb and Ta, whereas Er trends to core. Even though no reliable results were obtained with respect to the remaining REE it can be expected that the pyrochlores additionally contain a certain amount of Tb and may thus indeed be responsible for the negative Tb, Er and Yb anomalies observed for fluorapatite.

The Σ REE in pyrochlore ranges between 1.4 and 4.1 wt.%, with the highest values obtained for the smallest pyrochlore grains (Fig. 14.32a, b). All pyrochlores display straight REE patterns with high $(\text{La}/\text{Nd})_{\text{cn}}$ and $(\text{La}/\text{Yb})_{\text{cn}}$ ratios (1.4-4.4 and 12.5-162, respectively) and strong positive $(\text{Tm}/\text{Tm}^*)_{\text{cn}}$ anomalies (2.3-17.4), which are most accentuated in the larger pyrochlore grains (Fig. 14.32c). The high Tm amounts of the analysed pyrochlores agree well with the conspicuous negative Tm anomalies observed for both calcite and ankerite, thus suggesting that most of the Tm available was incorporated into the early crystallising pyrochlore. The pronounced LREE enrichment in the pyrochlores reflects the REE distribution in the ferrocarnatites.

15 Geochemistry

15.1 Major and trace element geochemistry

Geochemical data were obtained for 5 rock samples of the fenitized anorthosites, 8 rock samples of the fenitized syenites, 1 rock sample of the nepheline syenite, 21 rock samples of the carbonatitic breccia, 3 samples of sodalite accumulations from the carbonatitic breccia and 2 rock samples of the ferrocarbonatite veins. The investigation of the bulk rock geochemistry shall serve as a tool for constraining the nature and origin of the carbonatitic melts and for characterizing the carbonatite-induced fenitizing processes, which led to the formation of the Swartbooisdrif sodalite deposits. Moreover, 2 carbonatites, sampled close to the Namibian-Angolan border and presumably belonging to the Mesoproterozoic Luopongola complex of SW Angola, have been analysed for their major and trace element geochemistry, in order to investigate a possible genetic relationship between the Swartbooisdrif and the Luopongola carbonatite centres.

Fenitized anorthosite (A,f)

Ku-98-71, Ku-98-72, Ku-98-77, Ku-98-78, Ku-98-84

Fenitized syenite (S,f)

Ku-98-66, Ku-98-70s, Ku-98-73s, Ku-98-74, Ku-98-103s, Ku-99-09, Ku-99-19s

Fenitized nepheline syenite (S,ne)

Ku-99-15a

Carbonatitic breccia (CB)

Layered carbonatitic breccia (CB,l): Ku-98-05, Ku-98-28, Ku-98-56, Ku-98-70c, Ku-98-118, Ku-99-04, Ku-99-17, Ku-99-19c

Massive carbonatitic breccia (CB,m): Ku-98-08, Ku-98-73c, Ku-98-103c

Sodalite-rich carbonatitic breccia (CB,so): Ku-98-17, Ku-98-27, Ku-98-80, Ku-98-83, Ku-98-131 (sodalite-free zone), Ku-99-05, Ku-99-07, Ku-99-08

Sodalite accumulations from the sodalite-rich carbonatitic breccia (Sdl): Ku-98-18, Ku-98-47, Ku-01-OD3

REE-rich carbonatitic breccia (CB,REE): Ku-98-130a, Ku-98-130b

Ferrocarbonatite veins (FV)

Ku-01-04, Ku-01-05

Carbonatites of the Lupongola complex, NW Namibia – SW Angola

Ku-01-08, Ku-01-10

Geochemical data are listed in Table A.5.4.1 in the Appendix A.5.4. Analytical conditions are provided in the Appendix A.2.4.

15.1.1 Fentitized anorthosite

The five samples of fentitized anorthosites were taken from two metasomatically overprinted contact zones between the dark anorthosite suite and large dykes of the carbonatitic breccia. A principal problem for the interpretation of the geochemical data of the investigated samples is, that they represent fentitized equivalents of variable anorthosite lithologies (anorthosite and leucogabbronorite), displaying small-scale compositional variations.

The fentitized anorthosites of both sampled profiles reveal variable SiO_2 and Al_2O_3 amounts of 43-54 wt.% and 20-28 wt.%, respectively, with the lowest values being obtained for the most altered samples, thus suggesting an interaction between the anorthosites and strongly Si-deficient fluids (Fig. 15.1). The rocks show enrichment in Fe relative to Mg and strong increases in LOI (CO_2 and H_2O), which are reflected by increasing modes of ankerite and magnetite and the replacement of pyroxene by magnesio-riebeckite and/or biotite. Gains in Fe are suggested to be caused by the influx of fentitizing solutions carrying considerable amounts of Fe^{3+} , derived from the carbonatite magma.

Sodium may either increase or decrease with increasing proximity to the carbonatite (Fig. 15.1). It remains uncertain, however, if the apparent depletion of Na in part of the samples (1) results from the injection of Ca-rich fentitizing fluids or (2) reflects inherited compositional variations of the magmatic precursors, such as variable ratios of cumulus plagioclase and intercumulus Fe-Mg silicates. By now possibility (2) is the preferred model, since the progressive transformation of Ca-rich plagioclase into oligoclase, albite, and sodalite clearly testifies to the influence of fentitizing solutions carrying considerable amounts of Na.

Calcium decreases with increasing fentitization (Fig. 15.1), even though the modal amounts of carbonate increase in the same direction. It has to be mentioned, however, that Ca-rich phases of the precursor rocks, such as cumulus plagioclase, intercumulus clinopyroxene and

late-magmatic Ca-amphibole, were continuously replaced by sodium-rich minerals during fenitization, hence suggesting that the solutions were characterized by conspicuously high Na:Ca ratios.

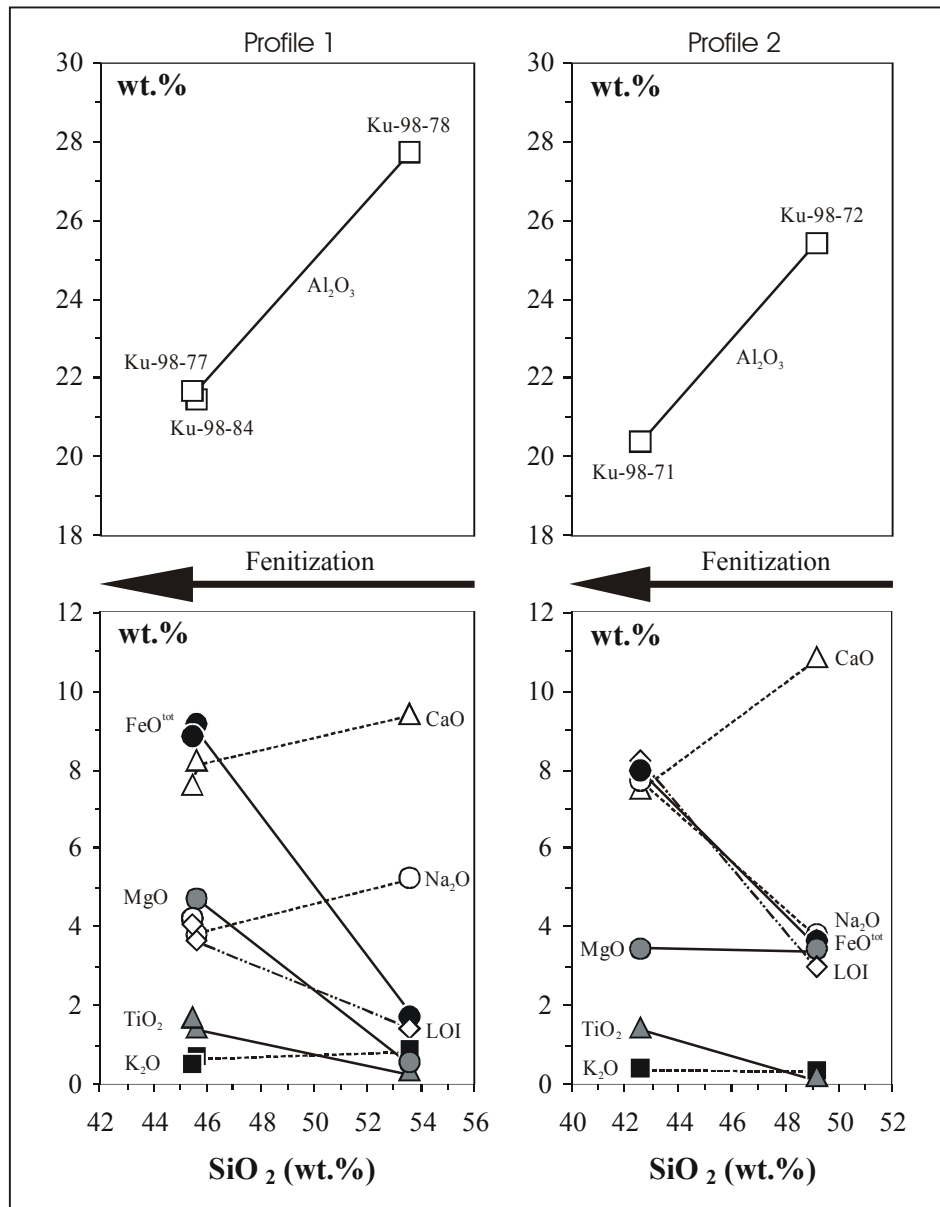


Fig. 15.1: Compositional changes during the progressive fenitization of anorthositic rocks sampled along two profiles at the contact zones between anorthosite and the carbonatitic breccia (arrows mark increase of fenitization of the two sampled profiles).

Trace elements such as V and Zn, incorporated in magnetite, and Co and Ni, incorporated in pyrite, became strongly enriched during fenitization. Sr is either weakly depleted or strongly enriched when compared to least altered samples, reflected by variable modes of ankerite and feldspar. In samples with small amounts of biotite, Ba and K are depleted. Elements which show an indifferent behaviour during metasomatism are P, Cr and Ga.

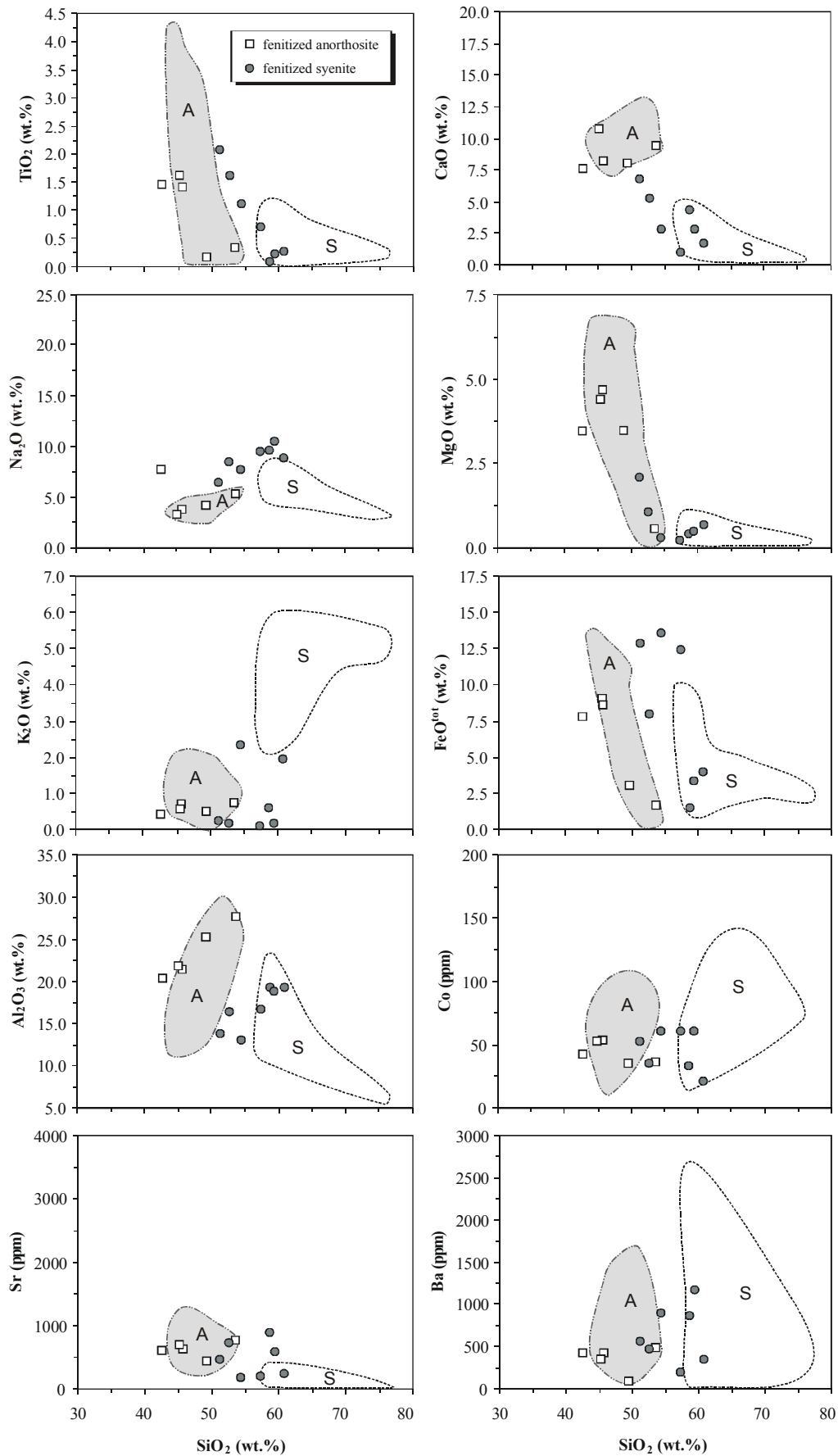


Fig 15.2: Compositional variation of the fenitized anorthosites and fenitized syenites compared to that of unaltered samples of the anorthositic suite (dash-dotted grey fields) and the felsic suite (dashed fields), illustrated in selected Harker-diagrams.

When compared to the compositional fields of unaltered samples of the anorthosite suite (Fig. 15.2) the fenitized anorthosites display a weak tendency towards lower Si, Ca, K and Ba, whereas Na trends to higher values. However, due to the generally wide compositional scatter of magmatic samples of the anorthosite suite (anorthosites, leucotroctolites and leucogabbronorites), most of the fenitized anorthosites fall into the fields of their magmatic counterparts.

The obtained spectrum of chemical compositions, i.e. increases in Na, Mg, Fe, LOI, V, Zn, Co and Ni accompanied by decreases of Si, Al and Ca, mirrors the continuously changing modes of the anorthosites during fenitization. Judging from the observed geochemical trends, the solution responsible for metasomatism of the anorthosites is suggested to be a Si- and Al-deficient Na-rich hydrous fluid, which additionally carried considerable amounts of Fe, Mg, V, Co, and Ti as well as traces of Ca, K, Sr, Ba, and S, in good accordance with a derivation from a carbonatite melt.

15.1.2 Fenitized syenite

Fenitized syenites differ from their unaltered counterparts by containing higher average amounts of Na, Ti, Fe, Ca, P, V, Ni, Sr, Nb, Zr, Th, U, CO₂, and H₂O and lower contents of Si, K, Rb, and Ba (Fig. 15.2), reflected by the observed mineralogical changes, i.e. (1) the progressive replacement of K-feldspar by albite accompanied by minor muscovite (losses: Si, K, Rb, Ba, H₂O; gains: Na), (2) the alteration of anhydrous Fe-Mg silicates to hydrous phases (gains: H₂O), (3) increasing modes of magnetite (gains: Fe, V, Ti), ankerite (gains: Fe, Ca, Sr, CO₂), apatite (gains: Ca, P), pyrite (gains: Fe, S, Ni) and zircon (gains: Zr, Th, U). It remains uncertain, however, which phase incorporates Nb, since the behaviour of Nb is not linked to any other element detected with the help of EMP analysis. It may, however, be possible that minor amounts of pyrochlore were formed during fenitization, which were too small to be observed with the available analytical facilities. Elements remaining mostly uninfluenced during fenitization are Al, Mn, Co, Zn, Ga, Y, Pb, La, and Ce. The investigated samples do not display a clear correlation for the respective elements but a scatter of data points, thus indicating a strongly varying degree of contamination with Si-deficient and sodium-rich hydrous fluids that were also capable of transporting appreciable amounts of Fe, Ca, V, Ni, Ti, and Sr as well as traces of Nb, P, Zr, Th, and U. Even though the proposed composition of this fluid deviates slightly from that assumed for the solutions which altered the anorthositic samples, both rock suites may have

interacted with the same fluid, since the chemical deviations are most likely a function of compositional differences between the respective source rocks.

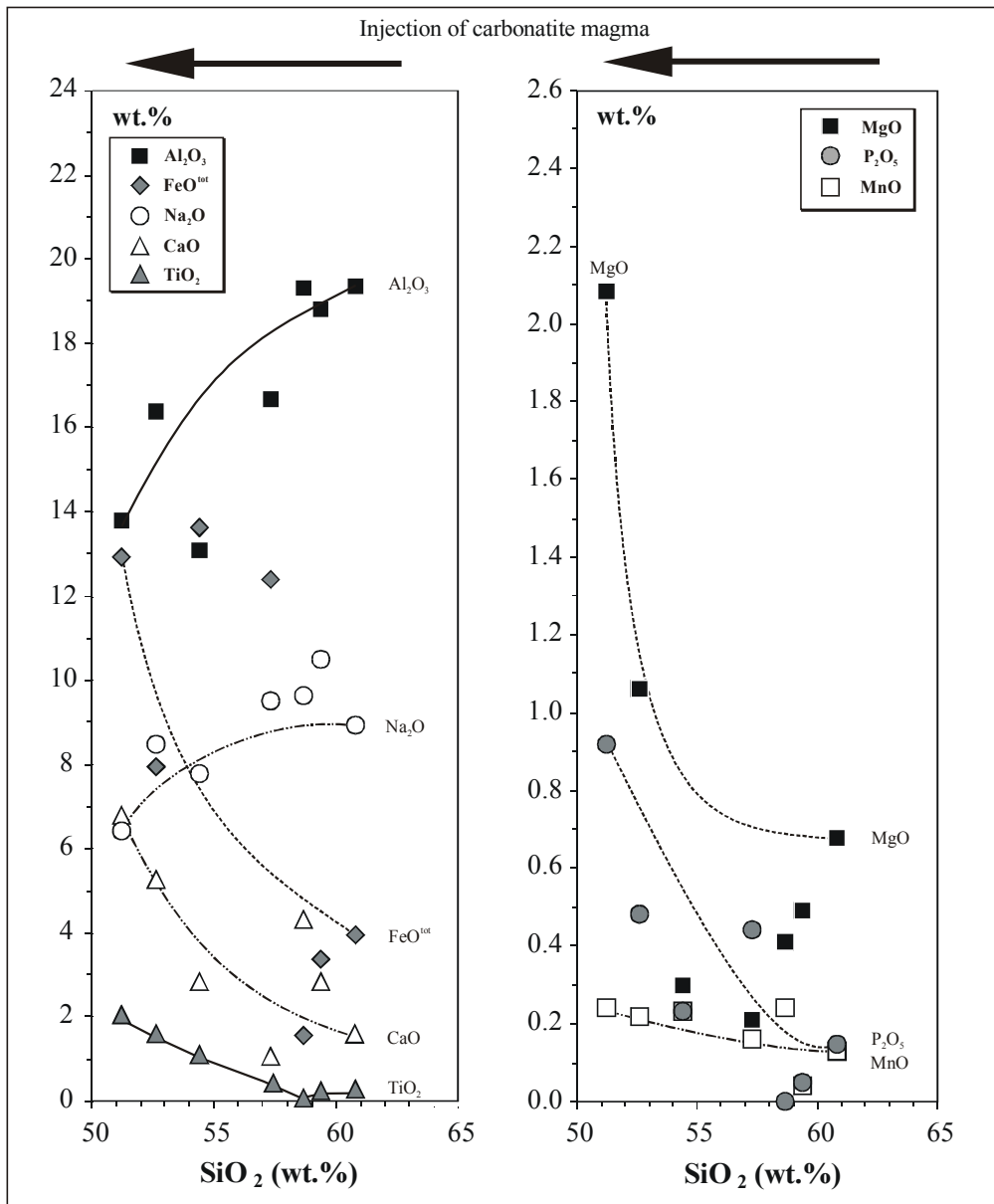


Fig 15.3: Compositional changes of the fenitized syenites, caused by the progressive injection of carbonatite melt (arrows mark increasing modal amounts of carbonatite minerals in the fenitized syenites).

Samples of the fenitized syenites themselves display distinct geochemical trends (Fig. 15.3), characterized by decreases of Si, accompanied by decreases in Al and Na and increases of Ca, Fe, Ti, Mn, Sr, and CO₃, which are reflected by the enrichment of both ankerite and magnetite with respect to albite. These trends, however, are not caused by the interaction of the syenites with fenitizing fluids but presumably result from a progressive injection of ferrocarbonatite magma, which intermingled with heavily sheared fragments of previously

fenitized syenites. It can thus be concluded, that the injection of fenitizing fluids predated the emplacement of the carbonatite melts for a certain time.

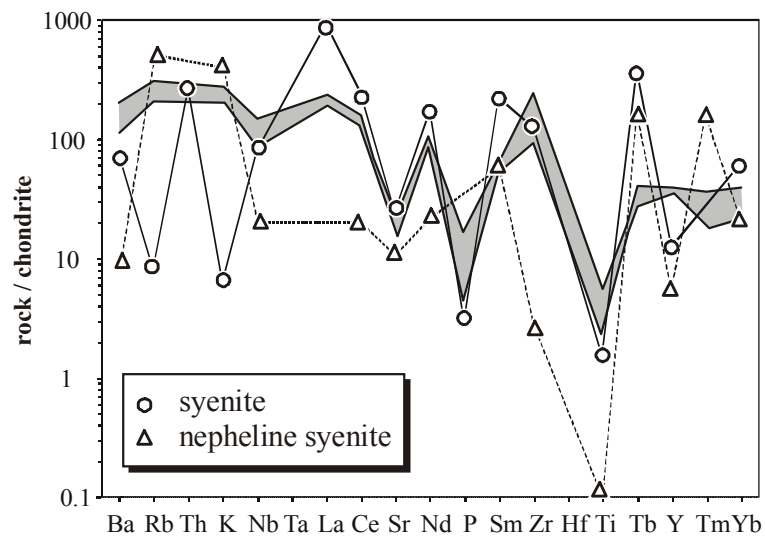


Fig. 15.4: Chondrite-normalized (except Rb, K, P) trace element abundance diagrams (Spider-grams) for the fenitized syenite (Ku-98-103s) and the fenitized nepheline syenite (Ku-99-15a), using the normalization factors of Thompson et al. (1983). Compositional ranges of the unaltered samples of the felsic suite (light grey) are marked for comparison.

Chondrite normalized trace element plots (Fig. 15.4) show depletion in Rb, K, Sr, P, Ti, and Y. When compared to unaltered samples of the syenite suite, the fenitized syenite sample contain reveal higher amounts of most of the plotted REE (La, Ce, Sm, and Tb) and distinctly lower contents of Rb, K, and Y, reflected by the breakdown of K-feldspar during fenitization. Increases of the REE are in excellent accordance with an interaction between the syenites and LREE- and Tb-rich, carbonatite-derived fluids.

15.1.3 Fenitized nepheline syenite

The partially fenitized nepheline syenite sample analysed (Ku-99-15a) has an alkali-rich, peraluminous and silica-undersaturated composition. The ratio $\text{FeO}^{\text{tot}}/(\text{MgO}+\text{FeO}^{\text{tot}})$ is 1.0. The Al, Na, K, and Rb contents are higher than those obtained for the fenitized syenites, whereas the nepheline syenite exhibits considerably lower amounts of Si, Ca, Fe, Sr, Ba, CO_2 , H_2O , and the REE.

The chondrite normalized trace element plot of the nepheline syenite (Fig. 15.4) displays accentuated troughs for Ba, Nb, Ce, Sr, Zr, Ti, and Y and a weak negative slope. The trace-

element patterns of the nepheline syenite thus differ significantly from those of all other syenites, constraining that the two rock types do not belong to one single suite. Remarkably however, the trace element patterns of the nepheline syenites display similarities (negative anomalies of Ba, Nb and Ti) with those of mantle-derived melts, weakly contaminated with crustal material (Thompson et al., 1983). The geochemical characteristics of the nepheline syenite could be explained by silicate-carbonate liquid immiscibility, even though textural evidence, as listed by Kjarsgaard & Hamilton (1989), is missing.

15.1.4 Carbonatites

15.1.4.1 Carbonatitic breccia

The 19 samples of the carbonatitic breccia (excluding the REE-rich samples), even though generally containing significantly lower absolute amounts of SiO₂ (22-45 wt.%), mostly display correlation patterns similar to those of the anorthosites when plotted in selected Harker diagrams (Fig. 15.5), hence suggesting that anorthosite rather than syenite is the dominant component of the incorporated fenitized wallrock xenoliths. Only one sample of the layered carbonatitic breccia (Ku-98-56), containing only minor amounts of carbonatite minerals, reveals relatively high SiO₂ contents (57 wt.%) and plots in the vicinity of the syenite field. The investigated samples were thus compared to the anorthositic rock suite in order to obtain information about the geochemical nature of the carbonatite matrix surrounding the anorthositic fragments.

With respect to the anorthositic rocks (Fig. 15.5), the samples of the carbonatitic breccia (excluding sample Ku-98-56) are strongly depleted in Si, Al and Ca, whereas they contain distinctly higher contents of Na, reflecting (1) the progressive replacement of plagioclase by albite and sodalite during fenitization followed by (2) relative decreases of the modal contents of feldspars and feldspathoids with progressive injection of carbonatite melts. Increasing ratios of carbonatite matrix/anorthositic xenoliths are mirrored by increases of Fe, Ca, P, S, Sr (up to 3695 ppm), Nb (up to 195 ppm), Zn, Ba, Th, U, the LREE (La: up to 444 ppm, Ce: up to 857 ppm, Nd: up to 170 ppm), and CO₂, thus suggesting that the above mentioned elements represent primary constituents of the carbonatite magma. High Fe:Ca ratios are taken as evidence that the carbonatite matrix is broadly ferrocarnatitic in nature. Sodalite-rich samples of the carbonatitic breccia (excluding sample Ku-98-131), like the Sdl-separates, trend to high Al and Na, whereas the sodalite-poor and -free samples of both the layered and the massive carbonatitic breccia as well as sample Ku-98-131, composed of almost sodalite-free zones from a sodalite-rich

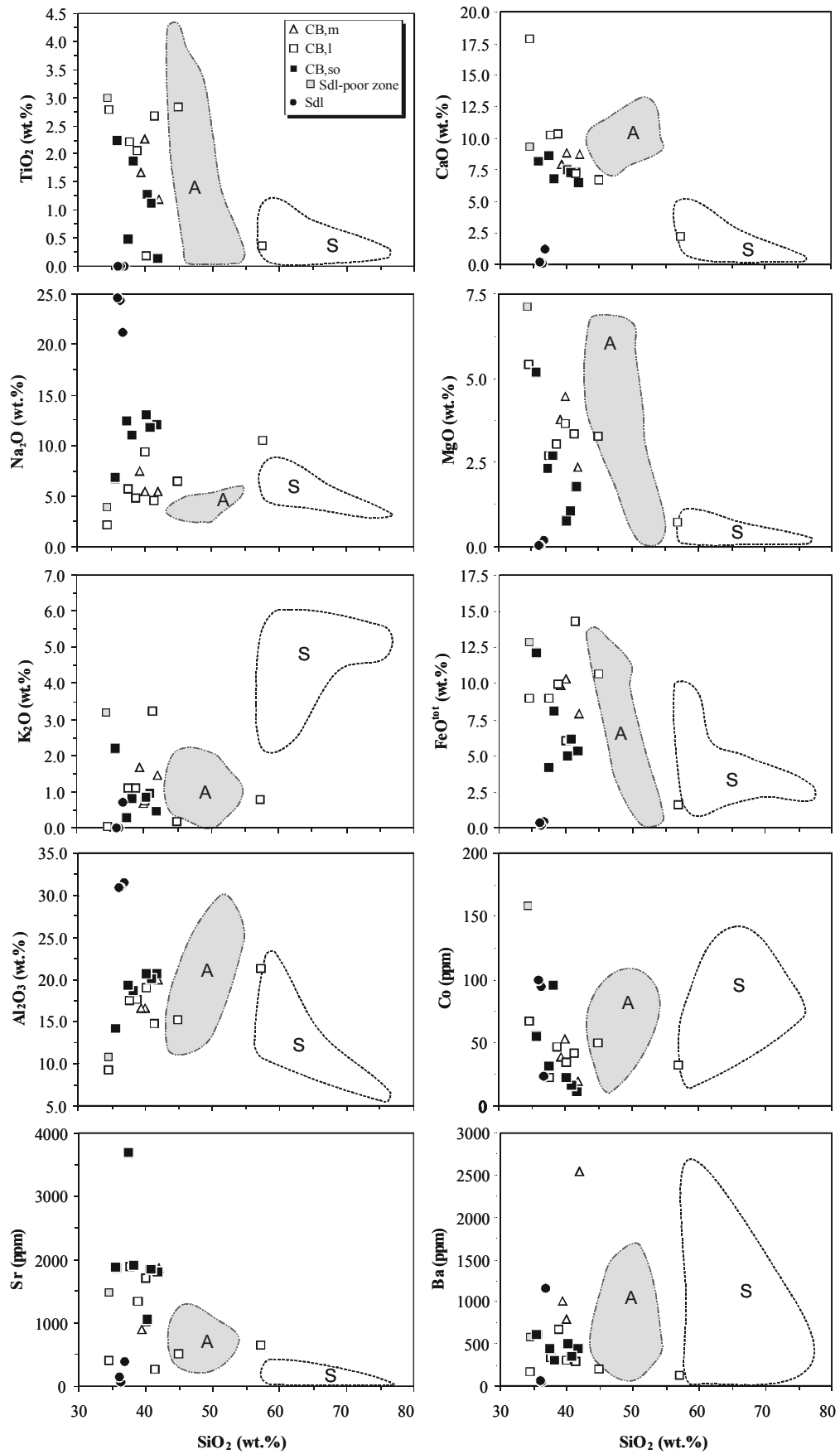


Fig 15.5: Compositional variation of the carbonatitic breccia (excluding samples containing SiO₂ < 30 wt.%), illustrated in selected Harker diagrams and compared to that of sodalite (black dots) as well as to those of unaltered samples of the anorthositic suite (grey fields) and the felsic suite (white fields).

carbonatitic breccia, are generally higher in Ti, Ca, Mg, Fe, and V, caused by lower modal amounts of sodalite and higher amounts of biotite, magnetite and ankerite.

REE-rich samples of the carbonatitic breccia exhibit low SiO₂ (4-11 wt.%) and Al₂O₃ contents (2-6 wt.%), hence pointing to a minor degree of wallrock contamination (sodalite and/or albite). Indeed, the Na₂O contents (6-8 wt.%) are positively correlated with both Al and Si. The amounts of FeO^{tot} (4-10 wt.%) and MgO (2-4 wt.%) are too low to classify the investigated samples as ferrocarnatites, whereas remarkably high values were obtained for Ca (15-16 wt.%), Sr (3.8-8.9 wt.%), Ba (0.8-2.2 wt.%), La (2.2-5.4 wt.%), Ce (3.3-7.9 wt.%), and Nd (1.1-3.0 wt.%), correlated negatively with the Si and Al contents and reflected by high modal amounts of Ca-Sr-REE carbonates. The trace element contents of the REE-rich carbonatite dykes agree well with the chemical composition obtained for a REE-rich calciocarnatite dyke in Rajasthan, India (Wall et al., 1993). However, regarding their major elements, the Swartbooisdrif dykes are characterized by higher amounts of Al, Fe, Mg, and Na and lower Ca and Mn, due to the effects of wallrock contamination and their ankeritic nature.

Since the wallrock fragments incorporated in the carbonatitic breccia are almost entirely composed of albite and/or sodalite (95-100 vol.%), subtraction of the respective oxides (Na₂O, SiO₂ and Al₂O₃) should give approximate values of the composition of the surrounding carbonatite matrix. Best-fit results were reached by subtracting the totals of Na₂O from the analyses, together with corresponding amounts of SiO₂ and Al₂O₃, calculated for the petrographically observed albite:sodalite ratios of each single sample (i.e. 0.7-1.0 in the massive and layered carbonatitic breccia and 0.45-0.55 in the sodalite-rich carbonatitic breccia). Subsequently, the remaining totals of oxides were recalculated to 100 wt.%, with the determined normalizing factor being also used for the recalculation of the trace elements incorporated in the carbonatite matrix. The calculation mode on the basis of Na was chosen, since almost the total of Na is incorporated in sodalite and albite of the fenitized wallrock fragment, whereas Si and Al may additionally be present in minerals crystallized from the carbonatite itself, such as biotite. Samples bearing relict magmatic biotite from the anorthositic suite as well as those containing abundant muscovite were excluded from the calculation. Recalculated compositions of the carbonatitic breccia are listed in Table 15.1. Recalculated SiO₂ and Al₂O₃ contents display ranges of 1.8-9.8 wt.% and 0.5-5.6 wt.%, respectively, with the highest values being obtained for samples which also contain significant amounts of K₂O (0.9-4.5 wt.%), reflected by the abundance of biotite. Values for FeO^{tot} (13.5-25.0 wt.%), CaO (16.7-28.5 wt.%), MgO (2.9-10.7 wt.%), MnO (0.5-2.1 wt.%), TiO₂ (0.6-5.5 wt.%), and P₂O₅ (0.1-3.0 wt.%) are generally high,

but mostly lie within the compositional range of ferrocarnatites world-wide (see Woolley & Kempe, 1989, for a review). Sr may reach values of up to 1.2 wt.%.

rock type sample	CB,l 98-28	CB,l 98-70c	CB,l 99-04	CB,m 98-08	CB,m 98-73c	CB,m 98-103c	CB,so 98-27	CB,so 98-80	CB,so 98-83	CB,so 99-05	CB,so 99-07	CB,so 99-08
wt. %												
SiO ₂	7.82	9.84	4.32	7.45	9.52	7.44	3.64	7.19	1.82	3.42	4.82	4.04
TiO ₂	4.75	4.31	0.55	5.16	2.94	4.04	5.55	4.61	1.58	0.47	3.86	4.87
Al ₂ O ₃	8.10	9.32	4.95	7.26	10.73	5.02	2.82	3.77	1.61	3.17	3.13	2.27
Fe ₂ O ₃	8.48	3.88	5.82	7.41	6.62	6.99	6.39	7.44	3.89	8.15	10.16	5.64
FeO	11.59	17.45	12.29	16.89	13.81	17.67	18.02	18.27	9.94	11.90	11.90	13.66
MnO	1.05	0.82	1.01	0.55	1.54	0.68	1.06	0.85	1.42	2.05	0.96	0.53
MgO	5.82	6.37	10.61	10.18	5.89	9.15	8.00	10.69	7.54	6.39	3.59	2.91
CaO	21.98	21.86	21.62	20.12	21.84	19.32	20.09	16.72	27.98	23.30	25.30	28.52
Na ₂ O	0.00	0.00	0.00	0.00	0.00	0.00	0.00	0.00	0.00	0.00	0.00	0.00
K ₂ O	2.39	2.34	2.14	1.53	3.58	4.04	2.39	4.53	0.93	1.62	3.28	3.29
P ₂ O ₅	0.13	0.46	0.20	0.55	0.07	1.24	0.18	1.74	3.00	0.18	0.62	0.60
S	b.d.l.	0.13	b.d.l.	0.09	b.d.l.	b.d.l.	0.12	b.d.l.	0.10	b.d.l.	b.d.l.	0.60
LOI	27.89	23.22	36.49	22.82	23.46	24.42	31.75	24.20	40.20	39.36	32.39	33.07
CO ₂	23.67	18.10	28.52	17.82	18.26	21.22	27.09	21.82	35.14	32.16	26.70	26.85
H ₂ O	4.22	5.13	7.97	5.00	5.20	3.20	4.66	2.38	5.05	7.21	5.69	6.21
Sum	100.00	100.00	100.00	100.00	100.00	100.00	100.00	100.00	100.00	100.00	100.00	100.00
ppm												
V	320	311	124	511	65	402	363	325	87	57	277	487
Cr	148	120	43	180	32	107	148	356	b.d.l.	43	465	559
Zn	211	435	283	434	527	596	463	575	232	190	362	374
Rb	60	50	43	43	45	100	86	159	35	32	103	79
Sr	4078	2821	4905	2301	4634	2180	5603	3840	11911	6467	6311	4000
Nb	60	135	159	155	234	209	148	387	461	312	198	212
Ba	722	1399	864	1804	6343	2458	888	1259	1431	1591	1173	1907
Pb	24	50	95	94	30	80	109	43	235	104	106	140
Th	b.d.l.	b.d.l.	b.d.l.	137	b.d.l.	b.d.l.	b.d.l.	b.d.l.	26	b.d.l.	b.d.l.	60
U	13	b.d.l.	b.d.l.	b.d.l.	b.d.l.	b.d.l.	41	19	19	25	b.d.l.	b.d.l.
Ce	125	505	231	548	b.d.l.	462	142	467	2763	700	304	933
Nd	b.d.l.	147	133	183	b.d.l.	243	65	194	812	233	85	325
Sum	5761	5974	6881	6391	11909	6838	8055	7623	18013	9756	9384	9076

Table 15.1: Recalculated composition of the carbonatite matrix of the carbonatitic breccia (see text for details).

Following the IUGS classification (Le Maitre, 1989), which is adopted for this study, the recalculated samples of the carbonatitic breccia can be classified as ferrocarnatite (Fig. 15.6a), but they cross the ferrocarnatite-ferruginous calciocarnatite–magnesiocarnatite borders after the revised carbonatite nomenclature of Gittins & Harmer (1997; Fig. 15.6b). Similar trends can be observed for the REE-rich samples of the carbonatitic breccia (Fig. 15.7), even though the classification of these samples in the ternary diagram Ca-Mg-(Fe+Mn) bears uncertainties, due to their comparably low amounts of Ca, Mg, Mn, and Fe and the high amounts of REE.

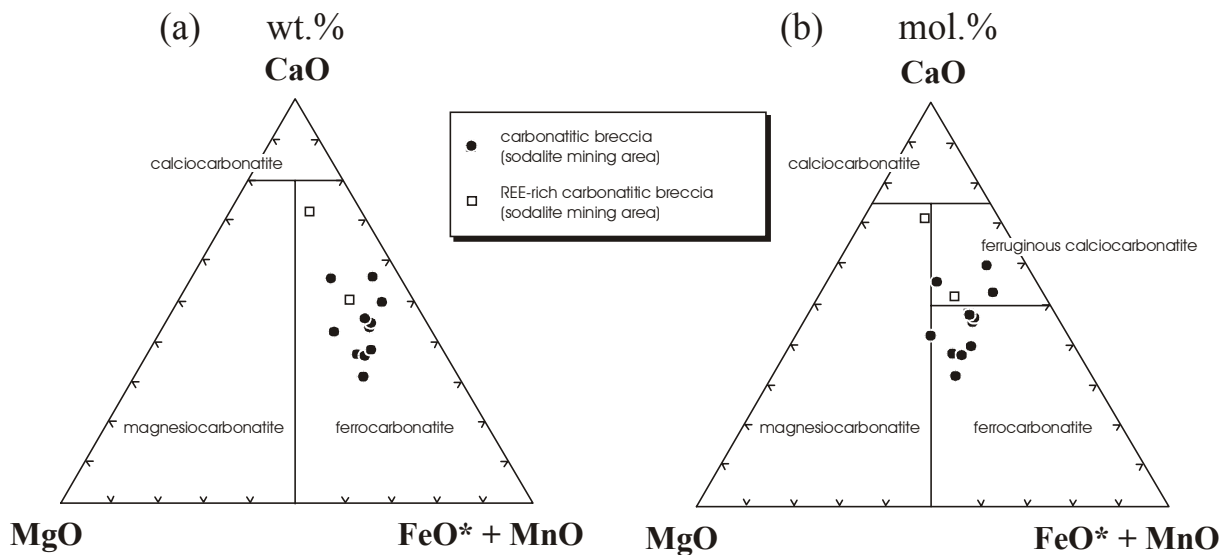


Fig 15.6: Classification diagrams for carbonatites, using their major element composition. **a)** IUGS classification (Le Maitre, 1989), **b)** classification after Gittins & Harmer (1997).

Chondrite normalized trace element plots of the investigated REE-poor samples of the carbonatitic breccia are illustrated in Fig. 15.7a. Most samples exhibit smooth patterns, peaking at Nb, La and Ce and displaying variably accentuated troughs at Rb, K, Sr, P, Zr, and Ti. The negative anomalies point to a K-, Sr-, P-, and Ti-depleted parental melt and thus suggest extensive biotite, apatite and Fe-Ti oxide crystallization prior to the emplacement of the carbonatites.

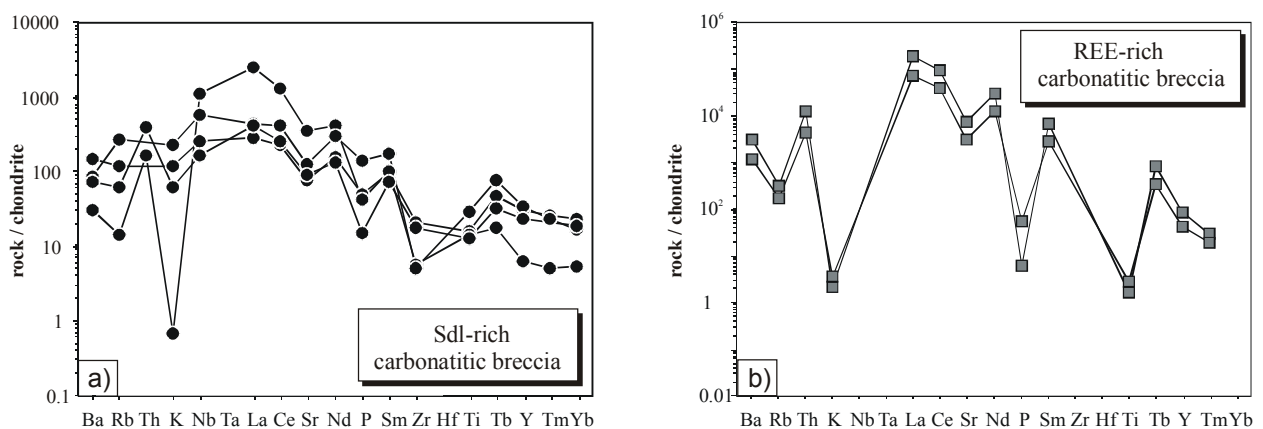


Fig. 15.7: Chondrite-normalized (except Rb, K, P) trace element abundance diagrams (Spider-grams) for the carbonatitic breccia. **a)** REE-poor samples (Ku-98-08, -103c, -118, -131). **b)** REE-rich samples (Ku-98-130a, Ku-98-130b).

Similar patterns are displayed by the REE-rich samples of the carbonatitic breccia (Fig. 15.7b), even though they contain higher absolute amounts of Ba, Th, La, Ce, Nd, Sm, and Tb, hence emphasising the negative anomalies at Rb, K, P, and Ti. It may thus be concluded, that the

formation of the REE-rich carbonatitic breccia post-dated the continuous crystallization of ankerite, apatite, biotite and Fe-Ti oxides from the carbonatitic breccia. Following this, the Ba-, Th- and REE-enrichment of these rocks may have been caused by strong fractionation of the previously intruded carbonatite melts of the carbonatitic breccia, even though secondary REE-enrichment by late-stage, REE-rich carbonatite fluids (autometasomatism) can not be ruled out. In general, the trace element patterns of all samples of the carbonatitic breccia display similarities with those characteristic of oceanic nepheline melilitites and basanites (e.g. Thompson et al., 1983).

15.1.4.2 Ferrocarbonatite veins

Compared to all other rock-types, the late ferrocarbonatite veins (Ku-01-04, -05) are characterized by the lowest SiO₂- (0-1.4 wt.%), Al₂O₃- (0.2-0.4 wt.%) and Na₂O-contents (0-0.2 wt.%) due to the low potential of these small-scaled dykes and veins to incorporate wallrock material.

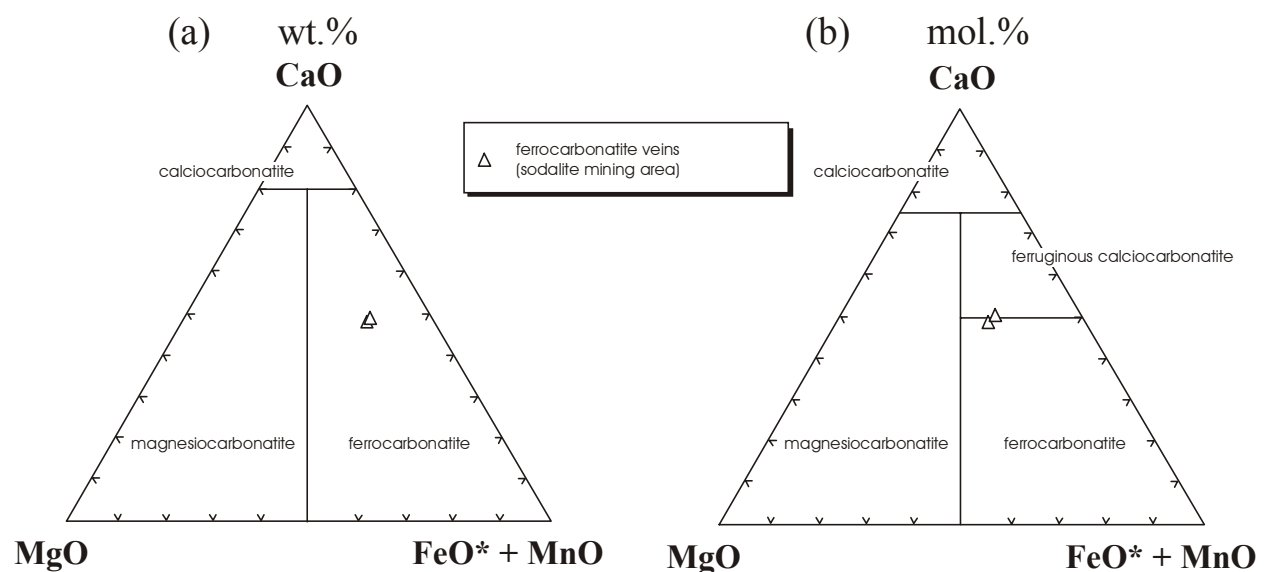


Fig 15.8: Classification diagrams for carbonatites, using their major element composition. *a*) IUGS classification (Le Maitre, 1989), *b*) classification after Gittins & Harmer (1997).

Values of Fe, Mg and Ca are similar to the mean values of ferrocarbonatites world-wide, as summarized by Woolley & Kempe (1989). The MnO contents are generally high (2.33-2.43 wt.%), whereas the amounts of K, Ti, P, and S are near the detection limit, presumably reflecting fractionation of K-, Ti-, P- and S-bearing minerals like biotite, Fe-Ti oxides, apatite and

sulphides from the carbonatitic breccia. The late ferrocarbonatite veins exhibit Sr, La, Ce, and Nd contents in the ppm range, although Sr may reach up to 0.5 wt.%. According to the classification of both Le Maitre (1989) and Gittins & Harmer (1997) the rocks are ferrocarbonatites (Fig. 15.8).

Chondrite normalized trace element plots of two ferrocarbonatite samples reveal quite different patterns (Fig. 15.9), i.e. (1) a smooth pattern, displaying accentuated troughs at Ba, P and Ti (sample Ku-01-04), similar to those obtained for the carbonatitic breccia, and (2) a straight pattern, characterized by a strong positive Sr anomaly and a negative Ti anomaly (sample Ku-01-05). The observed deviations of the trace-element patterns may reflect the abundance of pyrochlore in sample Ku-01-04, which is lacking in sample Ku-01-05.

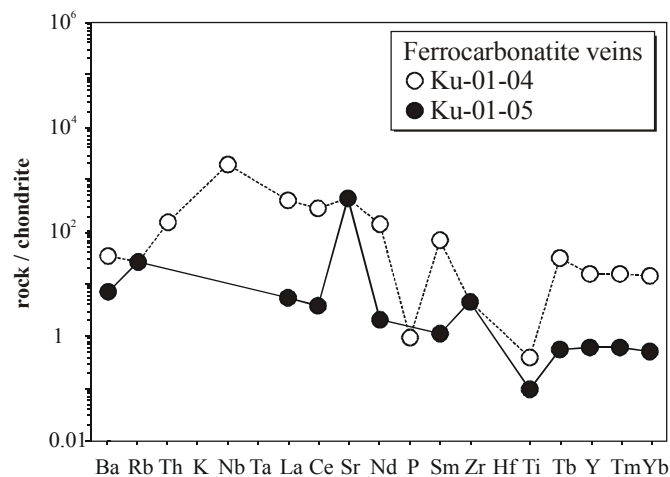


Fig 15.9: Chondrite-normalized (except Rb, K, P) trace element abundance diagrams (spider-grams) in the late ferrocarbonatite veins.

15.2 Rare earth element geochemistry

REE-analyses were carried out on one sample of the fenitized syenite (Ku-98-103s), one sample of the fenitized nepheline syenite (Ku-99-15a), four samples of the REE-poor carbonatitic breccia (Ku-98-08, -103c, -118, -131), two samples of the REE-rich carbonatitic breccia (Ku-98-130a, -130b) and two samples of the ferrocarbonatite veins (Ku-01-04, -05). Analytical results are given in Table A.5.4.2 in the Appendix A.5.4.

The *fenitized syenite* has a Σ REE of 868 ppm and high $(\text{La}/\text{Nd})_{\text{cn}}$ and $(\text{La}/\text{Yb})_{\text{cn}}$ ratios of 3.4 and 30.6, respectively. Like its unaltered counterparts, it displays a straight REE patterns lacking accentuated positive or negative anomalies (Fig. 15.9). When compared to syenites, which were not affected by metasomatism, the fenitized syenite has higher contents of LREE (La, Ce, Pr, Nd) whereas the contents of all other REE are almost identical to those of the unaltered syenites. It can thus be concluded, that the fenitizing fluids were exceptionally capable of transporting the LREE with respect to the HREE.

With a value of 43 ppm, the Σ REE of the *fenitized nepheline syenite* is extremely low. The sample is characterized by a straight REE pattern and comparably low $(\text{La}/\text{Nd})_{\text{cn}}$ and $(\text{La}/\text{Yb})_{\text{cn}}$ ratios of 1.2 and 3.4, respectively (Fig. 15.10). A distinctly negative $(\text{Eu}/\text{Eu}^*)_{\text{cn}}$ anomaly (0.5) suggests plagioclase fractionation prior to the nepheline syenite emplacement. The REE pattern of the nepheline syenite differs significantly from those of the syenites, thus constraining that the nepheline syenite represents an independent magmatic unit, which may be genetically related to the carbonatite suite.

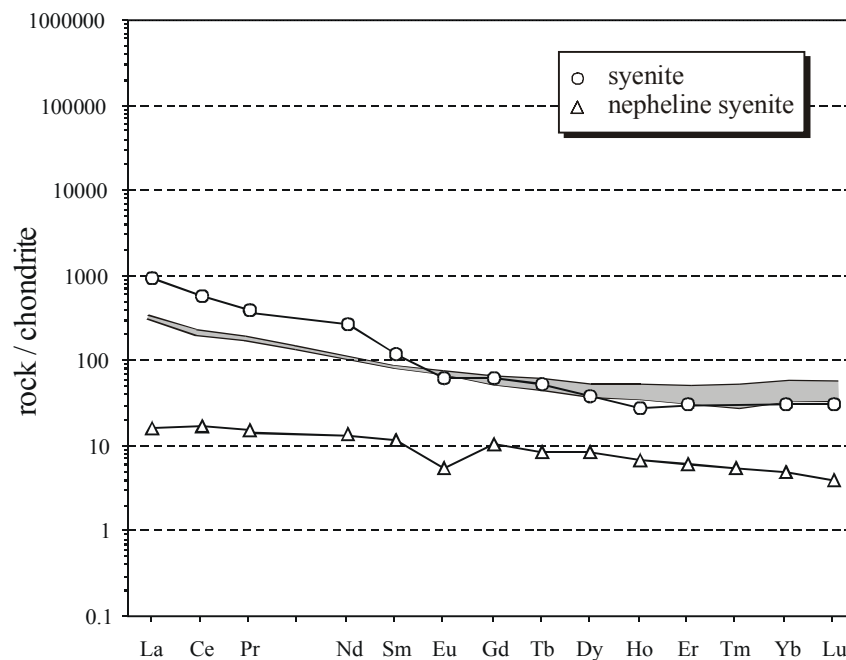


Fig. 15.10: Diagrams showing the variations in chondrite-normalized REE abundances for the fenitized syenite and the fenitized nepheline syenites compared to those of unaltered samples of the felsic suite (shaded grey).

The Σ REE of the *carbonatitic breccia* and the *ferrocarbonatite veins* range between 9 ppm and 17.7 wt.%, with the highest values obtained for the REE-rich carbonatitic breccia and the lowest for the ferrocarbonatite veins. All investigated samples have relatively high and

positively correlated $(La/Nd)_{cn}$ and $(La/Yb)_{cn}$ ratios, increasing from 2 to 6 and from 11 to 454 (except samples of the REE-rich carbonatitic breccia with Yb below the detection limit), respectively. Both, the carbonatitic breccia and the ferrocarnatite veins display straight REE patterns and weak positive $(Nd/Nd^*)_{cn}$ anomalies of 1.1-1.6 (Fig. 15.11). The samples of the REE-rich carbonatitic breccia have Tm-contents similar to those of the REE-poor samples of the carbonatitic breccia, but substantially more LREE, reflected by the high modal abundance of Ca-Sr-REE carbonates. The ferrocarnatite sample Ku-01-04 has REE abundances similar to the carbonatitic breccia, whereas the ferrocarnatite sample Ku-01-05 reveals significantly lower REE amounts but a similar overall pattern. The high ΣREE , $(La/Nd)_{cn}$ and $(La/Yb)_{cn}$ ratios and the straight REE patterns of the REE-rich carbonatitic breccia, when compared to the REE-poor samples of the carbonatitic breccia and the ferrocarnatite veins, suggest that they either represent highly fractionated carbonatite melts or that autometasomatism by late-stage carbonatite fluids is responsible for the strong enrichment of the LREE. In contrast, the REE abundances of the carbonatitic breccia and the ferrocarnatite veins are conspicuously low when compared to other carbonatites world-wide (e.g. Horning-Kjarsgaard, 1998). With values of 1-172 ppm the Y concentrations of most samples are extremely low, with the Y/Ho ratios (20-29) lying at or even below the chondritic value of 28.

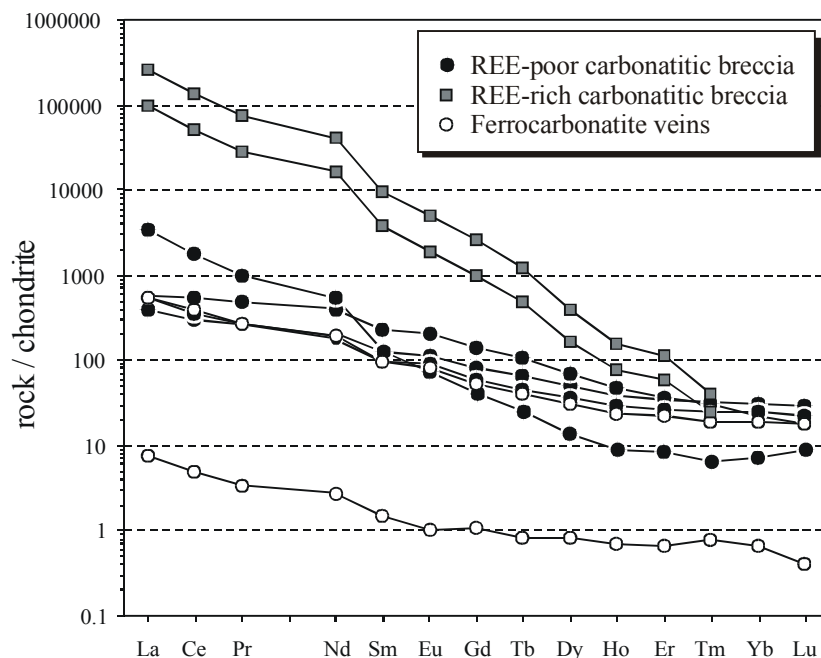


Fig. 15.11: Diagrams showing the variations in chondrite-normalized REE abundances for REE-poor and REE-rich samples of the carbonatitic breccia and the younger, almost silicate-free ferrocarnatite veins.

15.3 Discussion and interpretation of the carbonatite evolution

To summarize, the composition of the ferrocarbonatite veins is quite similar to that obtained for the carbonatites forming part of the carbonatitic breccia, even though, in contrast to the latter, the younger ferrocarbonatites contain lower amounts of Fe, Mg, K, Ti, P and S, which were presumably incorporated by previously crystallized biotite, ankerite, Fe-Ti oxides, apatite and sulphides from the carbonatitic breccia. Following this, the ferrocarbonatite veins may be interpreted as fractionation products of the ferrocarbonatite magma which forms the carbonatitic breccia. This interpretation is constrained by the $(\text{FeO}^{\text{tot}}+\text{MnO}+\text{MgO})$ vs. DI plot of Fig 15.12a. The DI ratio of the investigated carbonatites is in general negatively correlated with the $(\text{FeO}^{\text{tot}}+\text{MnO}+\text{MgO})$, with the highest DI being displayed by the late ferrocarbonatite veins, which may thus be interpreted to be the most fractionated members of this group. In contrast, REE-rich samples of the carbonatitic breccia plot in range of the corresponding REE-poor samples, thus suggesting that the REE-enrichment of the former is not the result of extensive fractionation, but rather caused by secondary processes.

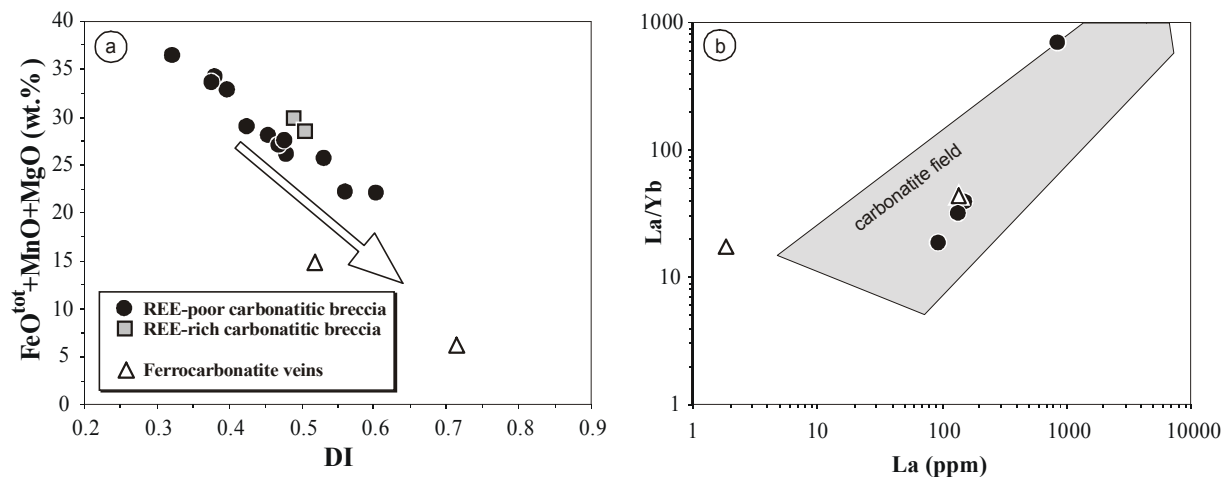


Fig 15.12: Chemical characteristics of the Swartbooisdrif carbonatite samples. **a)** Plot of DI vs. $\text{FeO}^{\text{tot}}+\text{MnO}+\text{MgO}$ (wt.%) (DI = $\text{CaO}/(\text{CaO}+\text{FeO}^{\text{tot}}+\text{MnO}+\text{MgO})$ molar ratios; arrow marks fractionation trend; values for the carbonatitic breccia are derived from recalculated analyses). **b)** Plot of La vs. La/Yb ratios (carbonatite field after Andersen, 1987).

Judging from the geochemical data the investigated carbonatite samples are supposed to represent the crystallization products of ferrocarbonatite magmas. Conformably, in the La vs. La/Yb diagram (Fig. 15.12b) most samples (except sample Ku-01-05) plot within the carbonatite field of Andersen (1987).

15.4 Comparison with the Lupongola carbonatites

Regarding their major and trace element geochemistry, the Swartbooisdrif carbonatites differ significantly from the carbonatites sampled from two north-west trending dykes, situated close to the Namibian-Angolan border ca 2.5 km south-west of the Lupongola Complex, SW Angola. Sample Ku-01-08, a magnesio-carbonatite, contains traces of Si, Fe, V, Sr, and La and high amounts of MgO (19.9 wt.%) and CaO (30.9 wt.%), reflecting the modal dominance of dolomite. All other elements are below the detection limit. In contrast, EMP analyses of sample Ku-01-10, a calciocarbonatite, reveals minor amounts of SiO₂ (1.6 wt.%), Al₂O₃ (0.5 wt.%) and P₂O₅ (0.6 wt.%), traces of Zn (70 ppm), Sr (1510 ppm), Y (191 ppm), Nb (201 ppm), Ba (120 ppm), La (290 ppm), Ce (780 ppm), and Nd (257 ppm), whereas remarkably high values are obtained for FeO (8.4 wt.%), MnO (2.5 wt.%) and CaO (45.9 wt.%), mirrored by the mineral assemblage of calcite, magnetite, together with minor apatite. In clear contrast to the Swartbooisdrif carbonatites, no metasomatic aureoles have been observed in the anorthosites bordering the magnesio- and calciocarbonatite dykes. If the Lupongola carbonatites indeed belong to the same magmatic suite like the Swartbooisdrif carbonatites, as has been suggested by several authors (e.g. Menge, 1998; Thompson et al., 2002), they represent a less fractionated carbonatite unit, presumably formed previous to the emplacement of the Swartbooisdrif dykes.

16 Mass Balance Calculations

Solidified carbonatites are the result of complex chains of interrelated processes, such as differentiation, fractional crystallization, element exchanges between the carbonatite magmas and coexisting fluids as well as subsolidus re-equilibration (e.g. Le Bas, 1977; Gittins, 1979; Andersen, 1984, 1987, 1989; Treiman & Essene, 1985; Dawson et al., 1987). Since fenites are the end-products of metasomatism, compositionally changed by the interaction between a precursor rock and emanations from carbonatite or alkaline silicate magmas, the investigation of alteration processes can convey important information about the nature and evolution of both the carbonatite intrusives and their wall-rocks. However, apparent element gains or losses, observed in the metasomatic aureoles must not per se infer element mobility but may also be attributable to volume changes, since elements that behave immobile during hydrothermal alteration are concentrated during net mass loss and diluted during net mass gains. An accurate calculation of the material changes during metasomatism therefore requires the knowledge of both, the compositional and the volume changes during fenitization.

16.1 The Gresens approach

An equation, assessing the compositional and volume changes of a parent rock during metasomatism has been formulated by Gresens (1967):

$$X_n = w \cdot \left\{ \left[F_V \cdot X^B \cdot \left(\frac{S^B}{S^A} \right) \right] - X^A \right\}$$

<i>where:</i>	$X_n =$	change in weight proportion of component n
	$w =$	initial weight of parent rock (generally set to 100 g, so that if X^A and X^B are in percent then X_n is in weight percent change of the component n)
	$F_V =$	volume factor (e.g. the volume ratio of altered rock to parent rock)
	$X^A, X^B =$	weight proportion of component n in parent rock A and altered rock B, taken from the respective chemical analyses
	$S^A, S^B =$	specific gravities of parent and altered rock, measured on representative rock chips

The equation contains two unknowns, X_n and F_V . However, a likely value of the volume factor can be deduced from composition-volume diagrams, with F_V being determined by the intersection points of lines of elements assumed to be immobile with the zero mass change axis

(i.e. $X_n = 0$; no loss or gain of the respective element). If the values for F_v for several elements and oxides coincide or only slightly differ, confidence is gained regarding their immobility. The average volume factor (calculated as an average of the volume factors of oxides and elements proven to be immobile) may then be applied to the mobile elements to obtain real mass changes.

An alternative method for the determination of F_v with the help of composition-volume diagrams was proposed by Kresten (1988). The fundamental assumption of Kresten (1988) is, that the sums of components supplied and removed during metasomatism roughly balance, thus resulting in minimum total mass changes of a rock during fenitization. Hence, values of minor and zero mass changes of a rock can be used to determine the corresponding F_v .

16.2 Mass change calculations for the fenitization of anorthosites and syenites

Mass balance calculations have been performed for three samples of the fenitized syenites and one fenitized anorthosite sample. In addition, six samples of the carbonatitic breccia, being almost entirely composed of fragments of fenitized wallrock anorthosite, have been investigated in order to obtain information about the evolution of the fenitizing fluids during continuous fluid-rock interaction. Composition-volume diagrams of the fenitized wallrock lithologies and fenite xenoliths show no preferential clustering of intersection points of the element lines with the zero mass change axis. Thus, values of minimum total mass changes have been used to determine F_v . A good fit was reached for minimum changes of oxygen, which indeed is generally thought to remain relatively constant during metasomatism. Results of the mass change calculations for the fenitization of anorthosites and syenites are listed in Tables 16.1 and 16.2, respectively.

The volume factor of 0.99, calculated for the fenitized anorthosite (Ku-98-71), infers a weak loss in volume of 1 % during fenitization. This volume decrease is most probably created by increasing modal contents of the high-density minerals magnetite and ankerite, leading to a density increase from anorthosite ($\rho = 2.76$) towards the fenitized anorthosite ($\rho = 2.81$). In clear contrast, volume factors determined for the transformation of anorthosite into fenitized xenoliths of the carbonatitic breccia ($\rho = 2.56$ - 2.76) mostly imply volume gains of 0.3-5.2 % (F_v : 1.00-1.085), which increase (1) with decreasing tectonic deformation of the samples and (2) with increasing modal amounts of sodalite ($\rho = 2.27$ - 2.33), formed at the expense of plagioclase ($\rho = 2.62$ - 2.76). Conformably, the sodalite-free and heavily tectonised sample Ku-98-103c ($\rho = 2.96$) is the only sample of the carbonatitic breccia that reveals a volume loss of 4 % (F_v : 0.96) during fenitization. Volume factors of 1.01-1.05 were applied to reveal the gains or losses of elements

caused by the transformation of syenites ($\rho = 2.65\text{-}2.77$) into fenitized syenites ($\rho = 2.67\text{-}2.70$). The factors infer gains in volume during fenitization of 1-5 %, which are reflected by increases of the modal abundance of feldspar with respect to the Fe-Mg silicates. Results of the mass balance calculations of fenitized anorthosites and fenitized syenites are shown in Fig. 16.1 and Fig. 16.2, respectively, in order to illustrate the differing activity gradients during the two types of equilibration.

Rock type	A / A, f	A / CB	A / CB	A / mean CB				
Sample	(98-72 / 98-71)	(98-72/99-04)	(98-72/99-05)	(98-72/99-07)	(98-72/98-08)	(98-72/98-73c)	(98-72/98-103c)	N(1:6)
F_v	0.989	1.027	1.031	1.052	1.085	1.003	0.957	1.024
changes in g / 100 g								
Si	-2.95	-4.61	-3.78	-3.68	-4.02	-3.30	-4.13	-3.92
Ti	0.76	-0.01	-0.04	0.56	1.25	0.59	0.90	0.54
Al	-2.61	-3.58	-2.69	-2.72	-4.57	-2.84	-4.46	-3.47
Fe ³⁺	1.45	0.92	1.10	1.63	1.83	1.40	1.59	1.41
Fe ²⁺	1.82	0.87	0.17	0.37	3.46	1.96	3.42	1.69
Fe ^{tot}	3.27	1.79	1.26	2.00	5.29	3.37	5.01	3.10
Mn	0.02	0.22	0.39	0.17	0.14	0.44	0.18	0.26
Mg	0.03	0.10	-1.01	-1.43	0.66	-0.63	0.26	-0.35
Ca	-2.25	-2.51	-3.19	-2.41	-1.37	-1.46	-1.94	-2.15
Na	3.04	4.07	6.10	6.13	1.37	1.31	2.95	3.67
K	0.04	0.30	0.06	0.50	0.26	0.89	1.11	0.51
P	0.01	0.02	0.01	0.07	0.09	0.00	0.22	0.07
C	1.04	1.96	1.72	1.47	1.47	1.33	1.75	1.62
H	0.13	0.25	0.16	0.13	0.19	0.18	0.09	0.17
O	0.00	0.00	0.00	0.00	0.00	0.00	0.00	0.00
Gains (F.I.)	14.88	18.13	18.29	18.93	19.62	14.30	20.58	17.94
Losses	-14.39	-20.15	-19.39	-18.75	-19.16	-15.50	-19.97	-18.53
G+L	0.48	-2.02	-1.09	0.18	0.46	-1.20	0.61	-0.59
changes in ppm / 100 g								
V	151.95	15.17	-11.26	54.80	200.06	-0.91	142.14	65.73
Co	8.23	-0.68	-13.36	-11.77	18.72	-15.93	4.98	-3.09
Ni	5.40	26.11	-59.18	-53.84	38.46	-	-15.67	-12.86
Zn	36.35	67.11	23.13	78.05	163.60	183.75	222.15	122.04
Ga	5.11	-0.31	11.54	6.22	8.33	1.06	13.73	6.72
Rb	-	14.71	8.85	30.30	19.26	18.06	42.03	22.05
Sr	102.20	1163.19	1270.38	1363.24	520.77	1368.57	417.51	1021.24
Y	-	15.69	-	26.26	29.40	-	55.36	25.06
Zr	34.18	56.88	43.28	43.42	181.44	58.20	149.67	88.22
Nb	-	53.94	85.57	58.57	68.93	94.33	88.16	74.85
Ba	241.31	98.22	240.71	151.39	605.79	2363.99	840.37	713.06
Pb	-6.00	26.36	22.52	25.31	35.56	6.04	27.83	23.91
Ce	-	78.45	191.79	89.88	243.28	-	194.77	159.19
Nd	-	45.11	63.93	25.25	81.09	-	102.51	63.36

Table 16.1: Calculated values of absolute compositional changes during the fenitization of the anorthosites (*A/FA* anorthosite/fenitized anorthosite, *A/CB* anorthosite/carbonatitic breccia, *F.I.* fenitization index, F_v assumed volume factor, *G+L* sum of gains and losses).

An immediate impression of Table 16.1 and Fig. 16.1 is, that the fenitization of the wallrock anorthosite was less severe than that of the anorthositic xenoliths forming part of the carbonatitic breccia. This interpretation is supported by the lesser petrographic and geochemical

grades of alteration observed for the fenitized wallrock anorthosites. Remarkably, however, both fenite types display almost similar chemical trends, suggesting that the composition of the fenitizing fluids did not change significantly during fluid-rock interaction and hence pointing to conspicuously high fluid:rock ratios. The main components subtracted during the fenitization of the anorthosites are Si, Al and Ca, whereas Fe, Na, H₂O, CO₂, Zn, Sr, and Ba and, to a lesser content, K, P, V, Zr Ce, and Nd, are the main components added. The ratio of FeO^{tot}/MgO is relatively high; MgO may be added or, more commonly, subtracted. The fact, that Fe³⁺ is not enriched with respect to Fe²⁺ provides evidence against elevated oxygen fugacities of the fenitizing fluid.

Sample	S / S, f	S / S, f	S / S, f	mean S / mean S, f
Rock type	98-40 / 98-73s	98-40 / 98-103s	98-40 / 99-19s	N (5 / 3)
F _v	1.024	1.047	1.010	1.024
changes in g / 100 g				
Si	-0.89	-0.05	-0.09	-0.42
Ti	-0.19	-0.10	-0.07	-0.12
Al	1.38	1.30	1.31	1.30
Fe ³⁺	-1.91	-1.06	-0.86	-1.28
Fe ²⁺	-2.02	-1.40	-1.22	-1.55
Fe ^{tot}	-3.93	-2.46	-2.07	-2.83
Mn	0.09	-0.07	0.00	0.01
Mg	0.01	0.06	0.17	0.08
Ca	1.10	0.09	-0.77	0.13
Na	2.66	3.44	2.09	2.71
K	-3.19	-3.56	-2.08	-2.94
P	-0.04	-0.02	0.02	-0.01
C	0.88	0.55	0.10	0.51
H	0.05	0.07	0.08	0.06
O	2.13	0.00	-1.76	0.00
Gains (F.I.)	7.69	5.67	6.68	8.88
Losses	-11.48	-8.01	-6.69	-8.48
G+L	-3.79	-2.34	0.00	0.40
changes in ppm / 100 g				
V	-	27.48	12.39	19.67
Co	-20.88	7.32	-34.08	-16.16
Ni	-	2.17	-0.02	1.03
Zn	-56.14	-77.25	199.40	22.62
Ga	-14.12	-9.61	-9.80	-11.25
Rb	-	-	-27.26	-26.68
Sr	750.51	459.35	86.04	429.48
Y	-	-5.41	-5.80	-5.85
Zr	-679.34	1352.17	360.95	335.64
Nb	379.92	-53.41	-47.56	92.97
Ba	315.03	635.39	-219.24	238.22
Pb	0.48	-0.14	0.32	0.16
Ce	-	192.64	-56.10	65.56
Nd	-	38.02	-30.03	3.14

Table 16.2: Calculated values of absolute compositional changes during the fenitization of the syenites (*S/FS* syenite/fenitized syenite, *F.I.* fenitization index, *F_v* assumed volume factor, *G+L* sum of gains and losses; *mean S* calculated for samples Ku-98-40, Ku-99-12, -13, -14, -20).

As shown in Fig. 16.2, fenitization of the syenites appears to be less pervasive than that of the anorthosites. Moreover, the major elements of the fenitized syenites show a quite distinct mobilisation behaviour compared to those of the fenitized anorthosites. Si, Fe^{tot} and K were strongly depleted during fenitization, whereas Al, Na, H₂O, and CO₂ are the main components added. Ti, Mn, Mg and P seem to have been constant during metasomatism and Ca displays no clear mobilisation trends. Regarding the behaviour of the trace elements, the fenitization of the syenites strongly resembles that of the anorthosites, as Zn, Sr, Ba, and Ce show a strong enrichment.

Fig. 16.1: Diagrams illustrating the main chemical changes of anorthositic protoliths caused by equilibration with fenitizing fluids emanating from the carbonatite magma (*Y axis:* results of the mass balance calculations compiled in Table 16.1).

However, the observed differences between the element mobilisation behaviour of the syenites and the anorthosites during alteration must not, per se, indicate compositional differences between the fluids responsible, but may be better explained by differences in the activity gradients between the carbonatite magma and the two rock suites, caused by contrasting bulk-rock compositions of the anorthositic and syenitic protoliths. In general, large compositional differences between the protolith and the source of fenitization will produce high gradients of activity, thus enhancing element transfer to the low activity environment until equilibrium is reached. In case of the anorthosites, the high activity of Ca, Al and Si with respect to the fenitizing fluid generates an activity gradient that causes the removal of these elements. In contrast, the low activities of Al and Ca in the syenites may have created an opposite trend, leading to addition of these components. Following this, the nature of the source of fenitization may be well constrained, if the fenitization patterns of both the syenites and the anorthosites are taken into consideration. As is evident from Fig. 16.1 and 16.2, metasomatism of both rock units provoked increases in Na, CO₂, H₂O, V, Zn, Sr, Ba Nb, and LREE, irrespective of the

compositions of the protoliths, thus suggesting that these elements form major constituents of the fenitizing fluid. In contrast, both the syenites and the anorthosites suffered a variably severe desilication, pointing to a very low silica activity of the magma responsible. Elements which, depending on the protolith composition, may be added or subtracted are Ti, Al, Fe, Mg, Ca, and K. These elements are thought to have been contained in the fenitizing fluids in only minor concentrations, thus creating strongly differing activity gradients between the fluid and the anorthosites and syenites, respectively. The abundance of hydrous ferro-magnesian phases in the fenites supports evidence for a high X_{H_2O} of the fluid.

Fig. 16.2 Diagrams illustrating the main chemical changes of syenite protoliths caused by equilibration with fenitizing fluids emanating from the carbonatite magma (*Y axis*: results of the mass balance calculations compiled in Table 16.2).

In order to constrain the grade of fenitization of the anorthosites and syenites, the chemical fenitization index (F.I.) has been determined from the quantitative mass transfer calculation (F.I. = sum of added components). Following Kresten (1988) the fenitization grade can be subdivided into (1) F.I. < 6.5: low-grade fenitization, (2) F.I. of 6.5-12: medium-grade fenitization and (3) F.I. > 12: high-grade fenitization. Following this, both the fenitized wallrock anorthosite (F.I. = 14.9) and the fenitized anorthositic xenoliths of the carbonatitic breccia (F.I. = 14.3-20.6) can be classified as high-grade fenites, whereas the F.I. of the fenitized syenites (F.I. = 5.7-8.9) indicates low- to medium-grade fenitization, in good accordance with the lack of metasomatically formed sodalite in the latter. Regarding the sodium to potassium ratios of the fenitized anorthosites and syenites related to their respective protolith compositions ($Na_2O/(Na_2O + K_2O)$ fenite/protolith; Fig. 16.3a) the fenitized anorthosites show an intermediate fenitization trend, lying in between the sodic and potassic trends (subdivision of fenitization trends by Kresten, 1988), whereas the fenitized syenites are characterized by a sodic fenitization trend. The different fenitization trends of the anorthosites and syenites may reflect chemical

gradients in the metasomatic aureoles, with sodium-rich fluids migrating into the bordering syenites (low- to medium-grade fenites), leaving back a K-enriched fluid. However, the apparent sodic and potassic trends may also simply mirror differences in the chemical compositions of the respective precursor rocks. Figure 16.3b displays the oxidation ratios ($X_{Fe_2O_3}$) of the fenites plotted against the fenitization index, reflecting the oxygen fugacity conditions during their formation. The oxidation ratios of the investigated samples are intermediate (low- to medium grade fenitized syenites) to low (high-grade fenitized anorthosites), hence suggesting that the fenitizing fluids were characterized by comparably low oxygen fugacities near QFM buffer conditions.

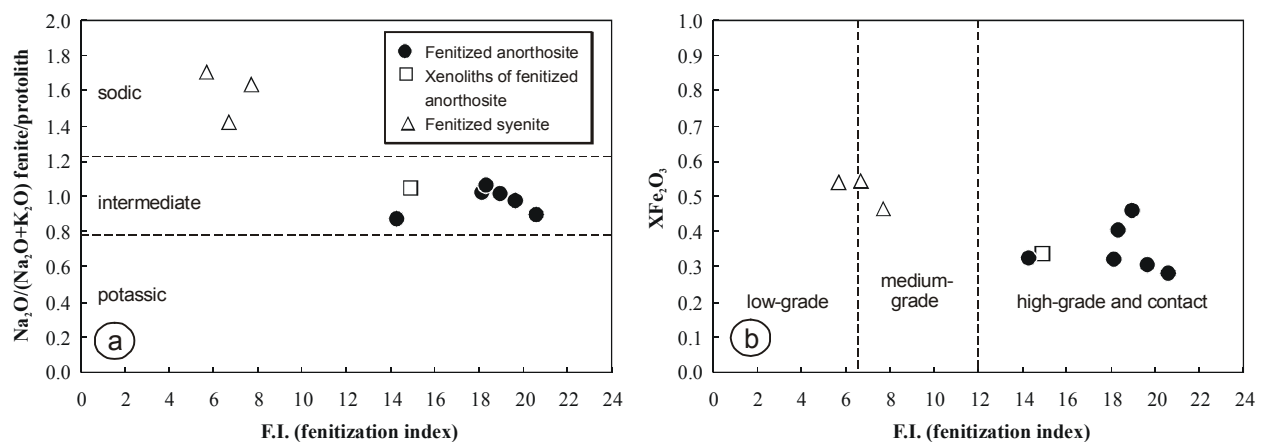


Fig. 16.3: Diagrams illustrating the variation of the fenitization index (F.I.) with progressive fenitization of anorthositic and syenitic protoliths. **a)** Fenitization index vs. protolith-normalized alkali ratios. **b)** fO_2 variation during progressive fenitization as reflected by the oxidation ratio of the fenites.

16.3 Origin and nature of the fenitizing solutions

Regarding the field-relationships of the investigated fenites, their metasomatic alteration appears to be directly linked to the intrusion of the ankeritic carbonatites since (1) the fenites occur within or in the direct neighbourhood of large carbonatite dykes and (2) no other rock type with the potential to cause large-scale fenitization has been observed in the studied area so far. In general terms, however, fenitizing reactions may be promoted by fluids emanating from both alkaline and carbonatite melts, that produce distinctive patterns of fenitization, differing in X_{CO_2} , a_{SiO_2} , $a_{Al_2O_3}$, a_{CaO} , X_{Mg} , fO_2 and T (e.g. Morogan, 1994). Since the possibility, that the fenitization at Swartbooisdrif was caused by another, not exposed magma source can not be safely ruled out, the obtained fenitization patterns were compared to the data of ijolite- and

carbonatite-related fenites of Oldoinyo Lengai, Tanzania, Fen, Norway, and Alnö, Sweden (compiled by Morogan, 1994). To summarize, fenitizing fluids related to ijolitic magmas are characterized by low X_{CO_2} , high activities of silica, magnesium, aluminium and alkalis, low a_{CaO} , and high f_{O_2} near the Hem-Mag buffer. Temperature gradients with distance to the magmatic source are shallow, falling gradually from $\sim 650^\circ\text{C}$ to $\sim 500^\circ\text{C}$. In contrast, fluids producing carbonatitic-type fenitization have high X_{CO_2} , low activities of silica and aluminium, and high activities of Ca. With respect to their alkali-, magnesium and iron-contents the fluids are quite variable. Temperatures and f_{O_2} are generally initially high ($T: \sim 700\text{-}800^\circ\text{C}$), but decrease sharply with distance to the magmatic source ($T: < 500^\circ\text{C}$), even though f_{O_2} may also increase.

<i>Fenitization</i>	<i>Carbonatitic-type fenitization</i>	<i>Ijolitic-type fenitization</i>	<i>Presumably ferrocarbonatite-related (this study)</i>
<i>Locality</i>	Oldoinyo Lengai Baräng and Stornäset areas, Alnö Holla, Ulefoss and Quarry areas, Fen	Hörningsholm area, Alnö Melteig area, Fen	anorthositic and syenitic fenites of Swartbooisdrif, Namibia
<i>X_{CO_2}</i>	high: $\text{CO}_2 > \text{H}_2\text{O}$ abundant calcite rare hydrous mafic phases Or and perthite in high-grade fenite	low: $\text{H}_2\text{O} > \text{CO}_2$ scarce calcite abundant hydrous mafic phases Ab and perthite in high-grade fenite	relatively low: $\text{H}_2\text{O} > \text{CO}_2$ minor ankerite abundant biotite Ab and Sdl in high-grade fenite
<i>a_{SiO_2}</i>	low no quartz present	high quartz even present in HGF	low no quartz present, abundant Sdl
<i>$a_{\text{Al}_2\text{O}_3}$</i>	low	high	low
<i>a_{CaO}</i>	very high	relatively low	relatively low
<i>FeO/MgO</i>	high	low	relatively high
<i>$\text{Na}_2\text{O}/\text{K}_2\text{O}$</i>	variable sodic, potassic and intermediate trends	$\text{Na}_2\text{O} \geq \text{K}_2\text{O}$ intermediate to sodic trend	$\text{Na}_2\text{O} > \text{K}_2\text{O}$ intermediate to sodic trend
<i>f_{O_2}</i>	variable	high	intermediate
<i>Temperature</i>	$\sim 700\text{-}800^\circ\text{C}$ to $< 500^\circ\text{C}$ steep T gradients	$\sim 650^\circ\text{C}$ to $\sim 500^\circ\text{C}$ shallow T gradients	$\sim 770^\circ\text{C}$ to $\sim 530^\circ\text{C}$ narrow aureoles; steep T gradients

Table 16.3: Main factors controlling the type of fenitization (modified after Morogan, 1994; data for Oldoinyo Lengai after Morogan (1982) and Morogan & Martin (1985), data for Fen after Kresten & Morogan (1986) and Kresten (1988), data for Alnö after Morogan & Woolley (1988) and Morogan (1989)).

Remarkably, the Swartbooisdrif fenites do not fit exactly in either of the schemes (Table 16.3). Like the carbonatitic-type fenites, they are severely desilicated and display relatively low $a\text{Al}_2\text{O}_3$ and relatively high FeO/MgO ratios (as evident from the biotite composition, see Chapter 14.10) and reveal high higher temperatures of fenitization (see Chapter 19). It can thus be concluded, that the fluids were definitely not derived from a silicate magma like ijolite or nephelinite. However, regarding the low $a\text{CaO}$ (absence of Ca-bearing hydrous mafic silicates, losses of Ca during fenitization) and low X_{CO_2} (abundance of hydrous mafic silicates, presence of albite even in the high-grade fenites) of the fenites, they also differ from most of the yet described carbonatite-related fenites. It has to be mentioned, however, that the latter two discrimination factors, i.e. (1) X_{CO_2} and (2) $a\text{CaO}$, must not imply that the fenitizing fluids are definitely not related to the ferrocarbonatite magmatism: (1) As has been mentioned by several authors (e.g. Wyllie & Tuttle, 1960; Currie & Ferguson, 1971; Andersen, 1986; Gittins, 1989), carbonatite fluids may have quite variable $\text{CO}_2:\text{H}_2\text{O}$ ratios, thus implying that CO_2 is neither the sole nor necessarily the dominant component of the fluids. Water saturation of carbonates may occur at various stages of the carbonatite evolution, with the solubility of water in the carbonatite magma increasing with increasing alkali-contents and thus with increasing fractionation (e.g. Gittins, 1989). (2) Judging from the abundance of sodalite in the fenitized anorthosites of the Swartbooisdrif area, the Na-rich aqueous fluids responsible for the metasomatism additionally carried substantial amounts of Cl, thus suggesting that they represent supercritical brines. Such a brine should generally be capable of removing alkalis, Fe, Mg, and Ca from the carbonatite magma as chlorides, thus leading to an enrichment of these elements in the fenites. The apparent depletion in Fe, Mg and Ca of the fenitizing fluids investigated in this study, when compared to the bulk composition of the carbonatite matrix of the carbonatitic breccia, implies that these elements were accumulated in readily fractionated minerals of the carbonatites such as biotite and ankerite, hence suggesting that fractionation was already active when the fluids were expelled.

To summarize, the qualitative retention series of the fenitizing fluids, as estimated from the calculated compositional changes of the Swartbooisdrif fenites (i.e. $\text{H}_2\text{O} > \text{Na} = \text{Cl} > (\text{Zn}, \text{Sr}, \text{Ba}, \text{Nb}, \text{Ce}, \text{Nd}, \text{V}, \text{CO}_2) > (\text{Ti}, \text{Fe}, \text{Mg}, \text{Ca}, \text{K}, \text{Al})$), implies that the fenitization was caused by late-stage fluids emanated from highly fractionated carbonatites. Consequently, the Swartbooisdrif ferrocarbonatites represent a potential source of fenitization.

17 Fluid inclusion Studies

17.1 Microthermometric studies

During the past thirty years it has become widely recognized, that the extensive fenitization of wall-rocks, surrounding magmatic carbonatite centres, is caused by the injection of large amounts of aqueous fluids released during the emplacement of the carbonatites (e.g. Currie & Ferguson, 1971; Rankin, 1975; Andersen, 1986; Kresten & Morogan, 1986; Wyllie, 1989; Gittins et al., 1990; Morogan, 1994; Morogan & Lindblom, 1995; Samson et al., 1995a, 1995b; Böhn & Rankin, 1999; Williams-Jones & Palmer, 2002). In order to develop a model for the hydrothermal systems around carbonatites it is important to gain knowledge about the chemical composition of the fluid responsible. As was suggested by Dawson (1989) and Wyllie (1989) these fluids may be capable of removing significant amounts of alkali-metals from the carbonatite magmas, thus accounting for the close association of alkali-poor Ca-Mg carbonatites with sodic or potassic fenites. Carbonatite fluids of quite variable compositions have been analysed, i.e. (1) simple aqueous inclusions (2) complex aqueous inclusions containing a variety of daughter minerals and (3) carbonic or mixed H₂O-CO₂ inclusions (e.g. Roedder, 1973; Rankin, 1975; Nesbitt & Kelly, 1977; Andersen, 1986; Böhn & Rankin, 1999). In general, these fluids are thought to evolve from a homogeneous, low-salinity carbonic into a heterogeneous fluid, i.e. (1) a high-salinity brine and (2) a low-salinity carbonic fluid. (Andersen, 1986; Morogan & Lindblom, 1995; Williams-Jones & Palmer, 2002). However, none of the above mentioned studies gives qualitative or quantitative data on the composition and evolution of fluids emanated by late-stage ferrocarnatite melts.

This study presents the first data on the nature of orthomagmatic fluids that were derived from ferrocarnatites. In order to characterize the chemical composition and evolution of these mineralising fluids, which caused the formation of the Swartbooisdrif sodalite occurrences, three samples of the carbonatitic breccia (REE-rich carbonatitic breccia: Ku-98-130a, Ku-98-130b; Sdl-rich carbonatitic breccia: Ku-98-131) and one quartz-syenite sample (Ku-98-40) were chosen for microthermometric and SRXRF studies. A description of the analytical techniques is given in the Appendix A.2.8 and A.2.9, respectively. Within the carbonatite and syenite samples four genetically different types of fluid inclusions can be distinguished, i.e. presumably primary inclusions of aqueous brines in sodalite and ankerite from the carbonatitic breccia, secondary inclusions of aqueous brines in quartz of a quartz-syenite and texturally later, CO₂-rich

inclusions in quartz of the quartz-syenite. In addition, aqueous fluid inclusions have been observed in apatite of the carbonatitic breccia, but were too small ($<0.5\text{-}2\ \mu\text{m}$) to be analysed with the available analytical facilities. Microthermometric fluid inclusion data were processed using FLINCOR (Brown, 1989). Results of the microthermometric investigations are listed in Tables A.5.6.1 to A.5.6.4 in the Appendix A.5.6.

17.1.1 H₂O-rich inclusions

17.1.1.1 Fluid inclusions in sodalite

The H₂O-rich inclusions in sodalite of the carbonatitic breccia (Ku-98-130a, Ku-98-130b, Ku-98-131) are either arranged in trails, groups or clusters or occur as solitary, randomly distributed inclusions, without a preferred orientation of their long axes. The fact, that inclusion-trails never cross the sodalite grain-boundaries is taken as evidence for their primary origin (Fig. 17.1a). Moreover, when occurring close to a fracture, the inclusions are empty. The fluid inclusions exhibit a distinct variability in both size and shape. Large inclusions ($15\text{-}21\ \mu\text{m}$) predominantly show amoeboidal shapes (Fig. 17.1 a) whereas the more common smaller ones ($3\text{-}10\ \mu\text{m}$) exhibit an either rounded or irregular shape (Fig. 17.1 b). The fluid inclusions consist of at least two phases, an aqueous liquid and a gas-bubble with a volume ratio of 0.9-1.0; small cubic isotropic daughter crystals ($<1\ \mu\text{m}$; presumably halite) have been observed in just a few inclusions.

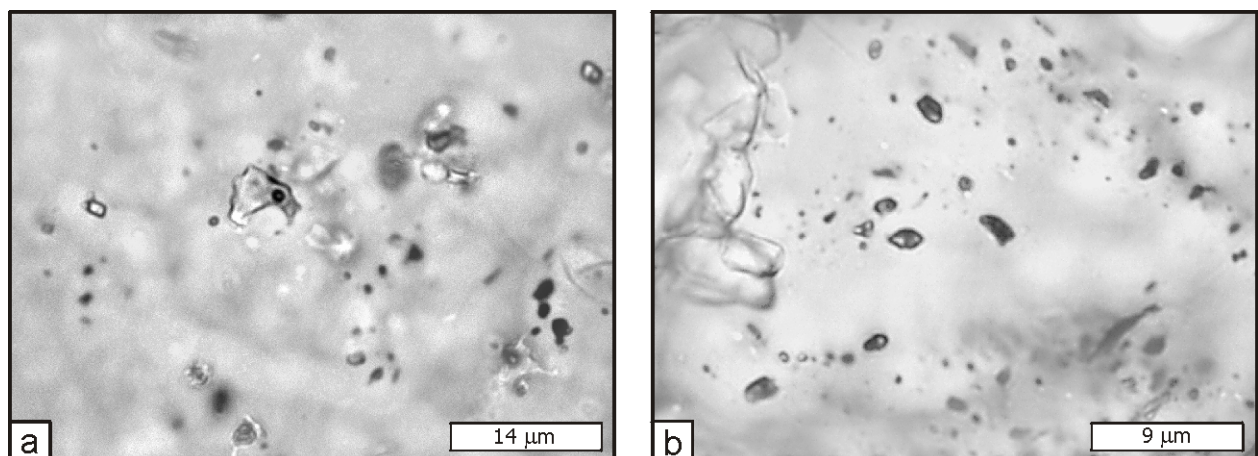


Fig. 17.1: Microphotographs of H₂O-rich inclusions hosted by sodalite from the carbonatitic breccia. *a*) Large inclusions display an amoeboidal shape, whereas *b*) the smaller ones are predominantly oval shaped.

The initial melting in the H₂O-rich inclusions (eutectic temperatures; T_e) occurred at temperatures of -32.7° to -23.1°C , close to the metastable eutectic of the NaCl-KCl-H₂O system

(Roedder, 1984). The salinity of the aqueous inclusions was calculated from the final melting temperatures (T_{mf}) which range from -22.5°C to -15.0°C (Fig. 17.2b). Conformably, the

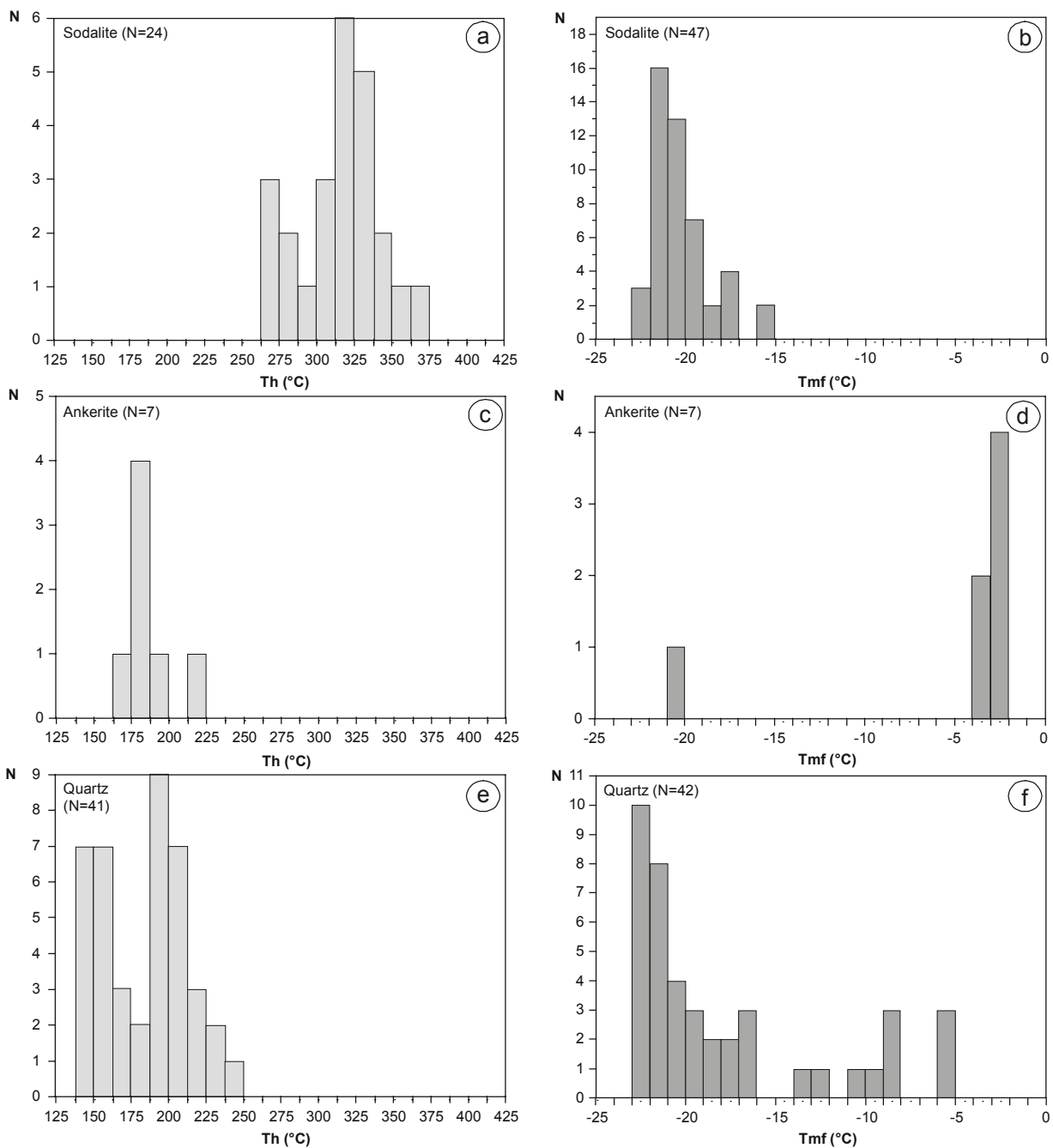


Fig. 17.2: Variation of the homogenization temperatures (Th) and the temperatures of final melting (T_{mf}) of aqueous fluid inclusions. *a)* and *b)* Aqueous fluid inclusions hosted by sodalite from the carbonatitic breccia. *c)* and *d)* Aqueous fluid inclusions hosted by ankerite from the carbonatitic breccia. *e)* and *f)* Aqueous fluid inclusions hosted by quartz from the quartz-syenite.

resulting salt concentrations calculated after Bodnar (1993) are quite variable but high, ranging between 19-30 wt.% NaCl equivalent (eq.) (average: 22.7 wt.%), thus indicating that the fenitizing fluid, released by the carbonatite melt was an alkaline brine. No phase transformation,

indicating the presence of CO₂ was observed in the temperature interval of -80°C to the critical point of CO₂. Densities of 0.86-0.98 g/cm³ have been calculated after Zhang & Franz (1987). Homogenization of fluid inclusions in sodalite takes place at temperatures varying in a range of 270-370°C with a well defined maximum at 320-330°C (Fig. 17.2a). Hereby, fluid inclusions hosted by sodalite of a REE-poor sample of the carbonatitic breccia (Ku-98-131) display a more restricted range of Th (320-350°C), when compared to those in sodalite of the REE-rich carbonatitic breccia (Ku-98-130a, Ku-98-130b; 270-320°C and 270-370°C, respectively).

A principal problem for the microthermometric analyses of the investigated fluid inclusions in sodalite is, that cracks in sodalite tend to propagate fast especially during heating, mostly leading to a sudden fragmentation of the thick sections into small particles. Thus, homogenization temperatures were determined for only 24 of 48 fluid inclusions, which remained unaffected during heating.

17.1.1.2 Fluid inclusions in carbonate

H₂O-rich fluid-inclusions in carbonates from the carbonatitic breccia are generally rare, due to extensive and repeated recrystallisation of carbonate. If present (Ku-98-130b), the fluid inclusions are mainly hosted by granular and mostly recrystallised ankerite (Fig. 17.3 a) but are also found in calcite. They show a tendency to form trails, which, however, never cross the carbonate grain boundaries and thus appear to be pseudosecondary (Fig. 17.3 b). The fluid-inclusions in ankerite of up to 18 µm (3-18 µm) in length are aligned and rather irregular to oval in shape (Fig. 17.3a). At room temperature, they contain a liquid phase (H₂O; 95 vol.%), a vapour phase (H₂O; 5-6 vol.%) and, rarely, an isotropic cubic phase (presumably halite).

First melting of ice (T_e) in fluid inclusions hosted by ankerite occurs in the interval between -7.0°C to -8.0°C (except one value of -29.3°C of an isolated fluid inclusion hosted by non-recrystallised ankerite). The temperatures of final melting of ice (T_{mf}) commonly vary from -5.6°C to -2.7°C (-20.7°C; Fig. 17.2d) and correspond to comparably low salinities of 4.5-6.3 wt.% NaCl eq. (22.8 wt.% NaCl eq.), thus indicating, that alkali-loss of the fluid, caused by previous sodalite formation, predated carbonate recrystallisation. Densities range between 0.88 g/cm³ and 0.94 g/cm³ (low-salinity subgroup) and 1.04 g/cm³ (high-salinity inclusion). The liquid and vapour phases of the fluid homogenize to liquid at significantly lower temperatures (170-220°C and 200°C, respectively) than fluid inclusions in sodalite (Fig. 17.2c).

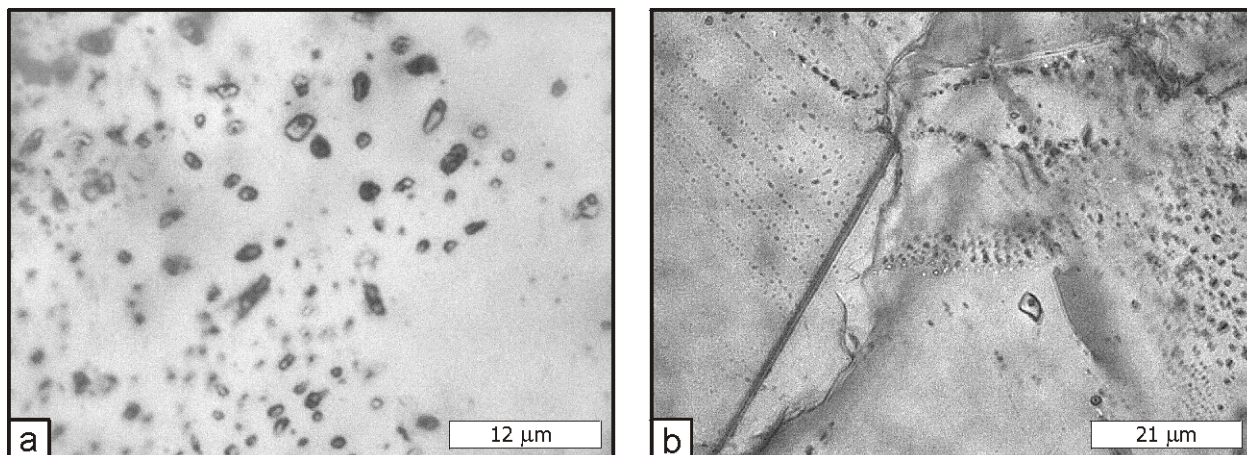


Fig. 17.3: Microphotographs of H₂O-rich inclusions hosted by carbonates from the carbonatitic breccia. **a)** Trail of pseudosecondary aqueous fluid inclusion in ankerite. **b)** Inclusion-trail in calcite.

17.1.1.3 Fluid inclusions in quartz

H₂O-rich 2-phase (liquid + vapour) inclusions of 4-30 μm in diameter are found in granular, interstitial quartz of a quartz-syenite sample. The inclusions are commonly arranged in trails (Fig. 17.4 a), frequently crossing the quartz grain boundaries and are thus suggested to be secondary in origin. They are oval to irregularly in shape with a length of up to 29 μm (2-29 μm; Fig. 17.4 a). Small daughter crystals of halite may occur in single inclusions.

Based on their physical properties the aqueous fluid inclusions in quartz were subdivided into three subgroups, each forming individual inclusion trails. Temperatures obtained for the initial melting of ice (Te) fall in the range of: (1) Te: -33.9°C to -24.0°C, (2) Te: -31.4 to -22.1 and (3) Te: -25.0°C to -11.6°C, suggesting a high compositional variability of the fenitizing fluids with respect to Na, K and Ca. The T_{mf} values vary between (1) -22.7°C and -17.1°C, (2) -22.7°C to -16.6°C and (3) -13.1°C and -5.8°C (Fig. 17.2f), corresponding to salinities of 20-24 wt.% NaCl eq., 20-24 wt.% NaCl eq. and 9-17 wt.% NaCl eq., respectively. Densities of (1) 1.06-1.11 g/cm³, (2) 0.99-1.06 g/cm³ and (3) 0.94-1.00 g/cm³ have been calculated for the three different populations of fluid inclusions. Liquid and vapour homogenize at temperatures of (1) 140-170°C, (2) 190-240°C and (3) 180-210°C, which are generally lower than the Th observed for aqueous inclusions in sodalite and in the range of the Th of aqueous fluid-inclusions in

carbonates of the carbonatitic breccia (Fig.17.2e). The high variability of the Th calculated for the fluid inclusions must be related to temperature changes during trapping of the fluid inclusions, since the homogenization temperatures remained constant during repeated heating, thus ruling out leakage of the inclusions.

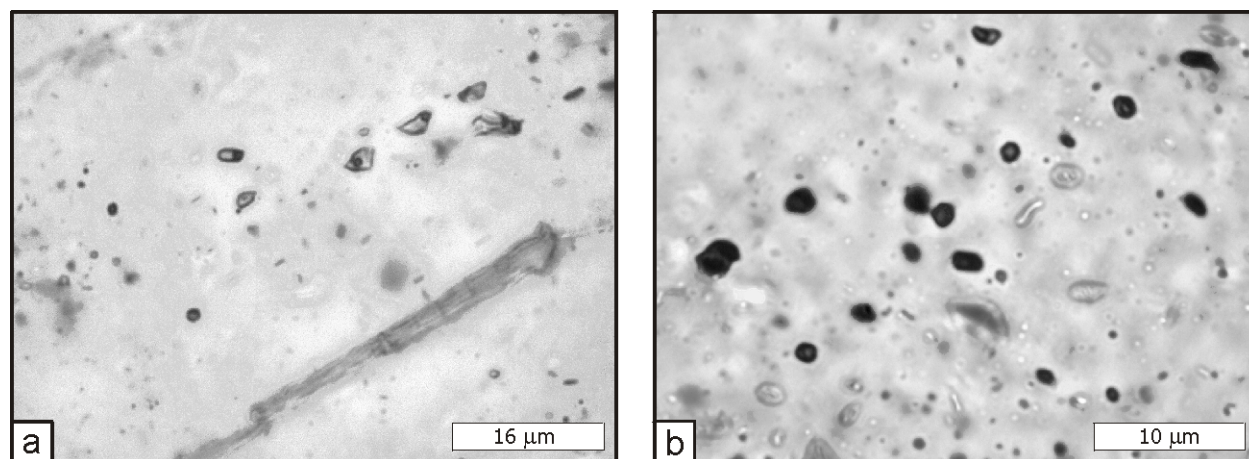


Fig. 17.4: *a)* Microphotograph of secondary aqueous inclusions hosted by quartz from the quartz-syenite. *b)* Microphotograph of secondary CO₂-rich inclusions hosted by quartz from the quartz-syenite.

17.1.2 CO₂-rich inclusions

The fourth type of fluid-inclusions, the CO₂ inclusions, are restricted to quartz of the syenite, slightly dark in appearance and can be distinguished from the H₂O-rich inclusions by shape and size. They are rather oval with a length of 4-21 μm and show no preferred orientation of their long axis within the inclusion trails (Fig. 17.4 b). The inclusion trails generally cut both the H₂O-inclusion trails and the quartz grain boundaries and are thus secondary in origin using the criteria of Roedder (1984). CO₂-rich fluid inclusions produced during the early stages of fenitization have never been observed.

Melting temperatures of 27 microthermometrically analysed inclusions cover a restricted range of -56.7°C to -56.5°C, with a well defined maximum at -56.6°C, the melting temperature of pure CO₂ and thus indicating that phases such as CH₄, N₂ and SO₂, which would lower the melting temperature, are absent or negligible (Fig. 17.5 a). Homogenization takes place into the fluid phase at 8.3-23.7°C with two distinct maximums, one at 13-17°C and a second one at 20-

24°C (Fig. 17.5 b). Densities of 0.73-0.87 g/cm³ for pure CO₂ have been calculated after Kerrick & Jackobs (1981).

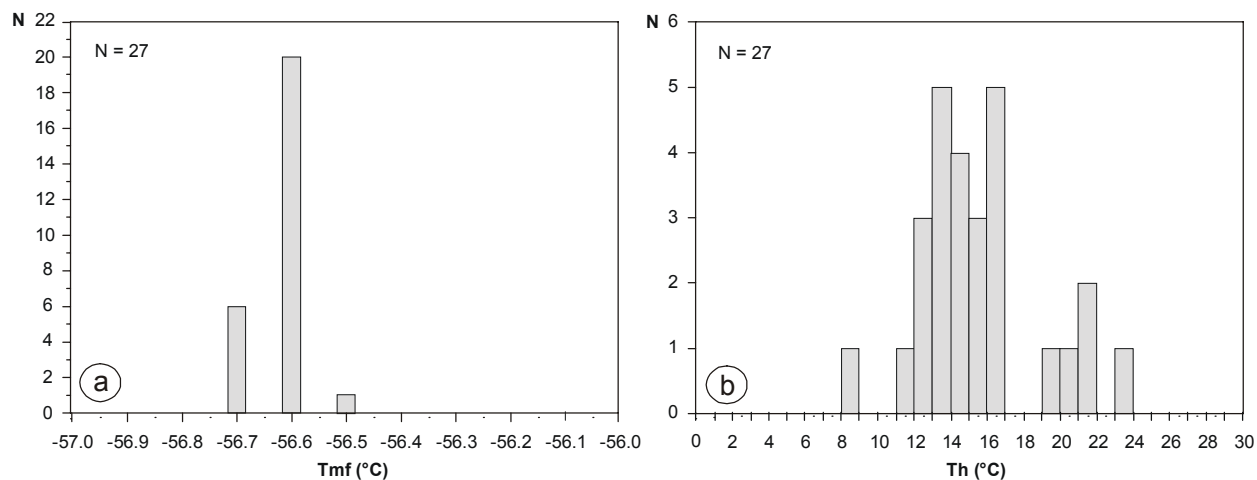


Fig. 17.5: Results of microthermometrical measurements of CO₂-rich inclusions in quartz from the quartz-syenite. *a)* Histogram showing the temperatures of final melting of CO₂-rich inclusions. *b)* Corresponding homogenization temperatures.

17.1.3 Discussion and interpretation

Except rare and small aqueous inclusions hosted by apatite, the primary aqueous, highly saline fluid inclusions in sodalite (19-30 wt.% NaCl, Th: 270-370°C) constitute the earliest recognisable generation of fluid in the carbonatitic breccia. Since textural relationships and microthermometrical measurements display no evidence for major post-genetic changes, the composition of these fluid-inclusions is presumably close to the initial composition of the fenitizing fluid. In contrast, primary to pseudosecondary aqueous fluid inclusions hosted by ankerite of the cementing carbonatite matrix of the carbonatitic breccia display lower minimum temperatures of entrapment (Th: 170-220°C). Rare fluid inclusions preserved in non-recrystallised ankerite display a similar salinity like those in sodalite (23 wt.% NaCl eq.), whereas those hosted by recrystallised ankerite reveal significantly lower salinities (4-6 wt.% NaCl eq.), thus suggesting that the recrystallisation of ankerite post-dated the major sodalite-forming event.

Secondary fluid inclusions in quartz of the quartz-syenite are characterized by a high variability of both the fluid composition and the Th (L-V). Since the three distinct types of fluid populations, occurring in the three individual inclusion trails, lack clear textural relationships, it

was impossible to constrain their relative temporal succession. High-salinity groups (20-24 wt.% NaCl eq.) were trapped at temperatures of 140-170°C and 190-240°C, whereas the low-salinity group (9-17 wt.% NaCl eq.) displays Th in a higher range (180-210°C). Two possible explanations may account for the conspicuous physical properties of the fluid inclusions, i.e. (1) injection of a high-salinity aqueous fluid leading to an extensive albite formation under still high temperatures (strong decreases of salinity, weak decreases of Th), followed by the crystallization of muscovite during cooling (increases of salinity and decreases of Th) or (2) injection of a high-salinity aqueous fluid leading to albite formation, followed by the repeated injection of a high-salinity aqueous fluid at lower temperatures. By now, possibility (2) is the preferred model, since the fluid inclusions seem to follow a continuous trend towards lower salinities, when plotted in the Th-salinity diagram. As textural evidence for a cogenetic formation of the CO₂ and the H₂O inclusions in quartz of the quartz-syenite is lacking, the late CO₂ inclusion trails are ascribed to a weak low temperature hydrothermal overprint.

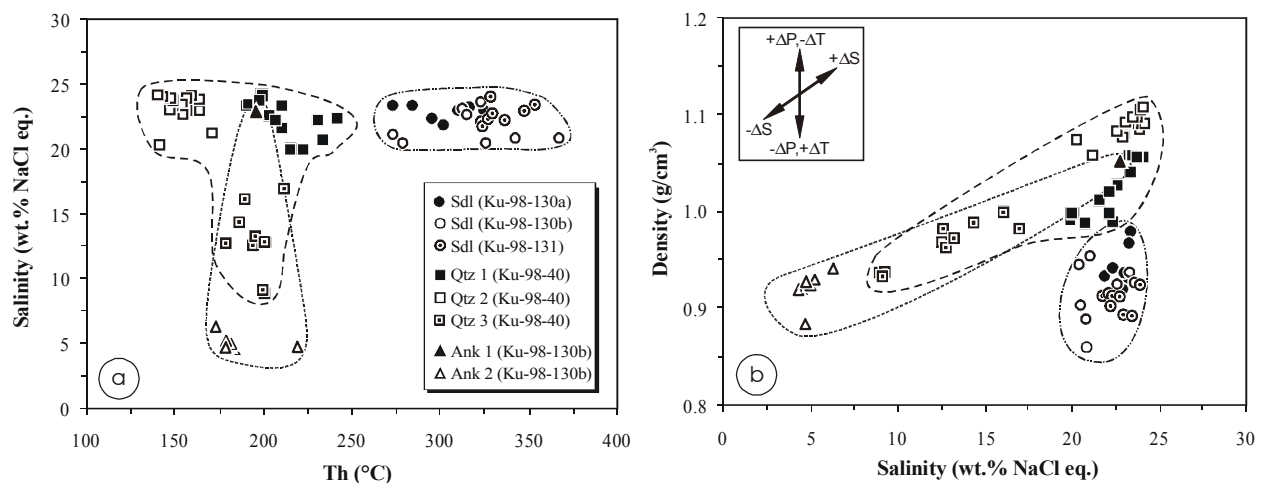


Fig. 17.6: *a*) Homogenization temperature (Th) vs. salinity for all inclusions as a function of inclusion type and host mineral. *b*) Salinity vs. density for all inclusions (the inset after Samson et al. (1995a) qualitatively illustrates the effects on density caused by increases or decreases salinity (S), temperature (T) and pressure (P)).

The temperature and pressure conditions at which the fluid was trapped (Fig. 17.6 a) as well as the salinity of the fluid inclusions (Fig. 17.6 b) strongly control the densities of the aqueous fluid inclusions. In a salinity-controlled system a strong positive correlation between salinity and density should be expected (e.g. Shepherd et al., 1985; Samson et al., 1995a), which indeed is recorded by the fluid inclusions hosted by ankerite from the carbonatitic breccia and by quartz of the quartz syenites (Fig. 17.6 b). Following this, the fenitizing fluid underwent major compositional changes which may be attributed mainly to a variable sodium-loss during the

formation of large amounts of Na- and NaCl-rich silicates (e.g. albite and sodalite) during the fenitization of the anorthosites and syenites. In contrast, the almost vertical trend displayed by the sodalite-hosted fluid inclusions in the density-salinity plot (Fig. 17.6 b) may be better explained by temperature and/or pressure variations during sodalite formation, whereas salinity-changes of the fluid seem to be of only minor importance (Fig. 17.6 a). However, the fluid inclusions in sodalite are generally less dense than those in ankerite and quartz, constraining that they were formed under higher temperatures and/or lower pressures (Fig. 17.6 b).

Given the postulated temporal succession of the fluid inclusions (e.g. sodalite → quartz, ankerite), the data indicates that the fenitizing fluids (1) led to the formation of albite and sodalite in the fenitized anorthositic xenoliths over a certain temperature interval under almost constant and high salinities, (2) caused the transformation of K-feldspar into albite in the fenitized syenites under lower temperatures, leading to a continuous decrease of the salinities of the fenitizing fluids followed by a repeated influx of high-salinity fluids and (3) were enclosed by the recrystallising carbonates from the carbonatitic breccia, with the comparably low salinities of the fluids reflecting previous albite and sodalite formation. The texturally late CO₂-inclusions are presumably formed during a later, independent event of low-temperature alteration. Absolute temperature and pressure conditions of trapping will be discussed in some detail in Chapter 19.3.

17.2 High-resolution synchrotron micro-XRF analysis

Due to the small sizes (5-20 μm) of the fluid inclusions trapped in sodalite, quartz, ankerite, calcite and apatite, the low concentrations of the elements of mineralogical interest (e.g. Sr, Nb, Ba and REE) and the sensitiveness of sodalite regarding temperature changes, a high spatial resolution combined with low detection limits of ppm to sub-ppm is needed for the measurements of their respective chemical compositions. The analyses of the fluid inclusions were performed with the standard polychromatic synchrotron radiation X-ray fluorescence set-up at beamline L at HASYLAB, Hamburg, which allows both, the multi-element analysis of even the high energetic REE and a destruction-free in situ measurement of the trace element geochemistry of the fluid inclusions under almost constant temperatures. In order to calculate the trace element compositions, solitary inclusions were selected and analysed with a beam size of 10 μm in diameter, covering the entire inclusion. The salinity of individual fluids was determined by microthermometric fluid inclusion measurements whereas their trace element contents were estimated from synchrotron micro-XRF analyses, which, in general, gives

reasonable results for elements with an atomic number > 15. EMP major element analyses (Ba, Sr or Fe) were used for the matrix correction and the SRXRF trace element quantification and standardisation. For the estimation of the composition of the fluid inclusions the element contents analysed for the inclusion-free host mineral were subtracted from the respective values of the total analyses (fluid inclusion + hosting mineral). The values calculated for the trace elements of the fluid inclusions must thus be regarded as minimum trace-element contents. The results for the investigation of 7 fluid inclusions in sodalite (Ku-98-14 and Ku-98-130b), 10 fluid inclusions in quartz (Ku-98-40) and 3 fluid inclusions in ankerite (Ku-98-14 and Ku-98-130b) are compiled in Table 17.1 (Drüppel & Rickers, in prep.).

<i>Mineral</i>	<i>Sodalite</i>		<i>Quartz</i>		<i>Ankerite</i>	
	Min (N=7)	Max (N=7)	Min (N=10)	Max (N=10)	Min (N=3)	Max (N=3)
<i>ppm</i>						
<i>S</i>	110	180	-	-	-	-
<i>K</i>	20	240	264	404	-	-
<i>Ca</i>	-	-	22	91	-	-
<i>Fe</i>	60	290	11	194	-	-
<i>Mn</i>	2	243	0	4	-	-
<i>Ti</i>	-	-	84	668	-	-
<i>Zn</i>	0	2	-	-	-	-
<i>Ga</i>	5	107	-	-	-	-
<i>As</i>	222	303	-	-	-	-
<i>Cu</i>	0	9	-	-	-	-
<i>Br</i>	27	924	-	-	-	-
<i>Sr</i>	5	875	35	943	150	700
<i>Ba</i>	9	298	5	1295	-	-
<i>Nb</i>	28	29	-	-	6	38
<i>Sb</i>	10	13	-	-	-	-
<i>La</i>	1	344	-	-	1069	1688
<i>Ce</i>	2	631	-	-	2611	3541
<i>Pr</i>	119	213	-	-	-	-
<i>Nd</i>	-	-	-	-	1270	1492
<i>Sm</i>	-	-	-	-	115	218
<i>Eu</i>	-	-	-	-	61	94
<i>Gd</i>	-	-	-	-	75	166
<i>Tb</i>	-	-	-	-	8	18
<i>Dy</i>	-	-	-	-	33	121
<i>Er</i>	-	-	-	-	15	38
<i>Yb</i>	-	-	-	-	6	29
<i>Lu</i>	-	-	-	-	3	17

Table 17.1: Trace element composition of aqueous fluid inclusions hosted by sodalite and ankerite from the carbonatitic breccia and by quartz of the quartz-syenite as revealed by SRXRF analyses.

SRXRF analyses of apatite crystals from the carbonatitic breccia (Ku-98-14) display similar spectra for the inclusion-free apatite matrix and the fluid inclusion-rich areas. This is

most probably an effect of the overall high Sr, Ba and REE contents of apatite and the comparably small volume of the fluid inclusions with respect to the apatite host, thus making a quantitative determination of the trace element compositions impossible.

Primary aqueous saline inclusions (19-30 wt.% NaCl eq.) trapped during the growth of sodalite from the carbonatitic breccia (Ku-98-14, Ku-98-130b) contain appreciable amounts of Sr (5-875 ppm), Ba (9-298 ppm), La (1-344 ppm) and Ce (2-631 ppm), in good accordance with the results of the mass change calculations for the fenitization of the anorthosites (see Chapter 16). Minor amounts of S (110-180 ppm), Nb (28-29 ppm), K (20-240 ppm), Fe (60-290 ppm), Mn (2-243 ppm), Zn (0-2 ppm), Ga (5-107 ppm), Sb (10-13 ppm), and Pr (119-213 ppm) may be present as well, indicating that the fluid was also capable of transporting these elements. The composition of the fluid inclusions is presumably close to the initial composition of the fenitizing fluid. The fact that Ca is below the detection limit, constrains the suggestion, that Ca was incorporated in previously crystallized carbonates, hence implying that the enclosed fluids represent a late-stage fluid-phase of a highly fractionated carbonatite magma. Judging from the low K contents of < 240 ppm, the fenitizing fluid is suggested to be characterized by a high Na:K ratio.

In clear contrast, secondary aqueous inclusions (9-24 wt.% NaCl eq.) trapped in quartz crystals of a bordering syenite (Ku-98-40) contain no La or Ce but display higher amounts of Sr (up to 943 ppm) and Ba (up to 1295 ppm), as well as minor amounts of K (264-404 ppm), Ca (22-91 ppm), Fe (11-194 ppm), Mn (0-4 ppm), and Ti (84-668 ppm). The composition of these fluids points to NaCl-loss of the fenitizing fluid during previous sodalite formation, accompanied by a relative enrichment of Sr, Ba Ca and H₂O.

The H₂O-rich fluid inclusions (4.5-6.3 wt.% NaCl eq.) hosted by recrystallised ankerite from the REE-rich carbonatitic breccia (Ku-98-130b) strongly differ from the other aqueous fluid inclusion-types in containing no Ba, Fe and K but revealing comparably high amounts of Sr (150- 700 ppm) and the REE (Σ REE: 5265-7421 ppm). As for the carbonatite, the $(La/Nd)_{cn}$ ratios are high, ranging from 1.4-2.4. The REE patterns of the fluid inclusions are straight, except a weak negative $(Sm/Sm^*)_{cn}$ anomaly of 0.4-0.7 (Fig. 17.7), which is also displayed by both the REE-poor $((Sm/Sm^*)_{cn}: 0.6-0.8)$ and the REE-rich carbonatitic breccia $((Sm/Sm^*)_{cn}: 0.6-0.7)$. The fluid inclusions reveal either an accentuated negative Ho anomaly or Ho contents below the detection limit, thus suggesting that Ho was either incorporated by a previously crystallized mineral or remained in the carbonatite melt. When compared to the carbonatitic

breccia, the fluid inclusions are characterized by flatter patterns overall, suggesting previous or contemporaneous crystallization of Sr-La-Ce carbonates. Regarding their high Sr and LREE contents, the fluids are a potential source for the Sr and REE enrichment of the REE-rich carbonatitic breccia. Following this, the REE-enrichment of the REE-rich carbonatitic breccia may better be explained by the influx of late-stage, highly evolved carbonatite fluids than by extensive fractionation of the carbonatite melt.

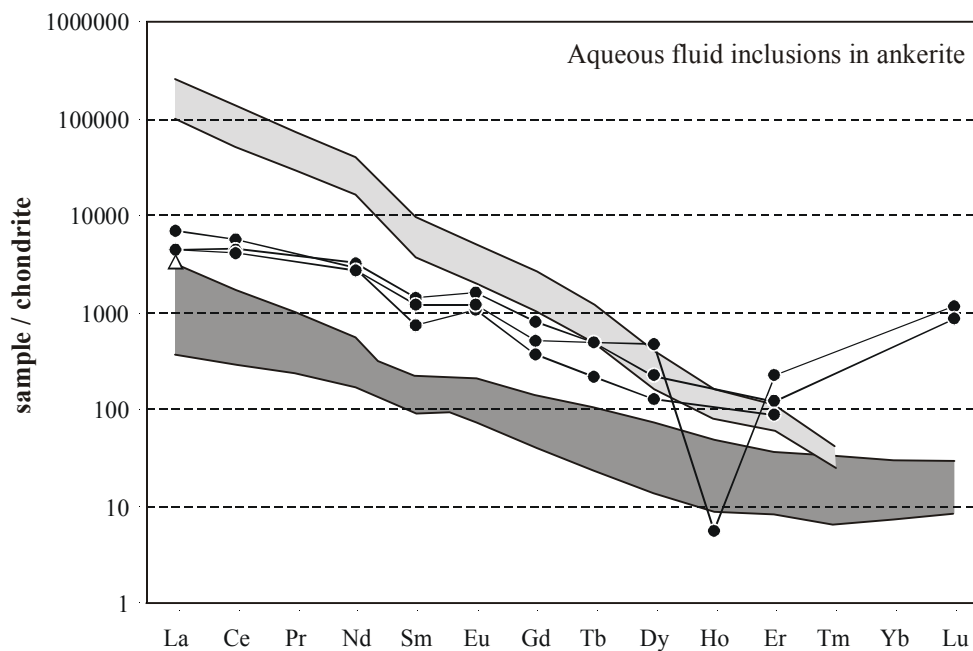


Fig. 17.7: Chondrite-normalized rare-earth element patterns of individual aqueous fluid inclusions in ankerite from the carbonatitic breccia. Chondrite-normalized REE-patterns of the REE-poor carbonatitic breccia (dark grey) and the REE-rich carbonatitic breccia (light grey; whole-rock ICP-AES analyses) are illustrated for comparison.

17.3 Implications for the evolution of the fenitizing fluids

This study was initiated in order to provide physicochemical data on the orthomagmatic fluids emanated by the Swartbooisdrif carbonatites. The data indicate that the fluids, even those enclosed in early crystallized sodalite from the carbonatitic breccia, are aqueous fluids containing no CO₂. Orthomagmatic CO₂-inclusions or low-salinity carbonic fluids, that are generally expected to be produced during the early stages of carbonatite evolution, have never been observed, thus constraining that carbonate fractionation was already active when the fluids were expelled. Following this, the aqueous fluid inclusions can be described as late-stage carbonatite fluids.

Aqueous fluid inclusions in sodalite from the carbonatitic breccia contain high concentrations of Na, Sr, Ba, Fe, Nb, and the LREE and may thus be responsible for the observed compositional changes of the anorthosites during fenitization (see Chapter 16). The fact that K is present in only minor proportions strongly suggests that the fluid is NaCl-dominated, in good accordance with the sodic fenitization type (i.e. the formation of large amounts of albite and sodalite). Since implications for post-genetic changes are lacking (e.g. necking down or decrepitation phenomena), the composition of the fluids is presumably close to the initial composition of the carbonatite fluid, even though previous and contemporaneous sodalite crystallization may have caused substantial NaCl-loss of the fluid before trapping.

Presumably later, H₂O-rich fluid inclusions hosted by recrystallised ankerite from the carbonatitic breccia strongly differ from those in sodalite in containing distinctly lower amounts of Na and no Ba, Fe and K, thus suggesting that these elements were incorporated in previously crystallized minerals like albite, sodalite, ankerite, magnetite and biotite, which were formed during the progressive fenitization of the wall-rocks and the crystallization of the carbonatite itself. Decreases of Na, K and Fe in the fluid may in turn have caused a relative increase in the remaining fluid species, such as Sr and the REE of the ankerite-hosted fluid inclusions. The fact, that these elements are highly concentrated in the REE-rich carbonatitic breccia, provides evidence that the REE-enrichment was caused by autometasomatic processes.

The secondary aqueous inclusions trapped in quartz crystals of quartz-syenite seem to preserve an intermediate stage of the fluid evolution. The highly variable composition of these fluids points to previous and contemporaneous Na-loss of the carbonatite-released fluid during albite and sodalite formation, accompanied by a relative enrichment of K, Ca, Fe, Ti, Sr and Ba. It has to be mentioned, however, that the occurrence of a low-temperature, high-salinity group of fluid inclusions testifies to repeated injections of high-salinity carbonatite fluids, thus making it impossible to unravel the exact chemical evolution of the fluids preserved in the quartz-syenite.

As a conclusion, the data imply, that the fluids preserved in sodalite and ankerite from the carbonatitic breccia and in quartz of the quartz-syenite represent direct samples of highly evolved, alkali-carbonatitic fluids, expelled from a fractionated carbonatite magma. Major compositional changes of the fluid are mainly caused by interrelated chemical reactions between the fluid and the lithologies bordering the carbonatite centres.

18 Stable Isotope Composition

18.1 Oxygen and Carbon Isotopic Composition

Stable isotopes can serve as a powerful tool for constraining the source rocks of carbonatites and their magmatic and post-magmatic evolution (e.g. Deines, 1989). In general, variations in the O and C isotopic ratios in carbonatite complexes are mainly attributed to (1) the isotopic composition of the magma sources, (2) fractionation processes during the carbonatite evolution (3) isotopic composition of the country rock and (4) post-magmatic alteration (see Deines, 1989, for a review). The range of the $\delta^{18}\text{O}$ and the $\delta^{13}\text{C}$ compositions of primary igneous carbonatites was first defined by Taylor et al. (1967) and called "carbonatite box", ranging between 6 and 10‰ for $\delta^{18}\text{O}$ and between -4 and -8‰ for $\delta^{13}\text{C}$. Recently, however, Keller & Hoefs (1995) supposed a more restricted composition for the "primary" isotope signatures of carbonatites ("primary" in this case means unaffected by secondary alteration processes), based on analyses of the stable isotope patterns of completely fresh natrocarbonatite from Oldoinyo Lengai (-6.3 to -7.1 ‰ $\delta^{13}\text{C}$ and 5.5-7.0 ‰ $\delta^{18}\text{O}$), which is adopted for this study. Remarkably, only part of the yet investigated carbonatites fall in the above mentioned compositional fields, whereas a considerable number of samples, especially the ankerite carbonatites, have significantly higher C and O ratios, which are generally thought to be caused by secondary processes (e.g. Deines, 1989; Horstmann & Verwoerd, 1997).

This study addresses the O and C isotope signatures of the Swartbooisdrif carbonatites as well as their influence on the O isotope patterns of the bordering syenites and anorthosites in the light of magmatic-metasomatic as well as hydrothermal or meteoric water alteration (Drüppel et al., *subm.*). The $\delta^{18}\text{O}$ and $\delta^{13}\text{C}$ data of separated minerals from carbonatites (ankerite, magnetite, biotite), anorthosites (plagioclase), fenitized syenites (albite) and the fenitized nepheline syenite (K-feldspar, nepheline, biotite) are listed in Table A.5.5.1 in the Appendix A.5.5. A description of the analytical techniques is given in the Appendix A.2.6.1.

18.1.1 Oxygen isotopic composition of anorthositic rocks

The oxygen isotopic composition of the anorthositic rocks of the Kunene Intrusive Complex has been discussed in some detail in Chapter 8.1. In order to investigate the influence of carbonatite-

related fluids on the anorthositic country rocks plagioclase was separated from 4 dark anorthosites sampled in the vicinity of the sodalite-mining area and from 4 dark anorthosites sampled in distinct parts of the anorthosite massif. The fact, that anorthosite samples from both areas display similar and magmatic $\delta^{18}\text{O}$ ranges for plagioclase (5.94 ± 0.21 ‰ and 5.82 ± 0.15 ‰, respectively) is taken as evidence, that the circulation of carbonatite-derived metasomatic fluids was confined to contacts between the carbonatites and their wallrocks and reached no large areal extent. The lack of broad metasomatic aureoles around the carbonatite dykes implies that the Swartbooisdrif ferrocarbonatites are deep-seated intrusions, emplaced in crustal levels where the effects of metasomatism are less prominent.

18.1.2 Oxygen isotopic composition of fenitized syenites and nepheline syenites

The oxygen isotopic ratios of orthomagmatic K-feldspar and plagioclase of the non-altered syenites of the Swartbooisdrif area are discussed in Chapter 8.2. In addition, metasomatically formed albite was separated from two samples of the fenitized syenite (Ku-98-70s, Ku-99-19s). Remarkably, the $\delta^{18}\text{O}$ values of feldspar separates of the non-altered syenite and the fenitized syenite are quite similar, ranging between 7.20-7.92 ‰ (average: 7.45 ± 0.24 ‰) and 7.53-7.77 ‰ (average: 7.65 ± 0.12 ‰), respectively (Fig. 18.1). Nepheline of the fenitized nepheline syenite (Ku-99-15a) exhibits a slightly lower $\delta^{18}\text{O}$ of 6.93, whereas the K-feldspar from the same

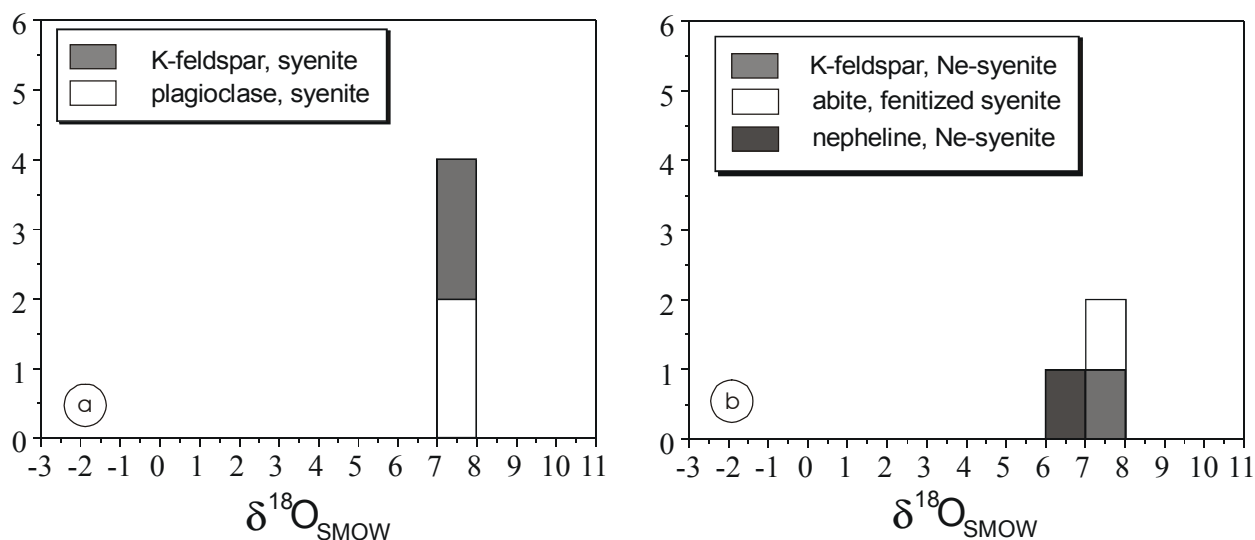


Fig. 18.1: Oxygen isotopic composition of hand-picked feldspar and nepheline separates from the syenites, fenitized syenites and the fenitized nepheline syenite. *a)* Oxygen isotope data of orthomagmatic feldspar from the syenites. *b)* Oxygen isotope data of metasomatically formed albite from the fenitized syenites and of K-feldspar and nepheline from the nepheline syenite.

sample has a $\delta^{18}\text{O}$ of 7.62 ‰, similar to those of syenite feldspars (Fig. 18.1b). Orthomagmatic biotite of the nepheline syenite sample shows a $\delta^{18}\text{O}$ of 1.73 ‰.

The homogeneity of the $\delta^{18}\text{O}$ values of feldspars and nepheline from the different rock-types is striking, since the two samples of the fenitized syenite and the nepheline syenite sample display clear textural and chemical evidence for the interaction with fenitizing fluids. Two explanations may account for the obtained results: (1) the carbonatitic fluids had no influence on the $\delta^{18}\text{O}$ of the feldspars and nepheline, or (2) the metasomatic fluid had magmatic temperatures and $^{18}\text{O}/^{16}\text{O}$ ratios similar to or only slightly higher than those of the syenites. By now, model (2) is favoured, as albite in the alkali-syenites and the sodium-rich rims of nepheline in the nepheline syenite are not magmatic in nature but were formed during the metasomatic event. Following this, the fenitizing fluids emanated by the carbonatites should have had $\delta^{18}\text{O}$ values of ≥ 7.5 -7.8 ‰ and magmatic temperatures of *c.* 600-890°C (see Chapter 9.2).

18.1.3 Oxygen and carbon isotopic compositions of the carbonatitic breccia and the ferrocarbonatite veins

Separated magnetite grains from the carbonatitic breccia (Ku-97-26, Ku-99-02, Ku-99-SA11) and from the ferrocarbonatite vein (Ku-01-03) reveal variable values of $\delta^{18}\text{O}$, in the range of -4.21 to -1.46 ‰ and of -2.63 ‰, respectively. Biotites from the carbonatitic breccia (Ku-98-48, Ku-99-5a) show ^{18}O values of 2.77-3.41 ‰ (Fig. 18.2).

Separated ankerite grains from 4 samples of the carbonatitic breccia (Ku-97-26, Ku-99-02, Ku-99-SA8, Ku-99-SA11) cover a narrow range in $\delta^{13}\text{C}$ (-6.86 to -6.98) and exhibit a stronger variation in $\delta^{18}\text{O}$ (8.95 to 9.73) Similar but slightly lower values are displayed by ankerite from a late ferrocarbonatite vein (Ku-01-03; $\delta^{13}\text{C}$: -6.73, $\delta^{18}\text{O}$: 8.91; Fig. 18.2), which agree well with the values obtained by Thompson et al. (2002) for similar samples. The ^{13}C contents of carbonates from both carbonatite generations are in good agreement with the $\delta^{13}\text{C}$ values of the fresh Oldoinyo Lengai natrocarbonatite lava and its carbonate phenocrysts (-6.3 to -7.1 ‰ $\delta^{13}\text{C}$) given by Keller & Hoefs (1995). In contrast, the ^{18}O values of the Swartbooisdrif dykes fall into the carbonatite box of Taylor et al. (1967) but are distinctly higher than those reported for unmodified partial mantle-melts from Oldoinyo Lengai (5.5-7.0 ‰ $\delta^{18}\text{O}$; Keller &

Hoefs, 1995), thus indicating the involvement of magmatic and/or hydrothermal phases during their petrogenesis (Fig. 18.3).

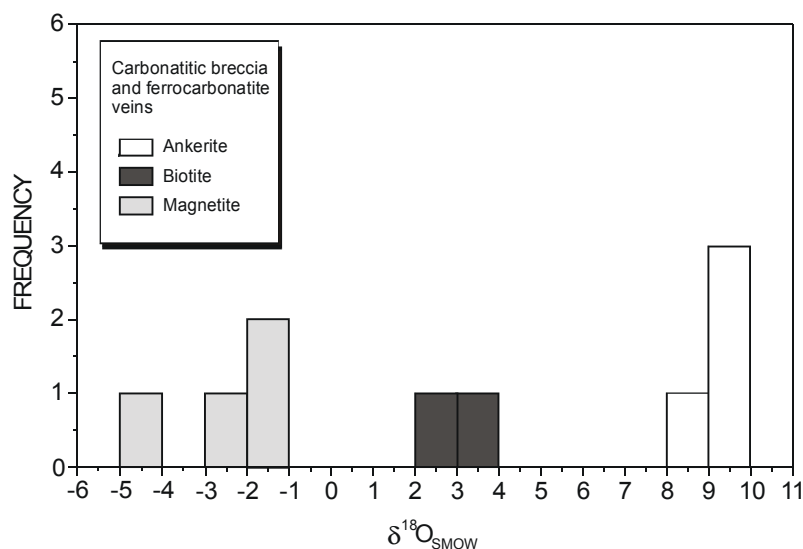


Fig. 18.2: Oxygen isotopic composition of hand-picked magnetite, biotite and ankerite separates from the carbonatitic breccia and the ferrocyanatite veins.

Following Deines (1989) enrichment of $\delta^{18}\text{O}$ of carbonatites may be due to: (1) emanation of fluids during pressure reduction at the time of emplacement (e.g. preferential escape of ^{18}O -depleted water or increase of the $\text{H}_2\text{O}:\text{CO}_2$ ratio in the remaining fluid), (2) exchange with magmatic, high ^{18}O fluids (e.g. carbonatite fluids with a low $\text{H}_2\text{O}:\text{CO}_2$ ratio), (3) retrograde exchange with magmatic fluids at temperatures of *c.* 100°C, (4) retrograde exchange with ^{18}O -rich hydrothermal fluids, displaying high $\text{H}_2\text{O}:\text{CO}_2$ ratios and (5) the influx of meteoric water at temperatures below 200-250°C, which previously had undergone isotopic exchange with ^{18}O -rich sedimentary or metasedimentary rocks at low temperatures. Both, point (1) and (5) after Deines (1989) may generally account for the elevated ^{18}O values of the ferrocyanatites investigated in this study. However, as has been demonstrated in Chapter 8.1, isotopic exchange between anorthosites and meteoric waters led to a decrease of the ^{18}O values of the anorthosites, thus suggesting that the circulating meteoric solutions in the investigated study area, at least those altering the anorthosites, rather had ^{18}O -poor compositions. Point (5) seems to be a plausible explanation for the ^{18}O patterns of the investigated samples, since the oxygen isotopic compositions of metasomatically formed albite and nepheline from the syenites and the nepheline syenites point to the influx of fenitizing fluids with comparably low ^{18}O values of 7.5-7.8 ‰, thus being indeed ^{18}O -depleted with respect to ankerite from the carbonatites (8.91 to 9.73 ‰ $\delta^{18}\text{O}$). However, regarding clear evidence for low-temperature alteration of the studied

samples (abundance of late CO₂-inclusions in quartz of a quartz-syenite, see Chapter 17.1.3), a combination of process (1) and (5) seems to be most likely.

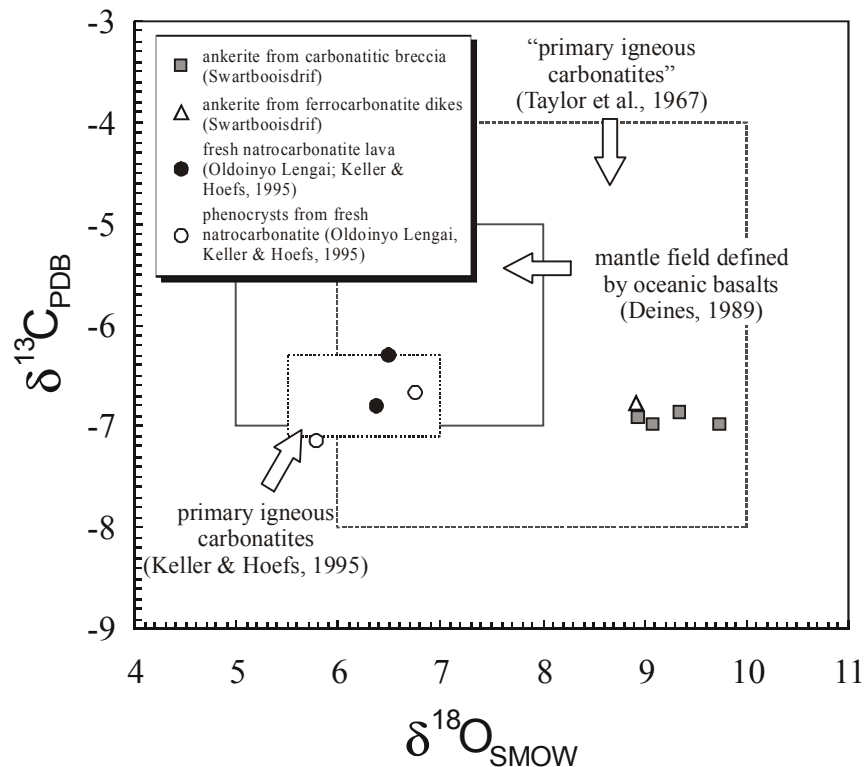


Fig. 18.3: $\delta^{13}\text{C}$ - $\delta^{18}\text{O}$ plot of hand-picked ankerite separates from both the carbonatitic breccia and the ferrocarbonatite veins of the Swartbooisdrif alkaline province (*dotted-line box*: based on C/O isotopes of fresh natrocarbonatite lava and phenocrysts (Keller & Hoefs, 1995), *solid-line box*: based on C/O isotopes in basalts (Kyser, 1986; Nelson et al., 1988; Deines, 1989), *dashed-line box*: based on C/O isotopes of carbonatites (Taylor et al., 1967)).

Regarding their oxygen and carbon isotopic composition, the Swartbooisdrif carbonatites differ significantly from most other ankerite and ankerite/calcite carbonatites, which are mostly characterized by variable and high ¹⁸O and ¹³C ratios (e.g. Deines, 1989; Horstmann & Verwoerd, 1997), lying outside the primary igneous carbonatite field as defined by Taylor et al. (1967; Fig. 18.4). The ankerites of these carbonatites are generally thought to be of secondary origin, with their formation being caused by the influx of Fe- and Mn-rich meteoric waters (e.g. Horstman & Verwoerd, 1997). Only two ankerite carbonatites, i.e. the ferrocarbonatites of Marinkas Quellen, Namibia (Verwoerd, 1993; Horstmann & Verwoerd, 1997), and the Barra do Itapirapuã ferro- to magnesiocarbonatites, Brazil (Andrade et al., 1999), have stable isotope ratios adjacent to those of the Swartbooisdrif carbonatites, plotting within the magmatic C-O field of Taylor et al. (1967; Fig. 18.4). Remarkably, however, oxygen and carbon isotope values

of calcio- and magnesiocarbonatites of the Lupongola complex, SW Angola (Alberti et al, 2000), are quite similar to those obtained for the Swartbooisdrif. Following these arguments, the stable isotope values obtained for the Swartbooisdrif ferrocarbonatites seem to be quite exceptional, as they are concordant with a magmatic origin.

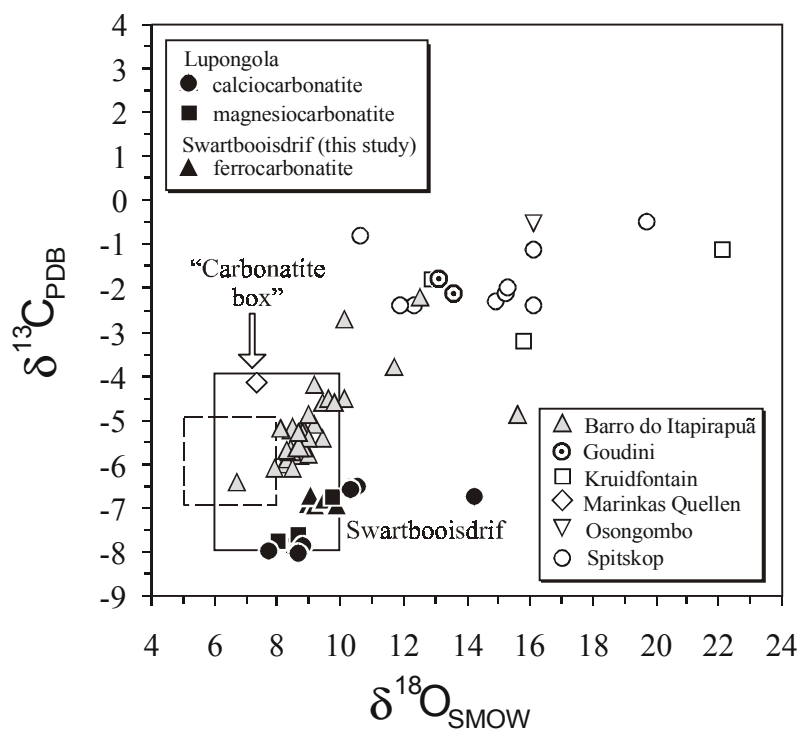


Fig. 18.4: $\delta^{13}\text{C}$ - $\delta^{18}\text{O}$ plot of hand-picked ankerite separates from both the carbonatitic breccia and the ferrocarbonatite veins of the Swartbooisdrif alkaline province and from carbonatites elsewhere in southern Africa and Brazil (*dashed-line box*: based on C/O isotopes in basalts (Kyser, 1986; Nelson et al., 1988; Deines, 1989), *solid-line box*: based on C/O isotopes of carbonatites (Taylor et al., 1967); isotopic data of ankerite and ankerite/calcite carbonatites from Goudini, Kruidfontain, Marinkas Quellen, Osongombo and Spitskop: Horstmann & Verwoerd (1997), isotopic data of magnesio- to ferrocarbonatites from the Barro do Itapirapuã complex, Brazil: Andrade et al. (1999), isotopic data of calcio- and magnesiocarbonatites of the Lupongola complex, Angola: Alberti et al. (2000).

18.2 Sulphur isotopic composition

Sulphur isotope data are yet available for relatively few carbonatites, with the analysed sulphides including pyrite, chalcopyrite, galena and pyrrhotite. The sulphur isotope composition of mantle-derived carbonatite melts can be estimated from the sulphur isotope ratios of meteorites, basic sills and ocean-floor basalts. Following Deines (1989) most of these analyses fall in a narrow

range of -1 to $+1$ ‰, a range, which is generally thought to be characteristic of the pristine mantle. However, significant ^{34}S enrichments with respect to these values have been observed in some basic intrusions, suggesting that parts of the mantle are enriched in ^{34}S (e.g. Deines, 1989). In contrast, the sulphur isotope composition of carbonatites is variable, ranging between -13 to $+2$ ‰ for $\delta^{34}\text{S}$ and thus deviating significantly from the isotopic ratio of the pristine mantle (see Deines, 1989, for a review). These differences are thought to be mainly caused by (1) isotope heterogeneity of S within the mantle or (2) changes in the O fugacity during the carbonatite formation (e.g. Deines, 1989).

This study addresses the S isotope signatures of the carbonatitic breccia and those of the fenitized anorthosites and syenites (Drüppel & Wagner, in prep.). In order to investigate the changes of $\delta^{34}\text{S}$ during the crystallization of the carbonatites, presumably early, euhedral pyrite from the sodalite-rich carbonatitic breccia (Ku-01-OD1, Ku-01-OD2) as well as pyrite and chalcopyrite from late-stage sulphide-oxide veins in the sodalite-rich carbonatitic breccia (Ku-99-SA8) and the REE-rich carbonatitic breccia (Ku-98-130b) have been analysed for their sulphur isotope composition. Moreover, the S isotope patterns of metasomatically formed pyrites from a fenitized leucogabbronorite (Ku-97-03b) and a fenitized syenite (Ku-97-05a) have been determined, to constrain the isotopic composition of the carbonatite fluids. The $\delta^{34}\text{S}$ data of the analysed sulphides are depicted in Table A.5.5.2 in the Appendix A.5.5 and are illustrated in Fig. 18.5. A description of the analytical method is given in the Appendix A.2.6.2.

The sulphur isotopic ratios of orthomagmatic pyrite grains, dispersed in the carbonatitic breccia range between 3.76 ‰ and 5.13 ‰ (Fig 18.5a, b), being about 4 ‰ higher than the ^{34}S range of the pristine mantle. These values may either reflect (1) a $\delta^{34}\text{S}$ -enriched mantle source or (2) fractionation governed by oxidised S species in the melt. In clear contrast, distinctly lower, negative $\delta^{34}\text{S}$ values have been determined for pyrite and chalcopyrite in late sulphide-oxide veins (-0.03 to -3.25 ‰ $\delta^{34}\text{S}$; Fig 18.5c, d), with the lowest values obtained for pyrite and chalcopyrite from the REE-rich carbonatitic breccia (-2.07 to -2.43 ‰ $\delta^{34}\text{S}$ and -2.84 to -3.25 ‰, respectively). Notably, late-stage chalcopyrite from the sodalite-rich carbonatitic breccia (-0.03 to -1.31 ‰ $\delta^{34}\text{S}$) is intimately associated with magnetite/hematite, whereas the REE-rich sample Ku-98-130b additionally contains accessory barite. Following this, the carbonatite sulphides follow a continuous trend towards more negative $\delta^{34}\text{S}$ values coupled with an increase of the oxygen fugacity. This trend can be interpreted in terms of changing proportions of oxidised and reduced S species in the melt: (1) During the early stages of crystallization the oxygen fugacity was presumably low (formation of magnetite) whereas the proportion of the

reduced S species (H_2S , HS^-) in the melt was high, promoting the precipitation of pyrite and the formation of almost pure, SO_4 -free sodalite and thus in turn leading to an increase of the oxidised

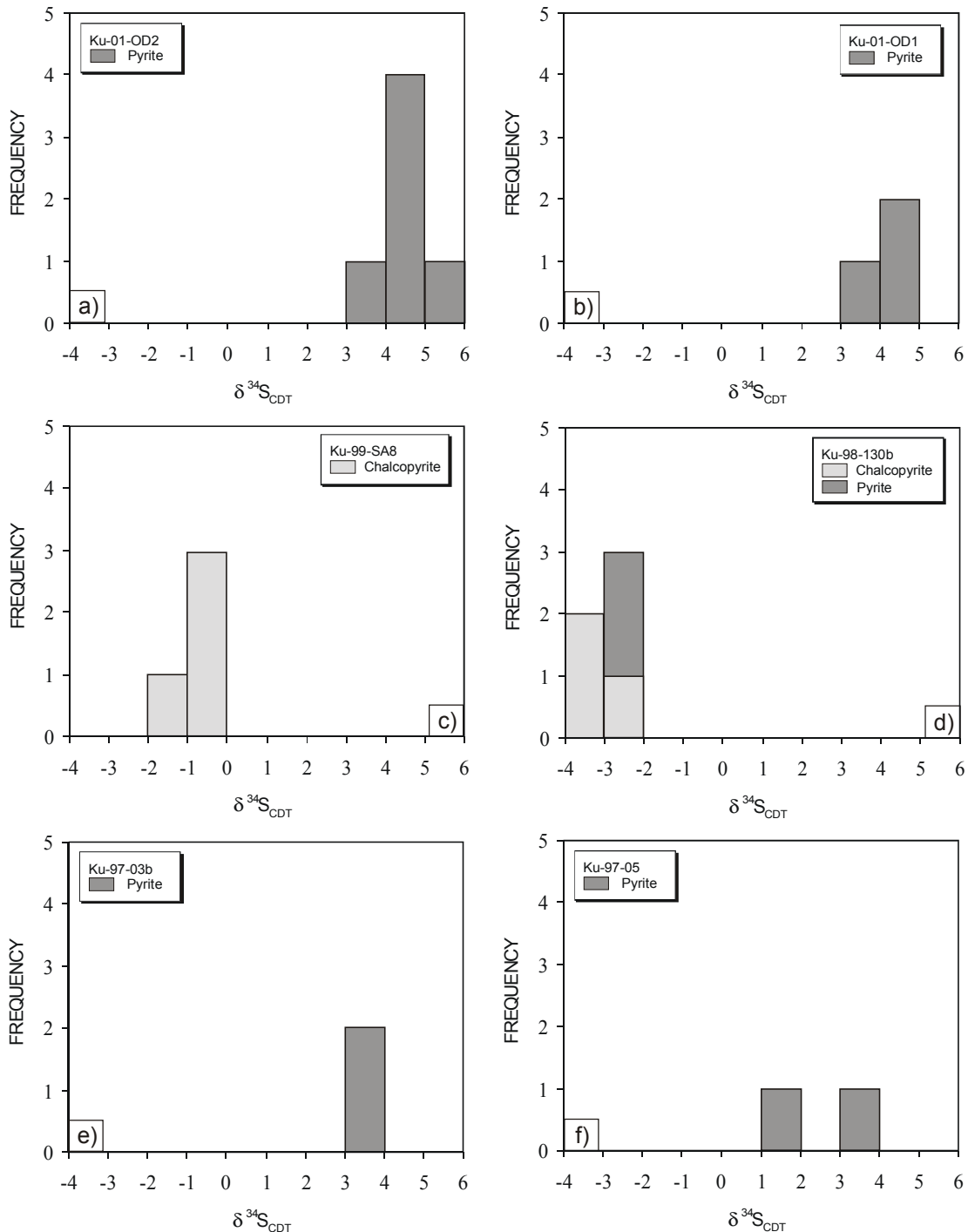


Fig. 18.5: Oxygen isotopic composition of pyrite and chalcopyrite from the carbonatitic breccia, the fenitized anorthosites and the fenitized syenites. *a)* and *b)* Isolated pyrite grains, dispersed in the carbonatite matrix of the carbonatitic breccia. *c)* and *d)* Pyrite and chalcopyrite occurring in texturally late sulphide veins of the carbonatitic breccia. *e)* Metasomatically formed pyrite from the fenitized syenite. *f)* Metasomatically formed pyrite from the fenitized anorthosite.

S species in the magma. (2) In contrast, both the oxygen fugacity and the proportion of the oxidised S species (HSO_4^- , SO_4^{2-}) continuously increased during the late stages of the carbonatite evolution, hence leading to the precipitation of barite and consequently increasing the relative abundances of the reduced S species in the carbonatite magma.

Remarkably, the $\delta^{34}\text{S}$ values obtained for metasomatically formed pyrite from both the fenitized syenites (1.17-3.40 ‰ $\delta^{34}\text{S}$; Fig. 18.5e) and the fenitized anorthosites (3.27-3.40 ‰ $\delta^{34}\text{S}$; Fig. 18.5f) are similar but slightly lower than those of early crystallized pyrite from the carbonatitic breccia, hence implying depletion of $\delta^{34}\text{S}$ in the carbonatite fluid with respect to the carbonatite melt. Following this, it may be possible that (1) the release of the fenitizing fluids predated the formation of pyrite in the carbonatitic breccia, thus preserving lower $\delta^{34}\text{S}$ contents of the carbonatite magma or (2) the fluid was characterized by a higher oxygen fugacity when compared to the carbonatite melt.

19 P-T evolution of the Carbonatitic Melts And fluids

Based on geobarometry studies on various mineral assemblages of the anorthosites of the KIC (1,385-1,347 Ma) and the associated felsic suite (~1,380-1,340 Ma) pressures of 6-8 kbar have been calculated for both their emplacement and subsolidus re-equilibration in the middle crust (Drüppel et al., 2000; see Chapter 9). Following this, the emplacement depth of the younger nepheline syenite and the ferrocarnatites (1,140-1,120 Ma) is confined to pressures below 6 kbar. The lack of broad metasomatic aureoles surrounding the carbonatite dykes as well as the sodic character of fenitization generally suggest the carbonatites to be deep-seated intrusions (Le Bas, 1987, 1989). The P-T conditions for the magmatic crystallization and subsolidus re-equilibration of the carbonatites and nepheline syenites and for the fenitization of anorthosites and nepheline syenites were estimated from the chemical compositions and textural relationships of their respective mineral assemblages, oxygen and sulphur isotope fractionation between mineral pairs and fluid inclusion isochore data. The results of the various calculations are summarized in the P-T plot of Fig. 19.4 (Drüppel et al., 2002a, *subm.*).

19.1 Emplacement and crystallization of the carbonatites

The following magmatic crystallization sequence was established for the carbonatitic breccia:

- (1) apatite, pyrochlore, biotite, ankerite, magnetite,
- (2) ankerite, interstitial calcite, magnetite,
- (3) chalcopryrite, pyrite, magnetite,
- (4) chalcopryrite, pyrite, millerite, polydymite/violarite, chalcocite/digenite, bornite, magnetite, hematite,
- (5) hematite, chlorite, barite, strontianite, and calcite of the second generation.

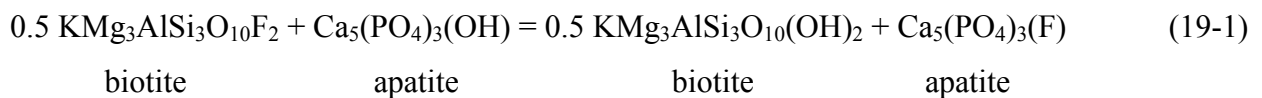
In the cementing carbonatite matrix, apatite, pyrochlore and biotite crystallized first accompanied and outlasted by ankerite and magnetite and followed by late interstitial calcite. Dispersed grains of chalcopryrite and pyrite are most probably synchronous with the second magnetite generation. During the end-stages of the carbonatite crystallization various sulphides, hematite as well as late chlorite, barite, strontianite, and calcite of the second generation were

formed. The rocks suffered extensive and repeated deformation, which, however, mainly affected ankerite and calcite.

To establish the *P-T* conditions during the crystallization of the carbonatites the following approaches have been used: (1) biotite-apatite thermometry and HF barometry, (2) calcite-dolomite thermometry, (3) equilibrium fractionation of oxygen isotopes in ankerite-magnetite pairs, (4) equilibrium fractionation of sulphur isotopes in pyrite-chalcopyrite pairs and (5) stability relations of Co-Ni-Fe sulphides using published thermodynamic data.

19.2.1 Biotite-apatite thermometry and HF barometry

The biotite-apatite geothermometer, first proposed by Stormer & Carmichael (1971), is based on the partition coefficient of fluorine and hydroxyl between biotite and apatite. The geothermometer was recalibrated by Ludington (1978), who additionally made allowance for the effect of iron and magnesium substitution on fluorine in biotite. A set of consistent thermodynamic properties of fluorine and chlorine end-member minerals and solid-solution properties for biotite (considering reciprocal (Mg,Fe²⁺,Al^{VI}) (F,Cl,OH) mixing properties) was given by Zhu & Sverjensky (1991), who later proposed a formulation of the biotite-apatite fluorine and hydroxyl geothermometer (Zhu & Sverjensky, 1992). The temperature-dependent F-OH exchange between coexisting biotite and apatite is expressed by the reaction



with the revised apatite-biotite geothermometer by Zhu & Sverjensky (1992) given by the equation:

$$T(^{\circ}\text{C}) = \frac{8852 - 0.024P(\text{bars}) + 5000X_{\text{Fe}}}{1.987 \ln K_{D,F}^{\text{Ap/Bt}} + 3.3666} - 273.15 \quad (19-2)$$

where: X_{Fe} = mole fraction of Fe in biotite
 $(X_{\text{Fe}} = (\text{Fe} + \text{Al}^{\text{VI}}) / (\text{Fe} + \text{Mg} + \text{Al}^{\text{VI}}))$

$$K_{D,F}^{\text{Ap/Bt}} = (X_{\text{F}}/X_{\text{OH}})^{\text{Ap}} / (X_{\text{F}}/X_{\text{OH}})^{\text{Bt}}$$

$X_{\text{F}}, X_{\text{OH}}$ = mole fractions of F and OH in biotite and apatite

The pressure dependence of this geothermometer is negligible, whereas it is highly sensitive to analytical errors in fluorine. The mean error (1σ) of the geothermometer is $\pm 50^\circ\text{C}$.

Sample	analyses	texture	KD	T ($^\circ\text{C}$)	T ($^\circ\text{C}$)	T ($^\circ\text{C}$)	$\log(f_{\text{HF}}/f_{\text{H}_2\text{O}})$
				$P_{\text{ref.}}: 3 \text{ kbar}$	$P_{\text{ref.}}: 4 \text{ kbar}$	$P_{\text{ref.}}: 5 \text{ kbar}$	
Ku-98-131	6-2-Ap1	core	12.29	1048	1045	1042	-3.84
	6-2-Bt1	core	11.65	1065	1062	1059	-3.82
		rim	15.14	985	982	980	-3.95
		rim	16.88	955	952	950	-4.00
		rim	36.93	774	771	769	-4.45
		rim	31.71	804	802	800	-4.36
		rim					
	6-2-Ap2	core	10.20	1121	1118	1115	-3.81
	6-2-Bt4	core	10.38	1115	1112	1109	-3.82
		rim	15.97	981	979	976	-4.02
		rim	33.15	805	803	800	-4.42
		rim					
	6-2-Ap3	core	11.74	1074	1071	1068	-3.87
	6-2-Bt2	rim	17.65	954	951	949	-4.07
	6-2-Ap4	core	14.31	1013	1010	1007	-3.97
	6-2-Bt2	rim	14.57	1008	1005	1002	-3.98
	6-2-Ap5	core	8.96	1168	1165	1162	-3.75
	6-2-Bt2	rim	21.21	906	904	901	-4.17
Ku-99-SA8	2-Ap1	core	9.91	1163	1160	1157	-3.89
	2-Bt1	rim	13.19	1067	1064	1061	-4.01
	2-Ap2	core	10.68	1161	1158	1155	-3.90
	2-Bt2	core	11.64	1132	1129	1126	-3.93
		rim	19.17	981	978	976	-4.15
		rim	13.11	1092	1090	1087	-3.98
		rim					
	3-Ap1	core	9.69	1197	1194	1191	-3.94
	3-Bt2	rim	12.42	1110	1107	1104	-4.04
	4-Ap1	core	10.28	1156	1153	1150	-3.89
	4-Bt1	rim	20.54	946	944	941	-4.20

Table 19.1: Representative T and HF fugacity ($\log(f_{\text{HF}}/f_{\text{H}_2\text{O}})$) estimates for biotite-apatite pairs of the sodalite-rich carbonatitic breccia, derived from biotite-apatite fluorine and hydroxyl geothermometry after Zhu & Sverjensky (1992).

The calculation of the relative hydrogen fugacity followed the approach of Andersen & Austrheim (1991), who suggested that the relative HF fugacity is independent of the phlogopite composition, which contains negligible octahedral aluminium. The equation of Andersen & Austrheim (1991), describing the relationship between apatite composition, temperature and the relative HF fugacity of the coexisting fluid phase and/or volatile-containing magma, is expressed as:

$$\log(f_{\text{HF}}/f_{\text{H}_2\text{O}}) = \log(X_{\text{F}}/X_{\text{OH}})^{\text{Ap}} - 1.523 - 3200 / T \quad (19-3)$$

The uncertainty of the relative HF fugacity is $c. \pm 0.15$ log units.

Temperatures have been calculated for individual biotite-apatite pairs in direct grain contact from two samples of the sodalite-rich and two samples of the layered (sodalite-poor or – free) carbonatitic breccia. The results obtained for temperatures and HF-fugacity data of the sodalite-rich carbonatitic breccia and the layered carbonatitic breccia are compiled in Tables 19.1 and 19.2, respectively, and are illustrated in a $\log(f_{\text{HF}}/f_{\text{H}_2\text{O}})$ vs. $10^4/T$ diagram (Fig. 19.1).

Sample	analyses	texture	KD	T (°C)	T (°C)	T (°C)	$\log (f_{\text{HF}}/f_{\text{H}_2\text{O}})$
				$P_{\text{ref.}}: 3 \text{ kbar}$	$P_{\text{ref.}}: 4 \text{ kbar}$	$P_{\text{ref.}}: 5 \text{ kbar}$	
Ku-98-14	2-ap1/2-Bt1	core	100.56	647	645	643	-5.03
	2-Ap2 2-Bt2	core	23.52	902	900	897	-4.15
		core	13.50	1054	1051	1048	-3.88
		rim	31.47	835	718	716	-4.92
		rim	57.12	720	833	831	-4.05
	2-Ap3 2-Bt2	core	19.46	950	947	945	-4.06
		core	14.01	1043	1040	1037	-3.90
		rim	39.07	791	788	786	-4.43
		rim	71.03	684	682	680	-4.81
	3-Ap1 2-Bt2	core	12.85	1069	1066	1064	-3.86
		core	14.16	1039	1036	1034	-3.90
		rim	58.66	716	714	712	-4.68
		recrystallised	163.66	566	565	563	-5.42
		recrystallised	147.90	583	581	579	-5.27
	6-Ap1 2-Bt2	core	44.51	765	763	761	-4.51
rim		45.95	759	757	755	-4.53	
Ku-98-48	a-Ap1 a-Bt4	core	31.62	888	886	884	-4.49
		core	24.49	949	946	944	-4.37
		rim	91.35	690	688	686	-5.07
		rim	134.93	633	631	629	-5.32
		rim	72.63	727	725	723	-4.93
		recrystallised	208.91	577	575	573	-5.62
	a-Ap2 a-Bt4	core	27.38	922	919	917	-4.42
		core	35.80	861	859	856	-4.55
		rim	84.56	702	700	698	-5.02
		rim	97.66	680	678	676	-5.11
	a-Ap3 a-Bt4	core	14.17	1103	1100	1097	-4.13
		core	15.75	1070	1067	1065	-4.18
		core	20.80	991	989	986	-4.30
		rim	123.63	645	643	641	-5.26
		rim	46.61	807	805	802	-4.69

Table. 19.2: Representative T and HF fugacity ($\log(f_{\text{HF}}/f_{\text{H}_2\text{O}})$) estimates for biotite-apatite pairs of the layered carbonatitic breccia, derived from biotite-apatite fluorine and hydroxyl geothermometry after Zhu & Sverjensky (1992).

Biotite-apatite pairs from the sodalite-rich carbonatitic breccia exhibit a cooling trend, reaching continuously from near-liquidus temperatures of 1220°C (Wyllie, 1966) down to 770°C at high corresponding relative HF fugacities ($\log(f_{\text{HF}}/f_{\text{H}_2\text{O}})$): -3.8 to -4.4). In contrast, samples of the layered carbonatitic breccia indicate a lower temperature range (1070-630°C) at lower relative HF fugacities ($\log(f_{\text{HF}}/f_{\text{H}_2\text{O}})$): -3.9 to -5.3). Recrystallised apatite-biotite pairs of the

layered carbonatitic breccia yield the lowest temperatures of 560-580°C and at the same time the lowest relative HF fugacities of -5.3 to -5.6 . Following this, it can be concluded that the original F-OH distribution between apatite and biotite is not easily disturbed by secondary processes, except recrystallisation, as has also been suggested by Andersen & Austrheim (1991) and Seifert et al. (2000).

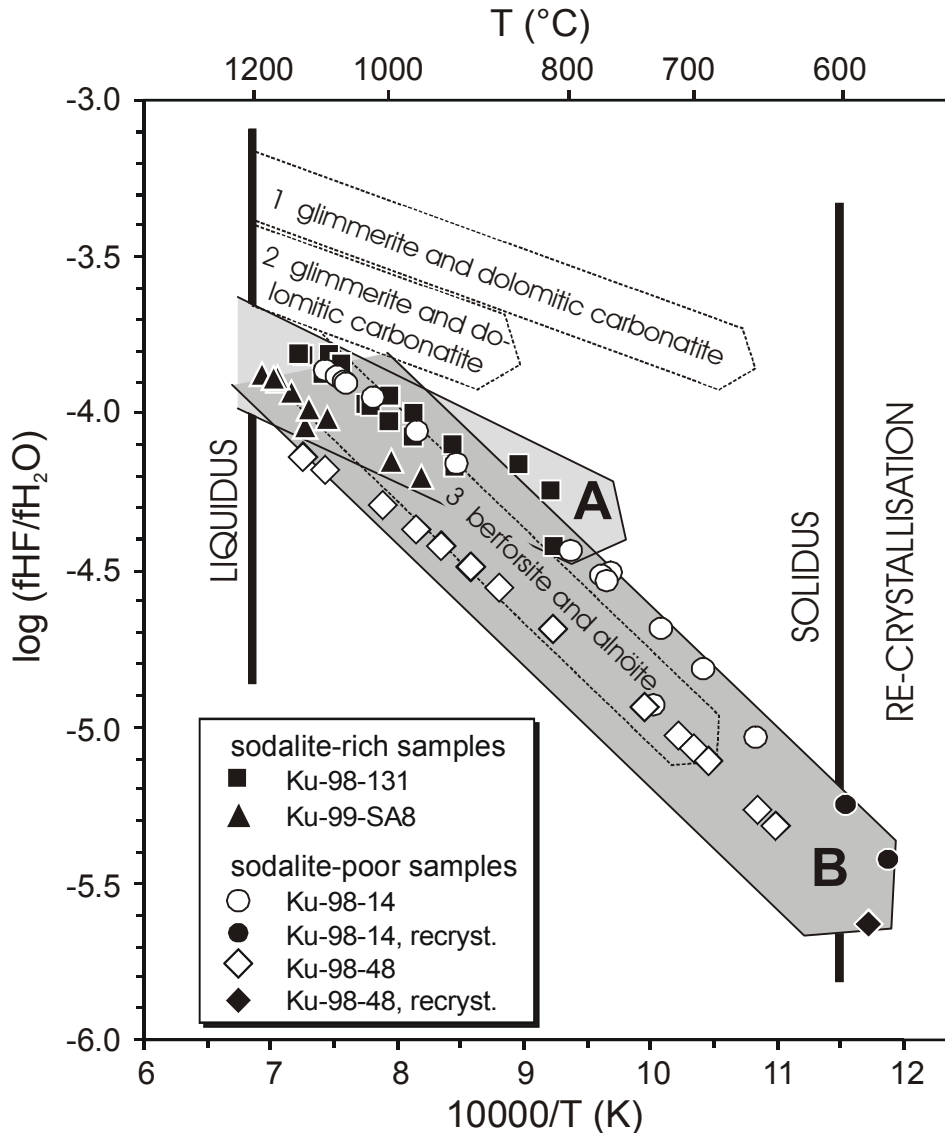


Fig. 19.1: $\text{Log}(f_{\text{HF}}/f_{\text{H}_2\text{O}})$ vs. $10^4/T$ diagram for magmatic and recrystallised apatite from the carbonatitic breccia of the Swartbooisdrif alkaline suite. *Arrow A:* cooling trend derived from apatite-biotite pairs of the sodalite-rich carbonatitic breccia, *arrow B:* cooling trend derived from apatite-biotite pairs of the layered (sodalite-poor) carbonatitic breccia, *arrows 1 and 2:* cooling trends of glimmerite and dolomite carbonatite of the Delitzsch complex, Germany (Seifert et al., 2000). *arrow 3:* cooling trend of alnöite of the Fen complex, Norway (Andersen & Austrheim, 1991) and of berforsite of the Delitzsch complex, Germany (Seifert et al., 2000). The liquidus of $T = 1200^\circ\text{C}$ is derived from the maximum thermal stability of phlogopite (Yoder & Kushiro, 1969) whereas the solidus of $625\text{--}650^\circ\text{C}$ is suggested by the experimental data of Wyllie (1966).

The obtained trends for the two carbonatite subgroups are in excellent accordance with the findings of Andersen & Austrheim (1991) and Seifert et al. (2000), who obtained similar trends for their relative sequence of carbonatite intrusions in the Fen complex (Norway) and the Delitzsch complex (Germany), respectively. The results indicate, that more than one magmatic event must have produced the carbonatitic breccia. In addition it can be concluded, that the transformation of albite into sodalite, which started during the end-stages and outlasted the biotite formation in the sodalite-bearing carbonatitic breccia, occurred at relatively high temperatures (up to $\sim 770^{\circ}\text{C}$) early in the magmatic-metasomatic history.

19.2.2 Calcite-dolomite thermometry

Calcite-dolomite thermometry was applied using the calibration Anovitz & Essene (1987), who provided the effect of Fe on the calcite-dolomite solvus. Temperatures were calculated for calcite-ankerite pairs in direct grain contact from the carbonatitic breccia and the fenitized syenite. The calculation yielded temperatures in the range of $410\text{--}530^{\circ}\text{C}$, the highest average values of 470°C being obtained by the REE-rich carbonatitic breccia sample Ku-98-130a (Table 19.3). When compared to the results of the apatite-biotite thermometry (see Chapter 19.2.1) these temperatures are relatively low, suggesting extensive recrystallisation and/or re-equilibration of the carbonates from the carbonatitic breccia, which is in excellent accordance with the petrographical findings.

Method of investigation	Rock type	Sample	Textural relationship	Tmin	Tmax	Taverage
Calcite-dolomite thermometry Anovitz & Essene (1987)	CB	Ku-98-130b	brownish carbonate aggregates	436°C	526°C	470°C
	S, f	Ku-98-59b	matrix overgrowths	406°C	534°C	438°C

Table 19.3: Temperature estimates for calcite-ankerite pairs of the carbonatitic breccia (CB) and the fenitized syenites (FS), derived from calcite-dolomite geothermometry after Anovitz & Essene (1987).

19.1.3 Ankerite-magnetite oxygen isotope equilibria

Stable isotope thermometry is an exchange thermometer, based on the partitioning of the heavy (^{18}O) and the light (^{16}O) isotope between coexisting phases. The fractionation between two mineral phases a and b ($\Delta^{18}\text{O}_{(a-b)}$, generally expressed as $1000\ln\alpha_{(a-b)}$) varies as a function of temperature, whereas pressure has no effect on the stable isotope fractionation. The temperature-

dependent fractionation between two phases (a, b) can be generally expressed as (e.g. Faure, 1986; Hoefs, 1997):

$$\Delta^{18}\text{O}_{(a-b)} = 1000\ln\alpha_{(a-b)} = A \cdot 10^6 \cdot 1/T^2 + B \quad (19-4)$$

Since published data for oxygen isotopic equilibria between mineral pairs, such as ankerite-magnetite, are missing, the fractionation factors have to be derived from the respective mineral-water curves. The $1000\ln\alpha$ values for ankerite-water and magnetite-water were calculated through the relations:

$$1000\ln\alpha_{(\text{Ank-water})} = 4.12 \cdot 10^6 \cdot 1/T^2 - 4.62 \cdot 10^3 \cdot 1/T + 1.71 \quad (19-4)$$

$$1000\ln\alpha_{(\text{Mag-water})} = 3.02 \cdot 10^6 \cdot 1/T^2 - 12.00 \cdot 10^3 \cdot 1/T + 3.31 \quad (19-5)$$

using the magnetite-water and the ankerite-water fractionation curves of Zheng (1991, 1999), calibrated for temperature ranges of 0-1200°C. Temperatures for equilibrium fractionation between ankerite and magnetite were estimated subsequently, by combining equation (19-6) and (19-7).

Method of investigation	Rock type	Sample	$\delta^{18}\text{O}_{\text{SMOW}} (\text{Mag})$	$\delta^{18}\text{O}_{\text{SMOW}} (\text{Ank})$	T (°C)
Equilibrium fractionation of oxygen isotopes in ankerite-magnetite pairs (Zheng, 1991, 1999)	CB	Ku-97-26	-1.82	8.95	449
	CB	Ku-99-02	-4.21	9.07	344
	CB	Ku-99-SA11	-1.46	9.73	479
	FV	Ku-01-03	-2.63	8.91	413

Table 19.4: Temperature estimates for ankerite-magnetite pairs of the carbonatitic breccia (CB) and the late ferrocarnatite veins (FV), calculated for ankerite-magnetite oxygen isotope equilibrium fractionation using mineral-water fractionation curves of Zheng (1991, 1999).

The temperatures calculated for oxygen isotope equilibration of magnetite-ankerite pairs from the carbonatitic breccia range between 344°C and 479°C (Table 19.4), thus being even lower than those obtained by calcite-dolomite thermometry (440-530°C; see Chapter 19.2.2). A similar temperature of 413°C was estimated for an ankerite-magnetite pair from a sample of a late-stage ferrocarnatite vein (Table 19.4). The lower temperatures obtained by the oxygen

isotopic ratios of ankerite-magnetite are interpreted in terms of a weak subsolidus re-equilibration of the carbonatites, which is also supported by the oxygen isotope values of the ankerites (see Chapter 18.1.3).

19.1.4 Pyrite-chalcopyrite sulphur isotope equilibria

The temperatures for the equilibrium fractionation of sulphur between coexisting pyrite and chalcopyrite were estimated indirectly, by combining the respective mineral-H₂S curves for temperature ranges of 200-600°C and 200-700°C, respectively, of Ohmoto & Goldhaber (1997), which are based on the general formulation (19-4):

$$1000\ln\alpha_{(\text{Py-H}_2\text{S})} = 0.40 \cdot 10^6 \cdot 1/T^2 \quad (19-6)$$

$$1000\ln\alpha_{(\text{Cpy-H}_2\text{S})} = -0.05 \cdot 10^6 \cdot 1/T^2 \quad (19-7)$$

Temperatures were calculated for three pairs of coexisting pyrite and chalcopyrite in late-stage sulphide veins from a REE-rich sample of the carbonatitic breccia (Ku-98-130b). The calculated temperatures range between 465°C and 488°C, thus suggesting that the sodalitization of anorthositic xenoliths, incorporated by the carbonatitic breccia, is confined to temperatures > 490°C (Drüppel & Wagner, in prep.). The fact, that the T estimates for the sulphides, which presumably formed during the end-stages of the carbonatite formation, are in the range of those calculated for calcite-ankerite pairs (440-530°C) and even higher than those obtained for ankerite-magnetite pairs (344-479°C) constrains the interpretation that at least the carbonates were affected by secondary processes such as recrystallisation and/or re-equilibration, which, however, did not effect the sulphur isotopic ratios of the investigated sulphides.

19.1.5 Stability relations of Co-Ni-Fe sulphides

The stability relations between various sulphide and oxide phases from samples of the carbonatitic breccia coexisting with an S₂-O₂ fluid have been investigated in some detail by von Seckendorff & Drüppel (1999) and von Seckendorff et al. (2000) and are illustrated in log *f*(S₂) vs. 1000/T and log *f*(S₂) vs. log *f*(O₂) diagrams, both constructed for 1 bar total pressure (Fig. 19.2a, b; modified after von Seckendorff & Drüppel, 1999; von Seckendorff et al., 2000). Stabilities of the different phases were calculated using published thermodynamic data (Toulmin & Barton, 1964; Barton, 1973; Barton & Skinner, 1979). Since composition-activity

relationships are available for only some of the investigated phases, the constructed $\log f(\text{S}_2)$ vs. $1000/T$ diagram must be regarded as semi-quantitative. The findings of von Seckendorff & Drüppel (1999) and von Seckendorff et al. (2000) for the crystallization sequence of the sulphide and oxide phases are summarized below.

(1) The starting point of the reconstructed T- $f(\text{S}_2)$ path (Fig. 19.2a) is given by coexisting igneous pyrrhotite and included magnetite, with the $f(\text{S}_2)$ and $f(\text{O}_2)$ values being buffered by the reaction (Fig. 19.2b)



During, subsequent cooling, high-T pyrrhotite broke down to lamellar intergrowths of at least two low-T pyrrhotite polytypes. A simultaneous increase of $f(\text{S}_2)$ and $f(\text{O}_2)$ (Fig. 19.2a, b), most probably accompanied by cooling, led to a coupled replacement of these pyrrhotite intergrowths by pyrite + hematite (\pm magnetite), according to reaction



followed by the reaction



The absence of vaesite suggests that the assemblage pyrite-hematite-magnetite became stable at temperatures $<320^\circ\text{C}$ and $\log f(\text{S}_2) < -8$ (Fig. 19.2a).

(2) No data are available to constrain the stability fields of siegenite, but from the established stability fields of polydymite and linnaeite (Rosenqvist, 1954; Leegaard & Rosenqvist, 1964; cf. Craig & Scott, 1974; Barton & Skinner, 1979), its maximum stability can be estimated at about 450°C with $\log f(\text{S}_2)$ in the vicinity of -6 (Fig. 19.2a). The replacement of siegenite by chalcopyrite limits $f(\text{S}_2)$ to values higher than the reaction:



(3) Millerite was probably derived from precursor $(\text{Ni,Fe})_{1-x}\text{S}$, stable at temperatures above 300°C (Fig. 19.2a). On the basis of the textural evidence, millerite coexisted with chalcopyrite and pyrite. In the absence of vaesite, the narrow stability field of $\text{Ni}_{1-x}\text{S} + \text{chalcopyrite} + \text{pyrite}$ extends from about 450°C and $\log f(\text{S}_2) = -3$ to the curve $\text{NiS} = \text{Ni}_{1-x}\text{S}$, where the stability field of millerite + chalcopyrite + pyrite is reached at about 290°C and $\log f(\text{S}_2) = -10.5$ (Fig. 19.2a).

(4) The replacement of millerite by polydymite-violarite took place with decreasing temperature. Since aggregates of millerite, polydymite, chalcopyrite and pyrite are transected or enclosed by veins of magnetite and titanohematite, $f(\text{S}_2)$ is most probably constrained by the buffer curve of

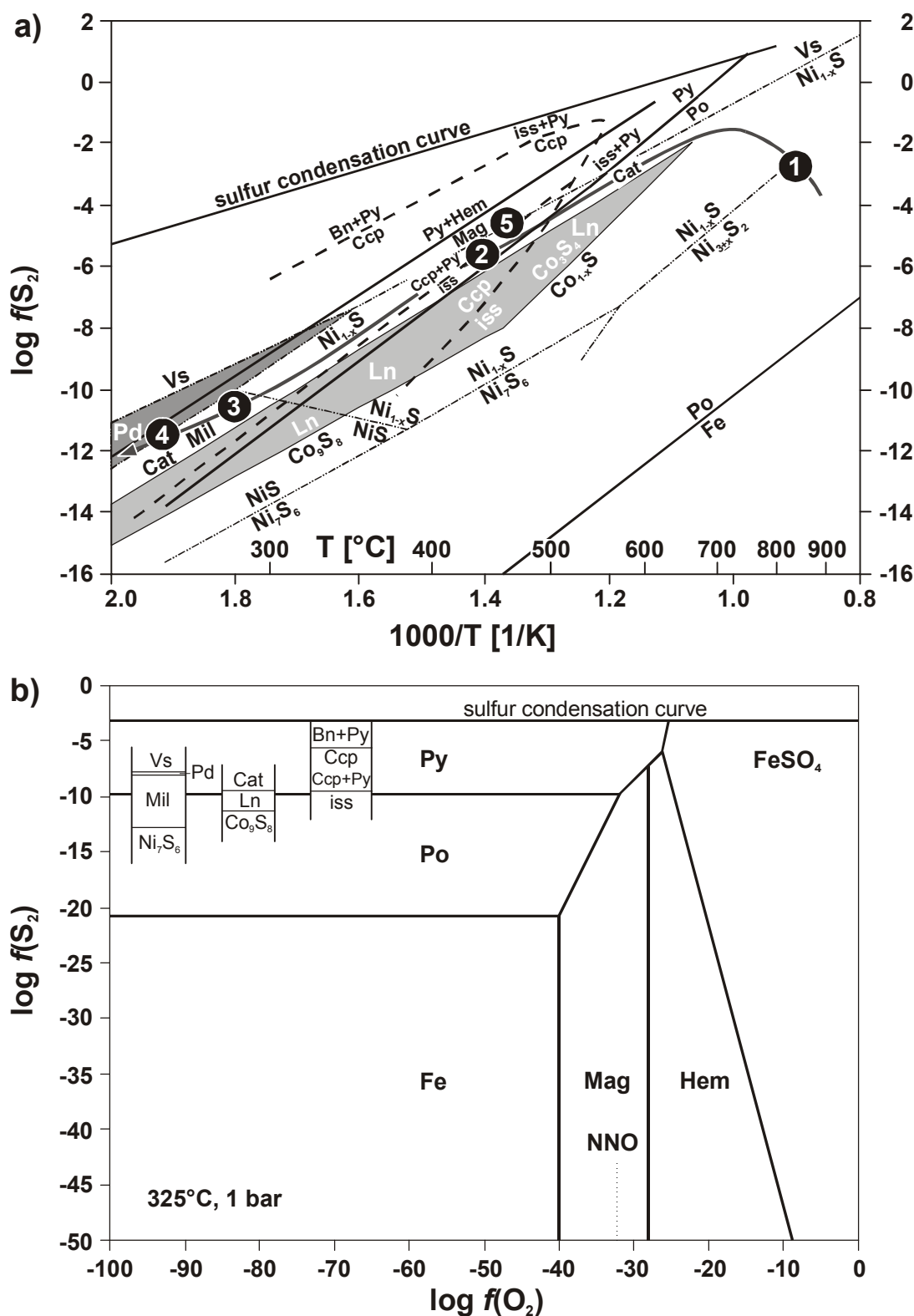


Fig. 19.2: *a)* Diagram $\log f(\text{S}_2)$ vs. $1000/T$ (modified after von Seckendorff & Drüppel, 1999; von Seckendorff et al., 2000) using thermodynamic data by Toulmin & Barton (1964), Barton (1973) and Barton & Skinner (1979). The stability fields for polydymite and linnaeite are shown in grey. The arrow depicts the reconstructed T - $f(\text{S}_2)$ path. *b)* Isothermal section of $\log f(\text{S}_2)$ vs. $\log f(\text{O}_2)$ at 325°C, 1 bar, calculated from thermodynamic data of Barton & Skinner (1979), following the approach of Holland (1959). For further details see text (*Bn* bornite, *Cat* cattierite, *Ccp* chalcopyrite, *Fe* metallic iron, *Hem* hematite, *iss* intermediate solid solution, *Ln* linnaeite, *Mag* magnetite, *Mil* millerite, *NNO* Ni-NiO-buffer, *Pd* polydymite, *Po* pyrrhotite, *Py* pyrite, *Vs* vaesite).

reaction (19-10), that is positioned within the polydymite stability field, thus suggesting that the replacement did not go to completion.

(5) The pyrites occurring in late-stage sulphide veins, which transect the oxide-sulphide aggregates appear to be the latest sulphides precipitated. As was assumed by von Seckendorff & Drüppel (1999) and von Seckendorff et al. (2000), this process took place during late hydrothermal alteration of the rocks, outlasting the metasomatic event. However, the high temperatures obtained for coexisting pyrite and chalcopyrite (\pm magnetite), occurring in late sulphide-oxide veins (465 - 488°C; see Chapter 19.1.4), constrain the $\log f(\text{S}_2)$ at comparably high values of *c.* -6, thus suggesting that the sulphide veins were rather formed during the repeated intrusion of carbonatite magmas than by low-temperature hydrothermal alteration of the carbonatitic breccia.

To summarize, the semi-quantitative T- $f(\text{S}_2)$ path of von Seckendorff & Drüppel (1999) and von Seckendorff et al. (2000; Fig. 19.2a) starts with igneous, high temperature conditions (*c.* 700-800°C), documented by coexisting ilmenite, Ti-magnetite and pyrrhotite, crossed the stability fields of iss, Ni_{1-x}S and siegenite, and ended in the polydymite stability field close to the magnetite + $\text{S}_2 =$ pyrite + hematite buffer curve at $<280^\circ\text{C}$ and $\log f(\text{S}_2) < -11$. The formation of late sulphide veins at comparably high temperatures of 465-488°C and $\log f(\text{S}_2)$ of *c.* -6 are ascribed to repeated magmatic activity, leading to a renewed elevation of both the temperature and the $f(\text{S}_2)$.

19.2 Emplacement and fenitization of the nepheline syenite

Temperatures of the nepheline syenite crystallization can be estimated from the chemical composition of orthomagmatic, concentrically zoned nepheline, using the nepheline liquidus thermometer after Hamilton (1964), which provides a temperature scale for the varying amounts of excess SiO_2 in natural nepheline coexisting with K-feldspar. The position of the approximate limit of nepheline solid-solution at 1068°C (Fig. 19.3) is based on determinations of the nepheline solid-solution limits in the systems $\text{NaAlSiO}_4\text{-NaAlSi}_3\text{O}_8$ (Greig & Barth, 1938) and $\text{NaAlSiO}_4\text{-KAlSiO}_4$ (Tuttle & Smith, 1958).

Calculated temperatures reveal a large spread, reaching from above the 1068°C isotherm for the SiO_2 -rich core compositions to temperatures as low as $\sim 770^\circ\text{C}$ at the SiO_2 -poor rims of

the individual nepheline grains (Fig. 19.3). In clear contrast, the outermost Ne-rich margins of the nepheline crystals, that were presumably formed by the interaction between the nepheline-syenite and the Na-rich and Si-deficient carbonatite magma, indicate lower temperatures of 700-775°C and may thus give a first idea of the temperature range of the wall-rock fenitization. Since both, the analyses of the nepheline mineral chemistry and the T estimates point to continuous nepheline growth, it might be possible that Na was introduced to the system before nepheline was fully crystallized.

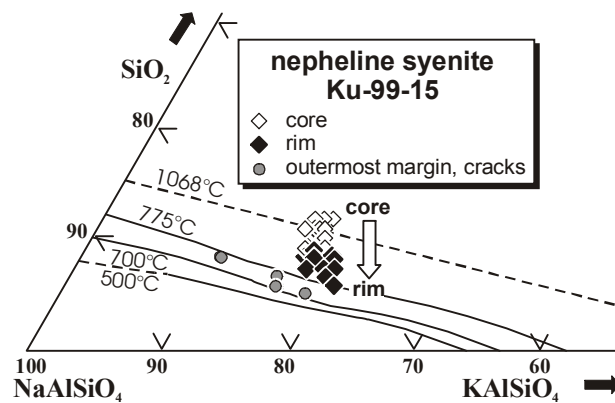


Fig. 19.3: Nepheline liquidus thermometry of nepheline from the Swartbooisdrif nepheline syenites after Hamilton (1964).

Moreover, the temperatures of the sodalitization of nepheline can be estimated from the stability field of sodalite formed by reaction (12-1), in relation to the NaCl concentration of the interacting fluids and temperature, based on the experimental investigations of Kostel'nikov & Zhornyyak (1995; see Chapter 12.1). Applying plausible ranges of 19-30 wt.% NaCl eq. for the primary salt concentrations of the fenitizing fluids (see Chapter 17.1), corresponding maximum temperatures of c. 630-730°C are obtained for the transformation of nepheline into sodalite, good in accordance with the temperatures obtained by Ne liquidus thermometry. Applying these T-estimates to the experimentally derived P-T stability fields of sodalite in the system NaAlSiO₄-SiO₂-NaCl of Sharp et al. (1989) and using reaction (12-1): $6 \text{ Ne} + 2 \text{ NaCl} \rightarrow \text{Sdl}$ (see Chapter 12.2), the sodalite stability with respect to nepheline is confined to pressures < 8 kbar.

19.3 Fenitization of anorthositic xenoliths and syenites– implications from fluid-inclusion isochore data

In order to constrain the P-T ranges of (1) the sodalite-formation in anorthosite xenoliths, incorporated by the carbonatitic breccia, and (2) the fenitization of syenites bordering the carbonatite centres, petrographical findings as well as temperature calculations for the carbonatite minerals were combined with fluid-inclusion isochore data. The resulting P-T paths are illustrated in Fig. 19.4a and Fig. 19.4b, respectively.

For an intermediate temperature range of 410-530°C, obtained for the carbonate recrystallisation (see Chapter 19.2.2), corresponding pressures of *c.* 4-5 kbar were obtained, using isochores calculated for pseudosecondary aqueous inclusions in ankerite from the REE-rich carbonatitic breccia (Fig. 19.4a). The resulting temperatures of sodalite formation for this P range are considerably variable, reaching from 800°C down to 530°C, using isochores of aqueous inclusions hosted by sodalite from the two REE-rich samples of the carbonatitic breccia (Ku-98-130a, Ku-98-130b). A more restricted T-range (725-625°C) is obtained for isochores of aqueous fluid inclusions in sodalite from a sample of the sodalite-rich carbonatitic breccia. Regarding the effects of secondary processes responsible for the REE-enrichment of the REE-rich carbonatitic breccia, the temperatures obtained for the REE-poor sample Ku-98-131 are suggested to give the more likely T conditions for transformation of albite into sodalite. It has to be mentioned, however, that the obtained temperature range for the sodalite formation is in excellent accordance with the previous findings, that (1) sodalite formation is confined to temperatures below those obtained for the co-crystallization of apatite and biotite (*i.e.* below *c.* 770°C) and higher than those calculated for coexisting pyrite and chalcopyrite (*i.e.* 465-488°C) and (2) sodalitization of nepheline of the bordering nepheline syenites presumably occurred at similar temperatures (*c.* 700-775°C). It is also noteworthy, that the formation of large masses of sodalite, both in the bordering anorthosites and in the fenitized anorthosite xenoliths can not be explained by a short magmatic episode in a narrow restricted temperature range but needs large amounts of NaCl-rich fluids, expelled during a certain time interval and temperature range.

For a given pressure range of *c.* 4-5 kbar, that is assumed to reflect the emplacement depth of the carbonatitic breccia (*c.* 12-15 km), corresponding temperatures of 330-500°C were obtained for the fenitization of the syenites, using isochores calculated for secondary fluid

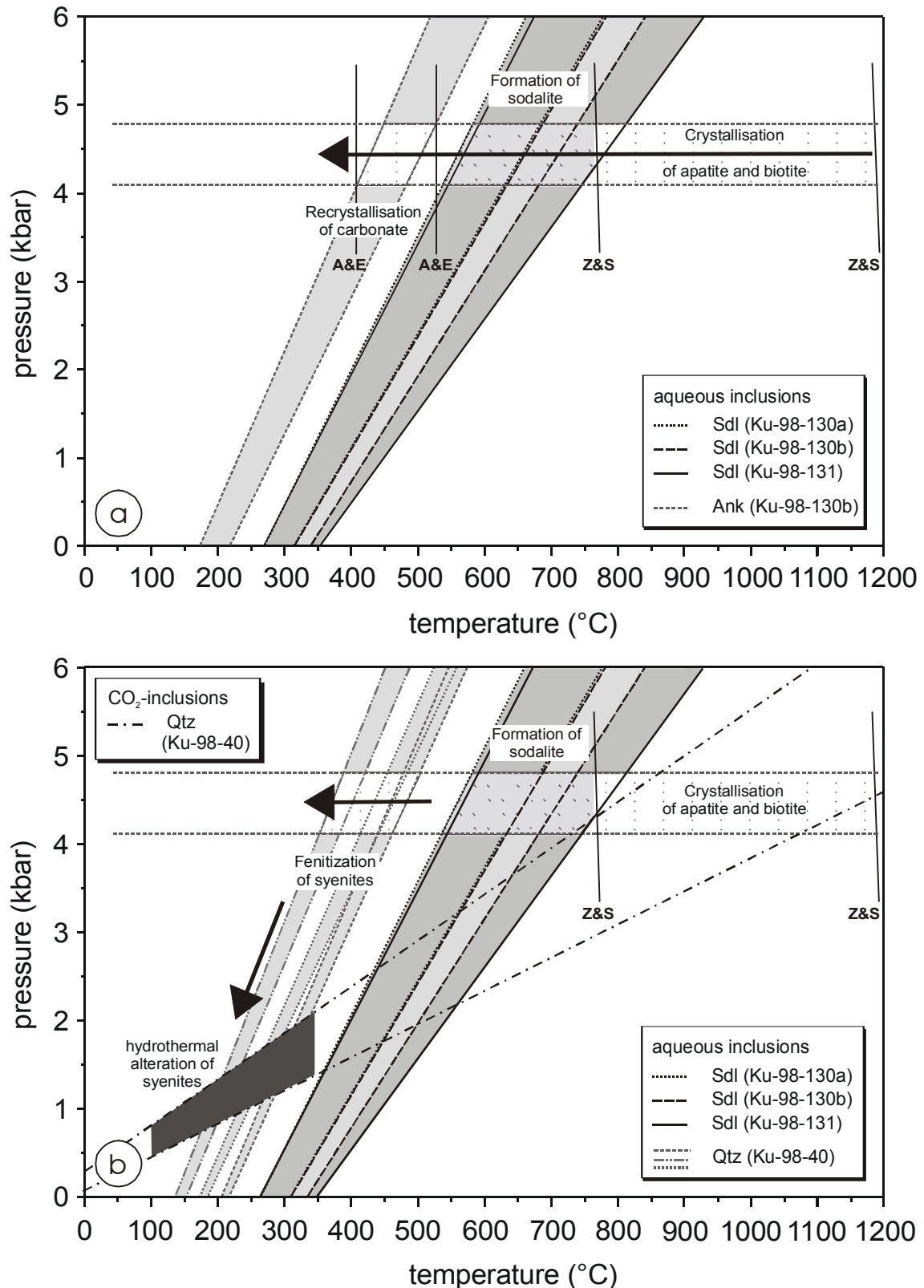


Fig. 19.4: P-T diagram for the carbonatite emplacement and the carbonatite-induced fenitizing processes in the Swartbooisdrif area, as deduced by conventional geothermometry combined with fluid-inclusion isochore data (see text for more detail). **a)** Carbonatite (re-)crystallization and fenitization of anorthositic xenoliths incorporated by the carbonatitic breccia. **b)** Fenitization and low-temperature alteration of syenites. (Arrows in a) and b) mark the respective evolutionary trends of the investigated rock units; A&E calcite-dolomite geothermometry after Anovitz & Essene, 1987, Z&S biotite-apatite fluorine and hydroxyl geothermometer after Zhu & Sverjensky, 1992).

inclusions in quartz of a quartz-syenite sample (Ku-98-40; Fig. 19.4b). Even though this sample suffered only minor alteration by the fenitizing solutions (e.g. a weak alteration of K-feldspar to albite), the obtained T-range is suggested to be a good proxy for the fenitization of the bordering syenites, since (1) steep temperature gradients in the vicinity of the carbonatitic centres can be assumed, judging from the lack of broad metasomatic aureoles surrounding the carbonatitic breccia, (2) the replacement of K-feldspar by albite-muscovite assemblages does not need high temperatures and (3) sodalite, which presumably formed under higher temperatures of 530-800°C, is virtually completely absent in samples of the fenitized syenites. Moreover, the low T-range obtained for the fenitization of the lithologies bordering the carbonatites, may also account for the formation of comparably narrow metasomatic aureoles in the anorthositic wall-rocks, where sodalite is restricted to the direct contacts between the carbonatite dykes and the anorthosites and hence confined to zones that rarely reach a width of 60 cm.

As textural evidence for a cogenetic formation of the CO₂ and the H₂O inclusions in quartz of the quartz-syenite is lacking, the late CO₂ inclusion trails are ascribed to a weak low temperature hydrothermal overprint of the syenites. Assuming a plausible T-range for hydrothermal activity (*c.* 100-300°C), corresponding pressures range of < 0.5 kbar to 1.5 kbar, in good accordance with an alteration by circulating meteoric waters confined to the shear-zones.

To summarize, the emplacement of the carbonatitic breccia at a depth of *c.* 12-15 km (*c.* 4-5 kbar) was followed by the early crystallization of apatite and biotite (\pm ankerite and magnetite) under igneous, high-temperature conditions (1200-770°C). Subsequently, NaCl-rich carbonatite fluids caused the partial replacement of albite-rich anorthosite xenoliths by sodalite under still high temperatures of 770-530°C. In the subsolidus stage the carbonates (ankerite/calcite) underwent extensive recrystallisation, confined to temperatures of *c.* 410-530°C. The fenitization of the syenites bordering the carbonatite centres occurred under comparably low temperatures of 330-500°C. The low-temperature alteration of the syenites by CO₂-rich solutions presumably reflects an independent event, restricted to subvolcanic crustal levels (<0.5 kbar to 1.5 kbar) and thus post-dating the magmatic and metasomatic evolution of the carbonatites.

20 Conclusions

20.1 Origin and evolution of the Swartbooisdrif carbonatites

There is striking field evidence that both the carbonatitic breccia and the late stage ferrocarbonatite veins are magmatic rather than hydrothermal in origin. They occur as dykes and veins with cross-cutting relationships and margins disturbed by fenitic aureoles, and contain abundant flow-oriented xenoliths from the surrounding anorthosite and syenite. In addition, the mineral assemblage of both carbonatite generations

- ankerite + calcite + magnetite + biotite ± apatite ± pyrochlore in the REE-poor carbonatitic breccia and
- ankerite + calcite + magnetite ± pyrochlore ± rutile in the late ferrocarbonatite veins,

their geochemical characteristics (high contents of incompatible elements like Sr, Ba and REE) and the values of O and C isotope ratios (8.91 to 9.73 and -6.73 to -6.98 , respectively) again indicate igneous derivation, with the $\delta^{18}\text{O}$ values suggesting only minor subsolidus alteration. Following these arguments the carbonatites of both generations can be described as mantle-derived, magmatic ferrocarbonatite magmas.

At least two magmatic events must have produced the carbonatitic breccia and the late ferrocarbonatite veins as is evidenced by (i) their temporal relationship (ii) their differing mineral assemblages and (iii) differences in their geochemical signatures. Moreover, evidence is provided that the carbonatitic breccia itself was formed by multiple magmatic events, i.e.: (1) the abundance of clasts of carbonatitic breccia cemented by a carbonate matrix, (2) elemental recurrences in the zoning patterns of apatite, biotite and ankerite, (3) repeated emanation of high salinity fluids recorded by quartz of the bordering quartz syenites, (4) the formation of texturally late pyrite under temperatures, which are higher than those obtained for previously crystallized sulphides and (5) the observation of at least two different cooling trends for sodalite-bearing and sodalite-free samples of the carbonatitic breccia, determined by apatite-biotite thermometry and HF barometry.

Based on general differences in their magmatic mineralogy and their mode of fenitization, the following simplified evolutionary trend can be established for the succession of the various carbonatite intrusions:

1. Magmatic evolution of the carbonatitic breccia and the ferrocarbonatite veins

The local presence of apatite and biotite phenocrysts in the carbonatitic breccia is suggestive of a ferrocarbonatite melt that additionally contained minor amounts of P, K, Si, and Al. The absence of these phases in the ferrocarbonatite veins, which are depleted in Fe, Mg, Si, Al, K, Ti, P, and S with respect to the carbonatitic breccia, implies that the ferrocarbonatite veins represent late-stage fractionation products of the ferrocarbonatite magma which forms the carbonatitic breccia, with their emplacement post-dating the extensive crystallization of biotite, ankerite, Fe-Ti oxides, apatite, and sulphides. However, the carbonatite-related fenitization style (sodic, hydrous fenitization), the primary composition of the fenitizing solution (Sr- and REE-bearing aqueous brine, virtually free of CO₂ and Ca), the trace-element composition of apatite (high SREE, high (La/Yb)_{cn} and (La/Nd)_{cn} ratios) and the chondrite-normalized trace element plots of the carbonatitic breccia (troughs at K, Sr, P, Ti), suggest that fractionation was even active previous to the emplacement of the older carbonatite unit, the carbonatitic breccia.

The high modal amounts of metasomatically formed sodalite in most samples of the carbonatitic breccia point to a high metasomatic potential of this rock type and, moreover, suggest, that these melts contained appreciable amounts of sodium before alkali-loss during fenitization. The abundance of sodalite correlates with high temperatures of apatite-biotite equilibria (~1200-770°C). In contrast, sodalite-free samples of the carbonatitic breccia reach lower apatite-biotite temperatures (~1070-630°C), thus evidencing that most of the fluids were expelled during the early and high-*T* intrusion stages of this rock type. This interpretation is in excellent agreement with the lack of extensive metasomatic aureoles around the youngest recognisable carbonatite unit, the late-stage ferrocarbonatite veins, which incorporated previously fenitized xenoliths but rarely show any wallrock alteration related to their emplacement. The occurrence of late barite in samples of the carbonatitic breccia as well as the sulphur isotopic data for pyrite and chalcopyrite imply a continuous trend towards higher oxygen fugacities with carbonatite evolution.

2. REE-enrichment of the carbonatitic breccia

The REE mineralization of REE-rich samples of the carbonatitic breccia appears to be of secondary origin, since the REE-minerals occur along the grain margins of ankerite, which display a similar or even REE-depleted composition when compared to those of the corresponding REE-poor samples. Moreover, the REE mineralization in the investigated samples is accompanied by the additional occurrence of barite and strontianite, which are commonly

found in carbonatites exposed to secondary alteration. A supergene origin for the REE enrichment can be ruled out, as ankerite from these rock types lacks fractionation to heavier $\delta^{18}\text{O}$, but has ^{18}O values in the range of ankerite from the REE-poor carbonatitic breccia. An in situ mechanism of hydrothermal solution and re-precipitation is not likely, as a concentration factor of over 100 times is required to achieve the REE-content of the REE-rich samples. Hence, an injection of Sr and REE-enriched, late-stage carbonatite fluids must be considered. A process like this would be in excellent accordance with the previous findings, i.e. (1) the REE-enrichment recorded by the samples is not accompanied by simultaneous Na enrichment, hence suggesting that the sodium contained in early fluids was already expelled during previous albite and sodalite formation and (2) late-stage, aqueous fluid-inclusions hosted by recrystallised ankerite, were found to be strongly enriched in Sr and the LREE, whereas they display comparably low salt concentrations. Following these arguments the REE enrichment of the two samples of the carbonatitic breccia resulted from a hydrothermal overprint by late-stage, fractionated carbonatite fluids.

3. P-T conditions of the carbonatite emplacement and crystallization

Judging from the lack of broad metasomatic aureoles and the sodic style of fenitization the Swartbooisdrif carbonatites may be generally assumed to be deep-seated intrusions. Conformably, the pressures obtained for the (re-)crystallization of the carbonatites (*c.* 4-5 kbar) point to emplacement depths of 12-15 km. The first minerals to crystallize are apatite, biotite, magnetite, and ankerite. Temperatures obtained for apatite-biotite pairs from the carbonatitic breccia reach from near-liquidus conditions of *c.* 1200°C (Wyllie, 1966) and proceed down to near-solidus conditions of 630°C. The formation of pyrrhotite, coexisting with magnetite, presumably occurred under high T conditions of *c.* 700-800°C. In contrast, most of the other sulphides (pyrite, chalcopyrite, millerite, siegenite, polydymite-violarite, fletcherite) were formed in the subsolidus stage, under comparably low temperatures of 490°C to < 280°C. Both biotite and apatite as well as the carbonates were subjected to extensive recrystallisation under T conditions of 560-580°C and 410-530°C, respectively.

4. The carbonatite-nepheline syenite association

The intimate association of the Swartbooisdrif carbonatites with nepheline-syenite and syenite dykes might suggest a genetic relationship between these rock-types. However, the syenites are ~150 Ma older than the carbonatite intrusions, thus providing evidence that their close spatial

association rather results from the preferred ascent of both the older silicate and the younger carbonatite magmas along pre-existing faults. It has to be mentioned, however, that no age has yet been constrained for the Swartbooisdrif nepheline syenite, which differs significantly from the ~1,380-1,340 Ma syenite dykes of the same area in both its mineralogy and its major and trace element composition. It is hence possible, that the nepheline syenite and the ferrocarnatite are part of one single magmatic suite, even though further age determinations are needed to constrain this assumption.

20.2 The breakdown of igneous minerals during fenitization

Fluids are commonly associated with carbonatite melts and are responsible for the formation of fenitic aureoles in the bordering lithologies. The fluids expelled by the carbonatite melts of Swartbooisdrif are mainly characterized by high NaCl- and H₂O-amounts, as is evident from the hydrous and sodalite-rich nature of the fenites. The composition and evolutionary trends of these fenitizing agents were estimated from both the sequence of metasomatic reactions within wallrock xenoliths in the carbonatitic breccia and fluid inclusions data (microthermometric fluid inclusion measurements combined with synchrotron micro-XRF analyses):

(1) From textural evidence, it is clear that the formation of almost pure albite at the expense of former plagioclase and alkali-feldspar from anorthosite and syenite, respectively, predated the emplacement of the carbonatite melts. This process presumably occurred simultaneously with the transformation of anhydrous Fe-Mg-silicates and amphibole into biotite in the respective rock types. From this it can be concluded that the carbonatite magma yielded water saturation already during its uprise and expelled large amounts of fluid, which migrated along the pre-existing pathways and pervasively altered the brecciated anorthosite and syenite exposed in the shear zones as well as the neighbouring lithologies. The metasomatic reactions require that Na and H₂O were the dominant components of this fluid, which, in addition, presumably contained Fe, Cl and K. In contrast, the Si necessary for the transformation of An-rich plagioclase into almost pure albite is supposed to be derived from the fenites themselves during Si-releasing metasomatic reactions, rather than being a primary constituent of the fenitizing agents.

(2) After its final emplacement in the crust (~12-15 km), the carbonatite magma again reached water saturation following cooling from ~1200°C to 770°C and fractionation of anhydrous minerals (apatite, ankerite and magnetite). In a temperature range of 800-530°C (maximum at 725-625°C) the circulation of NaCl-rich aqueous brines (20-30 wt.% NaCl eq.),

expelled by the crystallising carbonatite magma, caused the partial transformation of albite of the incorporated anorthositic xenoliths into sodalite. The sodalitization of nepheline from a nepheline syenite dyke in direct contact to the carbonatitic breccia, occurred under similar temperatures of *c.* 730-630°C. This fluid, whose composition was presumably close to the initial composition of the carbonatite fluid, was also capable of transporting minor amounts of Sr, Ba, Fe, Nb and the LREE. Most of the Na contained in the fenitizing agents was consumed during this major sodalite-forming event, which was restricted to the carbonatitic breccia and narrow reaction-zones (up to 60 cm in width) within the bordering anorthosite, syenite and nepheline syenite. Conformably, fluids trapped in quartz of a neighbouring quartz-syenite dyke display highly variable, but generally lower salinities of 20-24 wt.% NaCl eq. and 9-17 wt.% NaCl eq. and, at the same time, higher amounts of K, Ca, Fe, Ti, Sr and Ba, evidencing previous Na-loss during extensive sodalite and/or albite formation. Moreover, the temperatures obtained for the fenitization of the syenites (330-500°C) are distinctly lower than those of the direct contact zones between the nepheline syenite and the carbonatitic breccia. The low temperatures of fenitization, corresponding to comparably low salinities of the fenitizing fluids might be the reasons for the general lack of sodalite in the fenitized syenite.

(3) The fenitic mineral assemblage of cancrinite and muscovite, replacing albite and post-dating sodalite, implies that the evolved fluids were still aqueous brines but no longer contained sufficient Na to form sodalite. The Si-free composition of the subsequently formed Na-Al phase and its high Al:Na ratio of 4:1 when compared to sodalite ($Al/Na < 1$) strongly suggests that even the late-stage carbonatite fluids were still strongly deficient in Si but contained only minor amounts of Na. The K and Ca, required by most of the late metasomatic reactions, may be primary constituents of these fluids or derived by K- and Ca-releasing reactions. In the case of nepheline syenite, the close association of sodalite and muscovite, both formed at the expense of nepheline, favours the latter model. On the other hand, the clear temporal succession of the respective minerals observed in the other fenite types rather argues against a coupled process.

20.3 Links to other carbonatite complexes of NW Namibia and SW Angola

The ferrocarbonatite dykes of Swartbooisdrif have traditionally been grouped together with E-W and NE-SW trending calcio-carbonatite, lamprophyre and Ne-syenite dykes of the Epembe area (Ferguson et al., 1975; Menge, 1986, 1996; Verwoerd, 1993; von Seckendorff et al., 2000). In addition, syenite, calciocarbonatite and magnesiocarbonatite dykes of the Proterozoic Lupongola Complex of Angola, ~20 km north-west of Swartbooisdrif, have been considered part of the

same alkaline suite (Menge, 1996; Alberti et al., 2000; Thompson et al., 2002). Support for a genetic relation between at least the Lupongola and the Epembe suite is given by rock samples collected south of the Namibian-Angolan border about 2 km distant from the Lupongola Complex and forming the north-eastern extension of the NE trending Epembe dykes. In this area, the dykes are almost entirely composed of calciocarbonatites and magnesiocarbonatites with minor syenites, similar in mineralogy and geochemistry to those observed in the Epembe (Ferguson et al., 1975) and the Lupongola alkaline suite (Alberti et al., 2000). In clear contrast to the Swartbooisdrif ferrocarbonatites, however, the carbonatites in these areas lack the extensive formation of sodalite-bearing metasomatic aureoles and xenoliths.

Based on Sm-Nd and Rb-Sr isotopic data Alberti et al. (2000) concluded, that the age of the Lupongola carbonatites, even though yet undated, could be $\sim 1,100$ Ma. However, U-Pb pyrochlore ages of $\sim 1,204$ Ma have recently been constrained for the Epembe carbonatites whereas the Swartbooisdrif carbonatites yielded a distinctly younger U-Pb-pyrochlore age of $\sim 1,140$ - $1,120$ Ma (Littmann et al., in prep.). These age constraints strongly suggest that at least the Epembe and the Swartbooisdrif carbonatitic centres represent independent intrusions.

20.4 Concluding remarks

The present study has shown that the generation of carbonatite magmas and the associated contact metasomatism in the Swartbooisdrif area are the result of several magmatic and interrelated metasomatic processes, each inducing characteristic mineral reactions in the anorthositic and syenitic wall-rock. It is possible to relate the metasomatic reactions to both, the temporal succession of carbonatite intrusions and their respective magmatic crystallization history.

The metasomatic processes related to carbonatites can convey important information on the nature and evolution of the carbonatite melts. All present findings suggest that the Swartbooisdrif ferrocarbonatite intrusions represent deeply emplaced and highly evolved magmatic carbonatite melts, which contained appreciable amounts of sodium before alkali-loss during fenitization.

21 References

- Alberti, A., Castorina, F., Censi, P., Comin-Chiaramonti, P. & Gomes, C.B.** (2000): Geochemical characteristics of Cretaceous carbonatites from Angola. *Journal of African Earth Sciences* **29**: 735-759.
- Andersen, T.** (1984): Secondary processes in carbonatites: Petrology of "rødberg" (hematite-calcite-dolomite carbonatite) in the Fen complex, Telemark (South Norway). *Lithos* **17**: 227-245.
- Andersen, T.** (1986): Magmatic fluids in the Fen carbonatite complex, S.E. Norway: Evidence for mid-crustal fractionation from solid and fluid inclusions in apatite. *Contributions to Mineralogy and Petrology* **93**: 491-503.
- Andersen, T.** (1987): Mantle and crustal components in a carbonatite complex, and the evolution of carbonatite magma: REE and isotopic evidence from the Fen Complex, southeast Norway. *Chemical Geology* **65**: 147-166.
- Andersen, T.** (1989): Carbonatite-related contact metasomatism in the Fen complex, Norway: effects and petrogenetic implications. *Mineralogical Magazine* **53**: 395-414.
- Andersen, T. & Austrheim, H.** (1991): Temperature-HF fugacity trends during crystallisation of calcite carbonatite magma in the Fen complex, Norway. *Mineralogical Magazine* **55**: 81-94.
- Anderson, J.L.** (1980): Mineral equilibria and crystallization conditions in the late Precambrian Wolf River rapakivi massif, Wisconsin. *American Journal of Science* **280**: 289-332.
- Anderson, J.L.** (1983): Proterozoic anorogenic granite plutonism of North America. In: **Medaris, L.G., Byers, C.W., Mickelson, D.M. & Shanks, W.C.** (eds.): *Proterozoic geology: selected papers from an International Proterozoic Symposium*. Geological Society of America, Special Papers 161, pp. 133-154.
- Anderson, J.L. & Bender, E.E.** (1989): Nature and origin of Proterozoic A-type granitic magmatism in the southwestern United States of America. *Lithos* **23**: 19-52.
- Anderson, A.T. & Morin, M.** (1968): Two types of massif anorthosite and their implications regarding the thermal history of the crust. In: **Isachsen Y.W.** (ed.): *Origin of anorthosite and related rocks*. N.Y. State Museum and Science Service, Memoir 18, pp. 47-55.
- Andrade, F.R.D., Möller, P. & Höhndorf, A.** (1999): The effect of hydrothermal alteration on the Sr and Nd isotopic signatures of the Barro do Itapirapuã carbonatite, southern Brazil. *The Journal of Geology* **107**: 177-191.

- Anovitz, L.M. & Essene, E.J.** (1987): Phase equilibria in the system $\text{CaCO}_3\text{-MgCO}_3\text{-FeCO}_3$. *Journal of Petrology* **28**: 389-414.
- Ashwal, L.D.** (1993): Anorthosites. Minerals and Rocks Series 21. Springer-Verlag, Berlin, 422 pp.
- Ashwal, L.D., Hamilton, M.A., Morel, V.P.I. & Rambeloson, R.A.** (1998): Geology, petrology and isotope geochemistry of massif-type anorthosites from southwest Madagascar. *Contributions to Mineralogy and Petrology* **133**: 389-401.
- Ashwal, L.D. & Twist, D.** (1994): The Kunene complex, Angola/Namibia: a composite massif-type anorthosite complex. *Geological Magazine* **131**: 579-591.
- Barker, D.S.** (1976): Phase relations in the system $\text{NaAlSiO}_4\text{-SiO}_2\text{-NaCl-H}_2\text{O}$ at 400°-800°C and 1 kilobar, and petrologic implications. *The Journal of Geology* **84**: 97-106.
- Barton, M., Sheets, J.M., Lee, W.E. & van Gaans, C.** (1991): Occurrence of low-Ca clinopyroxene and the role of deformation in the formation of pyroxene - Fe-Ti oxide symplectites. *Contributions to Mineralogy and Petrology* **108**: 181-195.
- Barton, M. & van Gaans, C.** (1988): Formation of orthopyroxene-Fe-Ti oxide symplectites in Precambrian intrusives, Rogaland, southwestern Norway. *American Mineralogist* **73**: 1046-1059.
- Barton, P.B. Jr.** (1973): Solid solutions in system Cu-Fe-S Part I. The Cu-S and Cu-Fe-S join. *Economic Geology* **68**: 455-465.
- Barton, P.B. Jr. & Skinner, B.J.** (1979): Sulphide mineral stabilities. In: **Barnes, H.L.** (ed.): *Geochemistry of hydrothermal ore deposits*. Holt, Rinehart and Winston, New York, pp. 236-333.
- Beard, A.D., Downes, H., Vetrin, V., Kempton, P.D. & Maluski, H.** (1996): Petrogenesis of Devonian lamprophyre and carbonatite minor intrusions, Kandalaksha Gulf (Kola Peninsula, Russia). *Lithos* **39**: 93-119
- Beetz P.F.W.** (1933): Geology of South West Angola, between Cunene and Lunda Axis. *Transactions of the Geological Society of South Africa* **36**: 137-176.
- Bell, K. & Keller, J.** (eds.) (1995): Carbonatite volcanism: Oldoinyo Lengai and the petrogenesis of natrocarbonatites. Springer Verlag, Berlin, 210 pp.
- Berg, J.H.** (1977a): Dry granulite mineral assemblages in the contact aureoles of the Nain Complex, Labrador. *Contributions to Mineralogy and Petrology* **64**: 33-52.
- Berg, J.H.** (1977b): Regional geobarometry in the contact aureoles of the anorthositic Nain Complex, Labrador. *Journal of Petrology* **18**: 399-430.

- Berg, L.-P., Shamsheer, M.K., El-Daher, S.S., Kakkar, V.V., Authi, K.S., Buchanan, P.C., Zolensky, M.E. & Reid, A.M.** (1997): Petrology of Allende dark inclusions. *Geochimica et Cosmochimica Acta* **61**: 1733-1743.
- Bhattacharya, A., Krishnakumar, K.R., Raith, M. & Sen, S.K.** (1991): An improved set of a-X parameters for Fe-Mg-Ca garnets and refinements of the orthopyroxene-garnet thermometer and the orthopyroxene-garnet-plagioclase-quartz barometer. *Journal of Petrology* **32**: 629-656.
- Bhattacharya, A., Mohanty, L., Maji, A., Sen, S.K. & Raith, M.** (1992): Non-ideal mixing in the phlogopite-annite binary: constraints from experimental data on Mg-Fe partitioning and a reformulation of the biotite-garnet geothermometer. *Contributions to Mineralogy and Petrology* **111**: 87-93.
- Bingen, B., Demaiffe, D. & Delhal, J.** (1984): Petrologic and geothermobarometric investigations in the Kasai gabbro-noritic complex and associated metadolerite dykes (Zaire). *Bulletin de Minéralogie* **107**: 665-682.
- Binstedt, N.** (1981): The stability of sodalite minerals. *Progress in experimental petrology, N.E.R.C. Report* **5**: 54-56.
- Bodnar, J.R.** (1993): Revised equation and table for determining the freezing point depression of H₂O-NaCl solutions. *Geochimica et Cosmochimica Acta* **57**: 683-684.
- Bohlen, S.R., Wall, V.J. & Boettcher, A.L.** (1983): Geobarometry in granulites. In: **Saxena, S.K.** (ed.): *Kinetics and equilibrium in mineral reactions*. Advances in physical geochemistry, Volume 3, Springer-Verlag, New York, pp. 141-172.
- Bonshtedt-Kupletskaya, E.M.** (1966): On the questions of systematics of the pyrochlore-microlite group. (in Russian). *Zapiski Vsesoyuznogo Mineralogicheskogo Obshchestva* **95**: 134-144.
- Borthwick, J. & Harmon, R.S.** (1982): A note regarding ClF₃ as an alternative to BrF₅ for oxygen isotope analysis. *Geochimica et Cosmochimica Acta* **46**, 1665-1668.
- Bragg, W.L. & Claringbull, G.F.** (1965): *Crystal structures of minerals. Volume 4*. Bell and Sons Ltd., London, 149 pp.
- Brandt, S., Klemd, R. & Okrusch, M.** (2000): Evidence for ultra-high temperature metamorphism in the Pre-Pan-African Epupa Complex, NW Namibia. *GEOLUANDA 2000, Abstract volume*: 33-34.
- Brandt, S., Klemd, R. & Okrusch, M.** (2003): Ultrahigh-temperature metamorphism and multistage evolution of garnet-orthopyroxene granulites from the Proterozoic Epupa Complex, NW Namibia. *Journal of Petrology* (in press).

- Brandt, S., Will, T.M. & Klemd, R.** (2001): Metamorphic evolution of sapphirine-bearing orthopyroxene-sillimanite gneisses and associated felsic granulites from the Proterozoic Epupa Complex, NW Namibia. *EUG XI, Strasbourg, Abstract Volume*: 571.
- Brey, G.P. & Köhler, T.** (1990): Geothermobarometry in four-phase lherzolites II. New thermobarometers, and practical assessment of existing thermobarometers. *Journal of Petrology* **31**: 1353-1378.
- Brousse, R., Varet, J. & Bizouard, H.** (1969): Iron in the minerals of the sodalite group. *Contributions to Mineralogy and Petrology* **22**: 169-184.
- Brown, P.E.** (1989): FLINCOR - a microcomputer program for the reduction and investigation of fluid inclusion data. *American Mineralogist* **74**: 1390-1393.
- Bühn, B. & Rankin, A.H.** (1999): Composition of natural, volatile-rich Na-Ca-REE-Sr carbonatitic fluids trapped in fluid inclusions. *Geochimica et Cosmochimica Acta* **63**: 3781-3797.
- Bühn, B., Wall, F. & Le Bas, M.J.** (2001): Rare-earth element systematics of carbonatitic fluorapatites, and their significance for carbonatite magma evolution. *Contributions to Mineralogy and Petrology* **141**: 572-591.
- Cahen, L. & Snelling, N.J.** (1966): The Geochronology of Equatorial Africa. Elsevier, Amsterdam, 195 pp.
- Carvalho, H. de & Alves, P.** (1990): Gabbro-Anorthosite Complex of SW Angola/ NW Namibia. *Garcia de Orta, Série de Ciências da Terra, Comunicações* **2**, 1-66.
- Carvalho, H. de & Alves, P.** (1993): The Precambrian of SW Angola and NW Namibia. *Garcia de Orta, Série de Ciências da Terra, Comunicações* **4**: 1-38.
- Carvalho, H. de, Crasto, J., Silva, Z.C.G. & Vialette, Y.** (1987): The Kibaran cycle in Angola: a discussion. *Geological Journal* **22**: 85-102.
- Carvalho, H. de, Fernandes, F.C. & Vialette, Y.** (1979): Chronologie absolute du Précambrien du Sud-Ouest de l'Angola. *Comptes Rendus Académie Sciences Paris* **288**: 1647-1650.
- Carvalho, H. de, Tassinari, C., Alves, P.H., Guimarães, F. & Simões, M.C.** (2000): Geochronological review of the Precambrian in western Angola: links with Brazil. *Journal of African Earth Sciences* **31**: 383-402.
- Clifford, T.N.** (1970): The structural framework of Africa. In: **Clifford, T.N. & Gass, I.G.** (eds.): *African magmatism and tectonics*. Oliver and Boyd, Edinburgh, pp. 1-26.
- Craig, J.R.** (1971): Violarite stability relations. *American Mineralogist* **56**: 1303-1311.
- Craig, J.R. & Higgins, J.B.** (1975): Cobalt- and iron-rich violarites from Virginia. *American Mineralogist* **60**: 35-38.

- Craig, J.R. & Scott, S.D.** (1974): Sulfide phase equilibria. In: **Ribbe, P.H.** (ed.): *Sulfide Mineralogy. Reviews in Mineralogy 1*. Mineralogical Society of America, Washington D.C., pp. CS1-CS110.
- Craig, J.R., Vaughan, D.J. & Higgins, J.B.** (1979): Phase relations in the Cu-Co-S system and mineral associations of the carrollite (CuCo₂S₄) – linnaeite (Co₃S₄) series. *Economic Geology* **74**: 657-671.
- Currie, K.L., Eby, G.L. & Gittins, J.** (1986): The petrology of the Mont Saint Hilaire complex, southern Quebec: An alkaline gabbro-peralkaline syenite association. *Lithos* **19**: 65-81.
- Currie, K.L. & Ferguson, J.** (1971): A study of fenitization around the alkaline carbonatite complex at Callander Bay, Ontario, Canada. *Canadian Journal of Earth Sciences* **8**: 498-518.
- Dawson, J.B.** (1989): Sodium carbonatite extrusions from Oldoinyo Lengai, Tanzania: Implications for carbonatite complex genesis. In: **Bell, K.** (ed.): *Carbonatites: genesis and evolution*. Unwin Hyman, London, pp. 255-277.
- Dawson, J.B., Garson, M.S. & Roberts, B.** (1987): Altered former alkalic carbonatite lava from Oldoinyo Lengai, Tanzania: Inferences for calcite carbonatite lavas. *Geology* **15**: 765-768.
- Deer, W.A., Howie, R.A. & Zussman, J.** (1963): Rock-forming minerals, Volume 4: Framework silicates. Longmans, London, 435 pp.
- Deer, W.A., Howie, R.A. & Zussman, J.** (1992): An introduction to the rock-forming minerals, 2nd edition. Longmans, London, 696 pp.
- Deines, P.** (1989): Stable isotope variations in carbonatites. In: **Bell, K.** (ed.): *Carbonatites: genesis and evolution*. Unwin Hyman, London, pp. 301-359.
- de Waard, D.** (1970): The anorthosite-charnockite suite of rocks of Roaring Brook Valley in the eastern Adirondacks (Marcy Massif). *American Mineralogist* **55**: 2063-2075.
- Doherty, W.** (1989): An internal standardization procedure for the determination of yttrium and the rare earth elements in geological samples by inductively coupled plasma-mass spectrometry. *Spectrochimica Acta* **44B**: 263-280.
- D'Orey, F.L.C.** (1983): Cobaltopentlandite, siegenite ferifera e bravoite cobaltoniquelifera de Mocambique. *Garcia de Orta, Série de Geologia* **6**: 137-142.
- Drüppel, K.** (1999): Petrologie und Geochemie von Anorthositen des Kunene-Intrusiv-Komplexes, NW Namibia. Diploma thesis, University of Würzburg, 217 pp.
- Drüppel, K., Hoefs, J. & Okrusch, M.** (2002a): The polyphase magmatic and metasomatic history of ferrocarnatites from Swartbooisdrif, NW Namibia. *Berichte der deutschen Mineralogischen Gesellschaft, Beihefte zum European Journal of Mineralogy* **13**: 38.

- Drüppel, K., Littmann, S. & Okrusch, M.** (2000): Geo- und isotopechemische Untersuchungen der Anorthosite des Kunene-Intrusiv-Komplexes (KIK) in NW-Namibia. *Berichte der deutschen Mineralogischen Gesellschaft, Beihefte zum European Journal of Mineralogy* **12**: 37.
- Drüppel, K. & Okrusch, M.** (2000): Petrology and geochemistry of anorthositic rocks of the Kunene Intrusive Complex, NW Namibia. *GEOLUANDA 2000, Abstract volume*: 49-50.
- Drüppel, K., Rickers, K. & Okrusch, M.** (2002b): Characterisation of the trace element distribution in fenitizing fluids by synchrotron radiation x-ray fluorescence (SRXRF) microprobe analysis. *DESY Annual Report 2001* (online).
- Drüppel, K., von Seckendorff, V. & Okrusch, M.** (2001): Subsolidus reaction textures in anorthosites of the Kunene Intrusive Complex, NW Namibia. *European Journal of Mineralogy* **13**: 289-309.
- Duchesne, J.-C.** (1984): Massif anorthosites: another partisan review. In: **Brown W.L.** (ed.): *Feldspars and feldspathoids*. Reidel, Dordrecht, pp. 411-433.
- Duchesne, J.-C.** (1999): Fe-Ti deposits in Rogaland anorthosites (South Norway): geochemical characteristics and problems of interpretation. *Mineralium Deposita* **34**: 182-198.
- Dulski, P.** (1994): Interferences of oxide, hydroxide and chloride analyte species in the determination of rare earth elements in geological samples by inductively coupled plasma-mass spectrometry. *Fresenius Journal of Analytical Chemistry* **350**:194-203.
- Eckert, J.O. Jr., Newton, R.C. & Kleppa, O.J.** (1991): The ΔH of reaction and recalibration of garnet-pyroxene-plagioclase-quartz geobarometers in the CMAS system by solution calorimetry. *American Mineralogist* **76**: 148-160.
- Emslie, R.F.** (1975a): High pressure pyroxene megacrysts from anorthositic rocks and their bearing on the genesis of the parent magmas. *Geological Society of America, Abstracts with Program* **7**: 752-753.
- Emslie, R.F.** (1975b): Major rock units of the Morin Complex, southwestern Quebec. *Geological Survey of Canada Papers* **74-48**: 1-37.
- Emslie, R.F.** (1978): Anorthosite massifs, rapakivi granites, and late Proterozoic rifting of North America. *Precambrian Research* **7**: 61-98.
- Emslie, R.F.** (1980): Geology and petrology of the Harp Lake Complex, Central Labrador: an example of Elsonian magmatism. *Geological Survey of Canada Bulletin* **293**:1-136.
- Emslie, R.F.** (1985): Proterozoic anorthosite massifs. In: **Tobi, A. & Touret, J.L.R.** (eds.): *The Deep Proterozoic Crust in the North Atlantic provinces, NATO ASI Series*. Reidel, Dordrecht, pp. 39-60.

- Emslie, R.F.** (1991): Granitoids of rapakivi granite-anorthosite and related associations. *Precambrian Research* **51**: 173-192.
- Emslie, R.F., Hamilton, M.A. & Therault, R.J.** (1994): Petrogenesis of mid-Proterozoic anorthosite-mangerite-charnockite-granite, AMCG complex: isotopic and chemical evidence from the Nain Plutonic Suite. *Journal of Geology* **102**: 539-558.
- Evenson, N.M., Hamilton, P.J. & O'Nions, R.K.** (1978): Rare-earth abundances in chondritic meteorites. *Geochimica et Cosmochimica Acta* **42**: 1199-1212.
- Faure, G.** (1986): Principles of isotope geology (2nd edition). John Wiley & Sons, New York, 589 pp.
- Ferguson, J., McIver, J.R. & Danchlin, R.V.** (1975): Fenitisation associated with the alkaline-carbonatite complex of Epembe, South West Africa. *Transactions of the Geological Society of South Africa* **78**: 111-121.
- Ferry, J.M. & Spear, F.S.** (1978): Experimental Calibration of the partitioning of Fe and Mg between biotite and garnet. *Contributions to Mineralogy and Petrology* **66**: 113-117.
- Foster, M.D.** (1960): Interpretation of the composition of trioctahedral micas. *U.S. Geological Survey, Professional Papers* **254B**: 24-49.
- Franz, L. & Häussinger, H.** (1990): Die Anwendung interaktiver Programme in der Mineralogie am Beispiel des Programms "Amphibol". *Beiheft zum European Journal of Mineralogy* **2**: 68.
- Freestone, I.C. & Hamilton, D.L.** (1980): The role of liquid immiscibility in the genesis of carbonatites – an experimental study. *Contributions to Mineralogy and Petrology* **73**, 105-117.
- Frost, C.D., Frost, B.R., Bell, J.M. & Chamberlain, K.R.** (2002): The relationship between A-type granites and residual magmas from anorthosite: evidence from the northern Sherman batholith, Laramie Mountains, Wyoming, USA. *Precambrian Research* **119**: 45-71.
- Fuhrmann, M.L., Frost, B.R. & Lindsley, D.H.** (1988): Crystallisation conditions of the Sybille Monzosyenite, Laramie Anorthosite Complex, Wyoming. *Journal of Petrology* **29**: 699-729.
- Fuhrmann, M.L. & Lindsley, D.H.** (1988): Ternary feldspar modelling and thermometry. *American Mineralogist* **73**: 201-216.
- Gaspar, J. & Wyllie, P.J.** (1987): The phlogopites from the Jacupiranga carbonatite intrusions, and their petrogenetic significance. *Mineralogy and Petrology* **36**: 121-134.
- Geiger, C.A., Newton R.C. & Klepper, O.J.** (1987): Enthalpy of mixing of synthetic almandine-grossular and almandine-pyrope garnets from high-temperature solution calorimetry. *Geochimica et Cosmochimica Acta* **51**: 1755-1763.

- Gittins, J.** (1979): The feldspathoidal alkaline rocks. In: **Yoder, H.S. Jr.** (ed.): *The Evolution of the Igneous Rocks: Fiftieth Anniversary Perspectives*. Princeton University Press, Princeton, pp. 351-390.
- Gittins, J.** (1989): The origin and evolution of carbonatite magmas. In: **Bell, K.** (ed.): *Carbonatites: genesis and evolution*. Unwin Hyman, London, pp. 580-600.
- Gittins, J., Becket, M.F. & Jago, M.F.** (1990): Composition of the fluid accompanying carbonatite magma: a critical examination. *American Mineralogist* **75**: 1106-1109.
- Gittins, J. & Harmer, R.E.** (1997): What is ferrocarbonatite? A revised classification. *Journal of African Earth Sciences* **25**, 159-168.
- Grant, S.M.** (1988): Diffusion models for corona formation in metagabbros from the Western Grenville Province, Canada. *Contributions to Mineralogy and Petrology* **98**: 49-63.
- Grant, J.A. & Frost, B.R.** (1990): Contact metamorphism and partial melting of pelitic rocks in the aureole of the Laramie Anorthosite Complex, Morton Pass, Wyoming. *American Journal of Science* **290**: 425-472.
- Green, D.H. & Ringwood, A.E.** (1967): An experimental investigation of the gabbro to eclogite transformation and its petrological applications. *Geochimica et Cosmochimica Acta* **31**: 767-833.
- Greig, J.W. & Barth, T.F.W.** (1938): The system $\text{Na}_2\text{O}\cdot\text{Al}_2\text{O}_3\cdot 2\text{SiO}_2$ (nepheline, carnegieite)- $\text{Na}_2\text{O}\cdot\text{Al}_2\text{O}_3\cdot 6\text{SiO}_2$ (albite). *American Journal of Science* **35A**: 93-112.
- Gresens, R.L.** (1967): Composition-volume relationships of metasomatism. *Chemical Geology* **2**: 47-65.
- Griffin, W.L.** (1971): Genesis of coronas in anorthosites of the Upper Jotun Nappe, Indre Sogn, Norway. *Journal of Petrology* **12**: 219-243.
- Griffin, W.L. & Heier, K.** (1973): Petrological implications of some corona structures. *Lithos* **6**: 315-335.
- Griffin, W.L., Mellini, M., Oberti, R. & Rossi, G.** (1985): Evolution of coronas in Norwegian anorthosites: re-evaluation based on crystal-chemistry and microstructures. *Contributions to Mineralogy and Petrology* **91**: 330-339.
- Hamilton, D.L.** (1964): Nephelines as crystallisation temperature indicators. *Journal of Geology* **9**: 321-329.
- Hammarstrom, J.M. & Zen, E.-A.** (1983): Possible use of Al content in hornblende as a geobarometer for plutonic rocks. *Geological Society of America, Abstracts with Program* **15**: 590.
- Hammarstrom, J.M. & Zen, E.-A.** (1985): An empirical equation for igneous calcic amphibole geobarometry. *Geological Society of America, Abstracts with Program* **17**: 602.

- Hammarstrom, J.M. & Zen, E.-A.** (1986): Aluminium in hornblende: an empirical igneous geobarometer. *American Mineralogist* **71**: 1297-1313.
- Harley, S.L.** (1984): An experimental study of the partitioning of Fe and Mg between garnet and orthopyroxene. *Contributions to Mineralogy and Petrology* **86**: 359-373.
- Hedberg, R.M.** (1979): Stratigraphy of the Ovamboland Basin, South West Africa. *Precambrian Research Unit, University of Cape Town Bulletin* **24**: 1-325
- Helz, R.T.** (1973): Phase relations of basalts in their melting range at $P_{H_2O} = 5$ kbar as a function of oxygen fugacity, I, Mafic phases. *Journal of Petrology* **14**: 249-302.
- Helz, R.T.** (1976): Phase relations of basalts in their melting range at $P_{H_2O} = 5$ kbar, II, Melt compositions. *Journal of Petrology* **17**: 139-193.
- Hey, M.** (1954): A new review of chlorites. *Mineralogical Magazine* **30**: 307-340.
- Hibbard, M.J.** (1994): Petrographic classification of crystal morphology. *Journal of Geology* **102**: 571-581.
- Hodges, K.V. & Spear, F.S.** (1982): Geothermometry, geobarometry, and the Al_2SiO_5 triple point at Mt. Moosilauke, New Hampshire. *American Mineralogist* **67**: 1118-1134.
- Hoefs J.** (1997): Stable isotope geochemistry (2nd edition). Springer Verlag, Berlin, 208 pp.
- Hoffman, P.F.** (1989): Speculations on Laurentia's first gigayear (2.0 to 1.0 Ga). *Geology* **17**: 135-138.
- Hogarth, D.D.** (1977): Classification and nomenclature of the pyrochlore group. *American Mineralogist* **62**: 403-410.
- Hogarth, D.D.** (1989): Pyrochlore, apatite and amphibole: distinctive minerals in carbonatite. In: **Bell, K.** (ed.): *Carbonatites: genesis and evolution*. Unwin Hyman, London, pp. 105-148.
- Holdaway, M.J.** (1972): Thermal stability of Al-Fe epidote as a function of f_{O_2} and Fe-content. *Contributions to Mineralogy and Petrology* **37**: 307-340.
- Holland, H.D.** (1959): Some applications of thermochemical data to problems of ore deposits. I. Stability relations among the oxides, sulphides, sulfates and carbonates of ore and gangue metals. *Economic Geology* **54**: 184-233
- Hollister, L.S., Grissom, G.C., Peters, E.K., Stowell, H.H. & Sissom, V.B.** (1987): Confirmation of the empirical correlation of Al in hornblende with pressure of solidification of calc-alkaline plutons. *American Mineralogist* **72**: 231-239.
- Horning-Kjarsgaard, I.** (1998): Rare earth elements in sövitic carbonatites and their mineral phases. *Journal of Petrology* **39**: 2105-2122.
- Horstmann, U.E. & Verwoerd, W.J.** (1997): Carbon and oxygen isotope variations in southern African carbonatites. *Journal of African Earth Sciences* **25**: 115-138.

- Indares, A. & Martignole, J.** (1985): Biotite-garnet geothermometry in the granulite facies: the influence of Ti and Al in biotite. *American Mineralogist* **70**: 272-278.
- Ixer, R.A. & Stanley, C.J.** (1996): Siegenite-bearing assemblages found at the Great Orme mine, Llandudno, North Wales. *Mineralogical Magazine* **60**: 978-982.
- Jamtveit, B., Dahlgren, S. & Austrheim, H.** (1997): High-grade contact metamorphism of calcareous rocks from the Oslo Rift, southern Norway. *American Mineralogist* **82**: 1241-1254.
- Johnson, C.D. & Carlson, W.D.** (1990): The origin of olivine-plagioclase coronas in metagabbros from the Adirondack Mountains, New York. *Journal of metamorphic Geology* **8**: 697-717.
- Johnson, C.D. & Essene, E.** (1982): The formation of garnet in olivine-bearing metagabbros from the Adirondacks. *Contributions to Mineralogy and Petrology* **81**: 240-251.
- Keller, J. & Hoefs, J.** (1995): Stable isotope characteristics of recent natrocarbonatites from Oldoinyo Lengai. In: **Bell, K. & Keller, J.** (eds.): *Carbonatite volcanism: Oldoinyo Lengai and the petrogenesis of natrocarbonatites*. Springer Verlag, Berlin, pp. 113-123.
- Kerrick, D.M. & Jackobs, G.K.** (1981): A modified Redlich-Kwong equation for H₂O, CO₂ and H₂O-CO₂ mixtures at elevated temperatures and pressures. *American Journal of Science* **281**: 735-767
- Kjarsgaard, B.A. & Hamilton, D.L.** (1989): The genesis of carbonatites by immiscibility. In: **Bell, K.** (ed.): *Carbonatites: genesis and evolution*. Unwin Hyman, London, pp. 388-404.
- Kleemann, U. & Reinhardt, J.** (1994): Garnet-biotite thermometry revisited: The effect of Al^{VI} and Ti in biotite. *European Journal of Mineralogy* **6**: 925-941.
- Köstlin, E.C.** (1967): The geology of part of the Kunene basic complex, Kaokoveld, South West Africa. M.Sc. thesis, University of Cape Town, 92 pp.
- Köstlin, E.C.** (1974): The Kunene basic complex, northern South West Africa. In: **Kröner, A.** (ed.): *Contributions to the Precambrian geology of southern Africa*. University of Cape Town Bulletin 15, pp. 123-135.
- Kolker, A. & Lindsley, D.H.** (1989): Geochemical evolution of the Maloin Ranch pluton, Laramie Anorthosite Complex, Wyoming: petrology and mixing relations. *American Mineralogist* **74**: 307-324.
- Kostel'nikov, A.R. & Zhorniyak, L.V.** (1995): Stability of sodalite under hydrothermal conditions. *Geochemistry International* **32**: 87-90.
- Kreher, B.** (1992): Petrologie und Geochemie der Gabbrointrusion des Frankensteins (Odenwald). Dr. rer. nat. thesis, University of Würzburg, 229 pp.

- Kresten, P.** (1988): The chemistry of fenitization: Examples from Fen, Norway. *Chemical Geology* **68**: 329-349.
- Kresten, P. & Morogan, V.** (1986): Fenitization at the Fen complex, southern Norway. *Lithos* **19**: 27-42.
- Kretz, R.** (1983): Symbols for rock-forming minerals. *American Mineralogist* **68**: 277-279.
- Kyser, T.K.** (1986): Stable isotope variations in the mantle. In: **Valley, J.W.** (ed.): *Stable isotopes in high temperature geological processes. Reviews in Mineralogy 16*. Mineralogical Society of America, Washington D.C., pp. 141-164.
- Laird, J. & Albee, A.L.** (1981): High-pressure metamorphism in mafic schist from Northern Vermont. *American Journal of Science* **281**: 97-126.
- Large, R.R., Gemmell, J.B., Paulick, H. & Huston, L.** (2001): The alteration box plot: a simple approach to understanding the relationship between alteration mineralogy and lithogeochemistry associated with volcanic-hosted massive sulfide deposits. *Economic Geology* **26**: 957-971.
- Leake, B.E., Schumacher, J.C., Smith, D.C., Stephenson, N.C.N., Ungaretti, L., Whittaker, E.J.W. & Youzhi, G.** (1997): Nomenclature of amphiboles. *European Journal of Mineralogy* **9**: 623-642.
- Le Bas, M.J.** (1977): Carbonatite-nephelinite volcanism: an African case history. Wiley, London, 347 pp.
- Le Bas, M.J.** (1981): Carbonatite magmas. *Mineralogical Magazine* **44**: 133-140.
- Le Bas, M.J.** (1987): Nephelinites and carbonatites. In: **Fitton, J.G. & Upton, B.G.J.** (eds.): *Alkaline igneous rocks*. Geological Society Special Publications 30, Blackwell, Oxford, pp. 53-84.
- Le Bas, M.J.** (1989): Diversification of carbonatite. In: **Bell, K.** (ed.): *Carbonatites: genesis and evolution*. Unwin Hyman, London, pp. 428-447.
- Le Bas, M.J.** (1999): Ferrocarnatites: geochemistry and magma-fluid state. *Memoirs of the Geological Society of India* **43**, 785-802.
- Le Bas, M.J., Keller, J., Tao, K., Wall, F., Williams, C.T. & Zhang, P.** (1992): Carbonatite dykes at Bayan Obo, Inner Mongolia, China. *Mineralogy and Petrology* **46**: 195-228.
- Lee, H.Y. & Ganguly, J.** (1988): Equilibrium compositions of coexisting garnet and orthopyroxene: Experimental determinations in the system FeO-MgO-Al₂O₃-SiO₂, and applications. *Journal of Petrology* **29**: 93-113.
- Leegaard, T. & Rosenqvist, T.** (1964): Der Zersetzungsdruck und die Phasengleichgewichte der höheren Sulfide von Kobalt und Nickel. *Zeitschrift für Anorganische und Allgemeine Chemie* **328**: 294-298.

- Le Maitre, R.W.** (ed.) (1989): A classification of igneous rocks and glossary of terms. Blackwell, Oxford, 193 pp.
- Lindsley, D.H.** (1976): Experimental study of oxide minerals. In: **Rumble, D.** (ed.): *Oxide minerals, Reviews in Mineralogy 3*. Mineralogical Society of America, Washington D.C., pp. L61-L88.
- Lindsley, D.H.** (1983): Pyroxene thermometry. *American Mineralogist* **68**: 477-493.
- Littmann, S., Cook, N.J., Teigler, B. & Drüppel, K.** (2003): Ultramafic-mafic intrusives hosting Cu-Ni sulphide mineralisation, Itjitambi area, Kunene Region, N.W. Namibia: Investigation of drillcore, Hole OTD-1. *Communications of the Geological Survey of Namibia* (in press).
- Littmann, S., Romer, R.L. & Okrusch, M.** (2000): Nephelinsyenite der Epembe-Swartbooisdrif-Alkali-Provinz (ESAP)/ NW Namibia. *Berichte der deutschen Mineralogischen Gesellschaft, Beihefte zum European Journal of Mineralogy* **12**: 115.
- Longhi, J. & Ashwal, L.D.** (1985): Two-stage models for lunar and terrestrial anorthosites: Petrogenesis without a magma ocean. *Journal of Geophysical Research* **90**: C571-C584.
- Longhi, J., Vander Auwera, J., Fram, M.S. & Duchesne, J.-C.** (1999): Some Phase Equilibrium Constraints on the Origin of Proterozoic (Massif) Anorthosites and Related Rocks. *Journal of Petrology* **40**: 339-362.
- Ludington, S.** (1978): The biotite-apatite geothermometer revisited. *American Mineralogist* **63**: 551-553.
- Markl, G., Marks, M., Schwinn, G. & Sommer, H.** (2001): Phase equilibrium constraints on intensive crystallization parameters of the Ilímaussaq complex, South Greenland. *Journal of Petrology* **42**: 2231-2258.
- Martignole, J.** (1974): L'évolution magmatique du complexe de Morin et son apport au problème des anorthosites. *Contributions to Mineralogy and Petrology* **44**: 117-137.
- Martignole, J. & Schrijver, K.** (1971): Association of (hornblende-) garnet-pyroxene "subfacies" of metamorphism and anorthosite mass. *Canadian Journal of Earth Sciences* **8**: 698-704.
- Martin, H.** (1965): The Precambrian geology of South West Africa and Namaqualand. Precambrian Research Unit, University of Cape Town, 159 pp.
- Mayer, A., Sinigoi, S., Miguel, L.G., Morais, E. & Petrini, R.** (2000): Kibaran ages in the Kunene anorthositic complex. *GEOLUANDA 2000, Abstract volume*: 106.
- McLelland, J.M. & Whitney, P.R.** (1977): The origin of garnet in the anorthosite-charnockite suite of the Adirondacks. *Contributions to Mineralogy and Petrology* **60**: 61-181.

- McLelland, J.M. & Whitney, P.R.** (1980a): A geological garnet-forming reaction for meta-igneous rocks in the Adirondacks. *Contributions to Mineralogy and Petrology* **72**: 111-122.
- McLelland, J.M. & Whitney, P.R.** (1980b): Compositional controls on spinel clouding and garnet formation in plagioclase of olivine metagabbros, Adirondack Mountains, New York. *Contributions to Mineralogy and Petrology* **73**: 243-251.
- Menge, G.F.W.** (1986): Sodalite-carbonatite deposits of Swartbooisdrif, South West Africa/Namibia. In: **Anhaeusser, C.R. & Maske, S.** (eds.): *Mineral Deposits of Southern Africa*. Geological Society of South Africa, Johannesburg, pp. 2261-2268.
- Menge, G.F.W.** (1996): The eastern portion of the Kunene complex, its satellite intrusions and the alkaline suite between Epembe and Swartbooisdrif. Unpublished Report, 128 pp.
- Menge, G.F.W.** (1998): The antiformal structure and general aspects of the Kunene Complex. *Zeitschrift der Deutschen Geologischen Gesellschaft* **149**: 431-448.
- Minceva-Stefanova, J.** (1978): Paragenetische und geochemische Bedeutung der Mineralien von den Bravoit-, Cobaltin- und Linneit-Gruppen in den Polymetallvererzungen des "Strata-Bound"-Typs in den Balkaniden. *Verhandlungen der Geologischen Bundesanstalt, Wien*: 419-435.
- Minceva-Stefanova, J. & Kostov, I.** (1976): On siegenite and the 'miscibility' between linnaeite and polydymite. *Geochemistry, Mineralogy and Petrology, Sofia* **4**: 35-56.
- Moecher, D.P., Essene, E.J. & Anovitz, L.M.** (1988): Calculation and application of clinopyroxene-garnet-plagioclase-quartz geobarometers. *Contributions to Mineralogy and Petrology* **100**: 92-106.
- Mora, C.I. & Valley, J.W.** (1988): Channelized meteoric-hydrothermal alteration of the Boehls Butte and Bitterroot anorthosites, northern ID and MT. *Eos* **69**: 1489.
- Morais, E., Sinigoi, S., Mayer, A., Mucana, A., Miguel, L.G. & Rufino Neto, J.** (1998): The Kunene gabbro-anorthosite Complex: preliminary results based on new field and chemical data. *African Geoscience Review* **5**: 485-498.
- Morimoto, N.** (1988): Nomenclature of pyroxenes. *Mineralogical Magazine* **52**: 535-550.
- Morogan, V.** (1982): Fenitization and ultimate rheomorphism of xenoliths from the Oldoinyo Lengai carbonatitic volcano, Tanzania. M.Sc. thesis, University of Montreal, 193 pp.
- Morogan, V.** (1989): Mass transfer and mobility of REE during fenitization at Alnö, Sweden. *Contributions to Mineralogy and Petrology* **103**: 25-34.
- Morogan, V.** (1994): Ijolite vs. Carbonatite as sources of fenitization. *Terra Nova* **6**: 166-176.

- Morogan, V. & Lindblom, S.** (1995): Volatiles associated with the alkaline-carbonatite magmatism at Alnö, Sweden: A study of fluid and solid inclusions in minerals from the Langarsholmen ring complex. *Contributions to Mineralogy and Petrology* **122**: 262-274.
- Morogan, V. & Martin, R.F.** (1985): Mineralogy and partial melting of fenitized crustal xenoliths in the Oldoinyo Lengai carbonatitic volcano, Tanzania. *American Mineralogist* **70**: 1114-1126.
- Morogan, V. & Woolley, A.R.** (1988): Fenitization in the Alnö complex, Sweden: distribution, mineralogy and genesis. *Contributions to Mineralogy and Petrology* **100**: 169-182.
- Morrison, J. & Valley, J.W.** (1988): Contamination of the Marcy anorthosite massif, Adirondack Mountains, NY: petrologic and isotopic evidence. *Contributions to Mineralogy and Petrology* **98**: 97-108.
- Morse, S.A.** (1968): Layered intrusions and anorthosite genesis. In: **Isachsen, Y.W.** (ed.): *Origin of anorthosite and related rocks*. N.Y. State Museum and Science Service, Memoir 18, pp. 175-187.
- Morse, S.A.** (1982): A partisan review of Proterozoic anorthosites. *American Mineralogist* **67**: 1087-1100.
- Morse, S.A. & Nolan, K.M.** (1984): Origin of strongly reversed rims on plagioclase in cumulates. *Earth and Planetary Science Letters* **68**: 485-498.
- Munoz, J.L. & Swenson, A.** (1981): Chloride-hydroxyl exchange in biotite and estimation of relative HCl/HF activities in hydrothermal fluids. *Economic Geology* **76**: 2212-2221.
- Nelson, D.R., Chivas, A.R., Chappell, B.W. & Mc Culloch, M.T.** (1988): Geochemical and isotope systematics in carbonatites and implications for the evolution of ocean-island sources. *Geochimica et Cosmochimica Acta* **52**: 1-17.
- Nesbitt, B.E. & Kelley, W.C.** (1977): Magmatic and hydrothermal inclusions in carbonatite of the Magnet Cove complex, Arkansas. *Contributions to Mineralogy and Petrology* **63**: 271-294.
- Newton, R.C. & Perkins, D.** (1982): Thermodynamic calibration of geobarometers based on the assemblages garnet-plagioclase-orthopyroxene(clinopyroxene)-quartz. *American Mineralogist* **67**: 203-222.
- Nickel, H.E.** (1970): The application of ligand field concepts to an understanding of the structural stabilities and solid solution limit of sulfides and related minerals. *Chemical Geology* **5**: 233-241.
- Oberti, R., Smith, D.C., Rossi, G. & Caucia, F.** (1991): The crystal-chemistry of high-aluminium titanites. *European Journal of Mineralogy* **3**: 777-792.

- O'Connor, Y.-L. & Morrison, J.** (1999): Oxygen isotope constraints on the petrogenesis of the Sybille intrusion of the Proterozoic Laramie anorthosite complex. *Contributions to Mineralogy and Petrology* **136**: 81-91.
- Ohmoto, H. & Goldhaber, M.B.** (1997): Sulphur and carbon isotopes. In: **Barnes, H.L.** (ed.): *Geochemistry of hydrothermal ore deposits*. John Wiley & Sons, New York, pp. 517-611.
- Olson, K.E. & Morse, S.A.** (1990): Regional Al-Fe mafic magmas associated with anorthosite-bearing terranes. *Nature* **344**: 760-762.
- Ostwald, J.** (1978): Linnaeite series minerals from the Kalgoorlie district, western Australia. *Mineralogical Magazine* **42**: 93-98.
- Otten, M.T.** (1984): The origin of brown hornblende in the Artfjället gabbro and dolerites. *Contributions to Mineralogy and Petrology* **86**: 189-199.
- Papike, J.J. & Cameron, M.** (1980): Crystal chemistry of silicate pyroxenes. In: **Prewitt, C.T.** (ed.): *Pyroxenes. Reviews in Mineralogy* 7. Mineralogical Society of America, Washington D.C., pp. 5-92.
- Papike, J.J., Cameron, K.L. & Baldwin, K.** (1974): Amphiboles and pyroxenes: Characterization of other than quadrilateral components and estimates of ferric iron from microprobe data. *Geological Society of America, Abstracts with Program* **6**: 1053-1054.
- Pearce, J.A., Harris, N.B.W. & Tindle, A.G.** (1984): Trace element discrimination diagrams for the tectonic interpretation of granitic rocks. *Journal of Petrology* **25**: 956-983.
- Pearce, N.J.G., Perkins, W.T., Westgate, J.A., Gorton, M.P., Jackson, S.E., Neal, C.R. & Chenerly, S.P.** (1997): A compilation of new and published major and trace element data for NIST SRM 610 and NIST SRM 612 glass reference materials. *Geostandards Newsletter* **21**: 115-144.
- Peck, W.H. & Valley, J.W.** (2000): Large crustal input into high $\delta^{18}\text{O}$ anorthosite massifs of the southern Grenville Province: new evidence from the Morin Complex, Quebec. *Contributions to Mineralogy and Petrology* **139**: 402-417.
- Perchuk, L.L. & Lavrent'eva, I.V.** (1983): Experimental investigation of exchange equilibria in the system cordierite-garnet-biotite. In: **Saxena, S.K.** (ed.): *Kinetics and equilibrium in mineral reactions. Advances in Physical Geochemistry*, 3. Springer Verlag, New York, pp. 199-239.
- Pignolet, S. & Hagni, R.D.** (1983): Cobalt-nickel mineralization associated with lead-zinc-copper mineralization in the Mississippi Valley-type deposits at Fredericktown, Missouri. In: **Kisvarsanyi, G., Grant, S.K., Pratt, W.P. & Koenig, J.W.** (eds.): *International conference on Mississippi Valley Type lead-zinc deposits*. University of Missouri-Rolla, Missouri-Rolla, pp.187-194.

- Poldervaart, A. & Hess, H.H.** (1951): Pyroxenes in the crystallisation of basaltic magmas. *Journal of Geology* **59**: 472-489.
- Powell, R. & Holland, T.J.B.** (1988): An internally consistent dataset with uncertainties and correlations. 3. Applications to geobarometry, worked examples and a computer program. *Journal of metamorphic Geology* **6**: 173-204.
- Rae, D.A., Coulson, I.M. & Chambers, A.D.** (1996): Metasomatism in the North Qôroq centre, South Greenland: apatite chemistry and rare-earth element transport. *Mineralogical Magazine* **60**: 207-220.
- Rankin, A.H.** (1975): Fluid inclusion studies in apatite from carbonatites of the Wasaki area of western Kenya. *Lithos* **8**: 123-136.
- Riley, J.F.** (1980): Ferroan carrollites, cobaltian violarites, and other members of the linnaeite group: $(\text{Co},\text{Ni},\text{Fe},\text{Cu})_3\text{S}_4$. *Mineralogical Magazine* **43**: 733-739.
- Roedder, E.** (1973): Fluid inclusions from the fluorite deposits associated with carbonatite of Amba Dongar, India and Okoruso, South West Africa. *Transactions of the Institution of Mining and Metallurgy* **B 82**: 835-839.
- Roedder, E.** (1984): Fluid inclusions. Reviews in Mineralogy **12**. Mineralogical Society of America, Washington D.C., 646 pp.
- Rønsbo, J.G.** (1989): Coupled substitution involving REEs and Na and Si in apatites in alkaline rocks from the Ilímaussaq intrusion, South Greenland, and its petrological implications. *American Mineralogist* **74**: 896-901.
- Rosenqvist, T.** (1954): A thermodynamic study of the iron, cobalt, and nickel sulphides. *Journal of the Iron and Steel Institute* **176**: 37-57.
- Samson, I.M., Weining, L. & Williams-Jones, A.E.** (1995a): The nature of orthomagmatic hydrothermal fluids in the Oka carbonatite, Quebec: evidence from fluid inclusions. *Geochimica et Cosmochimica Acta* **59**: 1963-1978.
- Samson, I.M., Williams-Jones, A.E. & Weining, L.** (1995b): The chemistry of hydrothermal fluids in carbonatites: evidence from leachate and SEM-decrepitate analysis of fluid inclusions from Oka, Quebec, Canada. *Geochimica et Cosmochimica Acta* **59**: 1979-1989.
- Schliestedt, M.** (1980): Phasengleichgewichte in Hochdruckgesteinen von Sifnos, Griechenland. PhD thesis, University of Braunschweig, 142 pp.
- Seifert, K.E.** (1978): Anorthosite-mangerite relations on Barker Mountain, New York. *Geological Society of America, Bulletin* **89**: 245-250.
- Seifert, W., Kämpf, H. & Wasterneck, J.** (2000): Compositional variation in apatite, phlogopite and other accessory minerals of the ultramafic Delitzsch complex, Germany: implication for cooling history of carbonatites. *Lithos* **53**: 81-100.

- Seim, R. & Tischendorf, G.** (1990): Grundlagen der Geochemie. Deutscher Verlag für Grundstoffindustrie, Leipzig, 632 pp.
- Seth, B., Brandt, S. & Kramers, J.B.** (2001): First isotopic age determinations of mid-Proterozoic granulite-facies metamorphism in the Epupa Complex. *EUG XI, Strasbourg, Abstract Volume*: 597.
- Sharp, Z.D., Helfrich, G.R., Bohlen, S.R. & Essene, E.J.** (1989): The stability of sodalite in the system $\text{NaAlSiO}_4\text{-NaCl}$. *Geochimica et Cosmochimica Acta* **53**: 1943-1954.
- Shepherd, T. J., Rankin, A. H. & Alderton, D. H. M.** (1985): A Practical Guide to Fluid Inclusion Studies. Blackie, Glasgow & London, 239 pp.
- Silva, Z.C.G.** (1990): Geochemistry of the gabbro-anorthosite Complex of Angola. *Journal of African Earth Sciences* **10**: 683-692.
- Silva, Z.C.G.** (1992). Mineralogy and cryptic layering of the Kunene anorthosite complex of SW Angola and Namibia. *Mineralogical Magazine* **56**: 319-327.
- Simpson, E.S.W.** (1970): The anorthosite of southern Angola: a review of present data. In: **Clifford, T.N. & Gass, I.G.** (eds.): *African magmatism and tectonics*. Oliver Boyd, Edinburgh, pp. 89-96.
- Simpson, E.S.W. & Otto, J.D.T.** (1960): On the Pre-Cambrian anorthosite mass of southern Angola. *Proceedings of the 21st IGC, Part 13 (Petrographic provinces, igneous and metamorphic rocks), Copenhagen*: 216-227.
- Slejko, F., Demarchi, G. & Morais, E.** (2002): Mineral chemistry and Nd isotopic composition of two anorthositic rocks from the Kunene complex (South Western Angola). *Journal of African Earth Sciences* **35**: 77-88.
- Sörensen, H.** (1970): Internal structures and geological setting of the three agpaitic intrusions - Khibina and Lovozero of the Kola Peninsula and Ilímaussaq, south Greenland. *Canadian Mineralogist* **10**: 299-334.
- Spear, F.S. & Kimball, K.L.** (1984): RECAMP-A FORTRAN IV program for estimating Fe^{3+} contents in amphiboles. *Computers in Geology* **10**: 317-325.
- Spencer, K.J. & Lindsley, D.H.** (1978): New experimental results on the magnetite-ulvöspinel, hematite-ilmenite solution model using the Co-CoO buffer. *Geological Society of America, Abstracts with Program* **10**: 496.
- Spencer, K.J. & Lindsley, D.H.** (1981): A solution model for coexisting iron-titanium oxides. *American Mineralogist* **66**: 1189-1201.
- Stone, P. & Brown, G.M.** (1958): The Quihita-Cunene layered gabbroic intrusion of South-West Angola. *Geological Magazine* **95**: 195-206.

- Stormer, J.C. & Carmichael, I.S.E.** (1971): Fluorine-hydroxyl exchange in apatite and biotite: a potential igneous geothermometer. *Contributions to Mineralogy and Petrology* **31**, 121-131.
- Taylor, H.P.** (1968): Oxygen isotope studies of anorthosites, with particular reference to the origin of bodies in the Adirondack Mountains, New York. In: **Isachsen, Y.W.** (ed.): *Origin of anorthosite and related rocks*. N.Y. State Museum and Science Service, Memoir **18**, pp. 111-134.
- Taylor, H.P., Frechen, J. & Degens, E.T.** (1967): Oxygen and carbon isotope studies of carbonatites from the Laacher See district, West Germany and the Alnö district, Sweden. *Geochimica et Cosmochimica Acta* **31**: 407-430.
- Taylor, H.P. & Sheppard, S.M.F.** (1986): Igneous rocks I. Processes of isotopic fractionation and isotope systematics. In: **Valley, J.W., Taylor, H.P. & O'Neil, J.** (eds.): *Stable isotopes in high temperature geological processes*. Mineralogical Society of America, Chelsea, Michigan, pp. 227-269.
- Taylor, S.R., Campbell, I.H., McCulloch, M.T. & McLennan S.M.** (1984): A lower crustal origin for massif-type anorthosites. *Nature* **311**: 372-374.
- Tegtmeyer, A. & Kröner, A.** (1985): U-Pb zircon ages for granitoid gneisses in northern Namibia and their significance for Proterozoic crustal evolution of Southwestern Africa. *Precambrian Research* **28**: 311-326.
- Thompson, R.N.** (1982): Magmatism of the British Tertiary Volcanic Province. *Scottish Journal of Geology* **18**:49-107.
- Thompson, R.N., Morrison, M.A., Dickin, A.P. & Hendry, G.L.** (1983): Continental flood basalts ... arachnids rule OK?. In: **Hawkesworth, C.J. & Norry, M.J.** (eds.): *Continental basalts and mantle xenoliths*. Shiva Publishing Ltd, Nantwich, pp. 158-185.
- Thompson, R.N., Smith, P.M., Gibson, S.A., Matthey, D.P. & Dickin, A.P.** (2002): Ankerite carbonatite from Swartbooisdrif, Namibia: the first evidence for magmatic ferrocarnatite. *Contributions to Mineralogy and Petrology* **143**: 377-396.
- Torquato, J.R. & Carvalho, J.A.R.** (1992): Idade Rb-Sr do granito do Carculo, uma nova evidência para a existência do evento Namib no Sudoeste de Angola. *Revista Geologia* **50**: 157-167.
- Torquato, J.R. & Oliviera, J.T.** (1977): Sobre a idade dos granitos e do grupo vulcano-sedimentar da região de Chipindo, Angola. *Comunicações Serviços Geológicos Portugal* **61**: 223-238.

- Torquato, J.R., Silva, A.T.S.F. da, Cordani, U.G. & Kawashita, K.** (1979): A evolução geológica do Cinturão Móvel do Quipungo no Ocidente de Angola. *Anais Academia Brasileira Ciências* **51**: 133-143.
- Toulmin, P. III & Barton, P.B. Jr.** (1964): A thermodynamic study of pyrite and pyrrhotite. *Geochimica et Cosmochimica Acta* **28**: 641-671.
- Treiman, A.H. & Essene, E.J.** (1985): The Oka carbonatite complex, Quebec: geology and evidence for silicate-carbonate liquid immiscibility. *American Mineralogist* **70**: 1101-1113.
- Tröger, W.E.** (1982): Optische Bestimmung der gesteinsbildenden Minerale, Teil 2. Schweizerbartsche Verlagsbuchhandlung, Stuttgart, 822 pp.
- Trompette, R.** (1994): Geology of Western Gondwana (2000-500 Ma). Pan-African-Brasiliano aggregation of South America and Africa. Balkema, Rotterdam, 350 pp.
- Tuttle, O.F. & Smith, J.V.** (1958): The nepheline-kalsilite system: II. Phase relations. *American Journal of Science* **256**: 571-589.
- Valley, J.W. & O'Neil, J.R.** (1982): Oxygen isotope evidence for shallow emplacement of Adirondack anorthosite. *Nature* **300**: 497-500.
- Vaughan, D.J., Burns, R.G. & Burns, V.M.** (1971): Geochemistry and bonding of thiospinel minerals. *Geochimica et Cosmochimica Acta* **35**: 365-381.
- Vaughan, D.J. & Craig, J.R.** (1985): The crystal chemistry of iron-nickel thiospinels. *American Mineralogist* **70**: 1036-1043.
- Vermaak, C.F.** (1981): Kunene Anorthosite Complex. In: **Hunter, D.R.** (ed.): *Precambrian of the Southern Hemisphere. Developments in Precambrian Geology, Vol. 2.* Elsevier, Amsterdam, pp. 578-599.
- Vertainen, H. & Woolley, A.R.** (1974): The age of the Sokli carbonatite, Finland, and some relationships of the North Atlantic alkaline igneous province. *Bulletin of the Geological Society of Finland* **46**: 81-91.
- Verwoerd W.J.** (1967): The carbonatites of South Africa and South West Africa. *Handbook of the Geological Survey of South Africa* **6**: 1-452.
- Verwoerd, A.J.** (1993): Update on carbonatites of South Africa and Namibia. *South African Journal of Geology* **96**: 75-95.
- Volfinger, M., Robert, J.-L., Vielzeuf, D. & Neiva, A.M.R.** (1985): Structural control of the chlorine content of OH-bearing silicates (micas and amphiboles). *Geochimica et Cosmochimica Acta* **49**: 37-48.
- Von Seckendorff, V. & Drüppel, K.** (1999): Fe-Ti oxides and sulphide mineralisation in sodalite-bearing metasomatites at Swartbooisdrif (Kunene Region, NW Namibia). In: **de**

- Wall, H. & Greiling, R.O.** (eds.): *Aspects of Pan-African tectonics. Bilateral Seminars 32.* Forschungszentrum Jülich GmbH, Jülich, pp. 99-102.
- Von Seckendorff, V., Drüppel, K., Okrusch, M., Cook, N. & Littmann, S.** (2000): Oxide-sulphide relationships in sodalite-bearing metasomatites of the Epembe-Swartbooisdrif alkaline province, north-west Namibia. *Mineralium Deposita* **35**, 430-450.
- Wagner, T.** (1999): Spätvaristische hydrothermale Mineralisationen im Rheinischen Schiefergebirge. *Freiberger Forschungshefte, Freiberg C* **478**: VIII + 194 pp.
- Wall, F., Le Bas, M.J. & Srivastava, R.K.** (1993): Calcite and carbocernaite exsolution and cotectic textures in a Sr, REE-rich carbonatite dyke from Rajasthan, India. *Mineralogical Magazine* **57**: 495-513.
- Watkinson, D.H. & Wyllie, P.J.** (1971): Experimental study of the join $\text{NaAlSiO}_4\text{-CaCO}_3\text{-H}_2\text{O}$ and the genesis of alkalic rock-carbonatite complexes. *Journal of Petrology* **12**: 357-378.
- Wellman, T.R.** (1970): The stability of sodalite in a synthetic syenite plus aqueous chloride fluid system. *Journal of Petrology* **11**: 49-71.
- Wen, S. & Nekvasil, H.** (1994): SOLVCALC: an interactive graphics program package for calculating the ternary feldspar solvus and for two-feldspar geothermometry. *Computers & Geosciences* **20**: 1025-1040.
- Whalen, J.B., Currie, K.L. & Chappell, B.W.** (1987): A-type granites: geochemical characteristics, discrimination and petrogenesis. *Contributions to Mineralogy and Petrology* **95**: 407-419.
- Whitney, P.R. & McLelland, J.M.** (1973): Origin of coronas in metagabbros of the Adirondack Mts., N.Y. *Contributions to Mineralogy and Petrology* **39**: 81-98.
- Wiebe, R.A.** (1986): Lower crustal cumulate nodules in Proterozoic dykes of the Nain complex, Labrador: evidence for the origin of Proterozoic anorthosites. *Journal of Petrology* **27**: 1253-1275.
- Wiebe, R.A.** (1994): Proterozoic anorthosite complexes. In: **Condie, K.C.** (ed.): *Proterozoic crustal Evolution*. Elsevier, Amsterdam, pp. 215-261.
- Williams-Jones, A.E. & Palmer, D.A.S.** (2002): Fluid evolution of the Amba Dongar carbonatite complex, India. *Chemical Geology* **185**: 283-301.
- Woolley, A.R.** (1989): The spatial and temporal distribution of carbonatites. In: **Bell, K.** (ed.): *Carbonatites: genesis and evolution*. Unwin Hyman, London, pp. 15-37.
- Woolley, A.R. & Kempe, D.R.C.** (1989): Carbonatites: nomenclature, average chemical compositions and element distribution. In: **Bell, K.** (ed.): *Carbonatites: genesis and evolution*. Unwin Hyman, London, pp. 1-14.

- Wyllie, P.J.** (1966): Experimental studies of carbonatite problems: The origin and differentiation of carbonatite magmas. In: **Tuttle, O.F. & Gittins, J.** (eds.): *Carbonatites*. Interscience, New York, pp. 311-352.
- Wyllie, P.J.** (1989): Origin of carbonatites: evidence from phase equilibrium studies. In: **Bell, K.** (ed.): *Carbonatites: genesis and evolution*. Unwin Hyman, London, pp. 149-176.
- Wyllie, P.J. & Tuttle, O.F.** (1960): The system CaO-CO₂-H₂O and the origin of carbonatites. *Journal of Petrology* **1**: 1-46.
- Yang, H.-Y.** (1987): Stability of ilmenite and titanomagnetite in the presence of carbon dioxide a thermodynamic evaluation. *Contributions to Mineralogy and Petrology* **95**: 202-206.
- Yoder, H.S. & Kushiro, I.** (1969): Melting of a hydrous phase: phlogopite. *American Journal of Science* **267-A**, 558-582.
- Yund, R.A. & Kullerud, G.** (1966): Thermal stability of assemblages in the Cu-Fe-S system. *Journal of Petrology* **7**: 454-488
- Zhang, Y. & Franz, J.D.** (1987): Determination of the homogenization temperatures and densities of supercritical fluids in the system NaCl-KCl-CaCl₂-H₂O using synthetic fluid inclusions. *Chemical Geology* **64**: 335-350.
- Zheng, Y.F.** (1991): Calculation of oxygen isotope fractionation in metal oxides. *Geochimica et Cosmochimica Acta* **55**: 2299-2370.
- Zheng, Y.F.** (1999): Oxygen isotope fractionation in carbonate and sulfate minerals *Geochemical Journal* **33**: 109-126.
- Zhu, C. & Sverjensky, D.A.** (1991): Partitioning of F-Cl-OH between minerals and hydrothermal fluids. *Geochimica et Cosmochimica Acta* **55**: 1837-1858.
- Zhu, C. & Sverjensky, D.A.** (1992): F-Cl-OH partitioning between biotite and apatite. *Geochimica et Cosmochimica Acta* **56**: 3435-3467.
- Zuleger, E. & Erzinger, J.** (1988): Determination of the REE and Y in silicate materials with ICP-AES. *Fresenius Zeitschrift für Analytische Chemie* **332**, 140-143.

Lebenslauf

Kirsten Drüppel

Virchowstr. 18

97072 Würzburg

Geburtsdatum: 01.06.1974

Geburtsort: Würzburg

Familienstand: ledig

Schulischer Werdegang

09/1984-06/1993 Siebold-Gymnasium Würzburg

06/1993 Abitur

Studium

10/1993-09/2000 Studium der Geologie-Paläontologie an der Bayerischen Julius-Maximilians-Universität Würzburg

05/1997-10/1999 Studium der Mineralogie an der Bayerischen Julius-Maximilians-Universität Würzburg

05/1996 Diplom-Vorprüfung im Studiengang Geologie-Paläontologie

11/1997 Diplom-Vorprüfung im Studiengang Mineralogie

01/1999 Diplomhauptprüfung im Studiengang Mineralogie

01/1999-10/1999 Diplomarbeit im Studiengang Mineralogie über das Thema "Petrologie und Geochemie von Anorthositen des Kunene-Intrusiv-Komplexes, NW-Namibia"

10/1999 Diplom

seit 10/2000 Promotionsstudium am Mineralogischen Institut der Universität Würzburg

Tätigkeiten als wissenschaftliche Hilfskraft

02/1997-06/1997 Wissenschaftliche Hilfskraft am geologischen Institut der Universität Würzburg; Fachbereich: Strukturgeologie

08/1998-12/1998 Wissenschaftliche Hilfskraft am Mineralogischen Institut der Universität Würzburg; Fachbereich: Archäometrie

Tätigkeiten als wissenschaftliche Angestellte

- 10/1999-03/2000 Wissenschaftliche Angestellte am Fraunhofer-Institut für Silicatforschung (ISC), Würzburg; Fachbereich: Glas und Keramik
- 07/2000-03/2003 Wissenschaftliche Angestellte am Mineralogischen Institut der Universität Würzburg; Fachbereich: metamorphe und magmatische Petrologie

Tätigkeiten als Lehrbeauftragte

- 09/2001-07/2003 Lehrbeauftragte am Institut für Geologie und Mineralogie der Friedrich-Alexander-Universität, Erlangen; Lehrveranstaltungen: „Mikroskopie II: gesteinsbildende Minerale“ (WS 2001/2001, SS 2002, WS 2002/2003, SS 2003) und „Mikroskopisches Praktikum IV: Auflichtmikroskopie“ (SS 2002)

Auslandsaufenthalte

- 03/1998-05/1998, 03/1999-05/1999 & 08/2001 Forschungsaufenthalte in Namibia